INFORMATION TO USERS

This manuscript has been reproduced from the microfilm master. UMI films the text directly from the original or copy submitted. Thus, some thesis and dissertation copies are in typewriter face, while others may be from any type of computer printer.

The quality of this reproduction is dependent upon the quality of the copy submitted. Broken or indistinct print, colored or poor quality illustrations and photographs, print bleedthrough, substandard margins, and improper alignment can adversely affect reproduction.

In the unlikely event that the author did not send UMI a complete manuscript and there are missing pages, these will be noted. Also, if unauthorized copyright material had to be removed, a note will indicate the deletion.

Oversize materials (e.g., maps, drawings, charts) are reproduced by sectioning the original, beginning at the upper left-hand corner and continuing from left to right in equal sections with small overlaps.

Photographs included in the original manuscript have been reproduced xerographically in this copy. Higher quality 6" x 9" black and white photographic prints are available for any photographs or illustrations appearing in this copy for an additional charge. Contact UMI directly to order.

Bell & Howell Information and Learning
300 North Zeeb Road, Ann Arbor, MI 48106-1346 USA
800-521-0600

UMI®

Downloaded from SHAREOK. Persistent Handle URL: https://hdl.handle.net/11244/5955

NOTE TO USERS

This reproduction is the best copy available.

UMI

UNIVERSITY OF OKLAHOMA

GRADUATE COLLEGE

RESERVOIR CHARACTERIZATION AND GEOSTATISTICAL MODELING OF THE WEST JORDAN UNIT SAN ANDRES FORMATION, CENTRAL BASIN PLATFORM, ECTOR AND CRANE COUNTIES, WEST TEXAS

A DISSERTATION

SUBMITTED TO THE GRADUATE FACULTY

in partial fulfillment of the requirements for the

degree of

DOCTOR OF PHILOSOPHY

By

VICTORIA POLZIN-FRENCH

Norman, Oklahoma

2000

UMI Number: 9964629

UMI®

UMI Microform 9964629
Copyright 2000 by Bell & Howell Information and Learning Company.
All rights reserved. This microform edition is protected against
unauthorized copying under Title 17, United States Code.

Bell & Howell Information and Learning Company
300 North Zeeb Road
P.O. Box 1346
Ann Arbor, MI 48106-1346

RESERVOIR CHARACTERIZATION AND GEOSTATISTICAL MODELING OF THE WEST JORDAN UNIT SAN ANDRES FORMATION, CENTRAL BASIN PLATFORM, ECTOR AND CRANE COUNTIES, WEST TEXAS

A Dissertation APPROVED FOR THE
DEPARTMENT OF GEOLOGY AND GEOPHYSICS

BY

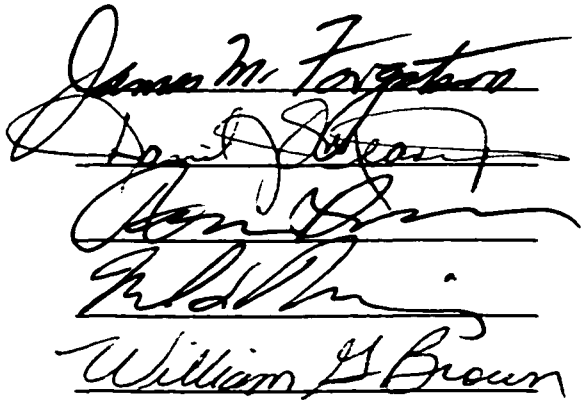

© Copyright by VICTORIA POLZIN-FRENCH 2000
All Rights Reserved

ACKNOWLEDGMENTS

Texaco Exploration and Production, Inc (TEPI) have graciously provided funding for this study not only through generous financial support but also by providing all necessary data needed to complete the study. In addition many individuals have provided professional and technical guidance which has made the completion of this study possible. I would like to thank the following professors at the University of Oklahoma for their continuous support while serving as committee members for this study; Dr. James M. Forgotson, Dr. Daniel J. O'Meara, Dr. Thomas A. Dewars, and Dr. Mark Morrissey. In addition, I would like to thank Dr. W. G. Brown (Baylor University), for serving as the outside member of the dissertation committee and for all the help and inspiration he has given me throughout my years spent at Baylor. I would like to give particular thanks to Anna Shaughnessy, Texaco Group Inc., for her interest in the Institute for Reservoir Characterization at the University of Oklahoma. Anna initiated this study by directing me to Texaco Exploration and Production, Inc (TEPI) scientists who worked together with committee members and myself to develop a suitable project.

A number of people at TEPI's Midland, Texas office have provided guidance and knowledge of the Permian basin area. I would like to thank Kim Moore, Monty Fields and Julie Gibbs for proposing the project. Kim has been my mentor through the project and given me much insight to the Permian basin area and provided considerable support in all aspects of the project where needed. Monty has helped me to understand the engineering aspects of the West Jordan unit and fluid movement through the reservoir. I would also like to thank Robert McKnaughton for long discussions on waterflood

management, particularly with respect to fluid movement and water chemistry within a waterflood environment and the considerable changes that can occur within a water-flooded reservoir. I would also like to thank Curtis Horn for showing me seismic data surrounding the West Jordan unit which enabled me to have a better understanding of broad seismic stratigraphic relationships of the San Andres Formation from the Midland basin onto the Central Basin platform. Appreciation is also extended to Dan George who aided me with a more regional structural analysis of the area surrounding the West Jordan unit.

Very special thanks are extended to Dr. Susan Longacre, Texaco Upstream Technology (TU) Department, Houston, Texas, for many hours spent guiding me through the world of carbonates and how they relate to the Permian Basin. Her expertise and input of core studies were instrumental to the understanding of the complexities of dolomitized rocks, their depositional environments, facies, and cyclic nature. Susan laid the foundation on which all my subsequent learning in the world of carbonates has been built. Mike Grammer, also at TU, was extremely helpful with describing facies partitioning within cycle boundaries and provided many useful suggestions for pulling all the chronostratigraphic work together. His suggested improvements on several figures seen within the text were sincerely appreciated. In addition, Mike provided use to his high powered microscope for analysis of samples under ultra violet florescence.

Gratitude is extended to Greg Hinterlong "the man who never sleeps" with the CO_2 Asset Team (TEPI, Midland, Texas). Greg provided insight into a number of topics affecting carbonate reservoirs including: petrophysical properties associated with San Andres dolomites; fluid flow within the reservoir; chronostratigraphic relationships

within carbonate ramp settings; and extensive discussions on depositional environments and the diagenetic events that that have influenced production within these rocks. Greg has also provided considerable help in maneuvering through the geostatistical program and explaining key concepts when needed. Greg has always made himself available to answer any questions or address concerns with the project and his efforts are sincerely appreciated. I would also like to thank all the regular members of the Texaco "Carbonate Café" lunch group not already mentioned including: Emily Stoudt, David Sivils, Mike Raines, Cory Hoffman, Denise Pfeffer, Dennis Dull and Dennis Prezbindowski. This group has provided informative presentations and discussions on carbonate reservoirs that have enhanced my knowledge considerably.

Bill Keyser and Dave Liebman of TEPI, Midland Texas, provided assistance with reformatting grid files so that they could be imported into StrataModel and Earth Vision three dimensional visualization programs. Without their help building a complete visualization model would have been a tedious and much longer process.

I would like to thank Steve Ruppel, Mark Holtz and Rick Major from the Bureau of Economic Geology, University of Texas. Information related to San Andres production within neighboring units was provided by these three gentlemen. Steve and Rick showed me core from the area and discussed their interpretations during a visit to the BEG. Mark provided me with data and information from work that he completed on the Jordan University Unit. I would also like to thank James Donnelly for many hours spent on the phone with me coordinating the shipment of BEG cores from Austin to the University of Oklahoma and Midland, Texas. Appreciation is also extended to OXY USA, Inc., for giving me permission to use one of their seismic lines within the body of

this paper. In addition to the people mentioned above, a vast number of individuals have given me moral support and assistance throughout the completion of this study. I would like to thank everyone within the TEPI former Central Basin Platform Asset Team and individuals within the Midland Asset Team and associated operating units who have supplied me with data or support. I would particularly like to thank the members of my team who have been supportive and understanding while I have taken time to finish this project including: Ryan Ott, Shilpa Abbitt, Bob Johnson, Curtis Horn, Kim Moore, Jim Ferrell, and Steve Chandler.

I would like to thank Patrick J. O'Connell for his emotional support and "you need to wrap it up girl" comments to help me stay focused; Brenda Braun for getting me out on the town on occasion, and Dinero for all the stress relieving rides. Finally, I thank my family for their continued support and encouragement without which this study would never have been possible. My mother Patsy A. Polzin has always encouraged me to be independent and motivated me to pursue my goals, my father Earl A. Polzin has provided me with a great respect for all individuals and high admiration for moral character while encouraging me to follow my heart and dreams, and my brother Douglas L. Polzin who has always been around for me when I need emotional support in my life or a ski buddy to get away for a while and play in the snow. Thank you all.

TABLE OF CONTENTS

ACKNOWLEDGMENTS iv

CONTENTS viii

LIST OF TABLES xii

LIST OF FIGURES xiii

ABSTRACT xviii

INTRODUCTION 1

Purpose 2

Location 3

Available Data 6

Methods 9

PREVIOUS WORKS 13

Tectonic and Sedimentary History of the Permian Basin Area 13

Early Rifting and Sedimentary Fill 16

Compressional Tectonics and Sedimentation Associated with the Marathon Ouachita Orogeny 19

Post Pennsylvanian Tectonism and Sedimentary Fill 27

San Andres Formation Descriptive Geology 28

Reservoir Characterization 31

Sequence Framework and Cyclicity within the San Andres Formation 33

Paleogeography and Geologic Setting 34

Hydrocarbon Maturation, Migration and Entrapment from the Midland Basin to the Central Basin Platform 36

WEST JORDAN UNIT HISTORY AND DESCRIPTIVE GEOLOGY 44

Jordan Field Discovery and West Jordan Unit Development 44

Descriptive Geology of Cycle Boundaries and Reservoir Zone Nomenclature within the West Jordan Unit 52

RESERVOIR LITHOFACIES OCCURANCE WITHIN FACIES TRACT DEPOSITIONAL ENVIRONMENTS 66

Introduction 66
Proximal Outer Ramp Facies Tract 73
Peloid Dolowackestone-Packstone Facies 75
Fusulinid Dolowackestone-Packstone Facies 78
Crinoidal Facies (Wispy Laminated Dolowackestone) 85
"Vertically Structured" Facies 88
Bioherm/Reef Facies 96
Ramp Crest 101
Peloid/Skeletal dolopackstone/dolograinstone Facies 107
Mixed Siliciclastic Facies 107
Middle Ramp Facies Tract 110
Skeletal/Peloidal Dolowackestone-Packstone Facies 113
Dolomudstone Facies 118
Inner Ramp Facies Tract -Tidal Flat and Nearshore Environments 121
Pisolite Dolopackstone-Grainstones and Associated Facies 124
Brecciated and Intraclast Facies 127

THE WEST JORDAN UNIT DEPOSITIONAL MODEL 133
Introduction 133
Morphologic Setting of San Andres Strata along the Eastern Margin of the Central Basin Platform 133
The Effect of Accommodation Space on Shoal Body Geometry 139
West Jordan unit Depositional Model 140
Proximal Outer Ramp through Ramp Crest Facies Tracts: (Zones IV-E2 - IV-C) 142
Middle Ramp Facies Tract (Zones IV-B and IV-A) 163
Inner Ramp Facies Tract (Zones III, II and I) 166

CLASSIFICATION OF PORE TYPES 172
Introduction 172
Intercrystalline 181
Interparticle 189
Moldic 192

Intraparticle 198
Fenestral 198
Fracture 206
Vuggy 214

DIAGENTIC AND SEDIMENTARY FEATURES 218
Dolomitization and Dissolution Features 219
Cement Types 239
Anhydrite 239
Gypsum 243
Calcite 243
Sedimentary Features 248
Stylolites 248
Pressure Solution Features and Clay Seams 256

THE PERMEABILITY TRANSFORM MODEL 262
The Lucia Petrophysical Class 263
The Lucia Permeability Transform 269
Application of the Lucia Permeability Transform within the West Jordan Unit 271

THE GEOSTATISTICAL DISTRIBUTION OF POROSITY AND PERMEABILITY WITHIN THE WEST JORDAN UNIT 282
Variogram Modeling 283
Probability and Cumulative Density Functions 297
Porosity and Permeability Grids 302

RESERVOIR VOLUMETRICS AND PREDICTION OF FUTURE RESERVOIR POTENTIAL 313
Calculation of Original Oil in Place 313
Pattern Analysis of Geostatistical Modeling and Cumulative Oil Production 316
Distribution of Remaining Oil within Cycle Boundaries 319

THREE DIMENTIONAL VISUALIZATION OF THE WEST JORDAN UNIT AND RECOMMENED ACTIONS FOR RESERVOIR RECOVERY IMPROVEMENT 331

Three-Dimensional Visualization Models 331
Recommendations for Waterflood Improvement 341

CONCLUSIONS 345

REFERENCES 349

APPENDIX A - AVAILABLE WELL LOG DATA, WELL LOG NORMALIZATION, AND LOG SUMMATION MAPPING TECHNIQUES 365
Available Well Log Data 365
Well Log Normalization 368
Neutron Curve Normalization 368
Casing Effects for GNT tools 369
Drift Problems within GNT Logs 370
Measuring the Effect of Gypsum 371
Log Summation Mapping Techniques 372

APPENDIX B - CORE DESCRIPTIONS AND XRD DATA ANALYSIS 374
Core Descriptions and XRD Analysis 374
Core Data 374
Core Description Chart 375
X-Ray Diffraction (XRD) Analysis 385

APPENDIX C - ZONE CHARACTERISTICS 389
Zone IV-E2 and IV-E1 389
Zone IV-C 391
Zone IV-B 393
Zone IV-A 394
Zone III 396
Zone II 397
Zone I 398

List of Tables

Figure **Page**

Table 1. Table of facies tracts, lithofacies and environments of deposition for West Jordan San Andres strata..... 71

Table 2. Table of original oil in place calculations from an earlier study and the present study from the 0.1 millidarcy geostatistical model and gross ultimate recovery estimates from the 0.5 millidarcy geostatistical model..... 314

Table 3. Table of primary and secondary oil recovery data and summary of gross ultimate recovery estimates from three methods used to calculate recovery factors..... 327

Table 4. Table of remaining oil in place calculations for the West Jordan unit 330

Table 5. Whole rock mineralogy from x-ray diffraction analysis..... 387

Table 6. Clay fraction mineralogy from x-ray diffraction analysis. 388

List of Figures

Figure **Page**

Figure 1. Location map illustrating the Permian basin structural components and physiographic provinces of Texas. 5

Figure 2. Stratigraphic nomenclature of the Permian basin region 8

Figure 3. Tectonic map of the Permian basin and surrounding tectonic features. 15

Figure 4. Isopach maps recording the early, middle and final stages of the formation of the Tobosa basin 18

Figure 5. Major structural divisions of the Central Basin platform 23

Figure 6. Diagrammatic cross section across the Central Basin platform. 25

Figure 7. Regional structural map on top of the San Andres Formation showing unitized boundaries of the West Jordan and surrounding units. 46

Figure 8. Average daily production chart for the West Jordan unit waterflood program since the initiation of water injection in 1969 49

Figure 9. Structural contour map of the West Jordan unit showing unit boundaries and the location of well and core data. 51

Figure 10. West Jordan unit type log showing zone nomenclature and chronostratigraphic relationships within the reservoir. 54

Figure 11. Structural cross section along depositional strike from north to south across the West Jordan unit 55

Figure 12. Structure contour maps of reservoir zones within the West Jordan unit. 59

Figure 13. Isopach maps of reservoir zones within the West Jordan unit. 62

Figure 14. Generalized depositional model of facies tract systems and related depositional environments within the West Jordan unit. 68

Figure 15. Core photographs and photomicrographs of subtidal peloid lithofacies 77

Figure 16. Cross section of facies indicator logs showing the occurrence of peloidal and shoal facies. 80

Figure 17. Core photograph of fusulinid and peloid lithofacies. 82

Figure 18. Core photographs and photomicrographs of subtidal fusulinid lithofacies. 84

Figure 19. Cross section of facies indicator logs showing occurrence of fusulinid lithofacies within the reservoir 87

Figure 20. Core photographs and photomicrographs of crinoid lithofacies. 90

Figure 21. Core photographs and photomicrographs of vertically structured lithofacies 92

Figure 22. Cross section of facies indicator logs showing the occurrence of vertically structured facies. 95
Figure 23. Core photograph of organic sponge-algal-bryozoan bioherm lithofacies. 98
Figure 24. Core photomicrographs of organic sponge-algal-bryozoan bioherm lithofacies 100
Figure 25. Core photograph of middle ramp, ramp crest and flanking ramp crest facies successions 104
Figure 26. Core photograph of ramp crest and flanking lithofacies. 106
Figure 27. Core photomicrographs of ramp crest and flanking ramp crest lithofacies... 110
Figure 28. Core photomicrographs of flanking ramp crest mixed siliciclastic lithofacies. 112
Figure 29. Core photograph of middle ramp nearshore lithofacies illustrating shallow subtidal to supratidal facies. 115
Figure 30. Core photomicrographs of middle ramp skeletal/peloidal wackestone to mud-rich packstone lithofacies. 117
Figure 31. Core photomicrographs of various middle ramp dolomudstone lithofacies.. 120
Figure 32. Core photographs of the fenestral pisolite dolopackstone-grainstone lithofacies. 123
Figure 33. Core photomicrographs of the fenestral pisolite dolopackstone-grainstone lithofacies. 126
Figure 34. Core photographs of brecciated intervals within the tidal flat environment. 129
Figure 35. Core photomicrographs of intraclast and exposure surfaces 132
Figure 36. General morphologic profiles for carbonate platforms and facies tracts described from the Algerita Escarpment 136
Figure 37. Seismic lines to the east and west of the West Jordan Unit. 138
Figure 38. Map view of facies tracts and three-dimensional block diagram of environments during deposition of zones IV-E2 and IV-E1. A). 144
Figure 39. Diagrammatic depositional model and satellite image of the modern analog for shoals within the West Jordan unit. 147
Figure 40. Paleogeographic reconstruction of the Permian basin and West Jordan unit area. 150
Figure 41. Average porosity (PHIA) maps of zones IV-E1 and IV-E2. 152
Figure 42. Outcrop photograph of shoal facies from Lawyer Canyon along the Algerita Escarpment in the Guadalupe Mountains. 154
Figure 43. Map of cumulative oil production from the West Jordan unit. 156

Figure 44. Outcrop photograph from Lawyer Canyon of mudstone barriers within shoal bodies along the Algerita Escarpment. 158
Figure 45. Map view of facies tracts and three-dimensional block diagram of environments during deposition of zones IV-E1 and IV-C. 161
Figure 46. Map view of facies tracts and three-dimensional block diagram of environments during deposition of zones IV-B and IV-A. 165
Figure 47. Stratigraphic cross section in the dip direction of cored wells. 168
Figure 48. Map view of facies tracts and three-dimensional block diagram of environments during deposition of zones III, II, and I 170
Figure 49. North-to-south stratigraphic cross section of cored wells showing pore types within the West Jordan unit.. 175
Figure 50. Porosity versus permeability cross plots of available core data for each zone within the West Jordan unit reservoir 177
Figure 51. Porosity versus permeability cross plots versus depth. 180
Figure 52. Core photomicrographs of intercrystalline porosity. 183
Figure 53. Core photomicrographs of intercrystalline porosity. 185
Figure 54. Cross plots of core porosity and permeability illustrating the relationship between intercrystalline porosity and dolomite crystal size. 188
Figure 55. Core photomicrographs of interparticle porosity. Interparticle porosity is the pore space occurring between particles.. 191
Figure 56. Photomicrographs of moldic porosity. 194
Figure 57. Cross plots of core porosity and permeability for moldic and dual moldic and intercrystalline pore types. 196
Figure 58. Core photomicrographs of intraparticle porosity 200
Figure 59. Core photomicrographs of fenestral pore types 202
Figure 60. Cross plot data of core porosity and permeability for fenestral pore types. .. 205
Figure 61. Core photographs and photomicrographs of tectonic and/or regional fractures seen within the West Jordan unit.. 208
Figure 62. Core photographs and photomicrographs of diagenetic fractures. 211
Figure 63. Cross plots of fracture and stylolite data versus depth.. 213
Figure 64. Core photomicrographs of vuggy pore types.. 216
Figure 65. Paragenetic sequence of diagenetic events interpreted for the West Jordan unit 222
Figure 66. Diagrammatic illustration showing the dolomitization reflux model 224
Figure 67 Core photomicrographs illustrating dolomite dissolution 227

Figure 68 Core photomicrographs illustrating alteration of grain-dominated fabrics due to recrystallization during dolomitization. 229

Figure 69. Cross plot of depth versus dolomite crystal size for the Seminole San Andres reservoir. 232

Figure 70. PHIH contour maps from zones IV-E1 and IV-E2 235

Figure 71. Porosity-permeability cross plot illustrating that solution enhanced porosity is not facies dependent. 238

Figure 72. Core photographs and photomicrographs illustrating examples of anhydrite cement from the West Jordan unit. 241

Figure 73. Core photographs and photomicrographs illustrating examples of gypsum cement from the West Jordan unit 245

Figure 74. Core photomicrographs of calcite cement observed within the reservoir.. ... 247

Figure 75. Core photomicrographs of stylolites within the reservoir 251

Figure 76. Core photographs of stylolites within the reservoir. 253

Figure 77. A structural cross section through the reservoir showing injection profile data. 255

Figure 78. Core photomicrographs illustrating pressure solution features including dissolution along stylolite seams and grain-to-grain dissolution. 258

Figure 79 Core photographs and photomicrographs of clay seams and clay laminations from the unit. 260

Figure 80. The petrophysical rock fabric classes defined by Lucia (1999). 266

Figure 81. Interparticle porosity-permeability cross plot data for nonvuggy limestones and dolostones and capillary pressure curves for petrophysical classes. 268

Figure 82. Diagrams illustrating the continuum porosity-permeability transform and rock fabric class for dolostones 273

Figure 83. Lucia rock fabric classifications for cycle boundaries within the West Jordan unit 275

Figure 84. Digital well data showing the constructed petrophysical class curve 277

Figure 85. A diagram of cored wells from the unit showing the correlation between core derived permeability and permeability modeled from the Lucia continuum transform model. 280

Figure 86. Variogram analysis of normalized porosity data for all zones. 285

Figure 87. Directional variograms and separation distance modeled for the West Jordan unit porosity and permeability data. 287

Figure 88. Variogram analysis of permeability data for all zones. 291

Figure 89. Horizontal and vertical variograms of porosity for zones II, IV-A, and IV-E1 294

Figure 90. Horizontal and vertical variograms of permeability for zones II, IV-A, and IV-E1 296

Figure 91. Graphs of probability and cumulative density functions for porosity. 299

Figure 92. Graphs of probability and cumulative density functions for permeability.... 301

Figure 93. PHIH contour maps from zone I through zone IV-C based on a 7% porosity cutoff. 306

Figure 94. A three-dimensional geostatistical model of the West Jordan unit illustrating the distribution of porosity within the reservoir. 309

Figure 95. A three-dimensional geostatistical model of the West Jordan unit illustrating the distribution of permeability within the reservoir. 311

Figure 96. Pattern analysis showing geostatistically generated PHIH maps from the 0.1 and 0.5 millidarcy models plotted with cumulative production contour line overlays. 318

Figure 97. PHIH maps by zone generated from the geostatistical 0.5 millidarcy cutoff model. 321

Figure 98. Semi-log plots of monthly oil production versus cumulative production for the West Jordan unit. 324

Figure 99. Decline curve analysis for the West Jordan unit. 326

Figure 100. Diagrams of porosity geobodies generated with a 10 percent porosity cutoff from the geostatistical model. 333

Figure 101. A diagram of porosity geobodies generated with a 12 percent porosity cutoff from the geostatistical model. 335

Figure 102. A diagram of permeability geobodies generated with a 0.5 millidarcy permeability cutoff from the geostatistical model. 338

Figure 103. A diagram of permeability geobodies viewed from the bottom southeast and generated with a 0.5 millidarcy permeability cutoff from the geostatistical model.. 340

Figure 104. The core chart used to describe cores for the West Jordan unit... 377

Figure 105. The key for microfacies observed within the West Jordan area..... 379

Figure 106. Legend of lithologic symbols used for core descriptions... 381

Figure 107. Legend for grain types, sedimentary structures, and diagenetic features described within cores... 384

ABSTRACT

The West Jordan unit produces from highly compartmentalized shoal facies that formed as a result of slight paleotopography on a gently dipping ramp. Productive shoal bodies developed within ramp crest facies tracts in an overall upward shallowing progradational sequence. Cycle boundaries defined within the unit mark chronostratigraphically significant surfaces that controlled deposition along platform areas. Two high frequency sequences (HFS I and HFS II) have been defined within the unit and each HFS culminates with a highstand systems tract (HST). Chronostratigraphic relationships were found to control porosity development and pore type distribution, diagenetic patterns of overprinting, and the geometric extent and degree of compartmentalization documented within productive shoal facies. Because these relationships occur within a chronostratigraphic architecture that has also been defined along outcrops in the Guadalupe Mountains, they can be extrapolated to other San Andres fields. Therefore, this study can be used as a predictive tool for better understanding where productive facies will occur within these reservoirs and the degree of compartmentalization that should be expected.

Productive ramp crest facies form a series of vertically stacked shoal bodies that formed during the end of HFS I and occur only below HST 1. Eustatic sea level changes and accommodation space within the HST resulting in laterally and vertically discontinuous facies controlled geometries of these stacked shoal bodies. Geostatistical models of porosity and permeability attributes incorporated into a three-dimensional model have allowed for a greater understanding of the reservoir heterogeneity. This heterogeneity is not confined to the vertically and laterally discontinuous shoal bodies.

Cycles defined within the reservoir have characteristic pore types that dominate from cycle-to-cycle, each exhibiting different petrophysical properties. In addition, diagenetic overprints have further compartmentalized the reservoir by changing original petrophysical properties through multiple periods of cementation and dissolution. Diagenetic events are also believed to be related to the chronostratigraphic framework established within HFS I and HFS II. This study will improve the ability to predict the distribution of reservoir shoal facies, their associated diagenesis, and the complexity of compartmentalization that can be expected within these reservoirs. This is an extremely valuable tool for application to all carbonate reservoirs deposited under similar environments along ramp platforms.

INTRODUCTION

The West Jordan unit reservoir produces from approximately 550 feet (168 meters) of dolomitized San Andres strata and exhibits considerable heterogeneity due to lateral and vertical facies variations and extensive diagenetic overprinting. The Texaco-operated unit is located along the eastern margin of the Central Basin platform, an area of prolific San Andres and Grayburg production. The West Jordan unit has produced over 17 million stock tank barrels (MMBST) since initial production in 1926 which represents a little over 30 percent of the 57 MMBST of original oil in place (OOIP) calculated for the reservoir under primary and secondary recovery. The Jordan University and East Penwell units, located directly east and northeast of the West Jordan unit, have significantly higher recovery efficiencies of 31 and 42 percent respectively (Holtz and Major, 1994; and Fields and Nelson, 1996).

Less efficient recovery within the West Jordan unit is believed to be the result of several factors including: 1) previously undefined reservoir compartmentalization in the form of shoal and intershoal areas within lower zones of the reservoir. Shoal bodies are areas of well-developed porosity and permeability while intershoal areas lack any appreciable permeability and create barriers to flow. The stacked nature of these shoal bodies results in vertical as well as lateral compartmentalization. Having not been previously defined these lower zones were water flooded as one continuous interval. 2) Channeling of injection water within waterflood "thief zones" through fracture networks and stylolite seams resulting in bypassed matrix pay; 3) bypassed hydrocarbons within middle zones of the reservoir due to a vertical change in pore types which are not

adequately drained by vertical wells and conventional waterflood techniques; 4) a less favorable land position within highly productive shoal facies than the Jordan University and East Penwell units; and 5) a lack of continuity within flow units between injection and producing wells. Core and injection profile data indicate fracturing and diagenetic features, which are believed to contribute to directional flow of injection water resulting in early breakthrough and unswept hydrocarbon zones. This reservoir characterization study was initiated to utilize all available data, in particular nine cores spaced throughout the reservoir were thoroughly examined to better understand the West Jordan unit reservoir architecture.

Purpose

With an increased understanding of how vertical and lateral facies relationships, depositional and diagenetic controls, and fracturing influence porosity and permeability distribution within the reservoir, waterflood efficiency can be maximized and increased hydrocarbon production may be possible through better reservoir management. Therefore, the objectives of this study were to: 1) determine the control of depositional facies distribution and cyclicity versus diagenetic controls on porosity and permeability within the reservoir; 2) define flow units and barriers within the reservoir; 3) construct a three-dimensional model of the reservoir; 4) apply geostatistical modeling of porosity and permeability attributes for more accurate distributions within the three-dimensional model; 5) Calculate up-to-date estimates of reserves based on a more concise geostatistically based reservoir model; and 6) determine a strategy to enhance

hydrocarbon production and to increase recovery efficiencies through waterflood management and specification of workover potential within the West Jordan unit.

Location

The West Jordan unit is located along the eastern margin of the Central Basin platform, straddling the boarder of Ector and Crane Counties, with the majority of the unit lying in Ector County (fig. 1). The unit is part of one field along a major productive trend within Permian carbonate shelf deposits that lie along the eastern margin of the Central Basin platform. The Central Basin platform, an area of stability during most of Permian time, lies between the deep Delaware basin to the west and the more shallow Midland basin to the east. Platform areas bordering the Permian basin include the Northwest, Northern and Eastern shelves (fig. 1).

Physiographically, the West Jordan unit lies along the southwestern-most boundary of the Llano Estacado (High Plains) approximately fifty miles southwest of Midland, Texas (fig. 1). The Llano Estacado is a surface of Tertiary sand, caliche, and gravel rising gently northwestward that is bounded on the west by the valley of the Pecos River (R. E. King, 1942). The southern boundary of the Llano Estacado is formed by carbonate mesas which characterize the Edwards Plateau. To the east are the North Central Plains (Osage Plains), an area of eroded, low-lying topography. The closest outcrop exposures of the San Andres Formation are located on the Northwest Shelf in the Guadalupe Mountains of eastern New Mexico and the west Texas panhandle (fig 1).

Figure 1. Location map illustrating the Permian basin structural components and physiographic provinces of Texas. The West Jordan unit is located along the eastern margin of the Central Basin platform and straddles southern Ector and northern Crane Counties (paleogeographic location map modified from Bebout and Harris, 1990; physiographic map modified from Bureau of Economic Geology, Physiographic Map of Texas).

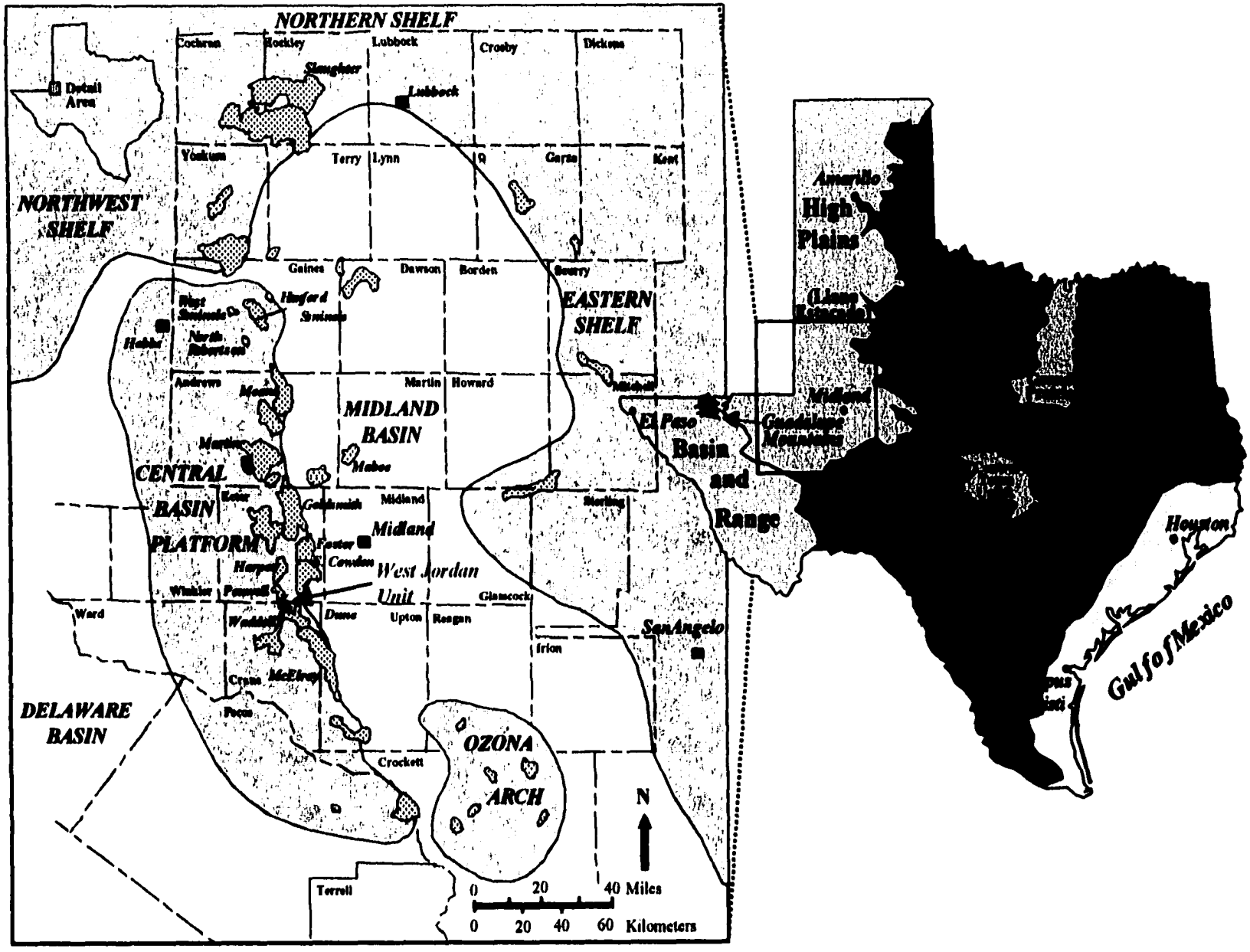
NORTHERN SHELF
Detail Area
NORTHWEST SHELF
EASTERN SHELF
MIDLAND BASIN
CENTRAL BASIN PLATFORM
DELAWARE BASIN
OZONA ARCH
Midland
West Jordan Unit
Cochran
Hockley
Lubbock
Crosby
Dickens
Slaughter
Yoakum
Terry
Lynn
Garza
Kent
Gaines
Dawson
Borden
Scurry
Andrews
Martin
Howard
Ward
Upton
Reagan
Crockett
Terrell
Amarillo High Plains
El Paso Basin and Range
Houston
San Angelo
Gulf of Mexico
N
0 20 40 Miles
0 20 40 60 Kilometers

The West Jordan unit produces from the San Andres Formation, part of the lower Gaudalupian Series of middle Permian time (fig. 2). The San Andres is comprised of a shallowing-upward, progradational carbonate sequence of subtidal, intertidal, and supratidal facies that have been interpreted as being deposited on a shallow-shelf platform within retrogradational, aggradational and progradational sequence tracts. Within the West Jordan unit, the San Andres reservoir is overlain by the Grayburg Formation and underlain by the Glorieta Formation.

Available Data

The foundation of this study is based on information gained through detailed core description from nine cores distributed throughout the West Jordan unit. A total of over 2800 feet of core was examined. Core analysis reports were available for each core as well as from three other cores that had not been located at the initiation of this study. Over three hundred thin sections were made from cores for petrophysical analysis. Capillary pressure data was available for only one cored well within the unit, the West Jordan unit (WJU) #505 well.

All available well log data was utilized in the study. In addition, tracer and injection profile data was available for twenty-nine injection wells throughout the unit. For a detailed list of electric log data available for each well location see Appendix A. Log data was digitized and normalized prior to being imported into the model. Production data was available for produced oil, water, and gas, and injected water since unitization of the waterflood in 1969. Production data prior to unitization was not available. In addition

Figure 2. Stratigraphic nomenclature of the Permian basin region. The San Andres Formation is within the Lower Guadalupian Series of the Permian System. The size of yellow circles to the right of productive formations indicate relative production. Note that the combined San Andres and Grayburg Formations are by far the most prolific producing reservoirs within the Permian basin region (modified from Frenzel and others, 1988; and Major, et al, 1990).

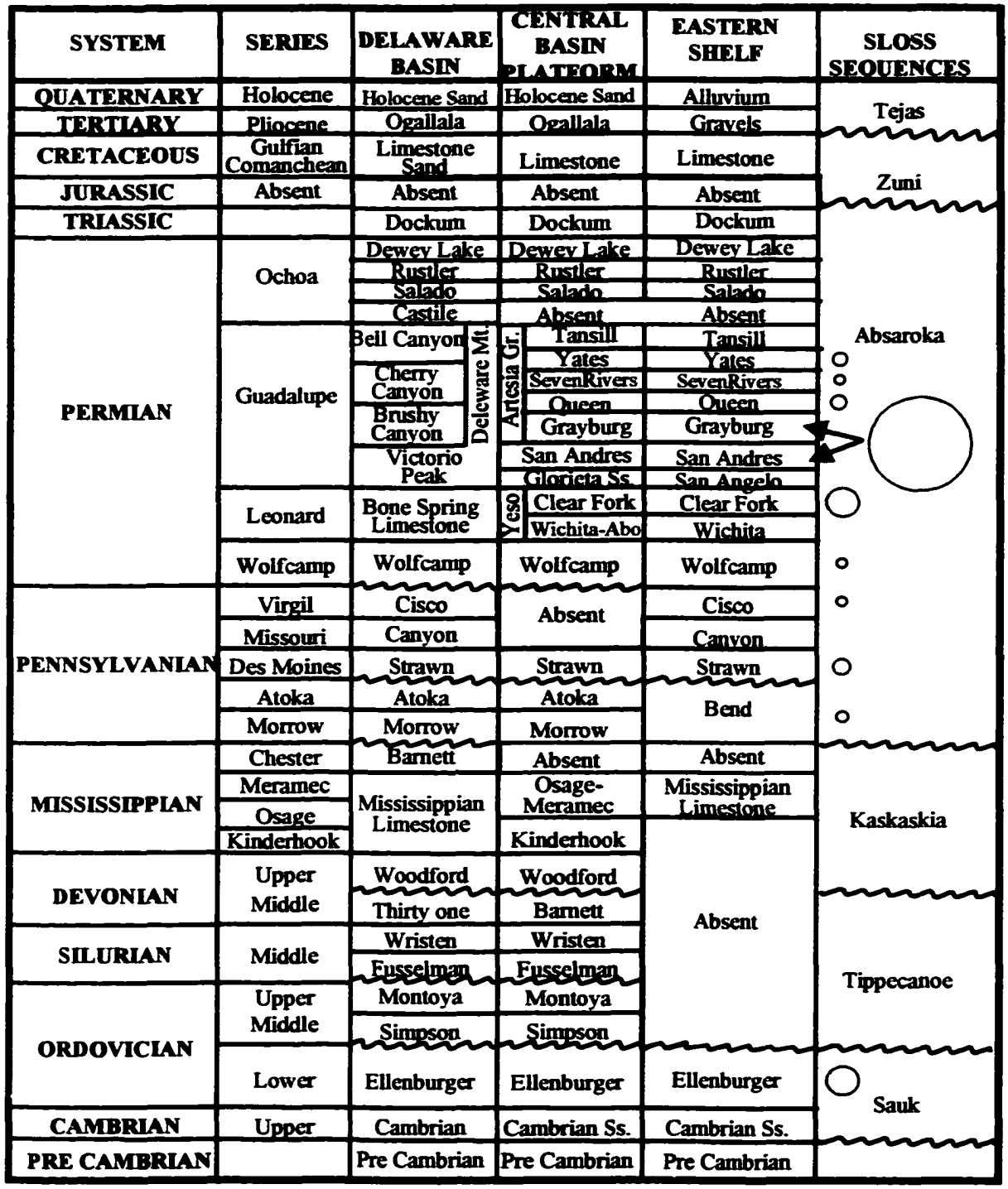
SYSTEM
SERIES
DELAWARE BASIN
CENTRAL BASIN PLATFORM
EASTERN SHELF
SLOSS SEQUENCES
QUATERNARY
Holocene
Holocene Sand
Holocene Sand
Alluvium
Tejas
TERTIARY
Pliocene
Ogallala
Ogallala
Gravels
CRETACEOUS
Gulfian Comanchean
Limestone Sand
Limestone
Limestone
Zuni
JURASSIC
Absent
Absent
Absent
Absent
TRIASSIC
Dockum
Dockum
Dockum
PERMIAN
Ochoa
Dewey Lake
Rustler
Salado
Castile
Dewey Lake
Rustler
Salado
Absent
Dewey Lake
Rustler
Salado
Absent
Guadalupe
Bell Canyon
Cherry Canyon
Brushy Canyon
Delaware Mt.
Victorio Peak
Artesia Gr.
Tansill
Yates
SevenRivers
Queen
Grayburg
San Andres
Glorieta Ss.
Tansill
Yates
SevenRivers
Queen
Grayburg
San Andres
San Angelo
Absaroka
Leonard
Bone Spring Limestone
Yeso
Clear Fork
Wichita-Abo
Clear Fork
Wichita
Wolfcamp
Wolfcamp
Wolfcamp
Wolfcamp
PENNSYLVANIAN
Virgil
Missouri
Des Moines
Atoka
Morrow
Cisco
Canyon
Strawn
Atoka
Morrow
Absent
Strawn
Atoka
Morrow
Cisco
Canyon
Strawn
Bend
MISSISSIPPIAN
Chester
Meramec
Osage
Kinderhook
Barnett
Mississippian Limestone
Absent
Osage-Meramec
Kinderhook
Absent
Mississippian Limestone
Absent
Kaskaskia
DEVONIAN
Upper
Middle
Woodford
Thirty one
Woodford
Barnett
SILURIAN
Middle
Wristen
Fusselman
Wristen
Fusselman
ORDOVICIAN
Upper
Middle
Montoya
Simpson
Montoya
Simpson
Absent
Tippecanoe
Lower
Ellenburger
Ellenburger
Ellenburger
Sauk
CAMBRIAN
Upper
Cambrian
Cambrian Ss.
Cambrian Ss.
PRE CAMBRIAN
Pre Cambrian
Pre Cambrian
Pre Cambrian

to data available for the West Jordan unit, log data and core descriptions from adjoining units (Jordan University, Penwell, and East Penwell) were also utilized within the study.

Methods

Methods involved in this study incorporate the use of all available data. Furthermore, a comprehensive review of previous works specific to the study was completed in order to gain a thorough understanding of both regional and local factors influencing the West Jordan unit reservoir. These include publications on regional structural geology and tectonics of the Permian Basin and Central Basin platform, oil generation and migration, outcrop analogs, sequence stratigraphy and cyclicity, reservoir scale heterogeneities, reservoir characterization, diagenesis, and geostatistical modeling.

Core and thin sections were used to describe the following rock properties occurring within the reservoir; textural classification, lithofacies, lithology, sedimentary and diagenetic textures, alteration, grain types, depositional environments, shallowing upward cycles, contacts, flow units, pore types, petrophysical classification and depth and occurrence of major pore filling cements. An example of a core description chart and further detail on the core description process is provided in Appendix B. Each core was depth shifted to log data and calibrated against core analysis reports to determine porosity and permeability trends that might exist within the reservoir. Because seven of the nine cores had undergone high temperature (vacuum retort) processing, porosity values from core analysis reports for these cores were considered suspect due to the presence of gypsum within the reservoir. High temperature core analysis results in the dehydration of

gypsum and higher porosity values than are actually present within the reservoir can be recorded.

Thin sections were stained for calcite with a solution of Alizarin Red-S and 0.2 percent hydrogen chloride. Thin sections were examined under a standard petrographic microscope using transmitted, cross-polarized (crossed nicols), and reflected light to determine mineralogical makeup of the samples. In addition, selected samples were examined under ultra-violet light on a high powered microscope in order to better visualize rock fabrics that had been obliterated by recrystallization during the dolomitization process. Thin sections were documented by depth to the presence of cement types (gypsum, anhydrite, dolomite and calcite), pore types (moldic, intercrystalline, fenestral, interparticle, etc.), dolomite crystal size, and rock fabric classifications.

Digital well data was used for the construction of cross sections, mapping and volumetric calculations within the reservoir. A cross-section grid across the study area (including bordering units Penwell, East Penwell and Jordan University units) was constructed. Within the West Jordan unit, cycle boundaries based on core descriptions were extrapolated to the cross section grid, which was then used to correlate zones throughout the reservoir. Subsurface mapping and grid construction was completed on all correlated zones including structure, gross and net isopachs, porosity feet (PHIH), average porosity (PHIA), cumulative production maps and others. Definitions for log summation mapping techniques are provided in Appendix A.

Permeability transforms were constructed incorporating geologic and petrophysical data from within each cycle boundary to predict the three-dimensional

interwell spatial distribution of permeability. Rock class types for each zone were determined based on dolomite crystal size and vuggy versus non-vuggy pore types. The rock classification was used with Lucia's (1999) global permeability transform to determine permeability values for each zone based on petrophysical properties within those zones.

Outcrop sections from the Algerita Escarpment along the northwestern shelf of the Guadalupe Mountains were studied to confirm similarities and differences to strata described within this study from cores within the West Jordan unit. While the brunt of outcrop work was completed in earlier studies (Sarg and Lehmann, 1986; Sonnenfeld, 1991; Kerans et al., 1991, 1992, 1994; Horvorka, 1993; and Kerans and Fitchen, 1995), four trips to the Guadalupe Mountains were made to look at outcrops and verify previous observations described within the literature. Sequence stratigraphic methods incorporating chronostratigraphic principles were followed while describing cores and mapping boundaries within the unit. Terminology used is as described in Kerans and Fitchen (1995) for San Andres and Grayburg outcrops along the Algerita Escarpment.

Geostatistical modeling of porosity and permeability allowed for more accurate interwell distribution of these attributes throughout the three-dimensional model. These geostatistical models were used to calculate more accurate volumes for determination of reserves within the reservoir. Geostatistical modeling was completed using GridSTAT, a geostatistical reservoir description software program that runs on both personal computer Windows and UNIX based workstations. GridSTAT was originally developed by Texaco in 1990, however, in 1995 the software was commercialized to Applied Computer Engineering and is assessable to the open market.

The construction of a three-dimensional model incorporating reservoir properties allowed for a detailed visualization of reservoir compartmentalization and flow unit distribution within the reservoir. The three-dimensional model was created using Stratigraphic Geocellular Modeling (SGM) software a product of Stratamodel, Incorporated and EarthVision, a product of Dynamic Graphics Incorporated. These software packages are used for geological analysis and visualization within heterogeneous strata and integrate rock and fluid properties into the three-dimensional model.

PREVIOUS WORKS

Tectonic and Sedimentary History of the Permian Basin Area

The Permian basin occupies an area of approximately 115,000 miles^2 (300,000 km^2) in southeastern New Mexico and west Texas (Hanson and others, 1991; Pinsonnault, 1996). Prior to the formation of present day subsurface structures within the Permian basin the area consisted of a broad, shallow, gently dipping structural sag referred to as the Tobosa basin (Galley, 1958; Hills, 1972 and 1985; Horak, 1985; Frenzel and others, 1988; Ewing, 1991; Hanson and others, 1991; and Shumaker, 1992). Shumaker (1992), described the Tobosa basin as being similar to other middle Paleozoic sag basins (Michigan, Interior and Williston) experiencing epeirogenic movements and deposition of stratigraphic sequences. Similar to these sag basins, intense uplift and deformation of pre-existing basement blocks (the Central Basin Uplift) later subdivided the Permian basin into a series of smaller basins (Hills 1970 and 1972; Keller et al, 1980; Dickinson, 1974; Shumaker, 1992).

The primary tectonic elements within the Permian basin today are the deep Delaware basin to the west, the more shallow Midland basin to the east, and between the two the Central Basin platform (figs. 1 and 3). The Permian basin contains sedimentary strata ranging from Cambrian through Triassic in age. The general tectonic history of the Permian basin can be broken down into three distinct stages: 1) early rifting and sedimentary fill, 2) compressional tectonics associated with the Marathon-Ouachita Orogeny; and 3) a second period of quiescence associated with basinal subsidence

Figure 3. Tectonic map of the Permian basin and surrounding tectonic features. Note area outlined in red is former location of the Tobosa basin. Fields producing from the San Andres and Grayburg Formations are indicated by blue. The West Jordan unit is centrally located along the eastern margin of the Central Basin platform (map modified from Bebout and Harris, 1990).

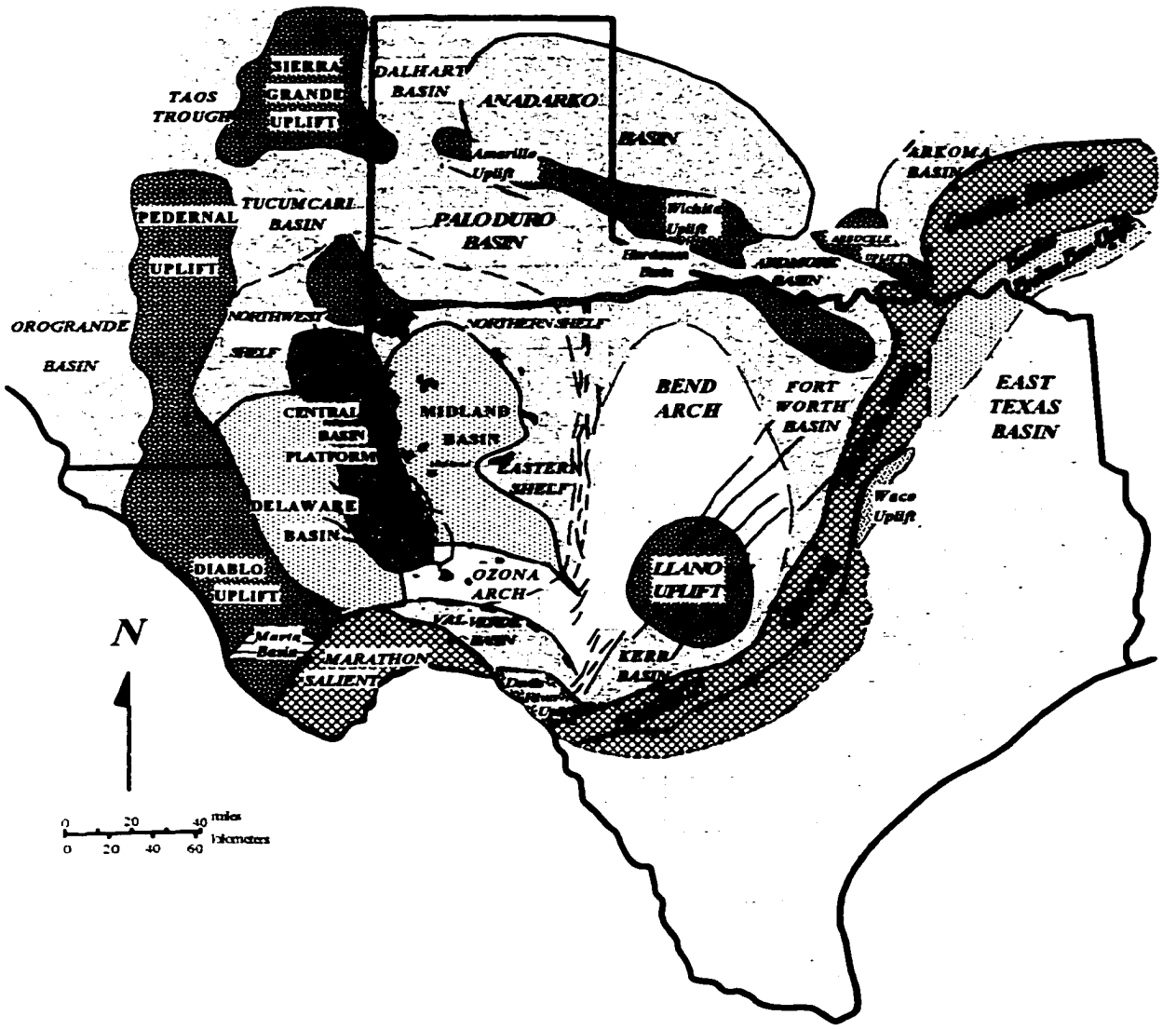
SIERRA GRANDE UPLIFT
DALHART BASIN
ANADARKO BASIN
TAOS TROUGH
Amarillo Uplift
Wichita Uplift
ARKOMA BASIN
PEDERNAL UPLIFT
TUCUMCARI BASIN
PALO DURO BASIN
Electra Basin
ARDMORE BASIN
OROGRANDE BASIN
NORTHWEST SHELF
NORTHERN SHELF
BEND ARCH
FORT WORTH BASIN
EAST TEXAS BASIN
CENTRAL BASIN PLATFORM
MIDLAND BASIN
EASTERN SHELF
Waco Uplift
DELAWARE BASIN
DIABLO UPLIFT
OZONA ARCH
LLANO UPLIFT
VAL VERDE BASIN
Marfa Basin
MARATHON SALIENT
KERR BASIN
N
0 20 40 miles
0 20 40 60 kilometers

resulting in the deposition of thick sequences of Permian age carbonates such as those of the San Andres reservoir at the West Jordan unit.

Early Rifting and Sedimentary Fill

Early rifting within west Texas has been described by several authors (Keller et al, 1980; Wuellner et al., 1986; Arbenz, 1989; Keller et al, 1989; Keller, 1983; and Ewing, 1985 and 1991; Adams and Keller, 1993). Keller (1989 and 1993) sited geophysical evidence and well data from the Central Basin uplift to suggest that the Tobosa basin may have been an area of Keweenawan rifting associated with the Mid-continent rift system. The area has also been suggested as part of the Interior Rift system (Wuellner et al, 1986). Arbenz (1989) and Ewing (1985 and 1991) describe the possibility of failed rift basins within the general area of the Tobosa basin during Cambrian time.

From Late Cambrian to Mississippian time the Tobosa basin was an area of relative quiescence interrupted by only mild tectonism and minor uplift resulting in deposition of carbonate and fine-grained clastic sediments (Hills, 1985; Frenzel and others, 1988). During the Ordovician thick deposits of Ellenburger dolomite record the position of the incipient Tobosa basin (fig. 4a). The absence of any thinning in Simpson strata over the position of the ancestral Central Basin uplift indicate that the area was quiescent during Middle Ordovician and independent tectonic features were not yet actively forming within the Tobosa basin (McGlasson, 1968; Frenzel and others, 1988, Ewing, 1991). However, the Tobosa basin was actively subsiding as evidenced by substantial thickening of sediments within the basin depocenter and progressive thinning toward the

Figure 4. Isopach maps recording the early, middle and final stages of the formation of the Tobosa basin. Figure 4A shows isopach contours of Cambrian and Lower Ordovician age rocks. Note that there is no indication of present day structural features during these time periods. Figure 4B illustrates the development of the Tobosa basin by Middle Ordovician time. There is no indication from this isopach map that the Central Basin uplift was beginning to form by this time. Figure 4C is an isopach map of post-Wolfcampian Permian strata. The Delaware and Midland basins were well formed by the end of Pennsylvanian time (figures 5A and 5B modified from Frenzel and Others, 1988; figure 5C modified from Ewing, 1991).

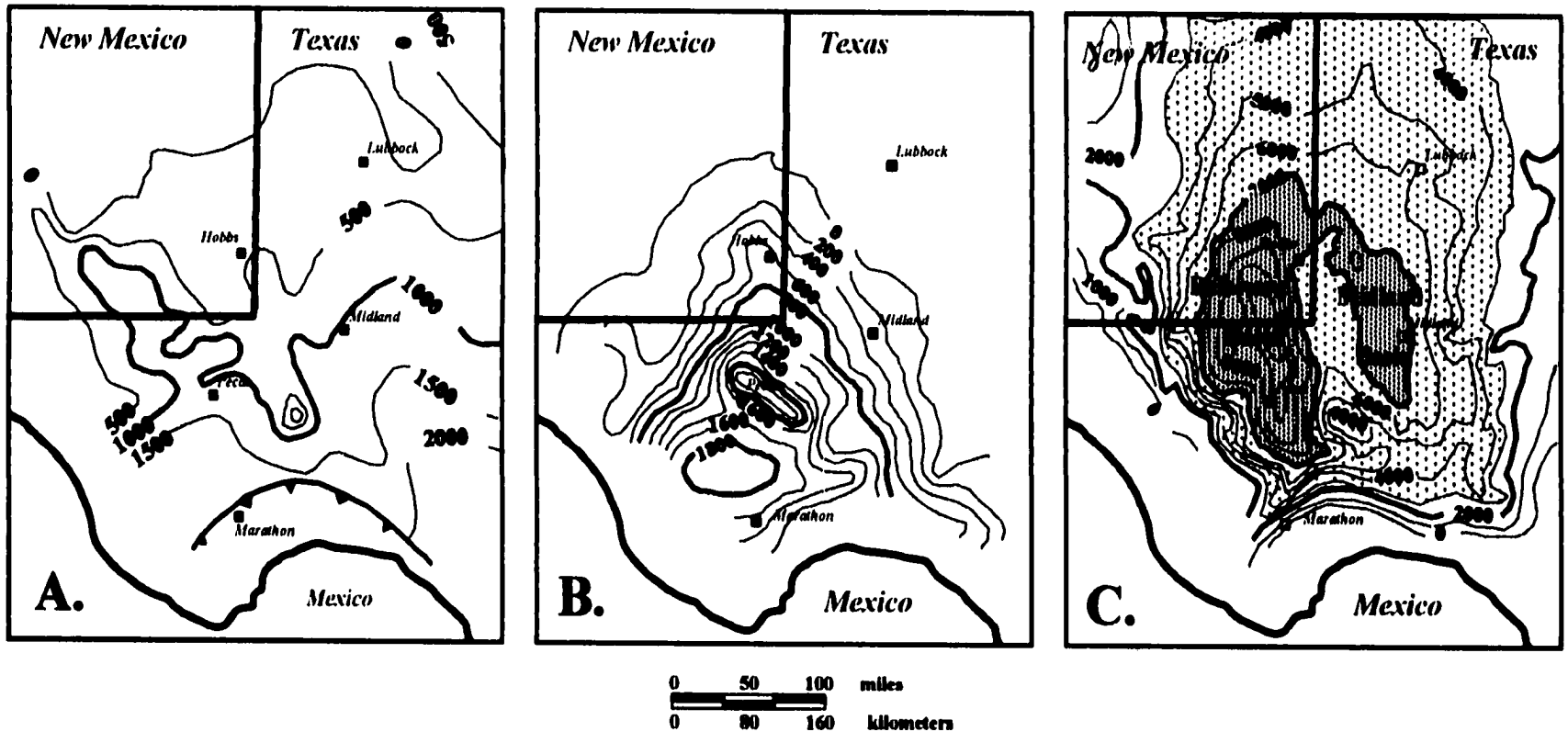
New Mexico
Texas
Lubbock
Hobbs
Midland
Marathon
Mexico
A.
B.
C.
500
1000
1500
2000
0 50 100 miles
0 80 160 kilometers

basin edges (fig 4b; Hanson and others, 1991). During the Silurian carbonate sedimentation continued on the shelf areas surrounding the Tobosa basin and the Wristen shales were deposited within the basin to the south. Stability within the area continued through at least Middle Devonian as evidenced by limestones of the Thirty-one Formation.

Late Devonian marked a time of distinct change in sedimentary environments within the Tobosa basin, as well as in much of the continent from the southwestern to the eastern United States (Frenzel and others, 1988; Ewing, 1991). The Woodford Formation, composed of highly organic-rich, dark brown to black shales was deposited. It has been suggested that the change in tectonic and paleogeographic environments resulting in Woodford deposition during late Devonian time may have been due to a mild epeirogeny (Frenzel and others, 1988).

Compressional Tectonics and Sedimentation Associated with the Marathon Ouachita Orogeny

From Cambrian age rifting until the Mississippian, the Tobosa basin region was a relatively stable part of the midcontinent craton receiving widespread carbonate deposits. In Late Mississippian the present day structures found within the Permian basin began to develop and become distinct identifiable features (Hills, 1970, 1972 and 1985; Keller et al, 1980; Hanson and others, 1991; Frenzel and others, 1991; Ewing, 1991; Shumaker, 1992). Sedimentation was affected by increased tectonism resulting in thick clastic deposits overlying the carbonates (Frenzel and others, 1988). Present day structural features that began to form in Late Mississippian include 1) the Matador Uplift; 2) the

Pecos Arch; 3) the Central Basin uplift, and; 4) the Diablo uplift which forms the western edge of the Permian basin (fig. 3).

The Permian basin was most affected by the Marathon-Ouachita orogeny that extended from approximately Late Mississippian through Pennsylvanian time. This orogenic stage was the result of north-directed convergence of the South American-African plate with the southern margin of the North American plate (Kluth and Coney, 1981; Kluth, 1986; Thomas, 1983; Ross, 1986; Hanson and others, 1991; Yang and Dorobek, 1995; Kerans and Fitchen, 1995). Rocks from Mississippian age down to the basement were exposed and eroded from southern areas of the Central Basin uplift suggesting uplift and faulting within this area during Late Mississippian (Hills, 1970).

By Middle Pennsylvanian time suturing between the two continents had increased from the Ouachita to the Marathon regions (Kluth and Coney, 1981). Convergence of the North American plate culminated in Late Pennsylvanian to earliest Permian (Wolfcampian) time and was followed by isostatic adjustment during the Wolfcampian (Kluth and Coney, 1981; Ross, 1986; Yang and Dorobek, 1993; Kerans and Fitchen, 1995).

Tectonism extending from Late Mississippian into the earliest Permian produces extreme variability in the distribution, thickness, and lithology of Pennsylvanian rocks within the Permian basin area. By the culmination of the orogeny the Tobosa Basin had ceased to exist and the present tectonic features of the Permian basin were in place. Many of the oil- and gas-producing anticlines of the Permian basin area were formed during this period (Hills, 1970 and 1972; Frenzel and others, 1988). The Central Basin uplift and the Diablo uplift were structurally high areas resulting in non-deposition of

Pennsylvanian strata over much of these positive features (fig. 3; Frenzel and others, 1988). Within the study area, parts of the Devonian through Pennsylvanian section are missing (Dan George, 1999, personal communication). Farther to the south erosion along the Fort Stockton uplift extends down to Precambrian basement (figs 5 and 6).

During much of the Pennsylvanian, the Central Basin uplift was an active high relief, north-south-oriented, positive element. Foreland deformation associated with the Marathon-Ouachita orogeny is believed to have initiated movement resulting in reactivation of preexisting basement faults along the Central Basin uplift (Hills, 1970; Frenzel and others, 1988). The Central Basin uplift is composed of strongly folded and faulted Paleozoic rocks with a pervasive unconformity truncating rocks of Precambrian to Late Pennsylvanian in age (Hills, 1985). Sediment being eroded from the Central Basin uplift was deposited along its margins into the surrounding basins (Hills, 1970).

The Central Basin platform is often described as a single uplifted block, however it is actually composed of several asymmetrical blocks that were eroded during the Late Pennsylvanian to form a relatively flat platform surface (Shumaker, 1992). The platform has been divided into tectonically discrete blocks that experienced east-west compressional stresses resulting in the structural variations seen within these blocks (fig. 5; Ewing, 1991; Yang and Dorobek, 1995). Differences in platform-to-basin relief along the margins of the blocks produced variations in sequence geometries, particularly in the lateral extent of onlapping siliciclastic and carbonate facies along the block margins (Yang and Dorobek, 1995; Pinsonnault, 1996).

The style of deformation leading to the complex structural faulting and folding along the Central Basin platform is a topic of considerable debate which is beyond the

Figure 5. Major structural divisions of the Central Basin platform as interpreted by Ewing, 1991. The West Jordan unit lies along the northern boundary of the Monahans Transverse Zone, an area of complex structures.

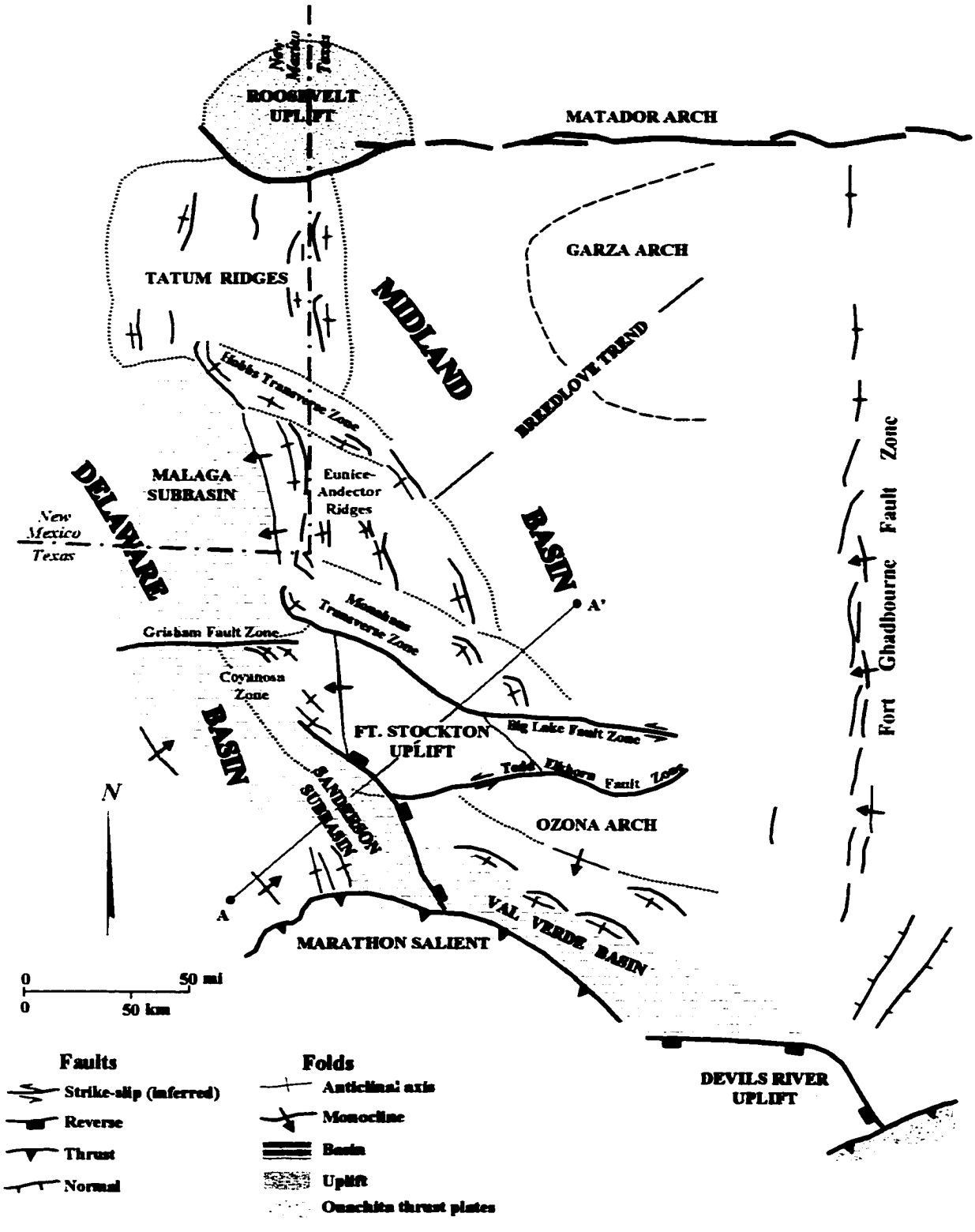
New Mexico Texas
ROOSEVELT UPLIFT
MATADOR ARCH
GARZA ARCH
TATUM RIDGES
MIDLAND
BREEDLOVE TREND
Hobbs Transverse Zone
MALAGA SUBBASIN
Eunice-Andector Ridges
DELAWARE
BASIN
A'
Grisham Fault Zone
Monahans Transverse Zone
Coyanosa Zone
FT. STOCKTON UPLIFT
Big Lake Fault Zone
Fort Chadbourne Fault Zone
BASIN
SANDERSON SUBBASIN
OZONA ARCH
A
MARATHON SALIENT
VAL VERDE BASIN
DEVILS RIVER UPLIFT
N
0 50 mi
0 50 km
Faults
Strike-slip (inferred)
Reverse
Thrust
Normal
Folds
Anticlinal axis
Monocline
Basin
Uplift
Ouachita thrust plates

Figure 6. Diagrammatic cross section across the Central Basin platform. The line of section trends southwest-northeast across the Fort Stockton uplift (see figure 5 for location of cross section A-A'). In this area erosion has removed strata below the Leonardian down to Precambrian basement along the Fort Stockton high. Structure underlying the Penwell-Jordan field complex is similar, although smaller in scope. In the study area erosion along the uplifted structure occurs down into the Devonian (modified from Ewing, 1991).

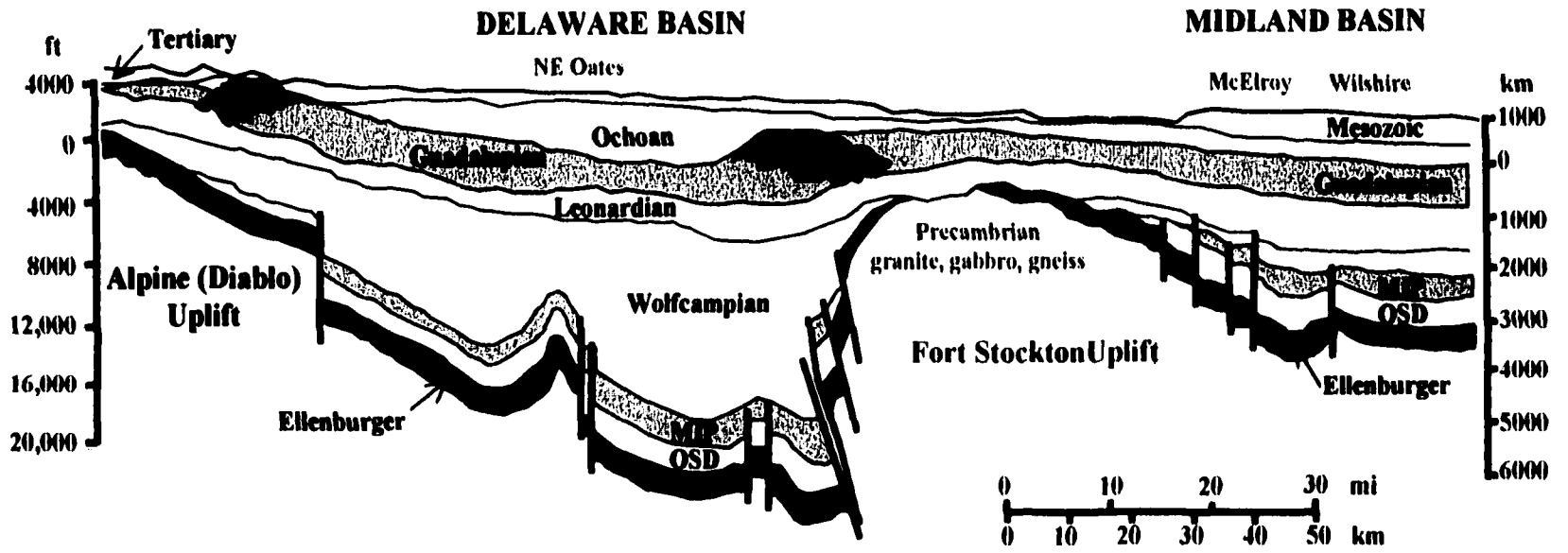
DELAWARE BASIN
MIDLAND BASIN
ft
Tertiary
NE Oates
McElroy
Wilshire
km
4000
0
4000
8000
12,000
16,000
20,000
Ochoan
Leonardian
Mesozoic
Precambrian
granite, gabbro, gneiss
Alpine (Diablo)
Uplift
Wolfcampian
Fort StocktonUplift
OSD
Ellenburger
1000
0
1000
2000
3000
4000
5000
6000
0 10 20 30 mi
0 10 20 30 40 50 km

scope of this study. For a brief synopsis of structural interpretations for the origin of the Central Basin platform the reader is directed to the previous investigation section of Shumaker (1992) and Yang and Dorobek (1995). Several authors have described the subsidence history of the associated Midland and Delaware basins as well (Hills 1970, 1984; Walper, 1977; Elam, 1967,1984; Horak, 1985; and Yang and Dorobek, 1993, 1995).

The exact timing of deformation along the Central Basin uplift is also uncertain. Initial stages of tectonism are believed to have began in Early Pennsylvanian (Hills, 1970; Ewing, 1991, Hanson, 1991; Yang and Dorobek, 1995). From Middle-to-Late Pennsylvanian extending into Early Permian the Central Basin uplift was tectonically active (fig. 4C; Ewing, 1991; Hanson, 1991, Yang and Dorobek, 1995). Prior to Wolfcampian deposition, uplift is indicated by erosional truncation of faulted and folded rocks ranging in age from Precambrian to earliest Permian in age which are overlain by younger Permian strata (Hills, 1970). The end of the Marathon-Ouachita orogeny is suggested by; fault termination, stratal onlap patterns and a regional unconformity in Wolfcampian age sediments (Silver and Todd, 1969; Yang and Dorobek, 1995). Other evidence also includes thrust faults along the frontal Marathon orogenic belt that terminate in lower Wolfcamp strata (Silver and Todd, 1969; Ross, 1981, Wuellner et al, 1986; Yang and Dorobek, 1995).

To the south of the Central Basin uplift lies the Val Verde basin, a foredeep basin which resulted from the Marathon-Ouachita foldbelt (fig. 3, Hills, 1985). As stresses from the orogeny advanced northward, large accumulations of flysh deposits within this foredeep basin were thrust toward the Central Basin uplift. In addition, the northward

thrust of the Marathon Salient overrode some Pennsylvanian rocks and under-thrust the southern end of the Central Basin uplift (Hills, 1985; Shumaker, 1992).

Post Pennsylvanian Tectonism and Sedimentary Fill

The Permian marked the beginning of a period of quiescence within the Permian basin area. By late Wolfcampian the Central Basin uplift had become a stable platform and the surrounding Northeastern, Northern and Northwestern shelves (fig. 1) accumulated thick sequences of cyclic shallow-water carbonates, siliciclastics, and evaporate deposits. During this time the tectonically stable Midland basin was relatively starved of terrigenous clastic sediments (Frenzel and others, 1988).

By Guadalupian time the Midland basin had filled to the same level as the Central Basin platform resulting in continuous sedimentation from the platform into the basin. At its depocenter sediments in the Midland basin have a thickness of over 15,000 feet (4,572 meters; Hills, 1985). The Delaware Basin continued to subside becoming one of the deepest intracratonic basins in North America containing over 24,000 feet (7,315 meters) of sedimentary rocks (Hills, 1985; Ewing, 1991). The Guadalupian was characterized by progradation of carbonate shelves into the basins. Depositional environments ranging from supratidal and shallow intertidal to high-energy ramp crest shoals and quite, subtidal, open-marine conditions were prevalent during this time (Frenzel and others, 1988).

During Ochoan time evaporite sequences deposited within the Delaware and Midland basins indicate a general lowering of sea level and the final stages of basin filling in an arid climate (Hills, 1970; Frenzel and others, 1988). These evaporites form the hydrocarbon seals confining oil accumulations in many of the underlying Permian

reservoir strata. Permian rocks, particularly the San Andres Formation, contain the vast majority of the hydrocarbon reserves of west Texas (Hills, 1970, 1984; Frenzel and others, 1988; Garber and Harris, 1990, Tyler et al, 1991; Holtz and Major, 1994). By the end of the Permian the Delaware and Midland basins had combined to form one large evaporite basin. (Hills, 1970, 1984; Ward et al, 1986; Frenzel and others, 1988).

The interior structures of the Permian basin were completely established by the Early Permian, however, the present day southern margins were formed by uplift and tilting during post-Permian to Pre-Cretaceous tectonism. The western margins of the Permian basin are the product of the Laramide orogeny that produces eastward tilting of the Delaware basin, followed by the formation of Basin-and-Range type structures and the erosion of Permian age strata from large areas (Hills, 1970; Keller, et al, 1980; Hanson, 1991; and Ewing, 1991).

San Andres Formation Descriptive Geology

The San Andres limestone was originally named by W. T. Lee and G. H. Girty (1909) after the San Andres Mountains in which the rocks are exposed in Socorro County, southern New Mexico. Only a brief description of the type locality was provided in their study and the location of the section is stated as "near the northern end of the San Andres range, in the canyon through which the road passed from Engle to Rhodes's ranch". From fossil assemblages within this limestone the age of the strata was placed within the uppermost Pennsylvanian Series.

With the onslaught of oil exploration in the Permian basin during the 1920's and 1930's a great deal of knowledge about subsurface rocks was gained. In 1939 the broader

subdivisions for the Permian Section (Wolfcamp, Leonard, Guadalupe, and Ochoa; see fig. 3) were formally named by Adams et al (1939). In 1941, Lewis attempted to correlate the San Andres Formation from its type section into the subsurface of the Permian basin where he extended the formation to a reef facies within the Guadalupe Series.

The exact placement of the San Andres Formation became a topic of considerable debate. In 1942, P. E. King also placed the San Andres within the Guadalupe Series. His interpretation was based on fusulinid evidence and a significant unconformity at the top of the San Andres within the southern Permian basin. King believed this unconformable surface corresponded to an unconformity of comparable magnitude occurring between the Leonard and Guadalupe Series within the Delaware basin and in the Guadalupe Mountains. Also in 1942, P. B. King worked out the general stratigraphy of the Guadalupe Mountain region placing the San Andres Formation within the upper Leonard Series based on brachiopods found within the formation that were similar to others found within Leonard strata. In this same study P. B. King disagreed with fusulinid evidence for placing rocks of the San Andres Formation within the Central Basin platform and Midland basin in the Guadalupe Series citing that the cuttings that contained the fusulinids were probably derived from younger aged strata.

Needham and Bates (1943) revisited Permian type sections and provided a detailed description of the San Andres at the location were it was originally described by Lee and Girty in 1909. They determined the type section outcrop to be located "...near the middle of the north line of section 29, T. 12 S., R. 2 E". The total thickness of the San Andres type section was measured to be 593.5 feet (180 meters) with the upper part

of the formation having been removed by erosion. Todd (1976) explained the two apparent ages of the San Andres Formation, Leonardian in the Delaware basin and on the Northwestern Shelf and Gaudalupian within the Midland basin, as an eastward progradation sequence in the Delaware and Midland basins. The age of the San Andres is generally well accepted to be Guadalupian by most stratigraphers.

The San Andres Formation outcrops in nearly continuous exposures along the Northwest Shelf including the Guadalupe Mountains. These outcrops have been described by numerous authors (Lewis, 1941; P. B. King, 1942, 1948; Needham and Bates 1943; Boyd, 1958; Hayes, 1959, 1964; Todd, 1976; Pray, 1985; Sarg and Lehmann, 1986; Sonnenfeld, 1991; Kerans et al., 1991, 1992, 1994; Horvorka, 1993; and Kerans and Fitchen, 1995).

Along the Central Basin platform, The San Andres Formation has generally been described as consisting of shallow shelf deposits representing a sequence of basinal prograding, shallowing upward environments. These environments range from open marine subtidal facies at the base of the formation, up through restricted intertidal and supratidal, tidal-flat deposits (Ward, et al., 1986; Ruppel and Cander, 1988a, b; Major et al., 1988; Garber and Harris, 1990, Major, et al., 1990; Major and Holts, 1990; Holts and others, 1992; Major and Holtz, 1997). As a result of basinal progradation in response to regressive seas, the San Andres shelf carbonates tend to be thicker on the shelf platforms, thinning toward the center of the basin (Frenzel, et al., 1988).

Since the early 1940's a plethora of previous work exists for Permian rocks and in particular the San Andres Formation which is the most prolific hydrocarbon reservoir along the Central Basin platform. The following sections are previous works directly

related to reservoir characterization, geostatistical modeling and cyclicity within the San Andres Formation and similar producing carbonate reservoirs.

Reservoir Characterization

Many of the advances in understanding San Andres reservoirs within the Permian basin have come from outcrop analogs along the Northwestern Shelf and within the Guadalupe Mountains of west Texas and New Mexico. Early work dealt with stratigraphic correlation and facies and cycle patterns within San Andres rocks (Silver and Todd, 1969; Meissner, 1972; Todd, 1976; Ramondetta, 1982; Cowen and Haris, 1986; Elliott and Warren, 1989). Reservoir characterization and management has become increasingly more important with time as mature San Andres reservoirs are reaching their economic limit with standard secondary recovery methods. Significant recoverable reserves still remain within the subsurface and with a better understanding of fluid flow within the reservoir these hydrocarbons can be produced more economically and efficiently.

Reservoir characterization work conducted at the Bureau of Economic Geology since 1982 indicates that over 70 percent of oil discovered in Permian age reservoirs (San Andres and Grayburg) remains unlikely to be recovered utilizing conventional primary and secondary oil recovery practices (Tyler, et al, 1991). Advanced secondary recovery techniques such as miscible CO2 floods are expensive and therefore to be economically feasible require detailed knowledge of the reservoir. It is becoming apparent that the complexity of San Andres reservoirs must be fully understood to produce the remaining movable hydrocarbons economically.

The fact that most of the easily recovered mobile oil has been produced from these mature fields has led to numerous studies designed to improve recovery and flatten out decline curves (Dulaney and Hadik, 1990; Ebauks, 1990; Purves, 1990; Friedman, et al, 1990; Major, et al 1990, 1992; Lucia, et al, 1990; Bebout, et al, 1991; Holtz, et al, 1992; Tyler, et al 1992; Whitman and Clemons, 1993; Grant, et al 1994; Kerans and Ruppel, 1994; Kerans, et al, 1994; Holtz and Major, 1994; Eisenberg, et al, 1994; Ruppel, et al, 1995; Major and Holtz, 1997; Tyler, et al, 1998; Saller and Henderson, 1998). These studies are demonstrating the financial gain that can be achieved when mature fields in secondary recovery stages are intimately understood. For example, Saller and Henderson (1998) determined that diagenetic and facies controls on porosity resulted in structurally lower wells within the South Cowden field having better porosity and permeability than structurally higher wells. The structurally low, platform margin wells produced three to ten times more oil than structurally higher platform-interior wells. In addition, simple strategies such as step-out wells, well deepening, recompletions, workovers, infill drilling, injection-profile modification, and waterflood optimization have added 12 billion cubic feet of gas and 2.1 million barrels of oil to the recoverable oil and gas reserve base remaining on State Lands (Tyler, et al, 1998).

With increased computer power, techniques utilizing statistics in reservoir characterization are becoming more common. Particularly in three-dimensional modeling of properties such as porosity and permeability that control fluid flow. Lateral and vertical relationships associated with shelf carbonates and diagenetic overprints produce heterogeneities that significantly affect fluid movement within the reservoir. Recent work is incorporating geostatistical methods to obtain a greater degree of accuracy in

determining the interwell distribution of key reservoir properties such as porosity and permeability (Fogg and Lucia, 1990; Kittridge et al, 1990, Senger et al, 1993, Dull et al, 1994; Ruppel, et al, 1995; Dull, 1995; Prieditis, 1998).

Sequence Framework and Cyclicity within the San Andres Formation

The importance of recognizing cycle boundaries and applying sequence stratigraphic principles when correlating well logs has been known for some time. Facies that may appear correlative can represent separate cycles and not be laterally continuous. High-frequency cycles based on sea level fluctuations define the genetic units of reservoir architecture. These cycle boundaries can define flow units within a reservoir and delineate diagenetically controlled porosity zones. The application of sequence stratigraphy has been widely applied to Permian age strata along the Northwest Shelf (Sarg and Lehmann, 1986; Elliot and Waren, 1989; Kerans and Nance, 1991; Sonnenfeld, 1991, 1993; Sonenfeld and Cross, 1993; Harris, et al, 1993; Hovorka, et al, 1993, Grant, et al, 1994, Kerans, et al, 1992, 1994; Kerans and Ruppel, 1994; Kerans and Fitchen, 1995; Lucia, et al, 1995). The sequence hierarchy of San Andres and Grayburg exposures along the Northwestern Shelf are described in detail by Kerans, et al (1992, 1994).

Subsurface studies that have attempted to place basinal Permian strata into the sequence stratigraphic relationships seen along the Northwestern Shelf are extremely limited in number and detail. (Lindsey, et al, 1992; Dedman and Dorobek, 1993; Keller, 1993, Eisenburg, et al, 1994; Barnaby and Ward, 1995; Lucia, et al, 1995; Ruppel and Ward, 1996; Ruppel and Lucia, 1996). The majority of these studies concentrate on

cyclicity and sequence stratigraphy of the Grayburg Formation. The most comprehensive published work to date that attempts to place Permian basin nomenclature into the sequence stratigraphic terminology applied to the Northwestern Shelf is that of Pinsonnault (1996). Through the use of core data and well logs this study establishes a sequence stratigraphic framework tied to outcrop analogs for the upper San Andres and Grayburg strata in the Waddell field (fig. 1). The Waddell field is located along the eastern margin of the Central Basin platform approximately three miles southeast of the West Jordan unit.

Paleogeography and Geologic Setting

The San Andres Formation extends from Central Texas to Arizona and Utah. In the Midland basin it reaches thickness of over 1,600 feet (533 meters) and a depth of burial of more than 5,010 feet (1,670 meters; Bein, and Land, 1982; Ramondetta, 1982). At present the San Andres Formation within the study area is covered by approximately 3500 feet (1070 meters) of sediment. Within the study area and along the Central Basin platform, the San Andres is almost entirely dolomitized, although limestone has been found in the lowermost part of the section in some areas along the platform (Ruppel and Cander, 1988a). To the north the formation grades into anhydrite, salt, and red beds. To the west exposures along the eastern flank of the Sacramento Mountains of New Mexico are predominantly carbonates (Bein, and Land, 1982; Ramondetta, 1982).

Paleogeography of the Permian basin was controlled by Pennsylvanian tectonism that resulted in reactivation of basement blocks and deformation of pre-Permian strata (Galley, 1958; Hills, 1972; Ward, et al, 1986; Frenzel, et al, 1988; Major, et al, 1990).

Present day structures trapping hydrocarbons within San Andres reservoirs result from structural drape and compaction over these pre-existing Pennsylvanian structural highs that are present at depth (Hills, 1972; Ward, et al, 1968).

The Central Basin platform was a stable paleotopographic high and the site of shallow-marine carbonate-ramp sedimentation during much of San Andres deposition (Galley, 1958; Ward, et al, 1986; Ruppel and Cander, 1988a; Major, et al, 1990; Kerans and Fitchen, 1995). During early San Andres deposition the Delaware basin was relatively starved of sediment, however, the basin received large amounts of siliciclastic-dominated sediment during the later part of San Andres deposition. Southwest trade winds provided the mechanism for sediment transport from the Kaibab Plateau-Colorado Plateau area and fine grained, wind blown clastic sediments were deposited with the basin (Parrish and Peterson, 1988; Peterson, 1988; Fischer and Sarntherin, 1988). Within the Midland basin large accumulations of platform carbonate sediments were deposited. These carbonates overly lower San Andres platform equivalent siliciclastic deposits in the basins depocenter (Galley, 1958; Ward, et al, 1986).

A major sea-level rise during early San Andres time resulted in carbonate deposition farther landward on the Central Basin platform and surrounding shelf areas of the Permian basin. As transgressive seas encroached landward over the stable shelf areas surrounding the Permian basin subtidal facies were deposited farther inland. This transgressive period was short lived thus most of the San Andres deposition represents a gradual upward shoaling, progradational sequence marked by numerous high frequency cycles suggestive of oscillating, shallow water deposition on a gently dipping shelf (P. E. King, 1942; Hills, 1972; Kerans and Fitchen, 1995). A wide scope of depositional

environments are characteristic of the San Andres Formation. These environments range from shallow shelf, open marine, bar and bank complexes of ooid and/or carbonate sand shoals, local patch reef and bioherm buildups to restricted lagoons and interior tidal flat environments (Tyler, et al, 1991).

Overlying the San Andres Formation are siliciclastics and dolomites of the Grayburg Formation that exhibit a shallowing upward cyclic nature similar to the San Andres (Longacre, 1980, 1983; Bebout, et al, 1987; Ruppel and Cander, 1988a). The contact between the two formations is unconformable along the Northwestern Shelf (P. E. King, 1942; Hayes, 1959, 1964) and speculative within the study area. Areas of at least localized truncation are indicated within the study area at the top of the San Andres Formation. The overall progradational nature of San Andres and Grayburg strata places the older San Andres Formation platformward (westward) of the younger Grayburg shelf edge deposits resulting in Grayburg production occurring predominantly basinward of producing San Andres fields (Bebout, et al, 1987; Tyler, et al, 1991).

Hydrocarbon Maturation, Migration and Entrapment from the Midland Basin to the Central Basin Platform

Permian strata have produced tens of millions of barrels of oil along the Central Basin platform and shelf areas, nevertheless very little is actually published on the source and migration of this oil. The following section presents potential source rocks and migration pathways put fourth by previous studies for the large accumulations of oil found within San Andres and Grayburg reservoirs.

One of the earliest classifications of oils within the Permian basin was by Jones and Smith (1965). Their study attempted to classify the physical and chemical

characteristics of crude oils produced from Upper Cambrian through Permian age reservoirs in an effort to determine organic rich rocks within the basin that may act as source rocks for the area. They generally concluded, "on the Central Basin platform where the Wolfcamp lies on a truncated surface of rocks as old as Precambrian, the age of the source rocks can be designated merely Woodford through Wolfcamp." Later studies reported the same conclusion. Oils sampled within the San Andres varied somewhat from each sample location and originated from source rocks deposited in two general environments, lagoonal and basinal. The vertical migration of oil along fault and fracture systems was suggested as a possible migration pathway. Although somewhat problematic given the scope of the distance this oil would have had to travel from deep basinal Woodford-Wolfcamp sources to shallow Permian shelf carbonates, and the impermeable nature of some strata between a basinal source and platform reservoirs (Jones and Smith, 1994).

Houde (1979) evaluated the Leonardian aged Spraberry sandstone as possibly self-sourcing within the Midland basin. The Spraberry is equivalent to the Middle and Upper Clear Fork Formation and is confined to the Midland basin. In this study it was determined that fine-grained intervals within the Spraberry contained adequate source-rock potential in dark, argillaceous carbonates and calcareous shales. It was concluded that the formation had the potential to be self-sourcing based on organic-rich Spraberry basinal rocks and similarities between hydrocarbons extracted from the presumed source beds and oil produced from the Spraberry (Houde, 1979).

Later work suggests that for the more shallow northern areas of the Midland basin, Pennsylvanian and Permian source beds are immature. Duton (1980 ab) studied

samples from the Palo Duro and Midland basins to determine source rock potential in these areas. Based on kerogen samples she compiled data on the total organic carbon (TOC), thermal alteration index (TAI), Vitrinite reflectance (Ro), and kerogen type (OMI). TOC measures the organic richness of a rock and carbonate values as low as 0.3 % can be fair source rocks. TAI is a measure of the kerogen color and ranges from 1.0 to 8.0, OMI index is a measure of the kerogen type and quality of organic matter within a rock and Ro is a measure of the amount of light reflected by vitrinite particles. Ro values less than 0.5% indicate immature source rocks with values between 0.5 % to 1.3 % falling within the oil generation window.

Within the central part of the Midland basin, higher TAI and TOC values were found for Permian rocks than that of the northern basin. For the northern Midland basin TAI values for Permian samples averaged 2.29 with TOC values averaging about 1 %. In the central parts of the Midland basin Permian sediments had TAI values averaging 2.82 and TOC values averaged 2.2 %, extending up to 5 %. Ro values for Pennsylvanian and Permian samples were found to be 0.6 % and 4.4 % respectively. While Ro values for the Sprayberry were less than 0.5 % indicating immaturity, cross plots of TAI and OMI data suggest that potential Spraberry source beds reached higher temperatures in the central Midland basin due to deeper depth of burial and therefore may have been mature enough in this area to generate hydrocarbons (Dutton, 1980a). If this is true then the Spraberry may have sourced some of the oil found within the San Andres. In addition, Dutton, (1980) found Wolfcampian shales to have significantly richer organic content than the overlying Spraberry with considerably higher TOC and Ro values of 2.8 and 0.6 %

respectively, indicating very good source-rock potential. Samples from Permian aged rocks lying above the Spraberry were found to be immature within the Midland basin.

The most comprehensive study published to date on the source rocks for San Andres reservoirs is that of Ramondetta (1982). This study determined that organic matter occurs predominantly in carbonate muds and thin laminae and lentils of dark-gray to black asphaltic shales intercalated with shelf carbonates within the San Andres Formation. Total organic carbon values in these laminae may be as high as 4 percent. The source of organic material within the San Andres was described as originating from both indigenous algal debris and terrigenous plant material that washed onto the shelf during storms and periods of subaerial exposure (Ramondetta, 1982). With a modern geothermal gradient of approximately 1.1 F/100 feet (Dutton, 1980a), a depth of at least 7,700 feet would be necessary for catagenesis within the San Andres (Ramondetta, 1982). His work demonstrated that San Andres shelf carbonates would probably be too immature for in situ sourcing. However, it was determined using the modern geothermal gradient and present day bottom hole temperatures from well bores that the Wolfcampian section possesses good source-rock potential. Wolfcampian rocks were found to have significantly greater TOC, OMI and Ro (vitronite reflectance) values compared to overlying Spraberry and underlying Pennsylvanian rocks and most likely were the source for San Andres oils (Ramondetta, 1982).

In this same study, Ramondetta (1982) suggested that migration from deeper source-rock beds might have resulted from compression and higher fluid pressure causing the expulsion of hydrocarbons. This may account for migration of oil within Pennsylvanian and earliest Permian aged rocks, nevertheless, compression took place

during the Marathon-Ouachita orogeny and predates San Andres deposition. However, compressional stress fields may have established an earlier network of fractures that were later connected up with younger strata through formation of younger fracture suites associated with Laramide and Basin and Range stress fields. Migration influenced by complex structural relationships may have also been responsible for the high degree of mixing of oils seen along the Central Basin platform as first indicated by Jones and Smith (1965).

Horak (1985) modeled the hydrocarbon generation window for potential source rocks within the Midland and Delaware basins following the Lopatin (1971) time/temperature dependent model. It was determined from this study that Lower Paleozoic source rocks for the Midland basin (Simpson and Woodford) generated oil during the Triassic and Jurassic with Woodford rocks being within the oil generation window during the Middle Jurassic to the present time. Oil generation from Upper Pennsylvanian – Lower Permian shales (Wolfcamp/Spraberry) began in the Middle Cretaceous and continued to the present. Rocks younger than Early Permian (Early Wolfcamp) are outside of the oil window and considered immature. Work by Horak (1985) provides a scientific model supporting previous work indicating that: 1) the San Andres is not self sourced; 2) Wolfcamp basinal deposits of the Midland basin are considered the most likely source rocks for the tremendous accumulations of oil found within the San Andres and Grayburg Formations; and 3) if these older, thermally mature rocks of the Midland basin depocenter are the source rocks for San Andres oil, then oil must have migrated across stratigraphic and structural boundaries, thousands of feet vertically and tens of miles laterally. It was postulated that "only a pervasive fracture

network can cut across the self-limiting stratigraphic pathways and connect source rocks with reservoir rocks." (Horak, 1985).

Dolomites are known for their brittle properties and tend to fracture more easily than other rock types. Fracturing seen in core from the West Jordan unit is believed to result from several different episodes. Fracturing resulting from localized stress fields set up through the drape and bending of strata over deeper structures can induce localized tectonic stresses associated with the formation of the anticlinal feature. In addition, stress fields associated with Laramide and Basin and Range tectonism probably resulted in fracturing within the area as well. It is very likely that a complex overprint of multiple fracture networks exists throughout the Permian basin region. The Permian basin is situated in the center of an area that has had an extremely complex structural history. It would not be unreasonable to suspect multiple fracture sets brought on by successive tectonic sequences through which oil would have migrated laterally and vertically for long distances from basin to shelf areas over geologic time. These fracture networks could easily provide avenues for hydrocarbon migration upward through the section. Although Basin and Range extension is not seen to extend to the eastern margins of the Permian basin the mild effects of crustal attenuation would most likely have extended great distances. Longacre (1990) suggests evidence for normal faulting within the Grayburg Formation at McElroy Field and minor faulting was seen in at least two cores within the West Jordan unit. Fractures were a common occurrence in all West Jordan unit cores.

Isopach maps indicate no structural development over the West Jordan unit until possibly latest San Andres time. The anticlinal structure comprising the Jordan field

appears to have been fairly well developed by middle-to-late Grayburg time. Dolomitization of the San Andres was an early diagenetic event and by the end of Grayburg time, San Andres strata would have been fairly well compacted. The initial fracturing within the area is believed to have began with stress fields associated with the bending of rock forming the anticlinal structure. Reactivation of older, deeper faults may have influenced structural development forming the present day traps up until at least late Guadalupian. As indicated by small faults seen within core from the West Jordan unit and substantial faulting within the Grayburg Formation at McElroy field as described by Longacre (1990), some degree of tectonic activity is documented to have occurred at least up until middle-to-late Guadalupian time. This period may have also resulted in a fracture network connecting basinal hydrocarbons and providing a migration path to Guadalupian aged rocks.

A regional network of fractures has been identified within many Texaco fields and other areas throughout the Permian basin. This regional fracture network is comprised of a conjugate set of fractures, with the dominant fracture set oriented east-northeast and its conjugate oriented north-west-north. This orientation is similar to a conjugate fracture network documented during this study along outcrops within the Guadalupe Mountains. As mentioned previously, Laramide stresses resulted in eastward tilting of the Delaware basin and Basin and Range structures are evidenced along the western margin of the Permian basin (Hills, 1970; Keller, et al, 1980; Hanson, 1991; and Ewing, 1991). The widespread regional occurrence of a conjugate fracture network suggests far extending stress fields as one would expect during basin and range attenuation. The nature of fracturing seen within the West Jordan unit and documented within other files and at

outcrop localities suggests the likelihood of multiple episodes of fracture development and an overprint of both tectonic fractures, derived from local stress fields forming the anticlinal structure, and regional fracture systems.

WEST JORDAN UNIT HISTORY AND DESCRIPTIVE GEOLOGY

Jordan Field Discovery and West Jordan Unit Development

The West Jordan unit is located along the southwestern end of a broad, gently dipping asymmetrical anticline (fig. 7). Initial development along the structure began in 1926 and the Jordan field was established in 1937 (Fields and Nelson, 1996; Major and Holtz, 1996). The early development of the field involved the drilling of thirty-seven wells on forty-acre spacing. Scout ticket data indicates that these early wells had initial production values ranging from several hundred to several thousand barrels with no water. In the 1950's and 1960's an infill drilling program resulted in twenty-acre spacing throughout the field (Fields and Nelson, 1996).

Texaco established current unit boundaries (fig. 7) on June 1, 1969 in order to begin a waterflood within the "San Andres" Formation. The unitized interval is based on the correlative interval as defined by the Hattie Connell et al well No. 6-T from 3,100 feet to 3,900 feet below ground level. Based on the unit agreement, the overlying Grayburg Formation is inclusive within the West Jordan unit boundaries although the entire unitized interval is termed San Andres. The initial waterflood program began with the development of an eight well peripheral pattern in an attempt to displace oil vertically by raising the water table through injection below the oil-water contact (Fields and Nelson, 1996).

In the mid to late 1970's, infill drilling brought the pattern spacing down to ten acres in order to begin a new waterflood expansion phase. The injection pattern was modified from a peripheral pattern to an inverted nine-spot pattern. Production data

Figure 7. Regional structural map on top of the San Andres Formation showing unitized boundaries of the West Jordan and surrounding units. This map shows two compartmentalized anticlinal structures representing the Jordan and Penwell fields. The Jordan field is comprised of the smaller asymmetrical anticlinal structure to the south and has been divided into the West Jordan and Jordan University units. The larger Penwell field to the north is divided into three units, the Penwell, East Penwell and the North Penwell units. The Penwell and Jordan units produce from the San Andres Formation and the Waddell field just to the southeast of West Jordan produces from porosity pinchouts within the Grayburg Formation.

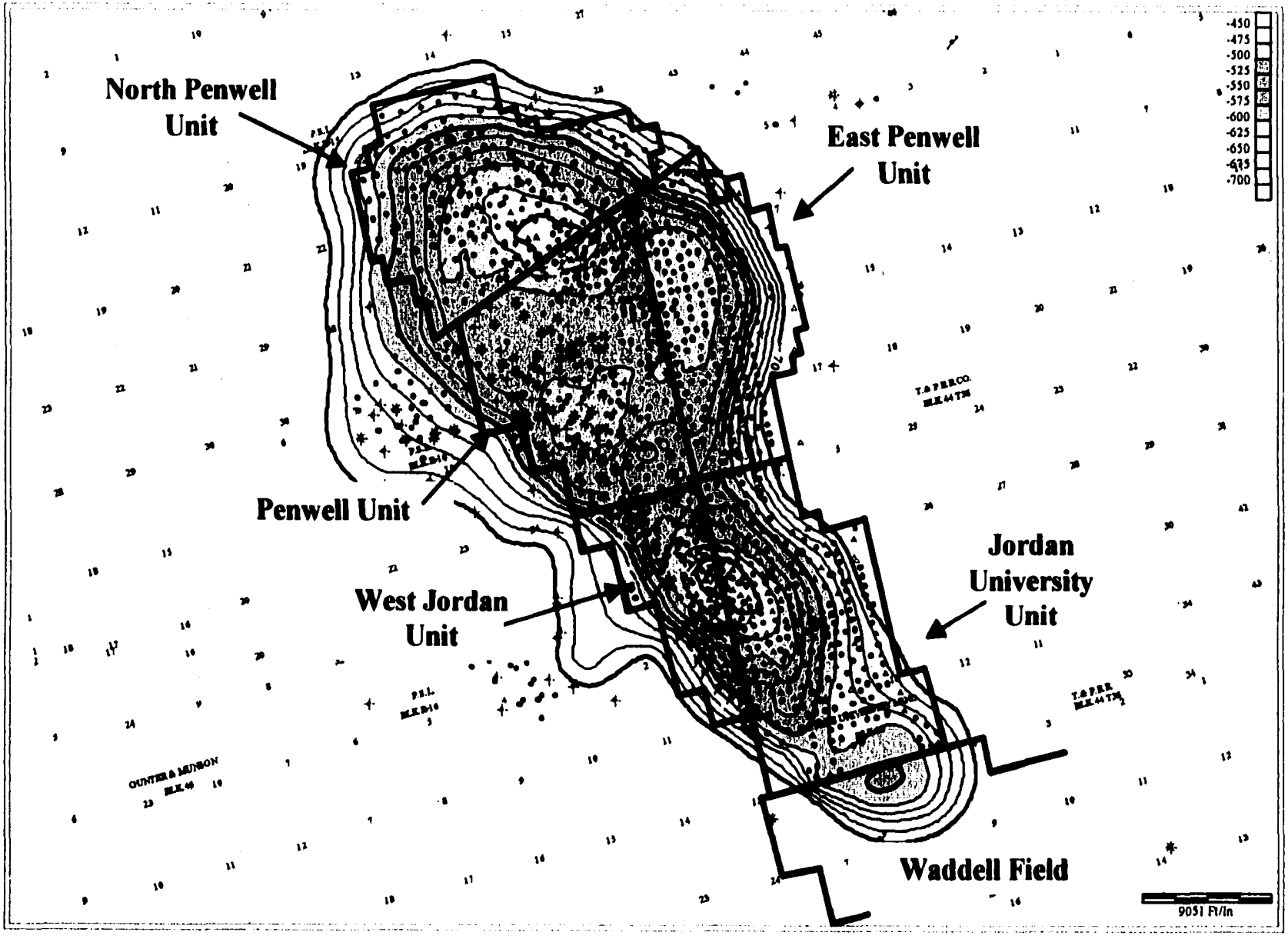
North Penwell Unit
East Penwell Unit
Penwell Unit
West Jordan Unit
Jordan University Unit
Waddell Field
-450
-475
-500
-525
-550
-575
-600
-625
-650
-675
-700
9051 Ft/In

available since unitization in 1969 indicate that this period was the most successful for the West Jordan unit waterflood program (fig. 8). A general overall decline in production was seen until 1982 during which time an aggressive workover program was initiated in which many of the wells were fracture stimulated (fig. 8). From the middle 1980's until 1993 decline within the unit was influenced by economics and a need to reduce operating expenses in reaction to the large decrease in oil prices (Fields and Nelson, 1996). During this time period injection was reduced and wells were shut in from production. In 1993, increase and stabilization of oil prices initiated a rejuvenation in the workover program at West Jordan. Fracture stimulation programs for numerous workover candidates leveled out the production decline for several years (fig. 8). At the present time there are a total of 133 wells within the West Jordan unit, of these 66 are active wells. Of the active wells within the unit 47 are producing wells and 19 are injectors (fig. 9).

Like many other San Andres and Grayburg fields along the eastern margin of the Central Basin platform, the West Jordan unit is an extremely mature waterflood. Since 1996 it has become clear that in order to maintain production within the unit and to capture the greatest quantity of remaining hydrocarbons, a better understanding of reservoir heterogeneity and flow unit architecture is imperative. It was decided that a detailed reservoir characterization study was needed to fully understand the West Jordan unit reservoir and its future economic potential. This study was initiated in late 1996 and began in earnest with the work presented here in the summer of 1997.

Figure 8. Average daily production chart for the West Jordan unit waterflood program since the initiation of water injection in 1969. Oil production was greatest in the late 1970's as a result of infill drilling which brought the unit spacing down to 10 acres during a waterflood expansion phase. From the early 1980's to the early 1990's the unit experienced substantial decline which was influenced by economics and a need to reduce operating expenses due to low oil prices. Since that time an aggressive workover program has flattened out decline to some degree.

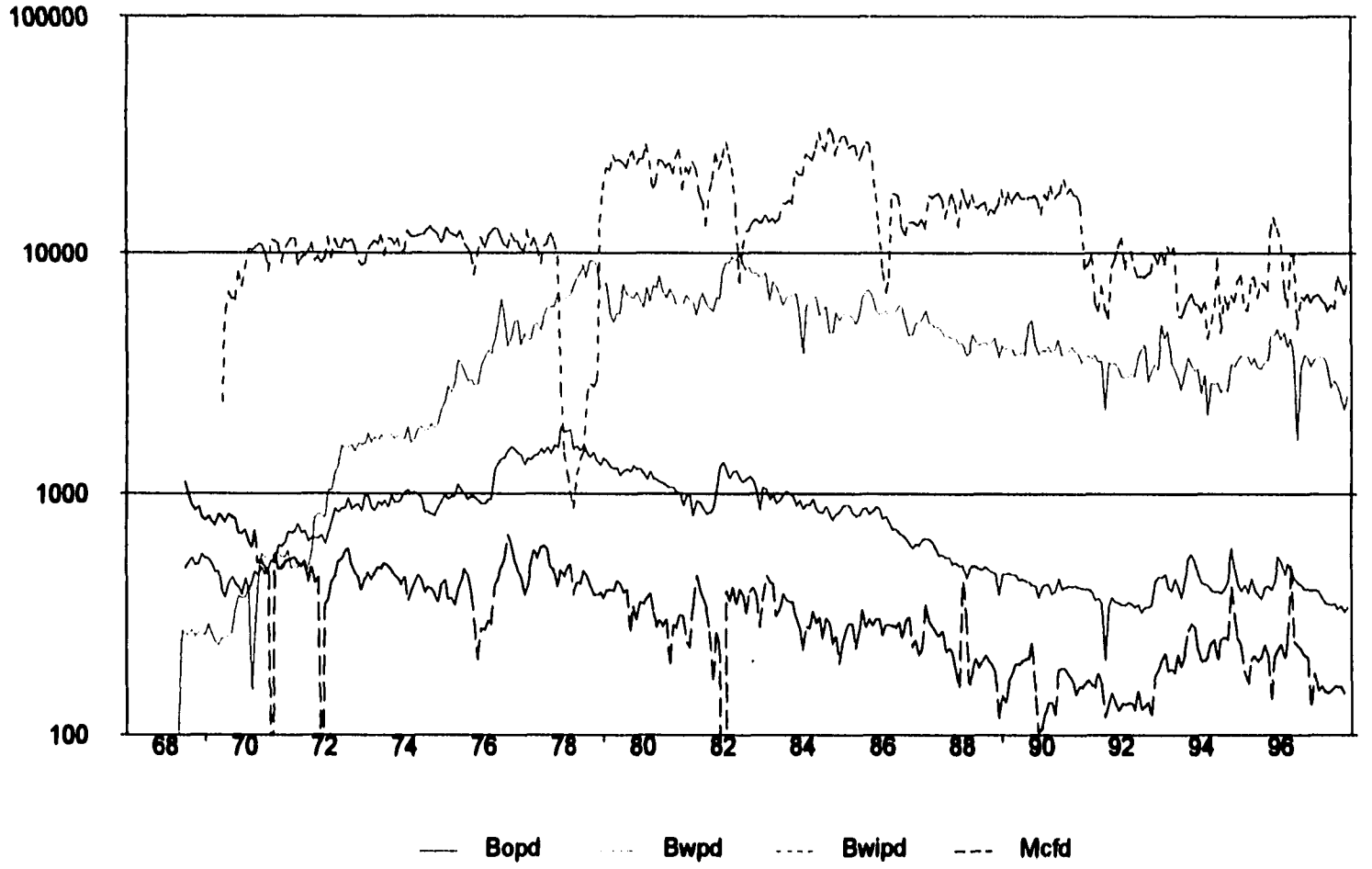
100000
10000
1000
100
68
70
72
74
76
78
80
82
84
86
88
90
92
94
96
Bopd
Bwpd
Bwipd
Mcfd

Figure 9. Structural contour map of the West Jordan unit showing unit boundaries and the location of well and core data. The twelve cores within the West Jordan unit are well distributed providing detailed information on vertical and lateral characteristics of pore and facies types within the reservoir. The large red circles indicate core locations and well symbols are defined in the upper right hand corner of the figure.

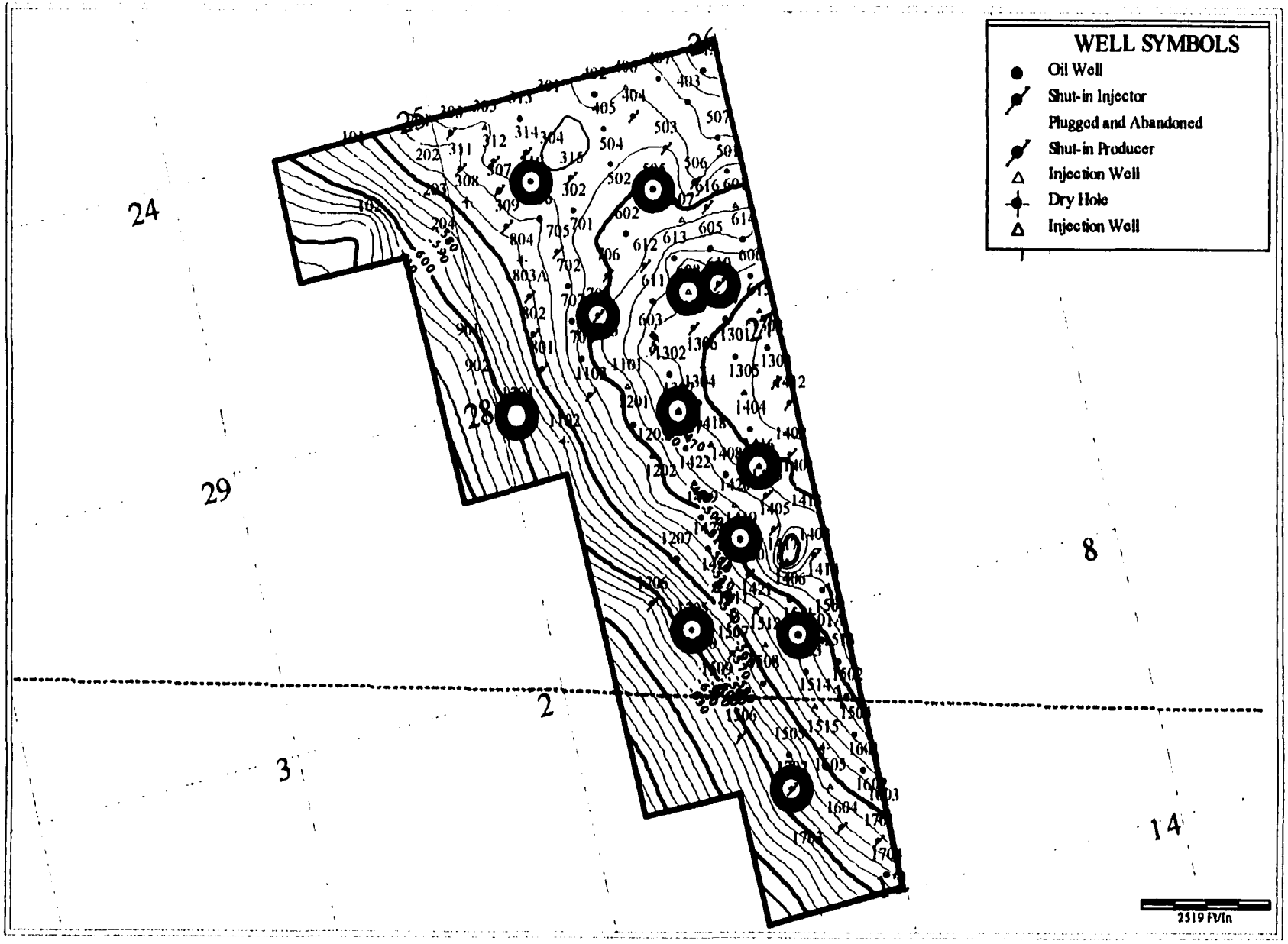
WELL SYMBOLS
Oil Well
Shut-in Injector
Plugged and Abandoned
Shut-in Producer
Injection Well
Dry Hole
Injection Well
24
29
28
2
3
8
14
2519 Ft/In

Descriptive Geology of Cycle Boundaries and Reservoir Zone Nomenclature within the West Jordan Unit

The West Jordan San Andres reservoir produces from several zones within an overall upward-shoaling, progradational sequence consistent with deposition on a shallow-ramp setting. The reservoir was originally divided into four correlative zones (zone I, II, II and IV) with the lowermost zone IV having five intervals (A, B, C, E1 and E2). The original nature of these divisions and their basis is not known. On the preference of other Texaco scientists working with the unit this nomenclature has been maintained. However, previous correlations that appear to be based on gamma ray curve picks were substantially modified to reflect shallowing upward cycle boundaries and flow unit properties.

Interpretations defined within this study are based on detailed examination of core employing chronostratigraphic principles to define cycle boundaries, as well as, petrophysical, injection profile, and production data that were then correlated throughout the unit. Maintaining the original nomenclature, these modified zones are from top to bottom: zone I, II, III, IV-A, IV-B, IV-C, IV-E1, and IV-E2 (fig. 10). It is important to keep in mind that zones within the unit are based on chronostratigraphic, shallowing upward vertical facies successions that form cycle boundaries. The chronostratigraphic nomenclature used in the study is discussed in further detail in a later section. Each zone within the reservoir was found to exhibit separate distinct petrophysical differences. For a detailed description of reservoir zones see Appendix C.

Figure 10. West Jordan unit type log showing zone nomenclature and chronostratigraphic relationships within the reservoir. Zones are based on core descriptions and petrologic work that has defined cycle boundaries within the unit. There are eight primary chronostratigraphic cycles defined for the reservoir. Each cycle boundary represents an overall shallowing of water depth followed by widespread deeper water conditions. In the figure triangles to the left of the type log represent facies partitioning within the reservoir. Deeper water vertical facies successions are volumetrically indicated by colored triangles at the base of each cycle while inverted white triangles represent volumetrically shallower water vertical facies successions. Not only is each cycle boundary capped by shallower water facies, but also an overall shallowing upward nature is seen within groups of cycles forming two high frequency sequences (HFS). HFS 1 represents an overall aggradational period within the reservoir that allowed for proximal outer ramp and ramp crest facies tracts (green) to be deposited within the unit area. Productive, stacked shoal bodies tend to form at the top of each cycle boundary within HSF I. HFS II is an overall progradational sequence that resulted in middle ramp (pink) and inner ramp (yellow) facies tracts to be deposited across the unit as sea level dropped. The culmination of each of these high frequency sequences represents a highstand systems tract (HST) within the unit.

WJU # 1416

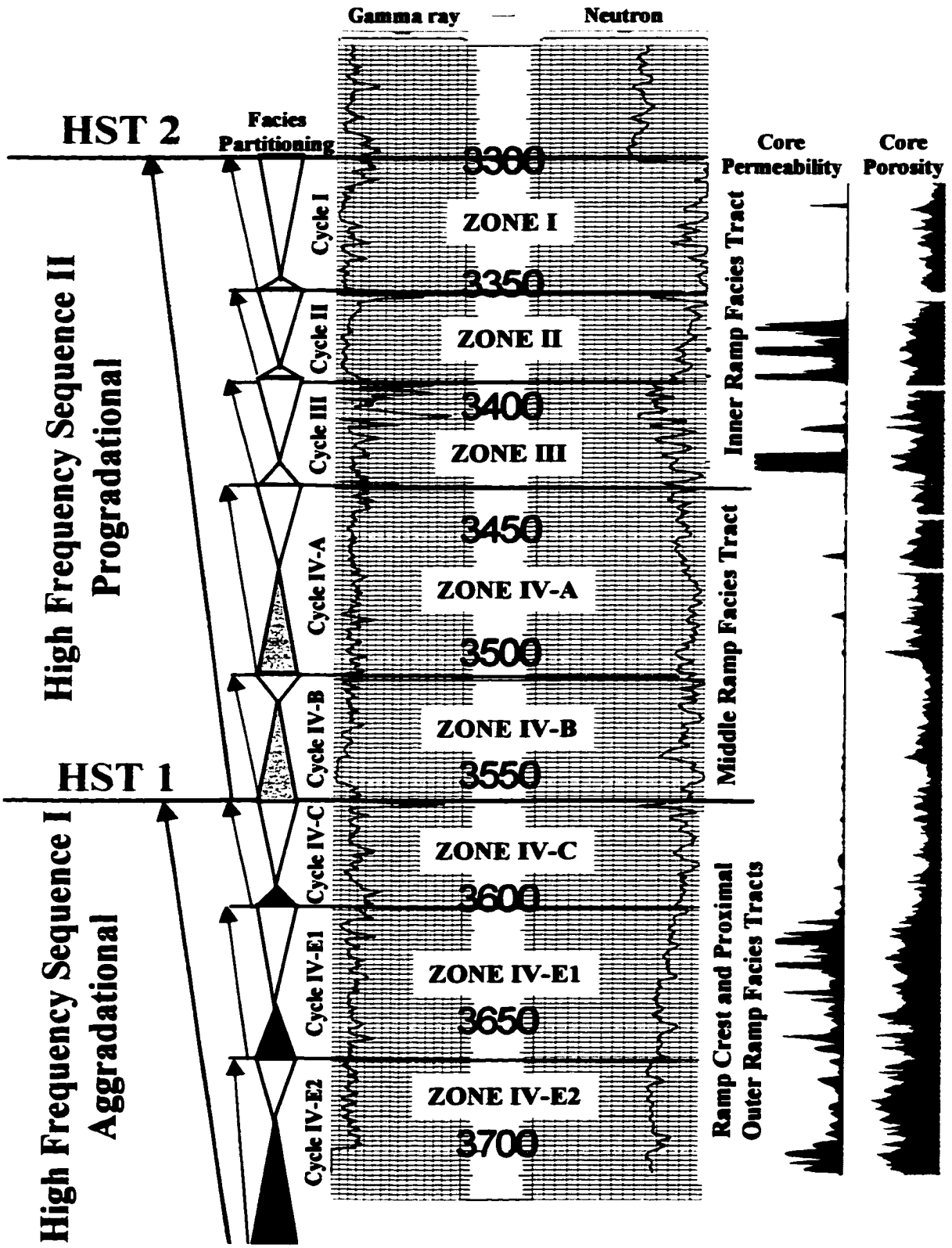
Gamma ray
Neutron
HST 2
Facies Partitioning
Core Permeability
Core Porosity
3300
ZONE I
Cycle I
3350
ZONE II
Cycle II
3400
ZONE III
Cycle III
3450
ZONE IV-A
Cycle IV-A
3500
ZONE IV-B
Cycle IV-B
HST 1
3550
ZONE IV-C
Cycle IV-C
3600
ZONE IV-E1
Cycle IV-E1
3650
ZONE IV-E2
Cycle IV-E2
3700
High Frequency Sequence II
Progradational
High Frequency Sequence I
Aggradational
Inner Ramp Facies Tract
Middle Ramp Facies Tract
Ramp Crest and Proximal
Outer Ramp Facies Tracts

A broad, gentle northwest-southeast trending anticline, the result of drape and compaction over Pennsylvanian aged structures, forms the primary trapping mechanism for the Jordan Field (figs 7 and 11). This anticlinal structure exhibits only minor changes up through cycle boundaries mapped within the unit (fig. 12). Structural closure within the unit is approximately 117 meters (385 feet). Tight supratidal dolomudstones and pisolite dolopackstone-grainstone facies that have been almost completely occluded by sulfate cement form the reservoir seal. Within the study area the San Andres Formation is approximately 875 to 925 feet thick (266-282 meters). Sparse well control and no core data is available for the San Andres Formation below the unitized interval. Within the unitized interval the formation ranges from 530 to 580 feet (161-177 meters). Thickness variations of up to 50 feet (13 meters) are primarily the result of localized exposure and truncation of isolated paleotopographic highs in the uppermost zone of the formation.

There is little evidence to suggest that the West Jordan unit structure was present during San Andres deposition. From deep wells that are available no appreciable thinning across the structure appears to have taken place within the overall San Andres Formation. Also, individual isopach maps of zones within the unit do not indicate an overall pattern of thinning over the present day structural high from which the unit produces (fig. 13). Actually, the opposite is seen in isopach maps of several zones that show thickening of strata in areas along the present day structural crest of the anticline (fig. 13). An exception is seen in zone IV-E1 that indicates a minor thinning along parts of the crest. This may or may not be related to structural development during deposition of facies within this zone. Significant localized thinning in the uppermost part of Zone I indicates

Figure 11. Structural cross section along depositional strike from north to south across the West Jordan unit illustrating zones defined within the San Andres Formation. The unit produces out of a broad, gentle anticlinal structure. Although the correlation of major cycle boundaries seen in zones I through IV-E2 appear laterally continuous, substantial vertical and lateral reservoir heterogeneity occurs within each zone. The location of the cross section is defined on the structure contour map of zone I to the left below the cross section. Vertical exaggeration is 10X. Zones I through III are composed of vertical facies successions (VFS) primarily from the inner ramp facies tract. Zones IV-A and IV-B consist of VFS from the middle ramp facies tract and zones IV-C through IV-E2 represent VFS primarily from ramp crest and proximal outer ramp facies tracts. Although cycles are usually seen to carry across multiple facies tracts this is not prevalent within the unit. Because of the location of the West Jordan unit so far inland on the ramp margin and due to the depositional dip being very slight (< 1 degree) during deposition of facies, lateral change in facies tracts within cycle boundaries across the unit is not substantial.

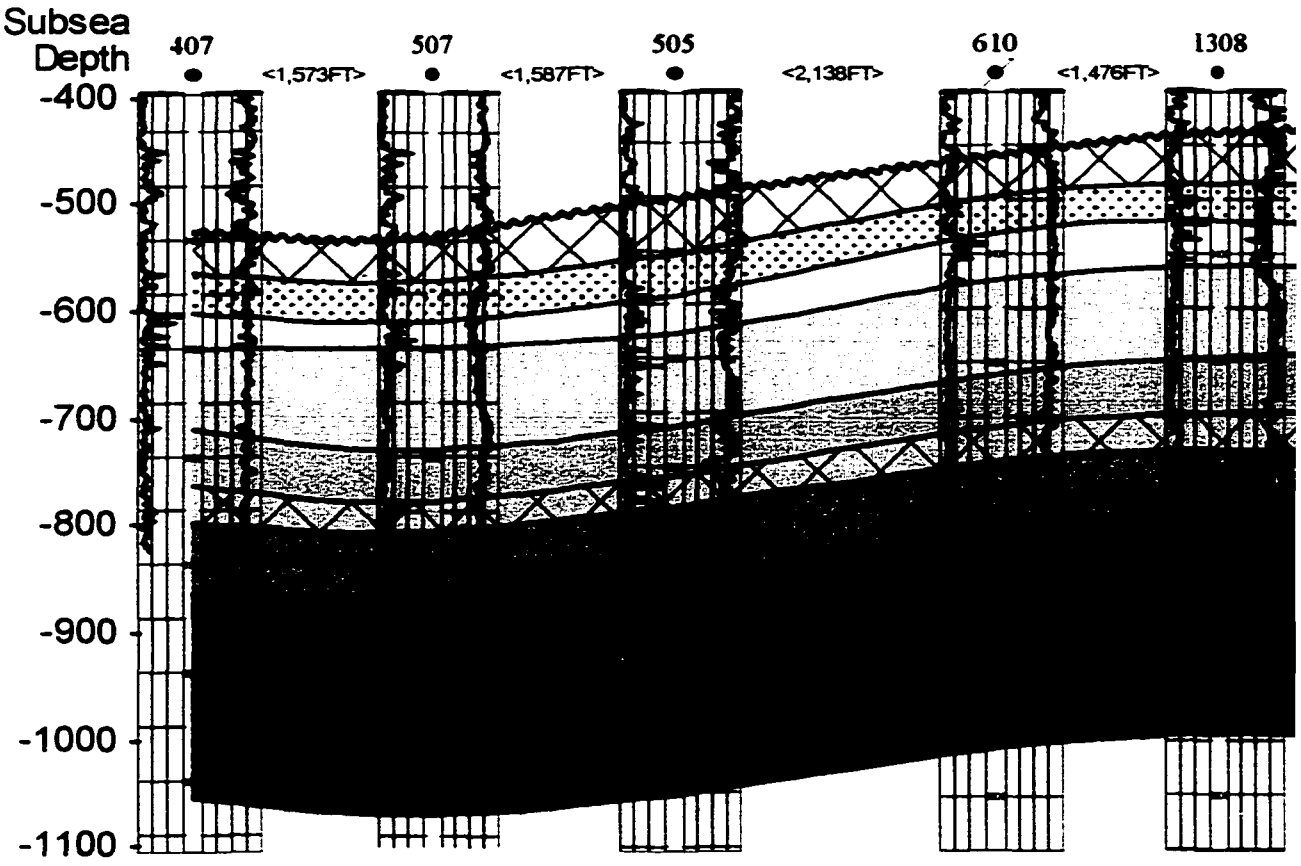

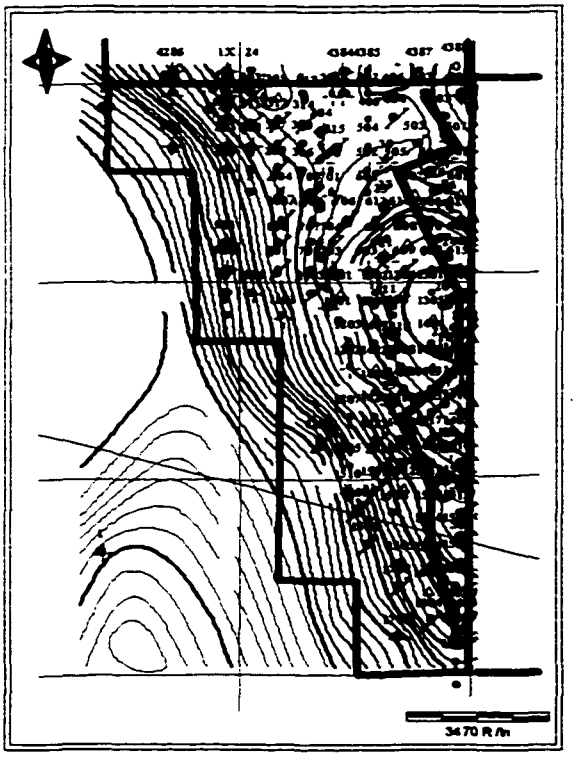

WELL SY
Oil Well
Shut-in Injector
Plugged and Aba
Shut-in Producer
Injection Well
Dry Hole
Injection Well

Cycles with inten
resulting in almo
of dolograinstone

Cycles that have
considerable sulf

Cycles that have
sulfate and dolon

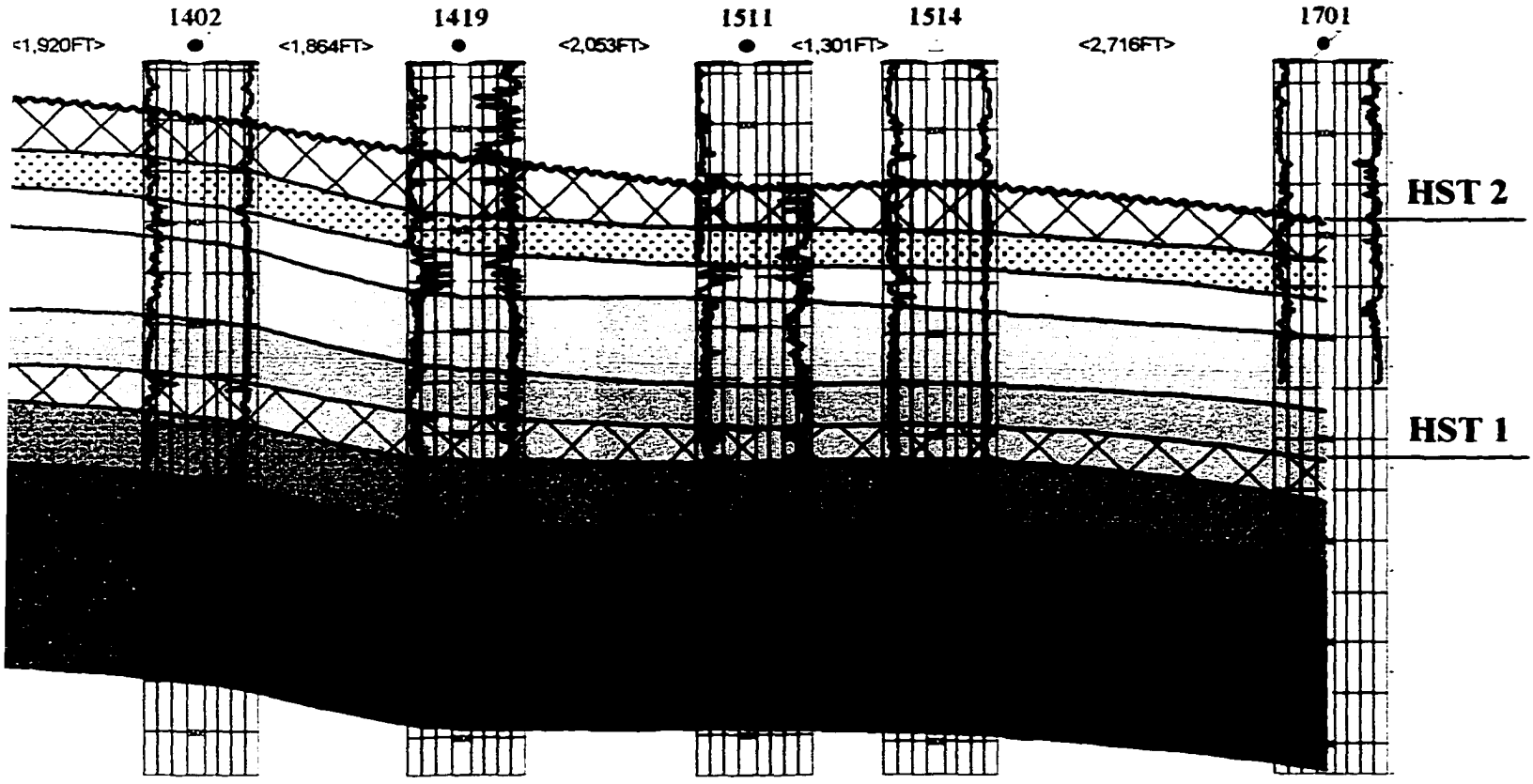

'MBOLS

ıdoned

se sulfate cementation
st complete occlusion
fabrics

undergone
ate dissolution

undergone considerable
nite dissolution

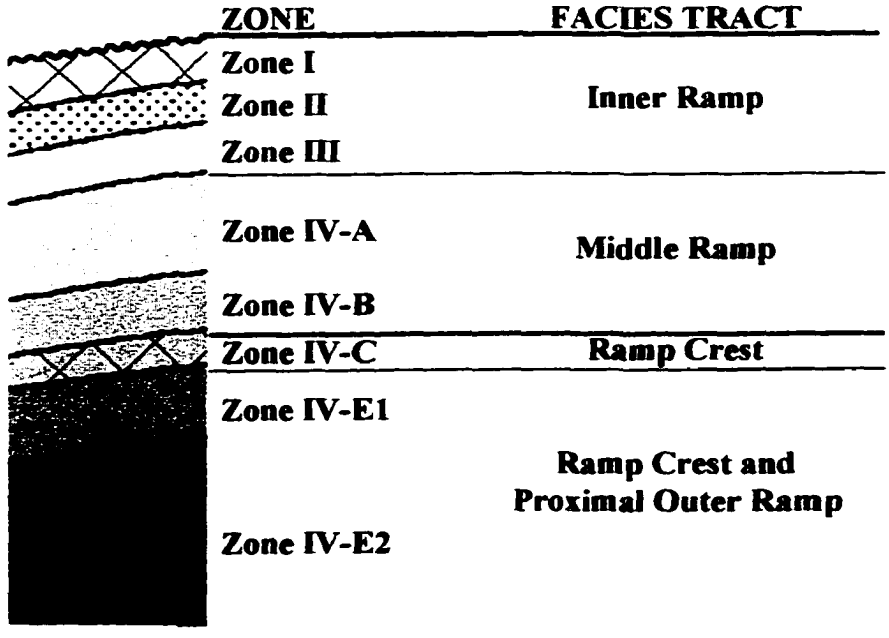

Figure 12. Structure contour maps of reservoir zones within the West Jordan unit. The anticlinal structure is carried upward through all zones within the reservoir. The crest of the anticline occurs along the central eastern margin of the unit. Contour maps for the unit have been rotated 18 degrees to the east to allow for a more uniform grid construction within models. A contour interval of 10 feet is used for all structure contour maps.

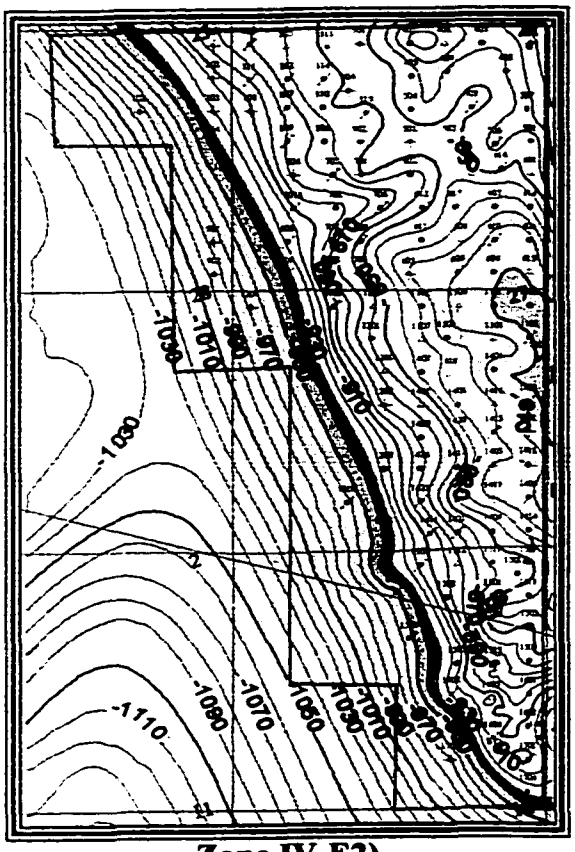

Zone IV-E2)

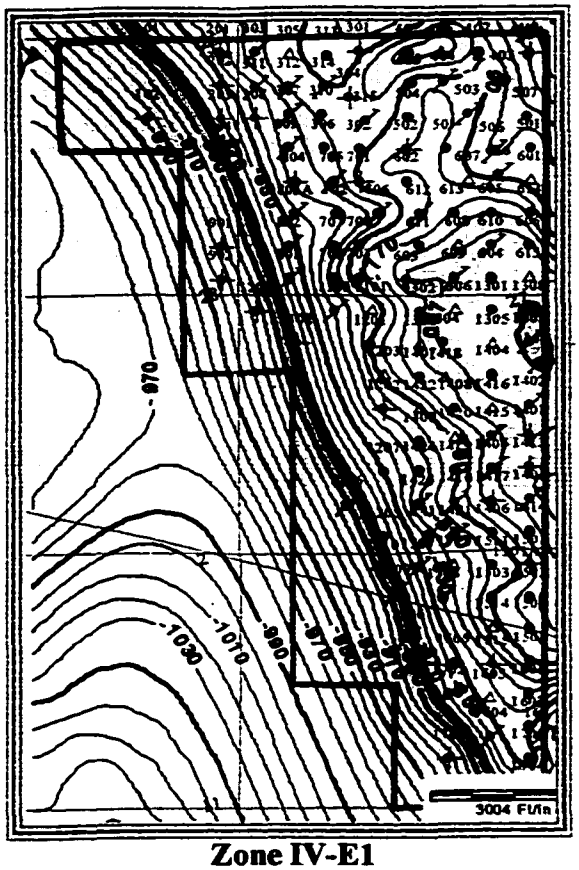

Zone IV-E1

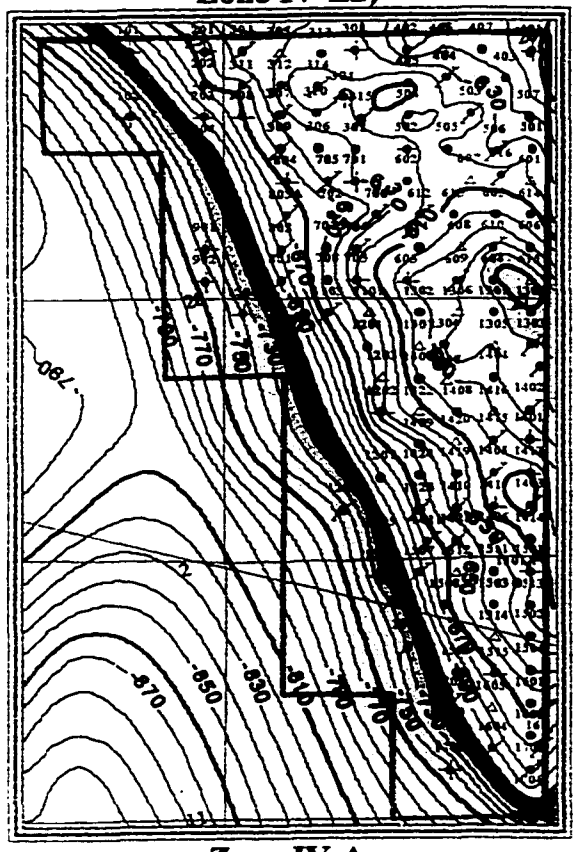

Zone IV-A

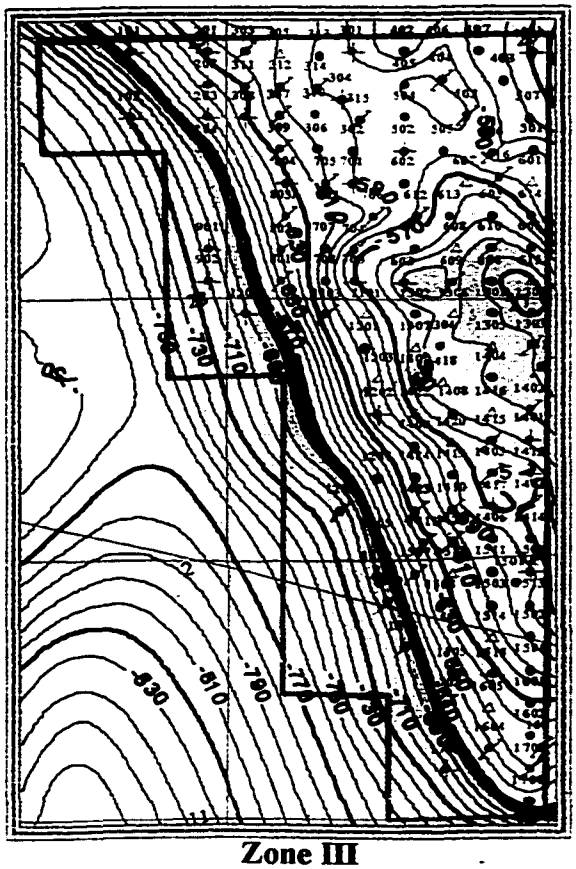

Zone III



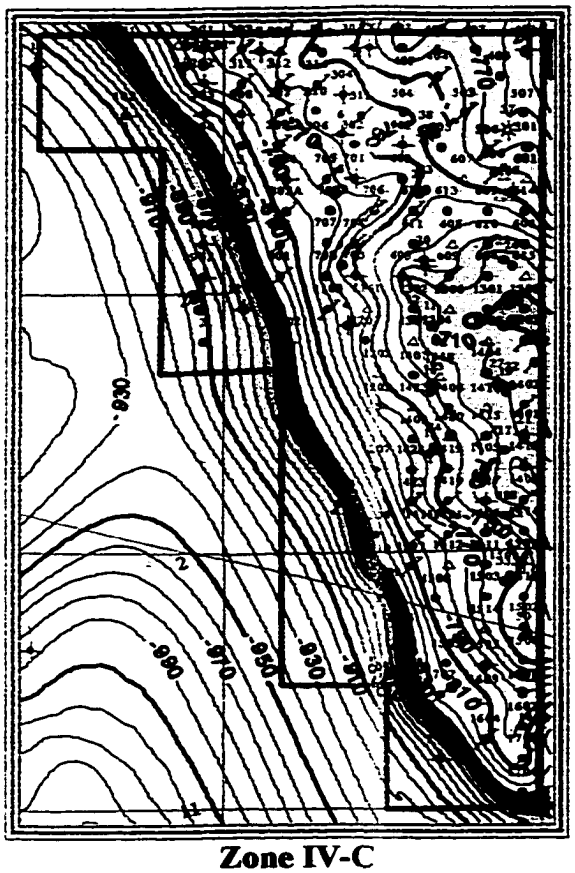

Zone IV-C

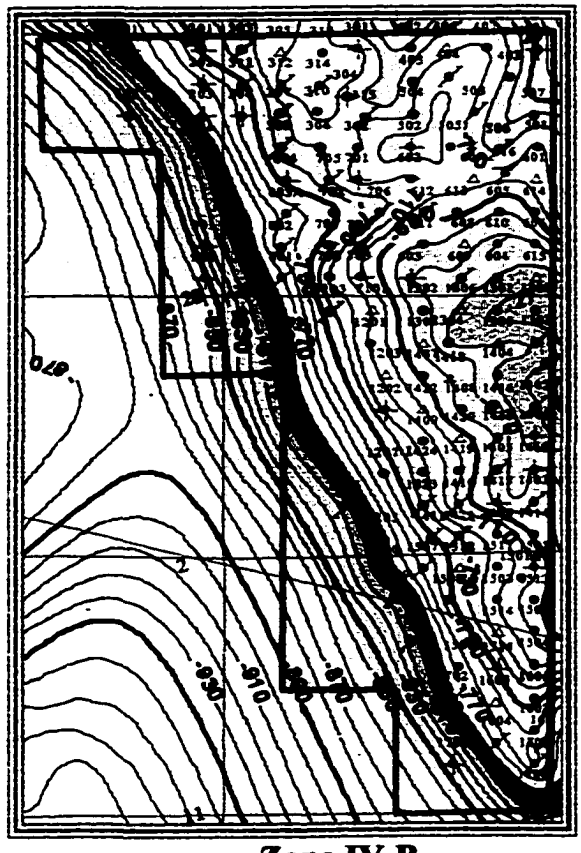

Zone IV-B



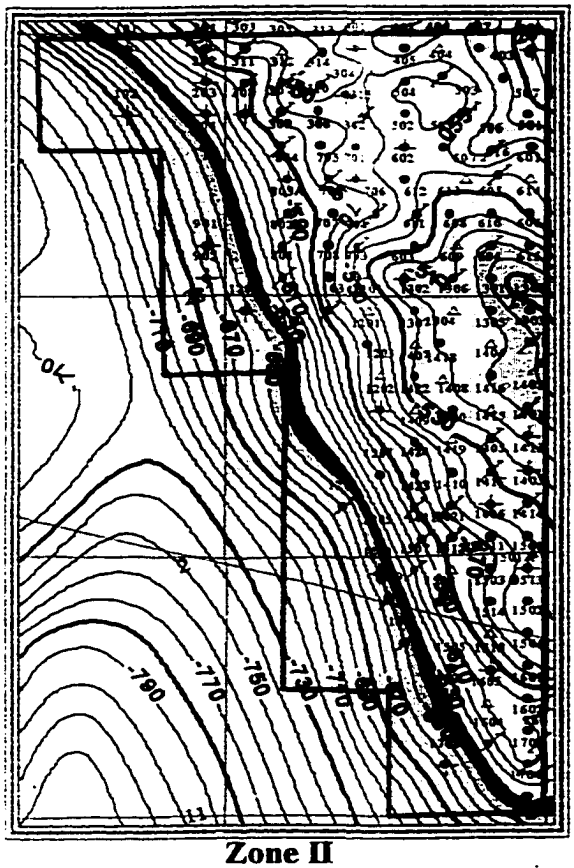

Zone II

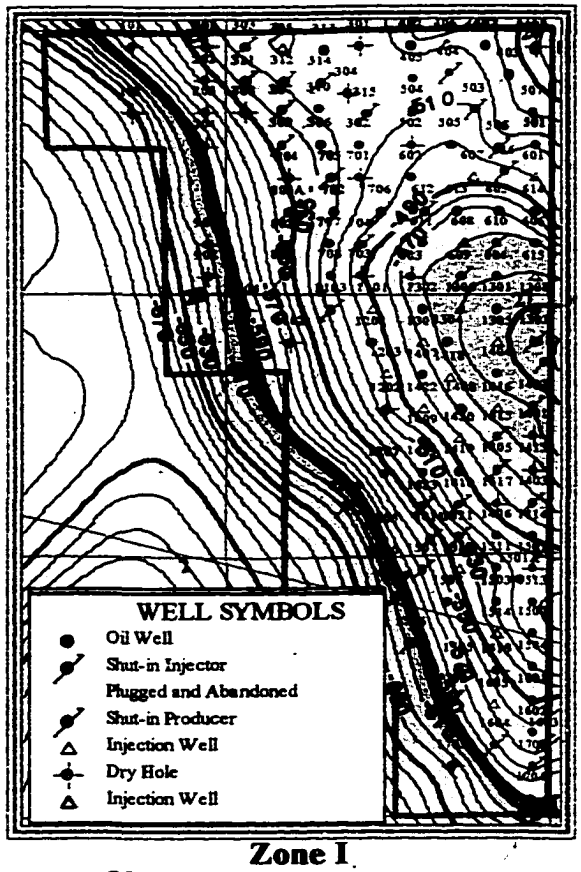

Zone I

the possibility of truncation of paleotopographic highs as the Gaudalupian sea migrated basinward during this time (fig. 13). Thin intervals seen within the upper part of the strata do not correlate directly to the structural high part of the anticline. This suggests that at best present day structure was just beginning to form at this time and zones of thinning are related to paleotopography.

Post San Andres tectonic activity is evident in the nearby McElroy Field. Longacre (1990) described faults with up to 850 feet (260 meters) of displacement in the Grayburg Formation. The McElroy field lies closer to the shelf-edge than the West Jordan unit (fig. 1). Possible down-to-the-basin faults described by Longacre (1990) for McElroy may have also formed east of the West Jordan unit in response to greater differential compaction and sediment loading along a platform hinge-line. Several small faults were observed in cores as evidenced by minor offset (inches) and by slickensides along fault planes, however no significant offset is evident from well-log data.

Deposition of the San Andres at West Jordan unit was influenced by paleotopography that controlled the nature and occurrence of lithofacies. Paleotopography influenced water depth, energy and sediment supply. Shoal bodies formed along paleotopographic highs within the unit. These shoal bodies developed within zone IV-E2 up through the middle of zone IV-C. Paleotopographic highs were most likely slightly influenced by underlying Pennsylvanian structure as the correlation of San Andres producing reservoirs along the eastern margin of the Central Basin platform is coincident with major underlying faults. Nevertheless, no thinning is seen in isopachs across the present day structural high suggesting deposition on a gentle, low dipping ramp where minor paleotopographic highs greatly influenced deposition. This

Figure 13. Isopach maps of reservoir zones within the West Jordan unit. Thicker areas are represented by red and yellow color filled contours and thinner areas are blue-to-green color contours. A contour interval of one foot was used for all maps. Note that predominantly subtidal facies within zones IV-E1 through IV-A are thickest to the north and east in a more basinal direction. Zones I through III are composed of more supratidal facies and as expected are seen to thicken to the west. Stacked shoal bodies are present in zones IV-C through IV-E2 and are reflective of thick intervals seen in isopach maps of zones IV-E1 and IV-C. No isopach map was constructed of zone IV-E2 due to a lack of deep well data penetrating the entire zone. A well-developed lagoon was present during deposition of lithofacies in zones IV-A and IV-B. Isopach maps and core descriptions suggest that this lagoon was present more to the north and east within the unit boundaries. Paleotopographic highs along the southern margin of the unit are believed to have restricted subtidal lagoonal facies to the northeast and favored supratidal deposition to the southwest during this time.

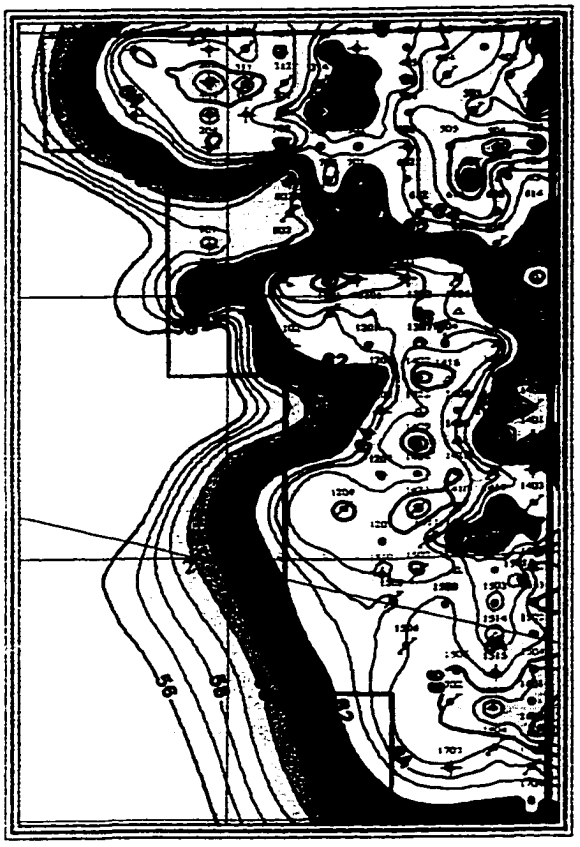

Zone IV-E1

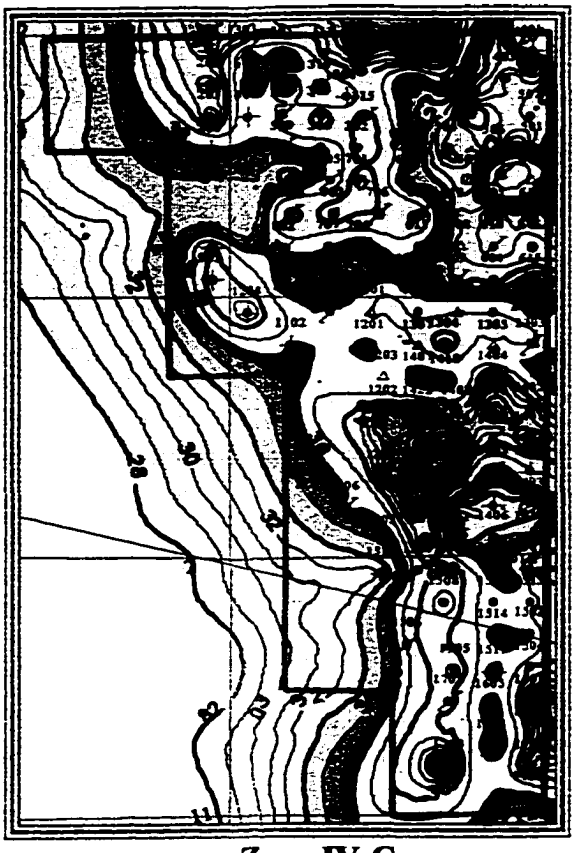

Zone IV-C

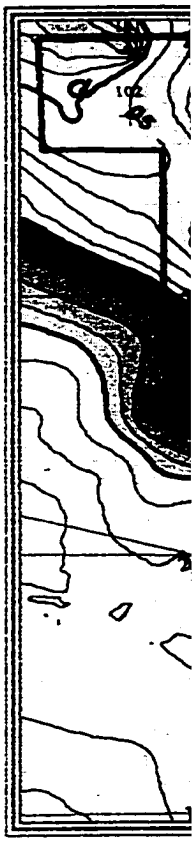



Zone III

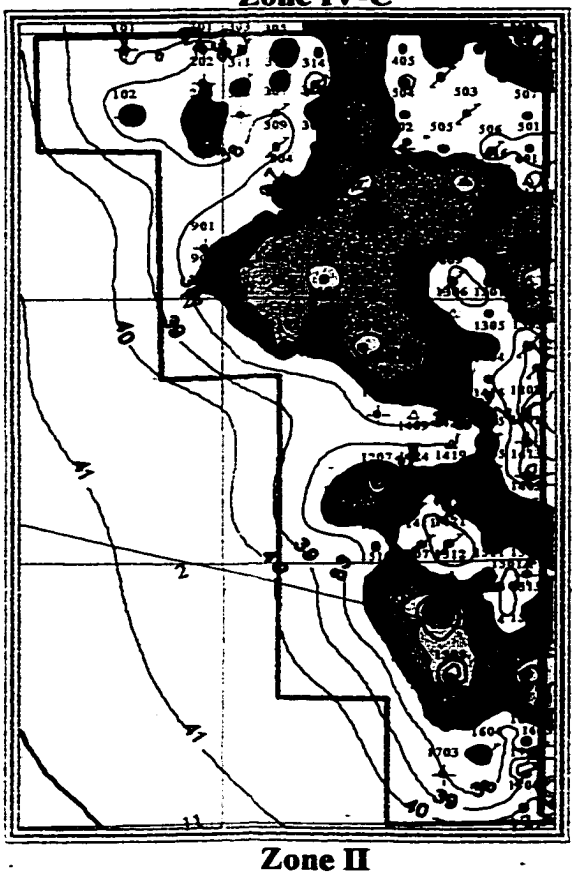

Zone II

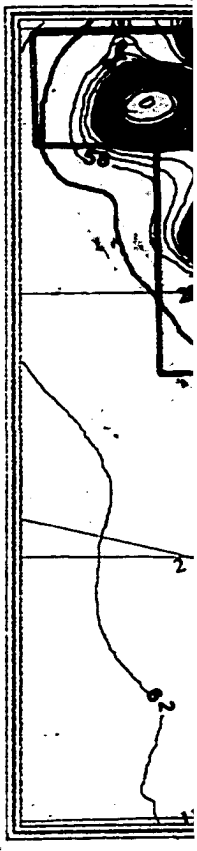



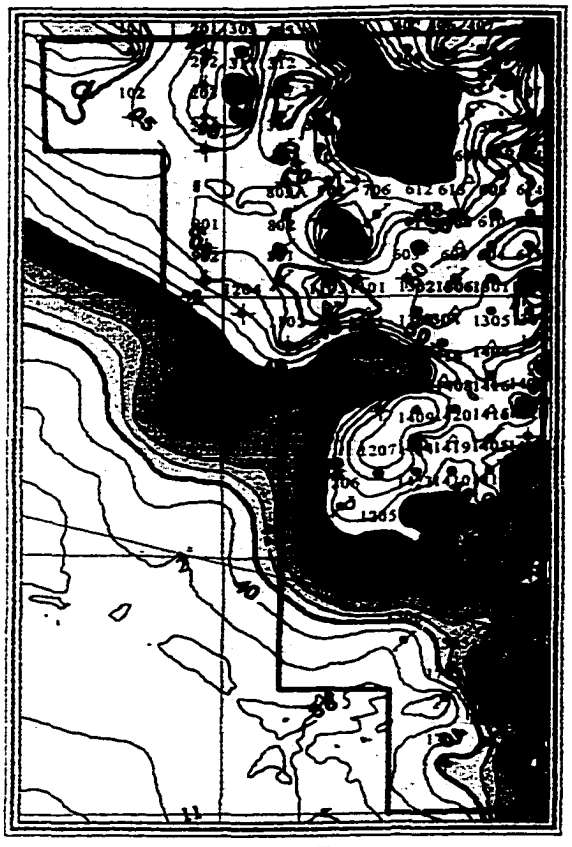

Zone IV-B

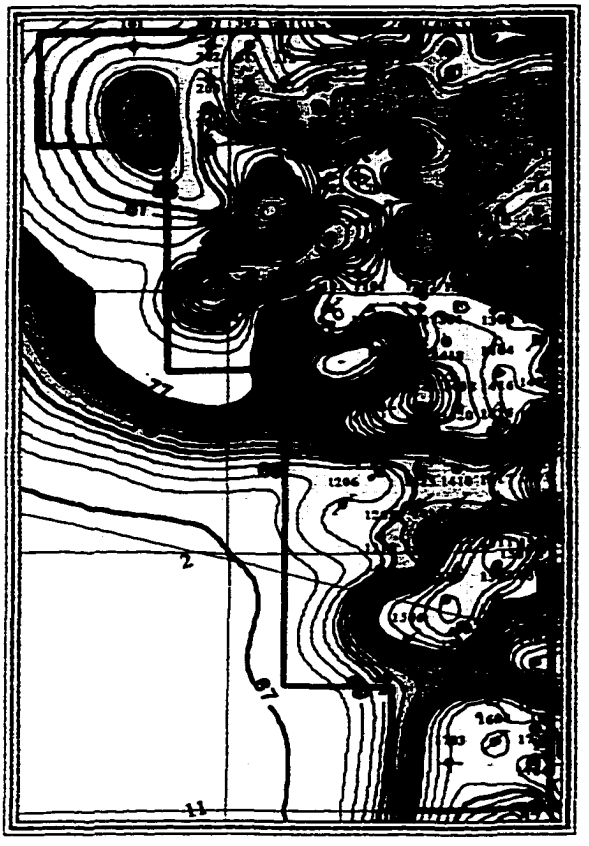

Zone IV-A



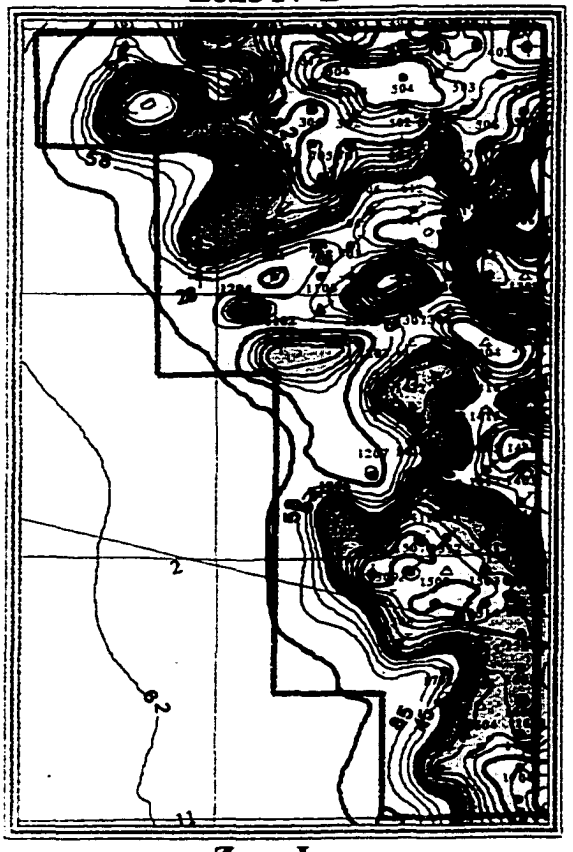

Zone I

WELL SYMBOLS

- Oil Well
- Shut-in Injector
- Plugged and Abandoned
- Shut-in Producer
- Injection Well
- Dry Hole
- Injection Well

may not be true with respect to later diagenesis and porosity formation within the reservoir.

The West Jordan unit carbonate reservoir has been completely dolomitized and detailed core analysis indicates that diagenesis played a key role in porosity development and preservation. Core data and isopach maps (fig. 13) show an increase in thickness of upper San Andres supratidal and tidal flat facies within the southern and western parts of the unit. These facies are found primarily in zones I, II, and III within the reservoir (see Appendix C). Prograding supratidal facies would be expected to show a general thickening to the west because they would be developed to a greater degree in the landward direction. Conversely, zones comprised of mainly subtidal facies (zones IV-E2 through IV-A) are thinner toward the west and thicker to the east and northeast (fig. 13). Overlying San Andres supratidal facies are siliciclastics of the Grayburg Formation. Porosity pinchouts were found to occur within the Grayburg Formation as you move structurally higher toward the anticlinal crest. This suggests that structurally influenced diagenetic processes controlled porosity development within the Grayburg. Isopach maps of the Grayburg Formation show a general northward thickening and a thinning to the west and south similar to subtidal facies within the San Andres Formation.

Maps of porosity feet (PHIH) indicate that solution enhanced porosity within zones IV-E1 and IV-E2 may be related to present-day structural development suggesting a late stage dolomite dissolution event. Widespread solution enhanced porosity is seen throughout cores in the lower portion of the reservoir. PHIH maps show a close relationship between diagenetically controlled solution enhanced porosity trends and present day structure within these lower zones. The greatest solution enhanced porosity

identified from core data was found to occur in an interval approximately 70 feet (21 meters) thick just above the oil-water contact. It is also believed that diagenetic trends follow high permeability facies tracts and that several episodes of sulfate dissolution have occurred within the reservoir. Sulfate dissolution is wide spread in zone II within the upper part of the reservoir as well, although there is no evidence of dolomite dissolution within this upper zone (fig. 11).

Zone intervals or cycle boundaries throughout the unit were based on defining vertical facies successions and facies tracts from detailed core analysis (Appendix B). Cycle boundaries were then carried throughout the unit by correlating gamma ray curve characteristics seen on electric logs from nearby cored wells. The distribution of cores throughout the unit allowed for a high confidence in extrapolating from core to well data even though modern log suites are lacking within the unit. The vast majority of electric log data available is in the form of antiquated gamma ray-neutron count (GNT) electric logs. Various vintages and scale variations required the rescaling of GNT logs. In addition, porosity logs had to be corrected for drift problems and normalized in an effort to compensate for the erroneous porosity values that can result from the presence of gypsum. The methods used for log normalization are described in detail in Appendix A.

Zones II, IV-E1 and IV-E2 are considered the primary flow units within the reservoir as determined from core descriptions and geostatistically based three-dimensional models. Zone IV-A was found to act as a water flood "thief zone" where much of the injection water is channeled through the reservoir resulting in poor contact with the matrix porosity. Although these zones, particularly zone IV-A, contain large volumes of oil in place, this oil not being recovered under current waterflood techniques.

Zones I, III and IV-C are thought to act essentially as flow barriers within the reservoir. Zone I is highly occluded with sulfate cement and provides the seal for the reservoir. Zones III and IV-C contain low permeability clay rich intervals that inhibit the flow of fluids vertically within the reservoir although the exact extent of their ability to transmit fluids is not fully understood. Although thin intervals of pisolite grainstones with well-developed fenestral porosity are found within zone III, they are not believed to be laterally continuous and are contained above and below by the non-permeable clay intervals. In addition, ramp crest dolograinstone facies observed in zone IV-C were also completely occluded with sulfate cement. Both zones I and IV-C represent the culmination of high frequency sequence boundaries and highstand systems tracts (figs. 10 and 11). Sulfate cementation within these zones is believed to be a result of these highstand systems tracts and changing environmental conditions associated with decreasing water depths.

RESERVOIR LITHOFACIES OCCURANCE WITHIN FACIES TRACT DEPOSITIONAL ENVIRONMENTS

Introduction

The San Andres reservoir at West Jordan unit consists of shallow-water carbonate strata that has been completely dolomitized. The formation is comprised of a vertical sequence exhibiting an overall upward shallowing, basinal prograding section including subtidal, intertidal and supratidal facies. These facies are interpreted to have been deposited within a low angle ramp setting. Wide ranges of depositional environments are indicated from core examination, all of which are interpreted to have occurred in water probably less than 80 feet. Depositional environments as determined by facies relationships seen in core data include four facies tract systems; proximal outer ramp, ramp crest, middle ramp and tidal flat (fig. 14). Similar environments have been described for San Andres outcrops along the northwestern shelf (Kerans and Fitchen; 1995). Within each of these broad depositional categories a wide range of lithofacies are combined to form numerous vertical facies successions which range from less than one foot to several feet in vertical extent. In turn, these vertical facies successions are combined together to form cycle boundaries defined within the unit

In order to more closely tie sequence stratigraphic relationships seen within the West Jordan unit to the outcrop, the lithostratigraphic terminology used within this study follows that of Kerans and Fitchen (1995) for their descriptions of San Andres and Grayburg rocks along the Algerita Escarpment and Guadalupe Mountains. In their report, chronostratigraphic units are composed of lithofacies, vertical facies successions, and facies tracts. These lithostratigraphic units reflect deposition in particular regimes of

Figure 14. Generalized depositional model of facies tract systems and related depositional environments within the West Jordan unit. The general association of zones with facies tracts is indicated at the base of the diagram. It should be understood that a considerable amount of overlap and interfingering occurs from one environment into another. Individual vertical facies successions can represent a number of varying environments and yet the overall cycle volumetrically reflects the most significant lithofacies found within cycle boundaries. Outcrop studies (Kerans and Fitchen, 1995) of similar facies stratigraphic architecture and correlations from the West Jordan unit indicate that the dip along the ramp platform would have been less than five degrees and more likely only around 1 to 2 degrees at the most. Approximate water depths for environment of deposition within each facies tract are presented on the right hand side of the diagram. The vertical exaggeration for this diagrammatic model is large and features are not drawn to scale.

GENERALIZED DEPOSITIONAL MODEL

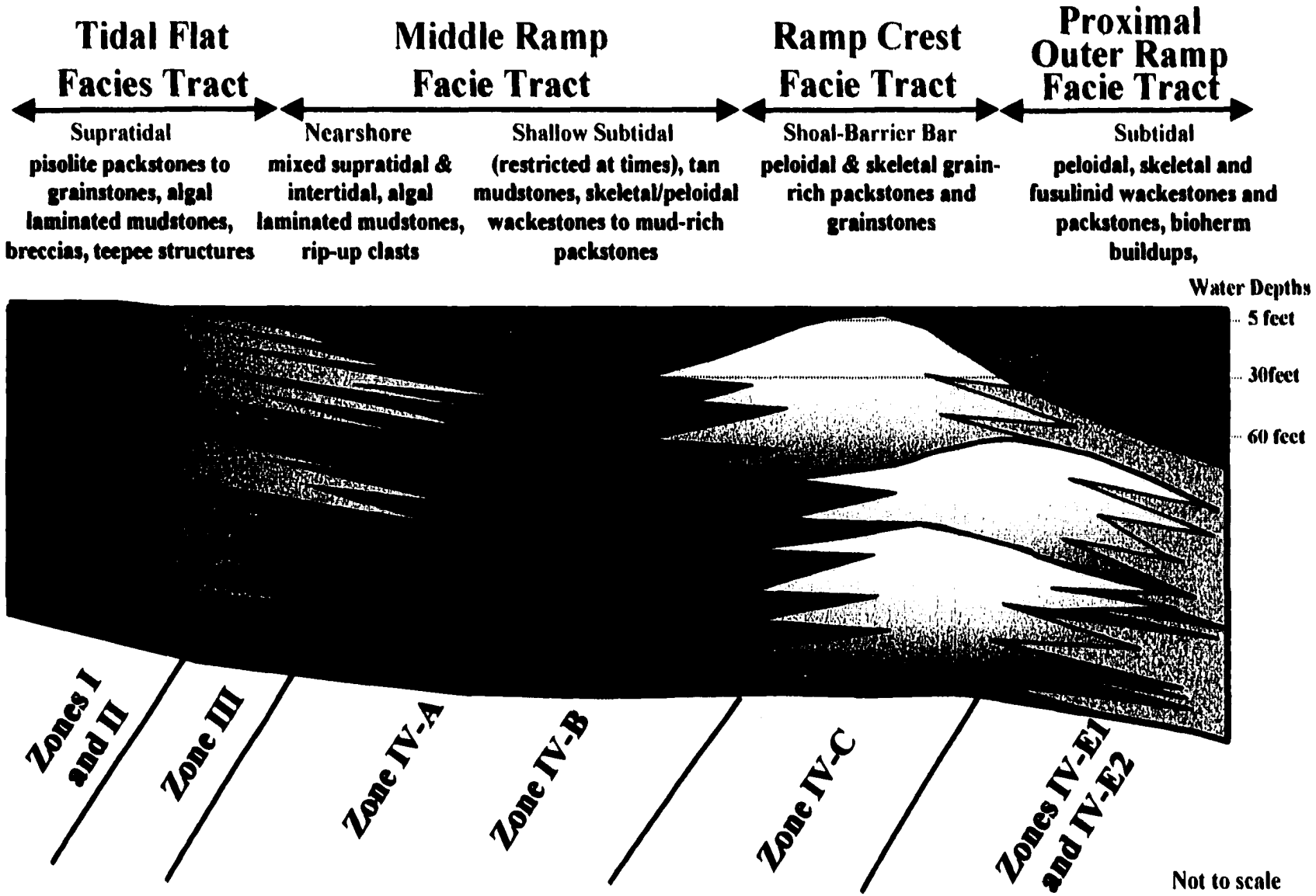

water depth, energy and physiochemical conditions. Lithofacies are defined as the basic descriptive three-dimensional rock element after the classification put forth by Dunham (1962). Vertical facies successions (VFS) record repeated upward shallowing of the carbonate platform as it fills accommodation space created during cycle-scale base level rise. Vertical facies successions that were found within varying depositional environments as described from the Algerita outcrop (Kerans and Fitchen, 1995) were extremely similar to those found within cores at the West Jordan unit. Within ramp crest and proximal outer ramp environments facies tracts were more likely to be composed of one or two lithofacies successions within a cycle. In the middle ramp environment multiple thinner vertical facies successions were common within cycles. Facies tracts are defined as a genetically linked association of lithofacies and vertical lithofacies successions that record a discrete energy/water depth/sediment supply setting (Kerans and Fitchen, 1995). Facies tracts defined within the West Jordan unit are as those described from San Andres outcrops within the carbonate ramp model including middle ramp, ramp crest and outer ramp. Modification to their descriptions include an inner ramp facies tract (nearshore and tidal flat) and the outer ramp facies tract is restricted to proximal outer ramp due to a lack of deeper water subtidal outer ramp facies encountered in cores (fig. 14).

Chronostratigraphic terminology described by Kerans and Fitchen (1995) includes three chronostratigraphically significant temporal and spatial scales including cycles, high frequency sequences (HFS) and composite sequences. Cycles are defined as multiple vertical facies successions that can be mapped across multiple facies tracts. They record the turnaround from base-level fall to base-level rise. The high-frequency sequence is

bounded by base-level-fall to base-level-rise turnarounds. These surfaces are identified on the bases of several components: 1) subaerial unconformities and karstification, 2) a turnaround from progradational to retrogradational cycles, 3) major basinward shifts or offsets in the location of facies tracts across a single surface, and 4) systematic trends in the thickness and facies proportion of cycles or stacking patterns (Kerans and Fitchen, 1995). Where unconformity bounded surfaces are not present high frequency sequences can be recognized by transgressive to highstand systems through the delineation of retrogradational, aggradational, and progradational cycle sets. This is the case at West Jordan unit where two high frequency sequences have been identified (figs. 10 and 11). Composite sequences are composed of sets of high frequency sequences. No composite sequences have been defined within the West Jordan unit due to a lack of data at depth. For further detail on chronostratigraphic and lithostratigraphic terminology the reader is directed to Kerans and Fitchen (1995).

Of the twelve cored wells at West Jordan unit, nine cores were available and described (fig. 9). For detail of core description methodology see Appendix C. From core descriptions and petrographic analysis of hundreds of thin sections, twenty-seven lithofacies were defined for the San Andres reservoir at West Jordan unit (Table 1). These lithofacies are the basic building framework comprising vertical facies successions found within the reservoir on which cycle boundaries are based. Facies indicator logs (FIL) were constructed of wells within the reservoir in order to determine the distribution of these facies within the reservoir model. These will be discussed in the following sections.

Table 1. Table of facies tracts, lithofacies and environments of deposition for West Jordan San Andres strata. Twenty-seven separate lithofacies were described from core analysis and thin sections for four facies tract systems; inner ramp, middle ramp, ramp crest, and proximal outer ramp. The inner ramp facies tract has been further divided into tidal flat and near shore environments. Facies tracts represent deposition further basinward as you move from top to bottom in the table.

Facies	Microfacies	Environment
Tidal Flat to Nearshore	Patterned dolomite	Evaporative restricted lagoon or pond
	Stromatolitic algal dolomudstones	Nearshore intertidal to tidal flat
Near Shore	Medium-pale green dolomudstone	Evaporative restricted lagoon or pond
	Dark green/gray laminated, silty dolomudstone	Middle ramp, restricted lagoon
	Intraclast dolowackestone/packstone	Shallow intertidal to periodically exposed
[redacted]	[redacted]	[redacted]
[redacted]	[redacted]	[redacted]
Open Ramp	Vertically structured, interbedded peloid, skeletal and fusulinid-mollusc dolowackestones-dolopackstones	Shallow open marine; possibly an indicator of the culmination of a highstand prior to basinal progradation
	Fusulinid dolopackstone / grainstone	Calm, open marine waters, subtidal
	Fusulinid dolowackestone / packstone	Calm, open marine waters, subtidal
	Bryozoan, sponge, algal baffiestones	Calm, open marine waters, subtidal
	Bryozoan, sponge, algal wackestone, dolopackstone, and grainstones	Calm, open marine waters, subtidal
	Wispy, argillaceous dolomudstone / wackestone	Calm, open marine waters, subtidal

Environments of deposition for lithofacies are based on grain constituents such as: allochem type (peloidal, skeletal, etc.); carbonate fabric, sedimentary structures and bedding after Dunham (1962). This classification encompasses mud versus grain supported textures including dolomudstone, dolowackestone, dolopackstone and dolograinstones; grain size and sorting; and the vertical relationship and occurrence of lithofacies within the reservoir with respect to each other. The following section provides a description of each of the primary lithofacies found within the West Jordan unit and broad depositional environments in which they are interpreted of being deposited.

Proximal Outer Ramp Facies Tract

Primary facies found within the subtidal, proximal outer ramp environment are peloidal dolowackestones to grain-dominated dolopackstones; fusulinid dolowackestones to mud-rich dolopackstones; crinoidal; vertically structured; and bioherm/reef facies. Peloidal dolowackestones to dolopackstones are the most common lithofacies within the proximal outer ramp environment. The fusulinid lithofacies are the second most common lithofacies observed from core data. Less commonly occurring are crinoidal dolowackestones and scattered bioherm facies consisting of sponge, algae, and bryozoan boundstones. Thin siliciclastic clay-rich intervals that are also common within the proximal outer ramp facies tract and have been interpreted as minor marine flooding surfaces often occurring at the base of vertical facies successions. Skeletal grains (mollusk, brachiopods, crinoids, etc.) occur as scattered grains within the primary

peloidal lithofacies and were therefore not seen to be a separate lithofacies prevalent within the outer ramp environment.

Proximal outer ramp subtidal facies are volumetrically more dominant within zones IV-E1 and IV-E2 and decrease as you move upward to HST 1 within the reservoir (fig. 10). Vertical facies successions within these lower zones (zones IV-C through IV-E2) consist volumetrically of more proximal outer ramp, deeper water lithofacies at the base of the cycle with a higher volume of shallow water ramp crest facies at the top of each cycle boundary (fig. 10). Similar lithofacies seen higher within the section are interpreted as being deposited within the middle ramp environment based on the vertical assemblage of lithofacies and criteria listed above. A lack of dolomudstones within zones IV-E1 and IV-E2 suggests deposition in the proximal outer ramp versus distal outer ramp where more dolomudstone facies should be present (see Kerans and Fitchen, 1995; fig. 7 for a summary of outer ramp environments described from outcrops of the San Andres Formation).

Vertically structured facies are also common within the outer ramp setting. This lithofacies does not represent any particular grain type (fusulinid, peloidal, etc.) but instead is the result of selective diagenetic alteration of localized porosity zones related to burrowing (Ruppel and Cander, 1988; Leary and Vogt, 1990; Major, et al, 1990; and Caldwell, et al, 1998). Production along the Central Basin platform has been attributed to "vertically structured" or "altered" texture and is included here as a separate lithofacies. The occurrence of this facies within cores has been documented throughout the unit because of its association to production in nearby reservoirs.

Sedimentary structures that are commonly associated with subtidal proximal outer ramp lithofacies include small stylolites, anhydrite nodules, burrows, and wispy carbonaceous clay intervals. Porosity is primarily from solution enhanced intercrystalline pores where original grain fabrics have undergone severe recrystallization.

Peloid Dolowackestone-Packstone Facies

Peloidal lithofacies are the most dominant lithofacies within the West Jordan unit. Due to the extreme dolomitization which has taken place in San Andres rocks within the unit no textural features have been identified to define these grains with certainty (fig. 15). It is also difficult to determine whether the fabric is dolowackestone, dolopackstone or dolograinstone in areas where complete recrystallization has resulted in only faint ghosts of the original grains being preserved. The peloid lithofacies is extremely variable in size, sorting and texture (fig. 15). Grain size ranges from less than one tenth of a millimeter to several millimeters in diameter and this lithofacies is usually poorly sorted.

Both pellet and ooid lithofacies have been described for similar San Andres reservoirs nearby (Leary and Vogt, 1990; Major, et al; 1990). Knowing the origin of the peloids would certainly enhance the accuracy of placing these lithofacies within their proper depositional environment, an important element in determining vertical facies succession within cycle boundaries. Ooid grains are deposited within moderate-to-high energy shallow waters whereas, pellets are usually formed in low-to-moderate energy regimes. Overall, the peloid lithofacies was placed in relatively quite, low-to-moderate energy regimes where the lithofacies is determined to be a dolowackestone or mud-rich dolopackstone and high energy when the facies was found to be grain-dominated.

Figure 15. Core photographs and photomicrographs of subtidal peloid lithofacies

A) Core photograph of peloidal grain-dominated dolopackstone-grainstone facies. Porosity and permeability for this sample is 18 percent and 42 millidarcies respectively (core photograph from WJU #3-10; 3538 feet).

B) Core photomicrograph of a typical peloidal packstone. Note that individual fabric is difficult to determine due to the degree of recrystallization that has occurred within this sample (core from WJU #1419; 3646.9 feet; magnification 32X).

C) Photomicrograph of peloidal grain-dominated dolopackstone to grainstone facies. Note the poorly preserved circular grain (red arrow) that has been leached within its interior. These grain-dominated fabrics are difficult to see in highly magnified thin sections and virtually impossible to identify visually in core samples. Grain-dominated solution enhanced peloidal fabrics like this example are common in zones IV-E1 and IV-E2. Porosity for this sample is approximately 17 percent and permeability was measured to be 2.4 millidarcies (core from WJU #505; 3670.5 feet; magnification 50X).

D) Close up of photomicrograph seen in C (magnification 100X).

E) Photomicrograph of a peloidal dolopackstone with excellent porosity and permeability development. Solution enhanced porosity has removed sulfate cement and enlarged intercrystalline areas improving porosity within this sample (core from WJU #505; 3614.3 feet; magnification 50X).

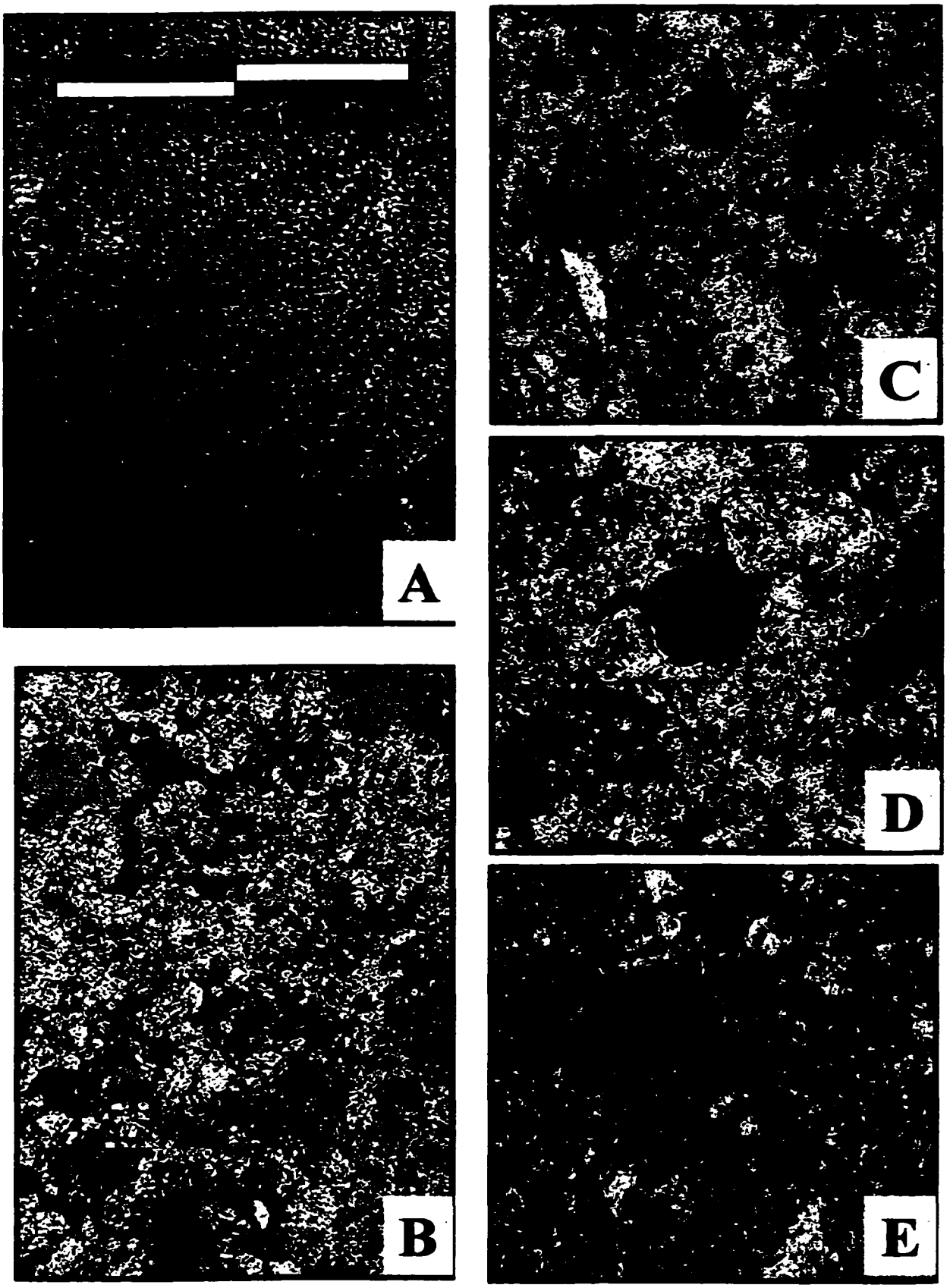
A
B
C
D
E

Facies indicator logs (FIL) show that the peloid lithofacies occurs most commonly in zones IV-E1 through IV-C where it is the primary grain component within compartmentalized shoal bodies (fig. 16). This facies was found from core data to be the most significant reservoir facies within the unit, particularly within lower zones where solution enhancement of porosity has occurred within shoal facies. Peloid lithofacies were found to a lesser degree in the middle ramp environment. Within the middle ramp these facies exhibit lower porosity and permeability values.

Fusulinid Dolowackestone-Packstone Facies

Fusulinid facies were found from core to occur in thin zones ranging in thickness from several inches up to eight feet (fig. 17). This lithofacies was observed primarily in the lower subtidal zones. The occurrence of this facies is significantly less than observed by other workers for nearby units suggesting shallower water depths for West Jordan than seen within the adjacent Jordan University and East Penwell units (Major, et al, 1990, East Penwell San Andres Unit; Holtz and Major, 1994, Jordan University Unit). This is consistent with the position of the West Jordan unit farther landward on the shelf (fig. 7). Fusulinid grains are often a component found within grain-dominated shoal facies.

Within the study area fusulinid facies occur most often in dolowackestones and mud-rich dolopackstones (fig. 18). These facies are indicative of open, normal marine waters and have been related to both middle ramp (Bebout, et al, 1987; Major, et al, 1990; and Ruppel, 1990) and outer ramp environments below fair-weather wave base (Longacre, 1980, 1990). Kerans and Fitchen (1995) place fusulinid dolowackestone-dolopackstones within a proximal outer ramp environment based on

Figure 16. Cross section of facies indicator logs showing the occurrence of peloidal and shoal facies. Facies indicator logs were created for all described cores and are represented by the color log fill in track two on the log curves. Most shoal facies are comprised primarily of peloid grains and therefore both peloidal and shoal facies are indicated in color fill in this cross section. Porosity and permeability in the lower section of the reservoir is enhanced by dissolution of dolomite and sulfate cements. Peloidal facies, particularly within shoals occurring in zones IV-E1 and IV-E2 are the most productive facies within the reservoir. Vertical facies successions within the West Jordan unit are very similar to facies tract characteristics described by Kerans and Fitchen (1996) in outcrops within the Guadalupe Mountains. Peloidal shoal bodies within the reservoir were found to be substantially compartmentalized lacking both lateral and vertical continuity.

Shoal - Peloidal and skeletal grain-dominated dolopackstones and grainstones

Fusulinid - Fusulinid dolowackestones/packstones.

Peloidal - Peloidal dolowackestone to mud-rich packstones.

Skeletal - Dolowackestone/packstones.

Vertically Structured- Distinct vertically oriented mottling due to porosity variation.

Reefal/Bioherm - Bryozoan-sponge-algal boundstones and dolowackestone/packstones.

Intraclasts- Facies indicates reworking in high energy to exposed depositional regime.

Pisolite - Dolopackstones/grainstones with characteristic fenestral porosity.

Dolomudstone - Calm water of the middle ramp, near-shore and tidal flat environments.

Siliciclastic - Fine grained quartz-rich coarse grained to silt size particles.

Clay - Green to dark black, fine grained, found within the middle ramp and tidal flat deposits.

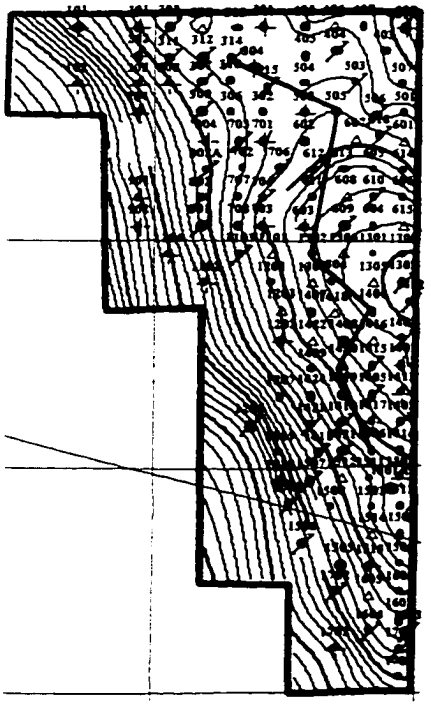

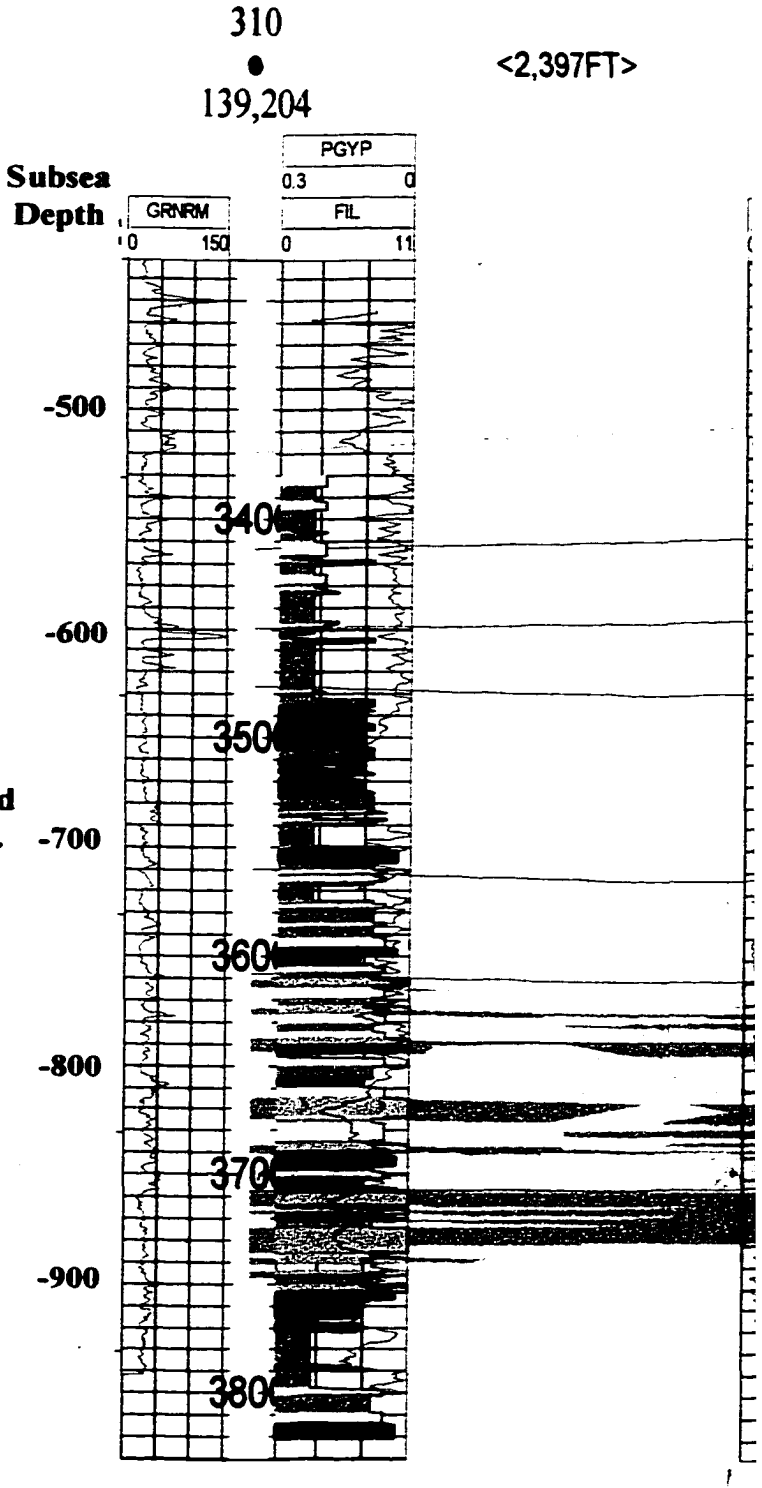

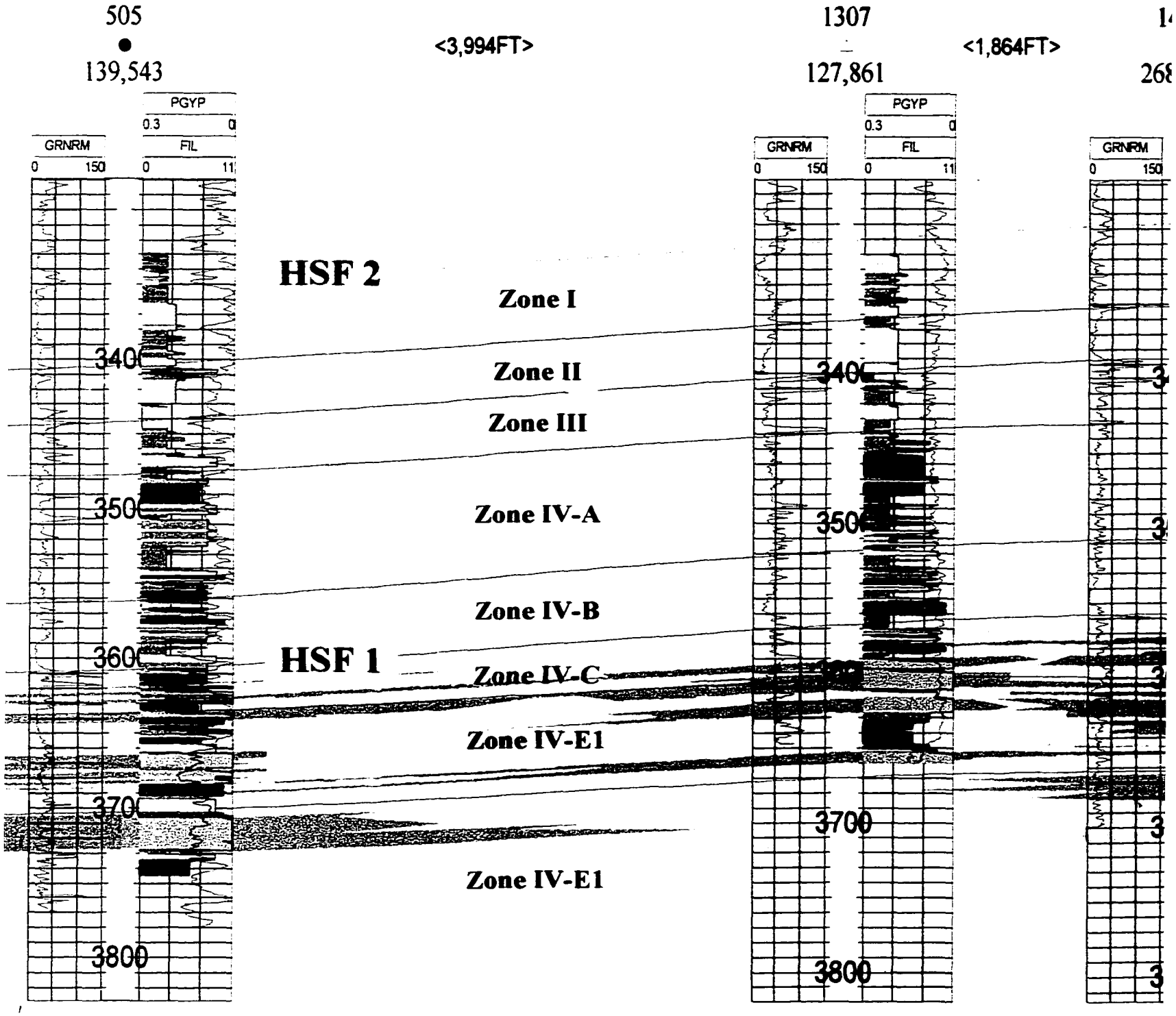
505
139,543
<3,994FT>
1307
127,861
<1,864FT>
PGYP
0.3
0
GRNRM
FIL
0
150
0
11
HSF 2
Zone I
Zone II
Zone III
Zone IV-A
Zone IV-B
HSF 1
Zone IV-C
Zone IV-E1
Zone IV-E1
3400
3500
3600
3700
3800

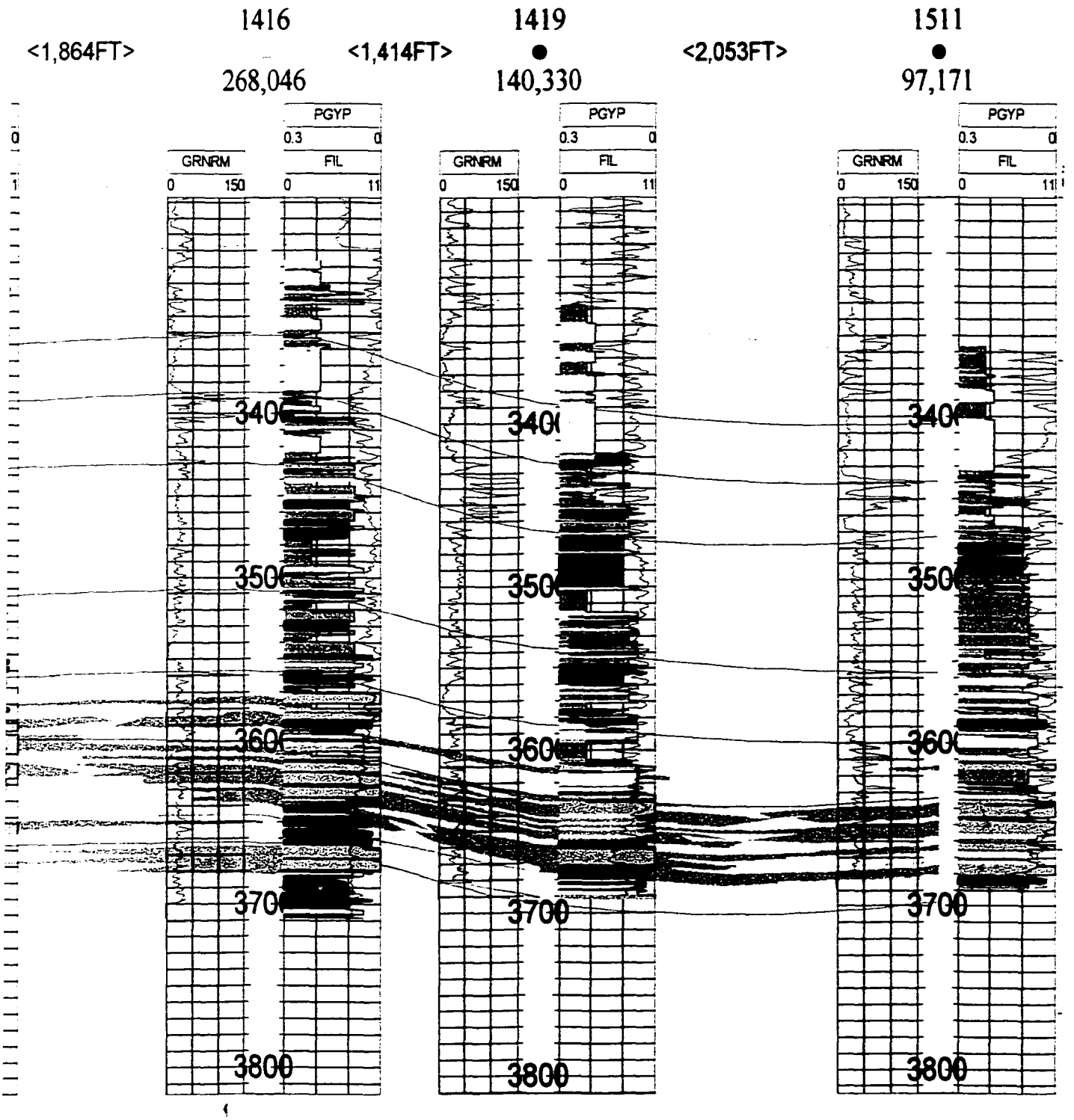
1416
<1,864FT>
268,046
1419
<1,414FT>
140,330
1511
<2,053FT>
97,171
PGYP
0.3
0
GRNRM
FIL
0
150
0
11
3400
3500
3600
3700
3800

Figure 17. Core photograph of fusulinid and peloid lithofacies. Thin fusulinid beds ranging from several inches to several feet are commonly interbedded with peloidal facies within the lower subtidal zones of the reservoir (zones IV-E2 and IV-E1). These facies are interpreted as being deposited in quite, open marine waters below fair-weather wave base. Thin intervals that exhibit lineation of grains are storm deposits. These intervals are typically less than three inches (eight centimeters).

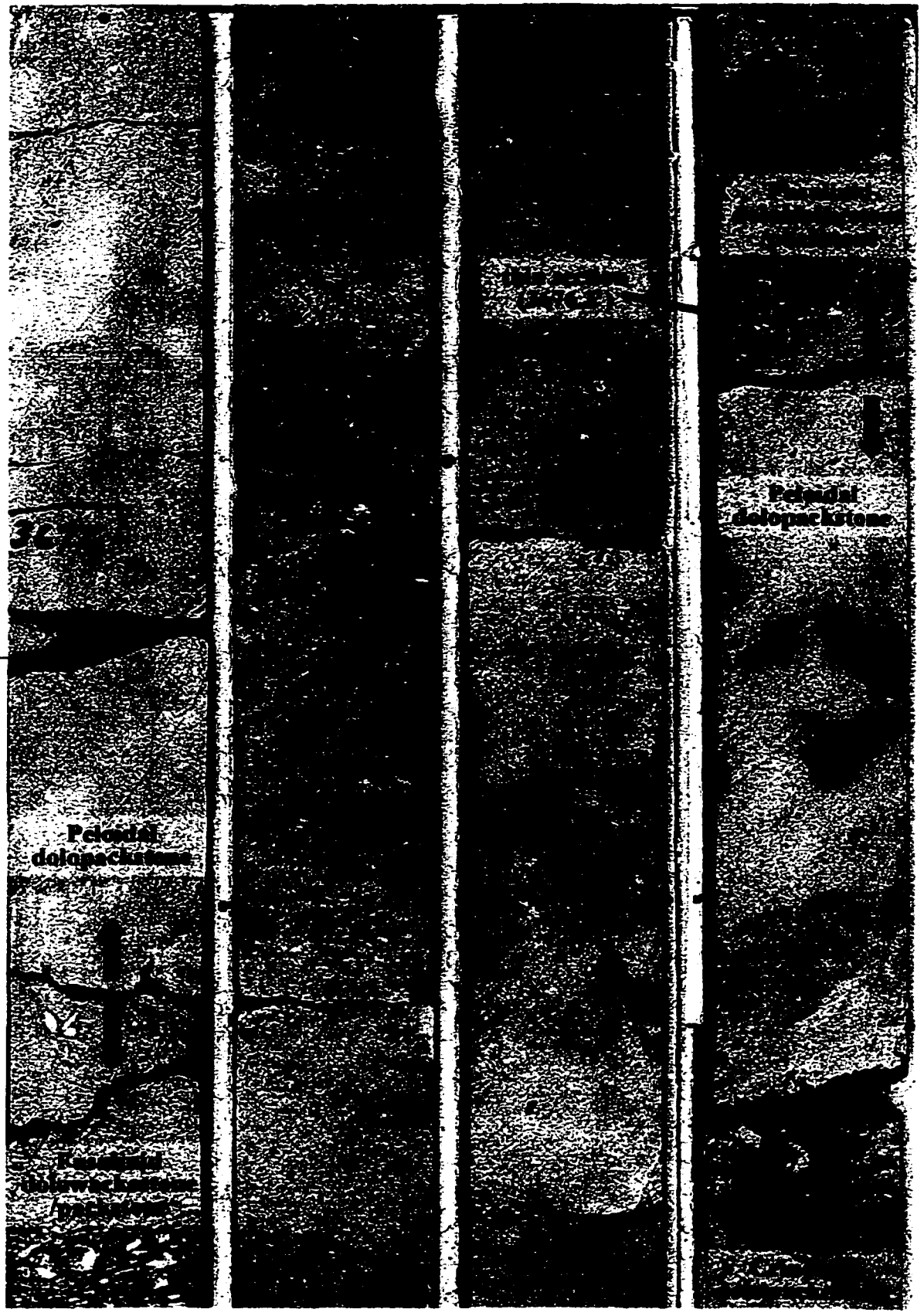
Pelagial
dolopsekstone
Pelagial
dolopsekstone

Figure 18. Core photographs and photomicrographs of subtidal fusulinid lithofacies. This facies was not found to be productive within the West Jordan unit although it has been found to be significant reservoir rock in nearby fields. In these fields fusumoldic porosity is well developed in grain-dominated facies and solution enhancement has increased the matrix porosity connecting fusumoldic pores.

A) Core photograph of a fusulinid wackestone to mud-rich packstone. Fusulinid grains are indicated by black arrows. (core photograph from WJU #505; 3601 feet).

B) Photomicrograph of fusulinid grains in a mud-rich dolopackstone. Intraparticle porosity is a common occurrence in fusulinid grains although it does not significantly increase permeability within the rock (core from WJU #1416; 3664 feet; magnification 6.3X).

C) Photomicrograph of fusulinid dolowackestone. Note the presence of intraparticle porosity within fusulinid grains and intercrystalline porosity with the dolomite matrix of the rock. The fusulinid grain located in the upper left-hand corner of the photomicrograph has been almost completely removed. Fusumoldic porosity, where voids are created by the complete removal skeletal grains is also a common occurrence within this facies (core from WJU #1416; 3661 feet; magnification 10X).

D) Photomicrograph of a fusulinid grain-dominated packstone facies (core from WJU #1419; 3676.2 feet; magnification 16X).

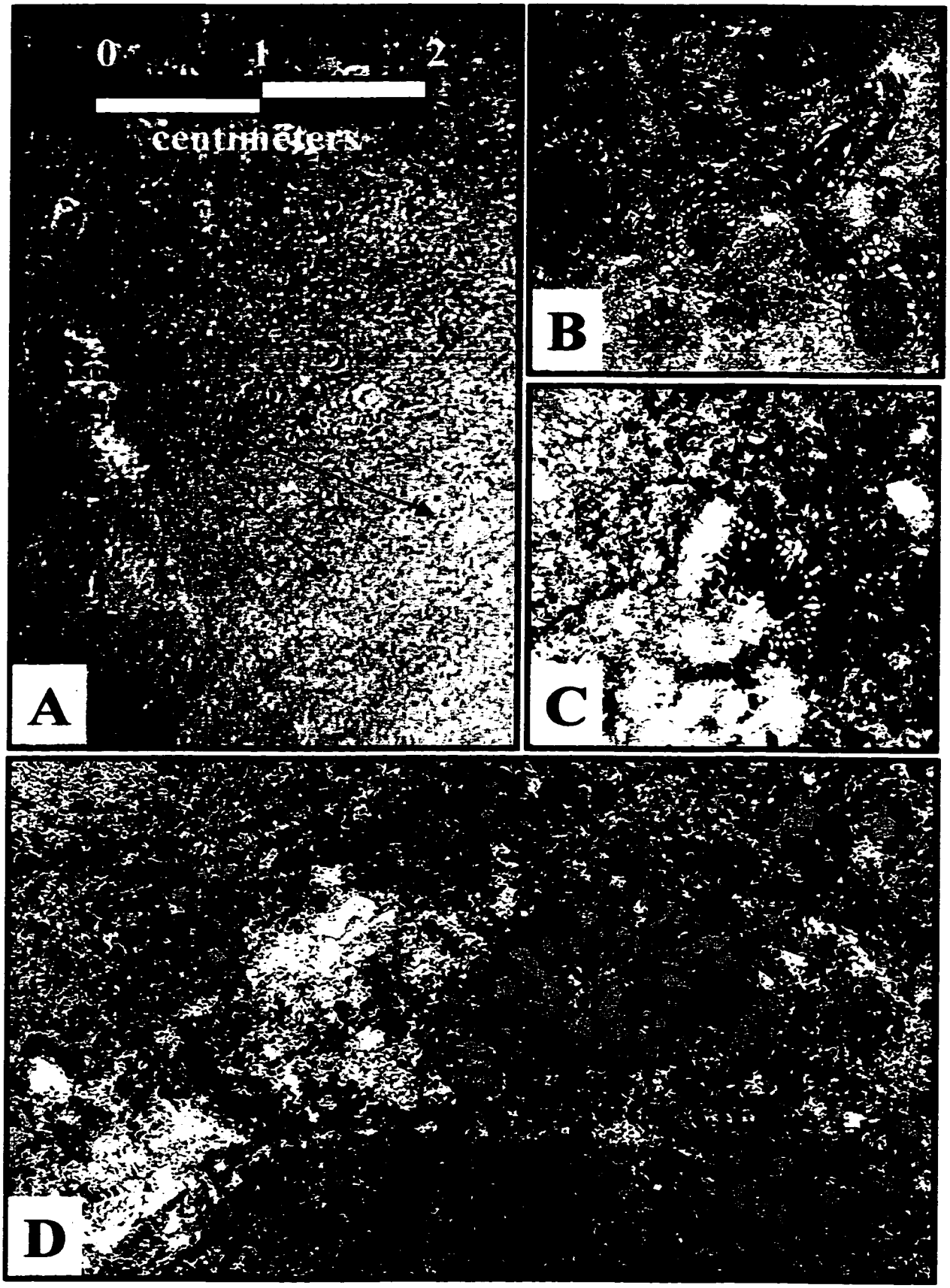
0
1
2
centimeters
A
B
C
D

detailed outcrop correlations from the Guadalupe mountain area. Within the West Jordan unit these facies are found primarily within zones IV-E1 and IV-E2, extending upward into the lowermost part of zone IV-A (fig. 19). Within zones IV-E2 and IV-E1 they are found to occur with alternating intervals of other outer ramp facies such as bryozoan sponge dolowackestones and dolopackstones suggesting deposition within the proximal part of the outer ramp setting. Fusulinid dolowackestones observed in conjunction with ramp crest and middle ramp deposits are believed to be the result of washover deposits where fusulinid grains are brought over ramp crests shoals and transported in tidal channels during unusually high tides and storm occurrences. In many instances an alignment of grains in thin lenses suggests deposition in moderate to high current regimes produced by storms.

Porosity in this lithofacies is usually poor, restricted to intraparticle porosity occurring within fusulinid grains and minor intercrystalline porosity occurring within the mud matrix. On occasion, in zones IV-E1 and IV-E2, fusulinid grains can be completely removed by leaching leaving fusumoldic porosity. Where this porosity is also accompanied by solution enhanced intercrystalline porosity it can result in excellent reservoir rock.

Crinoidal Facies (Wispy Laminated Dolowackestone)

Crinoidal lithofacies were common within the reservoir, nevertheless they were usually found to occur as subsidiary grains within peloidal lithofacies. Although their occurrence was documented on core description charts, they were not broken out into a

Figure 19. Cross section of facies indicator logs showing occurrence of fusulinid lithofacies within the reservoir. Fusulinid lithofacies are found primarily within zones IV-E2 through IV-C. Thin fusulinid intervals were also observed within zones IV-B through the base of zone IV-A. Fusulinid intervals were found to occur in varying thickness and locations within cycle boundaries suggesting that although they are common in the reservoir they do not appear to be laterally continuous, widespread deposits.

Shoal - Peloidal and skeletal grain-dominated dolopackstones and grainstones

Fusulinid - Fusulinid dolowackestones/packstones.

Peloidal - Peloidal dolowackestone to mud-rich packstones.

Skeletal - Dolowackestone/packstones.

Vertically Structured- Distinct vertically oriented mottling due to porosity variation.

Reefal/Bioherm - Bryozoan-sponge-algal boundstones and dolowackestone/packstones.

Intraclasts- Facies indicates reworking in high energy to exposed depositional regime.

Pisolite - Dolopackstones/grainstones with characteristic fenestral porosity.

Dolomudstone - Calm water of the middle ramp, near-shore and tidal flat environments.

Siliciclastic - Fine grained quartz-rich coarse grained to silt size particles.

Clay - Green to dark black, fine grained, found within the middle ramp and tidal flat deposits.

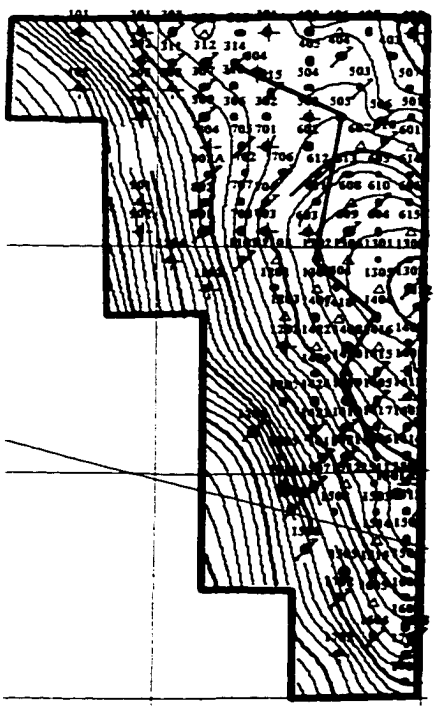

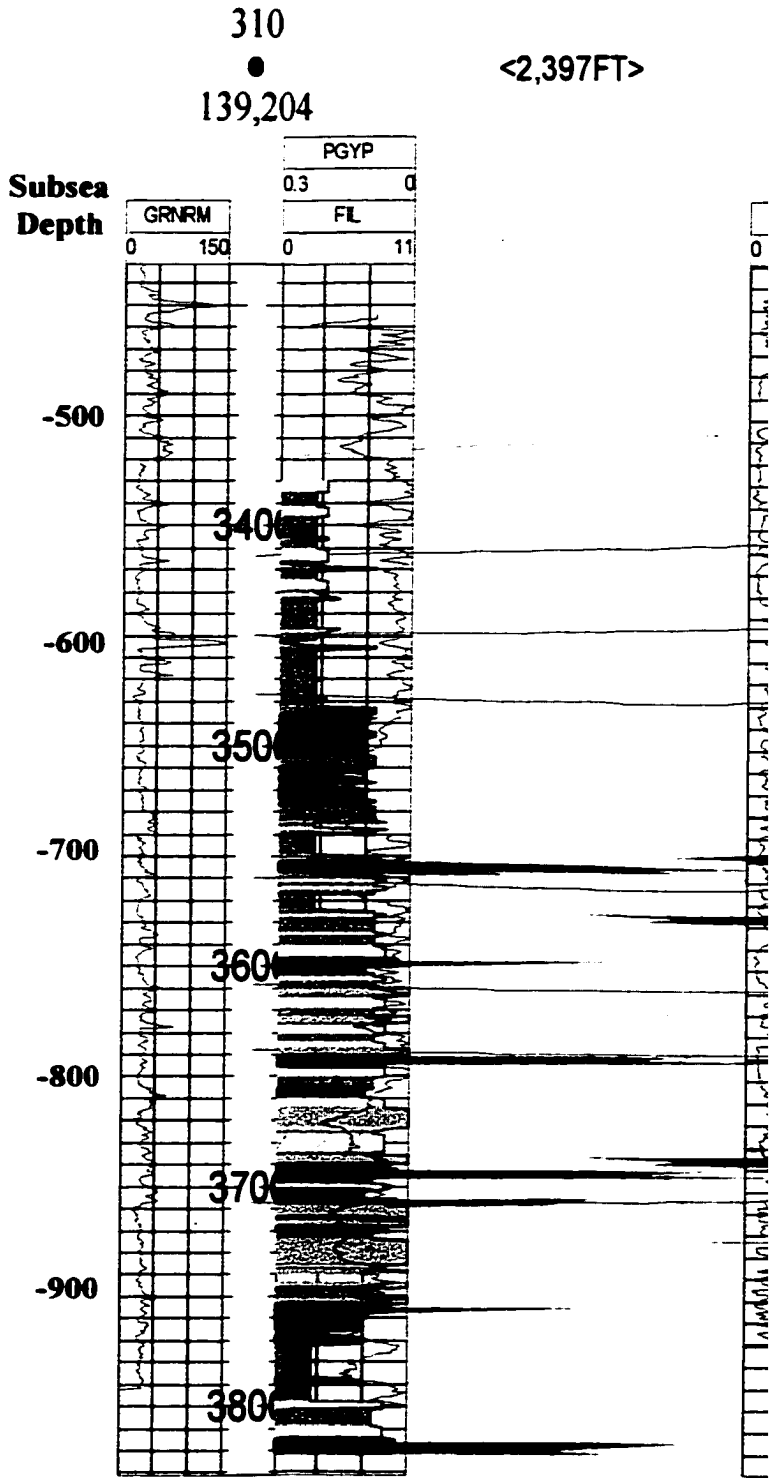

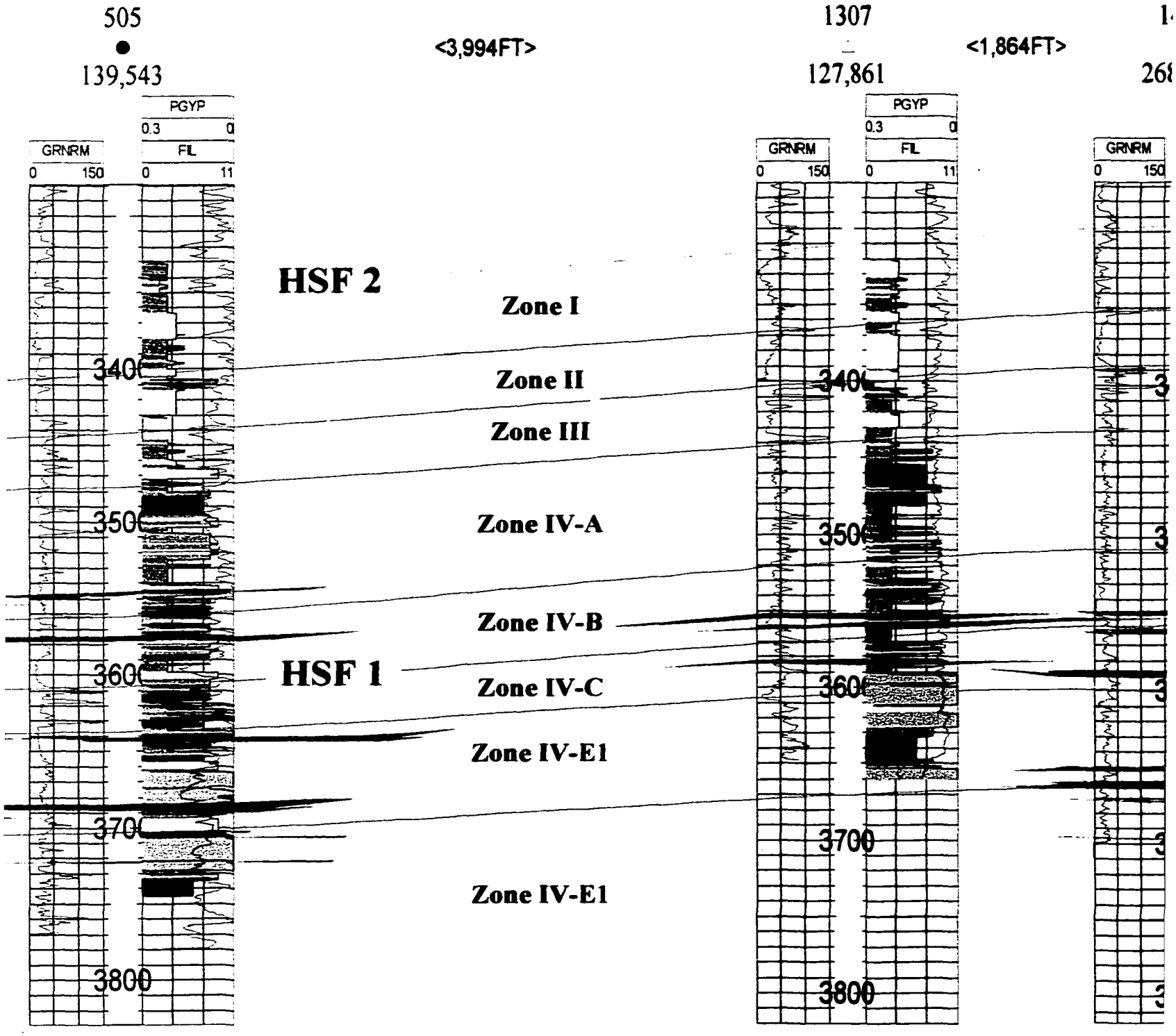
505
139,543
<3,994FT>
1307
127,861
<1,864FT>
PGYP
0.3
0
GRNRM
0
150
FIL
0
11
HSF 2
HSF 1
Zone I
Zone II
Zone III
Zone IV-A
Zone IV-B
Zone IV-C
Zone IV-E1
Zone IV-E1
3400
3500
3600
3700
3800

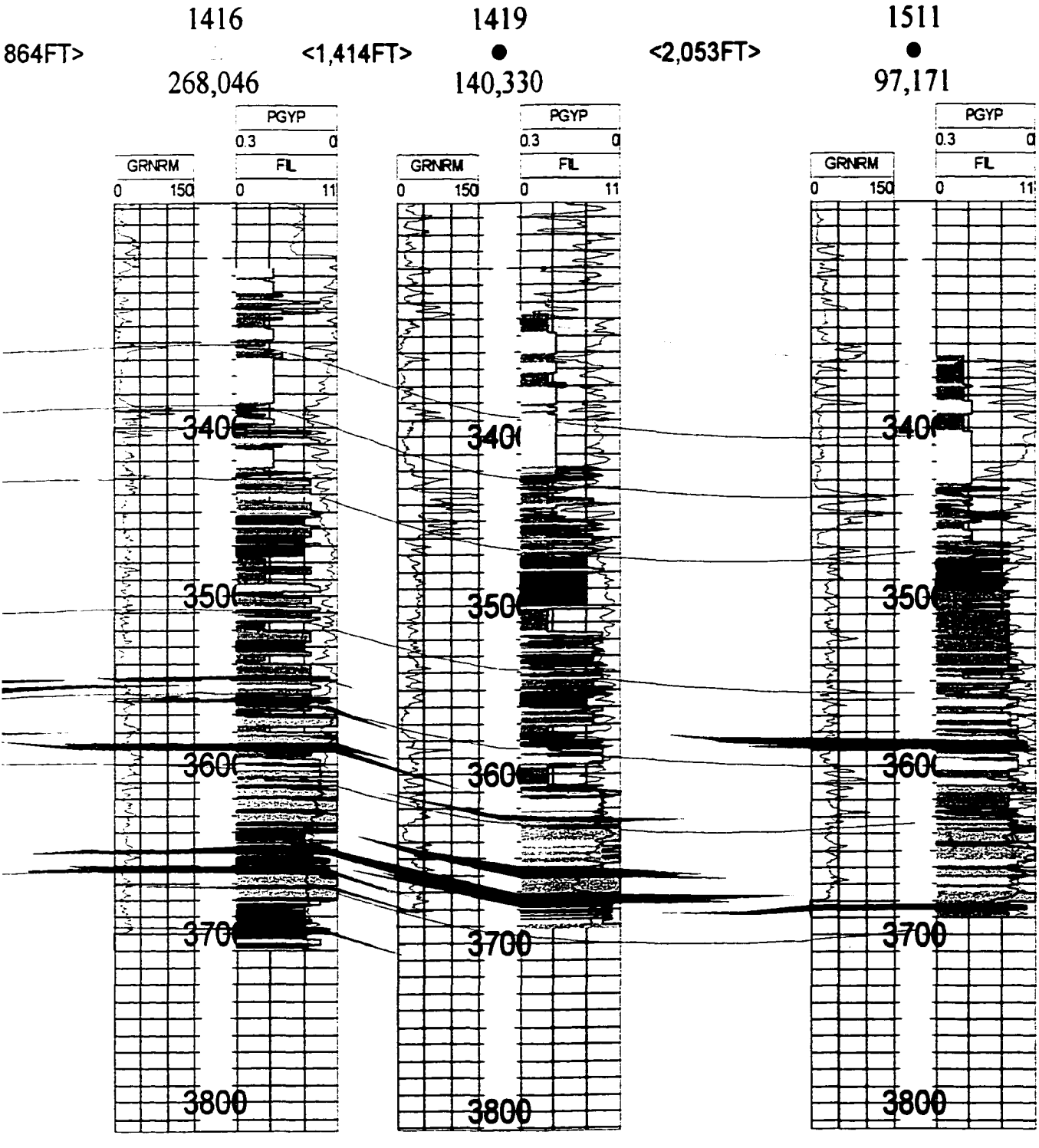
1416
864FT>
268,046
1419
<1,414FT>
140,330
1511
<2,053FT>
97,171
PGYP
0.3
0
GRNRM
FIL
0
150
0
11
3400
3500
3600
3700
3800

separate lithofacies for log and mapping purposes. Crinoid fragments occur from zones IV-E2 up into zone IV-A, encompassing both outer and middle ramp environments.

From core data the crinoidal lithofacies was seen to occur only within dolowackestone fabrics and commonly associated with clay and organic matter forming a wispy, laminated texture (fig. 20). Their occurrence within mud-rich rocks and association with peloid grains suggests calm, open marine waters. The presence of crinoidal lithofacies within the middle ramp environment as well as subtidal outer ramp environments is not unusual as crinoids have been found in water depths varying from shallow to moderately deep (Majewske, 1974). In nearby areas this lithofacies is productive. Within the Grayburg Formation to the south in Dune field, this facies is a good reservoir rock with permeability values in excess of 100 millidarcies (Lucia, et al 1990). This lithofacies does not contribute to reservoir flow properties within the West Jordan unit as seen from core data.

"Vertically Structured" Facies

Vertically structured facies exhibit a distinct vertically oriented mottling due to porosity variation believed to be the result of intense vertical burrowing within strata (Longacre, 1980, McElroy field; Bebout et al, 1987, Dune field; Ruppel and Cander, 1988a, Emma field; Major, et al, 1990, East Penwell Unit; Leary and Vogt, 1990, Seminole field; Ruppel and Lucia, 1998, South Cowden field; and Caldwell, et al, 1998, South Cowden field). These rocks typically exhibit gray-to-tan vertical mottling, which in thin section show significant porosity variations (fig. 21). Porosity variations have been interpreted to be the result of burrowing within mud-dominated facies, where burrows are

Figure 20. Core photographs and photomicrographs of crinoid lithofacies. This lithofacies was not found to be associated with productive intervals within the reservoir and occurs in mud-rich dolowackestones.

A) Core photograph of crinoidal lithofacies from WJU #505 core. Although crinoid fragments are common within the reservoir they usually occur within the peloidal dolowackestone facies.

B) Core photograph of crinoidal dolowackestone showing crinoid columnals and plates (core photograph from WJU #1307; 3638.3 feet).

C) Photomicrograph showing scattered crinoidal fragments and minor moldic porosity (core from WJU #1416; 3533.8 feet; magnification 10X).

D) Close up of C above showing a cross section through a well preserved crinoid ossicle. The original crinoid material has been almost completely replaced with anhydrite cement (magnification 50X).

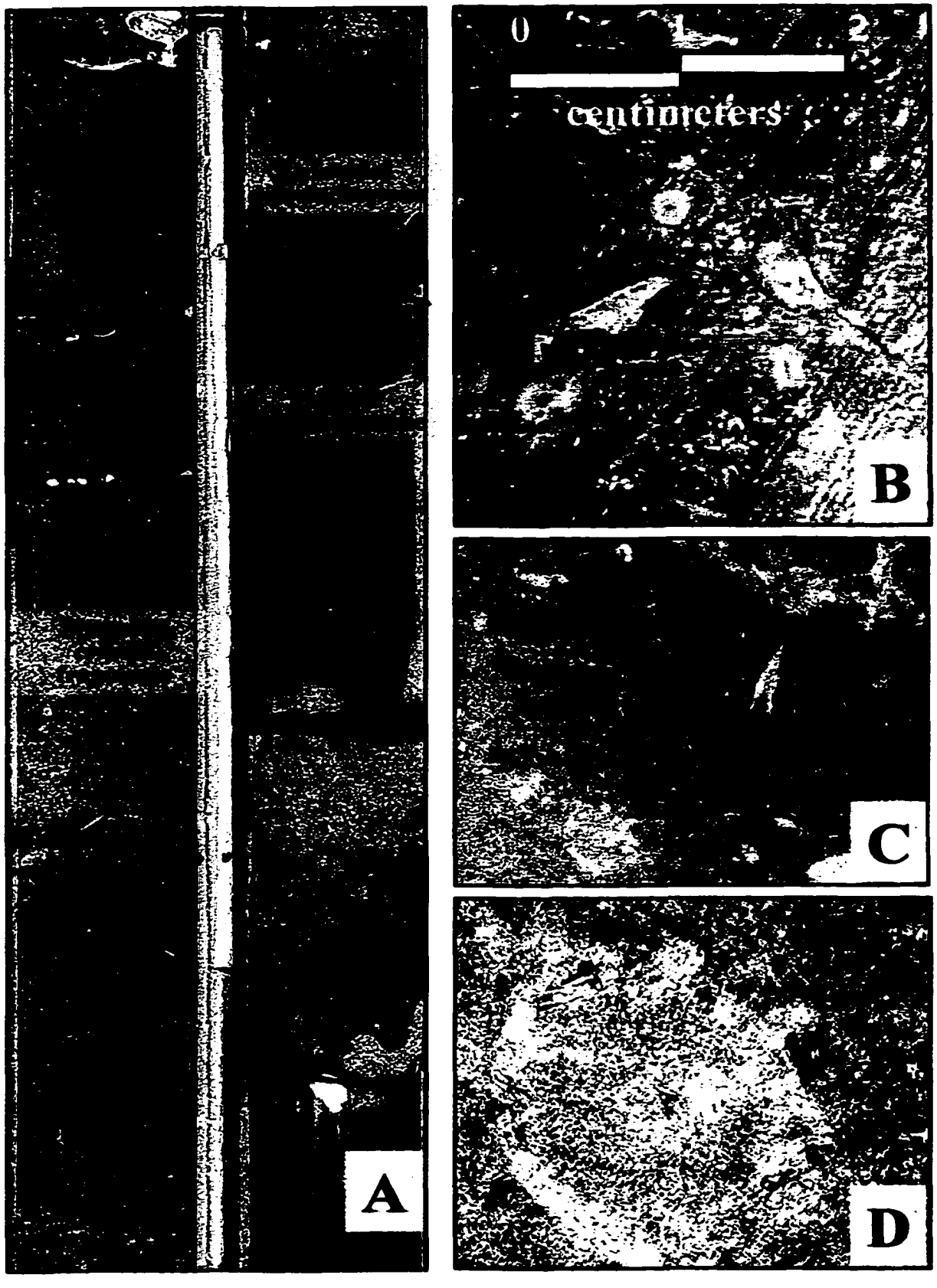
0
1
2
centimeters
A
B
C
D

Figure 21. Core photographs and photomicrographs of vertically structured lithofacies. This fabric is particularly prevalent at the top of zone IV-A and is believed to be the result of intense burrowing of organisms in response to shallowing water conditions and progradation of supratidal facies across the unit during the end of highstand system tract 2.

A) Core photograph from the WJU #310 core showing the vertical mottled texture characteristic of the vertically structured facies (depth of core is 3525 feet).

B) Close up of core photograph illustrating the noticeable contrast in porosity seen within the vertically structured facies (core photograph from WJU #505; 3660 feet).

C) Photomicrograph of a thin section again illustrating the noticeable variation of porosity within the vertically structured facies (WJU #505; 3670.5 feet; magnification 6.3X).

D) Close up of thin section photomicrograph above (magnification 32X).

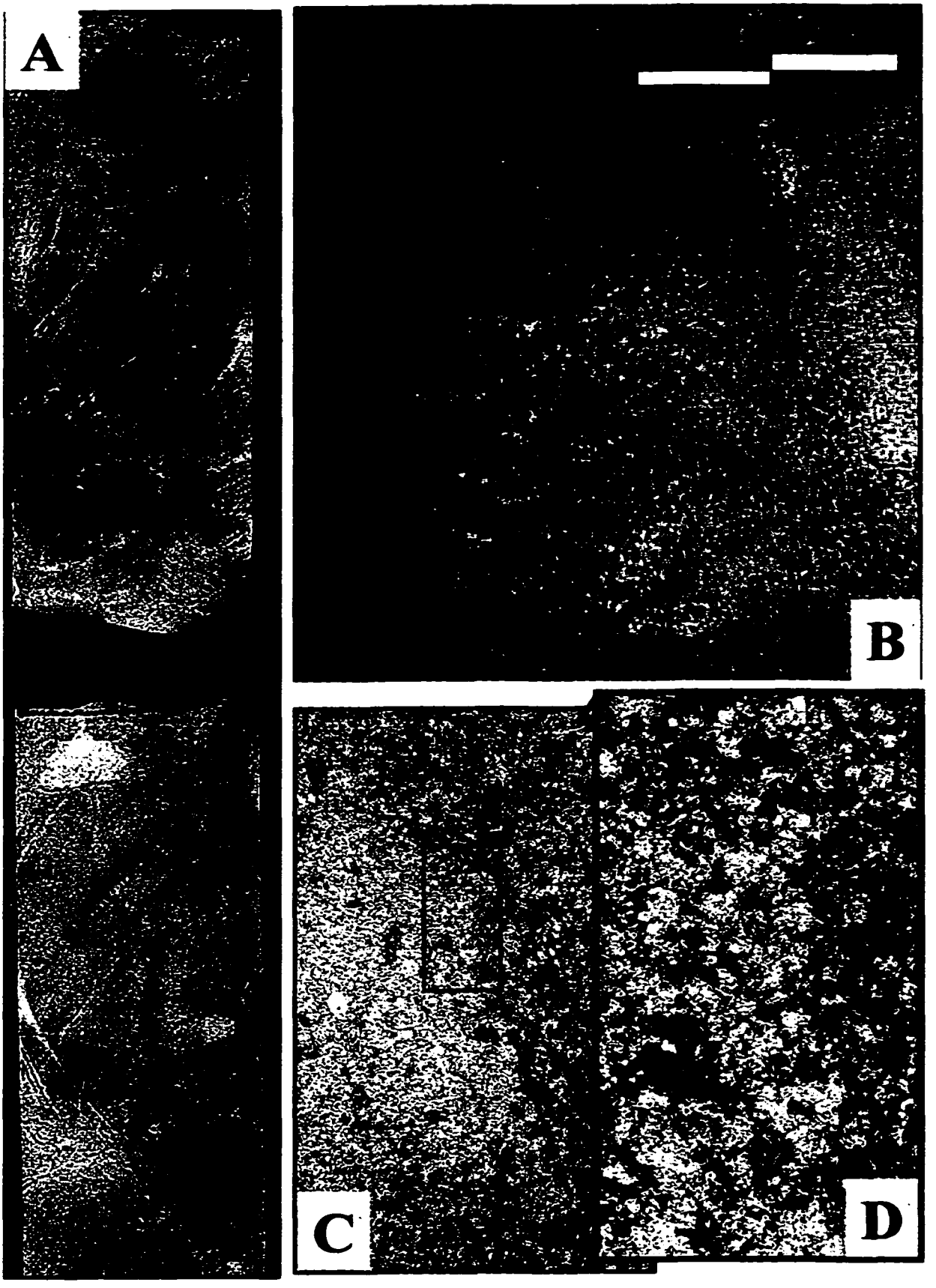
A
B
C
D

filled with coarser material and later diagenesis results in the coarser infilled areas to be more completely "altered" further increasing permeability (Ruppell, 1990; Major, et al, 1990; Ruppel and Lucia, 1998). The altered dolomite has been found to have porosity values twice that of the unaltered part of the rock and permeability values an order of magnitude greater (Ruppel and Lucia, 1998).

This texture was not found to be facies dependent within West Jordan unit and was observed in skeletal, fusulinid, and peloidal dolowackestones to mud-rich dolopackstones. Several different interpretations for the depositional environment of vertically structured facies exist ranging from an exposed flat (Longacre, 1990) to a shallow subtidal platform (Leary and Vogt, 1990). Ruppel and Lucia (1998) have interpreted these vertically mottled zones, which they term "altered", to have been deposited in largely restricted to highly cyclic, mud-dominated, inner-ramp highstand facies. If such a relationship can be established this would help to define cycle tops within many San Andres reservoirs along the Central Basin platform. Caldwell, et al (1998), suggests a depositional environment in subtidal marine waters, landward of the platform-crest oolite shoals, where the burrow-mottled dolopackstones record the initial phases of marine transgression. Within the unit this lithofacies was found to occur in two primary areas. The most substantial occurrence was seen just below the top of zone IV-A and was observed in all cores at this position (fig. 22). The top of zone IV-A is within the uppermost middle ramp environment where multiple, thin vertical facies successions are common. This position marks the end of shallow lagoonal deposition prior to prograding tidal flat facies tracts moving basinward of the area and the end of subtidal deposition within HST 2, supporting the conclusion of Ruppel and Lucia (1998).

Figure 22. Cross section of facies indicator logs showing the occurrence of vertically structured facies. Vertically structured lithofacies are found within subtidal proximal outer ramp and middle ramp environments. Porosity is much greater where solution enhancement of porosity and permeability has occurred. Note the interval below the top of zone IV-A that appears to be correlative in all cores. This marks the end of shallow marine deposition prior to migration of supratidal facies across the unit where burrowing organisms were responding to quickly changing water depths and environmental conditions during HST 2. This facies is also prevalent in HST 1 just below shallow water ramp crest facies tracts and is believed to be an indicator of rapidly changing water conditions (depth, salinity, etc...).

Shoal - Peloidal and skeletal grain-dominated dolopackstones and grainstones

Fusulinid - Fusulinid dolowackestones/packstones.

Peloidal - Peloidal dolowackestone to mud-rich packstones.

Skeletal - Dolowackestone/packstones.

Vertically Structured- Distinct vertically oriented mottling due to porosity variation.

Reefal/Bioherm - Bryozoan-sponge-algal boundstones and dolowackestone/packstones.

Intraclasts- Facies indicates reworking in high energy to exposed depositional regime.

Pisolite - Dolopackstones/grainstones with characteristic fenestral porosity.

Dolomudstone - Calm water of the middle ramp, near-shore and tidal flat environments.

Siliciclastic - Fine grained quartz-rich coarse grained to silt size particles.

Clay - Green to dark black, fine grained, found within the middle ramp and tidal flat deposits.

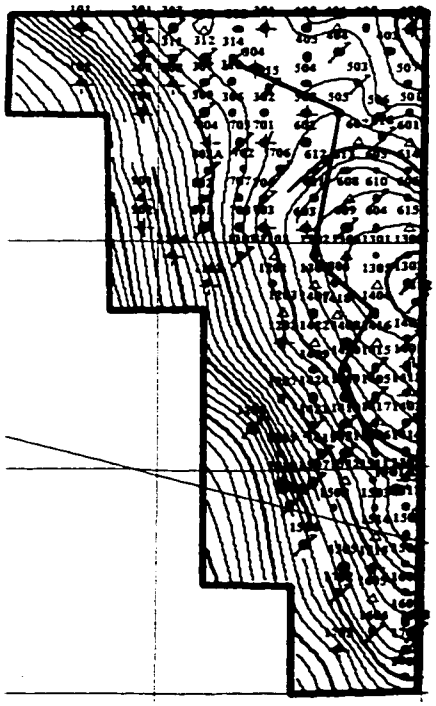

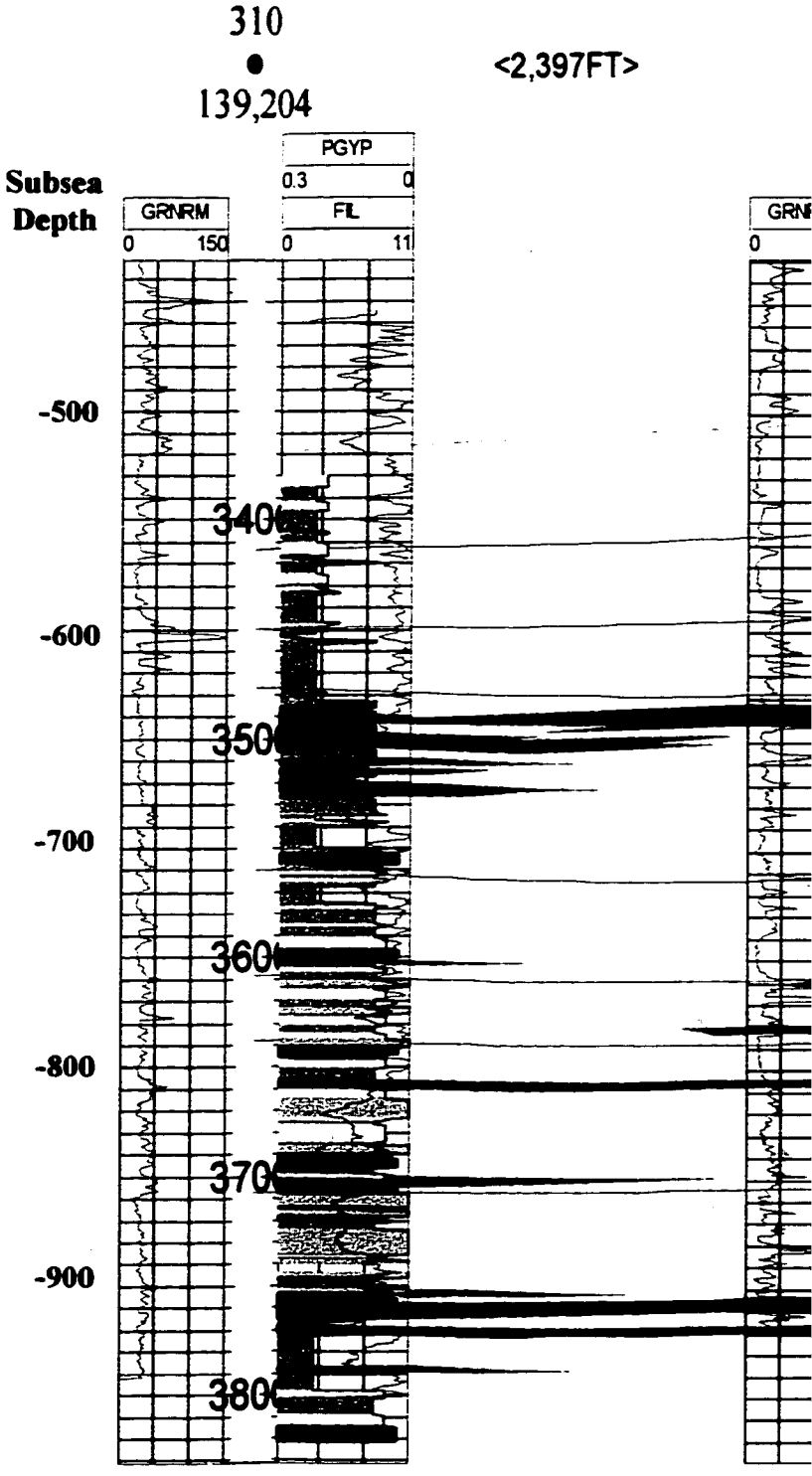

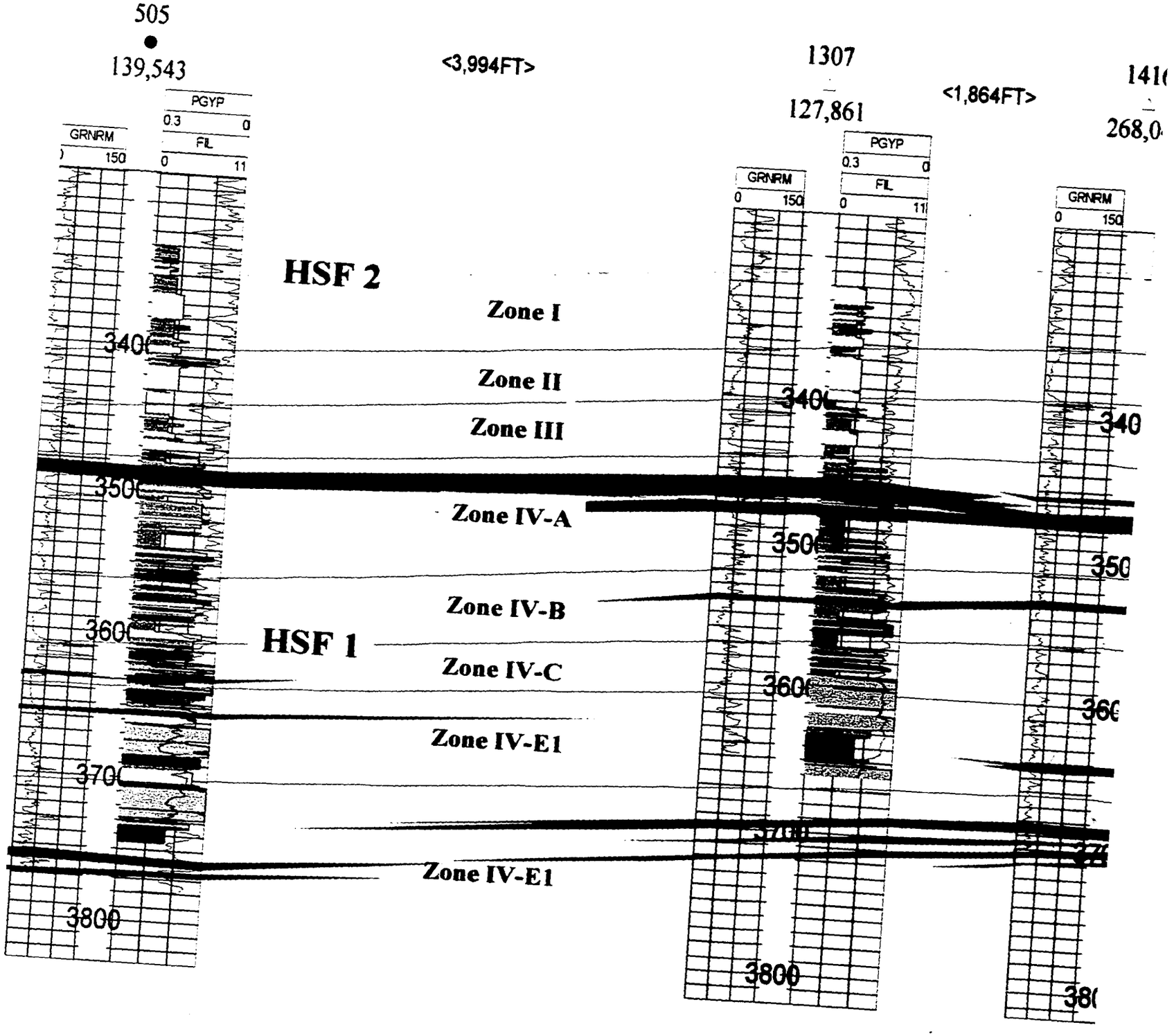
505
139,543
<3,994FT>
1307
127,861
<1,864FT>
141
268,0
PGYP
0.3
0
FIL
0
11
GRNRM
0
150
HSF 2
Zone I
Zone II
Zone III
Zone IV-A
Zone IV-B
HSF 1
Zone IV-C
Zone IV-E1
Zone IV-E1
340
350
360
370
3800

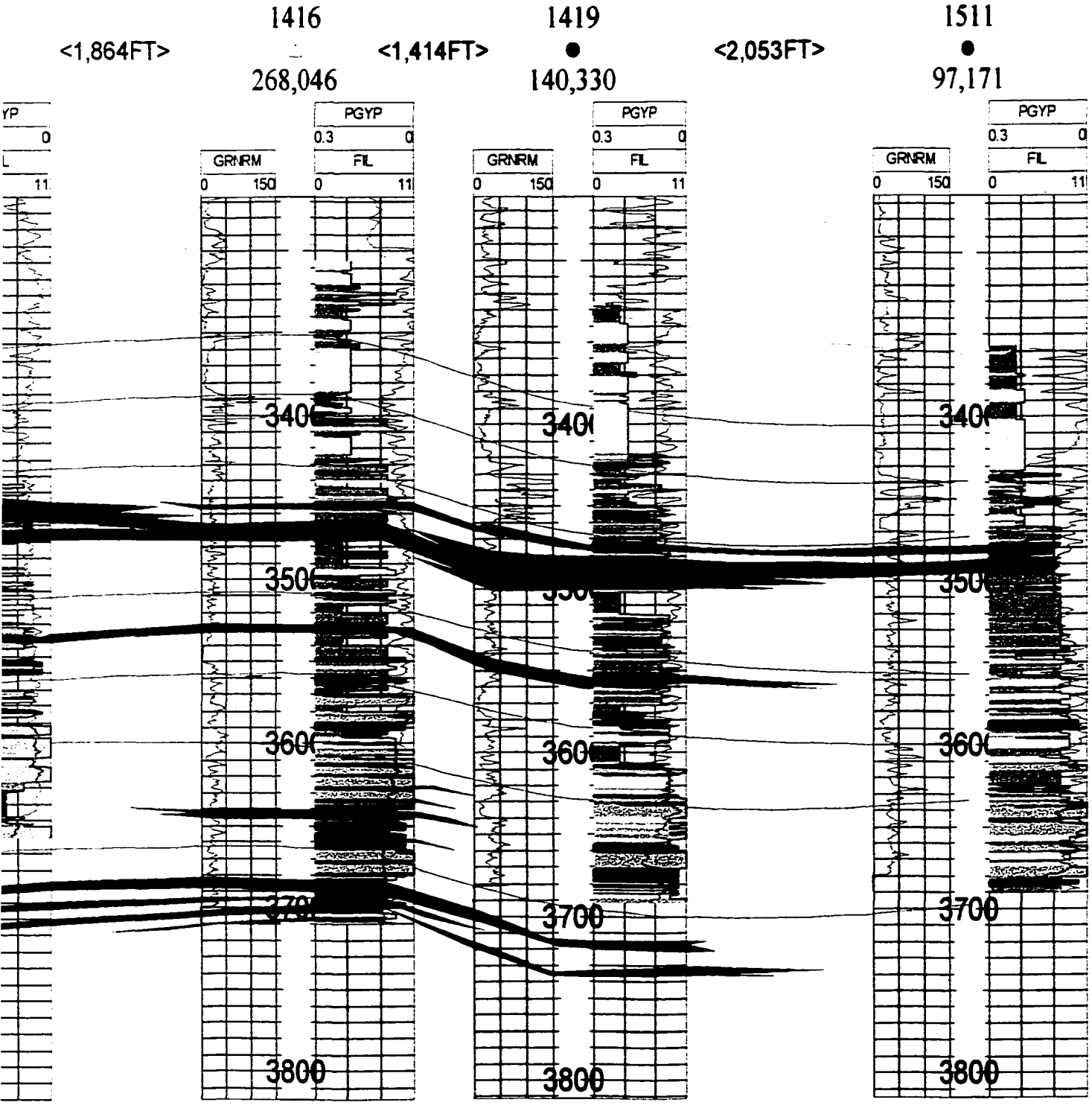
1416
<1,864FT>
268,046
1419
<1,414FT>
140,330
1511
<2,053FT>
97,171
PGYP
0.3
0
GRNRM
0
150
FIL
0
11
3400
3500
3600
3700
3800

Vertically structured facies were not found in cores to be as prevalent as described for nearby units within the San Andres and Grayburg Formations. This may be due to the position of the West Jordan unit farther landward on the shelf than other nearby units where vertically structured facies are found to be primary porosity zones. Where the facies is present within lower zones of the reservoir (IV-E2 and IV-E1), it typically contains good porosity and permeability as a result of diagenetic alteration. Unfortunately, this texture is only identifiable from cores, and therefore, it cannot be used for permeability prediction when core data is not available.

Bioherm/Reef Facies

The bryozoan-sponge-algal boundstone lithofacies was found within two of the nine cores studied (West Jordan unit #1307 and #505; figs. 9 and 22). This lithofacies was restricted to the lower zones of the reservoir (zones IV-E2 and IV-E1) where it was found to reach a thickness of up to twenty feet. In addition, flanking bryozoan-sponge dolowackestones to mud-rich dolopackstones were seen in several of the other cores (West Jordan unit #1416 and #1419). Aptly termed, the lithofacies typically consists of bryozoan and sponge framework material that has been bound together by calcareous algae (figs. 23 and 24). The absence of the boundstone lithofacies in other cores penetrating the lower intervals of the reservoir, suggests that these bioherm buildups are localized in nature. Porosity and permeability values for this lithofacies vary from poor to quite good, however the localized occurrence of these small bioherm buildups negates their significance with respect to reservoir volume.

Figure 23. Core photograph of organic sponge-algal-bryozoan bioherm lithofacies. This lithofacies was only found in the base of two cores (WJU #505 and 1307) within zones IV-E1 and IV-E2. The thickest bioherm encountered in core was approximately twenty feet thick. These small bioherms are interpreted as being deposited on the leeward side of the ramp crest within the proximal outer ramp environment.

A) Core photograph from the West Jordan unit #1307 well illustrating the algal-bryozoan-sponge bioherm lithofacies. These bioherm facies contain a significant amount of mud matrix suggesting deposition in quieter waters and are interpreted to have been deposited basinward of the ramp crest.

B) Core from the West Jordan unit#505 well showing the algal-bryozoan-sponge bioherm lithofacies. Anhydrite nodules are commonly seen within this lithofacies.

B

A

Figure 24. Core photomicrographs of organic sponge-algal-bryozoan bioherm lithofacies.

A) Photomicrograph of sponge-algal laminated boundstone within the boundstone lithofacies (core photomicrograph from WJU #505; 3737.7 feet; magnification 6.3X).

B) Photomicrograph illustrating bioherm internal structure of algae and sponge material. Note calcite cement indicated by pale red staining (core photomicrograph from WJU #505; 3737 feet; magnification 25X).

C) Photomicrograph of a bryozoan showing intraparticle porosity developed within the zooecia (core photomicrograph from WJU #505; 3739.3 feet; magnification 6.3X).

D) Photomicrograph showing a well preserved sponge within the bioherm lithofacies. Note that gypsum (bluish-gray colored mineral) has occluded porosity within the upper right portion of the sponge (photograph center). Also note laminated algae surrounding the sponge material (core photomicrograph from WJU #505; 3737; magnification 16X).

A
B
C
D

Similar buildups have been described within the East Penwell and Jordan University units (Major, et al, 1988, 1990; Bebout, et al, 1991) and other nearby fields such as Dune, Waddel and McElroy (Longacre, 1980,1983, 1990; Harris, et al, 1984; Harris and Walker, 1990). In these fields the boundstone lithofacies has been interpreted to have formed as isolated ramp-margin patch reef type mounds. This study concurs with this depositional model. Significant mud is found within the facies to suggest deposition in relatively quite calm waters. The lithofacies vertical association with peloid and fusulinid lithofacies supports deposition on the leeward side of the ramp crest within subtidal, proximal outer ramp environments. Similar reefal buildups are documented within the Guadalupe Mountains.

Ramp Crest

Ramp crest facies are indicative of shallow water, high-energy environments such as shoals or barrier bars. Lateral facies relationships seen from core data and porosity maps suggest a series of ramp crest shoals interrupted by either tidal channels or quite water intershoal areas. These shoal bodies developed in a north-south direction across the central and eastern margins of the unit. These intershoal or channel areas appear to be filled with finer grained sediment that exhibits considerably less porosity and permeability resulting in compartmentalization between shoal and non-shoal areas. Vertical facies successions seen from core show that ramp crest facies formed as a series of stacked shoal bodies containing low permeability dolomudstones and wackestones between successive shoals. These stacked shoal bodies result in reservoir compartmentalization in both vertical and lateral dimensions (figs. 14 and 16).

Ramp crest facies described from core data are predominately peloid and skeletal grain-dominated dolopackstones and dolograinstones with flanking ramp crest facies consisting of mixed siliciclastics and peloidal/skeletal mud-rich dolopackstones (figs. 25 and 26). Ramp crest lithofacies represent the top of upward shoaling cycles within aggradational high frequency sequence I (fig. 10). These facies were commonly seen interbedded with organic rich argillaceous dolomudstones and peloidal-skeletal dolowackestones to mud-rich dolopackstones indicating that small changes in sea level and paleotopography resulted in a dynamic environment with lateral changes in deposition of facies occurring over short distances and periods of time. The repetitive nature of vertical facies successions observed within zone IV-C indicates a shallow dipping ramp setting which was significantly influenced by only slight variations in sea level that moved depositional environments back and forth over the West Jordan unit area (figs. 25 and 26). Only slight changes in paleotopography (five feet or less) are needed for grainstone shoals to form within shallow water (Grammer, 2000; personal communication).

The top of zone IV-C is placed at a coal bed that was found in cores to occur consistently across the unit (fig. 25). Ramp crest and associated flanking facies observed zone IV-C were better preserved than fabrics seen within the lower zones. In zone IV-C early cementation is believed to have preserved grain fabric to a larger degree. Carbonate shoals prevalent within zones IV-E2 and IV-E1 have undergone intense dolomitization that has obliterated grain textures within these lower two zones making identification of dolograinstone fabric difficult to determine. Shoaling within these lower zones will be discussed in further detail in a later section.

Figure 25. Core photograph of middle ramp, ramp crest and flanking ramp crest facies successions. Large amounts of plant material were found within the ramp crest facies in the majority of cores examined. Coal intervals were observed in most of the cores, where preserved. The abundance of plant material and coal indicate climate changes to a more humid environment of deposition. A considerable amount of organic material would be necessary to form the coals seen within the unit that reach up to at least five inches thick (Core photographs from WJU #505 from 3605-3618.6 feet).

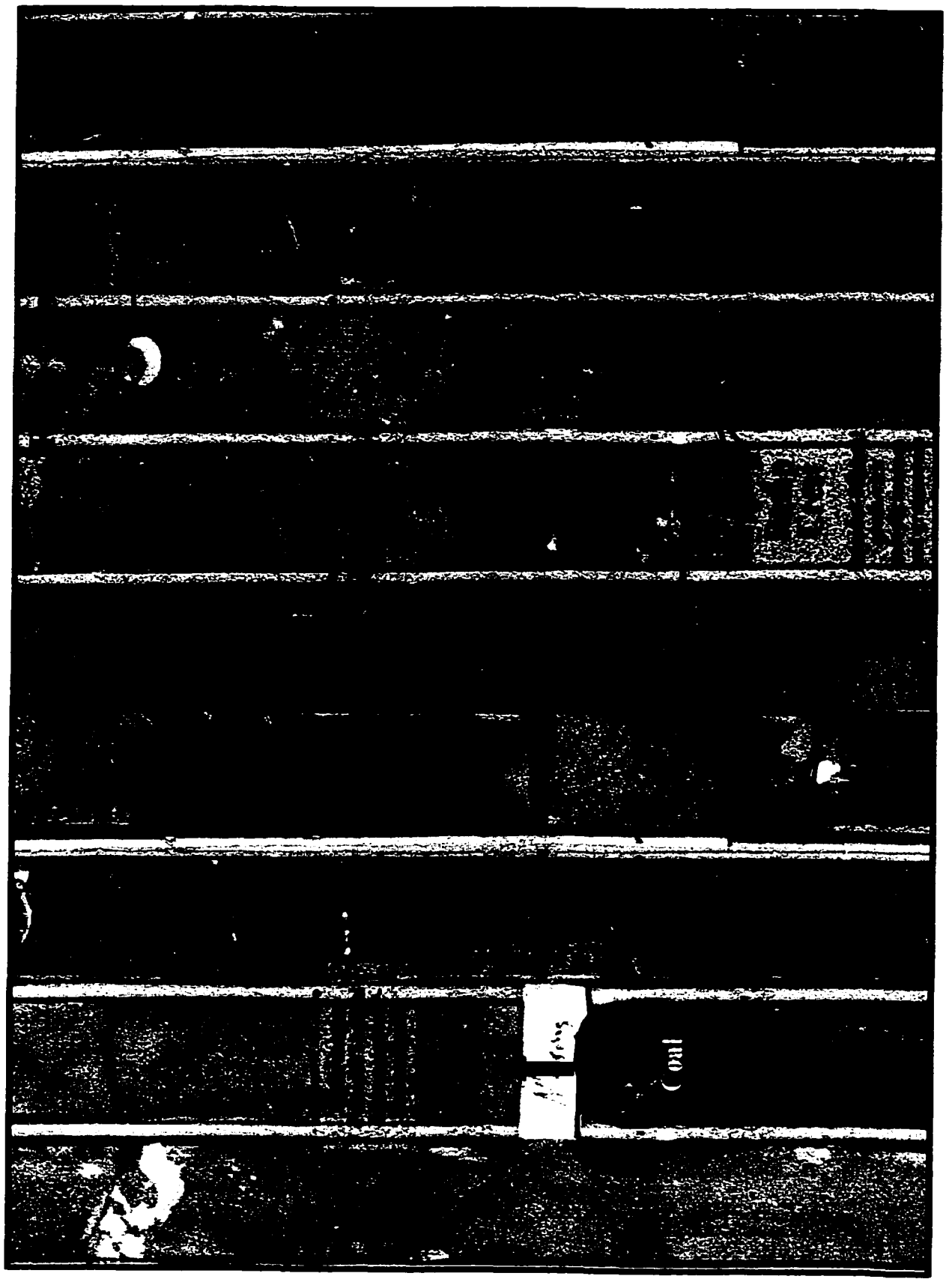

Figure 26. Core photograph of ramp crest and flanking lithofacies. Identifiable ramp crest facies in the form of dolograinstones and grain-dominated dolopackstones were found primarily within zone IV-C. While these facies are present within the lower zones as well they are not easily seen due to the degree of recrystallization that has taken place during the dolomitization process. Siliciclastic rich lithofacies are commonly found associated with ramp crest facies on landward side of these buildups. Argillaceous to organic-rich material is also commonly associated with the ramp crest facies indicating quite water inner-shoal areas where finer sediment was deposited. (core photograph from WJU #1307; 3597.5-3611 feet; magnification 6.3X).

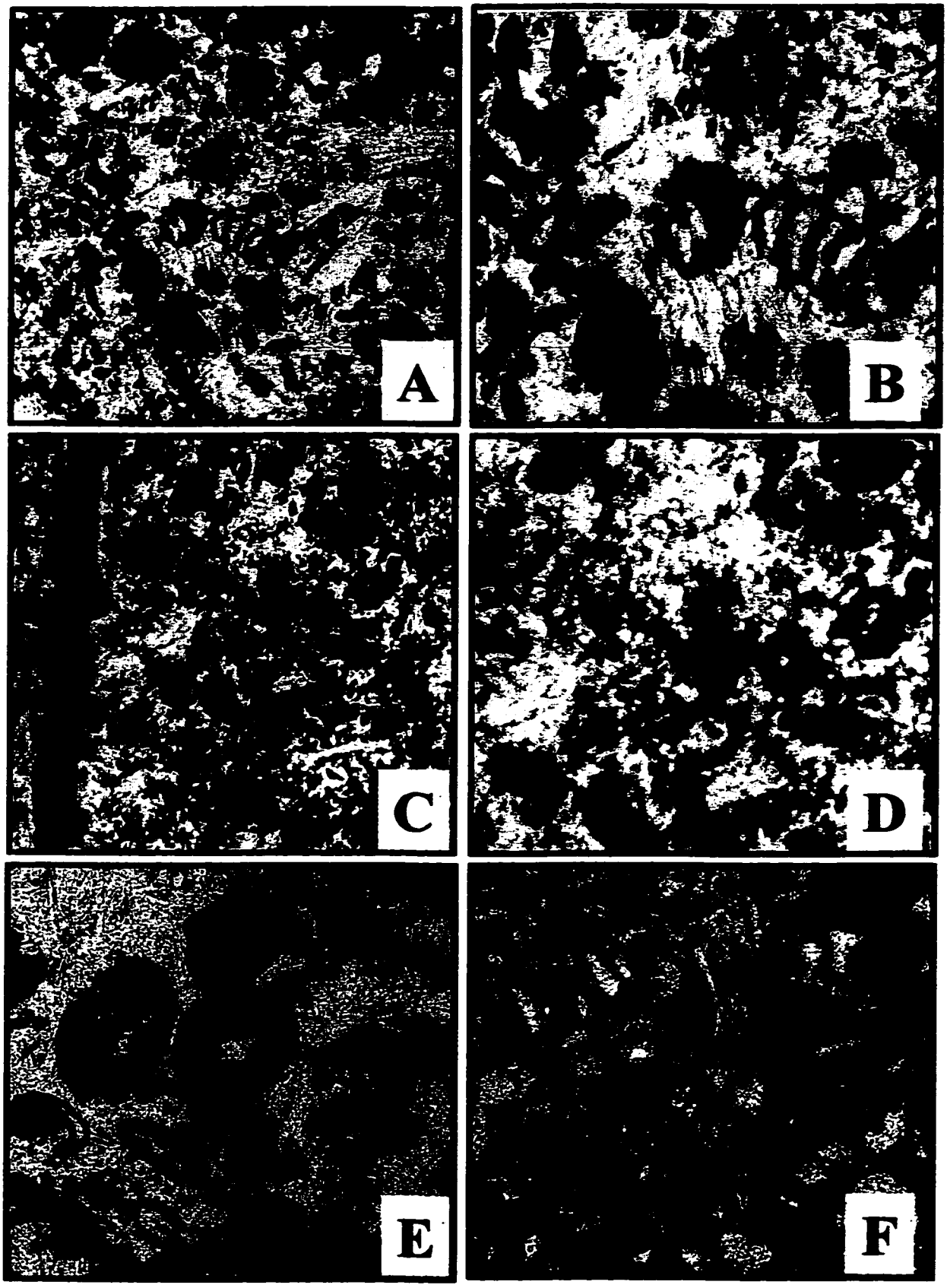
A
B
C
D
E
F

Missing
core

Peloid/Skeletal dolopackstone/dolograinstone Facies

Peloidal and skeletal lithofacies indicative of the ramp crest environment are grain-dominated fabrics consisting of dolopackstones and grainstones (fig. 27). The grain-dominated nature of these rocks along with the absence of any originally deposited mud-matrix suggests deposition in a high-energy environment. Within zone IV-C the original fabric of these shoal facies is fairly well preserved and individual grains are more easily identifiable. Skeletal constituents that are found within these grain-dominated facies include peloids, crinoids, mollusk fragments, coated grains, ooids and fusulinid grains. However, core and log data indicates that this dolograinstones facies is not productive within zone IV-C because the interparticle pore space has been completely occluded with sulfate cement, primarily anhydrite (fig. 27). Mud-dominated lithofacies within this zone have not undergone the degree of cementation that grain-dominated fabrics have. This suggests that dolomitizing fluids followed high permeability pathways present within these grain-dominated fabrics. The flanking ramp crest facies has the same grain constituents as the ramp crest, however it has a higher mud content. The peloid/skeletal content suggest deposition in moderate-to-high energy environments where skeletal grains were reworked along shoal margins.

Mixed Siliciclastic Facies

Mixed siliciclastic facies identified at West Jordan unit were found associated with flanking ramp crest facies on the landward side of shoal deposits (fig. 25). These facies were identified within three of the nine cores examined indicating this occurrence is fairly prevalent within flanking ramp crest facies. Fine-grained quartz-rich siliciclastic

Figure 27. Core photomicrographs of ramp crest and flanking ramp crest lithofacies. These facies are deposited in moderate to high-energy environments. The best preserved ramp crest facies were found in zone IV-C where early sulfate cementation is believed to have preserved original rock fabrics to a larger degree than in the lower zones that have undergone severe recrystallization of grains.

A) Core photomicrograph of ramp crest skeletal-peloidal, grain-dominated dolopackstone. Note that these grain-dominated facies have been completely occluded by sulfate (anhydrite) cement (core photomicrograph from WJU #1307; 3607.6 feet; magnification 8X).

B) Close up of A. above (magnification 20X).

C) Core photomicrograph of a peloidal dolopackestone-grainstone from the ramp crest to flanking ramp crest environment. A fracture (blue epoxy) allows for the migration of fluids through this otherwise fairly tight rock (core photomicrograph from WJU #1307; 3609.4 feet; magnification 8X).

D) Close up of C. above (magnification 16X).

E) Core photomicrograph of a fusulinid-peloidal grain rich dolopackstone. Again note that the grain-dominated ramp crest facies tend to be completely occluded by sulfate cement (core photomicrograph from WJU #1416; 3549.9 feet; magnification 8X).

F) Core photomicrograph of the peloidal-skeletal dolopackstone facies from the flanking ramp crest environment. The fine grained mud matrix is preserved within this sample indicting slightly less agitation of water conditions (core photomicrograph from WJU #1416; 3547.6 feet; magnification 8X).

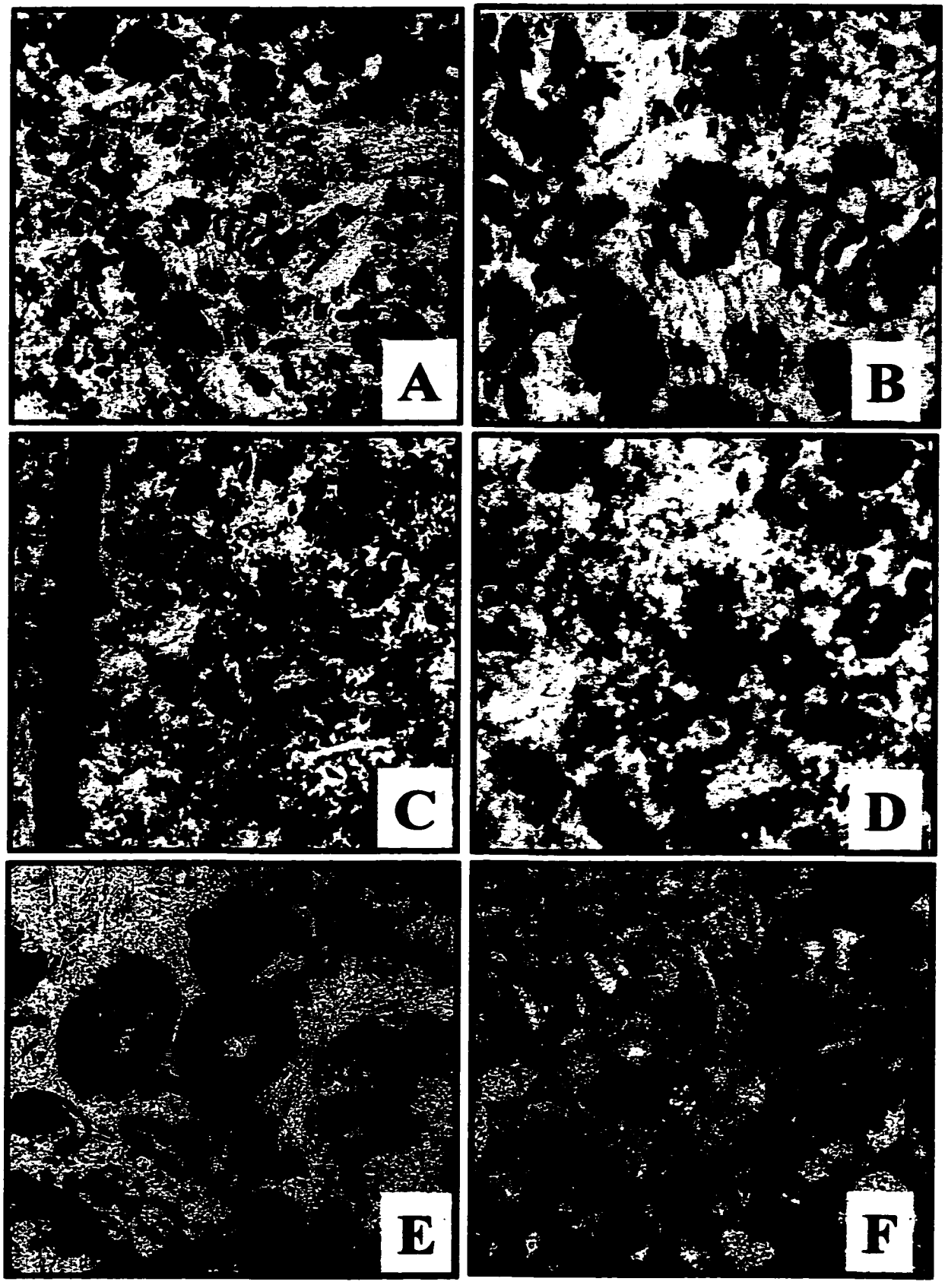
A
B
C
D
E
F

material is interpreted as being deposited as wind-blown sediment (fig. 28). Current and wave action may have concentrated siliciclastic material along the landward side of shoal areas where continued wave action resulted in the mixed carbonate-siliciclastic material found within cores. Siliciclastics are known to be common in the central parts of the basin and at the base of the Grayburg Formation.

Several different models have been described for deposition of siliciclastics within the Grayburg Formation. One interpretation suggests that siliciclastics of the Grayburg Formation record marine reworking of lowstand eolian sands during a sea level rise or marine transgression (Kerans, et al, 1995; Ruppel and Bebout, 1996; Trentham, et al, 1998). An alternate model, which is more consistent with siliciclastic deposition seen at West Jordan unit suggest that siliciclastics within the Grayburg may reflect deposition in subtidal marine waters landward of the platform-crest (Caldwell, et al, 1998).

Middle Ramp Facies Tract

The middle ramp environment consists primarily of skeletal, crinoidal and peloidal dolowackestones, tan to light brown dolomudstones and occasional algal laminated dolomudstones. The internal nature of thin, variable lithofacies seen in shallowing upward vertical facies successions within the middle ramp environment suggests that minor sea level changes and local paleotopography resulted in highly variable facies distribution. In addition, slightly exposed conditions within the overall middle ramp environment may have occurred at times as indicated by thin zones of algal laminated and fenestral dolomudstones within some cores.

Figure 28. Core photomicrographs of flanking ramp crest mixed siliciclastic lithofacies. Mixed siliciclastics were found to be very common on the landward margin of ramp crest facies within the West Jordan unit.

A) Fine-grained mixed siliciclastic and dolomitized carbonate material surround a well preserved plant fragment. These plant fragments were very common within the ramp crest and flanking ramp crest facies (core photomicrograph from WJU #1416; 3578.2 feet; magnification 32X).

B) Photomicrograph showing the contact between argillaceous rich material overlying fine siliciclastic lithofacies. Note that very fine siliciclastic material is present within the overlying argillaceous rock as well. The white areas are poikilotopic anhydrite cement (core photomicrograph from WJU #14-6; 3568.0 feet; magnification 7.5X).

C) Photomicrograph of the mixed siliciclastic flanking ramp crest facies. Siliciclastic material is believed to have been wind derived and then reworked on the landward margins of the shallow ramp crest area (core photomicrograph from WJU #1307; 3580.1 feet; magnification 10X).

D) A photomicrograph of mixed siliciclastic-peloidal dolopackstone. Note that the bluish-green material is not porosity but rather gypsum cement occluding pore space (core photomicrograph from WJU #1307; 3600.6 feet; magnification 32X).

B
D
A
C

Zones IV-B and IV-A consist of facies deposited within the middle ramp facies tract within a lagoonal environment. Zone III contains a wide range of lithofacies that oscillate back and forth between shallow subtidal, intertidal and supratidal facies. This peritidal zone is comprised of a diverse mixture of facies including: shallow subtidal to restricted marine mollusk-rich dolomudstones and dolowackestones, peloidal/skeletal dolowackestones, intercalated clay seams, intertidal algal laminated dolomudstones and occasional fenestral-algal dolomudstones, intraclast deposits and supratidal fenestral-pisolite dolopackestone-grainstone facies exhibiting poor to very well developed fenestral porosity (fig 29). These facies represent deposition in very shallow water where only slight sea-level changes greatly effected the facies being deposited. Lithofacies within zone III are representative of deposition within the near-shore area of the middle ramp environment (fig. 14).

Skeletal/Peloidal Dolowackestone-Packstone Facies

Middle ramp skeletal/peloidal facies have recognizable differences from those previously described for the proximal outer ramp and ramp crest environments. Within the outer ramp peloids are the main grain allochems. In contrast skeletal allochems are the main grains found within facies representative of the middle ramp lagoonal environment (fig. 30). Also, the middle ramp facies are considerably more mud-rich ranging from wackestones to occasional mud-rich packstones. Grain-dominated facies were not observed in core within zones IV-B and IV-A. The primary pore type for this lithofacies is moldic (fig. 30) versus intercrystalline for the proximal outer ramp

Figure 29. Core photograph of middle ramp nearshore lithofacies illustrating shallow subtidal to supratidal facies. Note the considerable fracturing developed off of anhydrite nodules and stylolite teeth. These fractures are referred to as "diagenetic" fractures within this study. In addition planar, tectonic and/or regional fractures are seen in the dolomudstone on the right side of the core photograph. Diagenetic fractures are short in duration and typically radiate outward from an anhydrite nodule or stylolite. The core was seen to commonly part along these fractures when brought to the surface. Also note that in between the shallow subtidal facies is an algal-laminated dolomudstone with fenestral porosity. This facies is indicative of shallow to exposed conditions (core photograph from WJU #1307; 3432.6-3440 feet).

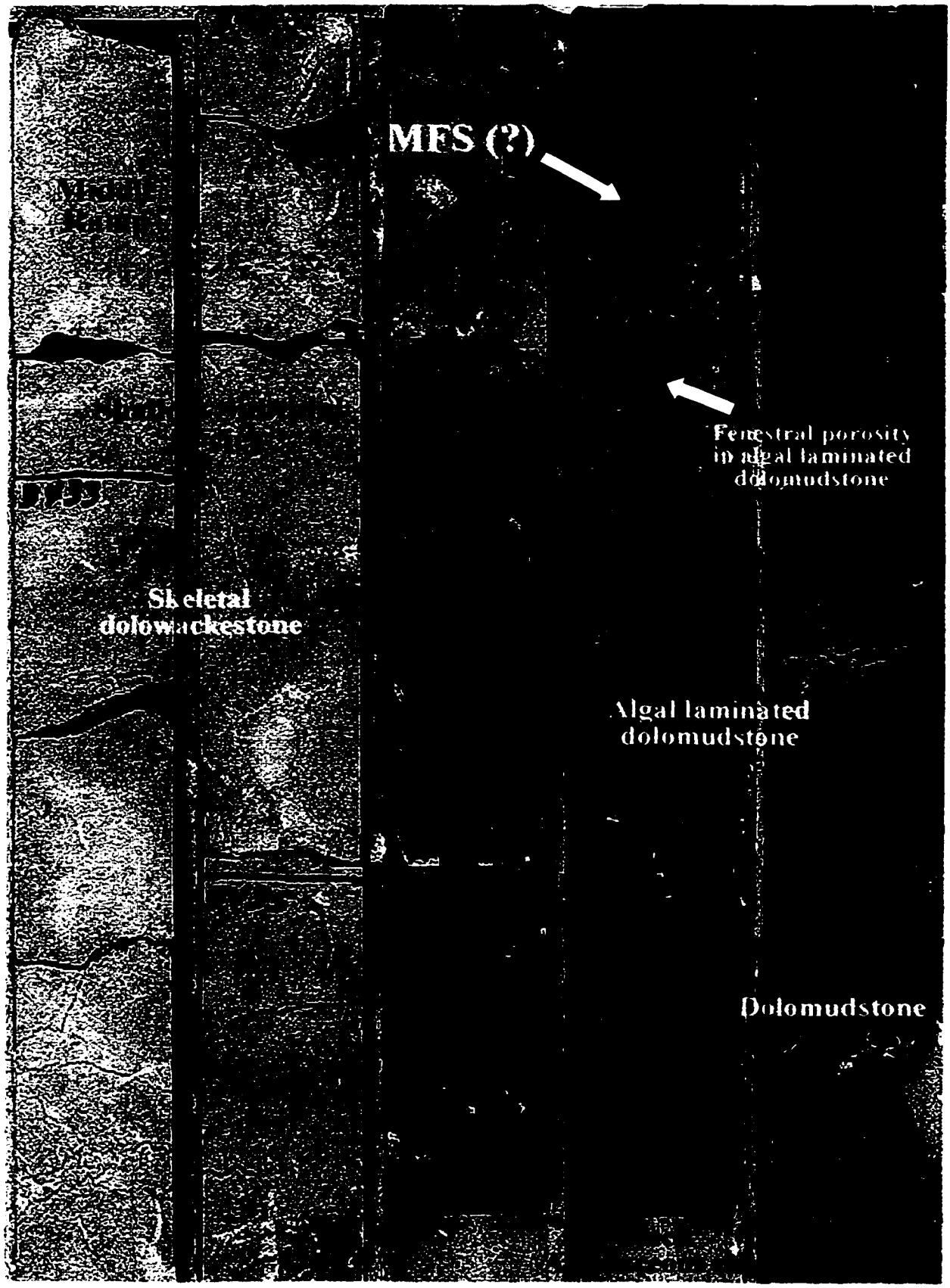
MFS (?)
Fenestral porosity in algal laminated dolomudstone
Skeletal dolowackestone
Algal laminated dolomudstone
Dolomudstone

Figure 30. Core photomicrographs of middle ramp skeletal/peloidal wackestone to mud-rich packstone lithofacies. These lithofacies contain considerably more mud and skeletal grains are primarily mollusk (gastropod and pelecypod fragments).

A) Photomicrograph of a mollusk (gastropod) dolowackestone-packstone. This thin section was photographed under crossed nicols and the blue color within the gastropod grain is anhydrite cement (core photomicrograph from WJU #1307; 3333.10 feet; magnification 32X).

B) Photomicrograph showing skeletal-mollusk dolowackestone-packstone. Note the longitudinal cross section of the gastropod grain. Both gastropod and pelecypod grains have undergone replacement of the original aragonite material forming the shell walls with anhydrite cement. Blue areas within this photomicrograph are the result of moldic porosity (core photomicrograph from WJU #1419; 3456.7 feet; magnification 20X).

C) Photomicrograph of a peloidal-skeletal, mud-rich dolopackstone. Note the considerable moldic porosity (blue epoxy filled areas) which is the dominant pore type found within middle ramp facies. While the leaching of grains forming these molds can result in good porosity, permeability values are typically quite low (core photomicrograph from WJU #1419; 3454.5 feet; magnification 8X).

C) Photomicrograph of a peloidal-skeletal dolowackestone from the middle ramp environment. Porosity (blue) is formed from the dissolution of peloid and skeletal grains and minor amounts of intercrystalline porosity. White areas are molds that have been filled with anhydrite cement. Porosity for this sample is about 10 percent while permeability is less than 0.2 millidarcies (core photomicrograph from WJU #1419; 3468.3 feet; magnification 8X).

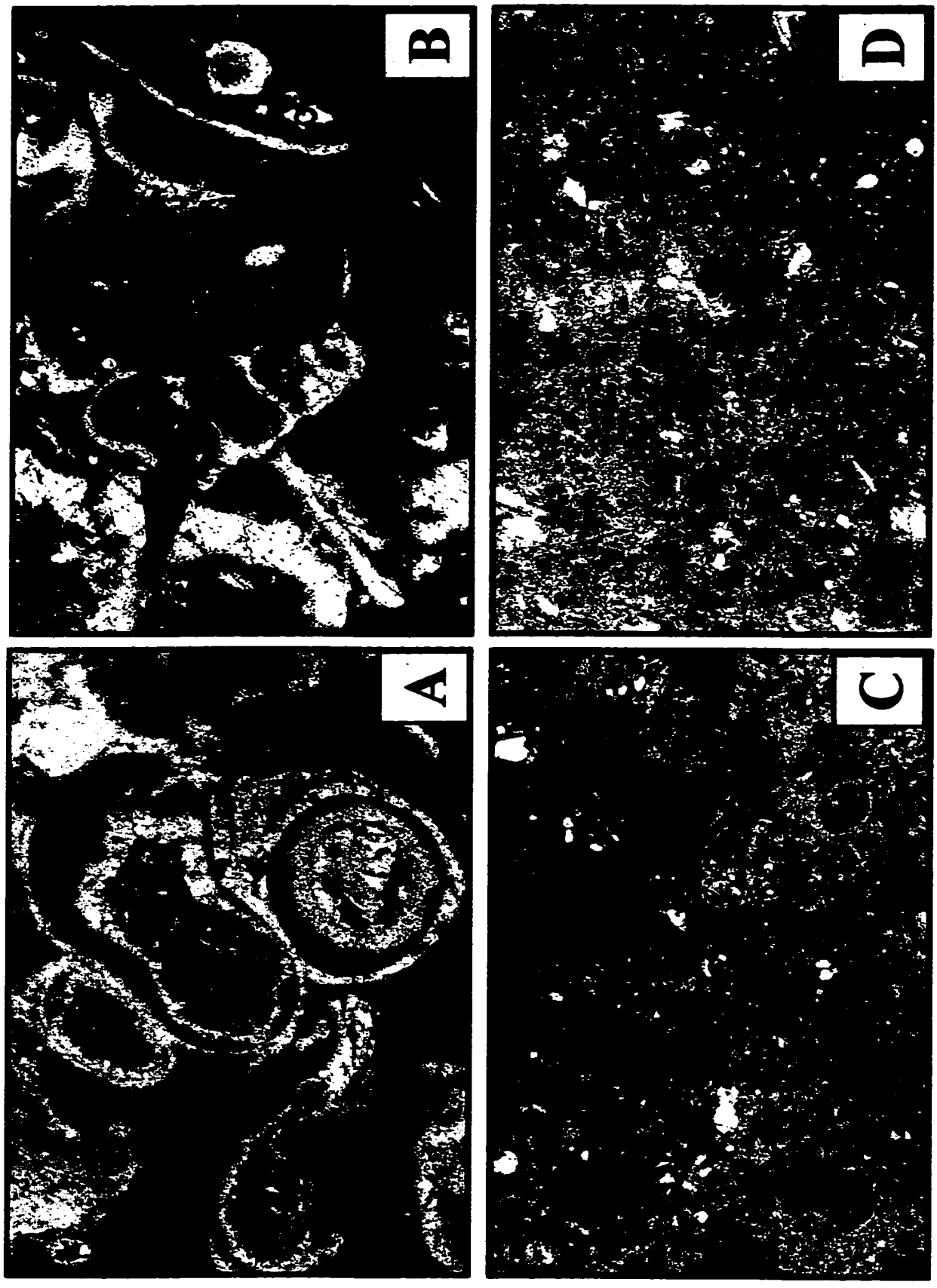
A
B
C
D

peloidal/skeletal lithofacies (moldic pores are present but they are not the primary pore type) and interparticle for ramp crest facies observed in zone IV-C.

Fracturing is much more common in these tighter, middle ramp facies (fig. 29). Other common sedimentary features are anhydrite nodules and numerous stylolites, particularly within zone IV-A where stylolites are very large in amplitude. Permeability associated with moldic porosity in these middle ramp facies is typically quite low and many moldic pores have been occluded by anhydrite cement (fig. 32 A, B).

Dolomudstone Facies

Dolomudstones are found within zone IV-B and become considerably more common in zone IV-A. These dolomudstones are typically homogeneous, finely crystalline and tan to light brown in color (fig. 31). Wispy argillaceous laminations are present within many of the dolomudstones within the lower parts of zone IV-A and in zone IV-B. Thin algal laminated dolomudstones occur within the near shore facies in zone III (fig. 31 C, D). All of these dolomudstones are characterized by microcrystalline dolomite with crystal size typically less than 10 microns ((m) and a lack of grain allochems. Middle ramp dolomudstones are interpreted as low energy, quite water lagoonal environments. Algal laminated dolomudstones are probably more common in the shallow intertidal and tidal flat environments representative of zone III. Features commonly occurring within these dolomudstones are fractures, stylolites and laminae (figs. 29, 31).

Figure 31. Core photomicrographs of various middle ramp dolomudstone lithofacies.

A) Photomicrograph of a microcrystalline dolomudstone. Note the tension fractures that have developed off of a small stylolite (core photomicrograph from WJU #1307; 3497.5 feet; magnification 6.3X).

B) Algal laminated silt-rich dolomudstone. Note the very fine-grained siliciclastic material (small white grains) intermixed within the matrix (core photomicrograph from WJU #1307; 3410.2 feet; magnification 6.3X).

C) Laminated dolomudstone lithofacies. Laminae are believed to be organic rich material probably of plant origin. Orange colored material was observed in much of the plant material seen within cores (see fig. 28 A) as well indicating a similar origin for its occurrence in the algal laminated dolomudstone lithofacies. The porosity (blue) formed by the removal or organic material in the center of the photomicrograph most likely occurred during the thin section making process (core photomicrograph from WJU #1307; 3492.7 feet; magnification 32X).

D) Photomicrograph of the tan to light brown colored dolomudstone. Note the numerous tension fractures that have developed off of the stylolite teeth. In many samples these fractures provided avenues for fluid movement. This sample also contains a small amount of intercrystalline porosity (core photomicrograph from WJU #1419; 3509.3 feet; magnification 8X).

A
B
C
D
organic plant
material (grape)

Inner Ramp Facies Tract -Tidal Flat and Nearshore Environments

The uppermost supratidal-to-shallow intertidal section of the San Andres reservoir at West Jordan unit is composed primarily of the following lithofacies: fenestral-pisolite dolowackestone-grainstone; algal laminated and light green to cream colored dolomudstones; argillaceous to silt rich clays ranging from dark black to green in color; thin intervals of intraclasts; brecciated zones and minor intervals of intertidal skeletal dolomudstone-wackestone facies. Facies representing tidal flat environments are found within zones III, II, and I, although zone III is composed of more facies representing nearshore intertidal depositional environments.

The seal for the San Andres reservoir is formed by a series of alternating dolomudstones and tightly cemented grain-dominated pisolitic facies within zone I. Sulfate cementation of original fenestral pore space is pervasive throughout most of zone I resulting in a tight interval impenetrable to oil migration upward into the overlying Grayburg Formation (fig. 32). Underlying zone I, well-developed open fenestrae are present within the pisolite facies of zone II, which has undergone considerable sulfate dissolution. Within zone II fenestrae are well connected and the facies exhibits some of the highest porosity and permeability values observed within the reservoir (fig. 32 B).

These facies are characteristic of tidal flat environments and mark the end of progradational HSF 2 (figs. 10 and 11). The presence of paleosols (caliche surfaces), sheet cracks, teepee structures, pisolites, fenestrae, exposure surfaces and brecciated intervals suggests conditions of exposure and alternating wetting and drying associated with tidal flat deposition (Longacre, 1980; Bebout and Harris, 1986; Ruppel, 1990).

Figure 32. Core photographs of the fenestral pisolite dolopackstone-grainstone lithofacies. In figure 28 A from zone I, fenestral porosity has been completely occluded by sulfate cement (anhydrite) forming the seal for the reservoir (see insert photograph). Figure 28 B illustrates the excellent porosity seen in zone II that can occur within this facies. Porosity values for the fenestral pisolite dolopackstone-grainstone lithofacies in zone II were found to be over 18 percent and permeability values of over 250 millidarcies were recorded (fig. 34A from WJU #1307 core; fig. 34B from WJU #1416 core).

Fenestral
Pores have been
occluded by sulfate
cement (anhydrite)
Tilting of pisolite
facies indicates
teepee structure
A
Well developed
Fenestral Pores
B

Pisolite Dolopackstone-Grainstones and Associated Facies

Poorly sorted pisolite grains exhibiting sparse to excellent fenestral porosity development characterize the pisolite dolopackstone-grainstone facies (fig. 33). This facies is usually found in core to be interbedded with cream colored and algal laminated dolomudstones, and clay intervals. Algal laminations are quite common within the pisolite facies as are associated teepee structures, birdseye texture, sheet cracks, and anhydrite filled fractures (figs. 32 and 33).

Where fenestrae are occluded by sulfate cement the facies forms an impermeable seal. The primary pore type within zone II is fenestral porosity developed within the pisolite packestone-grainstone facies. A distinct diagenetic event has resulted in nearly complete removal of sulfate cement within zone II producing excellent porosity and permeability that is not found within zone I (fig. 32). Zone II is believed to act as a flow unit within the reservoir although it has not been fully determined whether oil still remains in place within this zone or has been completely flushed due to the high permeability values and large pore apertures observed in core. If this zone has been flushed of oil then it is most likely acting as a waterflood thief zone, as well as zone IV-A.

Dolomudstones associated with the pisolite facies are light cream-colored, dense microcrystalline dolomites (dolomite crystal size is < 5 (m). The absence of fossil material within these dolomudstones and the close association with the pisolite facies has lead to the interpretation that these mudstones were deposited within hypersaline ponds within the tidal flat environment (Major and Holtz, 1997). Also interbedded within the

Figure 33. Core photomicrographs of the fenestral pisolite dolopackstone-grainstone lithofacies. This facies was found in zones I through III. The photomicrographs below are samples from zone II where fenestral porosity s often well developed resulting in excellent porosity and permeability for the reservoir.

A) The peloidal dolograinstone lithofacies exhibiting poorly sorted peloidal grains. Note the algal-laminated rings around some of the larger peloids and fenestral porosity indicated by blue epoxy (core photomicrograph from WJU #1416; 3380.4 feet; magnification 6.3X).

B) This photomicrograph illustrates tilted bedding associated with a teepee structure. A thin layer of pisolite grains is encompassed within algal laminated dolomudstone representing successive exposure and wetting of the sediment during deposition. Teepee structures are very common within this lithofacies. Also note fenestral porosity indicated by blue epoxy (core photomicrograph from WJU #1416; 3342.10 feet; magnification 6.3X).

C) Algal laminated pisolite dolowackestone/packstone. Other grains include intraclasts and very fine silts. Note fenestral porosity (blue) following algal laminations within the rock (core photomicrograph from WJU #1419; 3431.1 feet; magnification 8X).

D) A poorly sorted grain-dominated pisolite dolopackstone exhibiting very well developed fenestral porosity (blue). Note that anhydrite cement remnants (white color) still remain in several of the fenestral pores suggesting that this lithofacies may have been completely occluded by sulfate cement earlier in its history. This sample is from zone II within the reservoir (core photomicrograph from WJU #1307; 3372.3 feet; magnification 8X).

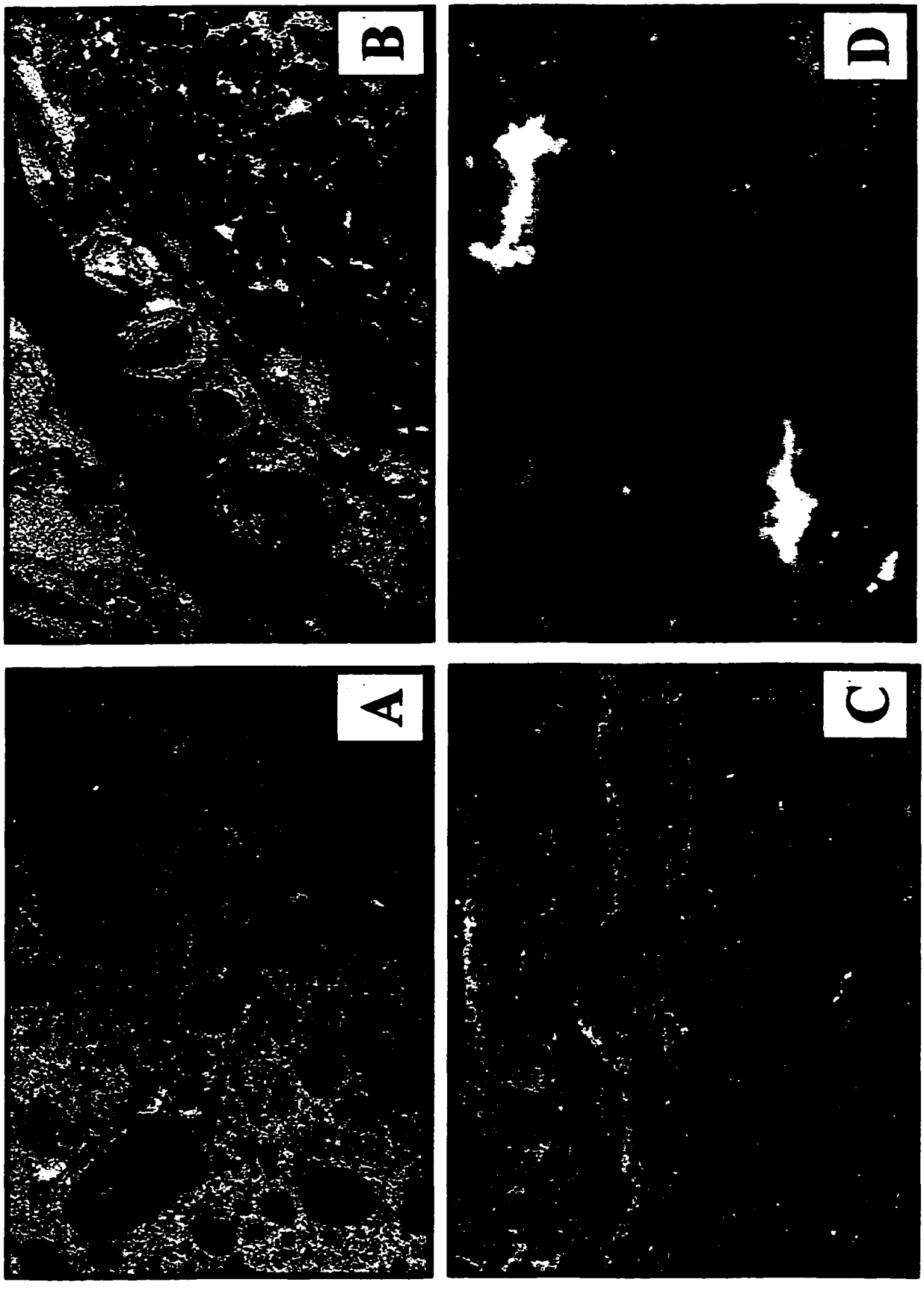
B
D
A
C

pisolite and mudstone facies are siliciclastic, clay-rich intervals that range from dark green to black in color and are laterally correlative throughout the unit.

Brecciated and Intraclast Facies

Brecciation within zones I and II was observed within several cores described within the West Jordan unit. Brecciated intervals associated with pisolite and dolomudstone facies are believed to be the result of solution collapse (fig. 34). Large fragments (over six inches) of rotated pisolite packstone/grainstone and dolomudstone facies are seen in core. Anhydrite cement and/or finer pale green sediment fills voids left between collapsed material. These brecciated intervals that indicate exposure and dissolution are not extremely common and are limited in thickness and extent. The thickest brecciated interval observed within core data is approximately 1.5 feet (43 centimeters). Substantial solution collapse zones have been described for San Andres reservoirs farther south along the Central Basin platform and along the northwestern shelf.

Brecciation seen within the San Andres has been related to a long-term sea level drop during the end of San Andres deposition (Trentham, et al, 1998). This sea level drop resulted in subaerial exposure and localized karstification within the upper parts of the formation at Foster and South Cowden fields just to the northeast of the West Jordan unit. In addition to brecciated zones seen in cores, isopach maps constructed for Zone I indicate patterns of exposure and localized truncation within the West Jordan unit, substantiating this widespread sea level drop (fig. 13).

Figure 34. Core photographs of brecciated intervals within the tidal flat environment. Brecciated intervals were found to be relatively thin, ranging from several inches to several feet in thickness. They occur most commonly within the pisolite lithofacies. Small blocks of the pisolite lithofacies surrounded by dolomudstone are usually found within brecciated zones. Nodular anhydrite is also a common constituent within the brecciated zones and is believed to have filled voids left within these zones (fig. 36A from WJU #1416 core; fig. 36B from WJU #1307 core).

Brecciated
zone
A

Brecciated
zone
Brecciated
zone
B

Intraclast and exposure surfaces were commonly seen in cores within the upper sections of the reservoir (fig. 35). These facies are also indicators of exposure and nearshore environments. The most common rip-up clasts observed within the intraclast facies were algal-peloids and grapestones formed from clusters of pisolite grains. Grapestone fabrics seen within intraclasts indicate formation within areas of intermittent agitation suggesting nearshore environments for this facies. It is interesting to note that a considerable increase in porosity is observed below exposure intervals (fig. 35 C, D), a common occurrence beneath major unconformity surfaces that is known to result in excellent reservoirs.

Figure 35. Core photomicrographs of intraclast and exposure surfaces. Intraclasts and exposure surfaces indicate nearshore to exposed conditions during deposition of the facies. Note that the intraclast sample from zone II (A) has well-developed porosity and the sample from zone I (B) is totally occluded by anhydrite.

A) Intraclast lithofacies from zone II composed of algal grapestone aggregates of pisolite and peloid grains. Note the interparticle porosity (blue) and the anhydrite cement (white) surrounding grains (core photomicrograph from WJU #505; 3453.9 feet; magnification 20X).

B) This photomicrograph shows an intraclast facies from zone I composed of peloids and grapestones. The dark minerals are pyrite, an abundant sulfide mineral found within the tidal flat and middle ramp environments of the San Andres formation. Note that pore space between grains in this particular sample has been completely occluded by gypsum cement (core photomicrograph from WJU #1307; 3366.11 feet; magnification 32X).

C) Photomicrograph showing the exposure contact between a silt-rich peloidal dolowackestone and a similar type facies below which appears to have undergone selective dissolution and cementation. Increased porosity below exposure surfaces is very common within the reservoir. In this sample much of the porosity has become occluded by anhydrite cement (core photomicrograph from WJU #1416; 3404.1 feet; magnification 8X).

D) Another example of an exposure surface within the nearshore environment. In this photomicrograph a dolomudstone has been exposed and then overlain by a deeper water skeletal-peloidal grain-dominated dolopackstone. Note the caliche layer between the two facies and the well developed fenestral porosity within the lower facies (core photomicrograph from WJU #1307; 3412.1 feet; magnification 6.3X).

B
D
A
C

THE WEST JORDAN UNIT DEPOSITIONAL MODEL

Introduction

The overall facies assemblage found within the West Jordan unit is strikingly similar to that observed on outcrop. The vast majority of cumulative oil production from the unit has been from stacked, compartmentalized shoal bodies within the lower part of the reservoir that formed within a moderate to high accommodation regime during a period of highstand (HST 1, fig. 10). Determining the shape and extent of these shoal bodies and their significance to reservoir production will be a valuable tool to extrapolate to other nearby fields.

The predictive nature of these productive shoal bodies is significant in that these highly compartmentalized reservoirs are not well understood within the Permian basin. The occurrence of these shoal bodies during HST 1 should be expected across the eastern margin of the Central Basin platform where paleotopography has allowed for their development behind a well-formed lagoon. Nevertheless, knowing where these shoals should be expected to develop is secondary to understanding their complex geometries that result in considerable compartmentalization of San Andres reservoirs. Only by having a well-defined depositional model can these bodies be predicted and fully understood.

Morphologic Setting of San Andres Strata along the Eastern Margin of the Central Basin Platform

Previous morphologic profiles for the San Andres carbonate platform along the eastern margin of the Central Basin platform have been primarily either ramp or shelf margin models. Ramp models consist of homoclinal and distally steepened while shelf

models include the attached rimmed shelf and flat-topped shelf (fig. 36 A). Along the eastern margin of the Central Basin platform the San Andres Formation has been interpreted as being deposited within rimmed shelf (Longacre, 1983; Hinricks et al, 1986, Garber and Harris, 1986, 1990, Harris and Walker, 1990) and ramp environments (Ward and others, 1986; Bebout and others, 1987; Ruppel and Cander, 1988 a,b; Fogg and Lucia, 1990; Garber and Harris; 1990; Longacre, 1990; Major and others, 1990; Lucial and others, 1992). The most widely accepted model for San Andres reservoirs along the eastern margin of the Central Basin platform is that of the distally steepened ramp (fig. 36).

Outcrop studies for the San Andres indicate a similar succession of facies along the Algerita Escarpment and Guadalupe Mountains (Kerans, et al, 1994; Eisenburg, et al, 1994; Grant et al, 1994; Kerans and Fitchen; 1995) as those deposited within the West Jordan unit. This has been established through comparison of cores examined within this study with comparative outcrop exposures. Outcrop studies show that San Andres carbonates record ramp to transitional rimmed shelf stages of carbonate platform development (Pray, 1985; Kerans, et al, 1992; Kerans and Fitchen, 1995). These broad morphologies are supported within the study area by seismic data to the immediate east and west of the West Jordan unit (fig. 37). The location of the Jordan field along the eastern margin of the Central Basin platform would have been very high (landward) on the carbonate ramp platform. Facies described within the West Jordan unit are strikingly similar to those described by Kerans and Fitchen (1995) for their Leonardian 7-8, and Guadalupian 1-4 high-frequency sequences (fig. 36 B).

Figure 36. Figure A shows the general morphologic profiles for carbonate platforms; distally steepened ramp, homoclinal ramp, rimmed shelf and flat-topped shelf. Figure B illustrates high frequency sequences (HFS) and associated facies tracts described from the Algerita Escarpment and western Guadalupe Mountains of west Texas and New Mexico. (A: modified from Handford and Loucks, 1993; B: modified from Kerans and Fitchen, 1995).

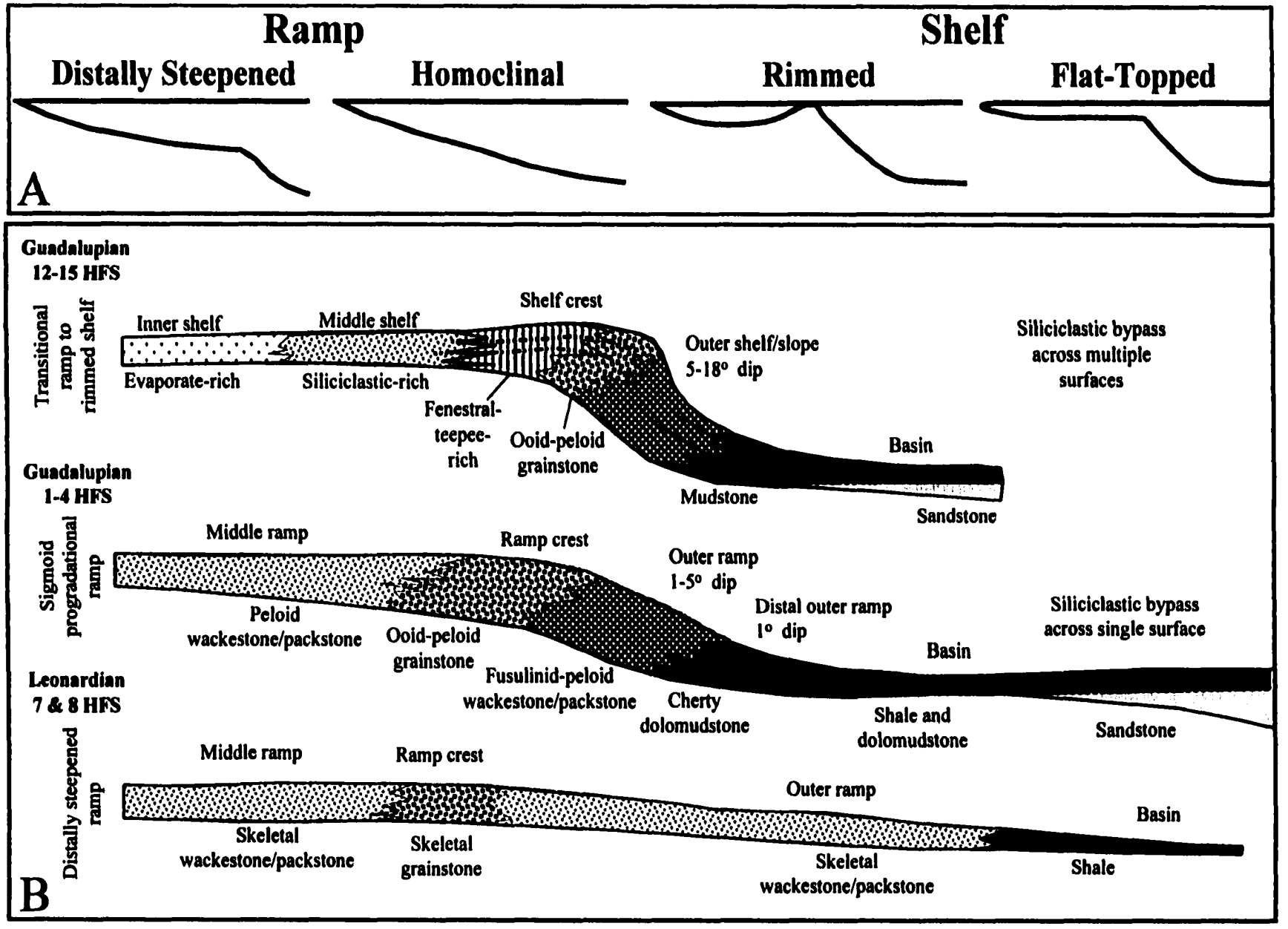
Ramp
Shelf
Distally Steepened
Homoclinal
Rimmed
Flat-Topped
A
Guadalupian
12-15 HFS
Transitional ramp to rimmed shelf
Inner shelf
Middle shelf
Shelf crest
Outer shelf/slope
5-18° dip
Siliciclastic bypass across multiple surfaces
Evaporate-rich
Siliciclastic-rich
Fenestral-teepee-rich
Ooid-peloid grainstone
Basin
Mudstone
Sandstone
Guadalupian
1-4 HFS
Sigmoid progradational ramp
Middle ramp
Ramp crest
Outer ramp
1-5° dip
Distal outer ramp
1° dip
Siliciclastic bypass across single surface
Peloid wackestone/packstone
Ooid-peloid grainstone
Basin
Fusulinid-peloid wackestone/packstone
Cherty dolomudstone
Shale and dolomudstone
Sandstone
Leonardian
7 & 8 HFS
Distally steepened ramp
Middle ramp
Ramp crest
Outer ramp
Basin
Skeletal wackestone/packstone
Skeletal grainstone
Skeletal wackestone/packstone
Shale
B

Figure 37. Seismic lines to the east and west of the West Jordan Unit. Note the lateral continuity of reflectors to the west of the unit. The West Jordan unit is located approximately eight miles from the San Andres shelf margin. Major cycle boundaries are correlative within the unit although not seen within the resolution of the seismic line. To the right of the diagram in the easterly direction, shelf margin progradation of the formation can be seen along with the significant thickening of strata into the basin. This thickening is related to the development of clinoforms at the shelf margin break (Seismic compliments of Texaco Exploration and Production, Inc. and OXY USA, Inc.)

Time in milliseconds

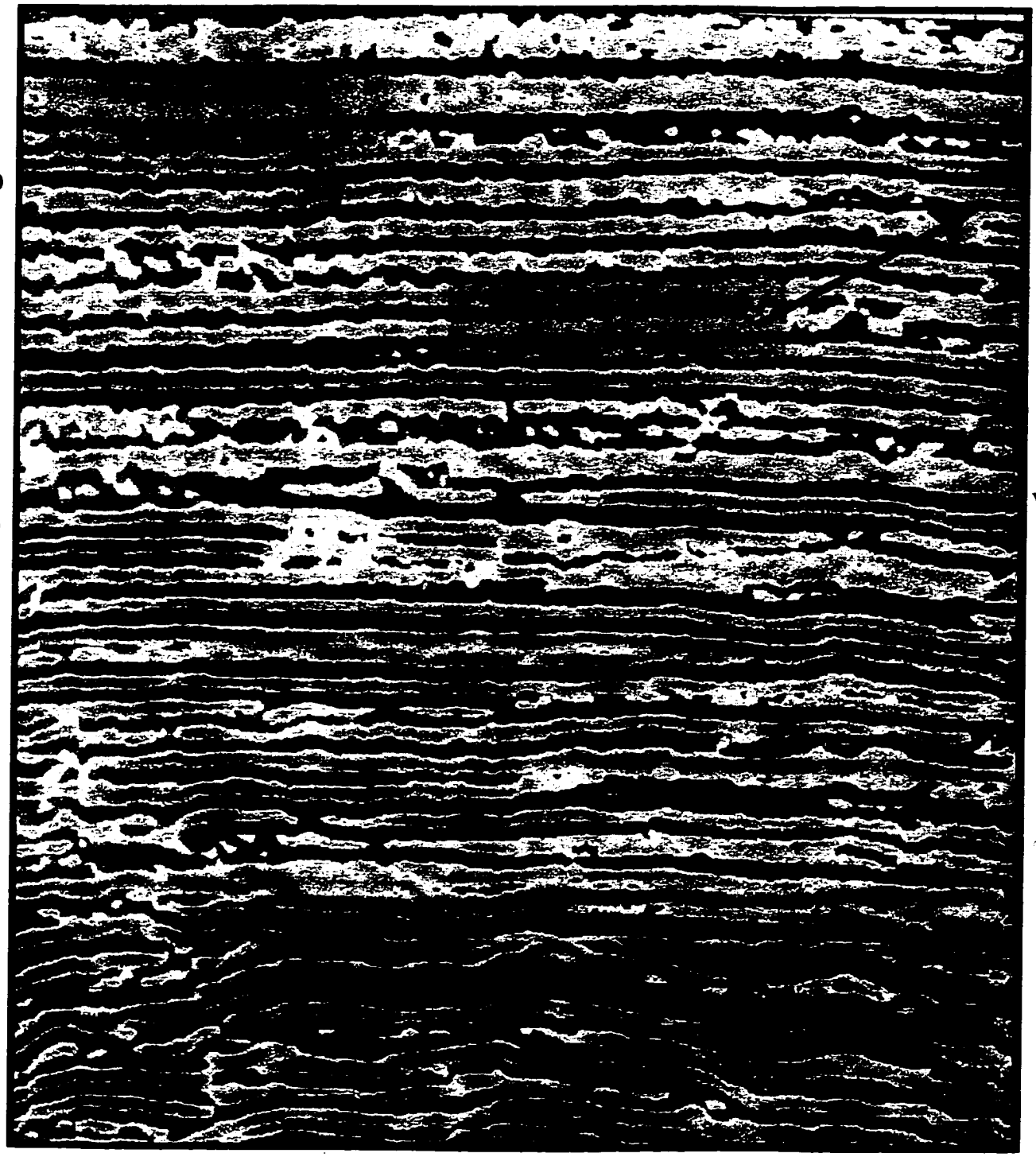

0.500

0.750

1.000

Area

West Jor

Area of the
West Jordan Unit.

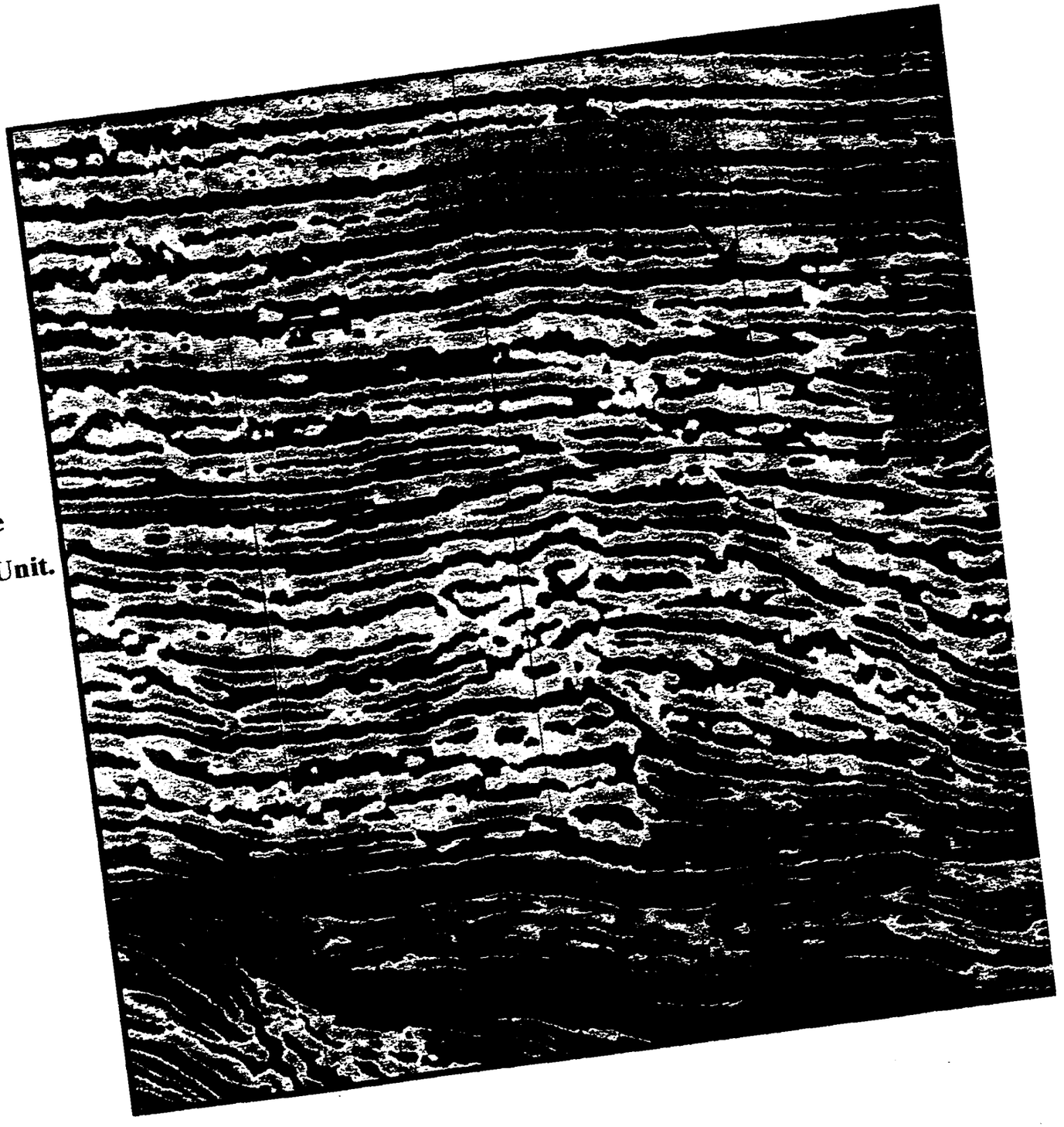

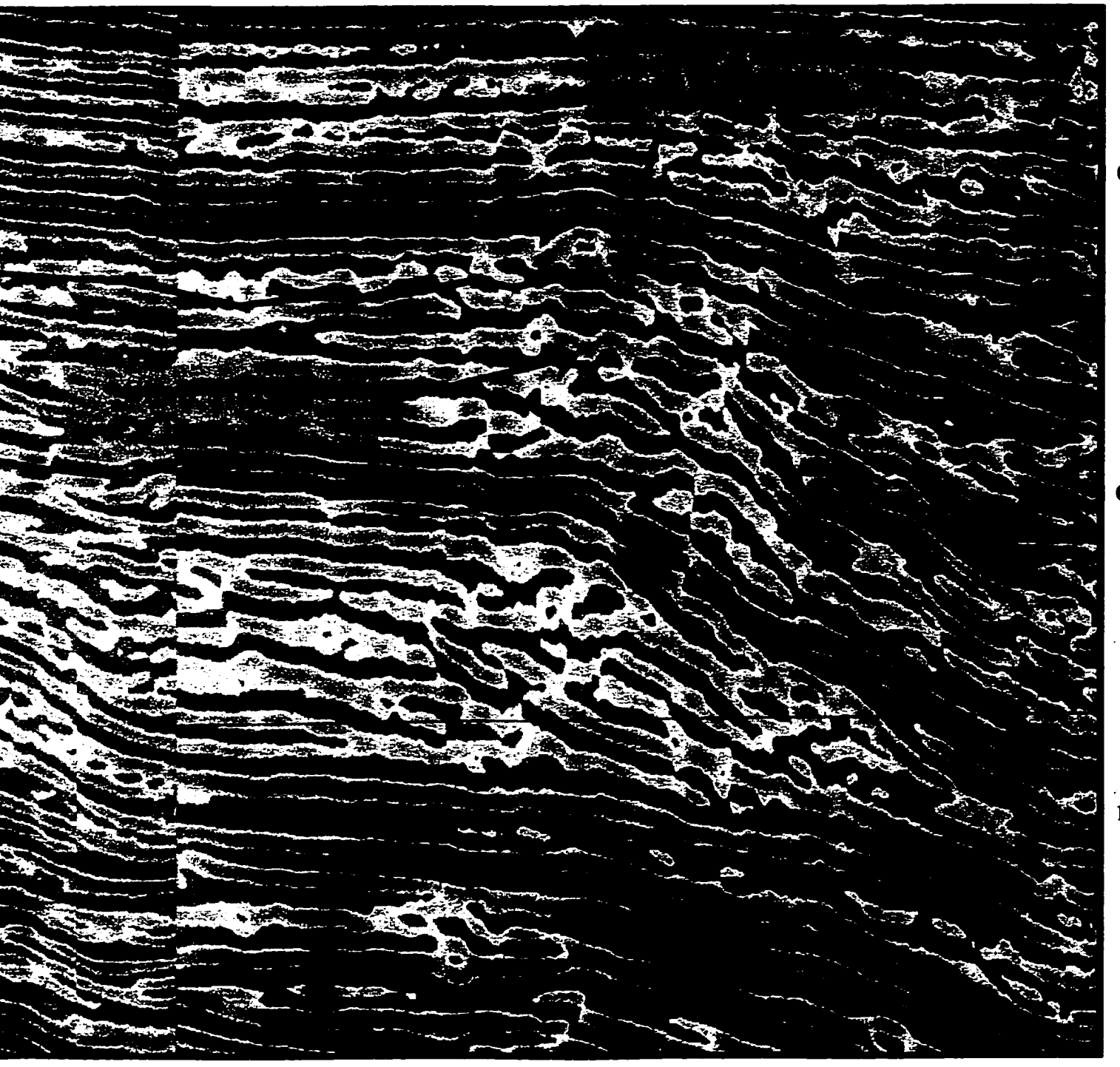
Time in
milliseconds
0.500
0.750
1.000

The Effect of Accommodation Space on Shoal Body Geometry

Heterogeneity within these shallow water, inner-ramp environments is primarily a result of fluctuations in sea level, accommodation space, and paleotopographic highs. These factors resulted in the development of localized grain-dominated shoals, a restricted lagoonal, and open marine facies that greatly compartmentalized the reservoir. The construction of an accurate depositional model and defining cycle boundaries within the reservoir is one of the most important elements in determining the lateral and vertical extent of the reservoir flow units.

The most productive intervals within the West Jordan unit are comprised of shoal bodies found within zones IV-E2 and IV-E1. Outcrop work indicates the importance of accommodation space on depositional environments and the overall geometry developed in San Andres shoal bodies. Outcrop sections through the San Andres recorded repeated upward shallowing of the carbonate platform as it filled accommodation space created during cycle-scale base-level rise (Kerans and Fitchen, 1995). Facies associations along with shoal body and intershoal geometries for described outcrops within Lawyer Canyon of the Algerita Escarpment are extremely similar to those found within the West Jordan unit. This is of particular importance as a predictive tool for fields that produce along the eastern margin of the Central Basin platform that lack sufficient core and well data in which to adequately map the lateral and vertical extent of these shoal bodies.

Kerans and Fitchen (1995) identified two primary shoal geometries within outcrops of San Andres strata along the Algerita Escarpment and Guadalupe Mountains. Their two shoal geometries were based on accommodation space, which reflects eustatic

trends and determines depositional environments. Their work illustrates that considerable variations occur within depositional environments and shoal body geometries under changing accommodation conditions. Under moderate to high accommodation during highstands, shoal bodies form stacked geometries with small tidal channels cutting shoals. Individual ramp crest shoal bodies exhibited up to 30 feet of thickness and separate well developed inner-ramp (middle ramp) lagoon facies from outer ramp facies. These geometries were observed within the overall highstand composite sequence and are placed within Guadalupian 2 and 3 high frequency progradational sequences (Kerans and Fitchen, 1995). Within low accommodation settings shoal bodies are thinner and laterally extensive (up to 10 miles) parallel to depositional dip, forming a shingled, oblique clinoform geometry. Low accommodation shoal bodies form shingled shoreface complexes and lack development of time-equivalent middle-ramp and tidal channel facies. Depositional dip within ramp crest and inner ramp environments is believed to have been 1 degree or less (Kerans and Fitchen, 1995).

Shoal body geometries observed within the West Jordan unit are the result of moderate to high accommodation during HST 1. Accommodation resulted in stacked shoals that are compartmentalized vertically by shifting facies tracts and laterally by intershoal mudbanks and tidal channels that resulted in the deposition of tight, impermeable strata.

West Jordan unit Depositional Model

The morphologic profile of the carbonate platform, ramp or shelf, is not nearly as important for characterizing San Andres reservoirs along the eastern margin of the

Central Basin platform as defining the internal pore type and geometry of lithofacies and facies tracts within cycle boundaries. Facies stacking patterns allow for the identification of the three-dimensional distribution of depositional environments related to facies tracts and the delineation of cycle boundaries, which in turn define flow units within the reservoir. The overall more generalized vertical sequence of San Andres strata along the eastern margin of the Central Basin platform is extremely uniform, exhibiting a shallowing upward sequence of subtidal through supratidal facies. However, facies variations and depositional environments from field to field show that substantial local variation does exist (Bebout and Harris, 1986; Garber and Harris, 1990). The West Jordan unit has been found to be highly compartmentalized based on depositional regimes controlling lithofacies distribution. Nevertheless, geometries of productive shoal bodies are very similar to documented in outcrop, and therefore, a predictive relationship can be established for determining their presence and general geometric extent.

The depositional model for the West Jordan unit is based on detailed core description and the spatial distribution of lithofacies described from core throughout the reservoir. Deposition within the West Jordan Unit was greatly influenced by minor paleotopographic variations along the gently dipping ramp. At times during middle San Andres deposition, the area probably became completely restricted as indicated by three to six inch thick coal intervals present over the unit (see Figure 25). Shoal complexes may have aided in restricting marine waters from entering into the area at times. Shoal facies are found just below the coal lenses in zone IV-C as seen in cores (fig. 27).

With continued progradation there was not enough wave action and water depth for the continued development of shoal bodies. The area became more restricted with

coal and argillaceous clay intervals deposited over previous areas where shoals once existed. Facies distribution indicates that the unitized interval was slightly higher to the west and south and most likely cut off from open marine waters to the east by paleotopography. During the culmination of HST 1, continued progradation and a lack of fresh marine waters produced hypersaline conditions that are believed to have resulted in early cementation of grain-dominated lithofacies within zone IV-C (fig. 11). A well-formed lagoon was present during deposition of zones IV-B and IV-A within the unit. A large vertical sequence of mud-dominated lithofacies eventually filled the lagoon resulting in distinct petrophysical differences between these middle ramp facies and earlier ramp crest facies. As tidal flat deposits continued their basinward migration, supratidal facies were deposited across the unit area. The culmination of HST 2 resulted in similar hypersaline conditions to occur as at the end of HST 1 and zone I was completely occluded with sulfate cement (fig. 11).

Proximal Outer Ramp through Ramp Crest Facies Tracts: (Zones IV-E2 - IV-C)

The lowermost zones (IV-E2 and IV-E1) consist of localized patch reefs/bioherm buildups, open marine facies and stacked shoal bodies (fig. 38). The distribution of stacked shoal bodies within the upper part of zone IV-E2 continuing upward through zone IV-C indicates relatively constant sea level conditions within a general aggradational sequence (fig. 38 B). Accommodation within the area allowed for stacked shoal sequences to form reaching total thicknesses of eighty vertical feet (24 meters) as seen in the WJU #1416 core. Planar bedding was seen in several of the cores although

Figure 38. Map view of facies tracts and three-dimensional block diagram of environments during deposition of zones IV-E2 and IV-E1. A). A map view of facies tracts present during deposition of these lower zones in the reservoir. Proximal outer ramp and ramp crest facies tracts are constrained by core data (large red circles). Bioherms and fusulinid facies within the lower parts of zone IV-E2 and IV-E1 suggest proximal outer ramp environments were present within the northeastern area of the unit. Stacked shoals within the ramp crest facies tract indicate a period of aggradation where vertically compartmentalized shoal bodies formed across the north-central and southeastern margins of the unit. Restricted mudflats and tidal channels that eventually filled with finer grained sediment resulted in lateral compartmentalization as well. Subtidal lagoonal facies are interpreted as being deposited to the west of the ramp crest facies although no core data exists at this depth in this area. B). A diagrammatic, three-dimensional block diagram illustrating the depositional environment occurring at this time. Low relief, localized paleotopographic highs resulted in the formation of stacked shoals along within the unit. Wave action was generated out of deeper water to the east allowing for the high-energy environment within the ramp crest facies tract that winnowed away mud rich sediment on these paleotopographic highs.

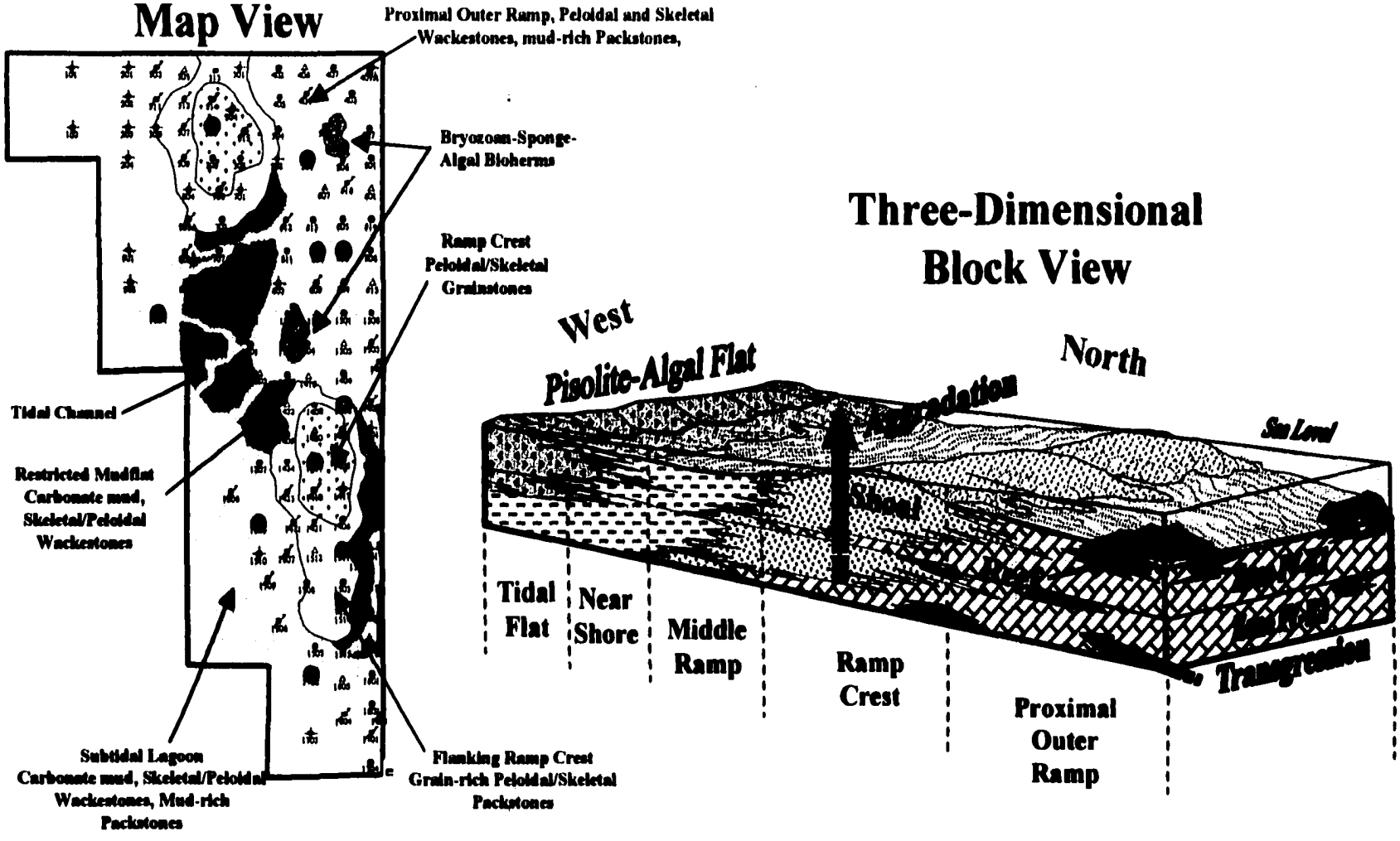
Map View
Proximal Outer Ramp, Peloidal and Skeletal Wackestones, mud-rich Packstones,
Bryozoan-Sponge-Algal Bioherms
Ramp Crest Peloidal/Skeletal Grainstones
Tidal Channel
Restricted Mudflat Carbonate mud, Skeletal/Peloidal Wackestones
Subtidal Lagoon Carbonate mud, Skeletal/Peloidal Wackestones, Mud-rich Packstones
Flanking Ramp Crest Grain-rich Peloidal/Skeletal Packstones
A.
Three-Dimensional Block View
West
North
Pisolite-Algal Flat
Sea Level
Tidal Flat
Near Shore
Middle Ramp
Ramp Crest
Proximal Outer Ramp
B.

destruction of original textures during dolomitization made identification of sedimentary structures and original grain fabric extremely difficult.

The distribution of lithofacies in the reservoir consisted of ramp crest and proximal outer ramp facies tracts over the majority of the unit as defined by core data (fig. 38 A). It is believed that a middle ramp facies tract was present to the west, however no core data exists to the west at this depth to substantiate the presence of lagoonal lithofacies. The distribution of ramp crest facies tracts seen in core indicates that a series of stacked shoal and intershoal areas formed similar to those seen in Figure 39 A. Deeper water fusulinid and bioherm facies indicate considerable lateral variation of water depth within the unit boundaries during deposition of these cycles. This is particularly evident within zones IV-E2 and IV-E1 where more quite water bryozoan-sponge-algal bioherm buildups and fusulinid facies are common. Water depths within the proximal outer ramp facies tract are believed to have reached sixty to eighty feet very quickly after moving away from the ramp crest facies tract (fig. 14). This would allow for the wave action needed within the ramp crest facies tract to form shoals and winnow away muddy sediments.

The Persian Gulf area, a subtropical arid, sabkha-type environment, is considered a modern analog for the San Andres along the eastern margin of the Central Basin platform (Purser and Evans, 1973; Friedman, et al 1990; Dull, 1995). This model fits nicely with the tidal flats and supratidal deposits of the upper San Andres formation and the evaporative reflux models for the diagenetic alteration of the San Andres to dolomite. It does not however, account for the large amounts of plant material needed to form the coal intervals found within zone IV-C. A satellite image from the coastline of the eastern

Figure 39. Diagrammatic depositional model and satellite image of the modern analog for shoals within the West Jordan unit. Detailed core analysis has identified vertically stacked shoal bodies within zones IV-E2 up through the middle of zone IV-C. A). A three-dimensional depositional model illustrating stacked shoal bodies similar to those occurring within the unit. Note the mud-dominated intershoal and mudflat deposits that result in both vertical and lateral compartmentalization between grain-dominated shoal facies. B). A satellite image from the Abu Dhabi coastline. This image shows complex ooid and skeletal sand shoals interspersed among islands. A large amount of plant debris found within shoal facies in zone IV-C indicates the possibility that shoals had become small, localized island features at the culmination of HST 1. Carbonate mud occurs adjacent to many of the islands in a similar manner as seen in the West Jordan unit as interpreted from core data. (A. Modified from Inden and Moore, 1983; B. modified from Harris and Kowalik, 1994).

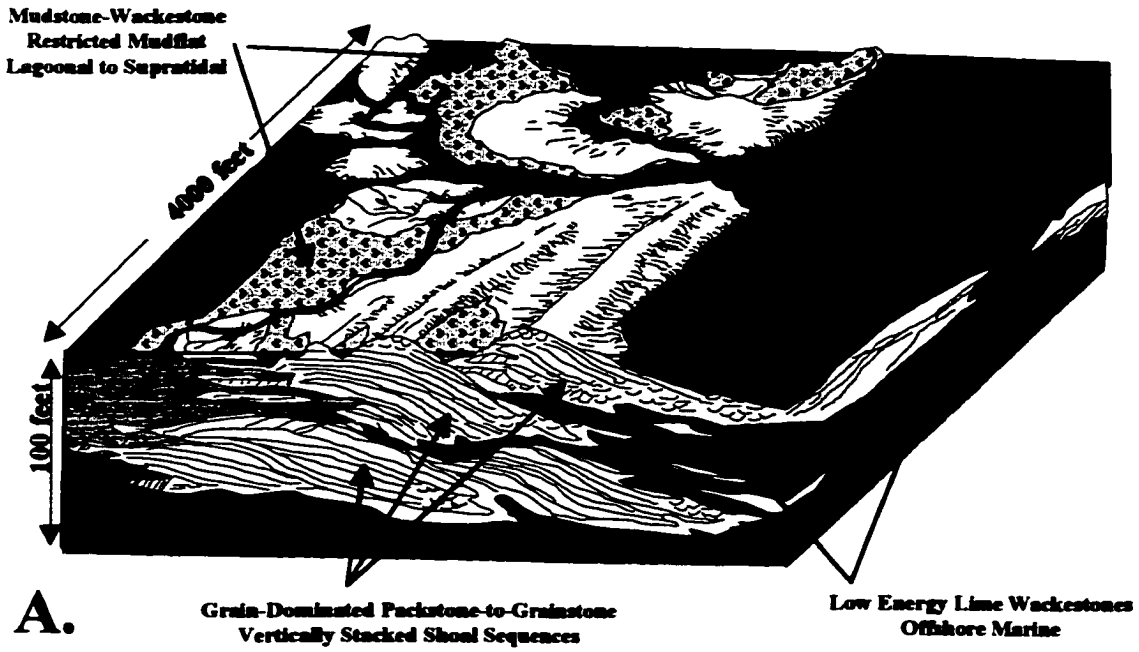
Mudstone-Wackestone
Restricted Mudflat
Lagoonal to Supratidal
4000 feet
100 feet
Grain-Dominated Packstone-to-Grainstone
Vertically Stacked Shoal Sequences
Low Energy Lime Wackestones
Offshore Marine

A.

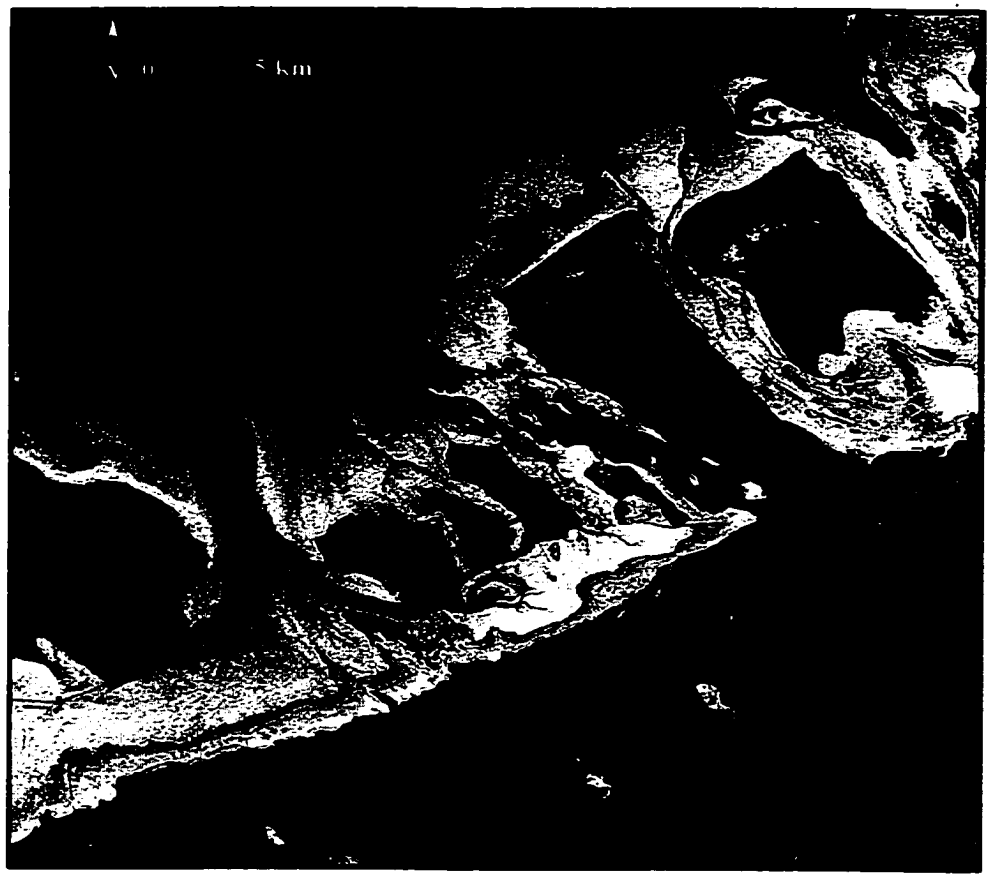

B.

Abu Dhabi area with the West Jordan unit outline superimposed over shoal complexes is presented in Figure 39 B. This model seems to fit nicely with the geometry of the shoal bodies seen within the West Jordan unit.

Paleogeographic reconstructions suggest that northeast prevailing winds and ocean currents produced a high-energy depositional environment along the eastern margin of the Central Basin platform (Walker, et al., 1991). These current and wind patterns also influenced the distribution and geometry of shoal bodies, however, to a less significant degree than accommodation space and paleotopography (fig. 40).

Average porosity maps (PHIA) were constructed using a high porosity cutoff value (13 percent porosity cutoff) in an attempt to filter out solution enhanced porosity so that primary depositional trends within each zone could be defined. Using these PHIA maps and core data, shoal bodies were mapped fairly accurately in zones IV-E2 and IV-E1 (fig. 41). Shoal bodies in these zones that extend laterally for 3,000 to 4,000 feet (approximately 900-1200 meters) and average vertically 10 to 30 feet (3 to 9 meters) are very similar to those seen on the Algerita outcrop and described within the literature (figs. 41 and 42).

A cumulative oil production map from the unit illustrates how closely production is tied to shoal bodies within the lower zones (fig. 43). Just as impressive is the correlation between non-permeable intershoal areas and low oil production within the unit. This illustrates that shoal and intershoal areas compartmentalize the reservoir laterally. These stacked shoal bodies are also often compartmentalized by dolomudstones and wackestones that formed vertically between successive shoal bodies (fig. 44). In addition, each zone boundary is capped by a shallowing upward facies overlain by a

Figure 40. Paleogeographic reconstruction of the Permian basin and West Jordan unit area. This reconstruction indicates that the Late Paleozoic north was forty-three degrees from present day north. Paleozoic northeast prevailing winds and ocean currents may have aided in the resulting geometry of high-energy shoal deposits. San Andres and Grayburg producing fields are indicated in red. A map of Zone IV-E2 shoal bodies identified from core and porosity maps has been rotated to the Late Paleozoic north to show their geometry with respect to northeast prevailing winds. It is felt that paleotopography, sediment accommodation and sea level oscillations probably had a greater affect on deposition of shoals within the West Jordan unit (map of Permian basin paleogeographic reconstruction modified after Walker, 1992).

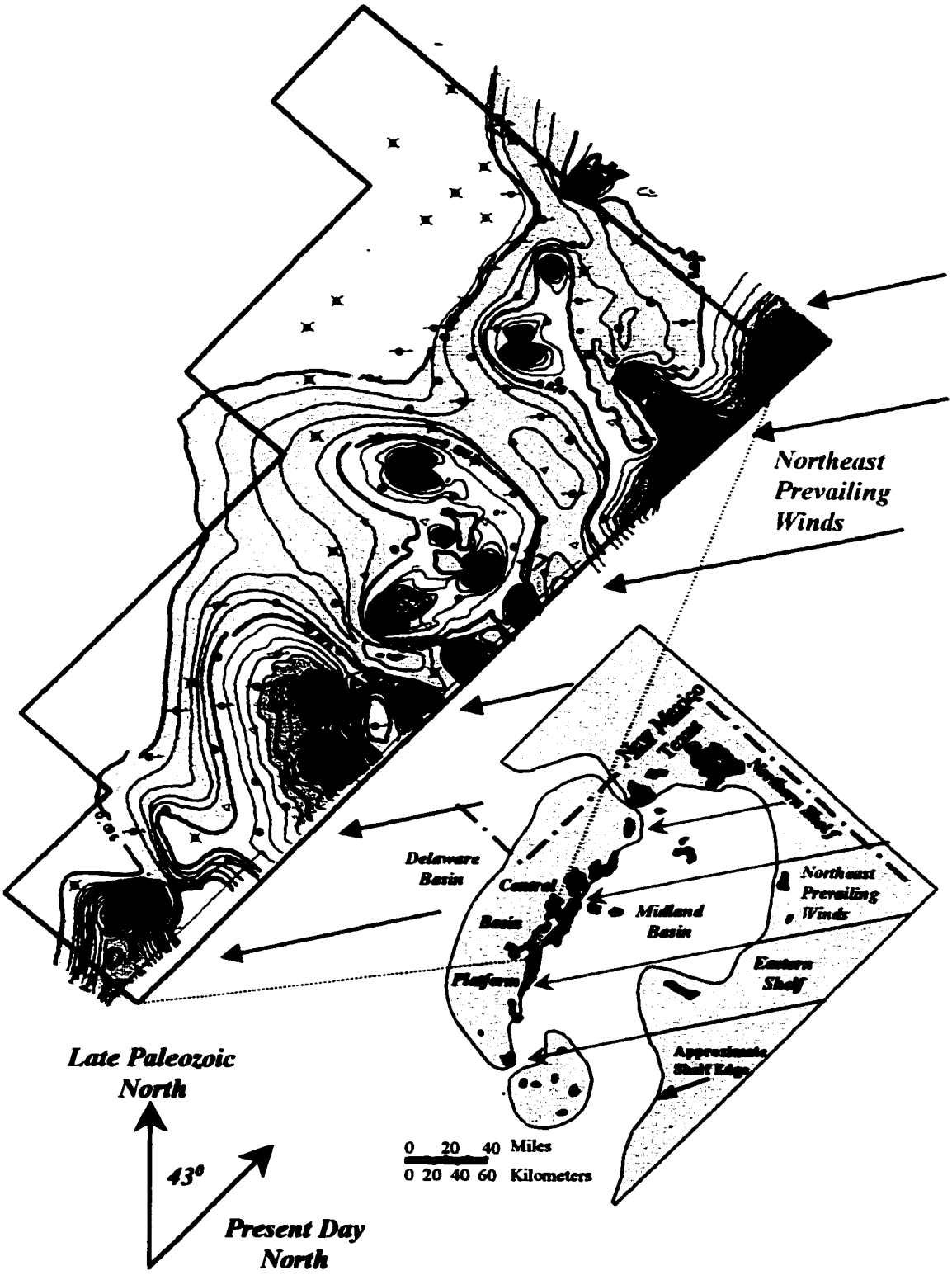
Northeast
Prevailing
Winds
Delaware
Basin
Central
Basin
Midland
Basin
Northeast
Prevailing
Winds
Eastern
Shelf
Platform
Late Paleozoic
North
43°
Present Day
North
0 20 40 Miles
0 20 40 60 Kilometers

Figure 41. Average porosity (PHIA) maps of zones IV-E1 and IV-E2. PHIA maps were created using a high porosity cutoff (13 percent) in order to filter out solution enhanced porosity within these lower zones and define primary porosity trends resulting from porous, grain-dominated ramp crest facies. PHIA maps along with a good distribution of core data indicate the lateral and vertical geometries of productive shoal bodies within the West Jordan unit. Shoal bodies are defined by yellow and blue color contours, intershoal areas are indicated by green. Large red circles indicate core locations.

Zone IV-E1

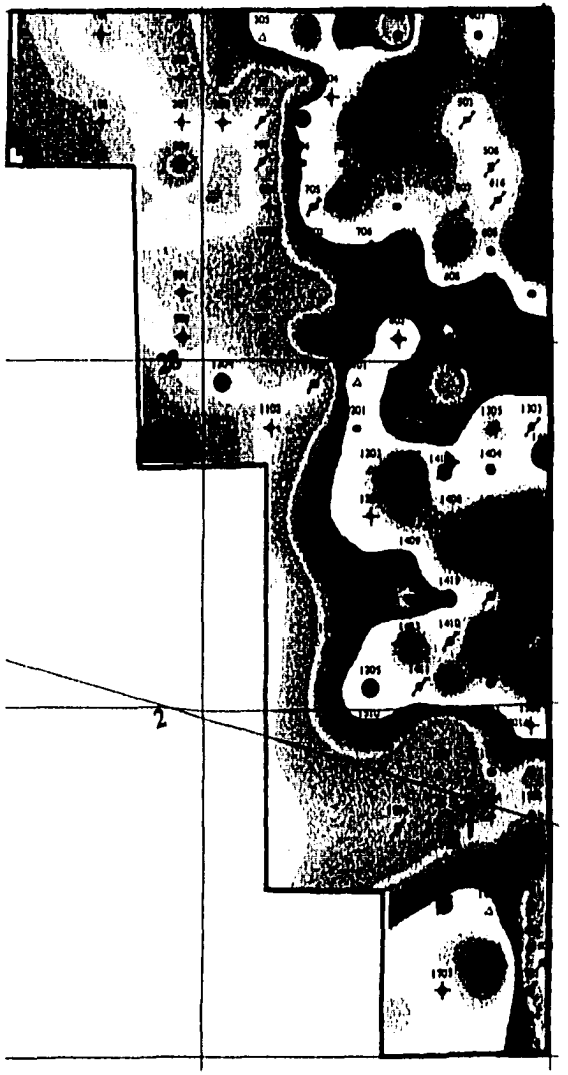

Porosity Scale (decimal)

0.100
0.098
0.096
0.094
0.092
0.090
0.088
0.086
0.084
0.082
0.080
0.078
0.076
0.074
0.072
0.070
0.068
0.066
0.064
0.062
0.060
0.058
0.056
0.054
0.052
0.050
0.048
0.046
0.044
0.042
0.040
0.038
0.036
0.034
0.032
0.030

Zone IV-E2

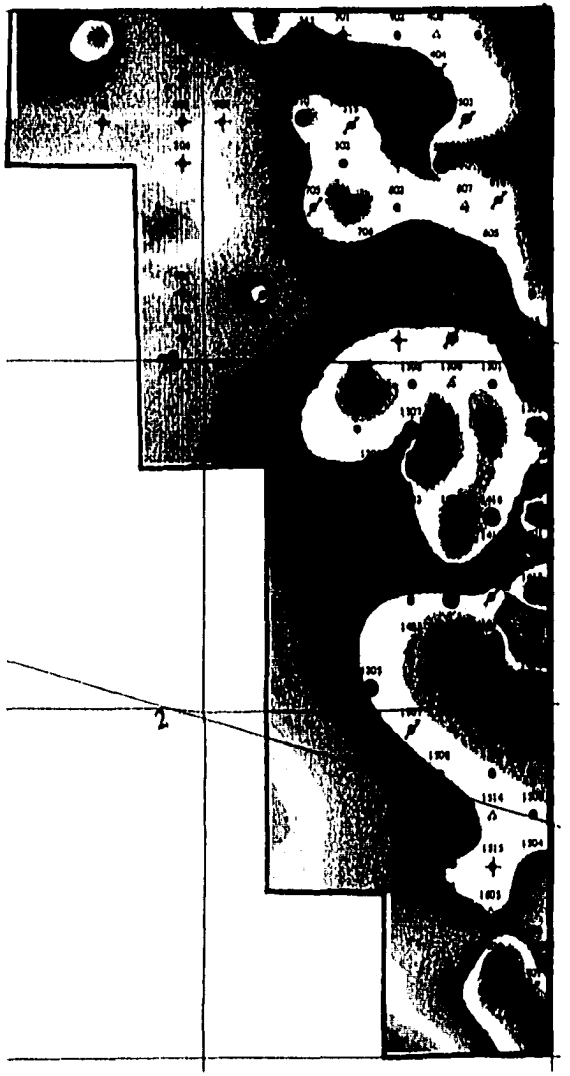

Figure 42. Outcrop photograph of shoal facies from Lawyer Canyon along the Algerita Escarpment in the Guadalupe Mountains. These shoals are seen to extend for several thousand feet laterally across the outcrop, similar to shoals indicated from core data and porosity maps form the West Jordan unit. The outcrop also exhibits tidal channel and mudflat deposits that interrupt the lateral continuity of these grain-dominated sequences. Dolomudstones are found at the base of each shoal, resulting in compartmentalization of stacked shoal bodies as well. Dashed red lines in the photograph indicate these dolomudstones. This shoal complex is about thirty feet high.

Figure 43. Map of cumulative oil production from the West Jordan unit. Cumulative oil is indicated by color contours, black contours represent structural feet above the oil-water contact (-875 feet subsea) for zone IV-E2. Cumulative oil production appears to be directly related to the location of shoal bodies within zones IV-E2 and IV-E1. Note that the best production is centered around the structural high area in the field, but overall, production appears to coincide with the location of shoal bodies rather than purely structural position. Also, note that intershoal areas result in low permeability non-productive reservoir. Vertical and lateral reservoir compartmentalization is substantiated by detailed core descriptions and outcrop correlations. Understanding reservoir compartmentalization is of particular importance under waterflood conditions when attempting to maintain continuity between injection and producing wells. Large red circles indicate core locations.

Cumulative Oil Map of the West Jordan Unit

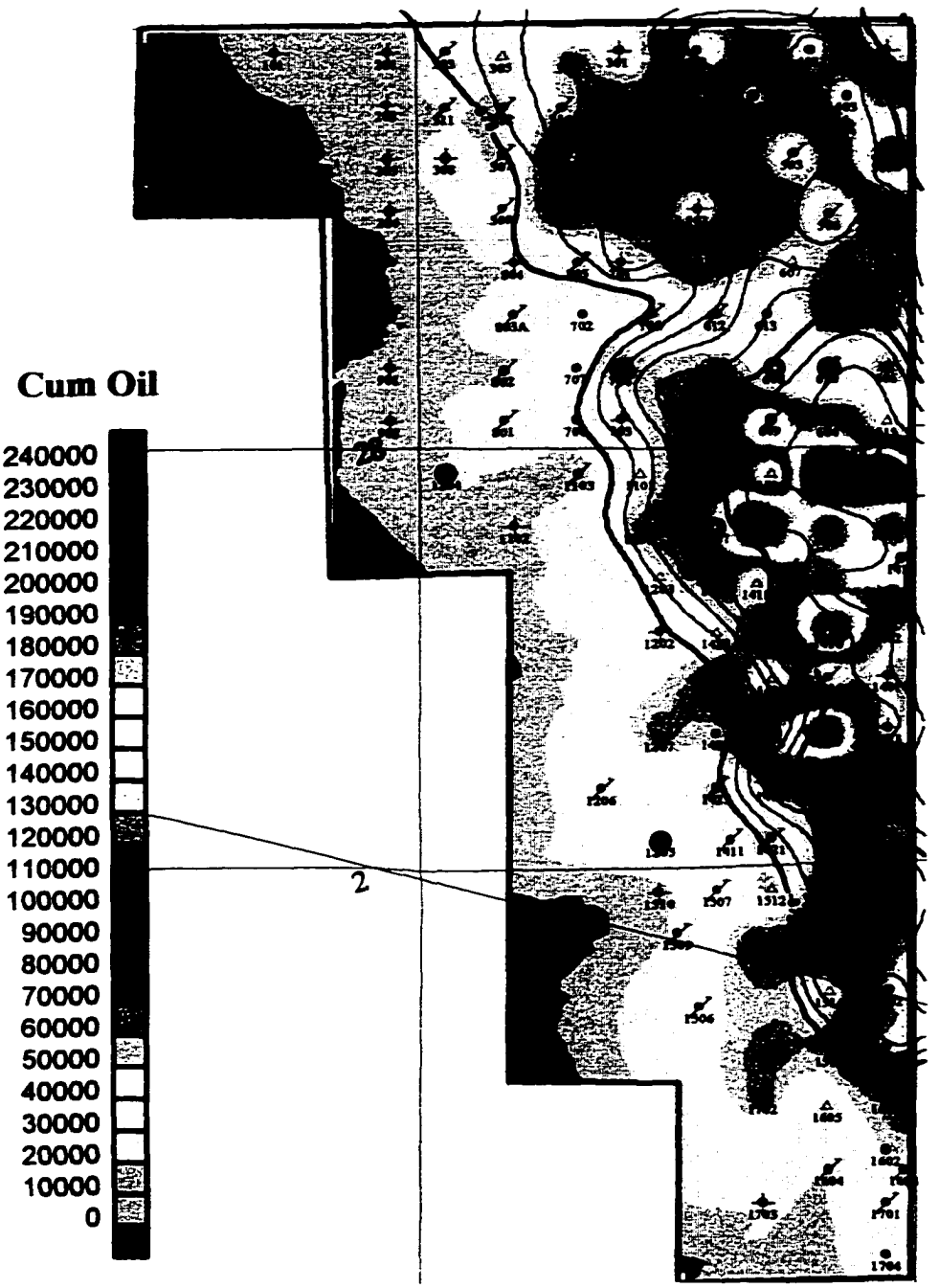

Figure 44. Outcrop photograph from Lawyer Canyon of mudstone barriers within shoal bodies along the Algerita Escarpment. As shoal bodies pinch out these dolomudstones can result in lateral heterogeneities. The insert (blue box) illustrates that permeability barriers as a result of mud-dominated facies can be present at all scales. The center shoal complex is approximately 10 feet high.

Shoalhaven

marine-flooding surface, which marks the cycle boundary. These marine flooding surfaces tend to be mud-rich, low permeability intervals. The cumulative production map illustrates that production patterns more closely follow shoal bodies than structure. Isopach maps of zones IV-E1 and IV-C also show the relationship of shoal bodies (fig. 13). Note that the isopach map of zone IV-E1 shows thick and thin intervals that correspond to a large degree to shoal and intershoal areas respectively, reflecting the patterns from porosity and cumulative oil maps.

The overall lack of dolomudstone occurrence within zones IV-E1 and IV-E2 suggests deposition within ramp crest to proximal outer ramp environments. Basinal or distal outer ramp environments in which dolomudstones have been found to occur have been described by many authors for the northwestern shelf and Central Basin platform (Harris et al, 1984; Sarg and Lehman, 1986; Bebout, et al, 1987; Harris and Walker, 1990; Ruppel and Cander, 1988; Leary and Vogt, 1990; Kerans and Fitchen, 1995). Distal outer ramp dolomudstones probably occur in the lower parts of the San Andres within the unit. Dolomudstones are found within the upper most part of zone IV-C where they are interpreted to be intershoal and middle ramp facies deposited in a quiet lagoonal environment.

Shoal bodies within the lower part of zone IV-C indicate continued aggradation. Lithofacies from the middle ramp facies tract in the upper parts of the zone indicate a change to progradation following highstand systems tract 1 (fig. 45). The entire zone was mapped as a single cycle based on the correlative nature of a maximum flooding surface at the base of zone IV-B. Shoal facies within the middle of zone IV-C may certainly mark the top of another cycle within the zone. However, shoal facies were not correlative

Figure 45. Map view of facies tracts and three-dimensional block diagram of environments during deposition of zones IV-E1 and IV-C. A). A map view of facies tracts present during deposition of these zones in the reservoir. Depositional environments within the reservoir were constrained to ramp crest facies tracts along the eastern margin of the reservoir and middle ramp facies tracts to the west. By the mid-to-upper part of zone IV-C deposition a series of vertically stacked shoals had formed, primarily along the eastern half of the unit. Shoal and intershoal mudflat lithofacies are constrained by core data (large red circles). B). Aggradation continued within the reservoir as evidenced by the presence of shoals within cores until the end of zone IV-C deposition. At this time high frequency sequence I was culminated by a highstand systems tract (HST 1). To the west mud-dominated middle ramp lagoonal lithofacies were being deposited within the unit boundaries. This area represents deposition within calm, shallow open to restricted marine waters.

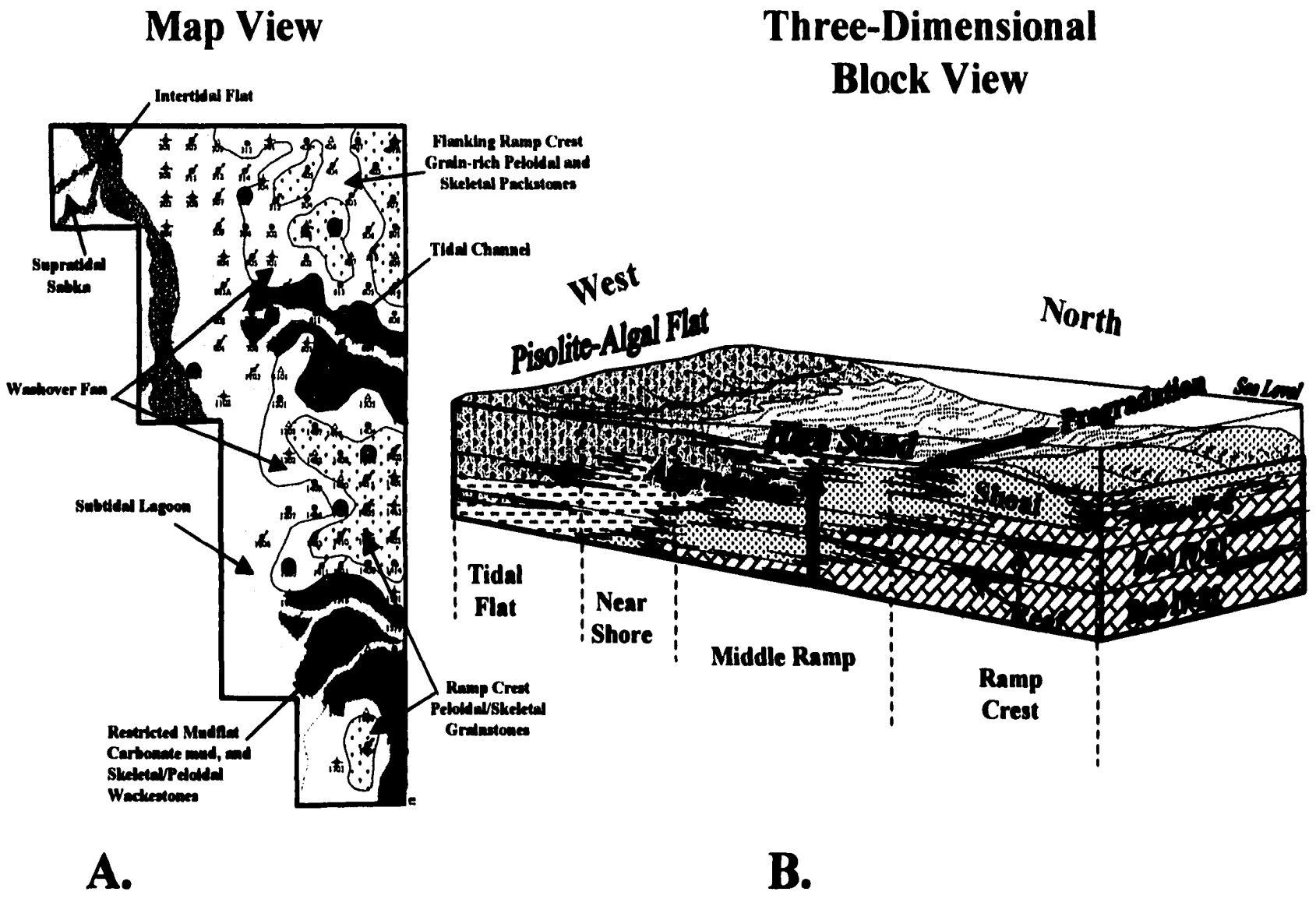
Map View
Three-Dimensional Block View
Intertidal Flat
Flanking Ramp Crest Grain-rich Peloidal and Skeletal Packstones
Supratidal Sabka
Tidal Channel
Washover Fan
Subtidal Lagoon
Ramp Crest Peloidal/Skeletal Grainstones
Restricted Mudflat Carbonate mud, and Skeletal/Peloidal Wackestones
West
Pisolite-Algal Flat
North
Sea Level
Tidal Flat
Near Shore
Middle Ramp
Ramp Crest
A.
B.

across the unit and because they could not be accurately mapped across the unit the cycle top was placed at the base of the correlative marine-flooding surface.

Porosity in the shoal facies within zone IV-C is completely occluded by sulfate cement making this facies nonproductive within the reservoir (fig. 27). Because of this porosity logs and PHIA maps do not delineate shoal bodies within this zone. Many of the cores along the eastern margin of the unit contained ramp crest, shoal facies within this zone. An isopach map of the interval attests to the continuation of aggregation within zone IV-C. The prominent thin zone representing an intershoal area seen in an isopach map of zone IV-E1 is also distinctly present within zone IV-C (fig. 13). This indicates that local paleotopography, which may be influenced by Pennsylvanian structure at depth, controlled deposition within the unit up through the middle of zone IV-C. Sulfate occlusion within zone IV-C is believed to be the result of exposure and early cementation occurring syndepositionally or shortly after deposition during the last stages of HSF I (figs.10 and 45). The highstand that culminated this event may have also allowed for meteoric waters to flow into the lower zones (IV-E1 and IV-E2) during periods of exposure resulting in the solution-enhanced porosity that occurs there.

In addition to these tight shoal facies numerous argillaceous clay intervals are present within this zone making it an overall barrier to flow (fig. 28). The upper part of zone IV-C shows a large degree of oscillation between ramp crest and restricted middle ramp facies as progradation was initiated within the area. The culmination of the cycle is marked by a three to six inch thick coal interval overlain by the marine flooding surface at the base of zone IV-B. Coal intervals seen at the top of zone IV-C indicate a change in climate conditions.

A considerable amount of organic material would be necessary to accumulate the coal intervals that reach up to six inches thick within the upper part of zone IV-C. These coal intervals indicate that a more humid climate was present during deposition of middle San Andres strata. Inland ponds that allowed for significant plant material to form in an oasis type environment might explain the formation of coal within the upper part of zone IV-C. If this were to be the case then the top of zone IV-C would represent a cycle boundary overlain by a minor transgressive pulse at the base of zone IV-B producing a laterally correlative marine flooding surface. Such a surface is seen at the base of zone IV-B allowing for deposition of the overlying more open marine middle ramp facies seen in the lower parts of the zone. Similar organic rich zones within San Andres rocks of the McCaney field are interpreted as being deposited within mangrove-type swamps bordering an island complex located seaward of the lagoon (Guiseppe and Trentham, 1999). This study and Guiseppe and Trentham's (1999) recent paper help to establish the presence of a more humid climate that occurred during middle San Andres time.

Middle Ramp Facies Tract (Zones IV-B and IV-A)

A marine flooding surface at the base zone IV-B indicates a minor transgression which was quickly followed by continued progradation (fig. 46). A thick succession of middle ramp facies comprises the bulk of zones IV-A and IV-B. The lateral extent and thickness (over 150 feet) of these middle ramp facies suggests that accommodation within the area was significant and progradation was a slow, long-term event Isopach maps of zones IV-B and IV-A suggest paleotopography was higher to the west and south within the unit based on thicker accumulations of middle ramp facies to the north and east

Figure 46. Map view of facies tracts and three-dimensional block diagram of environments during deposition of zones IV-B and IV-A. A). Deposition environments within the reservoir during zones IV-B and IV-A was dominantly shallow water, middle ramp lagoonal facies. Supratidal lithofacies of the inner ramp facies tract were being deposited along the western margins of the unit at times. Cores along the western and southern margins of the unit show periods of shallowing water conditions where supratidal facies were intermittently deposited within middle ramp facies tracts. Red circles indicate core locations. B). A minor transgressive pulse occurred at the base of zone IV-B and was quickly followed by progradation of middle ramp facies across the shelf.

Map View

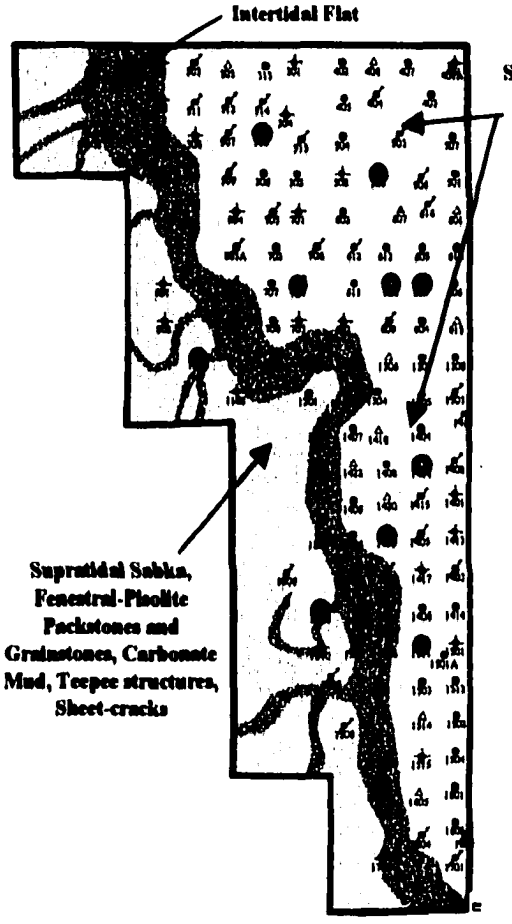

A.

Three-Dimensional Block View

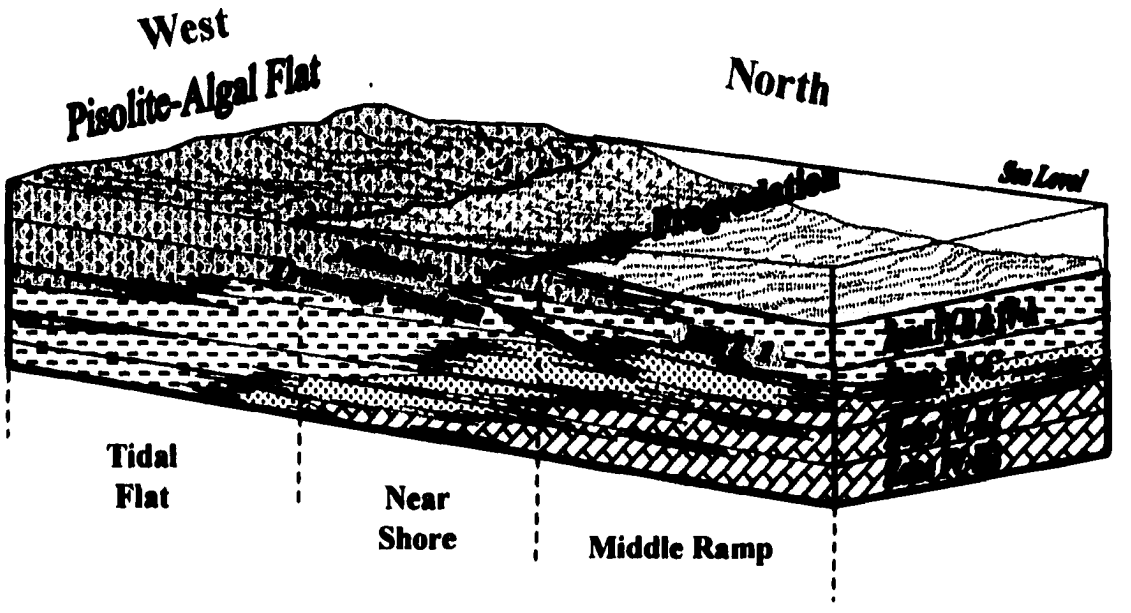

B.

(fig. 13). This is a distinct change in the depositional trend of the underlying zones. A cross section across the unit in the dip direction shows the transition within zone IV-A from an inner ramp facies tract to middle ramp facies tract systems (fig. 47). Zone IV-A has been further subdivided into minor cycle boundaries based on the presence of supratidal fenestral pisolite facies found within the WJU #1204 core in this zone. Core #1204 indicates that cycles prograded basinward from mixed near shore and supratidal facies to deeper middle ramp facies.

Lithofacies suggest deposition within a shallow lagoon exhibiting open to restricted marine conditions present during deposition of these zones. This environment resulted in the deposition of mud-rich skeletal and peloidal facies. The primary pore type found within the middle ramp facies tract is moldic that exhibits very low permeability within the West Jordan reservoir.

Inner Ramp Facies Tract (Zones III, II and I)

These zones represent continued progradation resulting in nearshore and supratidal facies being deposited over the unit (fig. 48). Zone III is a mixture of near shore skeletal and peloidal facies interbedded with supratidal pisolite facies. Algal laminated dolomudstones, intraclasts, and exposure surfaces are common within this zone as are thick argillaceous clay intervals. Intraclasts and exposure surfaces indicate intermittent periods of exposure followed by flooding. Very thick accumulations of supratidal pisolite facies were observed within zones II and I (fig. 47). Within zone II, the pisolite facies is both porous and permeable and was found to consistently form beds thicker than thirty-five feet.

Figure 47. Stratigraphic cross section in the dip direction of three cored wells. The cyclic nature of the facies can be seen as you move from west to east within zone IV-A. Zone IV-A has been further subdivided into minor cycle boundaries based on the presence of inner ramp supratidal capped vertical facies successions (pink) over middle ramp facies successions (gray) in the WJU #1204 core. The supratidal facies seen in the WJU #1204 core in zone IV-A mark the initiation of the eastward progradation of inner ramp facies tract across the unit. Unfortunately, only a partial section of the unit interval was cored in this well.

Shoal - Peloidal and skeletal grain-dominated dolopackstones and grainstones

Fusulinid - Fusulinid dolowackestones/packstones.

Peloidal - Peloidal dolowackestone to mud-rich packstones.

Skeletal - Dolowackestone/packstones.

Vertically Structured- Distinct vertically oriented mottling due to porosity variation.

Reefal/Bioherm - Bryozoan-sponge-algal boundstones and dolowackestone/packstones.

Intraclasts- Facies indicates reworking in high energy to exposed depositional regime.

Pisolite - Dolopackstones/grainstones with characteristic fenestral porosity.

Dolomudstone - Calm water of the middle ramp, near-shore and tidal flat environments.

Siliciclastic - Fine grained quartz-rich coarse grained to silt size particles.

Clay - Green to dark black, fine grained, found within the middle ramp and tidal flat deposits.

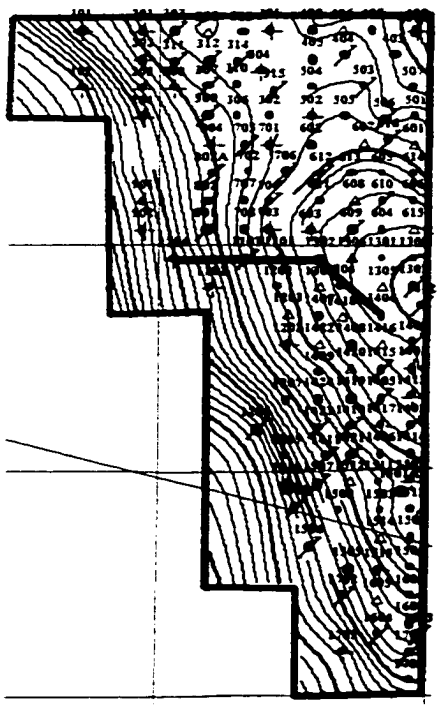

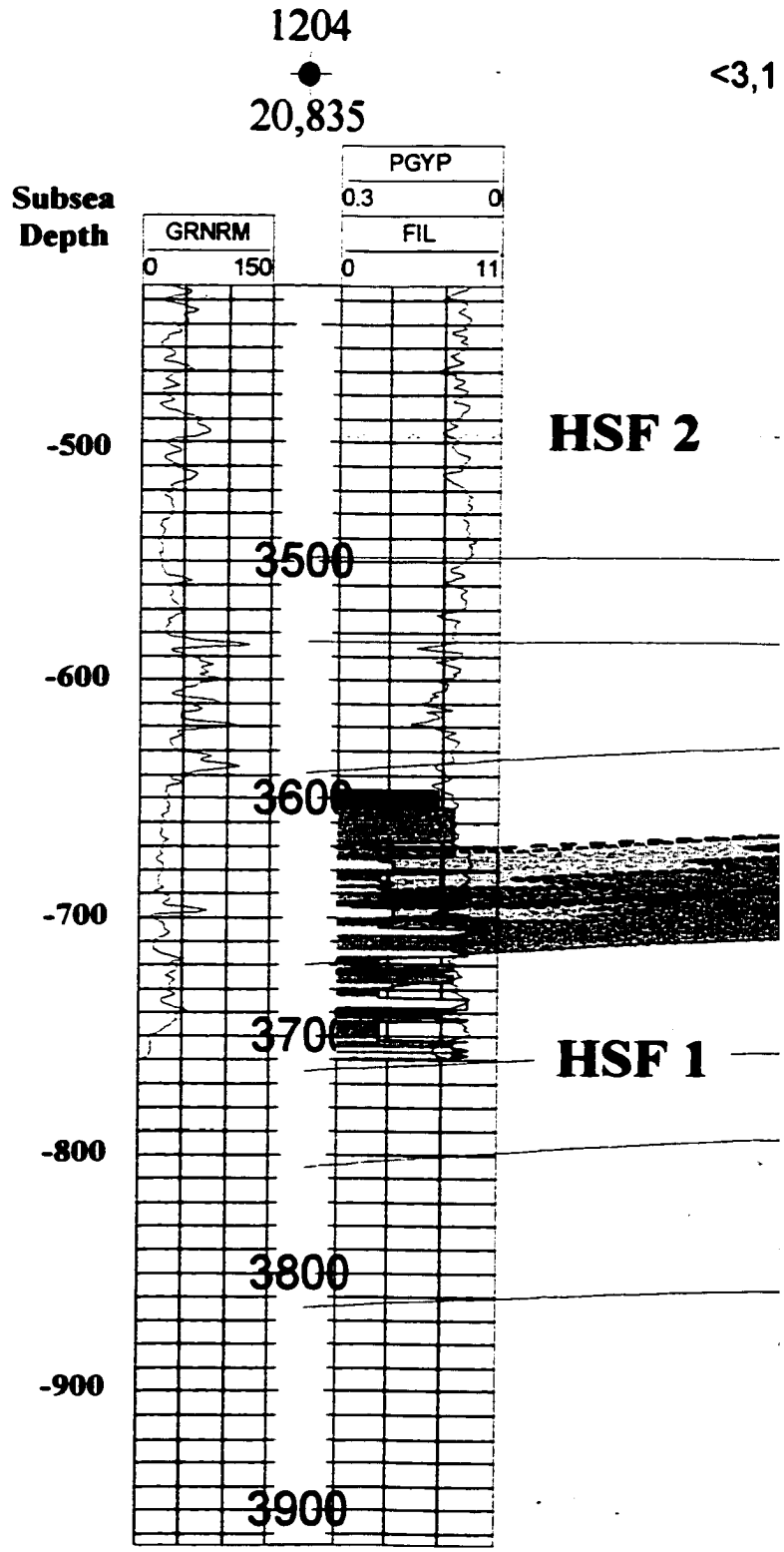

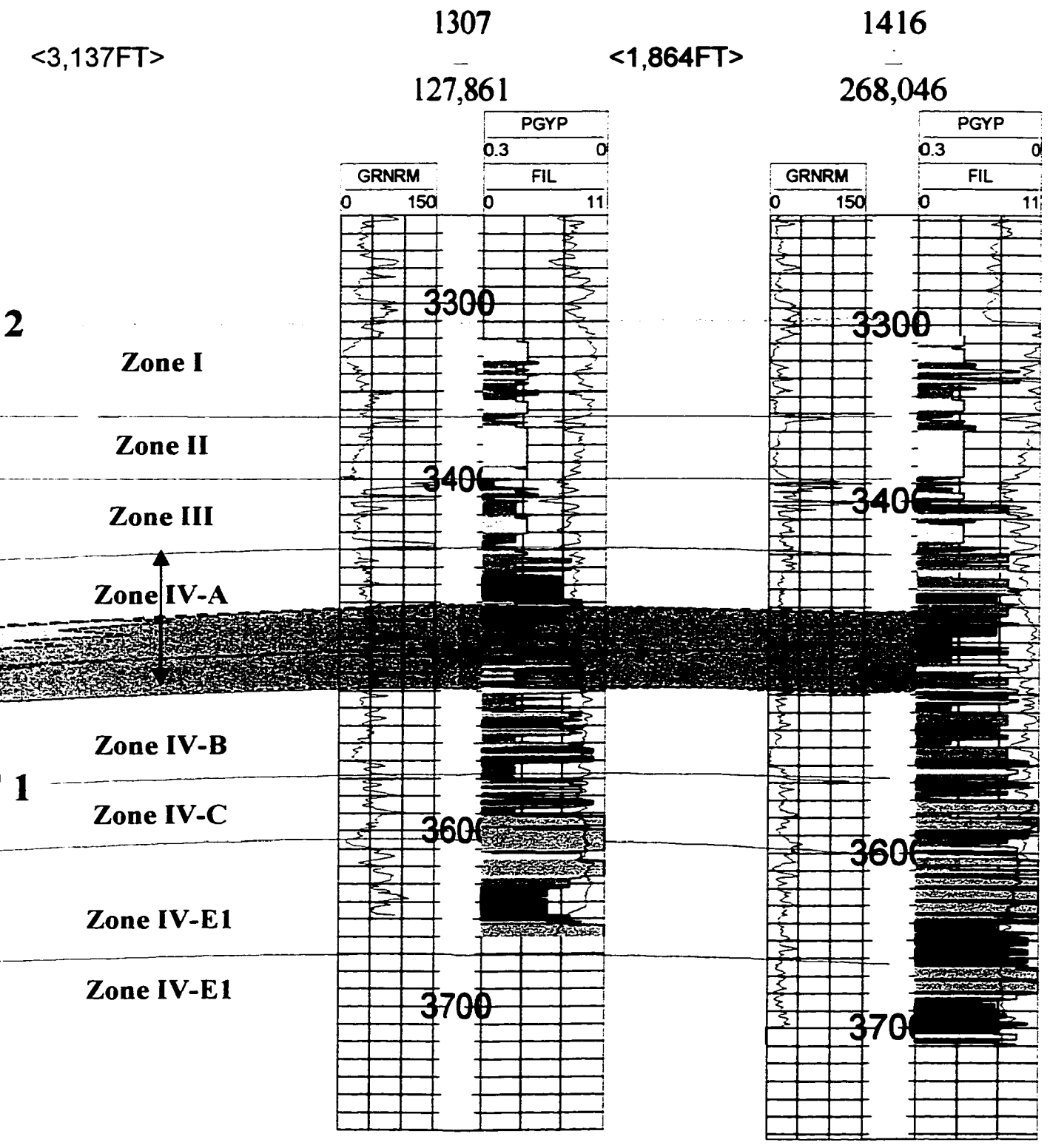
1307
<3,137FT>
127,861
1416
<1,864FT>
268,046
PGYP
0.3
0
GRNRM
FIL
0
150
0
11
3300
3400
3600
3700
Zone I
Zone II
Zone III
Zone IV-A
Zone IV-B
Zone IV-C
Zone IV-E1
Zone IV-E1

Figure 48. Map view of facies tracts and three-dimensional block diagram of environments during deposition of zones III, II, and I. A). During deposition of zone III nearshore environments were being deposited across most of the reservoir. Lithofacies range from shallow lagoonal skeletal lithofacies assemblages to supratidal fenestral pisolite grainstones. This suggests a dynamic environment where small changes in water depth greatly affected deposition of lithofacies. By the end of zone I, the entire unit area was overlain by supratidal, tidal flat deposits. B). The block diagram illustrates the continued progradation of middle ramp facies tracts across the unit. Middle ramp facies were followed by supratidal lithofacies of the inner ramp facies tract during deposition of zones III through I. The base of the overlying Grayburg Formation consists of a thick sequence of siliciclastics that were probably sourced by dunes migrating across inland areas as the sea moved basinward.

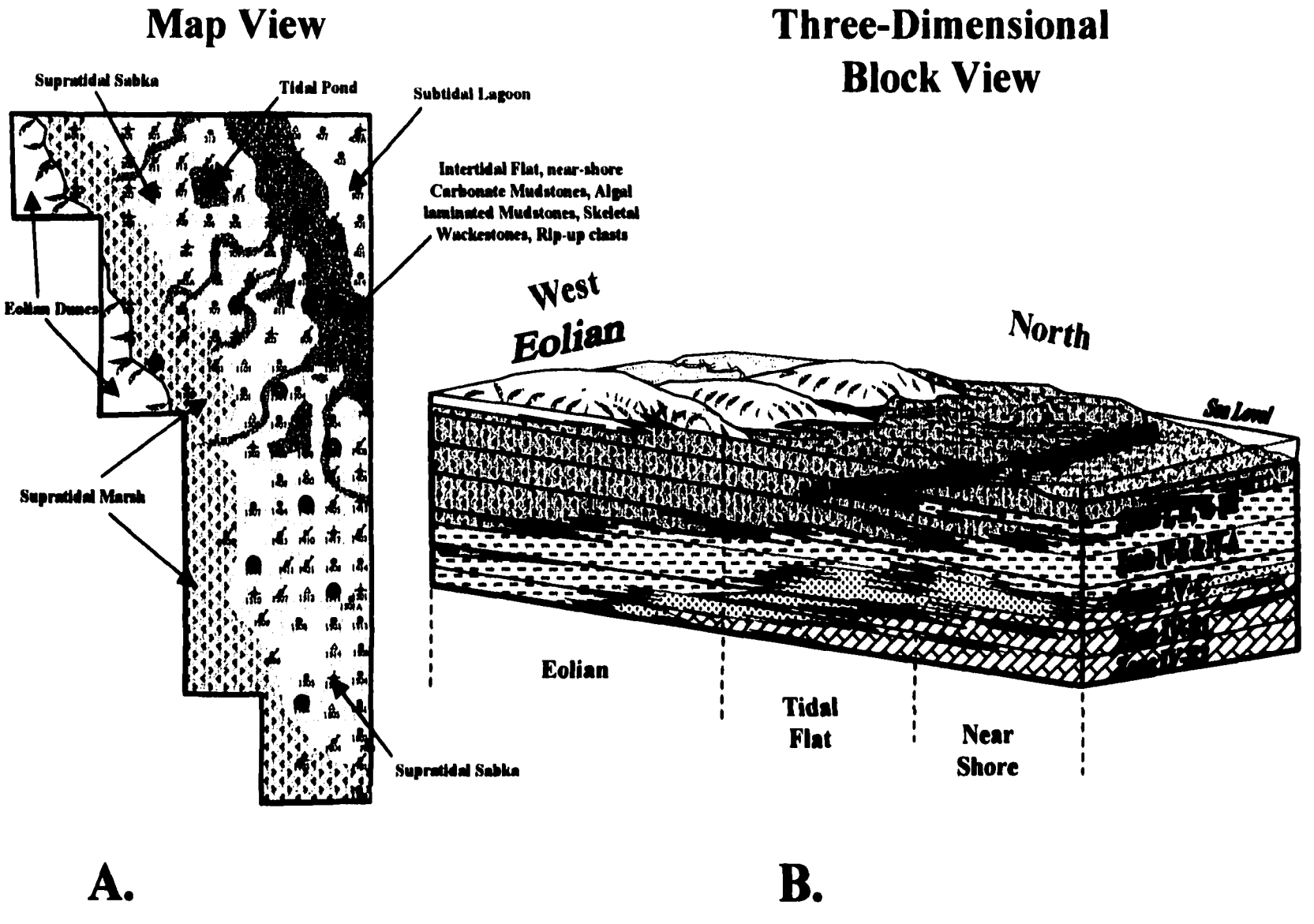
Map View
Three-Dimensional Block View
Supratidal Sabka
Tidal Pond
Subtidal Lagoon
Intertidal Flat, near-shore Carbonate Mudstones, Algal laminated Mudstones, Skeletal Wackestones, Rip-up clasts
Eolian Dunes
Supratidal Marsh
Supratidal Sabka
West
Eolian
North
Sea Level
Eolian
Tidal Flat
Near Shore
A.
B.

Zone I contains similar facies as zone II, however within zone I fenestral pores have been completely occluded by sulfate cement. Sulfate cementation within zone I is believed to have been syndepositional and related to the culmination of high frequency sequence II (fig. 10). Shallowing water conditions during HFS II are believed to have resulted in hypersaline waters and the precipitation of sulfate cements in a similar manner as suggested in zone IV-C. As with zones IV-E1 and IV-E2, zone II has been leached of all sulfate cement suggesting meteoric waters were able to filtrate into this cycle and remove earlier cementation. Meteoric water influx was most likely the result of a hydraulic head initiating fresh ground water seepage basinward into zone II where it was confined between cycle boundaries. The thickness of pisolite facies within zone I is not as extensive as within zone II. Pisolite beds are interbedded with thin intervals of cream to light tan dolomudstones and algal-laminated dolomudstones.

Isopach maps of zones III through I indicate a change back to a more north-south depositional trend across the unit (fig. 13). As expected, the pattern of thickening has increased in the west with the progradation of landward supratidal facies basinward. These supratidal facies thin significantly in the basinward direction. Overlying the San Andres Formation are the siliciclastics of the Grayburg Formation. These siliciclastic sediments suggest the continued progradation along the shelf with eolian wind swept sediments being transported and reworked over youngest San Andres strata (fig. 48).

CLASSIFICATION OF PORE TYPES

Introduction

Formation evaluation of complex, heterogeneous carbonate reservoirs requires detailed knowledge of pore types to accurately calculate reservoir properties responsible for fluid movement within cycle boundaries. This is particularly true for fields such as the West Jordan unit where the vast majority of the well logs are varying vintages of old style logs making core data a necessity to calibrate and normalize petrophysical properties calculated from these logs.

Fluid movement through a reservoir is directly related to pore characteristics that affect reservoir properties such as permeability, capillary properties, and m values (Lucia, 1983; Asquith, 1986 and 1995; and Wang, 1993). These reservoir properties are necessary to obtain accurate values for reservoir calculations used to predict the future economic potential of the field. Pore type development related to depositional environments, facies tract distribution, and diagenetic alteration is paramount to defining flow properties within the reservoir. Each cycle boundary within the West Jordan unit reservoir was found to contain unique properties that define whether it acts as a flow unit, barrier to flow, or as a waterflood thief zone.

The calibration of log data with core descriptions can greatly improve the accuracy of a reservoir model and improve secondary recovery programs. Each pore type found within the West Jordan unit has been documented by describing primary characteristics and statistical occurrence within each reservoir zone. Pore types within the

reservoir were found to change with facies tracts as you move from the inner ramp (tidal flat and near shore), middle ramp, ramp crest and proximal outer ramp environments (fig. 49). In addition, cycle boundaries within each facies tract also exhibit characteristic pore types or diagenetic alteration that further defines the petrophysical properties of the reservoir. This variation of pore types within cycle boundaries results in distinct changes in petrophysical properties as you move downward in depth within the reservoir and is directly related to facies tracts within the reservoir. Therefore, permeability transforms must be derived for each zone (cycle boundary) and it's characteristic pore type. This is a necessity to accurately model the reservoir and calculate more precise oil and gas recoveries.

The lack of a relationship between porosity and permeability is illustrated from cross plots of zones I through IV-E2 (fig. 50). Although there does seem to be some correlation between porosity and permeability within zones II, IV-E1 and IV-E2 it is weak at best. No correlation is seen between porosity and permeability within zones I, III, IV-A, IV-B and IV-C, which have extremely low correlation coefficients. Cross plot data clearly suggests that using a porosity to permeability transform for zones with a low correlation coefficient would have little accuracy. This data helps to illustrate the importance of defining pore types within cycle boundaries and various depositional environments within the reservoir. The permeability model for the West Jordan unit is based on the petrophysical behavior of pore types defined for each zone. This permeability model will be discussed in a later section.

The inner ramp facies tract (zones I, II, and III) is comprised mainly of finely crystalline dolomudstones, clay intervals and pisolite packstones and grainstones

Figure 49. North-to-south stratigraphic cross section of cored wells showing pore types within the West Jordan unit. Note that the upper reservoir inner ramp facies tract (zones I, II, and III) is comprised of primarily fenestral, fracture and moldic pore types in order of prevalence. The middle ramp facies tract of the reservoir (zones IV-A, IV-B, and the upper part of IV-C) is primarily moldic porosity and dual fine intercrystalline and moldic pore types. Fractures within the reservoir occur to a greater degree in zone IV-A. The lower part of the reservoir (zones IV-E1 and E2) within ramp crest and proximal outer ramp facies tracts contains principally medium-to-coarse intercrystalline porosity although moldic pores are present as well.

PORE TYPES



Interparticle

Intercrystalline (> 100 μm)

Intercrystalline (20-100 μm)

Intercrystalline (< 20 μm)

Moldic & Intercrystalline (> 100 μm)

Moldic & Intercrystalline (20-100 μm)

Moldic & Intercrystalline (< 20 μm)

Moldic

Moldic & Fracture

Fenestral

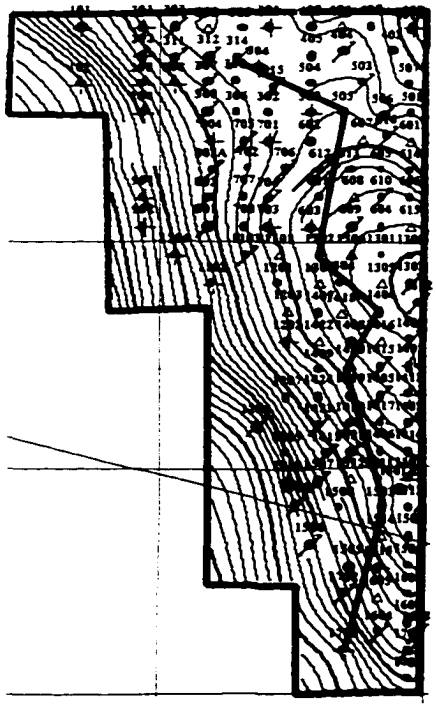

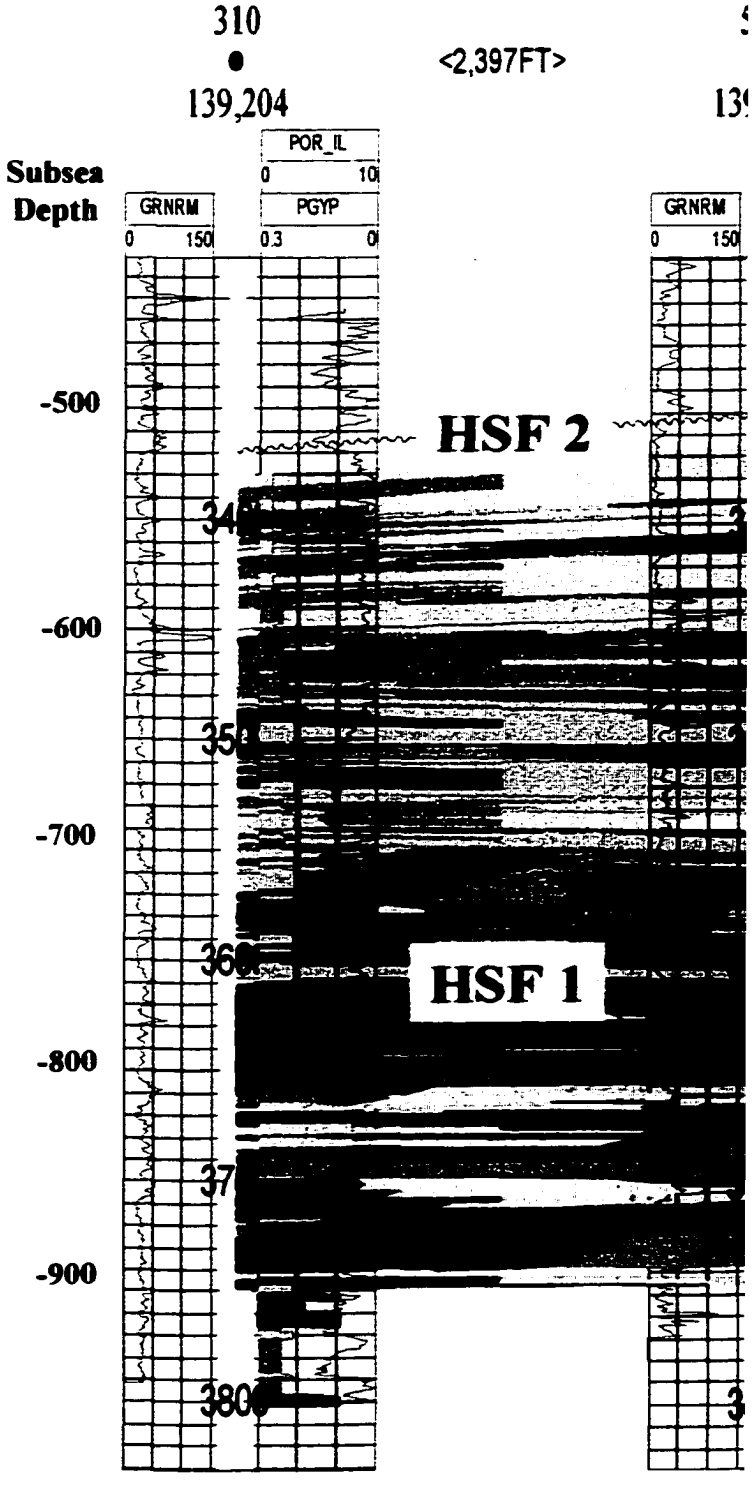

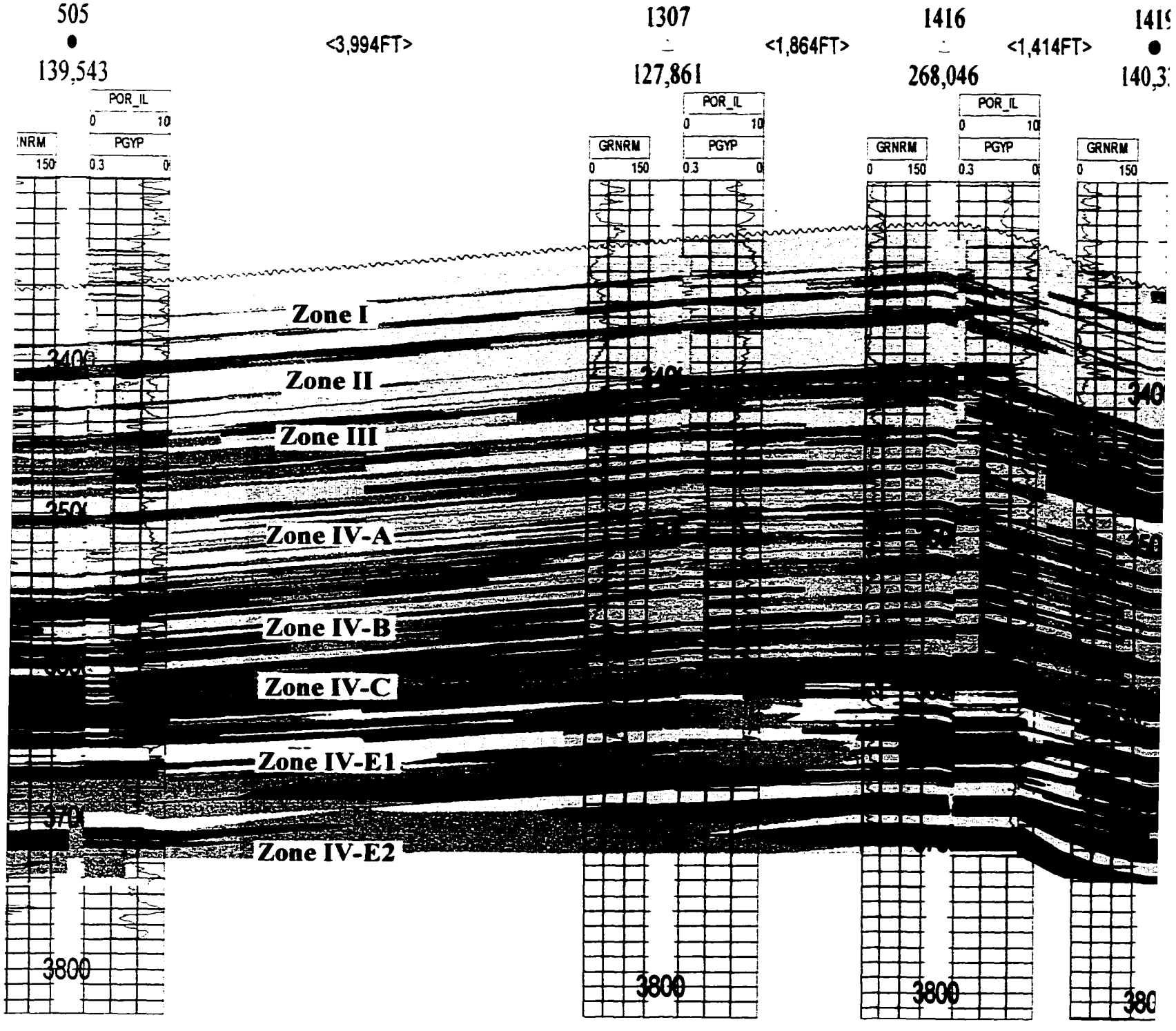
505
139,543
<3,994FT>
1307
127,861
<1,864FT>
1416
268,046
<1,414FT>
1419
140,3
POR_IL
0 10
PGYP
0.3 0
GRNRM
0 150
Zone I
Zone II
Zone III
Zone IV-A
Zone IV-B
Zone IV-C
Zone IV-E1
Zone IV-E2
3800

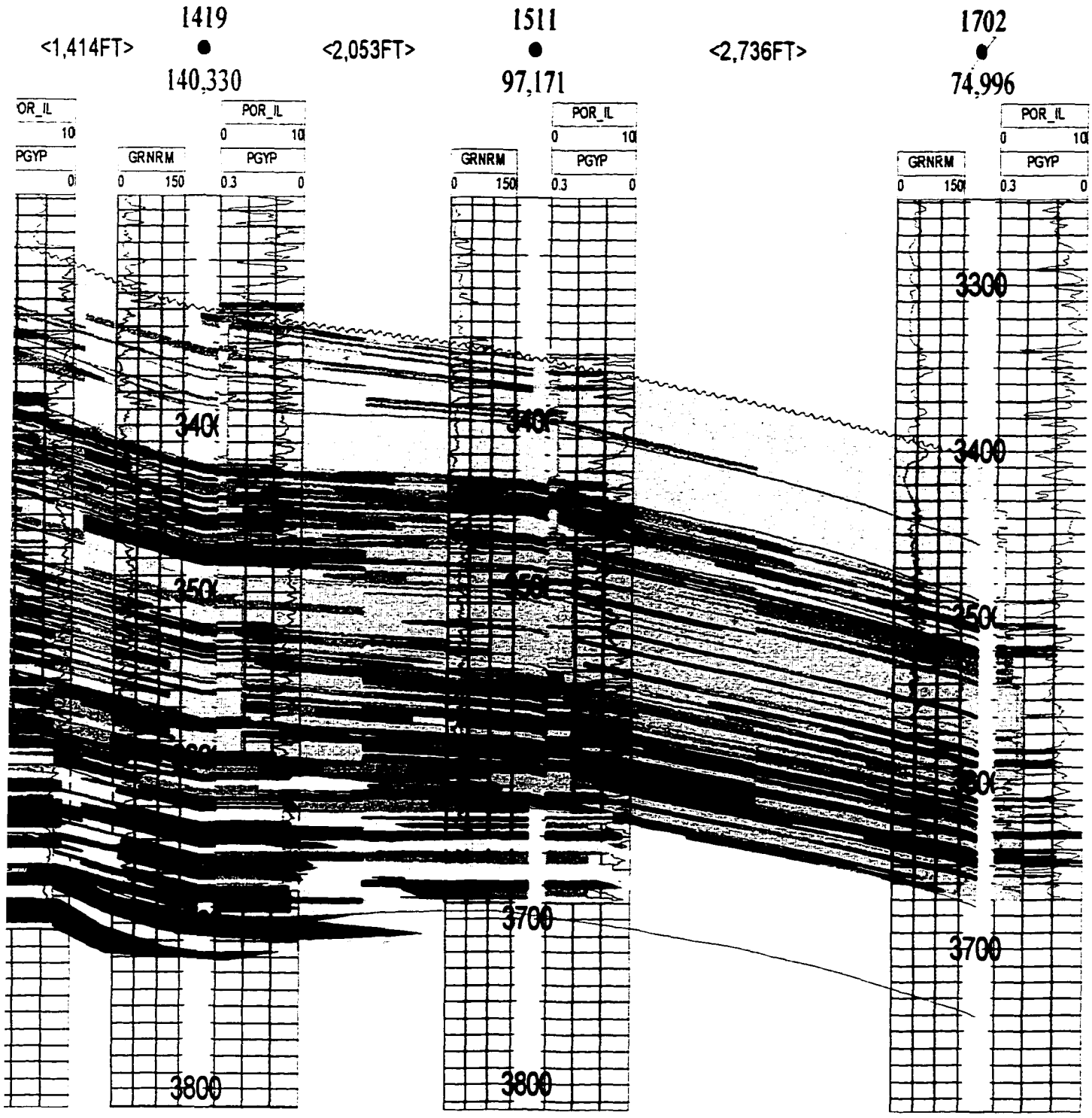
1419
<1,414FT>
140,330
1511
<2,053FT>
97,171
1702
<2,736FT>
74,996
POR_IL
PGYP
GRNRM
3300
3400
3500
3700
3800

Figure 50. Porosity versus permeability cross plots of available core data for each zone within the West Jordan unit reservoir. Correlation coefficients for each cross plot are provided. Zones II, IV-E1 and IV-E2 have the highest correlation coefficients, nevertheless, even these zones have a weak correlation and using porosity to construct permeability transforms would induce a considerable amount of error into the model. The determination of permeability by using porosity-to-permeability transforms is not an accurate method to apply in most carbonate reservoirs, particularly when a wide range of pore types are present such as seen within the West Jordan unit.

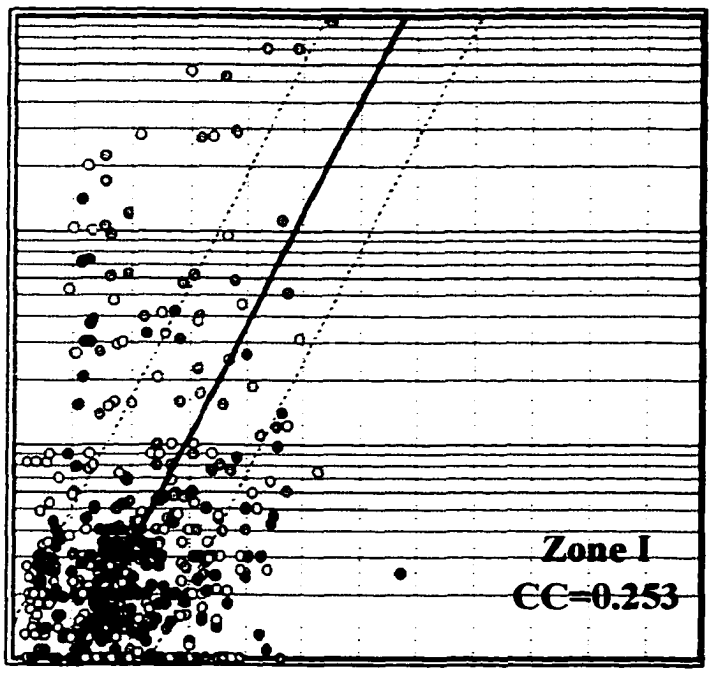
Zone I
CC=0.253

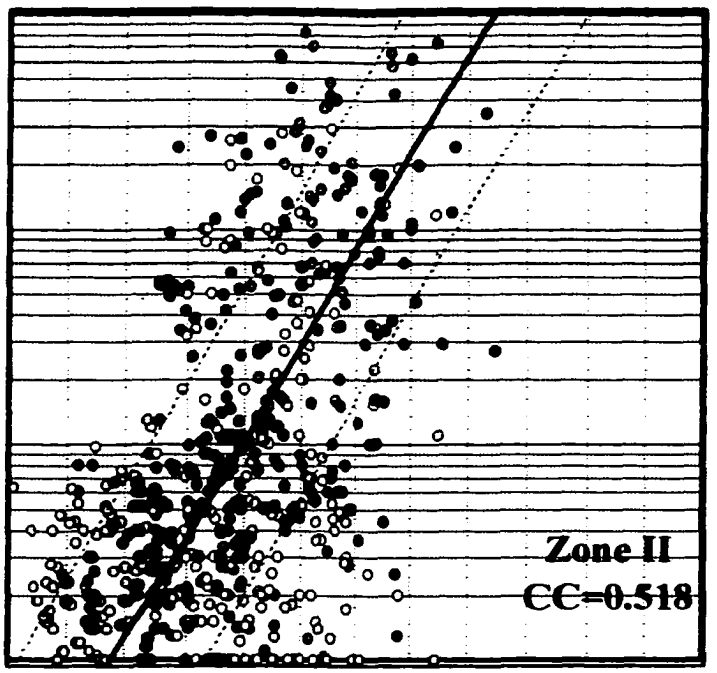
Zone II
CC=0.518

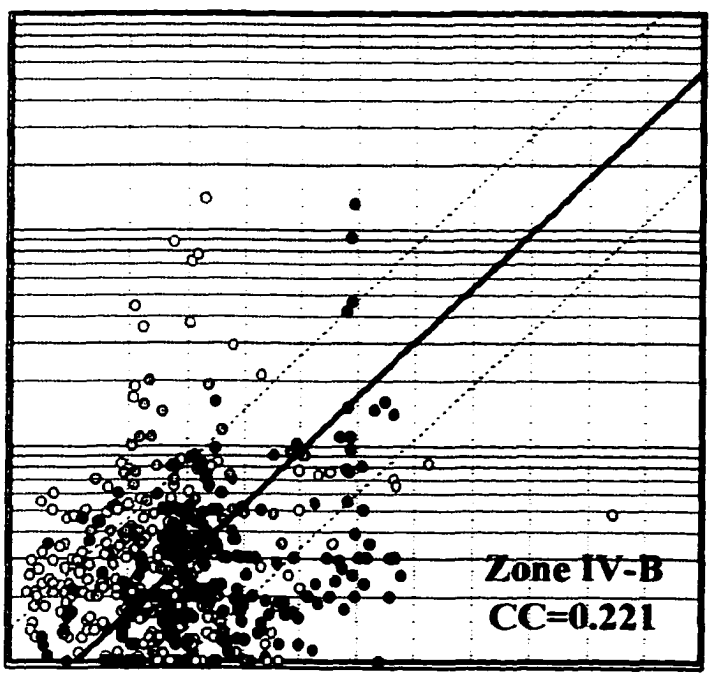
Zone IV-B
CC=0.221

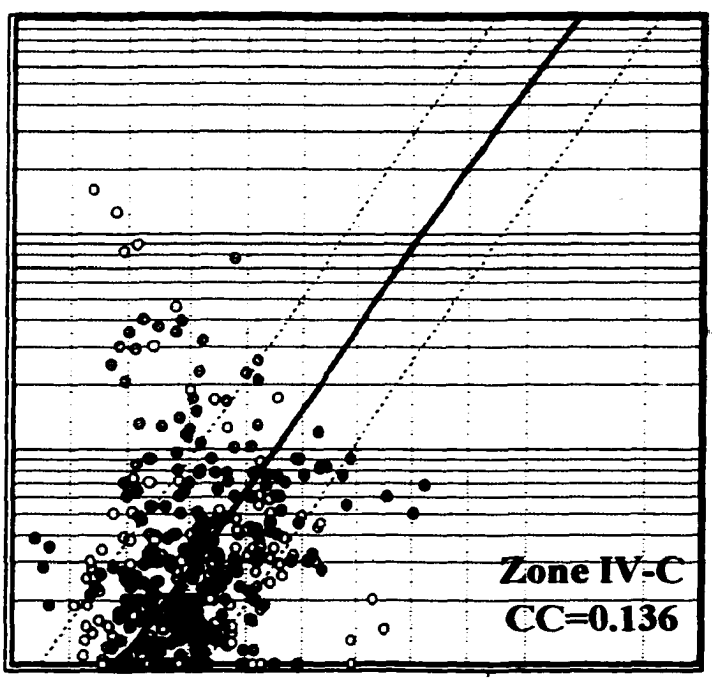
Zone IV-C
CC=0.136

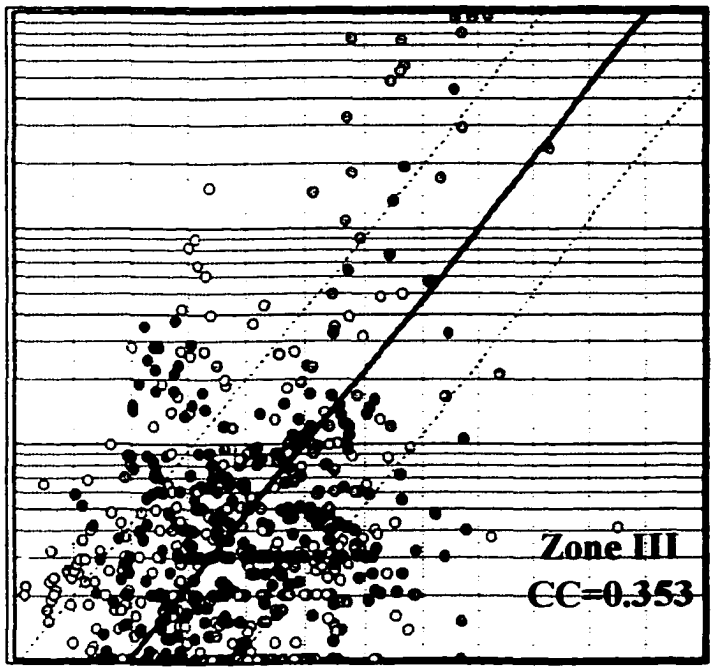
Zone III
CC=0.353

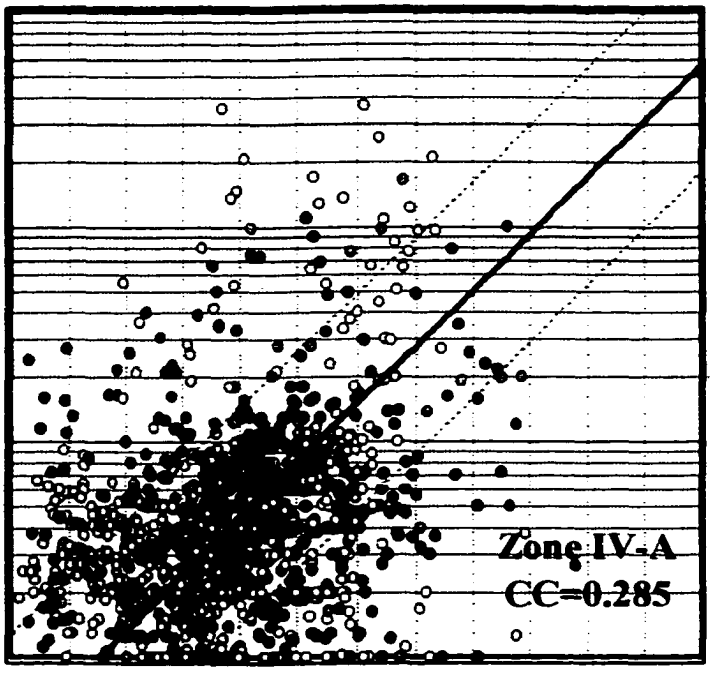
Zone IV-A
CC=0.285

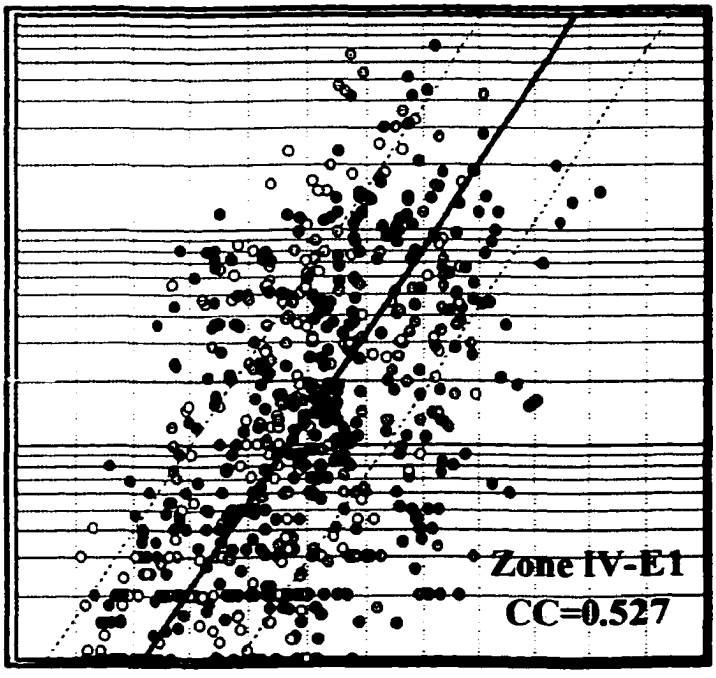
Zone IV-E1
CC=0.527

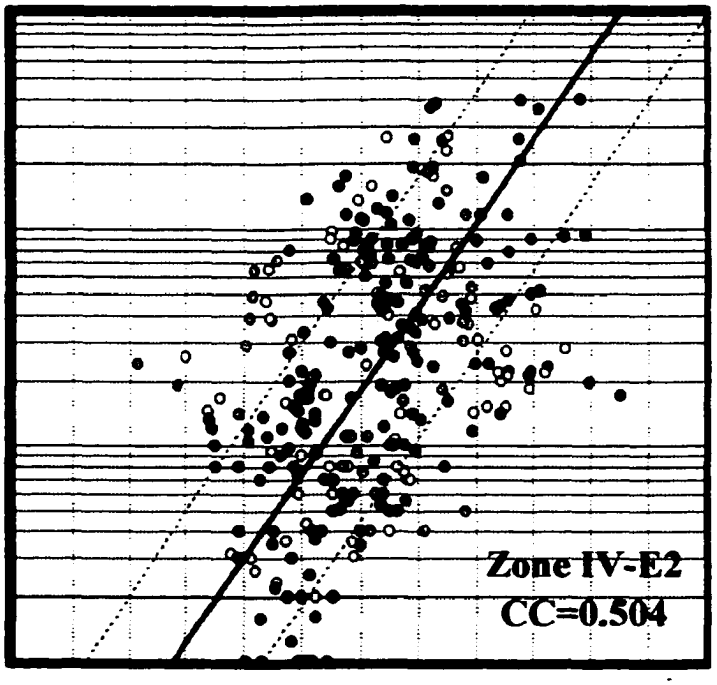
Zone IV-E2
CC=0.504

exhibiting fracture, fenestral, and moldic pore types (fig. 49). The middle ramp facies tract (zones IV-A and IV-B) contains dolomudstones and wackestones to mud-rich packstones. These zones are made up of lagoonal facies and exhibit fracture, moldic and dual moldic and intercrystalline pore types. Ramp crest facies seen within zone IV-C contain interparticle porosity. Although rarely preserved, almost all interparticle porosity occurs within sulfate occluded grain-dominated dolopackstones and grainstones within this zone. Ramp crest facies within zones IV-E1 and IV-E2 are comprised of large crystalline (< 100 (m) dolomites with well-developed intercrystalline porosity and intershoal and proximal outer ramp facies tend to be medium crystalline dolomites (50-100 (m; fig. 49).

Overall, zones II, IV-E1 and IV-E2 are the primary flow units within the reservoir. These zones consistently exhibit the highest porosity and permeability within the reservoir (fig. 50). Exceptions within these zones that compartmentalize the reservoir are low permeability intershoal areas within zones IV-E1 and IV-E2 and lateral facies changes from fenestral pisolite facies to tight dolomudstones within zone II. Another way to view this data is by looking at porosity-permeability cross plots versus zones for cored wells (fig. 51). Most of the cored wells show zones II, IV-E1 and IV-E2 (red, light blue, and dark blue colors respectively) to have the highest porosity and permeability. Where significant facies changes occur, such as in the West Jordan unit #310 core, cross plots vary from norm. For example, data points from zones IV-E1 and IV-E2 that plot lower permeability were found to be mud-rich intershoal facies (fig. 51, WJU #310 and 1419

Figure 51. Porosity versus permeability cross plots versus depth (defined zone intervals). Cores with the most complete section are shown in this figure to demonstrate general porosity-permeability trends within the reservoir. Data points are color coded to the representative zone color seen on the right hand side of each cross plot diagram. Note that zones II, IV-E1 and IV-E2 consistently have data points with greater porosity-permeability values. The effect of solution enhanced porosity and porous shoal versus non-porous intershoal areas can be seen in the WJU #310 and #1419 cores for zones IV-E1 and IV-E2.

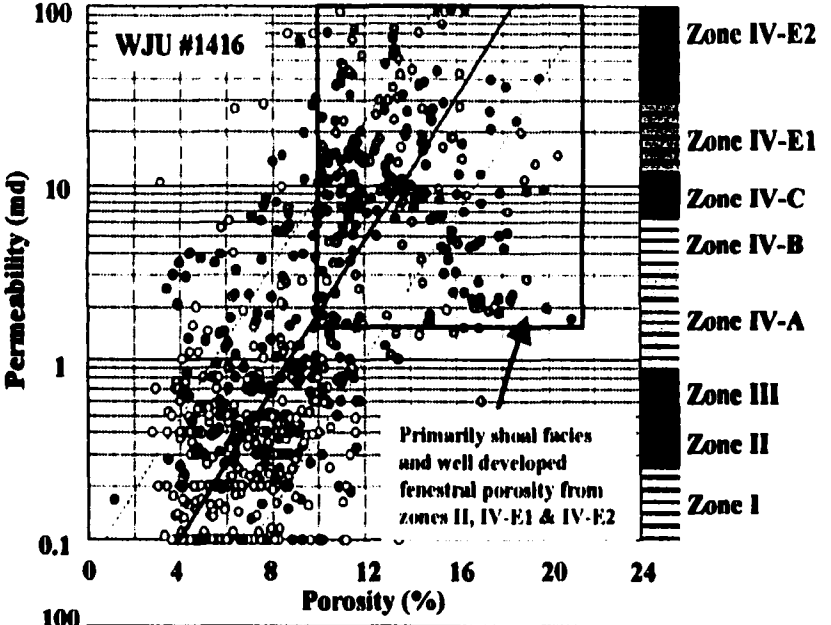
WJU #1416
Permeability (md)
100
10
1
0.1
0
4
8
12
16
20
24
Porosity (%)
Primarily shoal facies and well developed fenestral porosity from zones II, IV-E1 & IV-E2
Zone IV-E2
Zone IV-E1
Zone IV-C
Zone IV-B
Zone IV-A
Zone III
Zone II
Zone I

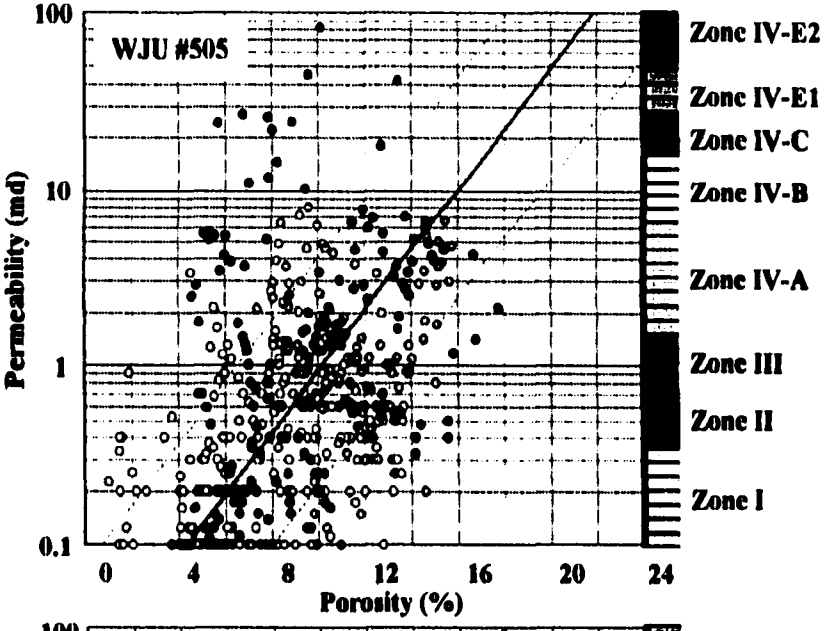
WJU #505
Permeability (md)
100
10
1
0.1
0
4
8
12
16
20
24
Porosity (%)
Zone IV-E2
Zone IV-E1
Zone IV-C
Zone IV-B
Zone IV-A
Zone III
Zone II
Zone I

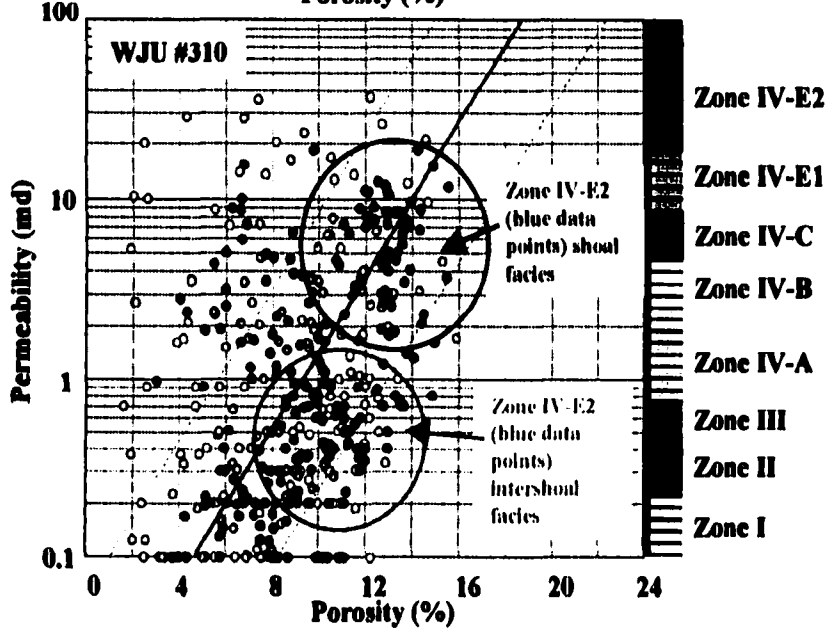
WJU #310
Permeability (md)
100
10
1
0.1
0
4
8
12
16
20
24
Porosity (%)
Zone IV-E2 (blue data points) shoal facies
Zone IV-E2 (blue data points) intershoal facies
Zone IV-E2
Zone IV-E1
Zone IV-C
Zone IV-B
Zone IV-A
Zone III
Zone II
Zone I

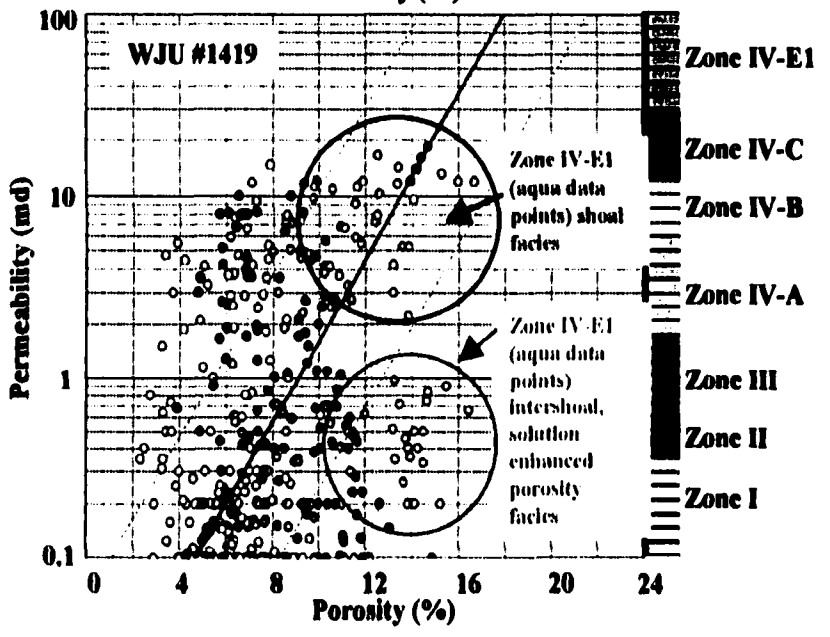
WJU #1419
Permeability (md)
100
10
1
0.1
0
4
8
12
16
20
24
Porosity (%)
Zone IV-E1 (aqua data points) shoal facies
Zone IV-E1 (aqua data points) intershoal, solution enhanced porosity facies
Zone IV-E1
Zone IV-C
Zone IV-B
Zone IV-A
Zone III
Zone II
Zone I

cores). Data points that exhibit high permeability and low porosity are the result of permeability anomalies such as fractures and stylolites within the data sample.

The following section provides descriptions of major pore types identified within the San Andres Formation at the West Jordan unit. Most pore types associated with carbonate reservoirs have been encountered in this heterogeneous reservoir, however, only several of these play a significant role in fluid movement within the reservoir. This study uses the terminology and classification put forth by Choquette and Pray (1970) for core chart and porosity descriptions (Appendix B).

Intercrystalline

Intercrystalline porosity is the pore space occurring between individual dolomite crystals and is typically described as secondary in nature (figs. 52 and 53). Intercrystalline porosity is most common within the lower zones of the San Andres Formation at West Jordan unit. Core descriptions indicate intercrystalline porosity within the unit to range from 1% to 21%, with a mean porosity value of 12%. Complex polyhedral shapes and tabular or sheet pore throats dominate intercrystalline pore space geometry and commonly result in good permeability. Permeability values associated with intercrystalline porosity in the unit were measured to range from 1 millidarcy to 70 millidarcies and have a mean value of 4.5 millidarcies.

Intercrystalline porosity within the unit does not appear to be strictly related to any particular lithofacies type. This pore type was seen in peloidal, fusulinid, and skeletal dolowackestones to dolopackstones and in finely crystalline dolomudstones. Analysis of core data from thin sections indicates an increase in intercrystalline porosity and

Figure 52. Core photomicrographs of intercrystalline porosity. Intercrystalline pores are common pore types within San Andres dolostone reservoirs along the eastern margin of the Central Basin platform. Well-developed intercrystalline porosity within large crystalline dolomites is most prevalent within the lower zones of the reservoir (zones IV-E1 and IV-E2).

A) Intercrystalline porosity in a medium crystalline (20-100 μm) peloidal packstone which has undergone solution enhancement. Note the intracrystalline pores seen within individual dolomite crystals. Porosity and permeability within this sample is 14.6 percent and 38 millidarcies, respectively (photomicrograph from WJU #505; 3712.8 feet; magnification 50X).

B) Solution enhanced intercrystalline porosity within a peloidal wackestone-packstone of zone IV-E1. Original fabric within these samples is extremely difficult to determine because of dolomitization that has taken place in these samples. Porosity and permeability within this sample is 13.7 percent and 32 millidarcies, respectively (photomicrograph from WJU #1416; 3606.7 feet; magnification 32X).

C) Medium crystalline dolomite (20-70 μm) with solution enhanced porosity. Almost all samples of intercrystalline porosity from lower intervals within the reservoir have been enhanced by dissolution. Note the small vugs that have formed throughout the sample (photomicrograph from WJU #505; 3671.4 feet; magnification 32X).

D) Photomicrograph of large crystalline dolomite (> 100 μm) with considerable solution enhanced vuggy and intercrystalline porosity (photomicrograph from WJU #505; 3694.2feet; magnification 32X).

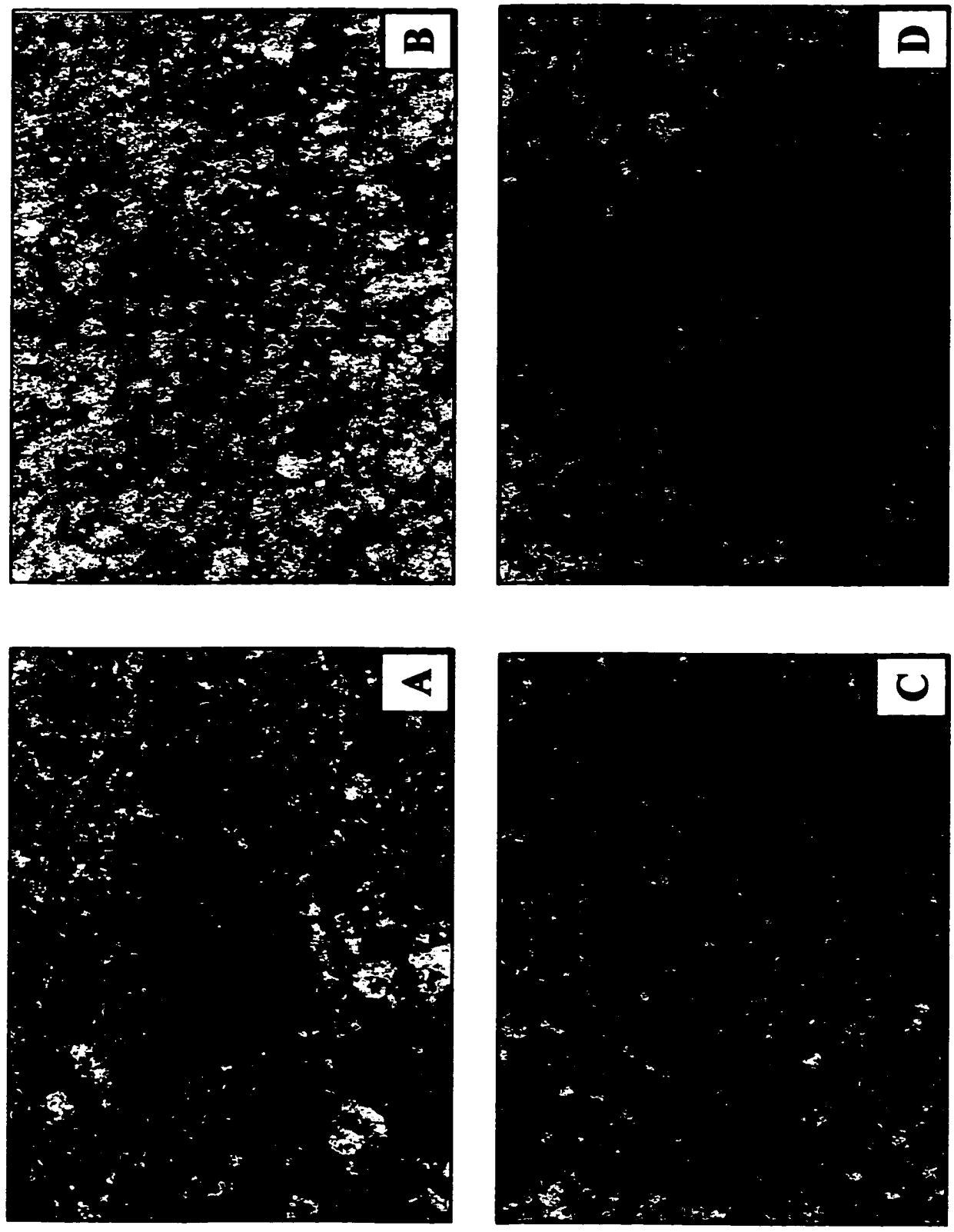
B
D
A
C

Figure 53. Core photomicrographs of intercrystalline porosity. Many of the original grain-dominated fabrics within the reservoir have been so severely crystallized that identification of fabric types is difficult. Intercrystalline porosity was found to occur in dolomites with crystal size ranging from <5 (m to over 200 (m. Intercrystalline porosity is seen to have the highest values of porosity and permeability within the lower zones of the reservoir.

A) Intercrystalline porosity occurring within a peloidal grain-dominated packstone to grainstone. Although difficult to recognize, peloid grains which have had their interior leached are present within this sample. The shape and size of these peloids suggest they may be ooids. Note the anhydrite cement (white) and oil (black) filling some of the pore space (photomicrograph from WJU #505; 3698.4 feet; magnification 100X).

B) Large crystalline dolomite with intercrystalline, intracrystalline and fusumoldic pore types. The intracrystalline pores form through the selective dissolution of the interior parts of dolomite rhombs and can contribute substantially to porosity and permeability. The original fabric of this sample is believed to have been a fusulinid-peloidal packstone. (photomicrograph from WJU #1416; 3606.7 feet; magnification 32X).

C) Well developed intercrystalline and interparticle porosity within a skeletal/peloidal packstone (photomicrograph from WJU #505; 3714.3 feet; magnification 25X).

H) Intercrystalline porosity within a large crystalline dolomite (>100 (m). This sample was photographed under ultra violet florescence in order to image original fabric type. As seen, fabrics are still unidentifiable in this thin section. Note the large dolomite crystals that have completely obliterated the original fabric of this sample. Yellow florescence within the diagram is due to hydrocarbons. Darer green areas are intercrystalline pore throats (photomicrograph from WJU #1419; 3669.10 feet; magnification 100X).

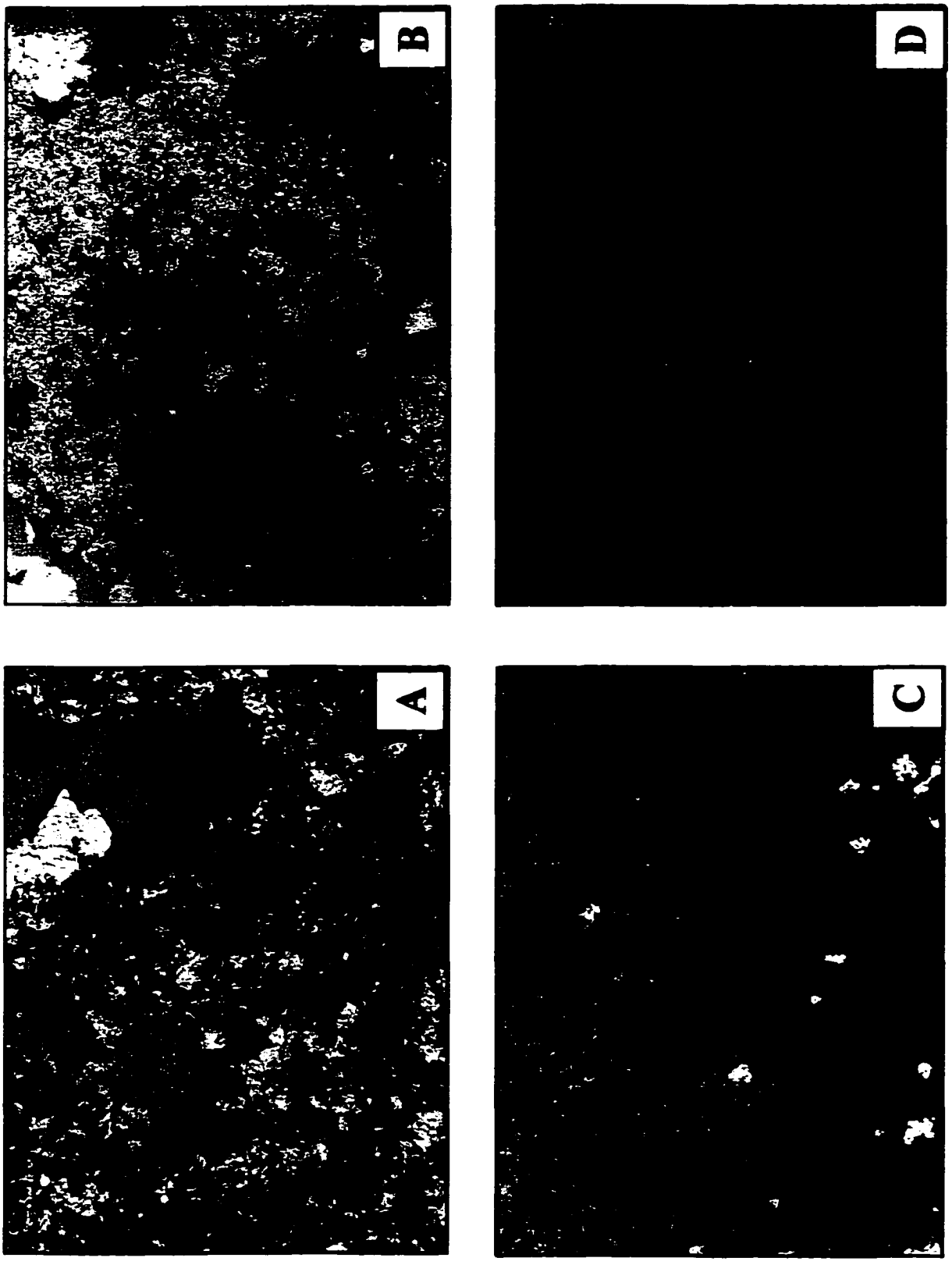
B
D
A
C

permeability values is associated with an increase in dolomite crystal size. Cross plots of porosity-permeability data versus dolomite crystal size illustrate a general increase in porosity and permeability with increased dolomite crystal size (fig. 54). Although significant scatter exists, a general trend is evident from these cross-plots. Scatter within the cross plots is substantially influenced by the class size used when measuring each sample. Dolomite crystal size was grouped into three classes, <20 (m, 20-100 (m, and >100 (m. Considerable overlap within the middle class is evidenced by scatter within the cross plots. This naturally is a function of the class size. Also of importance to note is the occurrence within facies tracts for fine (<20 (m), medium (20(m -100(m), and coarse (>100(m) crystalline dolomites as indicated by red bars on the left hand side of the log signatures (fig. 54 B,C, and D). A transition from finer to coarser crystalline dolomites is seen as you move downward in depth within the reservoir from tidal flat through proximal outer ramp facies tracts.

Intercrystalline porosity from fine crystalline dolomites occurs primarily in the middle ramp. Medium and coarse crystalline dolomites occur within the lower part of the reservoir within the ramp crest and proximal outer ramp facies tracts. The association of increase in dolomite crystal size as you move from more shallow water supratidal and nearshore facies to deeper water outer ramp facies is related to diagenetic and facies controls which will be addressed in the following section. Intercrystalline porosity as a dominant pore type occurs almost exclusively below zone IV-C, which marks the culmination of highstand systems tract I prior to progradation of more landward facies across the area. Above zone IV-C within the middle ramp, moldic porosity becomes the

Figure 54. Cross plots of core porosity and permeability illustrating the relationship between intercrystalline porosity and dolomite crystal size. Dolomite crystal size for samples with intercrystalline pore types has been broken out into three classes fine (<20 (m), medium (20-100 (m), and coarse (>100 (m). These samples are plotted in yellow, blue and red data points respectively. Also note that the concentration of data samples are plotted next to the log curves as indicated by the red bars in B, C, and D. The samples show an overall increase of dolomite crystal size with depth. This relationship is quite evident visually when comparing thin sections within the reservoir as you move downward in depth. IR, MR, and RC/POR on log curves stand for inner ramp, middle ramp, and ramp crest/proximal outer ramp facies tracts.

A) Cross plot diagram of fine, medium and coarse intercrystalline porosity. Note the general transition of fine crystalline dolomites plotting in lower permeability and porosity fields compared to the medium and then coarse crystalline dolomites that plot in the highest permeability and porosity fields.

B) Cross plot of fine crystalline dolomites with intercrystalline pore types. Samples with low porosity and high permeability most likely contain fractures or stylolites, which are prevalent in core from the West Jordan unit.

C) Cross plot of medium crystalline dolomites with intercrystalline pore types. The wide range seen in this group is a result of the large class used from 20-100 microns.

D) Cross plot of coarse crystalline dolomites with intercrystalline pore types. These data points clearly have the highest permeability and porosity substantiating the relationship between increased dolomite crystal size and increased permeability. Coarsely crystalline dolomites have permeability values on average that are over an order of magnitude higher than finely crystalline dolomites.

Permeability (md)
Porosity (%)
Intercrystalline Porosity
(A)
Interparticle
Intercrystalline (>100 μm)
Intercrystalline (20-100 μm)
Intercrystalline (<20 μm)
Fracture
Moldic &Inter-crystalline (>100 μm)
Moldic &Inter-crystalline (20-100 μm)
Moldic &Inter-crystalline (<20 μm)
Moldic
Fenestral
Fine Crystalline Dolomite (<20 μm)
(B)
Medium Crystalline Dolomite (20-100 μm)
(C)
Coarse Crystalline Dolomite (>100 μm)
(D)
IR
MR
RC/POR

principal pore type. All coarse crystalline dolomites (>100 (m) analyzed from available core data occur below the top of zone IV-E1 as do the vast majority of medium crystalline dolomites greater than 50 (m within the reservoir. Solution enhancement of intercrystalline pore space and leaching of dolomite crystals and grain constituents has significantly increased porosity and permeability in these lower zones (below zone IV-C).

Interparticle

Interparticle porosity is the pore space occurring between particles and is a broader term for intergranular porosity, which should be restricted to between-grain porosity of carbonates whose particles are coarse enough to be considered grains (Choquette and Pray, 1970,). In carbonates interparticle porosity is generally considered to be primary, although it can be secondary in occurrence if a finer matrix that originally occupied the space between grains has subsequently been removed since deposition.

Interparticle porosity observed within the unit occurs primarily between peloidal and mixed peloidal/skeletal grains (fig. 55). Although interparticle porosity is a dominant form of porosity in many San Andres dolomites, it is not commonly identifiable from core data within the unit. This is because crystallization during the dolomitization process has almost completely obliterated the texture of carbonate grain constituents making identification of grain-dominated facies extremely difficult. Where interparticle porosity is identifiable, it is almost always entirely occluded with anhydrite and gypsum cement suggesting early and substantial fluid movement through these grain-dominated facies. This is apparent in zone IV-C where grain-dominated fabrics are occluded with sulfate cements (fig. 55 e, f). It is believed that early cementation of this zone may have

Figure 55. Core photomicrographs of interparticle porosity. Interparticle porosity is the pore space occurring between particles. As depth increases within the reservoir it becomes increasingly difficult to determine the original fabric of the rock due to increasing crystallization due to dolomitization. As seen from the previous two figures, an increase in dolomite crystal size is associated with facies found deeper within the reservoir because dolomitization tends to more completely obliterate the original fabric of the rock making identification of grain content difficult. Because of recrystallization, well-preserved interparticle porosity rarely was seen from samples within the West Jordan unit.

A) Photomicrograph of peloidal packstone with interparticle porosity. Note that peloids are difficult to see within this sample but with close examination the peloid grains can be seen (photomicrograph from WJU #1419; 3646.9 feet; magnification 32X).

B) Photomicrograph of interparticle/intercrystalline porosity. Grain fabrics are difficult to determine in this peloidal/bryozoan packstone facies. The large grain in the upper right hand corner is a cross section through a bryozoan grain. Poorly preserved peloids can be seen with close examination (photomicrograph from WJU #505; 3714.3 feet; magnification 32X).

C) Interparticle porosity within this algal-pisolitic intraclast grainstone is well developed. White areas around grains are anhydrite cement, blue areas are interparticle porosity. Porosity and permeability measured from core analysis within this interval are 15.6 percent and 2.8 millidarcies, respectively. (photomicrograph from WJU #505; 3453.9 feet; magnification 20X).

D) Photomicrograph of well developed interparticle porosity within a mixed siliciclastic/peloidal grain-dominated packstone. Porosity and measured from core analysis within this interval are 16.6 percent and 2.4 millidarcies, respectively. (photomicrograph from WJU #1416; 3677 feet; magnification 32X).

E) Photomicrograph of a peloidal grain-dominated packstone from zone IV-C that originally had excellent interparticle porosity prior to cementation of pore space. All interparticle pore space has been completely occluded by gypsum cement (white areas). A very small micro-fracture running through the center of the photomicrograph has some porosity (photomicrograph from WJU #1307; 3538.3 feet; magnification 32X).

F) Photomicrograph of E) above under crossed-nichols showing birefringence of the anhydrite cement (photomicrograph from WJU #1307; 3538.3 feet; magnification 32X).

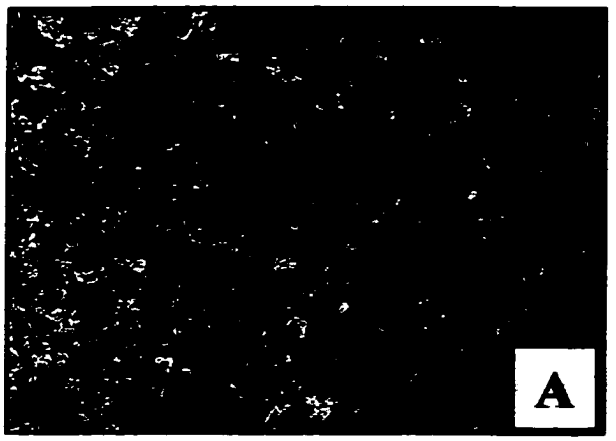
A

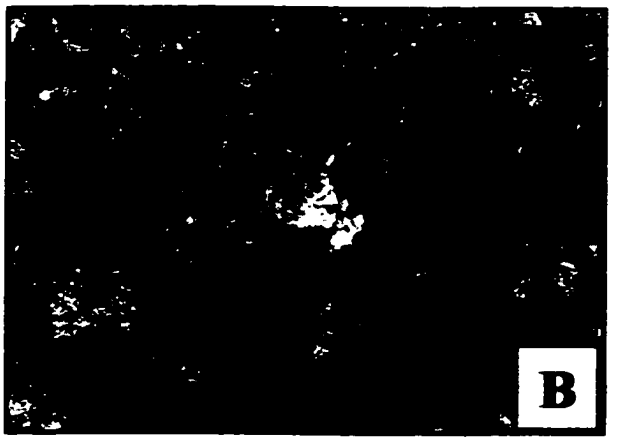
B

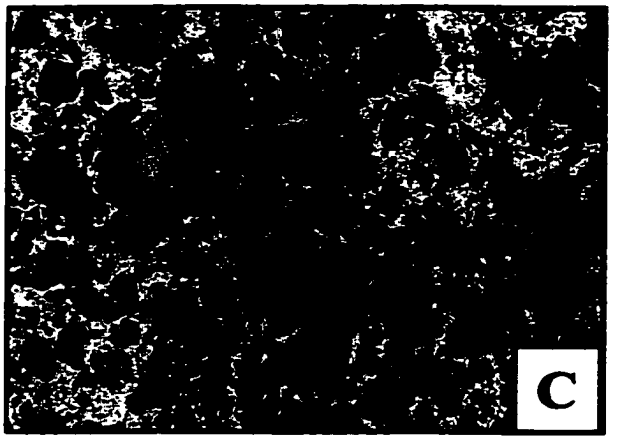
C

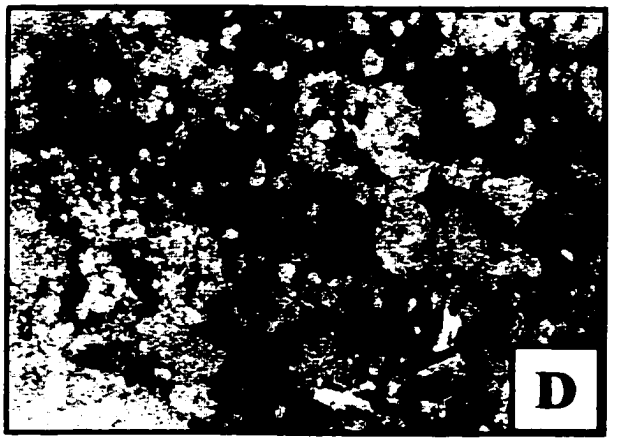
D


E


F

preserved particles from being completely recrystallized as occurred within the grain rich facies in zones IV-E1 and IV-E2.

Cross-plots from core data of interparticle porosity versus permeability show little correlation. This is the result of several factors, a lack of adequate samples and the effect of considerable cementation within this facies where it is well preserved. Maximum porosity and permeability values measured from core data are 11 percent and 0.8 millidarcies respectively.

Moldic

Moldic porosity is the porosity formed by the selective removal, normally by solution, of a former individual grain constituent of a rock such as a shell or oolith (Choquette and Pray, 1970, p. 248). Moldic porosity is typically visible to the unaided eye, unlike intercrystalline porosity and the term is often preceded by different discriminators such as oomoldic (ooid molds), fusumoldic (fusulinid molds), biomoldic (bioclast molds) and so on which are common skeletal constituents in the San Andres Formation (**fig. 56**). Although moldic porosity is more visible than intercrystalline porosity, the pores are usually not interconnected and therefore permeability values tend to be low.

Cross plots of moldic porosity indicate permeability values typically less than one millidarcy (**fig. 57**). Most moldic porosity ranges from 2% to 14% and corresponding permeability values range from <0.1 millidarcies to over 2 millidarcies according to core data. Geostatistical modeling has shown that almost all moldic porosity is actually less than 0.5 millidarcies within the reservoir. Data points reflecting higher permeability

Figure 56. Photomicrographs of moldic porosity. Moldic porosity is the porosity formed by the selective removal, normally by dissolution, of a former individual grain constituent of a rock. This pore type is the primary pore type within zones IV-A through the upper part of zone IV-C.

A) Photomicrograph of moldic porosity in a skeletal-peloidal wackestone/packstone. Moldic pores are filled with blue epoxy. Other pores have been filled with anhydrite cement (white). Most of the skeletal fragments within this sample are from mollusk. Porosity and permeability measured from core analysis within this sample are 10.4 percent and 0.9 millidarcies, respectively (photomicrograph from WJU #1419; 3698.1 feet; magnification 6.3X).

B) Photomicrograph of a skeletal wackestone. All the original grains within this sample have been removed by solution leaving only moldic porosity (photomicrograph from WJU #505; 3480.2 feet; magnification 20X).

C) This photomicrograph shows fusumoldic and intercrystalline porosity within a coarsely crystalline dolomite from zone IV-E2 within the reservoir. Dark material filling fusumolds is oil and the white material is anhydrite cement (photomicrograph from WJU #1419; 3468.3 feet; magnification 8X).

D) A photomicrograph of skeletal-peloidal, mud-rich packstone. Porosity in this sample is about 10 percent, permeability is less than 0.2 millidarcies. Note the peloid grains in the background that are more easily distinguishable in this fine crystalline dolomite than in coarser crystalline dolomites found at greater depths within the reservoir (photomicrograph from WJU #1419; 3468.3 feet; magnification 32X).

B
D
A
C

Figure 57. Cross plots of core porosity and permeability for moldic and dual moldic and intercrystalline pore types.

A) Cross plot of moldic only pore type. Note that most of the data points fall below one millidarcy of permeability. Samples within the blue box have high permeability/low porosity values and are either fractured or contain other permeability anomalies such as stylolites.

B) Cross plot of dual pore types consisting of moldic and intercrystalline porosity. These data points are from intercrystalline porosity that occurs within finely crystalline dolomites (<20 (m). Note that most of the intercrystalline data points within the fine dolomite crystal class fall in approximately the same area as moldic only pores. Fine-grained intercrystalline dolomites typically have relatively low permeability and porosity.

C) Cross plot of moldic and dual moldic and intercrystalline pore types. Medium and large crystalline dolomites have greater porosity and permeability than finely crystalline dolomites. As indicated by the overall low porosity and permeability seen in A) and B) above this increase in porosity and permeability is a function of intercrystalline porosity development in coarser grained dolomites. This helps substantiate the lack of effective porosity and related permeability development within moldic pore types.

D) Almost all pores consisting of moldic and finely crystalline dolomites with dual moldic and intercrystalline porosity occur within the middle ramp environment within zones III through IV-B. Because the primary pore type within these zones is moldic in nature, these zones have not been found to be significantly productive within the reservoir.

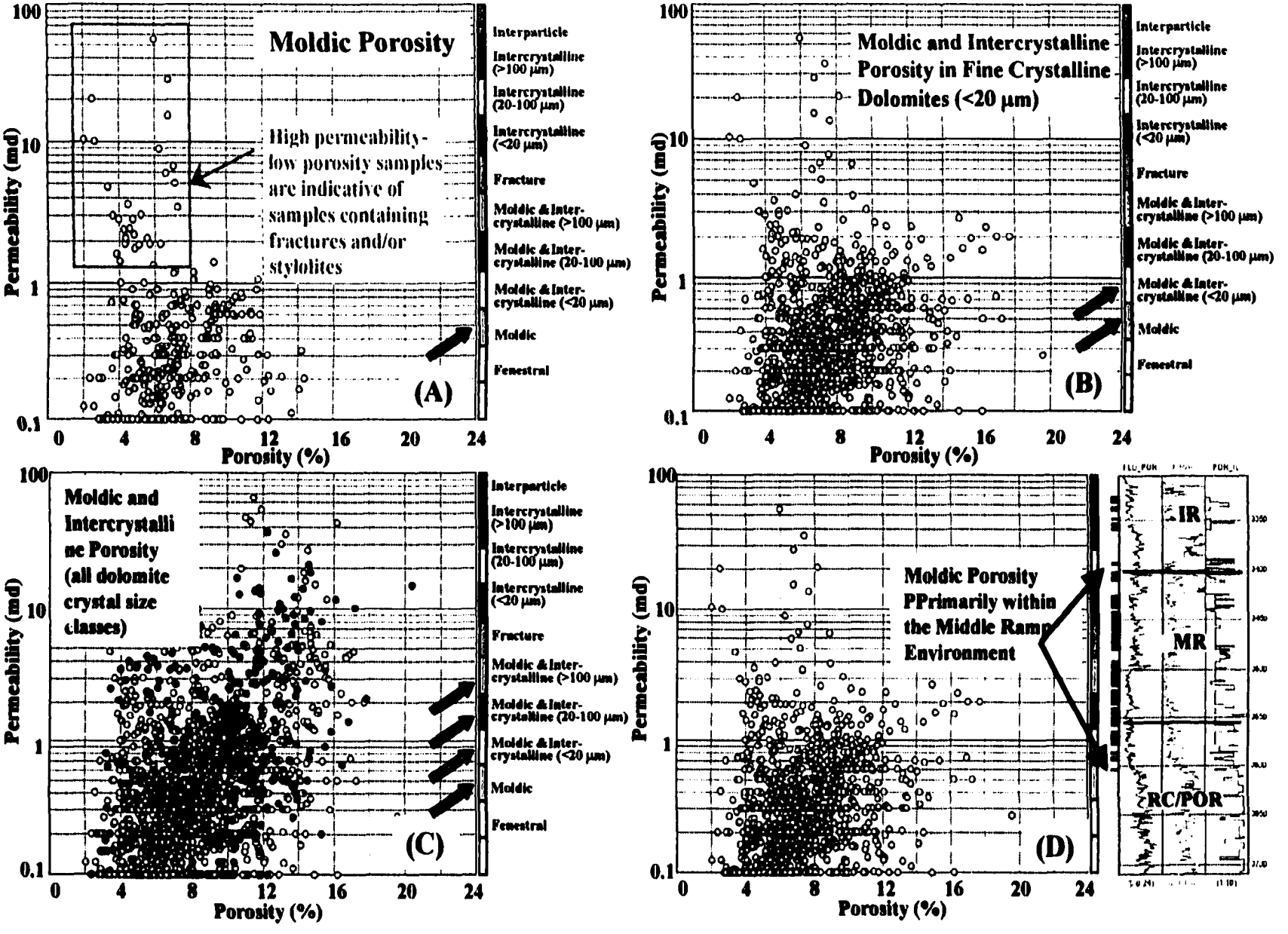
Moldic Porosity
High permeability-low porosity samples are indicative of samples containing fractures and/or stylolites
(A)
Moldic and Intercrystalline Porosity in Fine Crystalline Dolomites (<20 µm)
(B)
Moldic and Intercrystalline Porosity (all dolomite crystal size classes)
(C)
Moldic Porosity PPrimarily within the Middle Ramp Environment
(D)
IR
MR
RC/POR
Permeability (md)
Porosity (%)
Interparticle
Intercrystalline (>100 µm)
Intercrystalline (20-100 µm)
Intercrystalline (<20 µm)
Fracture
Moldic & Intercrystalline (>100 µm)
Moldic & Intercrystalline (20-100 µm)
Moldic & Intercrystalline (<20 µm)
Moldic
Fenestral

values either contain intercrystalline porosity within the sample or are fractured. An effort was made to remove data points that were influenced by fracturing or stylolites. However, samples with relatively low porosity and high permeability values are suspect and most likely not representative of true matrix values (fig. 57a). Moldic porosity and dual pore types consisting of moldic and fine intercrystalline porosity (<20 um) have comparable porosity and permeability ranges (fig. 57b). The general increase in porosity and permeability values that occurs with an increase in dolomite crystal size is a direct relationship to the increase in intercrystalline porosity that occurs within dual moldic/intercrystalline pore types as dolomite crystal size increases (fig. 57c).

Correlation between porosity and permeability in moldic and finely crystalline dolomites has substantial scatter. The bulk of the data points indicate that porosity and particularly permeability are low within facies dominated by these pore types. As you can see from the position within the reservoir where these data points fall, these pore types occur primarily within the middle ramp environment (fig. 57d). It is evident from core and cross plot data that moldic porosity is not facies selective within the reservoir. However, moldic porosity is concentrated in cycles within intertidal and shallow subtidal vertical facies successions within middle ramp facies tract, primarily occurring within zones IV-A through the upper part of zone IV-C. Moldic porosity increasingly enhances porosity and permeability in intercrystalline rocks as dolomite crystal size increases, however, moldic porosity alone is not a significant factor to reservoir flow.

Intraparticle

Intraparticle porosity is the porosity formed within individual grains, particles or plant chambers (fig. 58). This porosity typically forms when chambers within carbonate particles or grains are not filed after deposition. Although intraparticle porosity is most often primary it also results from selective solution of the original carbonate grain or skeletal constituent or solution of early replacement cements. Under certain conditions such as within dolograinstones or grain-dominated dolopackstones that already have appreciable interparticle porosity, intraparticle porosity can enhance overall effective porosity and permeability values.

Intraparticle porosity is quite common within the West Jordan unit, nevertheless, does not significantly contribute to flow within the reservoir. Although very striking in appearance, this porosity is usually associated with grain constituents common in dolowackestones to mud-rich dolopackstones even though overall porosity values are increased permeability is not.

Fenestral

The development of fenestral porosity has been attributed to decay of sediment-covered algal mats, shrinkage during drying, and accumulation of pockets of gas or water (Choquette and Pray, 1970). Fenestral porosity at West Jordan unit is thought to be the result of small gas pockets formed within sediment as it was deposited and occurs in the supratidal to intertidal pisolite packstones to grainstones and various dolomudstone facies. Fenestral pores are typically irregularly shaped, larger than associated pisolite grain constituents and often lenticular, occurring parallel with carbonate laminae or bedding planes (fig. 59).

Figure 58. Core photomicrographs of intraparticle porosity. Intraparticle porosity is prevalent within the West Jordan reservoir, nevertheless is does not enhance permeability to any significant degree.

A) Photomicrograph of a cross section through a fusulinid grain. Intraparticle porosity occurs in areas filled with blue epoxy. Anhydrite cement fills the majority of the chambers within the fusulinid grain (white areas). The grayish-blue areas filling intercrystalline pores within the matrix are a result of gypsum cement (photomicrograph from WJU #1416; 3591.3 feet; magnification 20X).

B) Photomicrograph of a bryozoan wackestone with impressive intraparticle porosity development (blue epoxy). Dissolution of part of the bryozoan grains has resulted in the development of small vugs within the upper right hand corner of the photograph (photomicrograph from WJU #1416; 3613.0 feet; magnification 6.3X).

C) Intraparticle porosity occurs within the fine chambers of a piece of plant debris that was commonly seen within zone IV-C within the reservoir (photomicrograph from WJU #1416; 3558 feet; magnification 32X).

D) A photomicrograph of intraparticle porosity within a bryozoan grain. This sample comes from within a bryozoan-algal-sponge bioherm within the proximal outer ramp facies tract (photomicrograph from WJU #505; 3739.3 feet; magnification 10X).

B
D
A
C

Figure 59. Core photomicrographs of fenestral pore types. Fenestral porosity occurs primarily within zones I through III, however, in some cores this pore type was found lower within the reservoir indicating shallow water environments with probable periods of subaerial exposure.

A) Photomicrograph showing irregular fenestral pores within an algal-pisolite dolopackstone. Pisolite grains within this sample are very faint and hard to recognize. Porosity and permeability within the interval where this sample was taken are 11.9 percent and 5.1 millidarcies, respectively (photomicrograph from WJU #1416; 3373.8 feet; magnification 20X).

B) A well developed pisolite grainstone exhibiting fenestral porosity. Note the fringing anhydrite cement around the margins of pores. The grayish-blue pore filling material in the upper right hand corner of the photomicrograph is gypsum. Porosity and permeability within this sample is 13.8 percent and 135 millidarcies, respectively (photomicrograph from WJU #1416; 3373.11 feet; magnification 10X).

C) Well connected fenestral porosity within a pisolite grainstone. Porosity and permeability within this sample is 14.9 percent and 252 millidarcies, respectively (photomicrograph from WJU #1307; 3372.3 feet; magnification 10X).

D) Photomicrograph of a finely crystalline dolomudstone with well developed fenestral porosity. Dolomite crystal size within this ample is < 5 (m (photomicrograph from WJU #1307; 3379.4 feet; magnification 32X).

A
B
C
D

Fenestral pores are not usually thought to contribute significantly to permeability within a reservoir due to a lack of interconnectivity even though porosity values may be very high. This is questioned within zone II where porosity and permeability values from the majority of cores studied show not only good porosity development but also considerable permeability as well. Porosity and permeability values from core analysis for fenestral pore types within zone II range from 1% to over 18% and 0.02 to 252 millidarcies respectively, with averages of 10% and 8.5 millidarcies respectively.

Fenestral porosity occurs in zones I, II, and III which represent supratidal and intertidal rocks within near shore and tidal flat facies tracts. The uppermost zone (zone I) has appreciable fenestral pore development that has been almost entirely occluded by anhydrite and gypsum cement. The underlying zone (zone II) is also composed of supratidal pisolite and algal-rich facies exhibiting considerable fenestral porosity. Pores within zone II are rarely occluded by sulfate cementation. Petrographic evidence in the form of sulfate remnant cement suggests late stage removal of sulfate cement by solution.

Porosity and permeability cross plots of core data show the relationship between fenestral pore types and permeability (fig. 60). Although the correlation coefficient is much higher for fenestral pore types than for moldic pore types (fig. 50) the correlation between porosity and permeability is still quite low. As expected almost all fenestral porosity occurs within pisolite lithofacies and minor fenestral porosity was seen in algal laminated and light colored dolomudstones and a few pisolite intraclast facies (fig. 60b). Thin, localized intervals of fenestral porosity do occur in algal laminated and pisolite facies within zones IV-A through IV-C at the top of some shallowing upward cycles

Figure 60. Cross plot data of core porosity and permeability for fenestral pore types. The 'z' axes on cross plots are from color-coded pore indicator logs (A) and facies indicator logs (B). Digital logs of pore and facies types were constructed to better determine their distribution within the reservoir.

A) Cross plot of core porosity versus core permeability on the 'x' and 'y' axis with pore types on the 'z' axis. This cross plot uses a discriminator to look only at fenestral pore types and their distribution within the reservoir. Fenestral porosity within the reservoir has one of the higher correlation coefficients although the correlation is still weak at 0.518.

B) Cross plot of core porosity versus core permeability on the 'x' and 'y' axis with facies types on the 'z' axis. The discriminator for this cross plot is fenestral porosity as in A) above. The primary facies types with fenestral porosity are pisolite grain-dominated packstone and grainstone facies. Secondary facies include dolomudstone, intraclasts and a few clay rich facies.

C) This figure illustrates the cross-plotted data curves and the depth at which fenestral pore data points fall within the reservoir. As the diagram illustrates, most fenestral pore types are found within the upper zones of the reservoir (zones I-III). Fenestral porosity is developed within shallow intertidal to supratidal conditions and indicates periods of exposure. Fenestral porosity located lower within the reservoir in zone IV-C suggests possible exposure within this zone as well. This is not uncommon within ramp crest environments.

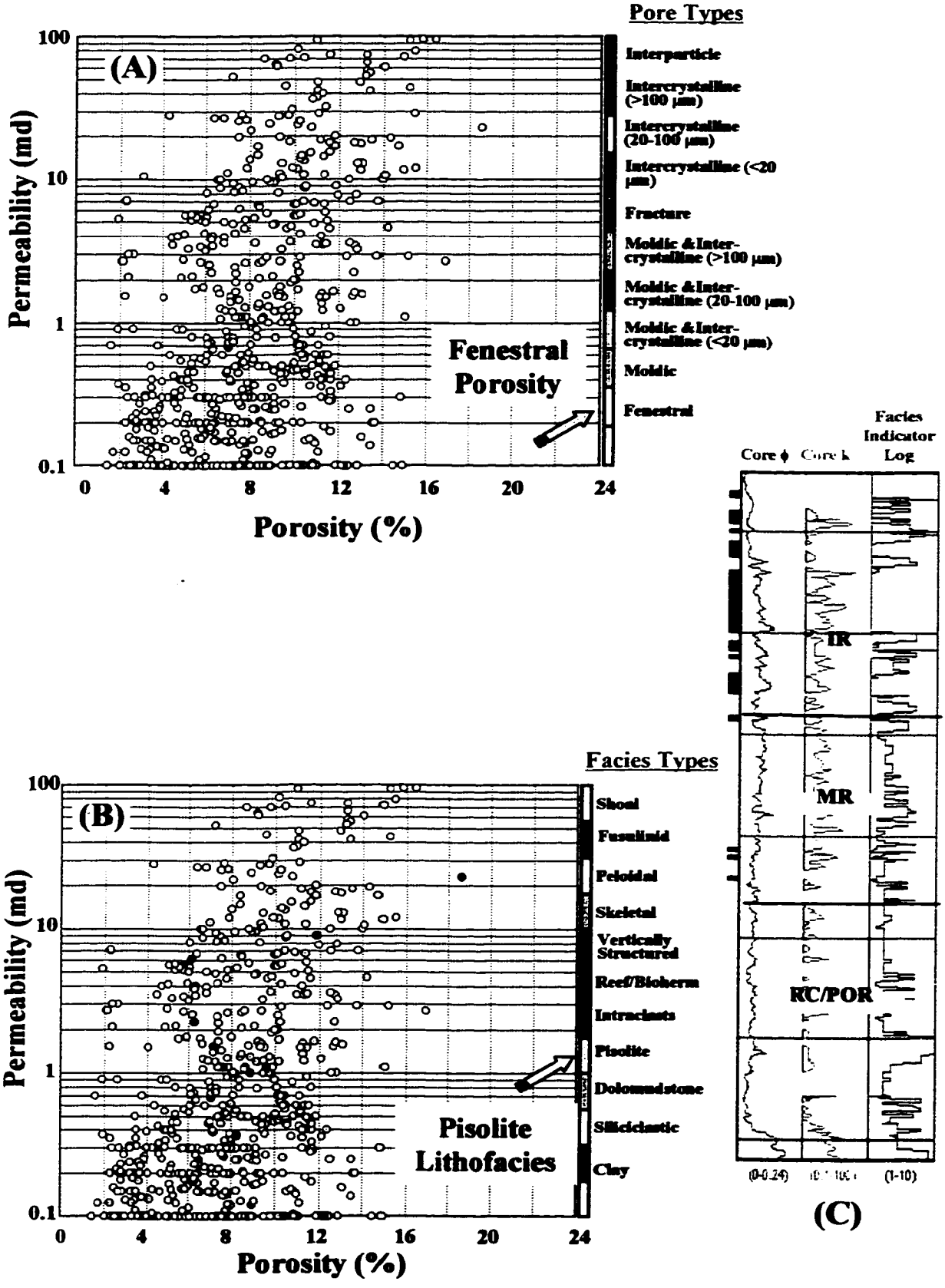
Pore Types
(A)
Permeability (md)
100
10
1
0.1
0
4
8
12
16
20
24
Porosity (%)
Fenestral Porosity
Interparticle
Intercrystalline (>100 μm)
Intercrystalline (20-100 μm)
Intercrystalline (<20 μm)
Fracture
Moldic & Inter-crystalline (>100 μm)
Moldic & Inter-crystalline (20-100 μm)
Moldic & Inter-crystalline (<20 μm)
Moldic
Fenestral
Facies Indicator Log
Core ϕ
Core k
IR
MR
RC/POR
(0-0.24)
(1-10)
(C)
Facies Types
(B)
Permeability (md)
100
10
1
0.1
0
4
8
12
16
20
24
Porosity (%)
Pisolite Lithofacies
Shoal
Fusulinid
Peloidal
Skeletal
Vertically Structured
Reef/Bioherm
Intraclasts
Pisolite
Dolomudstone
Siliciclastic
Clay

within the #1204 and #1702 cores. These cores are located along the western and southern margins of the reservoir and provide evidence that paleotopography was slightly higher to the south and west within the unit area.

Fracture

Fractures are planar breaks within rock along which negligible or no movement has taken place. Porosity forms from the voids created by fracturing and although they usually contribute only a few percent porosity they can contribute significantly to flow within a reservoir. Core data and photomicrographs show considerable fracturing within the San Andres Formation at West Jordan unit. Two vary different types of fracturing were seen from core data, primary fractures which include tectonic and/or regional fracture networks and what are termed within this study as "diagenetic fractures".

Primary fractures consist of tectonic and/or a network of regional fractures. Tectonic fractures are planar in nature and their origin is associated with nearby stress fields responsible for the formation of local structure such as the asymmetrical anticlinal structure comprising the Jordan field (fig. 61). Localized stress fields associated with compaction and drape over underlying deeper, fault related basement highs forming the anticline, as well as regional fractures most likely occur within the area. Regional fractures are vertical, planar fractures that develop over large geographic areas with relatively little change in orientation. A regional fracture network is also believed to overprint the area. A regional east-northeast and conjugate north-northwest network of fractures have been described for many fields within the Permian basin region. These fractures are probably related to stress fields created during Basin and Range extension.

Figure 61. Core photographs and photomicrographs of tectonic and/or regional fractures seen within the West Jordan unit. These fractures are planar in nature and their origin is associated with nearby stress fields responsible for the formation of local structure or from regional extensional stresses resulting in vertical planar fractures that develop over large geographic areas with relatively little change in orientation.

A) Photograph of a conjugate fracture set seen within the WJU # 1416 core from approximately 3482 feet. A network system of these fractures is believed to occur within the West Jordan unit area and may play a key part in channeling and early breakthrough of injection water within the reservoir. Note the cementation that has occurred along fracture faces.

B) Conjugate fractures from the #WJU 505 core at a depth of 3524.5 feet. Most fracturing was seen above zone IV-C within the reservoir. Again note the cementation along the fracture faces.

C) Photomicrograph of a microfracture within a fine crystalline dolowackestone. Microfractures within samples such as this one can help connect up intercrystalline porosity (photomicrograph from WJU #1416; 3532.2 feet; magnification 25X).

D) This large fracture plane provides the majority of the porosity within this nearly completely occluded mud-dominated peloidal packstone (photomicrograph from WJU #1307; 3609.4 feet; magnification 8X).

E) A photomicrograph of a microfracture connecting up intercrystalline porosity within a finely crystalline dolomudstone (photomicrograph from WJU #505; 3509.3 feet; magnification 32X).

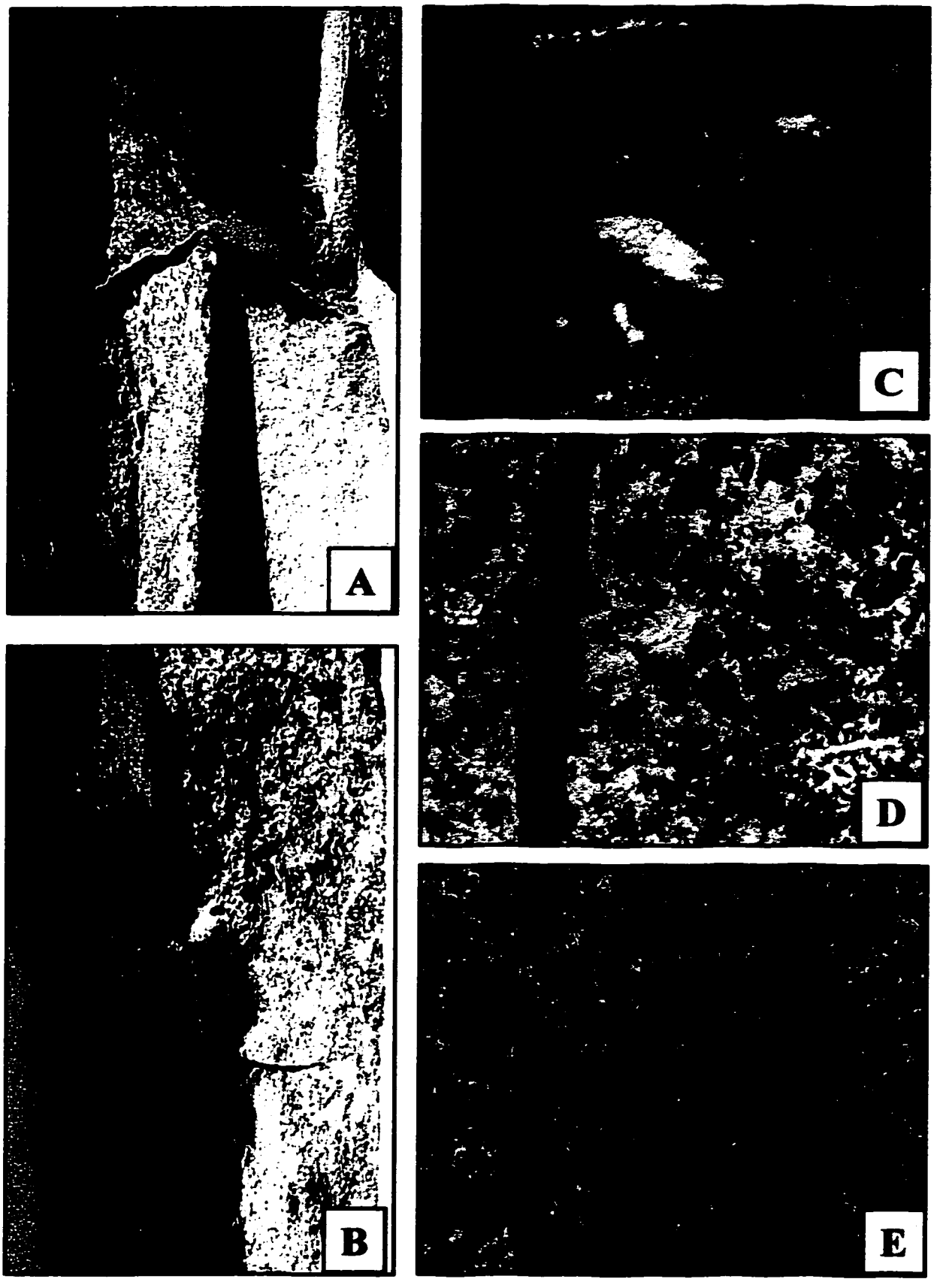
A
B
C
D
E

The second type of fractures, "diagenetic fractures", were observed in all cores throughout the unit and are associated with diagenetic processes such as nodular anhydrite and stylolite formation. Their exact influence on flow through the reservoir is not fully understood, nonetheless, they are believed to be of significant influence to warrant discussion within this study. These fractures are typically microfractures of short extent, less than about 10 inches (25 centimeters) and are non planar in nature (fig. 62)

Data points described as fractured and stylolitized on core analysis reports were incorporated into a digital well file. This file defines fracture and stylolite free samples as well as fractured only, stylolitized only, and fractured and stylotized samples. Each category was assigned a numeric value from zero to three and converted into a digital log file. This digital log curve (FRACT_DL) was plotted against well depth in an effort to substantiate visual occurrences seen within each zone during describing core and its relationship to facies (fig. 63). The majority of fractured samples were found to occur in zones I through IV-B within the inner ramp (tidal flat and near shore) and middle ramp facies tracts. Fractures tend to decrease significantly with depth within the reservoir, particularly into the proximal out ramp facies tract. This decrease of fractures with depth is believed to be the result of mechanical strength variances within the rock as you move downdip within the reservoir. As the reservoir changes from predominantly finely crystalline to coarsely crystalline dolomite the associated increase in porosity results in less brittle rock that is capable of transmitting greater amounts of stress.

Although fracturing can increase both porosity and permeability within the rock, most often it occurs in tight dolomudstones and wackestones, which lack matrix porosity. Fracture and/or stylolitized data samples which were not identified on core analysis

Figure 62. Core photographs and photomicrographs of diagenetic fractures. Diagenetic fractures were observed in all cores throughout the unit and are associated with diagenetic processes such as nodular anhydrite and stylolite formation. These fractures are typically microfractures of short length and are non-planar in nature. Within tight dolostones core tends to break along these fractures when brought to the surface suggesting that under waterflood pressures these features could be planes of weakness within the reservoir as well.

A) Core photograph showing the occurrence of diagenetic fractures developing off of anhydrite nodules and stylolite seams. These fractures are most common within the upper parts of the reservoir, particularly within zone IV-A (core photograph from WJU # 1419, 3484-3488.5 feet).

B) Photomicrograph of diagenetic fractures that have developed off of an anhydrite nodule. Much of the core breaks along these fractures and under water flood conditions these fractures may act as conduits for injection water (photomicrograph from WJU #1307; 3477.2 feet; magnification 16X).

C) Tension fractures often develop off of stylolite teeth and were found to be quite numerous within cores from the reservoir (photomicrograph from WJU #1307; 3483.11 feet; magnification 6.3X).

D) An enechelon pattern within a microfracture that has developed off of an anhydrite nodule within an extremely fine crystalline dolomudstone (photomicrograph from WJU #1416; 3388.8 feet; magnification 32X).

A
B
C
D

Figure 63. Cross plots of fracture and stylolite data versus depth. Data points known to be fractured and stylolitized as indicated on core data analysis reports were incorporated into a digital well file. This file defines fracture and stylolite free samples as well as fractured only, stylolitized only, and fractured and stylolitized data samples. Each category was assigned a numeric value from zero to three and converted into a digital log file. This digital log curve (FRACT_DL) was then plotted against depth in an effort to substantiate visual occurrences seen while describing core. The following cross plots show data points from core analysis reports that were documented to have stylolites and fractures. Stylolite and fracture free samples within the reservoir and their occurrence within zone boundaries are also plotted to show the general decrease in fracturing as depth increases within the reservoir. To the right of each cross plot is a color bar showing the location within the reservoir with respect to depth of were data points plot. As seen there is an overall decrease in fracturing with depth. From visual analysis of core data, fractures and large amplitude stylolites were found to be most prevalent within zone IV-A.

WJU #1416
FRACT_DL Curve
Depth
Stylolites
Fractures
Stylolite/Fracture free Samples
WJU #1419
Stylolites
Fractures
Stylolite/Fracture-free-Samples
WJU #1307
Stylolites
Fractures
Stylolite/Fracture free Samples
WJU #505
Stylolites
Fractures
Stylolite/Fracture free Samples
I
II
III
IV-A
IV-B
IV-C
IV-E1
IV-E2

reports can often be identified from porosity-permeability cross plots that show samples with low porosity associated with high permeability values. The influence of "diagenetic fractures" is believed to lie in their affect on overall rock competence. These fractures are concentrated in zone IV-A and tend to be zones of weakness within the reservoir along which the core breaks when brought to the surface. These zones of intense fracturing most likely contributed significantly to primary production, but under secondary recovery waterflood operations are believed to be conduits for channeling and early breakthrough of injection water. Completion techniques within the unit often have resulted in pressures above the reservoir fracture pressure that most likely further opened these zones up for injection water channeling. The possible influence of these fractures on reservoir flow will be discussed in the later section.

Vuggy

Vuggy porosity is secondary porosity most often formed by selective dissolution of carbonate particle constituents or the solution enlargement of interparticle and intercrystalline pore space (fig. 64). Choquette and Pray (1970) define a vug as a pore that is somewhat equant (not elongate), large enough to be visible to the unaided eye and non-fabric selective.

Vuggy porosity is more common in the lower zones of the reservoir (zones IV-E1 and IV-E2) where solution of original grain constituents such as fusulinid and pelloids resulted in small vugs typically less than one inch (2.5 millimeters). Also, vuggy porosity formed from the dissolution of dolomite crystals and enlargement of intercrystalline pore space is common in the lower part of the reservoir. Although intercrystalline porosity is

Figure 64. Core photomicrographs of vuggy pore types. Vuggy porosity is secondary porosity most often formed by dissolution of carbonate particle constituents or the solution enlargement of interparticle and intercrystalline pore space.

A) A small vug has enlarged this partially open microfracture within this peloidal wackestone. Vuggy porosity is not effective if the vugs are not interconnected. Most vugs observed within the West Jordan unit have formed by dissolution along fracture faces or grain constituents and are isolated within the rock matrix. Intercrystalline porosity (blue epoxy) as well as anhydrite cement (white) and calcite cement (red) are also seen within this sample (photomicrograph from WJU #1419; 3635.11 feet; magnification 32X).

B) Nice vuggy porosity has developed within this mixed siliciclastic rock. Although the fine crystalline nature of this sample may make it difficult to see, this sample has appreciable intercrystalline porosity within the matrix of this rock. Vugs are much more effective when they occur within zones where appreciable intercrystalline porosity is already present. Porosity and permeability for this sample is 14.4 percent and 70.6 millidarcies, respectively. This porosity and permeability is primarily the result of the well-developed micro porosity within this sample (photomicrograph from WJU #1416; 3624.4 feet; magnification 8X).

C) This vug would be considered fairly large within the West Jordan unit. Most vugs observed were very small and isolated. This vug probably developed from the mold of a peloid grain and became enlarged through dissolution of surrounding matrix (photomicrograph from WJU #1416; 3618.2 feet; magnification 10X).

D) This finely crystalline dolomite has developed several small vugs from intercrystalline pores within this interval. A small vug is seen within the lower middle part of the photomicrograph. This vug is the result of enlargement of intercrystalline pore space and dissolution of surrounding dolomite crystals (photomicrograph from WJU #505; 3502.2 feet; magnification 32X).

E) Vuggy porosity development has occurred within this peloidal packstone as a result of solution around previous molds and intercrystalline pores. Not the calcite cement (red) within the central right-hand side of the photomicrograph. Calcite cement is more prevalent within the lower zones of the reservoir (zones IV-E1 and IV-E2) where solution enhanced porosity has developed (photomicrograph from WJU #505; 3698.4 feet; magnification 32X).

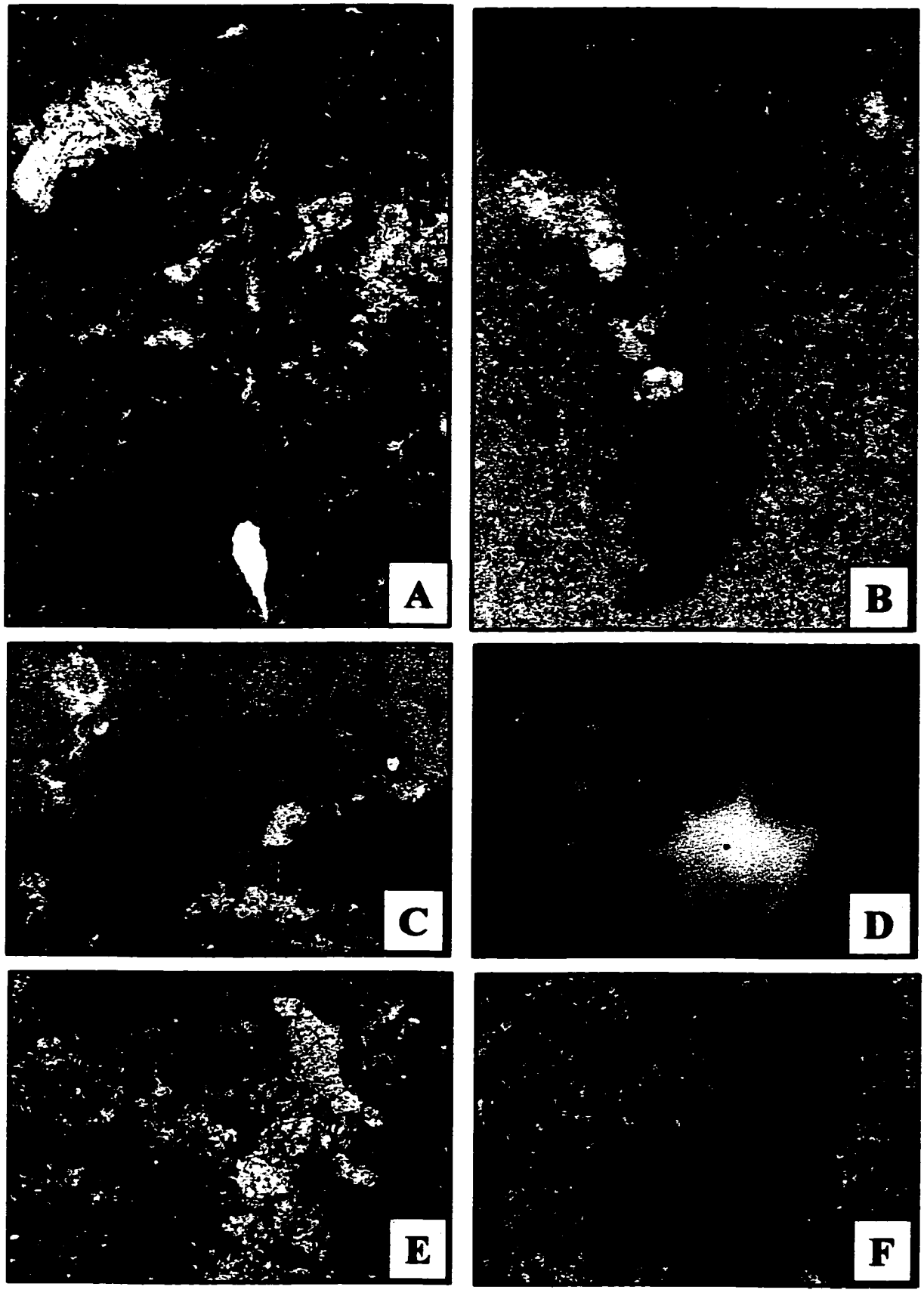
A
B
C
D
E
F

the most significant pore type affecting hydrocarbon flow within the West Jordan unit, the formation of small vugs by enlargement of intercrystalline pores and grains in the lower part of the reservoir has improved the overall flow properties within these zones. Where significant solution enhanced intercrystalline and vuggy porosity was seen in core and thin sections, it was almost always associated with secondary calcite cementation which is a by product of the dedolomitization process.

Above zone IV-E1, vuggy porosity is associated with muddier facies (skeletal and peloidal dolowackestones and mud-rich dolopackstones) and was formed by the solution enlargement of moldic pore space created by dissolution of carbonate grains. These pores were always isolated and not believed to contribute to the overall reservoir permeability. Where large vugs (greater than one inch) were observed in core they were always associated with anhydrite nodules, and therefore, are suspected of being recent voids caused by the displacement or dissolution of sulfate cement during coring or cleaning processes.

DIAGENTIC AND SEDIMENTARY FEATURES

Diagenetic and sedimentary features that most affect fluid flow within the West Jordan reservoir include dolomitization, sulfate and dolomite dissolution, cementation, stylolite and associated pressure solution features, and clay seams. Original carbonate rock once present within the San Andres Formation at the West Jordan unit has been completely dolomitized making grain and fabric identification in core difficult. Scatter within porosity-permeability cross plots is reflective of several factors, including differing pore types, multi-model pore size distribution, fractures, stylolites, and diagenetic processes such as cementation and dissolution that resulted in alteration of porosity and permeability within the reservoir. It is fortunate that diagenetic processes within the unit have concentrated within facies tracts following for the most part original depositional fabrics. This has allowed for a more predictable model based on geological and petrophysical characteristics.

San Andres rocks within the West Jordan unit have been significantly altered by diagenetic events. The most significant of these events was dolomitization of San Andres carbonates. Evaporative reflux is the most accepted mechanism for the dolomitization of San Andres carbonates along the Central Basin platform. In this model, dolomitization would be an early diagenetic event, most likely occurring syndepositionally.

Sulfate minerals (gypsum and anhydrite) comprise the primary pore filling cements in the reservoir and are common within all facies. Anhydrite is by far the most dominant sulfate mineral observed in cores, however, sufficient amounts of gypsum occur to make accurate porosity determinations difficult due to the bound water contained

in this mineral. Calcite cement occurs in the lower parts of the reservoir and is considered a late-stage replacement cement precipitated during the dedolomitization process.

Petrographic evidence indicates that sulfate cementation within the reservoir was a multistage diagenetic event. Displacive anhydrite nodules testify to early sulfate precipitation prior to solidification of sediment. Anhydrite within fractures identify late stage precipitation as well. Several episodes of dissolution and cementation within the reservoir are believed to be the result of periods of exposure and the influx of meteoric waters occuring at the end of high frequency sequences I and II (fig. 11). The occlusion of many skeletal molds by sulfate cement indicates dissolution must have proceeded some periods of sulfate cementation. At least one later period of dissolution is indicated within zones II and IV-E1 and IV-E2 by the almost complete solution of anhydrite within pore throats.

Clay intervals, stylolites and pressure solution features within the reservoir create low permeability zones that restrict vertical flow of fluid within the reservoir. Even though stylolites result in vertical permeability barriers, evidence suggests that horizontal lateral fluid flow occurs between stylolite planes within the reservoir and that injection water may be channeling horizontally through the reservoir along parted stylolite seams.

Dolomitization and Dissolution Features

Recrystallization during dolomitization has changed pore throat geometry thus altering the original characteristics of porosity and permeability within the reservoir. Later dissolution of dolomite and sulfate cements has further modified original porosity

and permeability trends within the reservoir. Although complex diagenetic events have altered the petrophysical properties of the reservoir, diagenetic patterns were found to follow depositional patterns to a large degree. This allowed for an accurate reservoir model to be built which closely follows the depositional facies tract model. The interpreted sequence of diagenetic events for the West Jordan unit is seen in Figure 65.

The most widely accepted mechanism for dolomitization of San Andres carbonates along the Central Basin platform is by evaporative reflux. Dolomitization within San Andres carbonates by evaporative reflux was originally proposed by Adams and Rhodes (1960). Since that time a number of studies have supported an evaporative reflux process for dolomitization within Permian carbonates along the Central Basin platform (White, 1984; Bebout et al., 1987; Ruppel and Cander 1988a; Leary and Vogt, 1986, 1990; Sun, 1995; Saller and Henderson, 1998; Lucia, 1999). Oxygen isotope data suggest that evaporative reflux, not deep burial diagenesis, is the most likely mechanism for dolomitization within the area (Saller and Henderson, 1998). Isotope studies within the area combined with petrographic studies of dolomitization within the West Jordan unit suggest that dolomitization occurred early, most likely syndepositionally (fig. 65).

In this model dolomitization and commonly associated evaporate mineralization (anhydrite and gypsum) are produced from an environment characterized by refluxing hypersaline evaporative seawater. Tidal flat environments result in evaporation of marine waters causing them to become denser (fig. 66). These dense, saline waters flow downward and seaward through underlying sediment resulting in dolomitization of carbonate strata and precipitation of sulfate minerals. In this system pervasive dolomitization occurs toward the top of each carbonate-evaporite cycle but decreases

Figure 65. Paragenetic sequence of diagenetic events interpreted for the West Jordan unit. Dolomitization of San Andres carbonates was an early diagenetic event occurring syndepositionally or within early burial of sediments within an evaporative reflux environment. At least several episodes of sulfate cementation and dissolution are indicated from petrophysical evidence. The presence of highly occluded cycles (zones I and IV-C) at the top of high frequency sequence boundaries representing highstand systems tracts 1 and 2 suggest that sea level and accommodation space controlled periods of cementation and dissolution to a large degree within the area. Dolomite dissolution and associated calcite precipitation are believed to be late stage diagenetic events because of their pattern association to present-day structural trends.

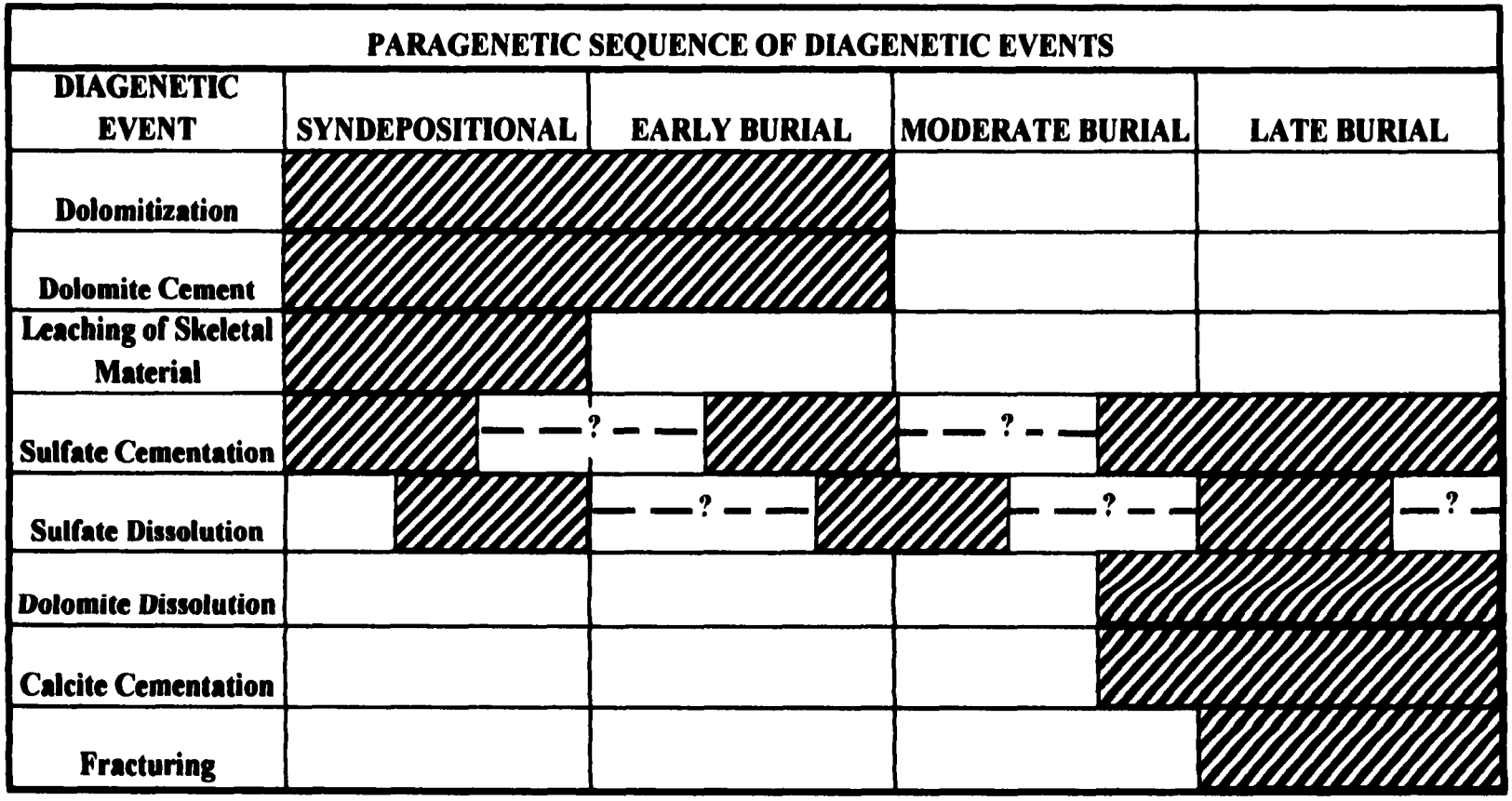
PARAGENETIC SEQUENCE OF DIAGENETIC EVENTS
DIAGENETIC EVENT
SYNDEPOSITIONAL
EARLY BURIAL
MODERATE BURIAL
LATE BURIAL
Dolomitization
Dolomite Cement
Leaching of Skeletal Material
Sulfate Cementation
Sulfate Dissolution
Dolomite Dissolution
Calcite Cementation
Fracturing
?

Figure 66. Diagrammatic illustration showing the dolomitization reflux model. Evaporation of shallow restricted marine waters results in the sinking of dense supersaturated fluids into the underlying substrate. Through reflux these supersaturated fluids with respect to magnesium and calcium are transported basinward and dolomitization begins to take place. Dolomitization occurs first in areas closest to the evaporative lagoons and tidal ponds and progresses basinward as these nearshore sediments become completely dolomitized.

Dolomitization Reflux Model

$$CaCo_3 + Mg^{2+} + Co_3^{2-} \rightleftharpoons CaMg(Co_3)_2$$

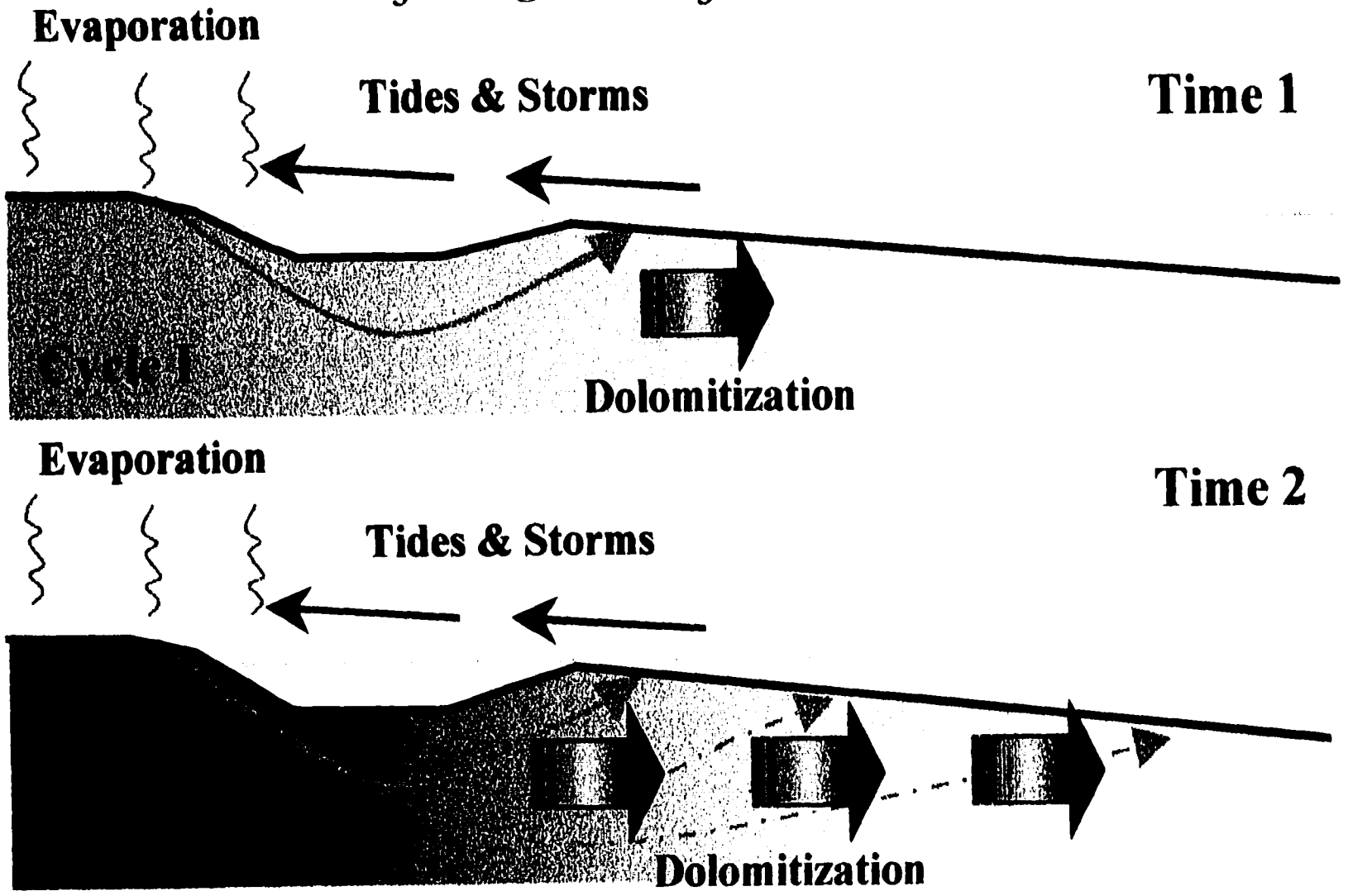

progressively downward toward more normal marine subtidal facies within the cycle (fig. 66; Sun, 1995; Lucia, 1999).

Dolomitization results in both the replacement of calcite or aragonite by dolomite and the cementation of pore space by dolomite cement (Lucia, 1999). The rapid nucleation and long term exposure within the nearshore environment results in the formation of finely crystalline, interlocked dolomites with little porosity and permeability due to dolomite cementation (overdolomitization; Sun, 1995). Overdolomitization allows for precipitation of additional dolomite, which fills remaining pore space and decreases porosity (Schmoker and Halley, 1982; Lucia and Major, 1994; Sun, 1995; Saller and Henderson, 1998; Lucia, 1999). Farther from the dolomitizing fluids the volume of fluid flow and magnesium/calcium ratio is lowered leading to the formation of more porous sucrosic dolomites.

Because of extreme recrystallization thin sections were examined under ultra violet light in an effort to better determine rock fabrics within the reservoir. Although ultra violet florescence was not successful in determining individual grain types, it did illustrate clearly the degree of recrystallization that has taken place within the reservoir (figs.67 and 68). Grain-dominated fabrics were identifiable with high magnification under ultra violet light.

The distinct relationship between increased dolomite crystal size as you move to more basinal facies tracts has been observed by other workers in the area (Murray, 1960; Lucia, 1962; 1999). Lucia (1999) writes that two factors affecting dolomite crystal size are (1) the saturation of the dolomitizing fluids (magnesium/calcium ratio) and (2) the surface area of the precursor fabric. He observed from the Seminole San Andres

Figure 67. Core photomicrographs illustrating dolomite dissolution (A), and the severe alteration and recrystallization of grain-dominated facies under ultra violet reflectance (B) through (D).

A) Photomicrograph illustrating solution enhanced porosity that occurs within the lower zones of the reservoir. Both anhydrite and dolomite have undergone dissolution within this sample. Note that many of the dolomite rhombs have been completely leached leaving only an exterior rim. In addition, remnant anhydrite can be seen in the upper left-hand corner of the picture (photomicrograph from WJU #1416; 3705.7 feet; magnification 32X).

B) Photomicrograph of thin section under ultra violet florescence. Arrows point out more obvious grains. Even at this magnification and using special techniques, grain-dominated fabrics are difficult to discern due to the large degree of recrystallization that has taken place within the reservoir. Note that many of the cores of grains have been completely leached as well. Dark areas are interparticle/intercrystalline porosity (photomicrograph from WJU #505; 3670.5 feet; magnification 50X).

C) Magnification of dolomitized grains (red arrows) illustrating the degree of recrystallization that has taken place. Only faint "ghost" outlines of grains remain. The circular nature and size of these grains suggests that they may be ooids. Much of the porosity within this sample is provided by the leaching of the internal part of the grains as well as intercrystalline/interparticle porosity (photomicrograph from WJU #1307; 3658.11 feet; magnification 100X).

D) A higher magnification of (C) above illustrating recrystallization of grains within the reservoir. The grain is located in the center of the photograph and only the outer remnant remains (photomicrograph from WJU #1307; 3658.11 feet; magnification 200X).

A
B
C
D

Figure 68. Core photomicrographs illustrating alteration of grain-dominated fabrics due to recrystallization during dolomitization.

A) Photomicrograph of thin section under ultra violet florescence illustrating a fusulinid-peloidal grain-dominated packstone. Bryozoan and fusulinid grains tend to be better preserved within the reservoir making their identification easier. Pore throats are indicated by dark colors (photomicrograph from WJU #1416; 3676.6 feet; magnification 100X).

B) Photomicrograph of thin section under ultra violet florescence illustrating a grain-dominated packstone. The large grain in the upper right hand corner is a bryozoan fragment. Ghost grains can be identified within the sample as well by their circular pattern. Porosity in this sample occurs within dark areas (photomicrograph from WJU #505; 3714.3 feet; magnification 50X).

C) Photomicrograph of thin section under plain light showing ghost remnants of grains within a grain-dominated packstone. Dark areas filling pore throats are hydrocarbons and anhydrite cement (white) is seen in the central top portion of the photograph. Note that grain centers have been leached (photomicrograph from WJU #505; 3698.4 feet; magnification 100X).

D) Photomicrograph of (C) above under ultra violet florescence. Hydrocarbons filling pore throats are yellow colors within the sample. Porosity within the sample is indicated by the green color (photomicrograph from WJU #505; 3698.4 feet; magnification 100X).

A
B
C
D
0.10 centimeters

reservoir (fig. 1) that dolomite crystal size increases with depth in both mud-dominated and grain-dominated facies (fig. 69). The influence of rock fabric is evident in the grain – dominated facies where the increase in dolomite crystal size is even more dramatic. Evidence to support both of these factors is seen within the West Jordan unit. Dolomudstones deposited in nearshore environments have much finer dolomite crystals (<10 (m) than intershoal dolomudstones and mud-rich wackestones within the proximal outer ramp environment where coarser dolomite crystals develop (20-50 (m).

The second relationship is particularly evident within the West Jordan unit where dolomitized grain-dominated facies have considerably coarser dolomite crystals than mud-rich facies. This substantiates that grain fabric is a control on the development of dolomite crystal size within the unit. Nevertheless, grain-dominated fabrics in the overlying zone IV-C exhibit less severe recrystallization and finer crystal size. This suggests that the occlusion of pore throats with anhydrite within zone IV-C occurred early within highly saturated dolomitizing fluids. This would result in the finer dolomite crystal size observed in this zone and at the same time anhydrite could have been precipitated precluding the movement of later dolomitizing fluids through the zone. Because this zone represents the culmination of highstand systems tract I (figs. 10 and 11) it would not be unlikely that shoals within the ramp crest facies tract cut off circulation of fresh marine waters resulting in more hypersaline conditions in the lagoon.

Dissolution within Permian reservoirs has been documented by numerous studies (Leary and Vogt, 1986, 1990; Bebout, et al., 1987; Ruppel and Cander, 1988a; Ruppel, 1990, Longacre, 1990; Major and Holtz, 1990; Major, et al., 1990; Ruppel and Lucia,

Figure 69. Cross plot of depth versus dolomite crystal size for the Seminole San Andres reservoir. This figure shows an overall increase in crystal size associated with increasing depth within the reservoir. This relationship is well documented within the West Jordan unit reservoir as well and is probably common to similar San Andres reservoirs across the eastern margin of the Central Basin platform. The increase in dolomite crystal size with depth is thought to be the related to 1) the distance and concentration of facies from hypersaline dolomitizing fluids during deposition 2) the precursor rock fabric, particularly grain-dominated versus mud-dominated (figure from Lucia, 1999).

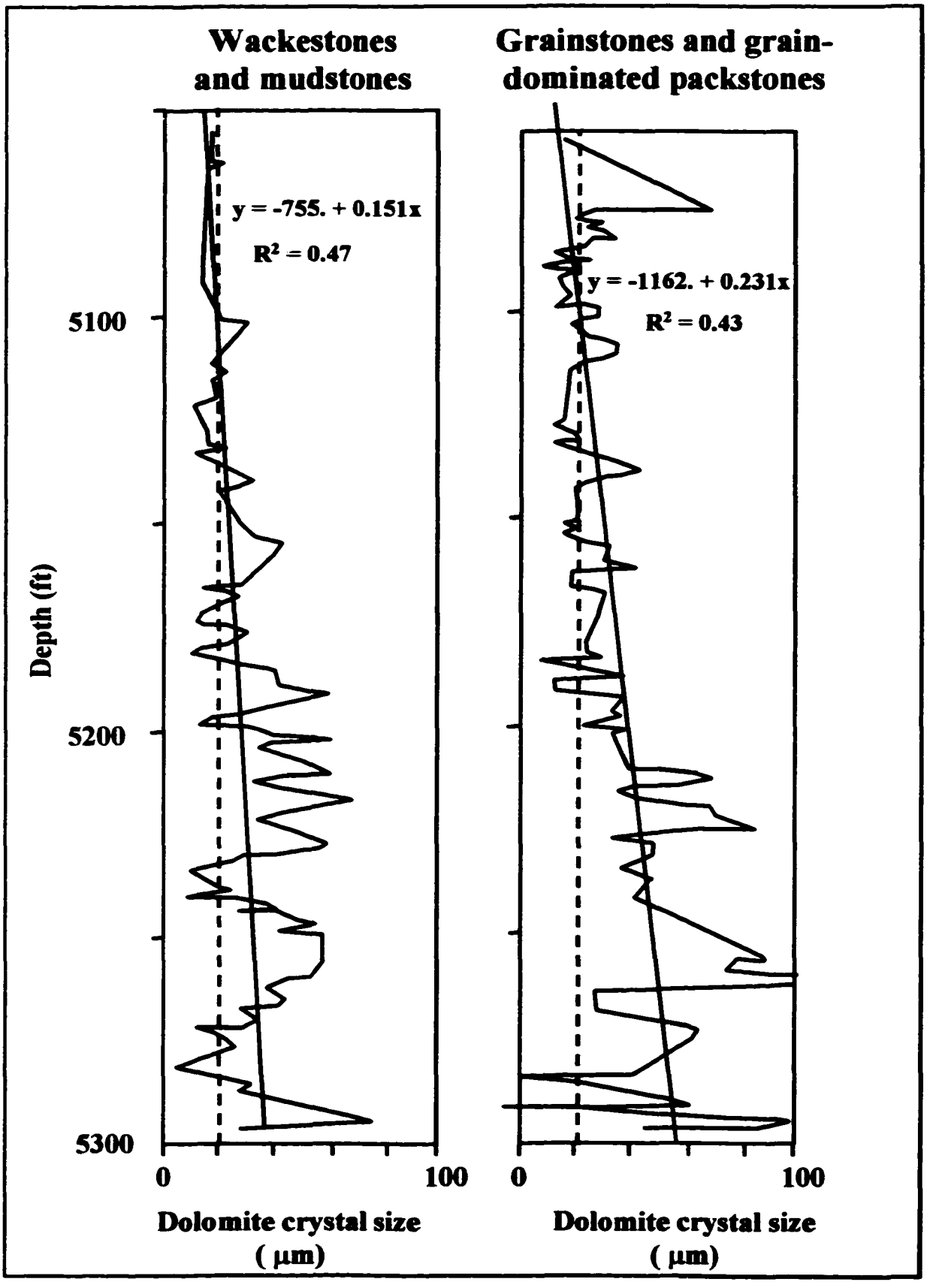
Wackestones and mudstones
Grainstones and grain-dominated packstones
y = -755. + 0.151x
R² = 0.47
y = -1162. + 0.231x
R² = 0.43
5100
5200
5300
Depth (ft)
0
100
0
100
Dolomite crystal size (μm)
Dolomite crystal size (μm)

1996; Lucia, 1999). Dissolution of sulfate cement is particularly evident within zones II, IV-E1 and IV-E2 (fig. 11) and dissolution of dolomite is seen only within the lower zones where selective dissolution of the interior of dolomite rhombs has resulted in increased porosity and permeability (fig. 67a).

Petrographic analysis indicates a complex series of multiple periods of dissolution within the West Jordan unit. Nevertheless, original reservoir facies have maintained their overall petrophysical characteristics and permeability trends resemble depositional facies trends within the reservoir. Exceptions to this occur within cycles containing grain-dominated facies that have been occluded by sulfate cements (zones I and IV-C). In these zones the petrophysical trends no longer mimic the depositional patterns.

Within the West Jordan unit a correlation between solution enhanced porosity and the paleo oil/water contact related to present day structure provides evidence that dolomite dissolution was a late stage diagenetic event. This relationship is evident only with dolomite dissolution and may not be synonymous with sulfate dissolution. Solution enhanced porosity is indicated to be post present day structure within the lower zones IV-E1 and IV-E2 because dissolution porosity patterns closely follow structural contours in these zones (fig. 70). Dolomite dissolution is confined to these cycle boundaries (zones IV-E1 and IV-E2) although it was not found to be facies dependent (fig. 71). Calcite cement, a precipitant of the chemical reaction occurring during the dissolution of dolomite was observed only in the lower parts of the reservoir near the original oil/water contact. Calcite precipitation associated with dolomite dissolution and solution enhanced porosity within these lower zones appears to be post present day structure and therefore, late stage diagenetic event. The precipitation of calcite from dolomite forms either by the

Figure 70. PHIH contour maps from zones IV-E1 and IV-E2. PHIH values are represented by color contours while black contours represent structural elevation for each zone. The approximate area of the oil/water contact is designated by the westernmost contour for each zone. West of these contours the relative permeability for oil becomes essentially zero and only water is produced. This eliminates a substantial portion of the western half of the unit for production within zone IV-E2. Note that solution enhanced porosity trends tend to follow structure indicating that solution enhancement of porosity occurred post modern day structural formation. Solution enhanced porosity within these zones is believed to be the result of both early and late stage diagenetic events. The early event related to mixing of meteoric waters during periods of exposure at the end of high frequency sequence I and the late stage event related to dolomite and/or sulfate dissolution after formation of the present day structure. The association of calcite cement (a product of dolomite dissolution) near the original oil/water contact helps lend support to this conclusion.

Zone IV-E1
Zone IV-E2
3.75
3.5
3.25
3
2.75
2.5
2.25
2
1.75
1.5
1.25
1
0.75
0.5
0.25
0

Figure 71. Porosity-permeability cross plot illustrating that solution enhanced porosity is not facies dependent. Almost all facies types have experienced dissolution within the reservoir if they occur within zones II, IV-E1 or IV-E2. The red polygon outlines data points that are believed to have at least some amount of dissolution. Data points within this polygon are plotted at depth to the left of log signatures of plotted data. Note that data points with the most significant porosity and permeability are found within zone II, IV-E1 and IV-E2. Zones I, III, IV-A, IV-B and IV-C have low porosity and permeability values, the result of moldic pore types (zones IV-A, IV-B and IV-C) and occlusion of porosity by cementation with sulfates (zones I, and IV-C).

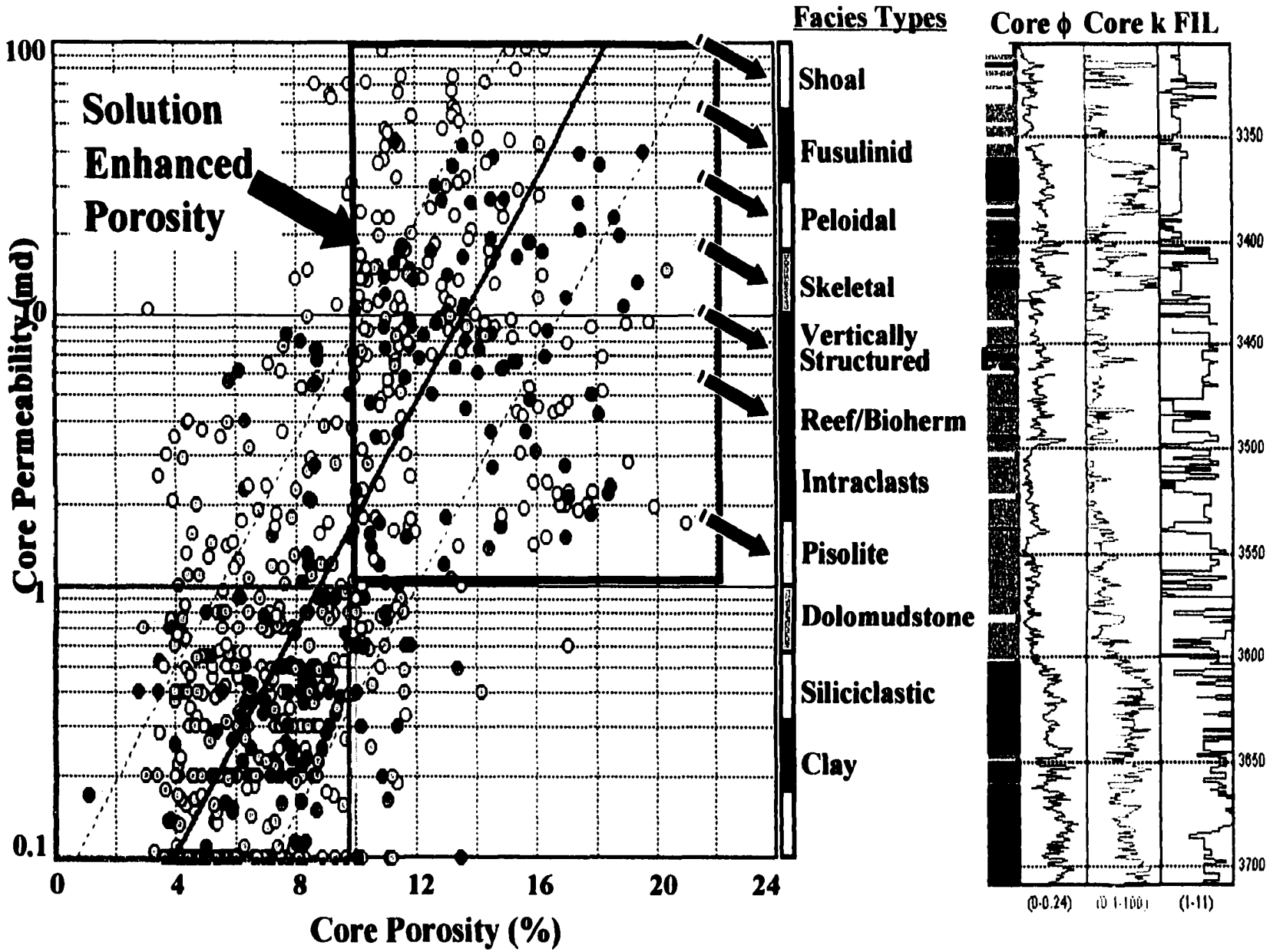
Facies Types
Core ϕ Core k FIL
100
10
1
0.1
Core Permeability (md)
Solution
Enhanced
Porosity
Shoal
Fusulinid
Peloidal
Skeletal
Vertically
Structured
Reef/Bioherm
Intraclasts
Pisolite
Dolomudstone
Siliciclastic
Clay
0
4
8
12
16
20
24
Core Porosity (%)
3350
3400
3450
3500
3550
3600
3650
3700
(0-0.24)
(0.1-100)
(1-11)

influx of meteoric or deep ground waters. Whether or not dolomite and sulfate dissolution were contemporaneous within zones IV-E1 and IV-E2 is not fully understood. It does appear likely that at least two separate periods of dissolution occurred between zone II and zones IV-E1 and IV-E2. If dissolution was associated with sulfate cementation in zones I and IV-C during highstand systems tracts 1 and 2, then at least three periods of dissolution have occurred within the reservoir.

Petrographic analysis indicates that sulfate dissolution probably occurred as a series of diagenetic events. Zones II, IV-E1 and IV-E2 have significantly greater porosity and permeability due to dissolution. The overlying zones (III and IV-C) are completely occluded with sulfate cement and represent supratidal to very shallow water ramp crest environments capable of subaerial exposure that would have allowed meteoric waters to come in contact with underlying rock cycles. Trentham (1998) writes that at the end of San Andres deposition there was a major long term sea level drop (+/- 250 feet) which subaerially exposed porous intervals and caused extensive dissolution and reprecipitation. Ruppel, (1999; personal communication) describes a large hiatus in middle San Andres deposits within the Fuhrman Macho field to the north of West Jordan. Preliminary correlation indicates this hiatus was contemporaneous with the deposition of zone IV-C. Therefore, it is possible that exposure occurred during deposition of zones directly overlying intervals of dissolution. If meteoric influx is responsible for sulfate dissolution within cycle boundaries then this would indicate that dissolution of dolomite, which follows late stage structural development, and dissolution of sulfates occurred at very different times during the diagenetic history of the unit.

Evidence previously stated suggests sea level drops occurred that could have allowed for the recharge of meteoric fluids through exposed platform deposits. Also, coal at the top zone IV-C indicates a humid environment suggesting a climate change from dry, semi-arid to more humid conditions. Climate changes resulting in increased rainfall would improve the likelihood of meteoric ground water percolating down within the underlying cycle boundary in zone IV-E1. Based on probable periods of exposure within cycle boundaries (zones I and IV-C), it seems likely that at least two periods of sulfate dissolution have taken place within the reservoir. Whether or not zones I and IV-C were occluded with sulfate cement early on during dolomitization or dissolution within zones II, IV-E1 and IV-E2 resulted in reprecipitation of sulfate cements in overlying zones I and IV-C is unclear. Diagenetic events that occurred in the reservoir are very complex and the paragenetic sequence is only a broad spectrum of possible diagenetic sequences for the reservoir. This is an area that is not fully resolved at this time.

Cement Types

Anhydrite

Anhydrite was found to form as nodules and to occur as pore filling cement within fractures, molds, and poikilotopic textures (fig. 72). Anhydrite was seen from core data to be present throughout the reservoir but was found to be more prevalent in zones I, IV-A, IV-B and IV-C. The most common form of anhydrite within zones IV-A and IV-B are anhydrite nodules with pore filling anhydrite cements most common in zones I, and IV-C. Anhydrite was found to occur within all facies and pore types.

Figure 72. Core photographs and photomicrographs illustrating examples of anhydrite cement from the West Jordan unit.

A) Core photograph of an anhydrite nodule with anhydrite filled fractures radiating out from the nodule. Anhydrite filled fractures associated with nodules suggest late stage precipitation under conditions where sediments had already become at least partially lithified (photograph from WJU #1307 at approximately 3434.10 feet).

B) Photomicrograph illustrating poikilotopic anhydrite filling pore throats in this peloidal dolopackstone (photomicrograph from WJU #1416; 3529.8 feet; magnification 6.3X).

C) Anhydrite filling diagenetic fractures and pore space within a dolomudstone-wackestone. Dark blue areas are porosity within the sample (photomicrograph from WJU #1419; 3648.0 feet; magnification 8.8X).

D) Photomicrograph under crossed nichols of blocky anhydrite cement filling fusulinid molds (photomicrograph from WJU #1307; 3552.3 feet; magnification 32X).

E) Photomicrograph under crossed nichols of fibrous or bladed anhydrite cement. This particular sample is from an anhydrite nodule from within the supratidal environment (photomicrograph from WJU #1416; 3330.9 feet; magnification 16X).

F) Bladed anhydrite filling pore throats between a peloidal/fusulinid grainstone. This sample is typical of grain-dominated facies within zone IV-C where interparticle pore space has been completely occluded by sulfate cement, primarily anhydrite (photomicrograph from WJU #1416; 3549.9 feet; magnification 16X).

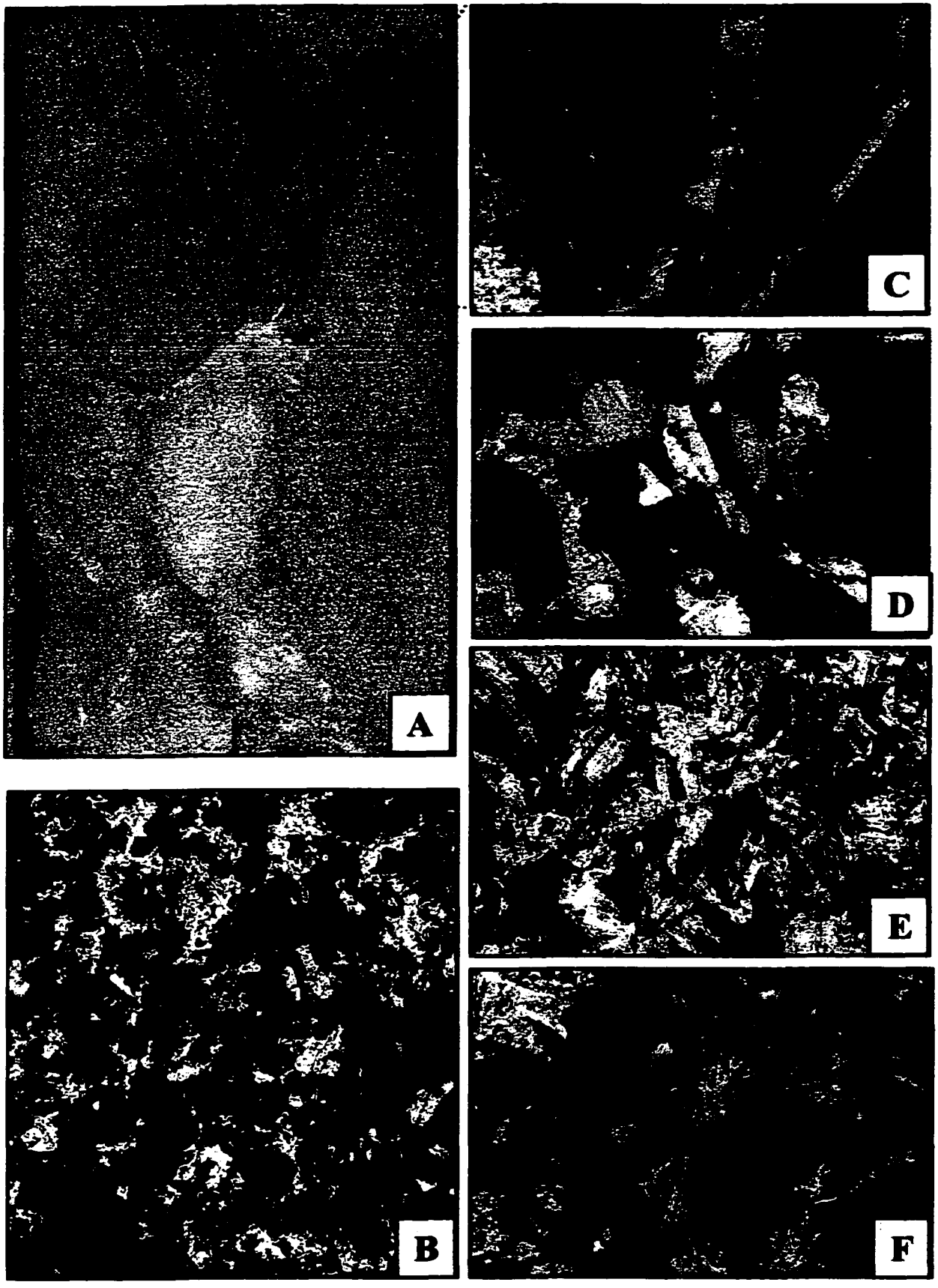
A
B
C
D
E
F

Anhydrite nodules range in size from a few millimeters (less than one half inch) to tens of centimeters (six inches) being greater than the diameter of the core. Both displacive and replacive nodules were seen within core, although displacive nodules were less common and observed only in supratidal facies. Displacive nodules are identified by disturbed strata surrounding the nodule and indicate growth before lithification and compaction of soft sediment. Amalgamation of anhydrite nodules forming a "chicken wire" texture was also common within the reservoir.

Although anhydrite formation may have occurred early in the diagenetic history of the reservoir, there is substantial evidence pointing to a later stage of formation as well. Within the West Jordan unit fracturing and organic matter are quite common around anhydrite nodules. This is particularly true of zone IV-A and suggests over pressuring within the reservoir where fractures and organic matter are concentrated around the nodules in a similar manner as that seen within stylolite formation. These nodules do in fact tend to be present in areas of concentrated stylolite formation. Fractures around anhydrite nodules show that sediment was already lithified prior to the nodule formation. Blocky anhydrite cement was commonly seen to occur within skeletal molds and fractures. The presence of blocky anhydrite within fractures also suggests precipitation of anhydrite after dolomitization and solidification of the sediment.

Other common anhydrite forms are fibrous to bladed and poikilotopic anhydrite (fig. 72 b and e). Poikilotopic anhydrite is the most common pore throat filling cement within the reservoir. It can be difficult to see with the unaided eye due to its fine crystalline nature (fig. 72 b). Although anhydrite nodules are most common in zones IV-A and IV-B, pore-filling anhydrite is more common in zone I and zone IV-C.

Gypsum

Gypsum is found in limited amounts throughout all zones within the reservoir although cores suggest a greater concentration in middle ramp, lagoonal facies (zones IV-A and IV-B). Gypsum seen in thin sections occurred within molds, fractures, nodules, and as pore filling cements replacing anhydrite (fig. 73). Most often gypsum only partially replaced anhydrite cement or nodules. The presence of gypsum within the reservoir is significant because of its affect on porosity determination by core analysis and wireline logs. Seven of the cores studied within the unit have undergone high temperature "vacuum retort" core cleaning procedures. High temperature core analysis alters unstable gypsum to bassanite by driving off bound water contained in the mineral (Lucia, 1999). As bound water is driven off pore space and free water are produced resulting in large errors in porosity measurements. Pore space is increased because bassanite has a smaller molar volume than gypsum (Lucia, 1999). Porosity logs within the reservoir have been corrected in an effort to offset the presence of gypsum (see Appendix A).

Calcite

Calcite cement was observed in zones IV-E1 and IV-E2 within molds, fractures and between pores as a replacement of anhydrite and dolomite (fig. 74). Calcite precipitation within the reservoir is believed to be a product of dedolomitization. Calcite cement occurs within the reservoir beside dolomite dissolution, as evidenced by partially dissolved dolomite rhombs. Calcification of dolomite can involve meteoric or deep ground waters. Lucia (1999) writes that the infiltration of meteoric water can reduce the

Figure 73. Core photographs and photomicrographs illustrating examples of gypsum cement from the West Jordan unit.

A) Gypsum cement (bluish-gray) is replacing anhydrite (white) within this fracture. Porosity is indicated by bright blue epoxy (photomicrograph from WJU #505; 3498.1 feet; magnification 32X).

B) The replacement of anhydrite (white) by gypsum (bluish-gray) along the margins of an anhydrite nodule and within the radiating fracture (photomicrograph from WJU #1416; 3385.8 feet; magnification 32X).

C) Another example of anhydrite being replaced by gypsum within a fracture. Gypsum tends to replace the margins of voids filled with anhydrite first and then move inward (photomicrograph from WJU #505; 3493.5 feet; magnification 20X).

D) This photomicrograph shows almost total replacement of anhydrite by gypsum within a seam and connected vug. Note that this entire peloidal grainstone has been completely occluded by sulfate cement (photomicrograph from WJU #1307; 3408.10 feet; magnification 25X).

A
B
C
D

Figure 74. Core photomicrographs of calcite cement observed within the reservoir. Calcite cement is interpreted as being precipitated during the dissolution of dolomite (dedolomitization) and occurs close to the original oil/water contact of the reservoir.

A) Calcite cementation has filled most of this microfracture and small vug within this medium crystalline peloidal wackestone. This sample is representative of intershoal and proximal outer ramp lithofacies within zones IV-E1 and IV-E2 (photomicrograph from WJU #505; 3656.8 feet; magnification 6.3X).

B) Photomicrograph of a medium crystalline peloidal dolowackestone that has undergone anhydrite and dolomite dissolution with associated calcite precipitation (photomicrograph from WJU #1416; 3618.2 feet; magnification 32X).

C) Calcite cement fills a large portion of the interparticle pore space within this photomicrograph. The large grain in the center of the picture is a bryozoan grain (photomicrograph from WJU #1416; 3657.1 feet; magnification 32X).

D) Calcite cement appears to be replacing anhydrite in this solution enhanced peloidal packstone (photomicrograph from WJU #505; 3656.8 feet; magnification 32X).

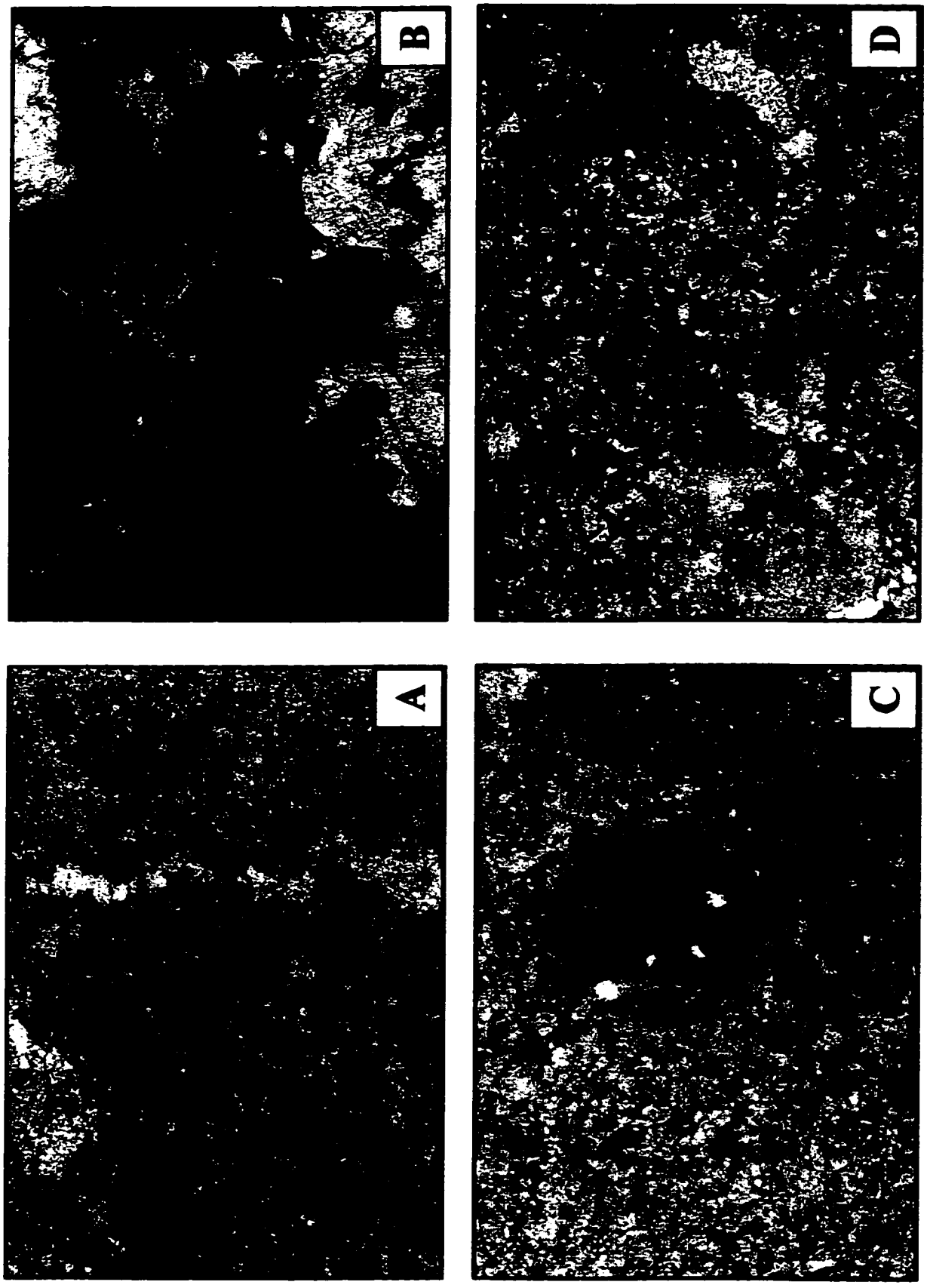
B
D
A
C

magnesium/calcium ratio to such a degree that dissolution of dolomite occurs and calcite is precipitated. Also, calcium-rich water can migrate upward along faults from deeper saline waters.

Calcite can also be precipitated from the dissolution of anhydrite due to contact with meteoric waters. The reduction of sulfates is commonly seen where meteoric water interacts with hydrocarbons in evaporite-bearing formations (Leary and Vogt, 1986). Calcite precipitation is believed to be a late stage diagenetic event (fig. 65) because of its occurrence near the original oil/water contact. This has also been documented within several other fields within the area (Leary and Vogt, 1986, 1990; Ruppel and Lucia, 1996).

Sedimentary Features

Stylolites

Stylolites are major stress-related diagenetic features forming irregular, interlocking suture zones along which dark fine grained material tends to precipitate resulting in vertical permeability barriers (Nelson, 1981, 1983; Wanless, 1979). Stylolites can form under overburden and tectonic stress conditions developing perpendicular to the principle plane of stress. Overburden stress and compaction results in solution and formation of stylolites that tend to form horizontal, parallel to bedding within a rock unit. Tectonic stylolites, common in compressional regimes, form at large angles to primary bedding within the rock. Although most stylolites within the reservoir are the result of overburden stress, tectonic stylolites are present as well.
Stylolites are usually believed to act as vertical barriers to flow, nevertheless within the

West Jordan unit evidence suggest that horizontal lateral flow is occurring along parted stylolite seams.

Stylolites are extremely common within the unit and are believed to play a significant role in channeling of injection water within zone IV-A. Petrological and petrophysical data indicate that stylolites were and are an avenue of fluid movement within the reservoir. Thin sections and core data illustrate that fluids have migrated through stylolite seams and that stylolite seams act as planes of weakness along which the core breaks when brought to the surface (figs. 75 and 76). Under waterflood injection pressures, it is likely that the same thing is happening within the reservoir as well. Large amplitude stylolites (millimeters to tens of millimeters) along which the core separates were primarily restricted to zone IV-A, although many smaller stylolites, stylolite swarms, and wispy laminations were seen throughout the reservoir. Injection tracer logs obtained throughout the unit have identified zone IV-A as the primary zone of flow within the reservoir capturing over thirty-two percent of injected fluids into the reservoir (fig. 77). Contradictory to injection profile data, core and thin section data indicate zone IV-A is relatively tight, comprised primarily of dolomudstones and dolowackestones. Where porosity is seen, it is for the most part moldic in nature and lacks permeability. After examining core, thin sections, and production and injection/tracer data, it becomes clear that the only permeability pathway through this zone occurs laterally through large amplitude stylolites and fracture planes (fig. 76).

Dawson (1988) writes that stylolite seams have served as conduits for calcium carbonate undersaturated fluids and that stylolites may be reopened by partial uplift and unloading. This enables stylolites to provide conduits for diagenetic fluids and

Figure 75. Core photomicrographs of stylolites within the reservoir along which dissolution has resulted in increased porosity in the area around the stylolite. As seen in these photomicrographs, porosity increase is typically restricted to either above or below the stylolite surface, but never was seen occurring on both sides of the stylolite.

A) It is easy to see within this photomicrograph that fluids have traveled along these stylolite seams. Anhydrite is precipitated and replaced by calcite (?) and dissolution has occurred within matrix rock below the stylolite (photomicrograph from WJU #1419; 3638.1 feet; magnification 6.3X).

B) In this photomicrograph blocky anhydrite has been precipitated within large stylolite tension fractures while dissolution has occurred within the matrix under the stylolite (photomicrograph from WJU #1419; 36142.6 feet; magnification 6.3X).

C) The same type feature is seen within this photomicrograph as above. Dissolution along stylolites was seen to be more prevalent in tighter, finer crystalline dolomites (photomicrograph from WJU #1419; 3513.2 feet; magnification 8X).

D) Magnification of C above. Note the intercrystalline porosity (blue) occurring above the stylolite seam and the precipitated anhydrite cement (photomicrograph from WJU #1419; 3513.2 feet; magnification 32X).

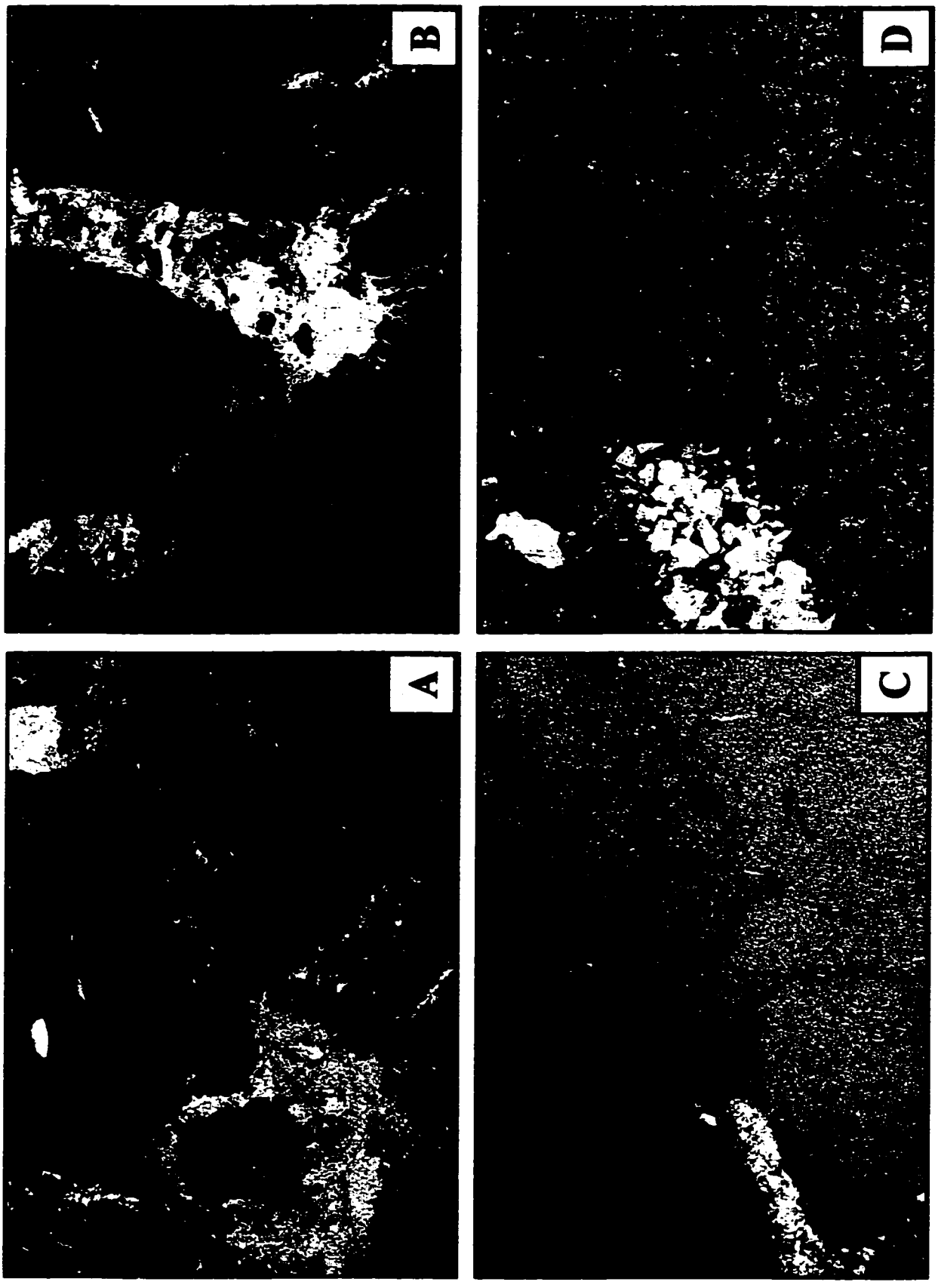
B
D
A
C

Figure 76. Core photographs of stylolites within the reservoir. Figures A) through C) show examples of core parting along large amplitude stylolite seams within the reservoir. These photographs illustrate typical stylolite formation within zone IV-A where core parts along stylolite seams about every two to six inches. Injection tracer data indicate that over 32 percent of the water being injected within the reservoir is entering this zone. The lack of effective porosity and low permeability within Zone IV-A and the presence of these large stylolite seams and fractures suggest that this zone is waterflood their zone within the reservoir.

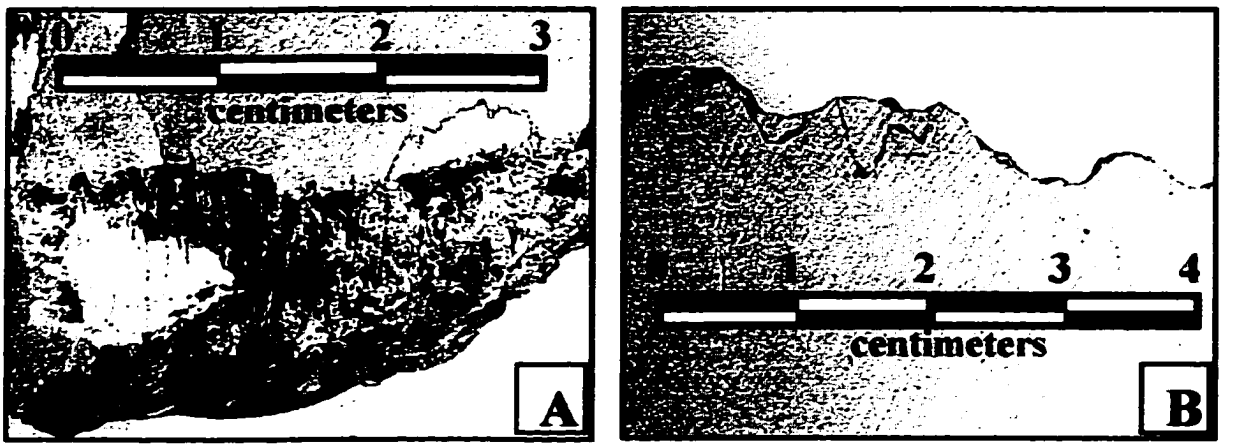
0
1
2
3
centimeters
A
1
2
3
4
centimeters
B

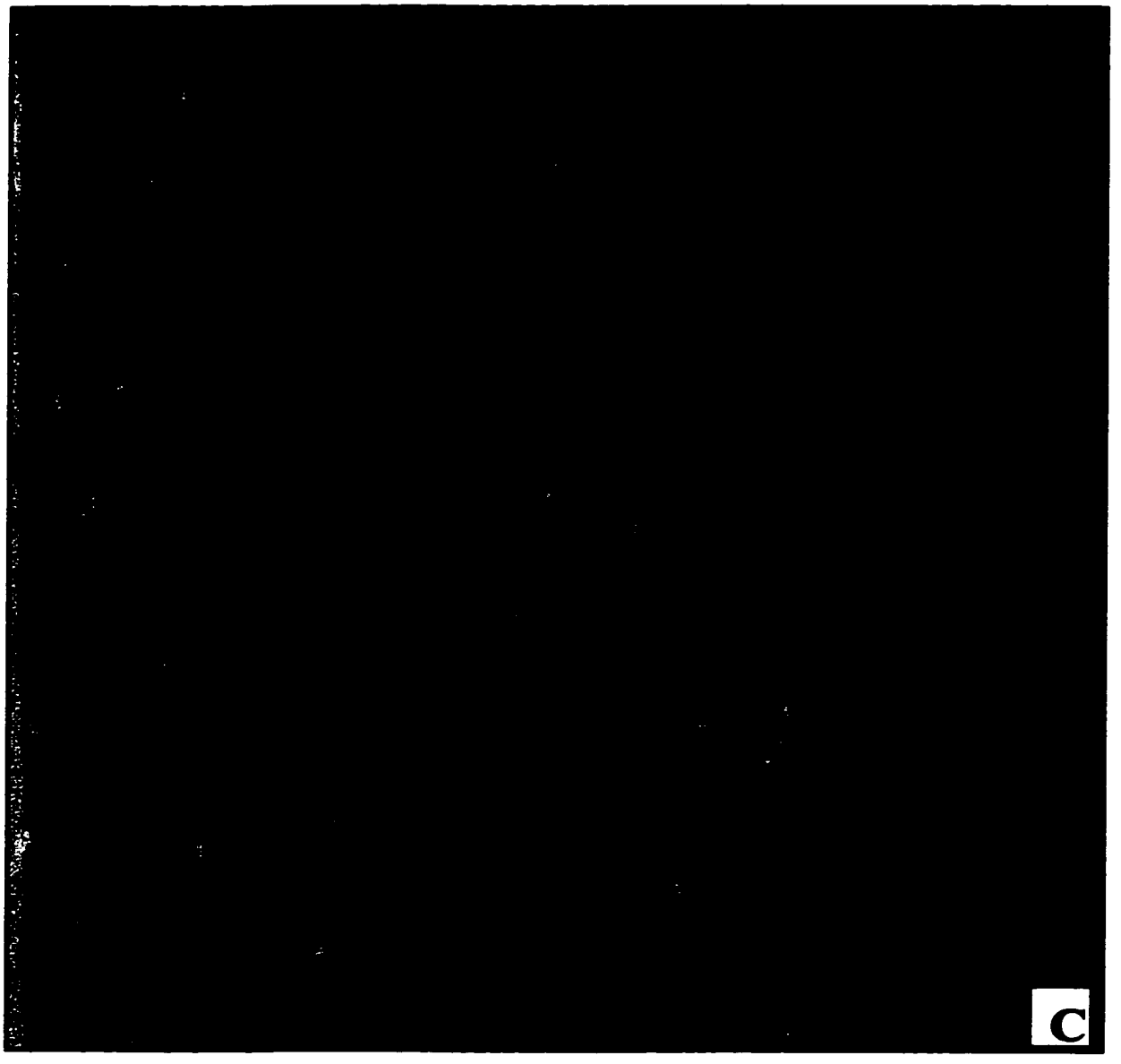
C

Figure 77. A structural cross section through the reservoir showing injection profile data for selected logs (see location map to the left). Zone IV-A takes over 32 % of the total flow seen from injection tracer logs. Colored circles on the location map indicate the location of wells with tracer and velocity data. Each color represents a separate log run for that well over a period of time. All injection tracer data was compiled for each zone and then normalized to determine the overall percent entering each zone. Percentages for injection profiles for each zone are as follows: zone I = 1.8 %, zone II = 6.5 %, zone III = 9.4 %, zone IV-A =32.1 %, zone IV-B = 12.5 %, zone IV-C = 10.1 %, zone IV-E1 = 7.3 %, and zone IV-E2 = 10.3 %. It is interesting to note that the primary flow units within the reservoir take the least amount of injection. This can partially be attributed to a lack of injectors being placed within productive shoal bodies within the lower zones of the reservoir. Pressure differentials within cycle boundaries may also play a key role in the profile of injection data. Red boxes within the center tract between log curves indicate perforations within wells and the color scale is seen to the left of the cross section.

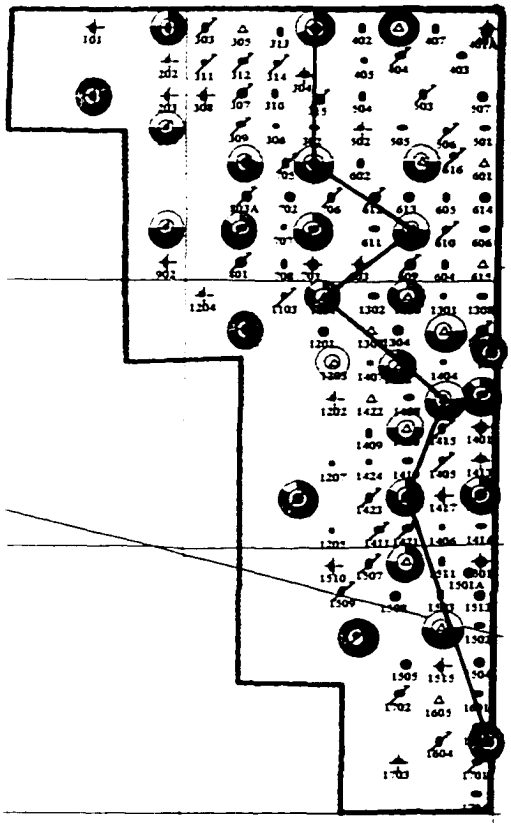

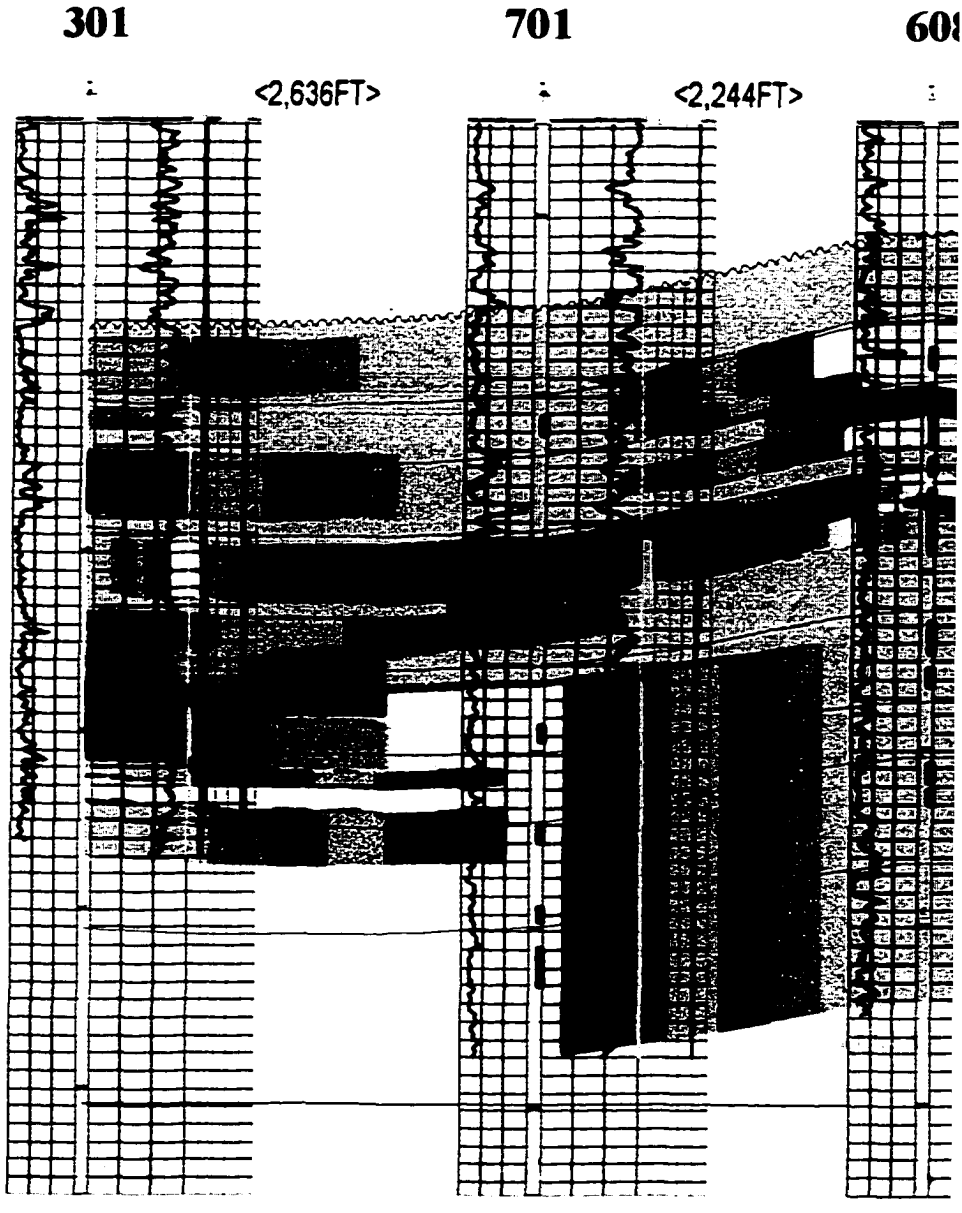
301
701
608
<2,636FT>
<2,244FT>

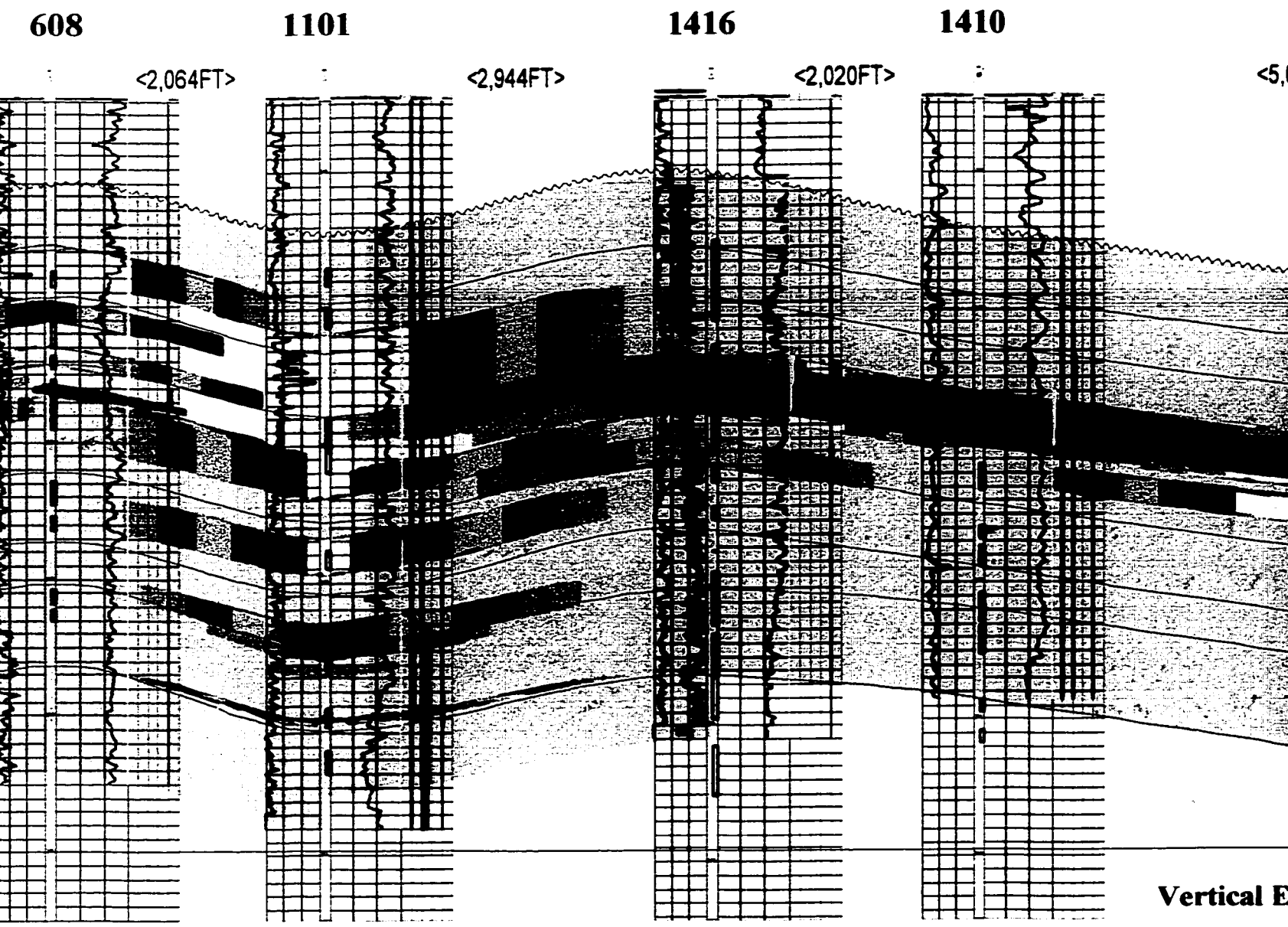

INJECTION TRACER SCALE IN PERCENT



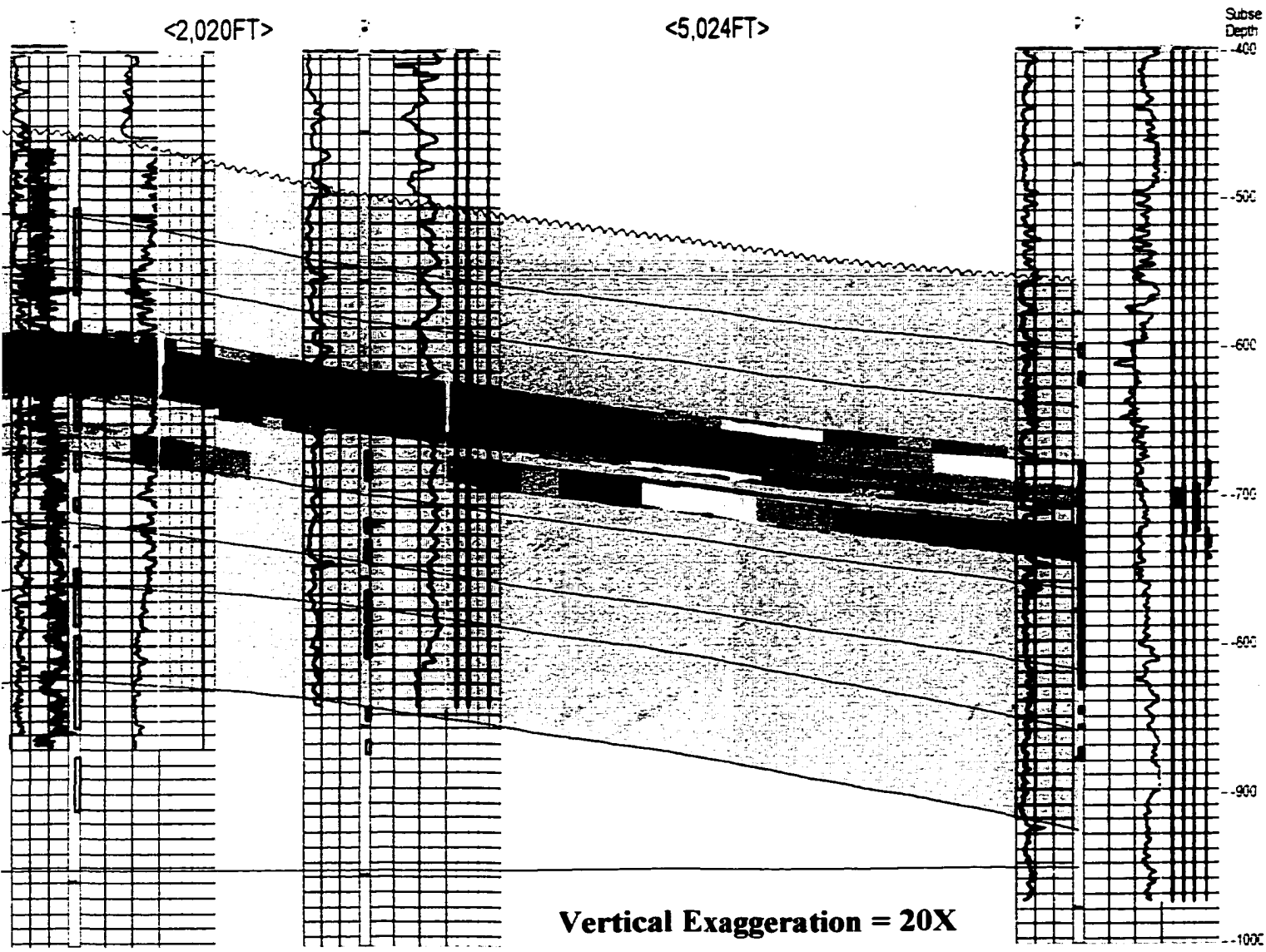

LE IN PERCENT

0 30

hydrocarbons in otherwise impermeable strata. Within the West Jordan unit injection fluids are channeling through the reservoir resulting in inefficient waterflood sweep. A large percentage of injection water is moving laterally through stylolite seams and fractures within zone IV-A and bypassing the majority of matrix porosity within the reservoir. Much of this water is never recovered resulting in an injection withdrawal ratio of 2.4:1.

Pressure Solution Features and Clay Seams

Grain-to-grain suture; microstylolites, microstylolite swarms, wispy laminations and clay seams have the ability to effect vertical permeability within the West Jordan unit reservoir (figs. 78 and 79). Microstylolites, microstylolite swarms, wispy laminations and clay seams are non-sutured solution surfaces that contain a significant amount of platy insoluble material such as clay, silt, or organic rich material (Wanless, 1979).

Microstylolites and microstylolite swarms were commonly observed within all zones of the reservoir. Lamellar stylolitic porosity is commonly associated with microstylolite swarms that typically occur as anastomosing groups of small amplitude stylolites (fig. 78 A, B). Wispy laminations are also very common in cores from the reservoir (fig. 78). Less commonly observed were grain-contact sutures (fig. 78). Grain-to-grain pressure solution features are rare, nevertheless, they were observed within two samples from two different cores within the reservoir. Wispy laminae within carbonate reservoirs similar to the West Jordan unit formed from concentration of significant amounts of fine insoluble material (Wanless, 1979; Lucia, 1962) and thin (less than several centimeters) clay seams are related to stress related pressure solution (Wanless,

Figure 78. Core photomicrographs illustrating pressure solution features including dissolution along stylolite seams and grain-to-grain dissolution.

A) Solution occurring along microstylolite swarms is very common within the West Jordan unit. Note the remnant anhydrite cement (white) left within small vugs created by fluids migrating through these stylolite swarms (photomicrograph from WJU #1307; 3644.8 feet; magnification 6.3X).

B) Porosity created along stylolite swarms such as seen in this photomicrograph are often the primary porosity within tight dolomudstones like the one seen in this example (photomicrograph from WJU #1307; 3658.2 feet; magnification 12.5X).

C) Grain-to-grain pressure solution was seen within two cores in the unit but was not found to be common. The lack of well preserved grains within the reservoir limits the occurrence of this feature as well. Most of these grains have been almost completely replaced by anhydrite cement (photomicrograph from WJU #1307; 3637.9 feet; magnification 16X).

D) This photomicrograph is the same as C above only under crossed nichols and a smaller scale. Note that at grain-to-grain contacts some of the grains have been dissolved (photomicrograph from WJU #1307; 3637.9 feet; magnification 6.3X).

B
D
A
C

Figure 79 Core photographs and photomicrographs of clay seams and clay laminations from the unit. Clay intervals were most prevalent in zones III and IV-C although thin clay intervals representing maximum flooding surfaces within vertical facies successions were found throughout the reservoir interval. A) through D) Core photographs of various clay intervals seen within the reservoir. Photographs A) and B) are from the inner ramp facies tract and occur within fenestral algal laminated dolomudstones. C) is a clay-rich interval from zone IV-C and D) is a small clay interval representing a marine flooding surface.

E) Photomicrograph of wispy laminations within a finely crystalline dolomudstone. Note the small displacive anhydrite nodule (photomicrograph from WJU #1307; 3492.7 feet; magnification 32X).

F) Fine grained clay with abundant quartz.(photomicrograph from WJU #1416; 3568.0 feet; magnification 32X).

G) Microstylolite swarms formed by coalescing microstylolites in a very fine crystalline dolomudstone. The yellow material is organic in origin similar to that seen in the plant fragment in figure 28 A (photomicrograph from WJU #1307; 3498.6 feet; magnification 32X).

H) Very thin microstylolite swarms in a finely crystalline dolowackestone. Note the sparsely developed intercrystalline porosity within this sample (photomicrograph from WJU #1307; 3589.11 feet; magnification 32X).

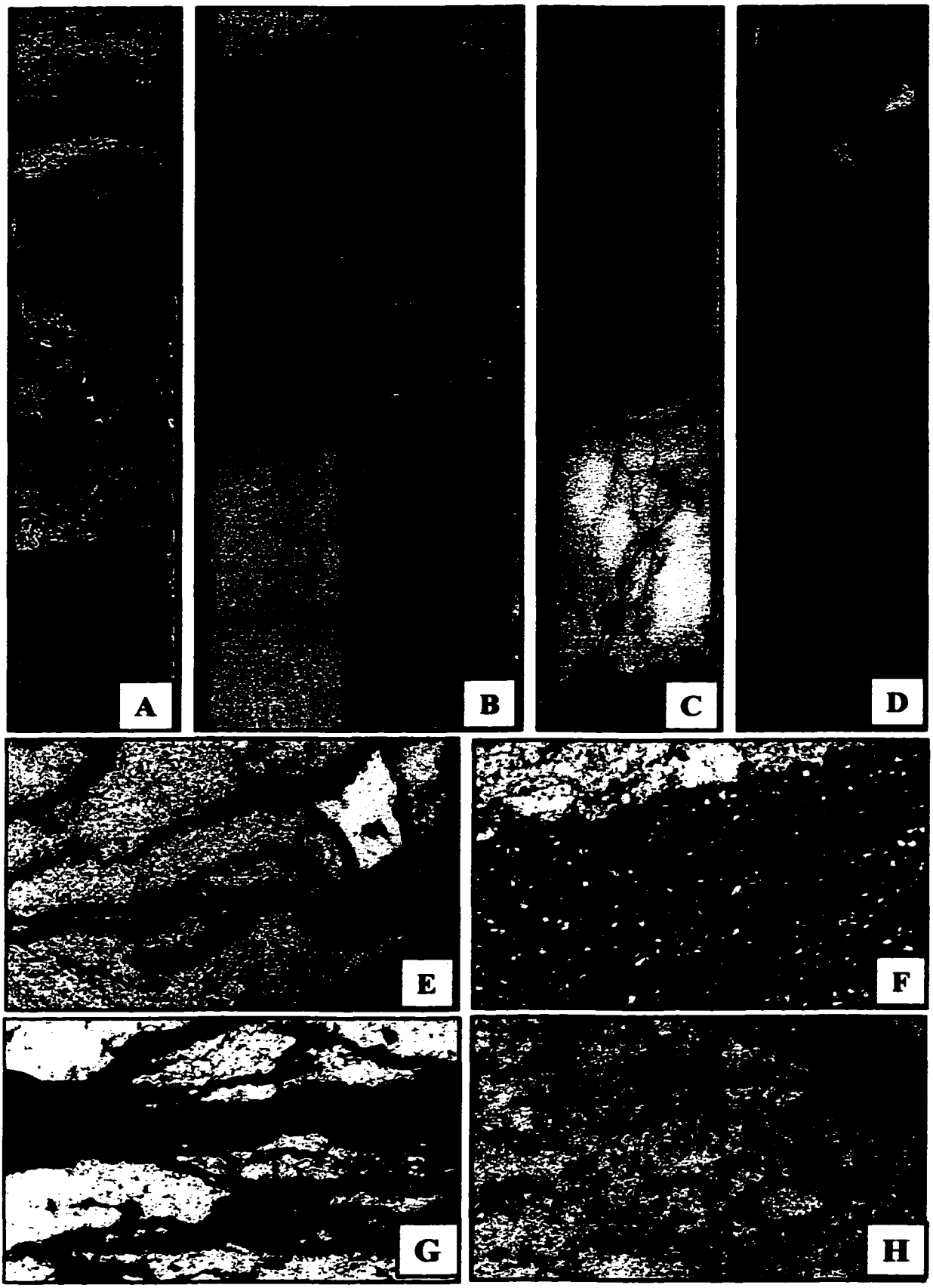
A
B
C
D
E
F
G
H

1979). Within the West Jordan unit most clay seams are believed to be sedimentary depositional features due to their thickness and lateral correlative nature over the unit suggesting deposition during maximum flooding surfaces.

Clay seams described to have formed from pressure solution are typically thin (<2cm) and contain little siliciclastic material (Wanless, 1979). XRD analysis indicates the presence of a large amount of quartz within clay seams. (fig. 79). XRD analysis was employed unsuccessfully in an attempt to more accurately define cycle boundaries by determining clay mineral structures that have environmental significance. XRD data are presented in Appendix B. Regardless of their origin clay seams within the reservoir act as vertical permeability barriers that compartmentalize and complicate the reservoir.

THE PERMEABILITY TRANSFORM MODEL

The method used to measure permeability within the reservoir integrates both geological and petrophysical data to predict the three dimensional spatial distribution of permeability within the West Jordan reservoir. The model, incorporating recent work by Lucia (1995, 1999) that integrates the distribution of petrophysical rock-fabric into a chronostratigraphic geological model, has been applied very successfully within the unit. Lucia (1999) has demonstrated a method for linking facies to petrophysical properties such as porosity, permeability, and water saturation and has derived a permeability transform that incorporates the flow properties characteristic of rock fabric pore types found in carbonates. This method was applied to cored wells within the unit in order to measure its accuracy within cycle boundaries and then extrapolated to all wells with porosity data. The method was found to be effective even with the wide range of old-style neutron-count logs that make up the bulk of porosity data for the unit.

Within the West Jordan unit a permeability transform derived simply from porosity-permeability cross plots would be fraught with inaccuracies. As clearly seen within the unit, little correlation exists between porosity and permeability and previous sections have demonstrated the inherent error that would occur by using a single porosity-permeability transform for this reservoir (fig. 50). More accurate results could be obtained by deriving permeability transforms for each zone within the reservoir. Nevertheless, most pore types within the reservoir lack any porosity to permeability correlation. Although intercrystalline and well-developed fenestral pores have a higher correlation coefficient than other pore types, the correlation within these pore types is weak at best (fig. 50).

The use of capillary pressure curve data has been shown to effectively calculate permeability in some reservoirs. Reasons why this method would be less effective within the West Jordan unit evolve around the available data set and heterogeneity present within the reservoir. Capillary pressure curves were available for only one cored well within the unit (WJU #505). The heterogeneous nature of the reservoir and the various pore types would decrease the effectiveness when using capillary pressure curves from this core. The Leverett "J" Function is most accurate when it is used to correlate capillary pressures from cores within a narrow classification of lithofacies and pore types. Capillary pressure curves illustrate that pore throat size has a larger affect on permeability than porosity. The large variation in pore types, which occur singularly or together, as well as diagenetic factors and a lack of sufficient data make this method less attractive in and of itself. However, the permeability transform model used within this study is based in part on capillary pressure data from well defined rock fabrics. The following section gives an introduction to the Lucia petrophysical class and permeability transform used within this study. For in-depth study of the petrophysical rock fabric classification the reader is directed to Lucia (1983, 1985, and 1999).

The Lucia Petrophysical Class

The basis of the Lucia permeability transform model is that pore-size distribution controls permeability and saturation and that pore-size distribution is directly related to rock fabric (Lucia, 1999). Lucia (1999) determined three major pore type classes; 1) interparticle, 2) separate vugs, and 3) touching vugs, where each class has a different type of pore size distribution and interconnection. Interparticle pore space is the pore space

located between grains or crystals and all other pore space is vuggy. The two types of vuggy pore space are: 1) separate vugs interconnected only through the interparticle pore network such as moldic and intracrystalline pores; and 2) touching vugs interconnected by pore systems such as fractures and fenestral porosity. Lucia (1983) used capillary pressure data from rock samples of interparticle pore-types to determine permeability fields defined by particle-size boundaries of 100 and 20 microns. He later determined that particle sorting was also a key element in defining these permeability fields. This geological/petrophysical classification divides pore-space into grain-dominated and mud-dominated fabrics (fig. 80).

The presence of vuggy pores within interparticle pore space alters the petrophysical properties of the rock. Examples of non-vuggy, interparticle pore-space within the West Jordan unit are seen in figures 52 (A, B, and C) and 53 (C and D), non-touching vugs in figures 56 and 58, and touching vug pore types in figures 59 and 61. This petrophysical class divides rock fabrics into categories based on particle or crystal size and grain-dominated versus mud-dominated fabrics (figs. 80 and 81). Each rock fabric type within the petrophysical class exhibits different petrophysical properties (Lucia, 1999). This work has established that grainstones, grain-dominated packstones, and mud-dominated fabrics are fairly well constrained within these three permeability fields. Grain or crystal size and sorting define the permeability fields and interparticle porosity defines the pore-size distribution and therefore, permeability within each field (Lucia, 1999).

The Lucia classification illustrates a porosity-permeability relationship between interparticle pore space in dolograinstones, grain-dominated packstones and mud-

Figure 80. The petrophysical rock fabric classes defined by Lucia (1999). These classes are based on capillary properties and permeability transforms of interparticle porosity. Three petrophysical classes are defined within the classification scheme, classes 1 through 3. The Class 1 field is composed of limestones and dolomitized grainstones and large crystalline grain-dominated dolopackstones and mud-dominated dolostones with a crystal size greater than 100 μm. The fabrics that make up the Class 2 field consist of grain-dominated packstones, fine to medium crystalline grain-dominated dolopackstones, and medium crystalline mud-dominated dolostones whose crystal size ranges from 100-to 20 μm. The Class 3 field contains mud-dominated fabrics including dolomudstones, wackestones, and mud-dominated packstones with crystal size less than 20 μm.

PETROPHYSICAL CLASSES

GRAIN-DOMINATED FABRIC **MUD-DOMINATED FABRIC**

Grainstone **Packstone** **Packstone** **Wackestone** **Mudstone**

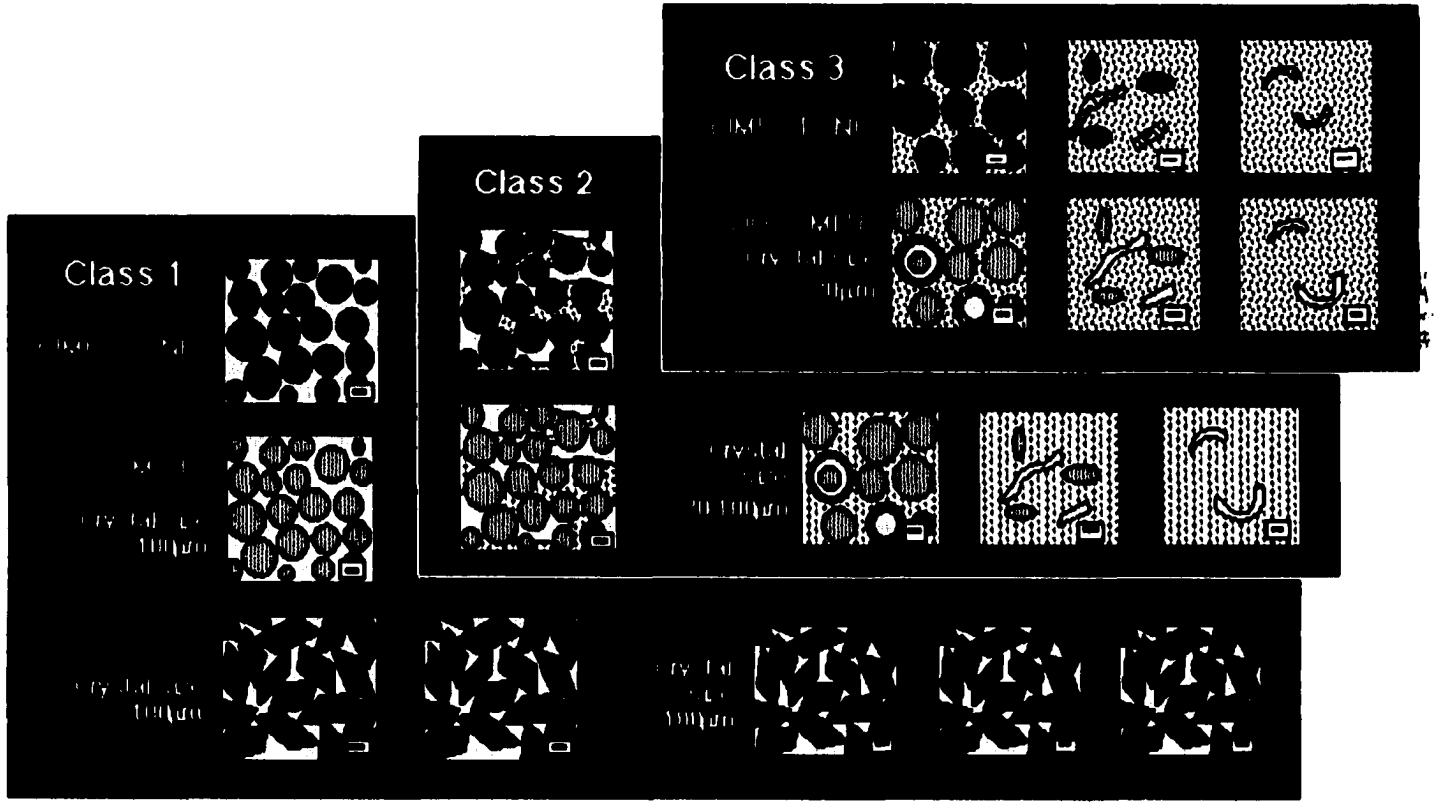

Note: bar is 100 microns

Figure 81. Interparticle porosity-permeability cross plot data for nonvuggy limestones and dolostones and capillary pressure curves for petrophysical classes. The cross plot illustrates were class types plot within the petrophysical divisions based on interparticle grain size greater than 100 μm or less than 20 μm. The solid lines represent the class divisions while the dashed lines show the statistical reduced-major-axis transforms representing class permeability linear regression equations provided in the text for classes 1, 2 and 3. Capillary pressure curves were used to quantify saturation characteristics of the three petrophysical classes. Within each class several samples are shown that have varying interparticle porosity values. Displacement pressures within each class are similar for varying interparticle porosity values but saturation is seen to vary significantly with porosity percent within each sample (figures modified from Lucia, 1995).

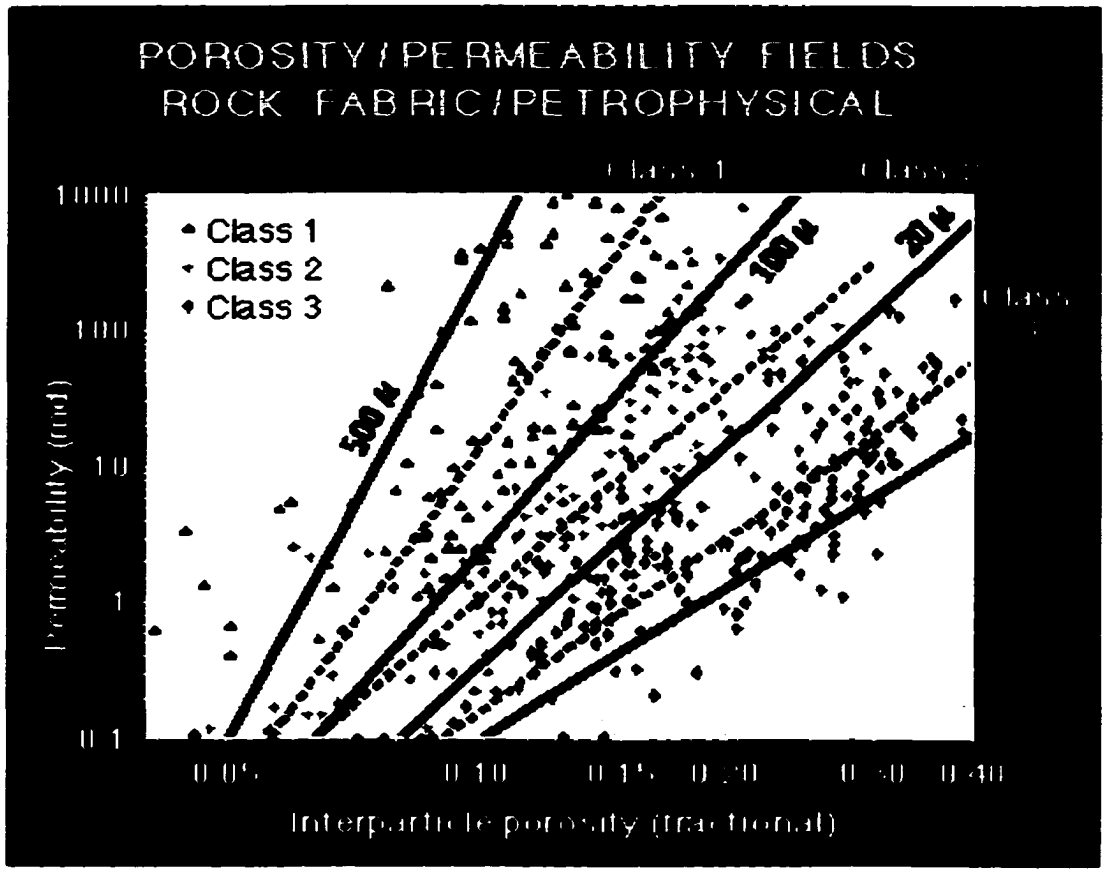
POROSITY / PERMEABILITY FIELDS
ROCK FABRIC / PETROPHYSICAL
Class 1
Class 2
Class 3
500 μ
100 μ
20 μ
10000
1000
10
1
0.1
Permeability (md)
0.10
Interparticle porosity (fractional)

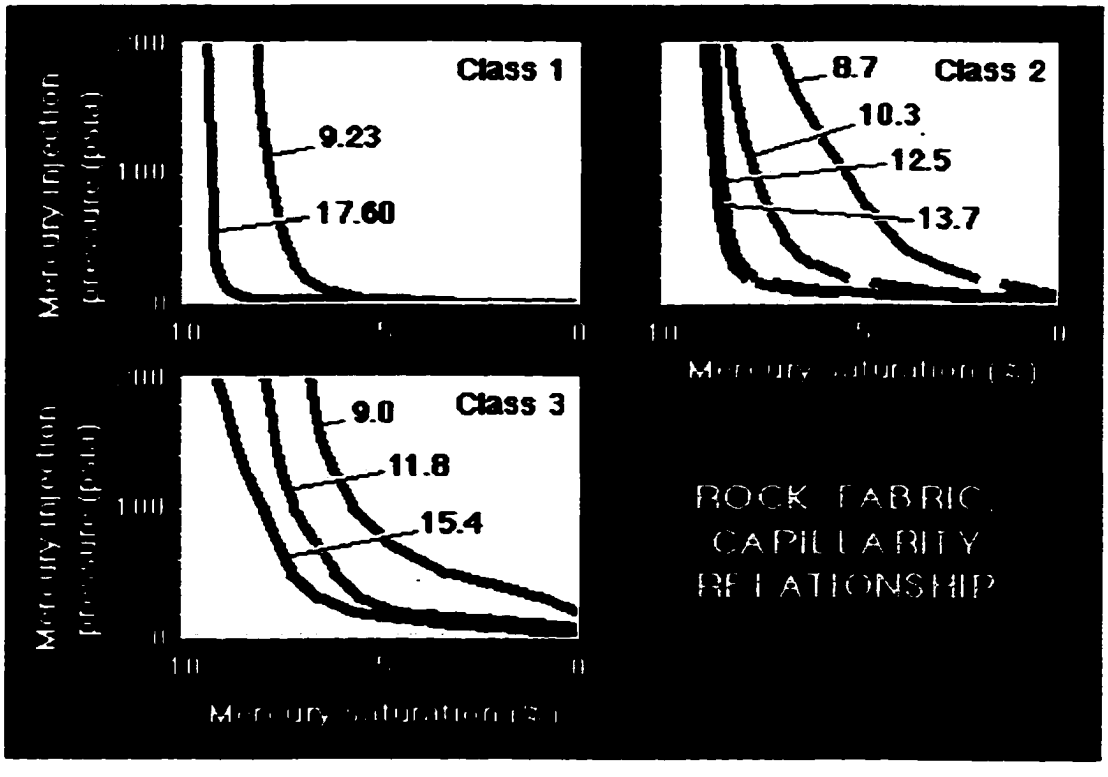
Class 1
9.23
17.60
Class 2
8.7
10.3
12.5
13.7
Class 3
9.0
11.8
15.4
ROCK FABRIC / CAPILLARITY RELATIONSHIP

dominated fabrics. It is important to understand that this petrophysical classification is based on interparticle pore-space within these rock types in the absence of vuggy porosity. Samples for his study were carefully collected and cleaned. Class type was determined by subtracting out any vuggy pore-space that would skew results and add considerable scatter of data points within permeability fields. As defined by Lucia (1999), fabrics that make up the Class 1 permeability field have pore throats > 100 microns and consist of limestone and dolomitized grainstones, large crystalline grain-dominated dolopackstones and mud-dominated dolostones (fig. 80). The fabrics that make up the Class 2 field (100-to 20-micron pore throat field) are grain-dominated packstones, fine to medium crystalline grain-dominated dolopackstones, and medium crystalline mud-dominated dolostones. Mud-dominated fabrics including dolomudstones, wackestones, and mud-dominated packstones characterize rock fabrics within Class 3 in which pore throat sizes are less than 20-microns (figs. 80 and 81).

The Lucia Permeability Transform

Permeability transforms based on fractional interparticle porosity (total interparticle porosity minus vuggy porosity) for each class are used to determine reduced major axis within which rock-fabrics fall (fig. 81). In addition, Lucia (1999) presented a continuum transform for mudstone through grainstone fabrics from 5 microns to over 500 microns for dolostones. Major axis permeability transforms for each individual class are provided below:

Class 1 $k = (45.35*10^{8})*\Phi ip^{8.537}$ $r = 0.71$

Class 2 $k = (2.040*10^{6})*\Phi ip^{6.380}$ $r = 0.80$

Class 3 $k = (2.884*10^3)* \Phi ip^{4.275}$ $r = 0.81$

Where: k is permeability in millidarcies and Φip is equal to the fractional interparticle porosity. The correlation coefficients (r) are provided for each class permeability transform as determined from Lucia's statistical data. Lucia (1995, 1999) used capillary pressure curves to quantify the saturation characteristics of the three petrophysical classes comparing different interparticle porosities for each class. Capillary pressure curves were seen to change shape and saturation properties within class types and relative to the amount of interparticle porosity present within each sample (fig. 81).

To more accurately model carbonates with pore throat fabrics ranging from 5 microns to 500 microns, Lucia (1999) developed a complete continuum of rock-fabric specific porosity-permeability transforms (fig. 82). The equation relates permeability to a continuum of petrophysical classes and interparticle porosity through the development of multiple linear regression. The equation for the rock-fabric continuum transform is provided below:

$$Log(k) = (A-B*log(class))+(C-D*log(class))*log(\Phi ip)$$

Where:

A = 9.7982
B = 12.0838
C = 8.6711
D = 8.2065

Class for the continuum equation is the rock fabric petrophysical class ranging from 0.5 to 4 (fig. 82) rather than 1, 2 or three in the previous class transforms (fig. 81). Φip is the fractional interparticle porosity and A, B, C, and D are numerical constants derived from Lucia's regression analysis of interparticle rock-fabric classes. Within the rock fabric

continuum for dolomite textures each class increases from finely crystalline to coarsely crystalline dolomites (fig. 82). Class 1 consists of large crystalline dolomites increasing from 100- to-500 microns; Class 2 consists of medium crystalline mud-dominated dolostone and fine-to-medium crystalline grain-dominated dolopackstones increasing from 20-to-100 microns; and Class 3 is composed of fine crystalline mud-dominated dolostone increasing from 5-to-20 microns (fig. 80 b).

Application of the Lucia Permeability Transform within the West Jordan Unit

The Lucia transform model was applied within the West Jordan unit by comparing permeability data based on core analysis to the derived permeability model based on petrophysical rock fabric classes determined for each zone within the reservoir. This comparison was used to calibrate the petrophysical rock fabric model. Pore type descriptions from each cycle (zones I through IV-E2) along with porosity-permeability cross plots were used to determine the petrophysical rock class for each zone (fig. 83). It is important to note that the presence of permeability anomalies such as stylolites and fractures and vuggy porosity create scatter within the plots.

Log curves were constructed of class types for each zone for all cored wells within the unit (fig. 84). Well logs within areas mapped to have shoal bodies were given a higher petrophysical class within zones IV-E1 and IV-E2 than those known to occur within intershoal and more mud rich facies tracts. Large crystalline shoal facies were assigned class values of 1.8 and 2.0 for zones IV-E1 and IV-E2 respectively and medium crystalline mud-dominated intershoal and proximal outer ramp facies were assigned a

Figure 82. Diagrams illustrating the continuum porosity-permeability transform and rock fabric class for dolostones. A) Class boundaries showing rock fabric designations as defined by the continuum transform model. The continuum ranges from 0.5 to 4.0. B) Rock fabric continuum for nonvuggy dolostone fabrics. Within each class crystal size increases upward to the left (figures A and B modified from Lucia, 1999).

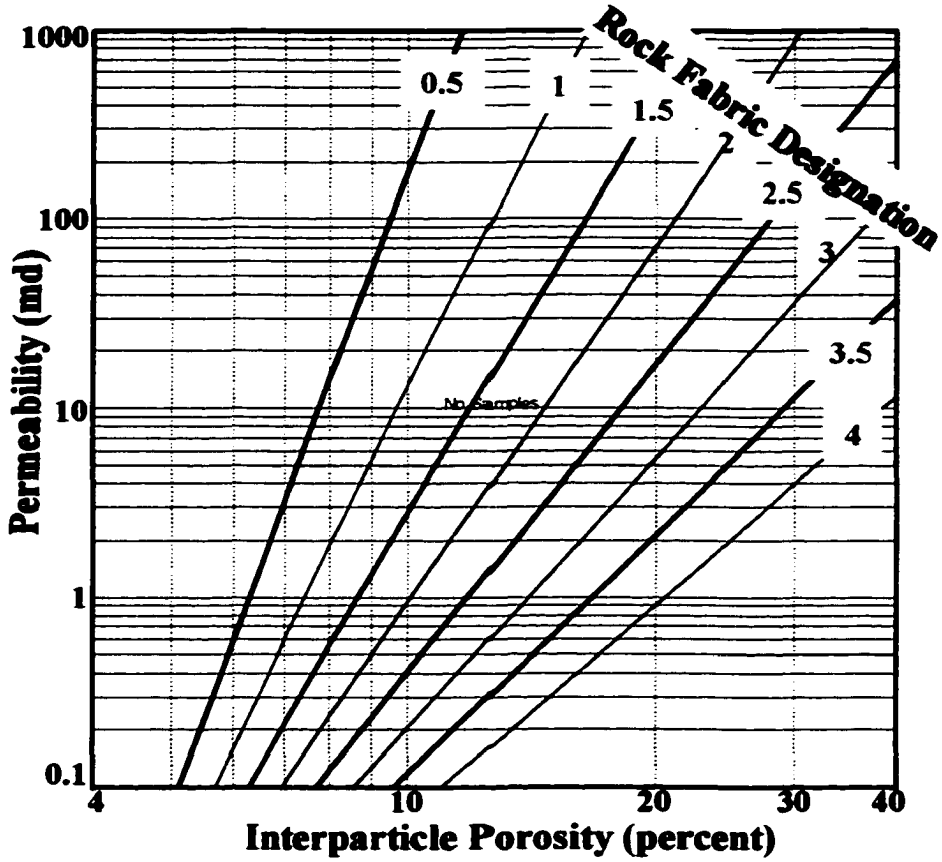
Rock Fabric Designation
0.5
1
1.5
2
2.5
3
3.5
4
No. Samples
Permeability (md)
1000
100
10
1
0.1
4
10
20
30
40
Interparticle Porosity (percent)

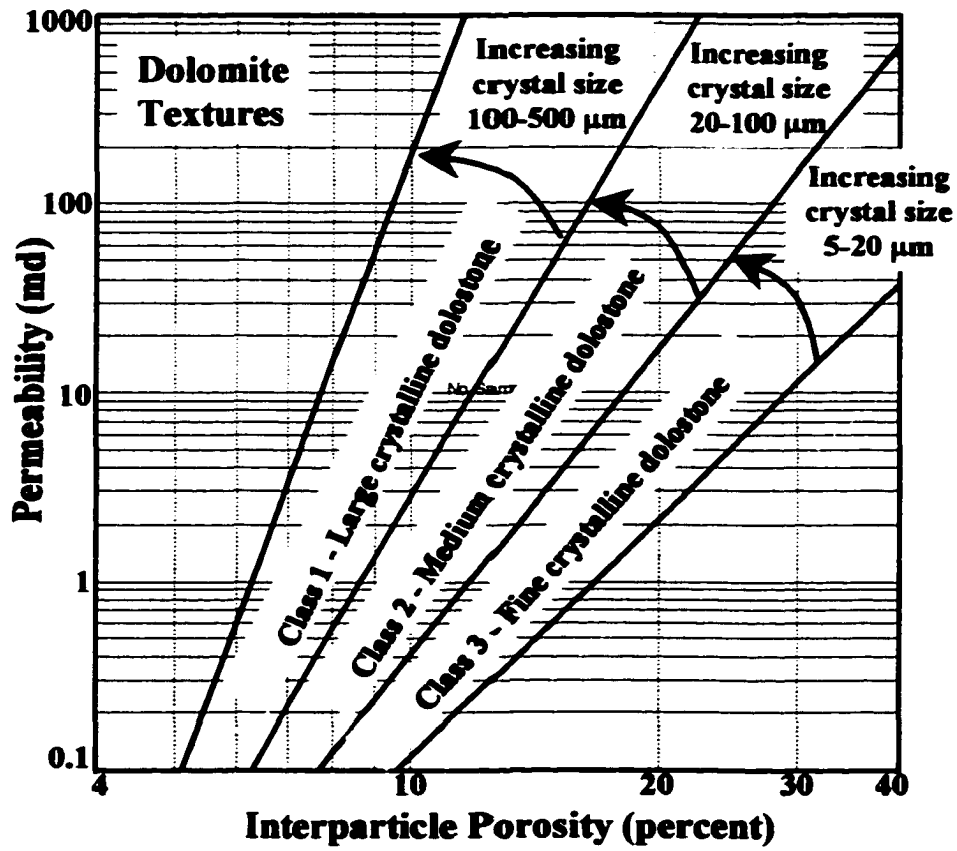
Dolomite Textures
Increasing crystal size 100-500 µm
Increasing crystal size 20-100 µm
Increasing crystal size 5-20 µm
Class 1 - Large crystalline dolostone
Class 2 - Medium crystalline dolostone
Class 3 - Fine crystalline dolostone
Permeability (md)
1000
100
10
1
0.1
4
10
20
30
40
Interparticle Porosity (percent)

Figure 83. Lucia rock fabric classifications for cycle boundaries within the West Jordan unit. Scatter within the plots is caused by vuggy porosity and permeability anomalies such as fractures and stylolites. Rock fabric classes are based on interparticle porosity and vuggy porosity within the sample will affect the data points. The class type value assigned to each zone was determined primarily on the application of the Lucia rock-fabric classification from core descriptions. Cross plot data can be used in absence of core and modern log suites, nevertheless, a considerable amount of scatter complicates the interpretation of rock classes within San Andres strata. Class values assigned to each one are present on the cross plots.

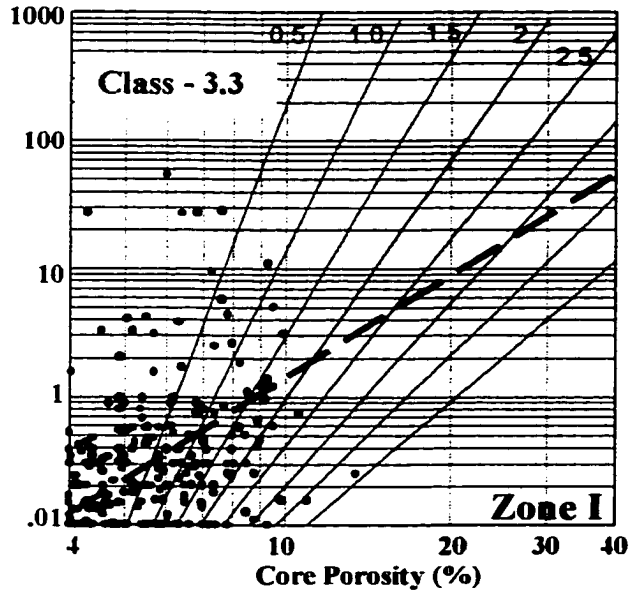
Class - 3.3
0.5
1.0
1.5
2
2.5
Zone I
1000
100
10
1
.01
4
10
20
30
40
Core Porosity (%)

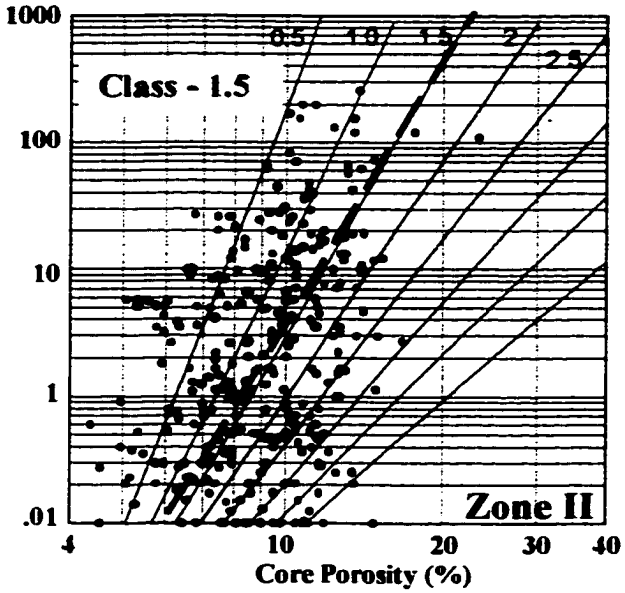
Class - 1.5
0.5
1.0
1.5
2
2.5
Zone II
1000
100
10
1
.01
4
10
20
30
40
Core Porosity (%)

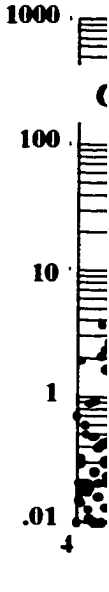
1000
100
10
1
.01
4

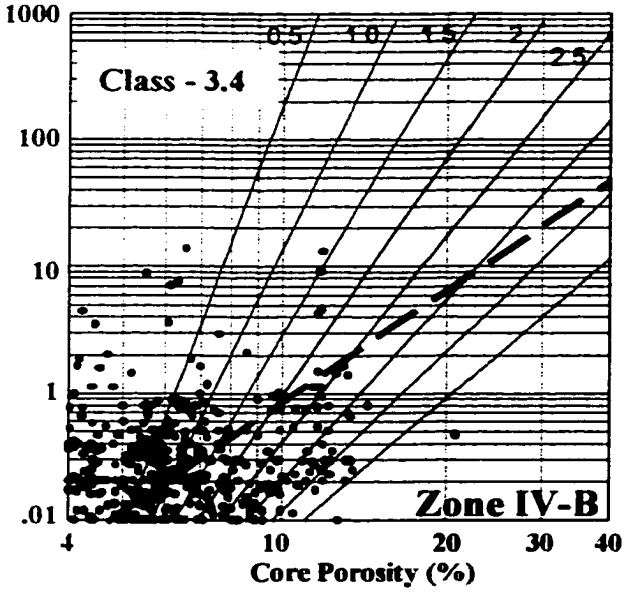
Class - 3.4
0.5
1.0
1.5
2
2.5
Zone IV-B
1000
100
10
1
.01
4
10
20
30
40
Core Porosity (%)

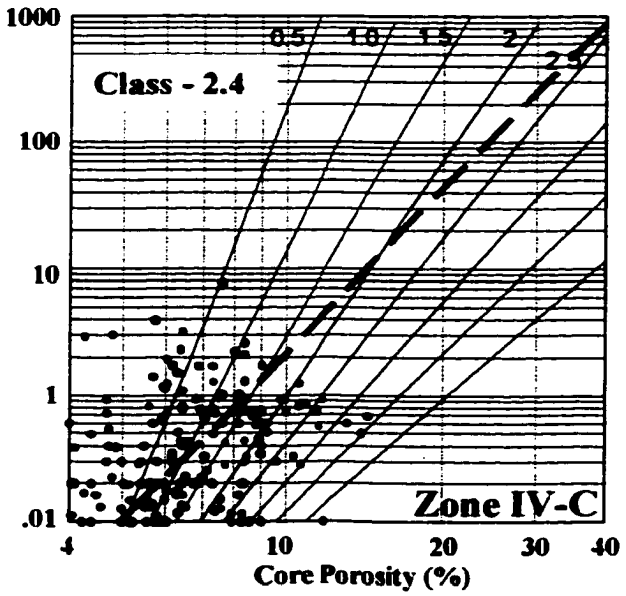
Class - 2.4
0.5
1.0
1.5
2
2.5
Zone IV-C
1000
100
10
1
.01
4
10
20
30
40
Core Porosity (%)

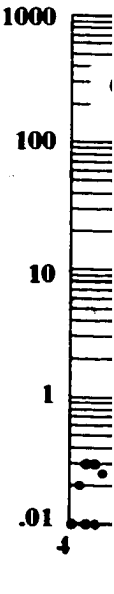
1000
100
10
1
.01
4

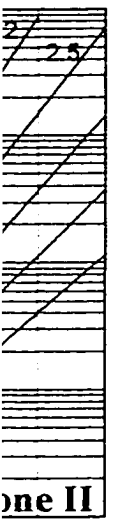
2
2.5
one II
30
40

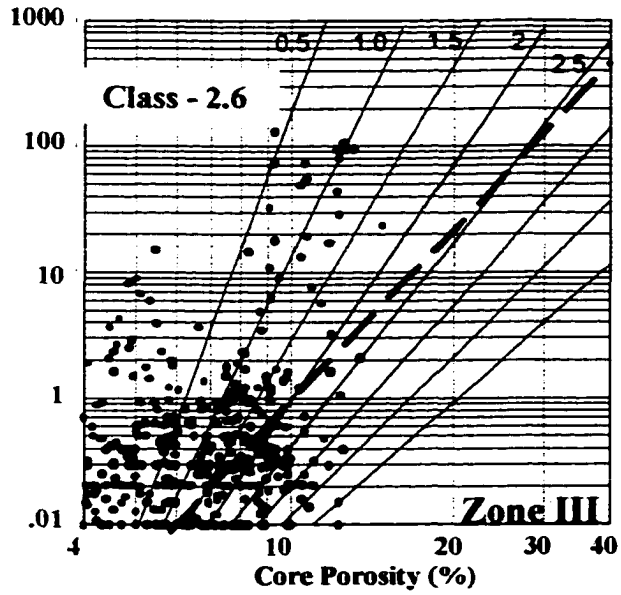
1000
100
10
1
.01
0.5
1.0
1.5
2
2.5
Class - 2.6
Zone III
4
10
20
30
40
Core Porosity (%)

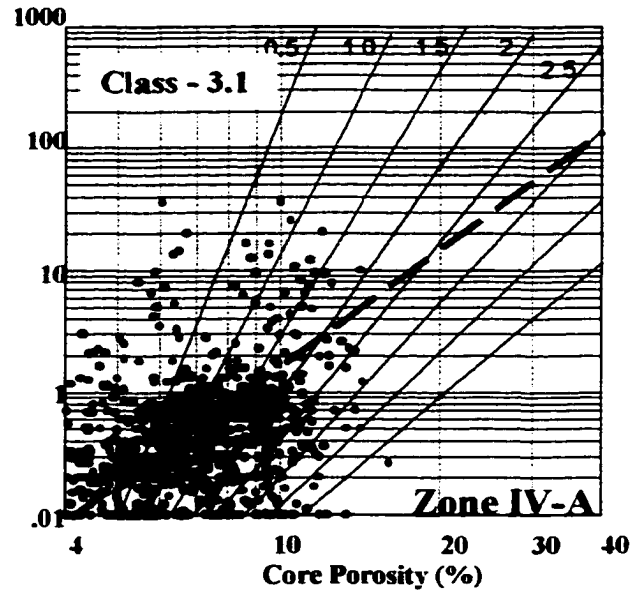
1000
100
10
1
.01
0.5
1.0
1.5
2
2.5
Class - 3.1
Zone IV-A
4
10
20
30
40
Core Porosity (%)

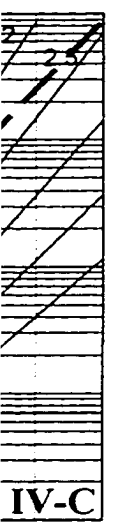
2
2.5
IV-C
30
40

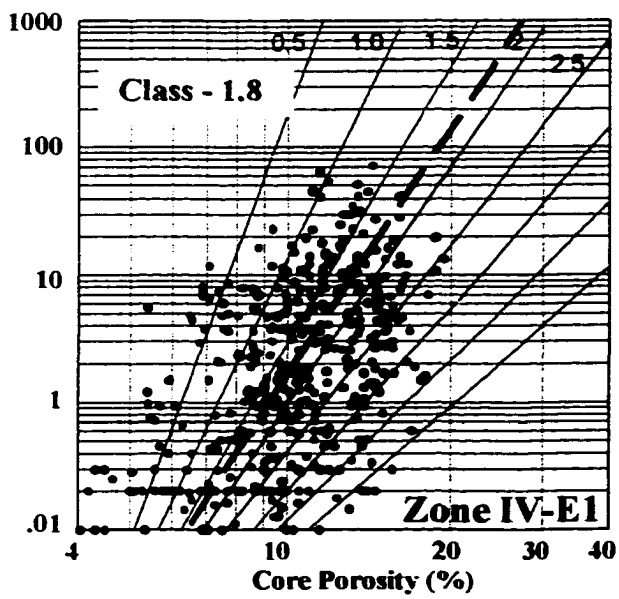
1000
100
10
1
.01
0.5
1.0
1.5
2
2.5
Class - 1.8
Zone IV-E1
4
10
20
30
40
Core Porosity (%)

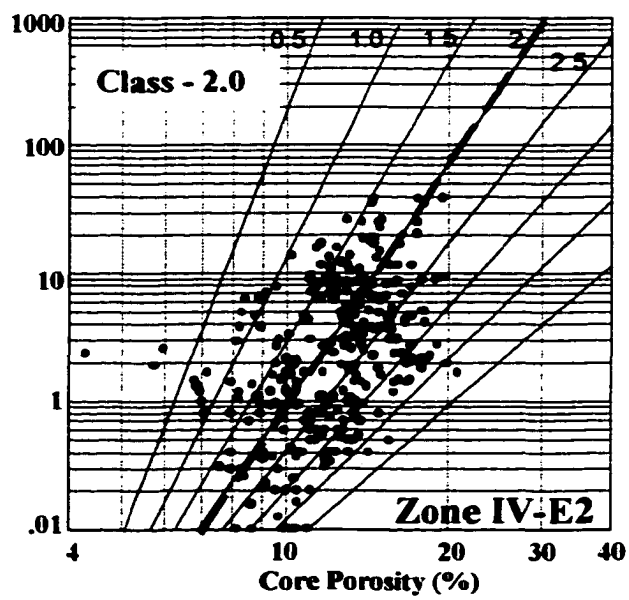
1000
100
10
1
.01
0.5
1.0
1.5
2
2.5
Class - 2.0
Zone IV-E2
4
10
20
30
40
Core Porosity (%)

Figure 84. Digital well data showing the constructed petrophysical class curve (black line), the normalized porosity curve (thin blue curve), and the facies indicator log (colored bars). The petrophysical class curve and the normalized porosity curve are used in the permeability transform equation to calculate permeability throughout the unit. The class curve value is based on the petrophysical rock-fabric classification (fig. 80) which reflects the primary pore type present within each zone and whether the rock fabric is grain-dominated or mud-dominated. Except for zones IV-E1 and IV-E2, each zone was assigned a class value based on the overall pore and rock-fabric characteristics of that zone as these features were seen to be fairly consistent across the unit area. Within zones IV-E1 and IV-E2, wells known to penetrate shoal bodies were assigned a lower class value of 1.5 than wells within intershoal and outer ramp facies tracts which were assigned a class value of 2.5.

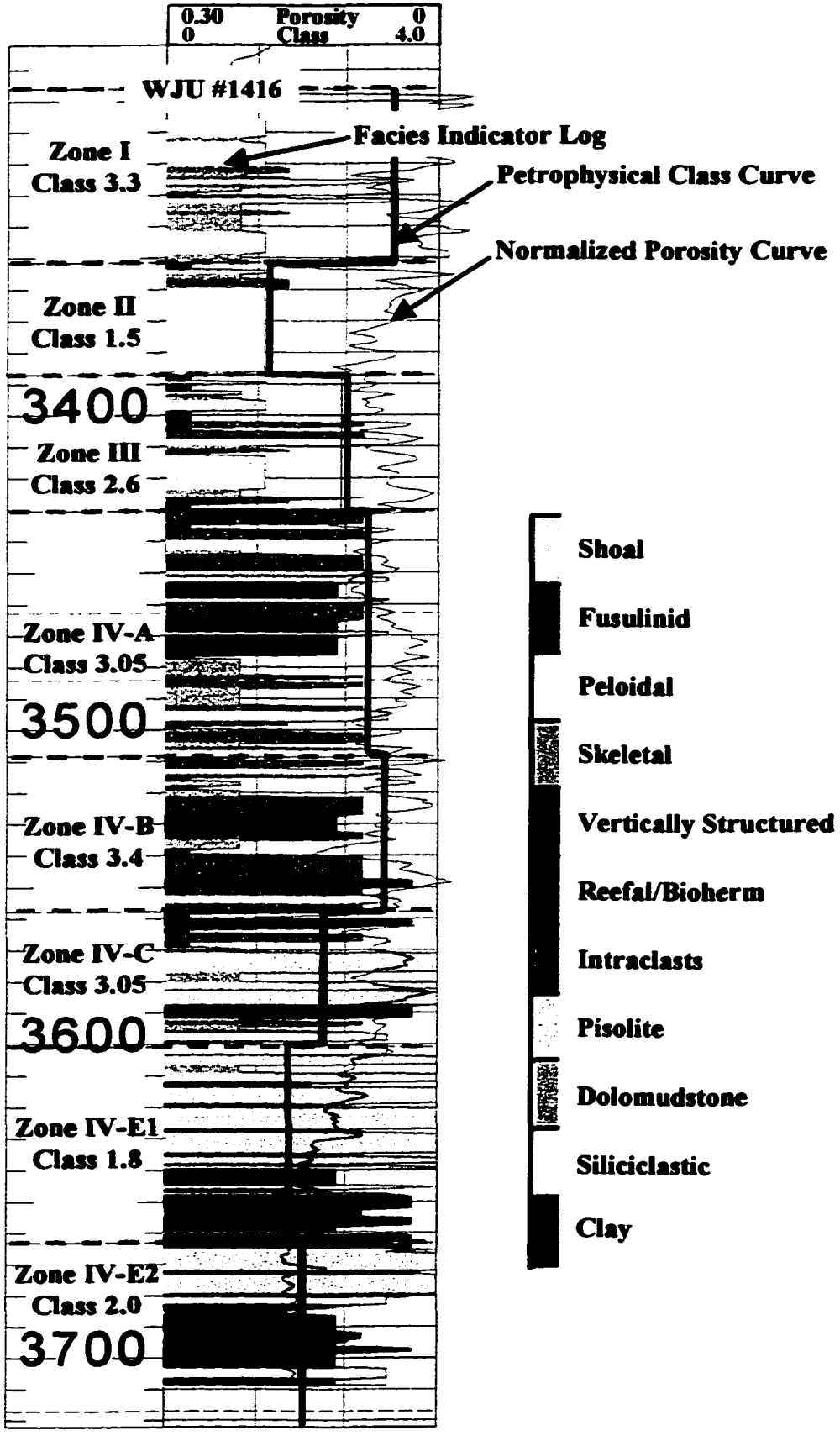
0.30 Porosity 0
0 Class 4.0
WJU #1416
Facies Indicator Log
Petrophysical Class Curve
Normalized Porosity Curve
Zone I
Class 3.3
Zone II
Class 1.5
3400
Zone III
Class 2.6
Zone IV-A
Class 3.05
3500
Zone IV-B
Class 3.4
Zone IV-C
Class 3.05
3600
Zone IV-E1
Class 1.8
Zone IV-E2
Class 2.0
3700
Shoal
Fusulinid
Peloidal
Skeletal
Vertically Structured
Reefal/Bioherm
Intraclasts
Pisolite
Dolomudstone
Siliciclastic
Clay

class of 2.3 for both of the lower zones. Therefore, classes within the lower cycles were further refined based on the dominant fabric and facies type occurring within each well. Zones I through IV-C were given one class type value based on the overall pore type and rock-fabric characteristics within each zone, which were found to be fairly consistent within the unit boundaries.

Permeability from the transform model was calculated using the Lucia continuum permeability transform equation with the determined class type (fig. 83) and the normalized porosity curve. Porosity curves for the unit have been normalized to account for problems such as drift and the presence of gypsum within the reservoir (see Appendix A for further detail). Core porosity was not used with the transform because the model was being tested in an effort to see how closely porosity logs available for the unit (primarily old style gamma ray-neutron count logs) would match core permeability derived from laboratory analysis when applying the transform model. Correlation between core derived permeability and the petrophysical/rock fabric transform were found to match reasonably well (fig. 85).

Factors that influence areas were a pore match is seen include permeability anomalies such as fractures and stylolites within upper zones of the reservoir. Lab calculated permeabilities are higher in these zones due to the presence of these permeability anomalies, which are well documented on the core analysis reports. The transform model is not affected by these features and therefore, may provide a more accurate model of matrix related permeability for the reservoir. Other factors that affect the transform are thin intervals of clay with high porosity values. Although a shale cutoff was applied to zone III within the upper parts of the reservoir is was not applied within

Figure 85. A diagram of cored wells from the unit showing the correlation between core derived permeability and permeability modeled from the Lucia continuum transform model. Although the correlation is not one-to-one, the petrophysical characteristics of the reservoir are being modeled more accurately than previous porosity-to-permeability transform models applied to these carbonate reservoirs in the past. Within the upper parts of the reservoir fractures and stylolites give erroneous core permeability readings for rock matrix. These erroneous data values are not reflected in the transform model. Within productive shoal facies the transform model both overestimates and underestimates permeability. This is believed to reflect the wide range of porosity logs of varying age vintages found and the affect of vuggy porosity within the reservoir. Curve scales are at the top of each well where: CLASS = rock fabric petrophysical class; PGYP_VCL = normalized porosity log; FIL = facies indicator log; K_LUCIA = permeability calculated with the Lucia global continuum transform model; and K_MAX = core measured permeability.

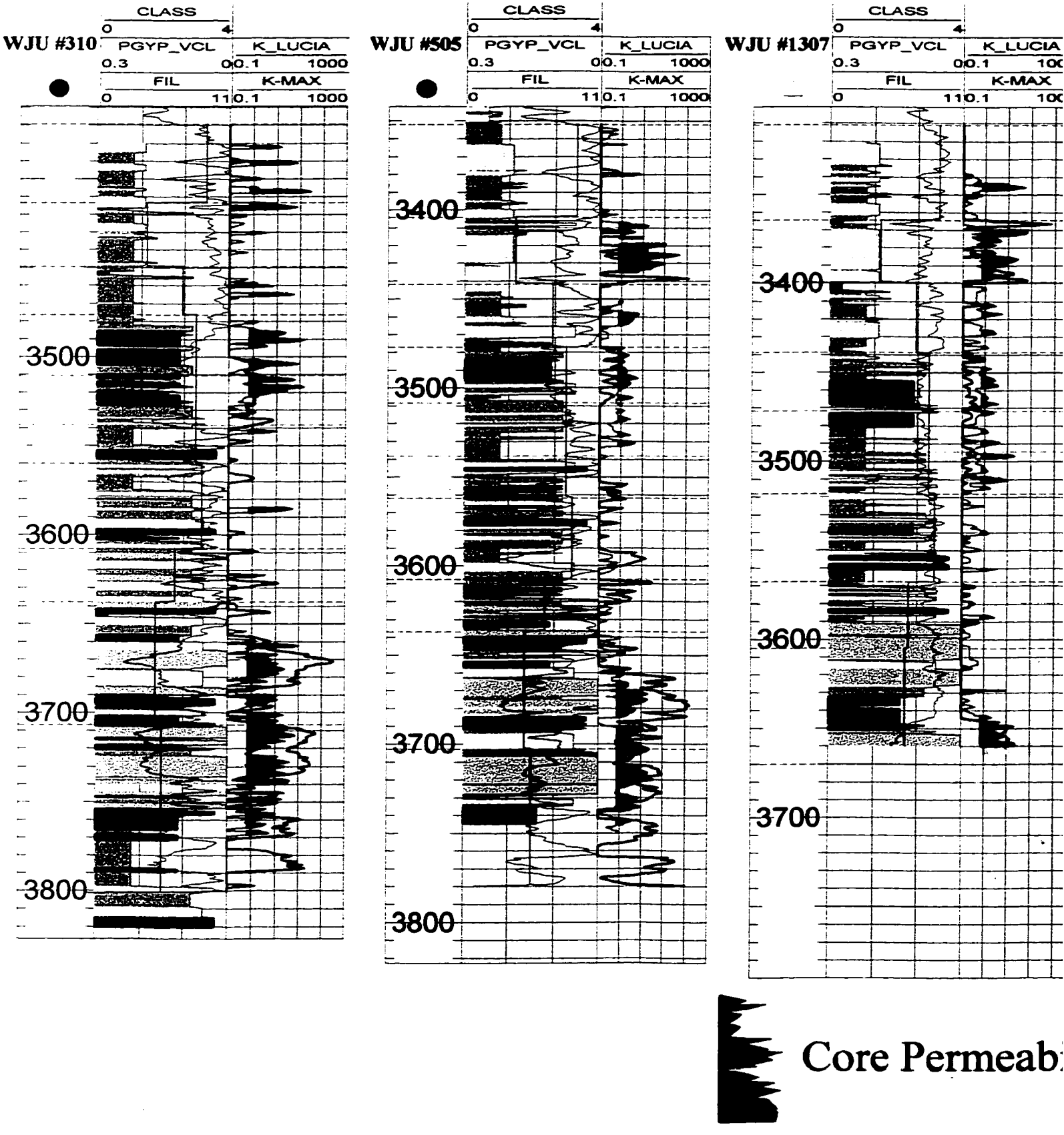
WJU #310
WJU #505
WJU #1307
CLASS
0
4
PGYP_VCL
0.3
0
K_LUCIA
0.1
1000
FIL
0
1
K-MAX
0.1
1000
3400
3500
3600
3700
3800
Core Permeab

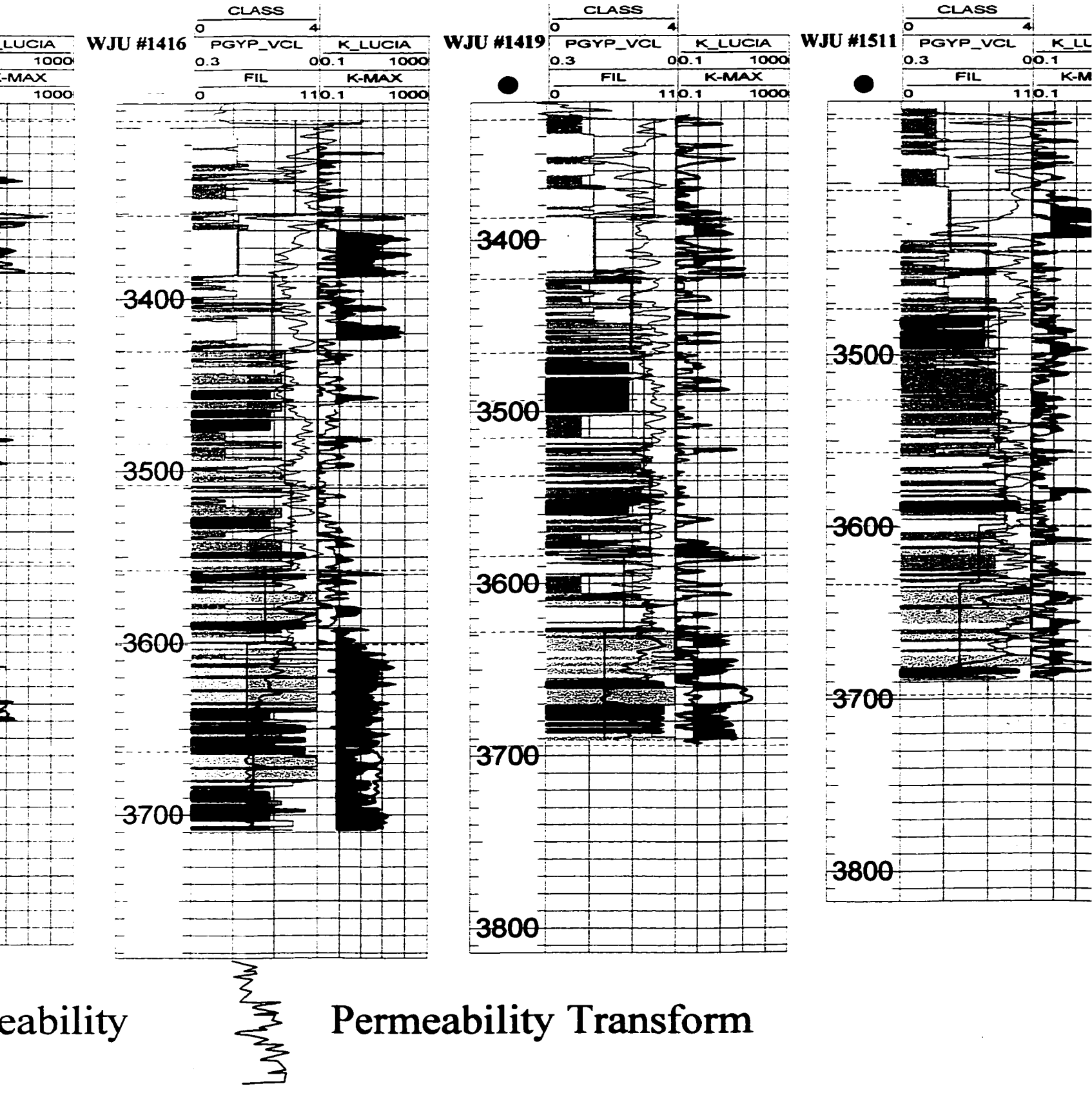

eability Permeability Transform

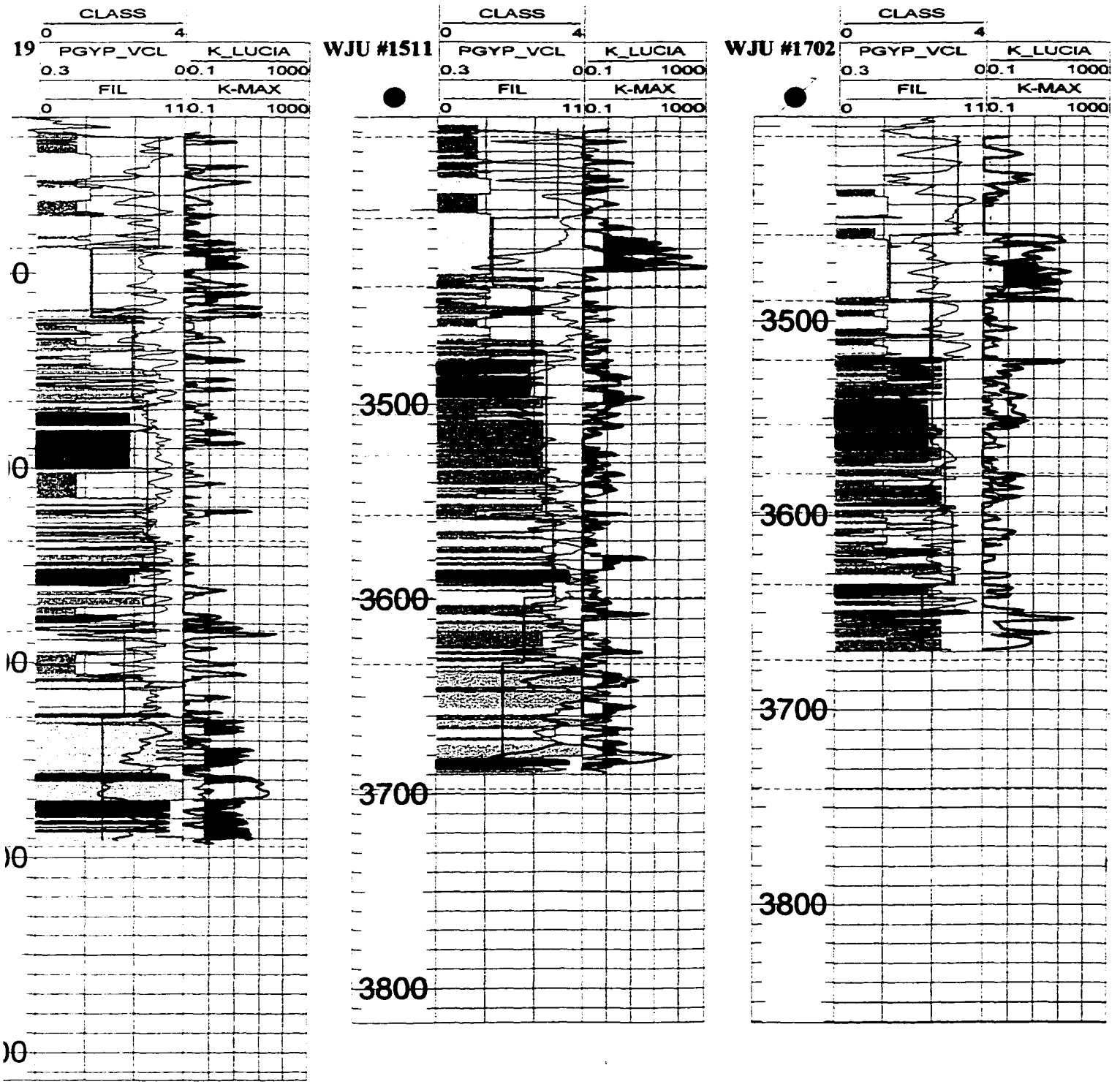

ity Transform

lower zones. High gamma ray readings unrelated to clay intervals are common within the San Andres. It was determined that most of the high gamma ray readings within zone III are the effects of clays, however, that is not always true within lower parts of the reservoir where highly radioactive minerals (uranium and potassium) affect gamma ray readings.

Within productive shoal facies the transform model both overestimates and underestimates permeability. This may be the result of using a wide range of porosity logs of varying age vintages, the normalization corrections applied to logs, and the affect of vuggy porosity within the reservoir. After taking these factors into account, it was felt that the petrophysical/rock fabric permeability transform model was successful within the cored wells. The permeability transform was then applied to all wells within the unit where porosity logs were available. The resulting curve, K-Lucia, was used in the geostatistical model along with the normalized porosity curve to create a three dimensional distribution of these attributes throughout the reservoir.

THE GEOSTATISTICAL DISTRIBUTION OF POROSITY AND PERMEABILITY WITHIN THE WEST JORDAN UNIT

Use of the GridSTAT software provided a consistent method of interpolation of well control into the interwell areas. Geostatistical methods were applied within the West Jordan unit to distribute porosity and permeability values calculated at the wellbore locations into a three-dimensional grid volume. The porosity and permeability three-dimensional models have resulted in significantly more accurate reserve calculations than earlier studies for the West Jordan reservoir. These are discussed in the next section. Geostatistical models have determined that a higher permeability cutoff should be used to accurately model oil production within the reservoir under waterflood conditions than previously used for the unit.

Quality control of the data is important when using geostatistical models to remove poor data that can severely effect the accuracy of the model. Therefore, all data going into the model must be thoroughly examined. Quality control for this study began with porosity data that had already been normalized for drift and the affect of gypsum within the reservoir. Because of varying vintages and types of logs many logs needed to be rescaled so that all data scales were consistent. Other factors that require particular attention include the picking of tops, which must be precise. Many tops are picked off of the gamma-ray log that may not strictly coincide with the porosity log. Tails due to bottom hole calibrations are very common at the end of logs and must be removed from all digital data. Poor quality data from logs run within liner or casing that affect readings if not corrected during the logging run should be eliminated from the data set. Effective ways to examine data for inaccuracies include looking at statistical properties such as

mean, and standard deviation. Histograms and cumulative histograms allow for visual representation of the distribution of data. Scatter plots and graphs of various statistical properties such as data minimums and maximums for all wells can help to identify aberrant data. These and other procedures were used to determine erroneous data obtained from log curves prior to the gridding process.

Variogram Modeling

Geological data are spatially dependent, thus it has spatial correlation. This means that data spaced close together are more likely to have similar values than data spaced far apart (Isaaks and Srivastava, 1989). Because geological data exhibit spatial continuity, unknown data points can be estimated by the extrapolation of data values from nearby known data points. This can be accomplished on a two-dimensional surface or within the three-dimensional volume. The primary measures of distribution used in geostatistics are the mean, covariance and the variogram (semivariance). The variogram is used within this study to populate interwell grid blocks.

The variogram is a statistical function that describes how data variation increases with separation distances in certain directions. The spatial continuity seen within the variogram decreases as the variance increases with increasing separation distance. A plot of the well pair variance shows separation distance versus variance (fig. 86). There is a general increase in variance with increase in separation distance. Well pair data samples that are closely spaced (660 feet) tend to have lower variance than those that are spaced farther away from one another (1990 feet). The variogram function and examples of well pair spacing for the unit are seen in Figure 87. As seen from the areal and horizontal

Figure 86. Variogram analysis of normalized porosity data for all zones. Horizontal, vertical and areal variograms are shown for all combined zones within the reservoir. Note that the experimental variograms (e) and the theoretical variograms (t) only match at very close separation distances of approximately 25 feet and 300 feet for the vertical and horizontal variograms, respectively. Calculated parameters from the theoretical variogram are provided at the bottom of the diagram. Variogram analysis of porosity from all zones results in high error and unrealistic correlation lengths. The well pair variance diagram shows the relationship of increasing variance with increasing separation distance. The areal or omnidirectional variogram shows directions of maximum through minimum correlation within the reservoir. This ellipse model for two-dimensional variograms shows the range of correlation for various directions within the reservoir.

VARIOGRAM ANALYSIS OF POROSITY DATA FOR ALL ZONES

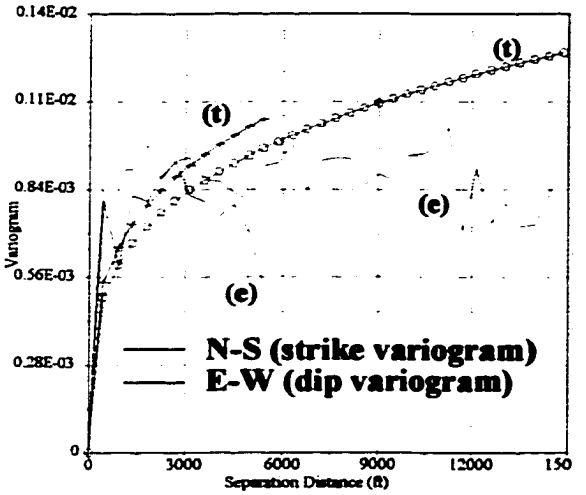

Horizontal Variogram

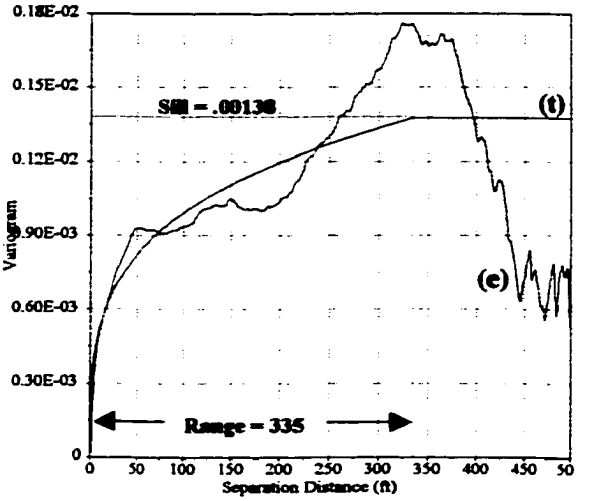

Vertical Variogram

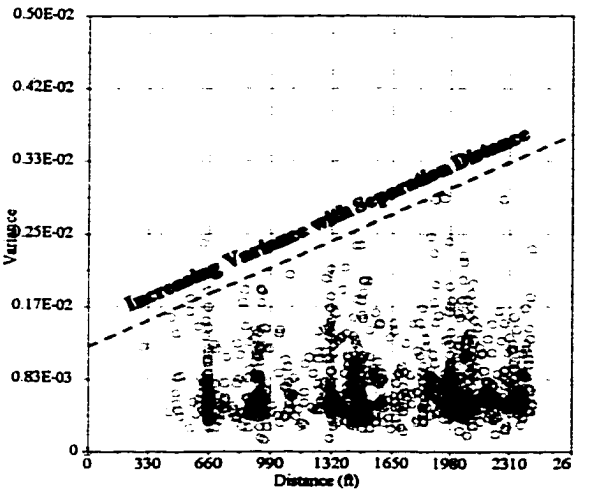

Well Pair Variance

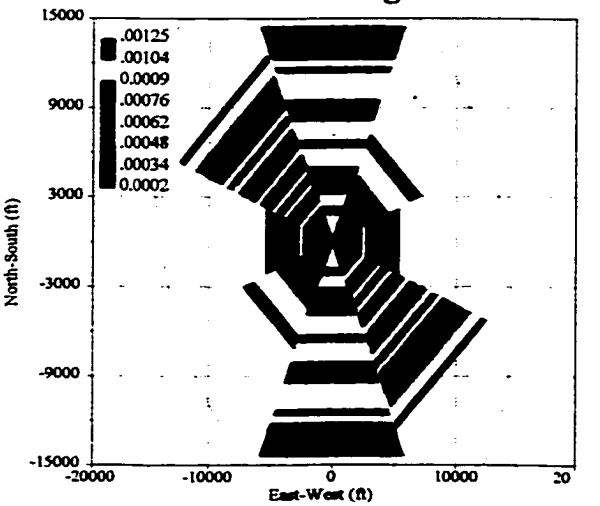

Areal Variogram

(e) Experimental Variogram

(t) Theoretical Variogram

Theoretical Variogram Calculated Parameters

Model - Fractal power-law variogram of 0.27	
Major Correlation length	**21074**
Minor Correlation length	**13704**
Vertical Correlation length	**335**
Correlation length ratio	**1.538**
Error	**51.64**

Figure 87. Directional variograms and separation distance modeled for the West Jordan unit porosity and permeability data. Directional variograms were calculated for porosity and permeability data in the N-S, E-W, NE-SW, and NW-SE directions. Examples of how variograms are calculated in one dimension as separation distance increases are seen in the N-S example where h_1, is the initial separation distance at 330 feet (ten acre spacing) with increasing separation distance up to h_6= 1980 feet. Directional variograms are calculated in the specified direction to a distance determined by the initial and maximum search radius. The equation for the variogram is provided at the base of the figure where: ((h) is the calculated variogram; v_1 ..., v_n ; are the data values; (h) is the separation distance; (i, j) are all the data pairs separated by h, and N is the total number of pairs. Therefore, the variogram is the half the average squared difference between the paired data values (Isaaks and Srivastava, 1989).

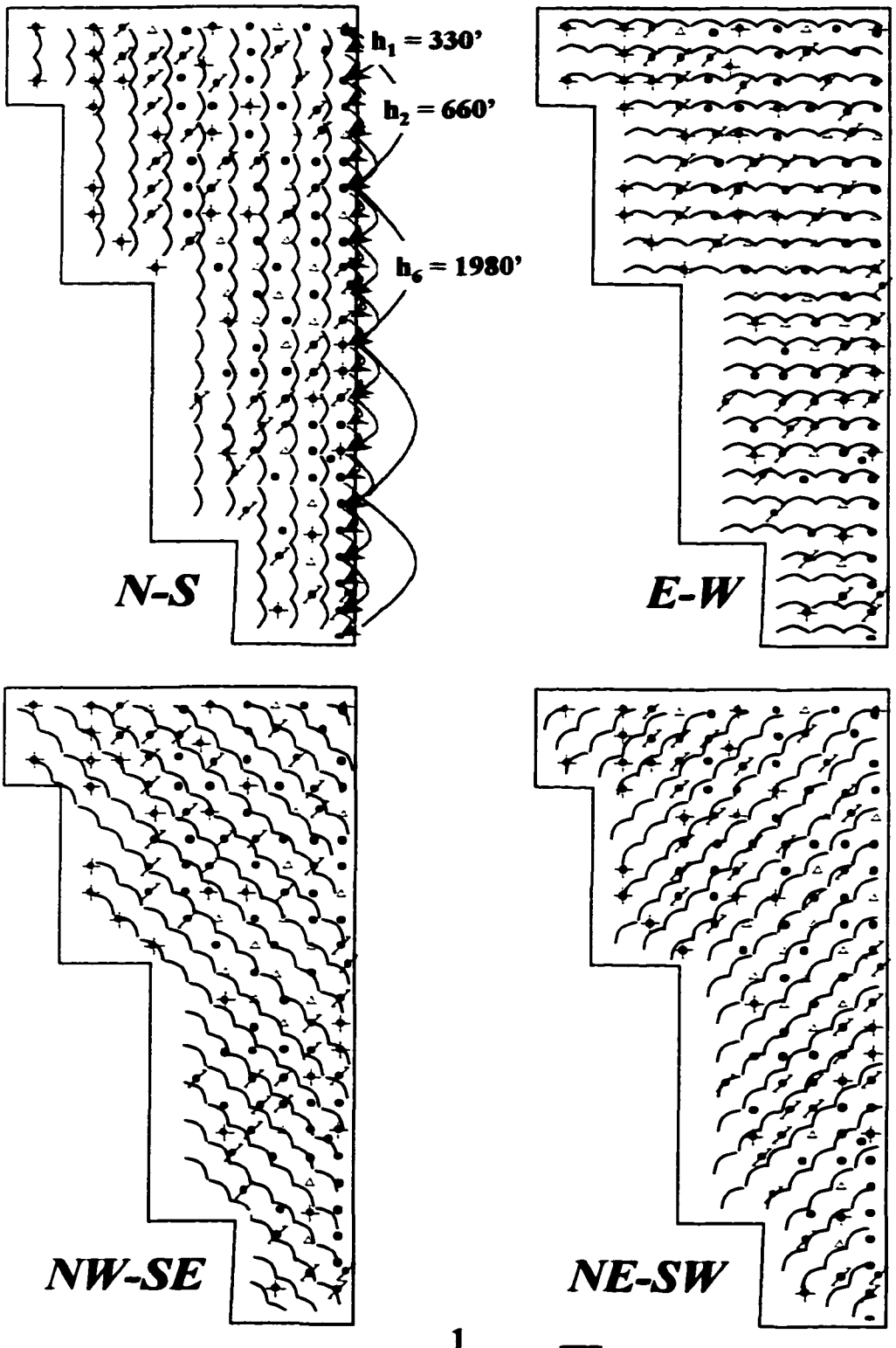

$$\gamma(h) = \frac{1}{2N(h)} \sum_{(i,j)|hij=h} (vi - vj)^2$$

variograms of porosity for all zones (fig. 86), the most dominant directions within the reservoir are to the north and the northwest-southeast. The shortest correlation length is within the dip direction (east-west). Although depositional facies tracts align north-south within the unit boundaries (figs. 38 and 45), a significant amount of the directional correlation seen in variograms is likely due to the affect of preferential north-south well spacing within the unit (fig. 87). The largest number of well pairs occurs within the north-south direction with the least in the east-west direction.

High variance at small separation distances can indicate problem data or a well with unusually high and/or low porosity values (fig. 86). This can be used as another means of quality control for the data. When the increase in separation distance no longer causes a corresponding increase in the variance then the variogram has reached the maximum distance between points over which some correlation can be demonstrated. This separation distance is referred to as the range or correlation length. The variance at which the range is reached is referred to as the sill (fig. 86; Eacmen, et al, 1998). The vertical and horizontal variograms of porosity for all zones show experimental (e) and theoretical (t) variograms. Experimental variograms are calculated from the actual porosity data and theoretical variograms are based on a statistical function that best describes the attribute in question, in this case porosity. The theoretical variogram model that describes most of the West Jordan San Andres reservoir is a fractal variogram model. This type of variogram model is a power-law function that shows similar proportional variation in different scales. For example, a fractal model of 0.48 is a power-law function with an exponent of 0.48. The theoretical variogram for porosity from all combined

zones within the reservoir indicates a range (vertical correlation length) of 335 feet and a sill of 0.00138 (fig. 86).

The calculated values for theoretical variograms from porosity and permeability are seen at the bottom of Figures 86 and 88. The variogram for permeability for all zones is particularly poor with an error of over 334. Errors calculated within GridSTAT are unitless and are relative to varying models and lag distances applied to the data. Based on errors seen within individual cycle boundaries of less than 30, an error of 334 represents a very poor correlation of data at any reasonable separation distance within the variogram model. This high error is reflective of the large degree of heterogeneity seen within the unit. The vertical correlation length of 976 feet is almost twice the actual thickness of zones I through the base of the unit. Experimental and theoretical variogram models do not correlate at all except at extremely short separation distances. This model is not realistic in terms of actual reservoir properties.

Having examined in detail the rock fabric and petrophysical properties of individual cycle boundaries, both porosity and permeability models based on these variograms would be subject to considerable error. The vertical correlation length for porosity at 335 feet is known to transcend several very different pore types with considerably different petrophysical properties. Variogram models for porosity and permeability for all combined zones help to demonstrate the difficulty of modeling these attributes when the reservoir is lumped into one package. To maintain the greatest accuracy within the model each cycle boundary within the reservoir was modeled in order to determine the statistical properties for the overall rock fabric and petrophysical characteristics found within these discrete boundaries.

Figure 88. Variogram analysis of permeability data for all zones. The variograms of permeability for all zones show little correlation between experimental variograms (e) and the theoretical variograms (t). The calculated error is extremely high at over 334, indicating that a reservoir grid populated by this variogram model would not provide very accurate results. This is not unexpected within the West Jordan unit reservoir. It has been shown that each cycle boundary defined within the reservoir has varying pore types with very different petrophysical properties and therefore should be modeled separately.

VARIOGRAM ANALYSIS OF PEMEABILITY DATA FOR ALL ZONES

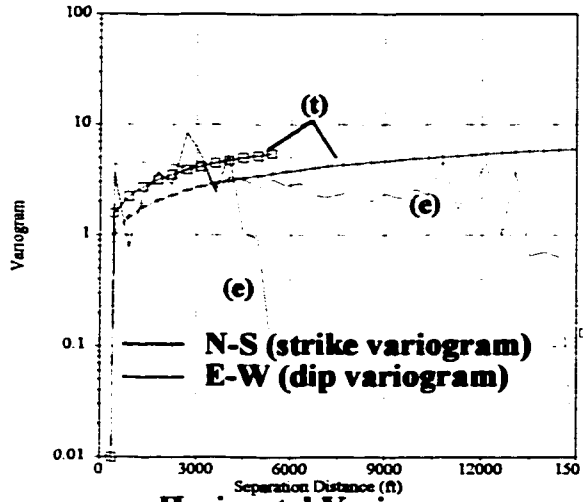

Horizontal Variogram

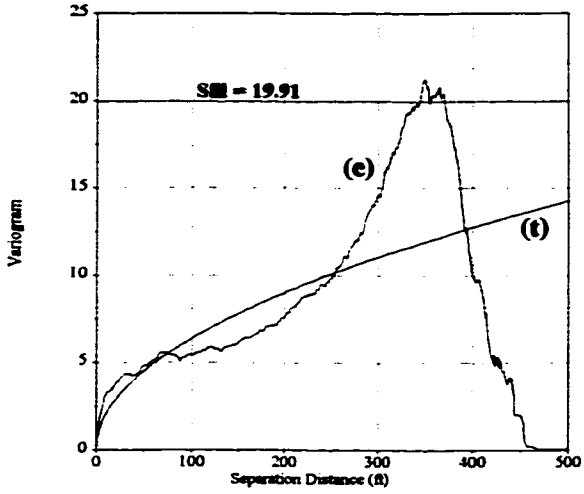

Vertical Variogram

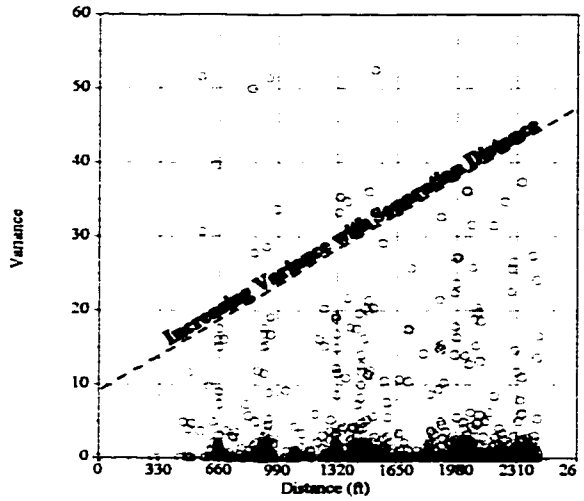

Well Pair Variance

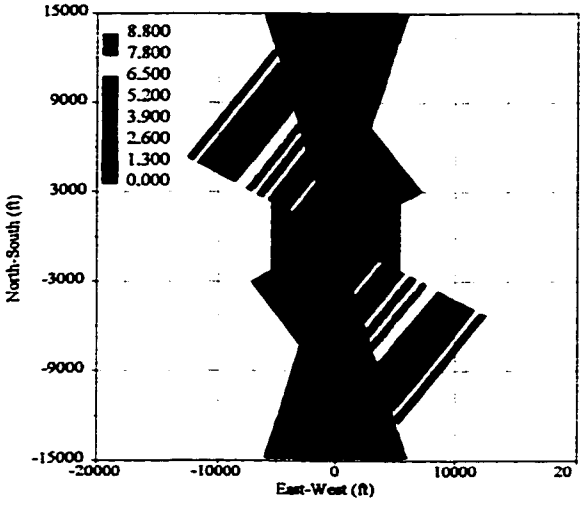

Areal Variogram

(e) Experimental Variogram

(t) Theoretical Variogram

Experimental Variogram Calculated Parameters

Model - Fractal power-law variogram of 0.50	
Major Correlation length	**199108**
Minor Correlation length	**69698**
Vertical Correlation length	**976**
Correlation ratio	**2.8567**
Error	**334.70**

Variograms for porosity and permeability from zones II, IV-A, and IV-E1 are presented in Figures 89 and 90. These variograms represent the primary pore types found within the reservoir. Zone II is primarily well developed fenestral porosity or touching vugs within the Lucia classification; zone IV-A is moldic or non-touching vuggy porosity; and zone IV-E1 is composed primarily of intercrystalline porosity or interparticle porosity within the Lucia classification. A substantially higher degree of correlation is seen within variograms of porosity and permeability within individual zones. Vertical correlation lengths (range) are reasonable for average zone thicknesses within the reservoir. Theoretical variogram models for porosity and permeability fit the experimental variograms much better than seen in those for the entire unit interval.

Comparing theoretical variogram models of porosity and permeability zone by zone shows that porosity models have less error and variance than permeability models (figs 89 and 90). Within zone IV-A the porosity model error is 4.44 compared to the permeability model error of 65.82, suggesting the influence of permeability anomalies such as fractures and stylolites. Zone II has the longest correlation lengths for both porosity and permeability variograms. This is not surprising since the majority of this zone is comprised of one dominant pore type, well developed fenestral porosity, that is laterally continuous. Variograms indicate that porosity has a larger correlation length than permeability, which is not uncommon. The distribution of permeability ranges within the reservoir is tied to petrophysical rock fabrics much more closely than the range of porosity distribution that is similar for all rock types.

Figure 89. Horizontal and vertical variograms of porosity for zones II, IV-A, and IV-E1. Vertical variograms for individual zones show the correlation between theoretical and experimental variograms to be much closer than those seen for the entire reservoir. Zone II represents primarily touching vuggy pore types (fenestral porosity); zone IV-A non-touching vuggy porosity (moldic porosity) and zone IV-E1 interparticle porosity (intercrystalline). Correlation lengths and calculated errors from theoretical variogram models are much more reasonable for each individual zone.

VARIOGRAM ANALYSIS OF POROSITY DATA FOR ZONES IV-E1, IV-A, AND II

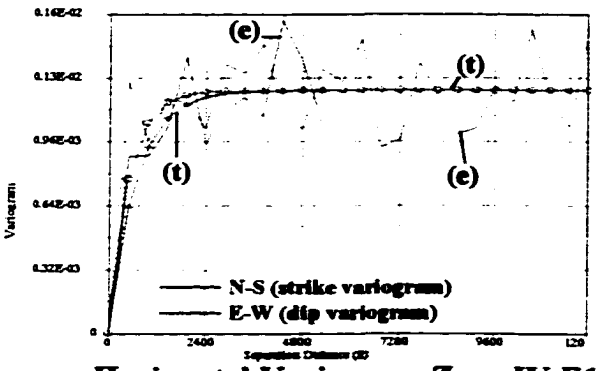

Horizontal Variogram Zone IV-E1

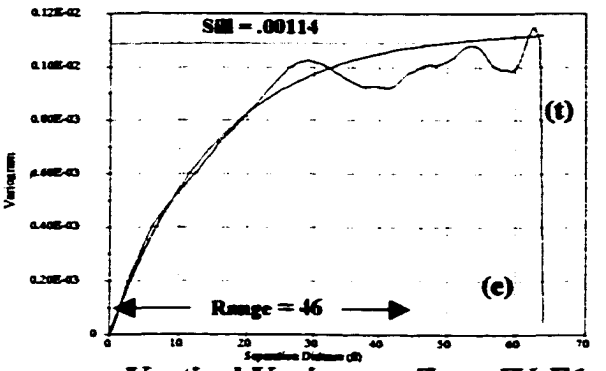

Vertical Variogram Zone IV-E1

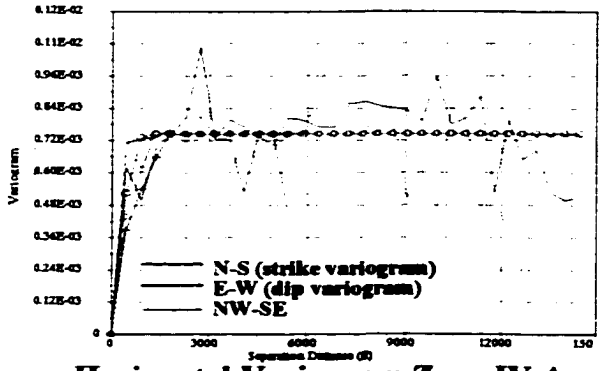

Horizontal Variogram Zone IV-A

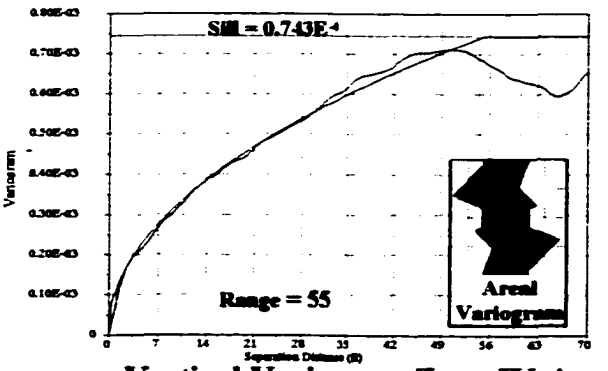

Vertical Variogram Zone IV-A

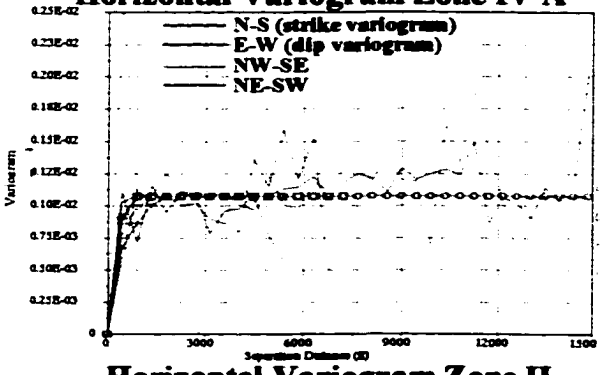

Horizontal Variogram Zone II

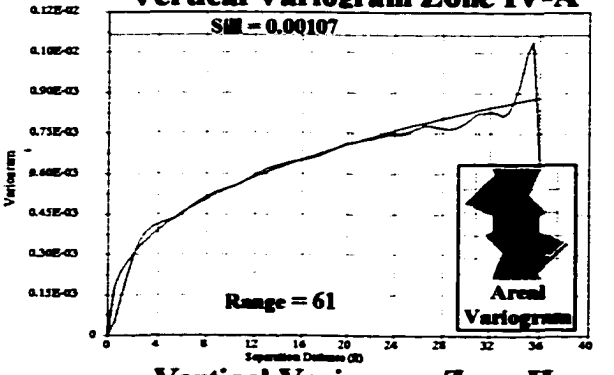

Vertical Variogram Zone II

Theoretical Variogram Calculated Parameters

	Zone IV-E1	Zone IV-A	Zone II
Model	Exponential	Fractal power-law	
		0.48	0.37
Major Correlation length	2406	1886	1902
Minor Correlation length	1337	917	670
Vertical Correlation length	46	55	61
Correlation length ratio	1.79	2.06	2.84
Error	6.33	4.44	3.87

Figure 90. Horizontal and vertical variograms of permeability for zones II, IV-A, and IV-E1. Note that correlation lengths for permeability are much shorter than those indicated for porosity in the previous figure. In zone IV-A the correlation length is very short for permeability suggesting high variance at short distances. This is not surprising after examining porosity-permeability cross plot data. Zone IV-A also has the greatest degree of error indicating the difficulty in modeling dolostones with multi pore types with primarily vuggy porosity.

VARIOGRAM ANALYSIS OF PERMEABILITY DATA FOR ZONES IV-E1, IV-A, AND II

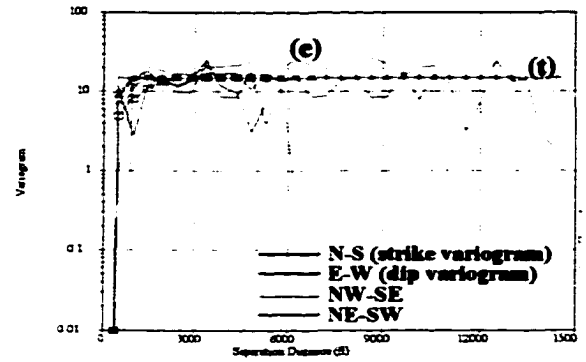

Horizontal Variogram Zone IV-E1

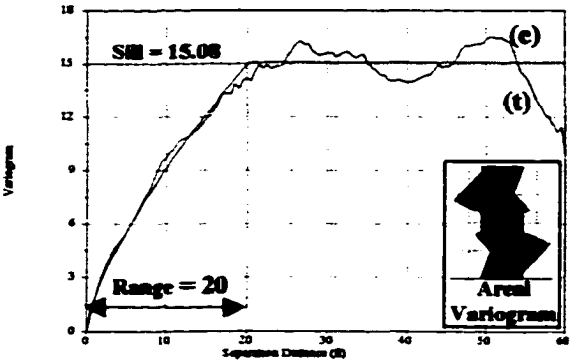

Vertical Variogram Zone IV-E1

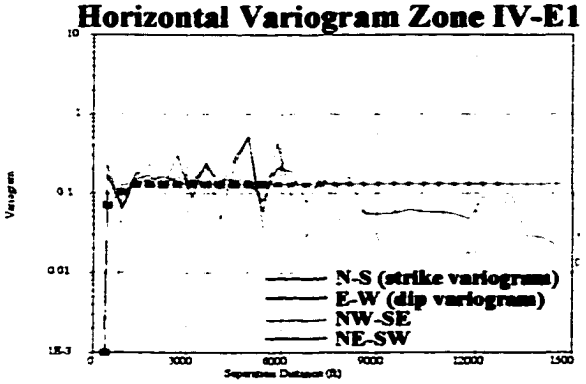

Horizontal Variogram Zone IV-A

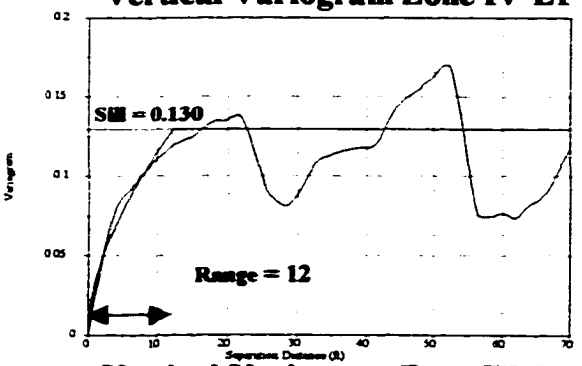

Vertical Variogram Zone IV-A

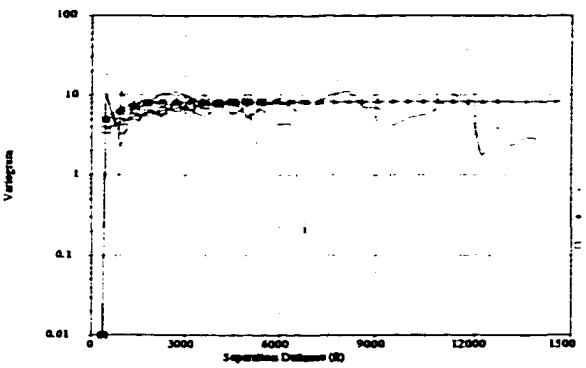

Horizontal Variogram Zone II

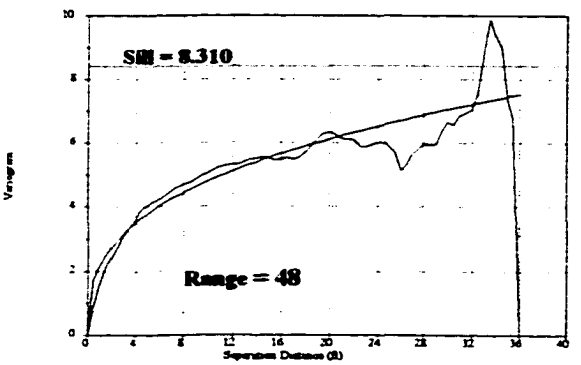

Vertical Variogram Zone II

Theoretical Variogram Calculated Parameters

	Zone IV-E1	Zone IV-A	Zone II
Model - fractal power-law	0.72	0.55	0.35
Major Correlation length	2505	1362	4719
Minor Correlation length	877	1356	1652
Vertical Correlation length	20	12	48
Correlation length ratio	2.86	1.01	2.86
Error	22.23	65.82	27.01

Probability and Cumulative Density Functions

Graphs of probability density functions (PDF) and cumulative density functions (CDF) also indicate differences in the distribution of porosity and permeability within the reservoir (figs. 91 and 92). The PDF function is a graph illustrating the proportional number of data points in each data value range. It is similar to the histogram except that the area under the curve is equal to one making it easier to compare between different data sets (Easmen, et al, 1998). The CDF function is the is a graph of the cumulative values from the PDF and shows the fraction of data below a certain value starting at a minimum of zero and ending at a maximum value of one. The PDF graphs of porosity (fig. 91) for the entire reservoir and zones II, IV-A, and IV-E1 show a similar spread. Most of the reservoir porosity falls between five and twelve percent for each graph although the frequency varies. CDF graphs for porosity can be used to examine the percent of porosity below a certain cutoff within various zones. For the entire reservoir (zones I through IV-E2) seventy-five percent of the porosity is less than ten percent. Values below the ten percent porosity cutoff for other zones are; seventy percent for zone II, seventy eight percent for zone IV-A and sixty-three percent for zone IV-E1 (fig. 91). We have already seen that porosity cutoffs are not a good method for determining permeability within the reservoir. After applying the Lucia permeability transform we can evaluate permeability and understand why permeability cutoffs are important when calculating reservoir economics.

When PDF and CDF graphs of porosity and permeability are compared, petrophysical properties of the reservoir are more revealing. PDF graphs of permeability

Figure 91. Graphs of probability and cumulative density functions for porosity. Graphs are from porosity data for all zones, and from individual zones (II, IV-A, and IV-E1). Although the frequency of the probability density function (PDF) curves change, the spread of data values remains fairly constant for all zones (between 5% and 12% porosity). The cumulative density function (CDF) curves show the fraction of data below a certain value. Examples of the percent of data values below 10 % porosity are indicated for each graph. Although differences are seen in the CDF curves of porosity, they are not nearly as extreme as those seen for permeability.

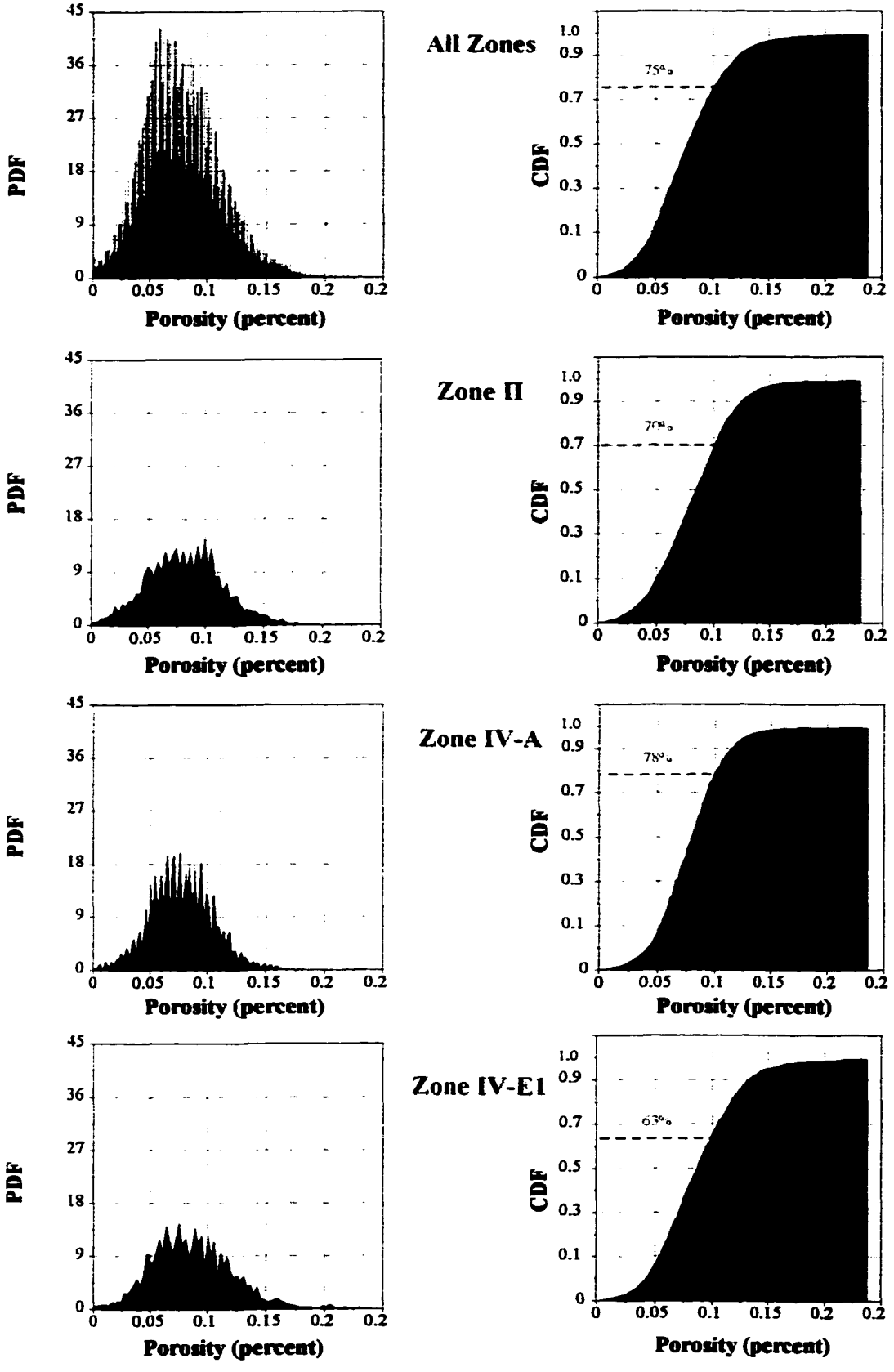
All Zones
Zone II
Zone IV-A
Zone IV-E1
PDF
CDF
Porosity (percent)
0
9
18
27
36
45
0.1
0.3
0.5
0.7
0.9
1.0
0.05
0.15
0.2

Figure 92. Graphs of probability and cumulative density functions for permeability. The PDF and CDF curves of permeability show the importance of using permeability to model carbonate reservoirs. The spread of permeability values is much narrower than the spread seen for porosity data. The direct relationship to rock fabric petrophysical characteristics is particularly evident in the CDF graphs of permeability. For all zones, 82% of the reservoir permeability is below 0.5 millidarcies (md) based on the transform model. For moldic porosity (non-touching vugs) within zone IV-A, 94% of permeability is below 0.5 md and for fenestral pore types (touching vugs) seen in zone II only 67% of permeability falls below 0.5 md. The CDF graph from zone IV-E1 shows that 70% of the intercrystalline porosity falls below 0.5 md. However, when wells are selected that only penetrate productive shoal bodies 50 % of the porosity becomes greater than 0.5 md for this zone.

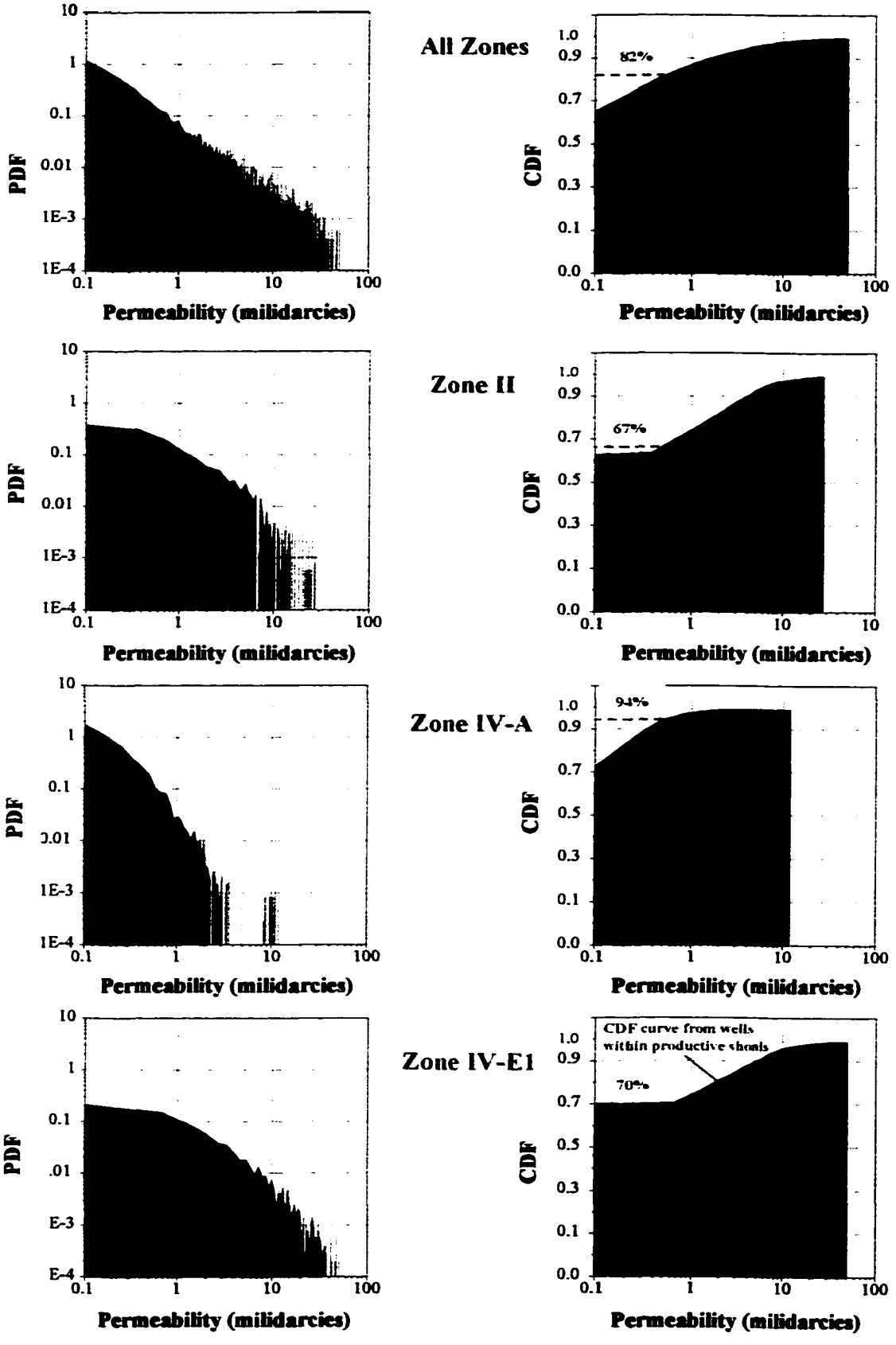
All Zones
Zone II
Zone IV-A
Zone IV-E1
PDF
CDF
Permeability (milidarcies)
82%
67%
94%
70%
CDF curve from wells within productive shoals

show the frequency of permeability within the reservoir (fig. 92). As expected higher permeability values occur within zones II and IV-E1 than in zone IV-A. Samples within zone IV-A with very high permeability values are considered suspect. The distribution of permeability within the reservoir is most telling within the CDF graphs. Geological modeling within this study has determined that using a permeability cutoff of 0.5 millidarcies most accurately calculates oil recovery within this reservoir under secondary waterflood recovery. This will be discussed in more detail in the next section. Graphs of CDF curves show that eighty-two percent of the reservoir has permeability values below a 0.5 millidarcy cutoff. Values below the 0.5 millidarcy cutoff for other zones are; sixty-seven percent for zone II, ninety-four percent for zone IV-A, and seventy percent for zone IV-E1. When wells were selected that contained only productive shoal bodies within zone IV-E1 the CDF curve indicated that only fifty percent of the permeability values fell below the 0.5 millidarcy cutoff. In evaluating a reservoir it is the petrophysical parameters that determine flow within the reservoir and these are the parameters that should be used when modeling the reservoir, primarily permeability.

Porosity and Permeability Grids

The primary statistical properties used for the gridding process include correlation lengths (major, minor, and vertical) and the correlation length ratio (Cra). The major correlation length is the correlation length in the major direction of the omnidirectional or areal variograms (figs. 86 and 88). The major axis represents the longest axis of the ellipse defining the areal variogram and the most correlative direction. The ellipse is a model for a two dimensional variogram that has a range of correlation for various

directions. The minor correlation length is perpendicular to the major correlation length and represents the direction with the least correlation. Variogram models provide correlation lengths for the input data, however, if geological trends are know it is best to constrain the model based on known reservoir properties. For example, within lower zones of the reservoir shoal bodies tend to be slightly elongate, longer in the north-south direction than in the east west direction. The geometries of the shoal bodies are modeled using the major and minor correlation lengths. Likewise, the vertical correlation length should be representative of the bed or cycle thickness. The correlation length ratio is the ratio of the major to minor correlation lengths and determines the elliptical shape of the search radius. A Cra ratio of one would occur when the major and minor correlation lengths are the same, resulting in an equal correlation length in all directions. These geological properties are defined for the variogram model prior to the gridding process.

GridSTAT interpolates interwell grid points using ordinary kriging, a point estimation method commonly referred to as B.L.U.E., for "best linear unbiased estimator" (Issaaks and Strivastava, 1989). Kriging is considered best because it aims at minimizing the variance of errors; linear because estimates are weighted linear combinations of the available data; unbiased because kriging tries to have the mean residual or error equal to zero and weights sum to one; and estimate because it does not attempt to reproduce the variability (Issaaks and Strivastava, 1989; Eacmen, et al, 1998). Ordinary kriging involves multiple unknown means in which the mean is constant only within the local neighborhoods. The local mean calculated within GridSTAT is determined by the maximum search radius used for griding.

The general process within GridSTAT involves determining the variogram model to be used for the kriging process and then setting up the gridding options. Correlation lengths were based on geologic trends determined by core descriptions and mapping (isopach, PHIH, and PHIA). PHIH maps were used to determining the maximum and minimum correlation lengths (figs. 68 and 93). Lateral extents of shoal bodies were mapped from core and porosity maps (PHIH and PHIA). Vertical correlation lengths were determined by several methods. In zones such as IV-A where petrophysical properties were fairly consistent from the top to base of the zone the vertical correlation length was assigned the zone thickness. In zones where considerable heterogeneity was found, such as productive shoal versus non-productive intershoal facies seen in zones IV-E1 and IV-E2, the average thickness of the desired petrophysical fabric was used as the vertical correlation length. Correlation lengths were determined in this manner to more accurately distribute these productive facies.

The same correlation lengths and gridding options were used to generate the porosity and permeability. A minimum of three data pints per node was used for gridding purposes. The initial search radius was set at 1320 feet (20-acre spacing) in order to have a sufficient number of data points to determine interwell grid values. The maximum search radius was set at 2640 (80-acre spacing) feet to control the distance of data point that influence the grid point values. Gridding was done proportionately along cycle boundaries where thickness changes result in a thickening or thinning of cells rather than maintaining cell thickness within zones and adding additional layers. The grid model contained a total of 2,114,859 cells with the number of cells in the x, y, and z directions being 53, 141, and 283, respectively. The grid spacing is 100 feet in the x and y

Figure 93. PHIH contour maps from zone I through zone IV-C based on a 7% porosity cutoff. PHIH maps along with average porosity maps and detailed core descriptions were used to determine the most accurate correlation lengths for geostatistical modeling based on reservoir characteristics. Zone IV-A has higher PHIH values than other zones, although pore types are primarily moldic. This zone is thicker than other zones within the reservoir and using an average porosity cutoff can lead to misinterpretations when evaluating carbonate reservoirs. PHIH maps of zones IV-E1 and IV-E2 are shown in figure 70. These PHIH maps derived from a 7% porosity cutoff will be compared to PHIH maps using permeability cutoffs in a later section. High porosity values in carbonates often do not contribute to flow in these reservoirs and can be misleading.

Zone I
Zone II
Zone III
Zone IV-A
Zone IV-B
Zone IV-C
PHIH
(ϕ /feet)
3.5
3.0
2.5
2.0
1.5
1.0
0.5
0.0

directions and 2 feet in the z direction. The theoretical variograms derived from experimental variograms were used for kriging after modification to reflect known geologic properties.

The three-dimensional geostatistical model of porosity (fig. 94) shows a greater degree of heterogeneity than the permeability model (fig. 95). Higher porosity values within much of the reservoir are associated with low permeability values. This is clearly evident when examining the two figures. Although the geostatistical model of porosity shows high porosity within zones IV-E1 and IV-E2 it does not model the actual geometries of shoal bodies that occur within those zones. High permeable "stacked shoal bodies" from zones IV-E1 and IV-E2 are well defined within the permeability model as are intervals of high permeability within zone II. The permeability model could be used as a predictive tool for facies tracts and geometry of productive bodies. Even with limited core data a fairly accurate geologic model could be defined by a geostatistical model of permeability provided lateral changes along the ramp setting are not severe within the field.

San Andres rocks along the eastern edge of the Central Basin platform are known for their shallowing upward progradational character. Similar pore types are described from field to field. A reasonable model can be constructed by defining the general vertical distribution of pore types within a chronostratigraphic framework. This can be accomplished even from a few cores and then applying the permeability transform to well data. The three-dimensional geostatistical model of permeability provides a predictive tool by defining shoal bodies more accurately than the porosity model. Any depositional facies with well-developed interparticle porosity will be modeled nicely with the

Figure 94. A three-dimensional geostatistical model of the West Jordan unit illustrating the distribution of porosity within the reservoir. Porosity is seen within most zones of the reservoir, although to a larger degree in zones IV-E1 and IV-E2. The lack of porosity seen within zone III is due to the clay cutoff applied to this zone eliminating non-permeable porosity as a result of clays. Even though high porosity can be seen within zones IV-E1 and IV-E2, the porosity model does not lead to easy interpretations of shoal body morphology or the delineation of shoal geometries present in the reservoir. This is not the case when looking at the geostatistical model of permeability.

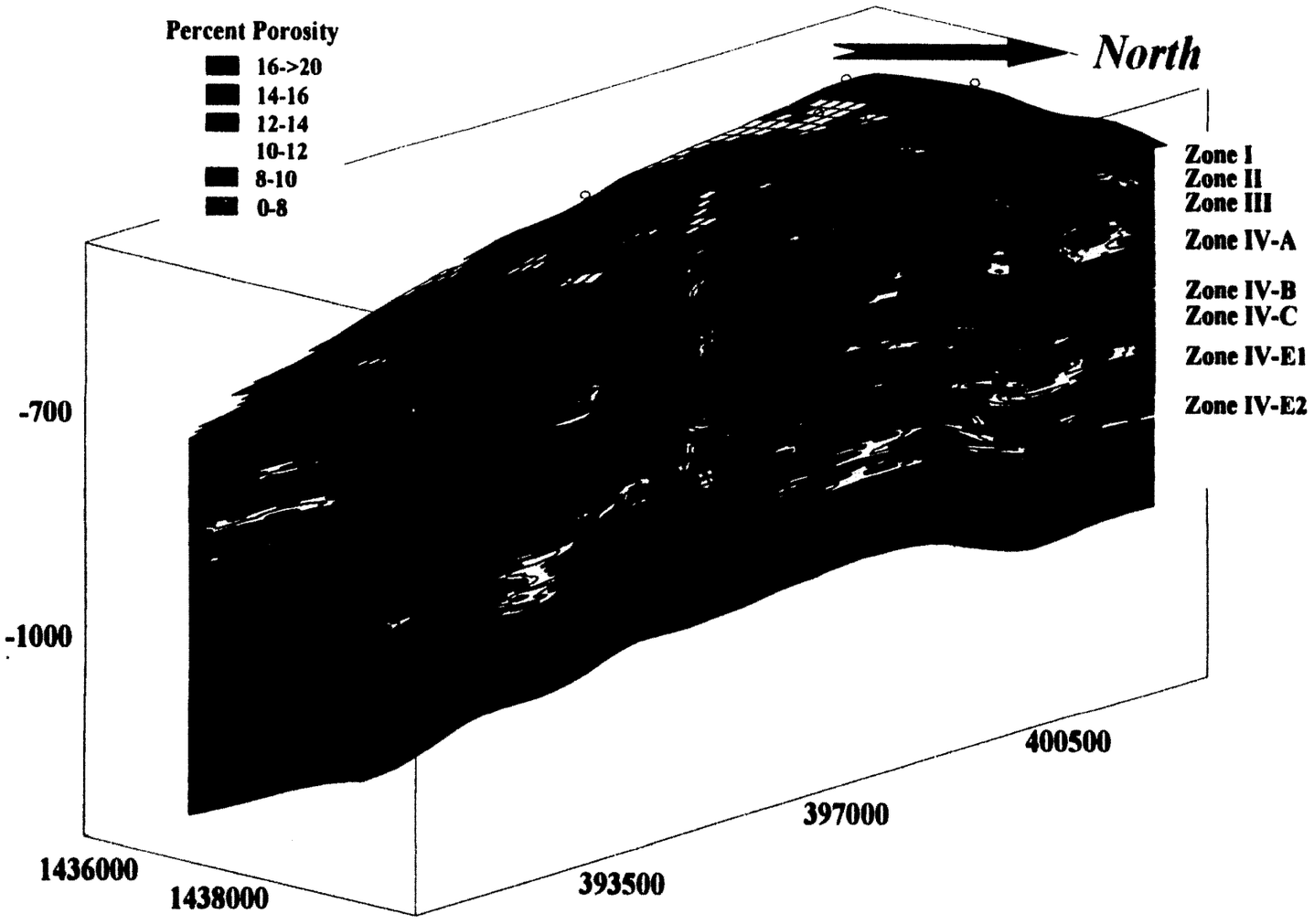
Percent Porosity
16->20
14-16
12-14
10-12
8-10
0-8
North
Zone I
Zone II
Zone III
Zone IV-A
Zone IV-B
Zone IV-C
Zone IV-E1
Zone IV-E2
-700
-1000
400500
397000
393500
1436000
1438000

Figure 95. A three-dimensional geostatistical model of the West Jordan unit illustrating the distribution of permeability within the reservoir. The permeability model more accurately shows flow units within the West Jordan unit under secondary waterflood recovery techniques. This has been established through correlation to cumulative production since initiation of the waterflood project. Within the model everything less than 0.5 millidarcies is blue. Stacked shoal bodies are easily identified and are extremely similar in geometry to those seen on the outcrop. Intershoal areas are also clearly seen as are high permeability streaks within zone II. Inner ramp facies consisting primarily of non-touching vuggy porosity (moldic) have little permeability and are not found to contribute to flow within the reservoir.

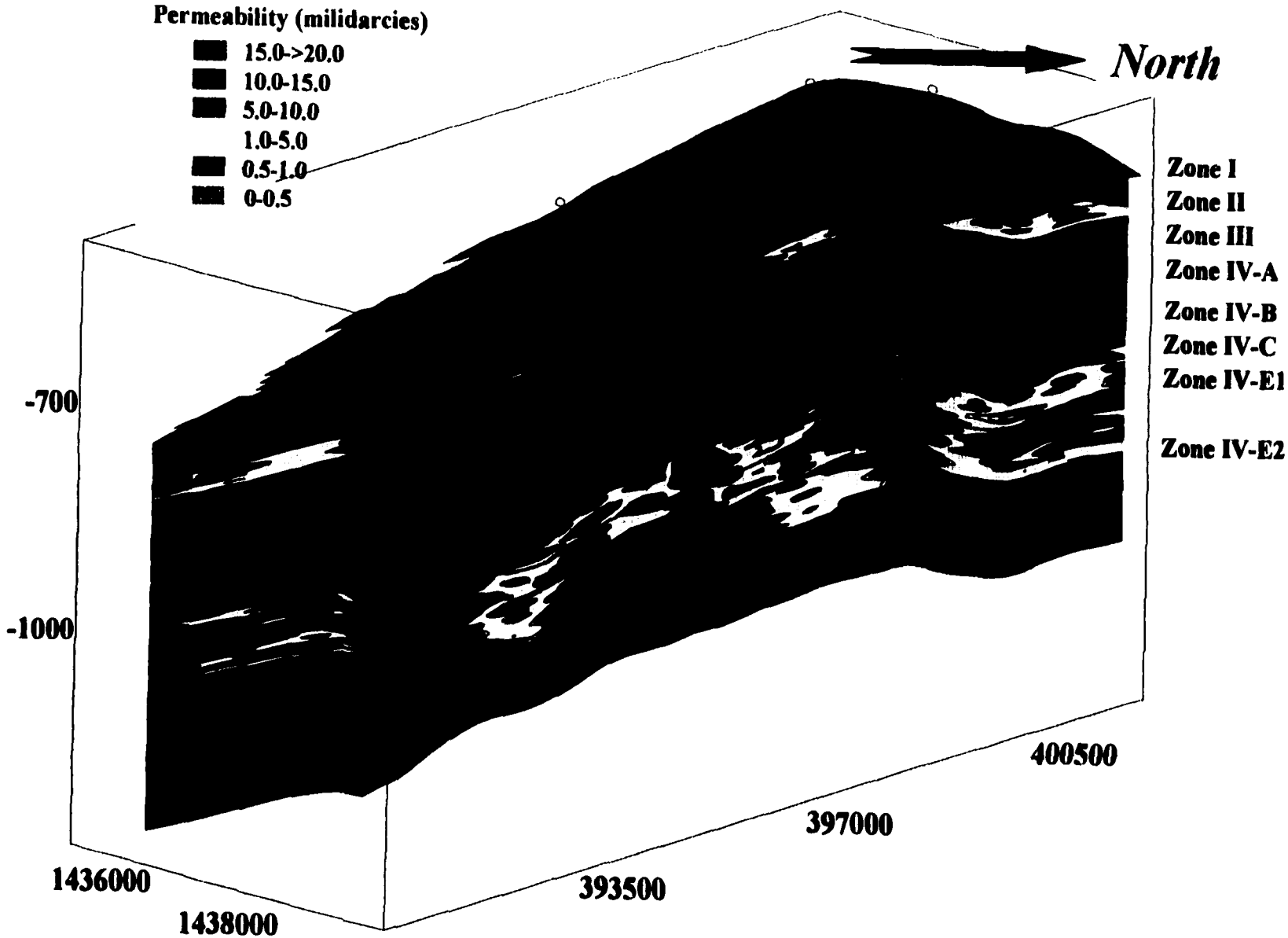
Permeability (milidarcies)
15.0->20.0
10.0-15.0
5.0-10.0
1.0-5.0
0.5-1.0
0-0.5
North
Zone I
Zone II
Zone III
Zone IV-A
Zone IV-B
Zone IV-C
Zone IV-E1
Zone IV-E2
-700
-1000
1436000
1438000
393500
397000
400500

transform. Lateral and vertical geometries of shoal bodies from the model were found to have the same geometries as those described from outcrop further supporting the model (figs. 42 and 44).

Analysis of the geostatistical models and cumulative production since waterflood injection indicates that under secondary recovery conditions a permeability cutoff of 0.5 is needed to model cumulative oil production within the West Jordan unit reservoir and most likely within all San Andres reservoirs under waterflood. Previous cutoffs used for the reservoir were 3.9 percent porosity which corresponds to 0.1 millidarcies on porosity/permeability cross plots. This lower porosity cutoff value makes a considerable difference in modeling oil production within the reservoir. This becomes critical when evaluating reserves and the economic potential of waterflood projects. Evidence for avoiding porosity cutoffs and using a permeability cutoff of 0.5 will be addressed in further detail in the last section.

RESERVOIR VOLUMETRICS AND PREDICTION OF FUTURE RESERVOIR POTENTIAL

Calculation of Original Oil in Place

Reserve estimates for the West Jordan unit were calculated from volumes generated within the three-dimensional geostatistical model for the entire reservoir above –875 feet subsea. This is the depth below which water saturation becomes high enough to reduce the relative permeability for oil to essentially zero. Original oil in place (OOIP) values, limited by a permeability cutoff of 0.1 millidarcies, were calculated for each reservoir zone to quantify reserves within individual cycle boundaries. The reservoir was modeled using various cutoff values for porosity and permeability in order to determine the most appropriate cutoff to match cumulative oil production since initiation of the waterflood project. As expected from previous geostatistical modeling, PHIH maps using porosity cutoffs were not found to adequately match reservoir production patterns, and therefore, were not used for reserve calculations.

Determining reservoir volumes from a geostatistically populated three-dimensional grid increases the accuracy in reserve calculations compared to the methods previously used. Three previous studies (Lalicker, 1985; Whitfield, 1993; and Fields and Nelson, 1996) used average values for net pay and porosity. The two most recent of those studies used the same reservoir properties determined in the Lalicker study for reservoir volumetrics and applied a constant net pay thickness of 109 feet for all wells within the unit. The average porosity used for this net pay was given at 9.3 percent (Table 2).

	From Lalicker study (1985)				
Zone	Net Pay	Volume = A*h*ϕ	OOIP	MMSTBO	OOIP %
Zone I	0	0.00	0.00	0	0.00
Zone II	6	910.86	3,478,019.28	3.48	5.13
Zone III	8	1,214.48	4,637,359.05	4.64	6.84
Zone IV-A	20	3,036.20	11,593,397.62	11.59	17.09
Zone IV-B	0	0.00	0.00	0.00	0.00
Zone IV-C	32	4,857.92	18,549,436.19	18.55	27.35
Zone IV-E1	43	6,527.83	24,925,804.87	24.93	36.75
Zone IV-E2	8	1,214.48	4,637,359.05	4.64	6.84
TOTAL	117	17,761.77	67,821,376.05	67.82	100.00

OOIP = Original oil in place

Where:
A = 1614
h = 109 feet
ϕ = 0.093
$(1-Sw_i)$ = 0.63
Boi = 1.28

OOIP = 7758 * A * H * *(1-Sw)/Boi
A = Developed unit areal extent
h = height or thickness of the net pay
ϕ = Average porosity of the net pay above a 3.9 % cutoff
$(1-Sw_i)$ = Initial water saturation
Boi = Formation volume factor for oil at initial conditions

MODEL 1 - Present study using a 0.1 millidarcy cutoff					
Zone	Net Pay	Volume = A*h*ϕ	OOIP	MMSTBO	OOIP %
Zone I	Variable	78.2	298,598.15	0.30	0.52
Zone II	Variable	2837.34	10,834,072.46	10.83	19.00
Zone III	Variable	147.23	562,181.65	0.56	0.99
Zone IV-A	Variable	3148.73	12,023,081.11	12.02	21.09
Zone IV-B	Variable	842.32	3,216,306.79	3.22	5.64
Zone IV-C	Variable	1961.98	7,491,606.04	7.49	13.14
Zone IV-E1	Variable	3901.42	14,897,145.55	14.90	26.13
Zone IV-E2	Variable	2013.19	7,687,145.82	7.69	13.48
TOTAL		14930.41	57,010,137.57	57.01	100.00

Where:
A = 1614
h = Variable - calculated for each well
ϕ = Variable - calculated for each well $(1-Sw_i)$ = 0.63
$(1-Sw_i)$ = 0.63
Boi = 1.28

MODEL 2 - Present study using a 0.5 millidarcy cutoff					
Zone	Net Pay	Volume = A*h*ϕ	GUR	MMSTBO	GUR %
Zone I	Variable	77.79	297,032.61	0.30	1.35
Zone II	Variable	1328.84	5,074,030.20	5.07	23.14
Zone III	Variable	22.75	86,868.39	0.09	0.40
Zone IV-A	Variable	144.74	552,673.86	0.55	2.52
Zone IV-B	Variable	29.26	111,726.11	0.11	0.51
Zone IV-C	Variable	340.31	1,299,436.51	1.30	5.93
Zone IV-E1	Variable	2219.06	8,473,237.90	8.47	38.65
Zone IV-E2	Variable	1578.77	6,028,360.57	6.03	27.50
TOTAL		5741.52	21,923,366.14	21.92	100.00

Where:
A = 1614
h = Variable - calculated for each well
ϕ = Variable - calculated for each well $(1-Sw_i)$ = 0.63
$(1-Sw_i)$ = 0.63
Boi = 1.28

The present study has shown that pore types and permeability dramatically change within facies tracts and related depositional environments within each cycle. Permeability has no direct relationship to porosity values within the reservoir. High porosity does not equate to higher permeability but rather permeability is directly related to the pore type and may have been enhanced or reduced by diagenetic processes. Volumetrics in this study are calculated using varying net pay based on log analysis for each well. Within the model, the determination of ($h * \phi$) or PHIH is based on permeability cutoffs obtained from petrophysical properties related to pore size distribution. In this study petrophysical characteristics of each well within the reservoir are calculated to determine volumetrics. This method more accurately matches production patterns and flow within the reservoir since initiation of the waterflood in 1970 than did the previous studies using average volumes.

An earlier study (Lalicker, 1985) of the West Jordan unit determined OOIP for the reservoir to be 67.82 million stock tank barrels of oil (MMSTBO; Table 2). The Lalicker study used a porosity cutoff of 3.9 percent which corresponds to 0.1 millidarcies on the porosity-permeability cross plot used in that study. Using a 0.1 millidarcy cutoff from the geostatistical model, the calculated OOIP is approximately 57 MMSTBO, 16 percent less than previous studies. Although the Lalicker study did not calculate OOIP for each zone it did determine average net pay for each zone making the calculation possible. The percent of OOIP represented by each zone is provided in the far right-hand column of the three models presented (table 2). Both the Lalicker study and the geostatistical model

from this study using a 0.1 millidarcy cutoff indicate that zone IV-A contributes 17 to 21 percent depending on the model of the total OOIP.

Petrographic study of this zone indicates the dominant porosity type is non-touching vuggy (moldic) porosity with very low permeability compared to other pore types. Probability density functions of porosity (fig. 91) and petrographic analysis show porosity has a similar range of values throughout all zones within the reservoir. Although these values indicate potential volumes of oil in place, this oil is not being recovered under present waterflood techniques. In addition, the Lalicker study also found zone IV-C to have very high net pay values resulting in over 27 percent of the OOIP for the reservoir. The high OOIP calculations for zone IV-C are based on using net pay values for the WJU#616 well for the entire reservoir.

Pattern Analysis of Geostatistical Modeling and Cumulative Oil Production

To determine the most accurate permeability cutoff to use for modeling the reservoir, cumulative production patterns since waterflood initiation were compared to geostatistically generated PHIH maps of the reservoir based on permeability cutoffs. Models were run using permeability cutoffs of 0.1 to 1.0 millidarcies at 0.1 millidarcy steps. The 0.1 and 0.5 millidarcy models are shown in Figure 96, as colored contour fill maps with cumulative production indicated by contour lines. The three dimensional geostatistical model of permeability distribution shows that shoal bodies are defined when using a 0.5 millidarcy cutoff. Comparison of the geostatistical permeability and porosity models (figs. 94 and 95) shows that moldic pore types within the reservoir have permeabilities below 0.5 millidarcies. The geostatistical model using a 0.1 millidarcy

Figure 96. Pattern analysis showing geostatistically generated PHIH maps from the 0.1 and 0.5 millidarcy models plotted with cumulative production contour line overlays. Color contour fill ranging from 0 to 11.0 porosity feet represents the geostatistical models with the 0.1 millidarcy model on the left and the 0.5 millidarcy model on the right. Cumulative production for the reservoir since the initiation of waterflood is indicated by contour lines. The maps indicate low correlation between the 0.1 millidarcy model and cumulative production and a very close match between the 0.5 millidarcy model and cumulative production.

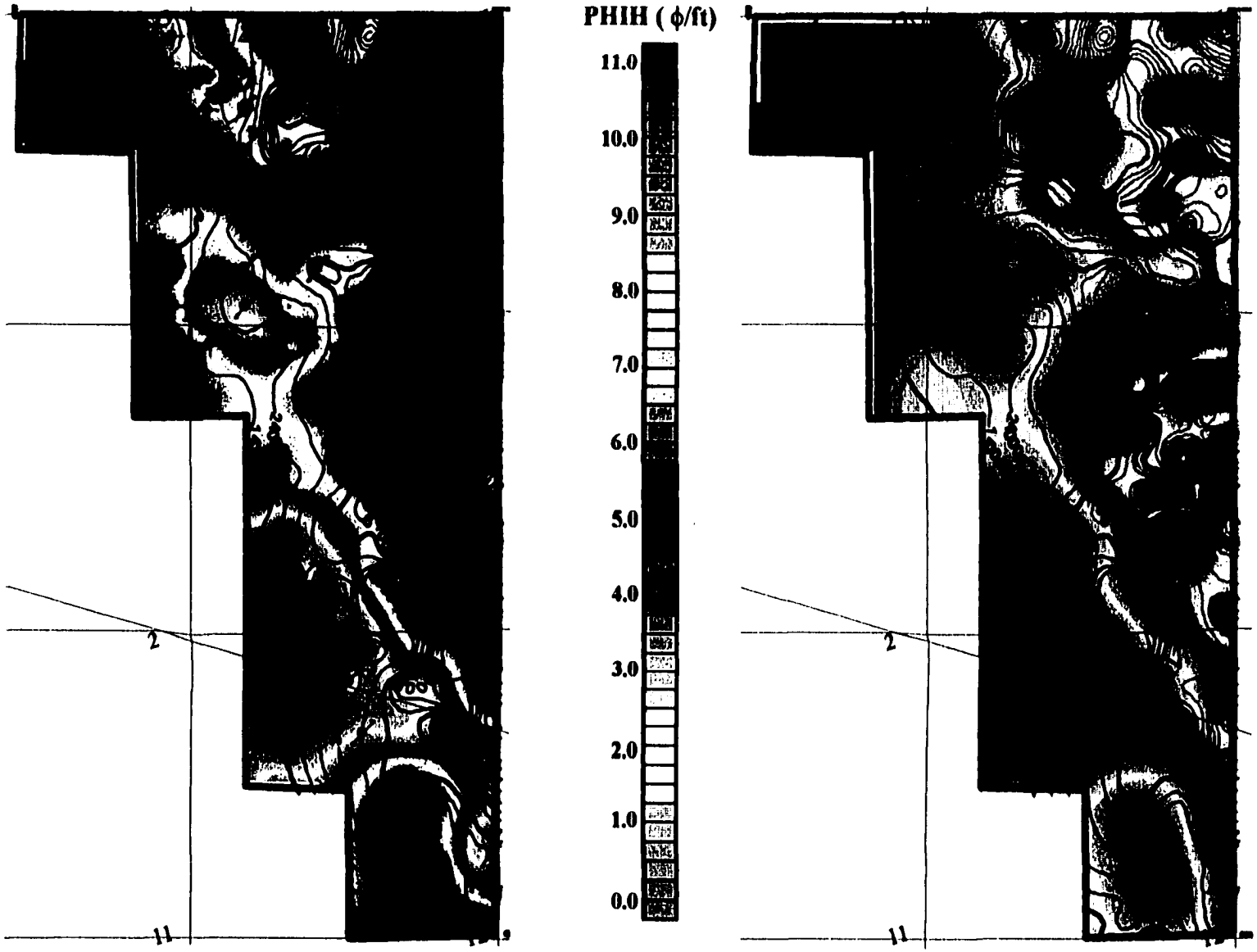

0.1 milidarcy cutoff model

0.5 milidarcy cutoff model

cutoff does not match patterns of cumulative production for the reservoir. The 0.5 millidarcy model shows almost a one-to-one match to the cumulative production pattern (fig. 96). This model also shows that the intershoal areas create considerable compartmentalization within the reservoir. The degree of this compartmentalization is evident within the three-dimensional visualization models shown in the next section. This strongly suggests that the majority of production since the initiation of the waterflood has come from shoal bodies within zones IV-E1 and IV-E2 that have permeability greater than 0.5 millidarcies. The lack of correlation to oil production patterns (figs. 43 and 96) within zone IV-A compared to a good correlation in zones IV-E1 and IV-E2 is also apparent when evaluating PHIH maps constructed from the geostatistical model (fig. 97) to earlier PHIH maps seen using a 7 percent porosity cutoff (figs. 70, 93).

PHIH maps for each zone are presented for the 0.5 millidarcy model (fig. 97). A comparison of PHIH maps of zones IV-E1 and IV-E2 from the 0.5 millidarcy geostatistical model and the 7 percent porosity cutoff model do not show significant variation (figs. 70 and 97). The most distinct differences are seen in the vuggy pore types, particularly zones IV-A and IV-B. A comparison of these maps to cumulative production (figs. 43 and 96) indicates that a 0.5 millidarcy cutoff is needed to model flow under present recovery techniques.

Distribution of Remaining Oil within Cycle Boundaries

Three methods where utilized in order to estimate total gross ultimate recovery (GUR) for the West Jordan unit reservoir. The first method already described is the

Figure 97. PHIH maps by zone generated from the geostatistical 0.5 millidarcy cutoff model. These maps indicate that most of the production since waterflood has been from zones IV-E1 and IV-E2 with some production from zone II. A comparison of these maps to earlier PHIH maps constructed using a seven percent porosity cutoff shows a dramatic difference in the location of produced oil within the reservoir (see figs. 70 and 93).

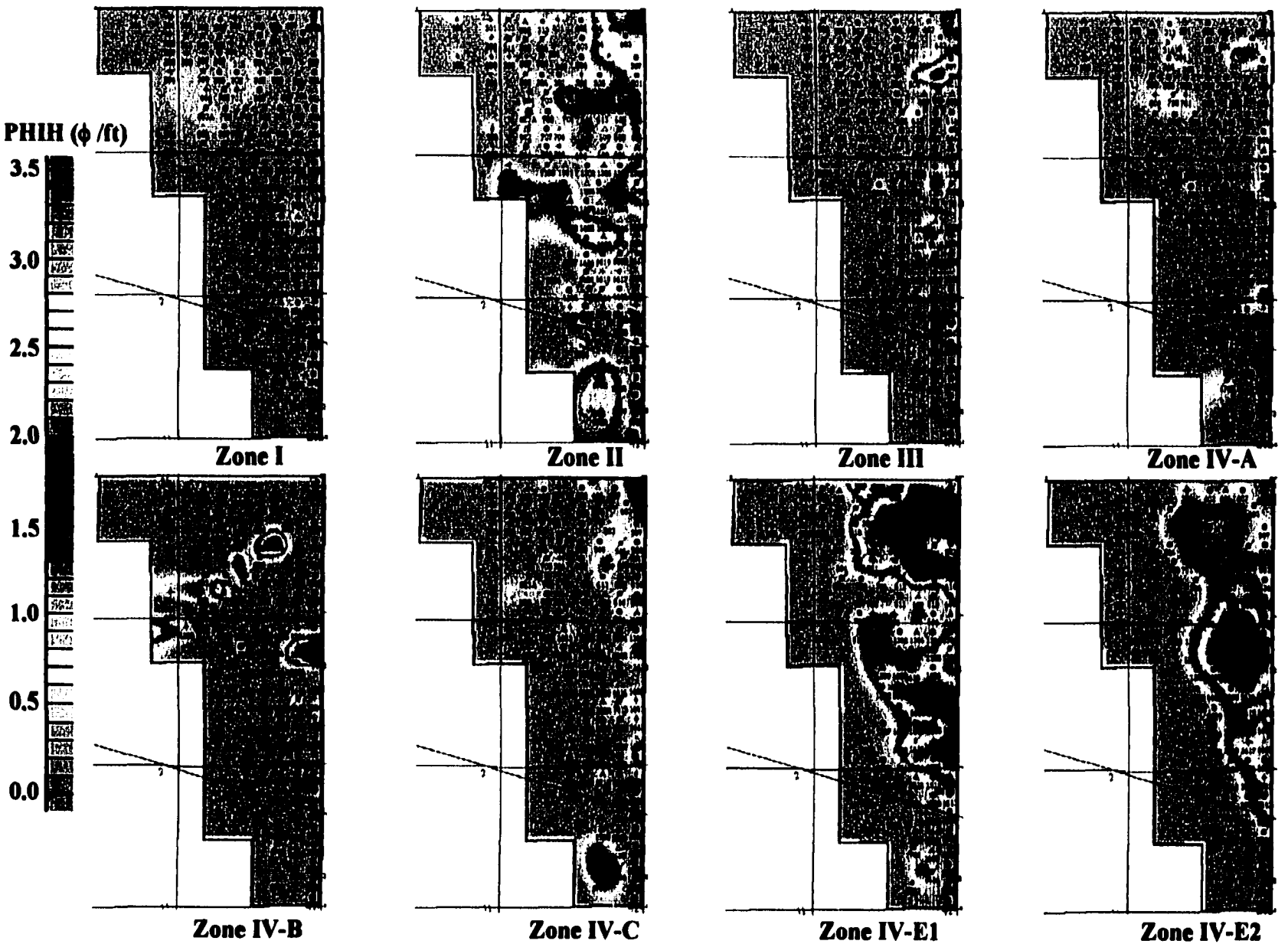
PHIH (ϕ /ft)
3.5
3.0
2.5
2.0
1.5
1.0
0.5
0.0
Zone I
Zone II
Zone III
Zone IV-A
Zone IV-B
Zone IV-C
Zone IV-E1
Zone IV-E2

geostatistical model using a 0.5 millidarcy cutoff. The second method is based on analysis of monthly oil production versus cumulative production (fig. 98) and the third method is based on decline curve analysis (fig. 99). Each of these methods estimates the gross ultimate recovery (GUR) expected from the field under current waterflood conditions. In addition, these methods can be used to determine remaining oil in place values for each zone within the reservoir by applying recovery factors derived from the methods.

Original oil in place for the West Jordan unit is calculated from the 0.1 millidarcy cutoff model to be 57,010,138 stock tank barrels of oil (STBO; Table 3). Primary recovery for the unit is 8,922,166 STBO, a recover efficiency of 15.7 percent. Secondary recovery since initiation of the waterflood in 1970 is 8,297,958 a recovery efficiency of 14.6 percent. GUR for the reservoir is 17,220,124 STBO, for a gross ultimate recovery factor of 30.2 percent (Table 3).

The 0.5 millidarcy cutoff method effectively models oil production under waterflood conditions within the reservoir as seen from comparison to cumulative production patterns. In this model the predicted GUR for the reservoir is 21.9 MMSTBO, resulting in a recovery factor of 38.25 percent (table 3). This number represents movable oil within the reservoir that should be producible under current waterflood techniques. In addition, this method provides a deterministic model for calculating remaining oil in place values for individual cycle bounders (table 4A). By subtracting cycle boundary GUR values within the 0.5 millidarcy model from OOIP values in the 0.1 millidarcy model, a good approximation of remaining oil in place can be estimated for each zone. These values represent oil still trapped in the reservoir after waterflood recovery reaches

Figure 98. Semi-log plots of monthly oil production versus cumulative production for the West Jordan unit. Gross ultimate recover (GUR) estimations are determined by an exponential fit of monthly oil production versus cumulative production. Decline values for the three plots were based on best fit through data values from three separate time periods resulting in varying decline rates and GUR values. The estimated GUR values are totals for curve fits through time periods represented by total cumulative oil production. Steep changes in the decline rate seen for cumulative oil production are based on several factors. The substantial increase in production seen at about 13.7 MMSTBO involved expansion of the waterflood and decreasing the unit spacing from 20 to 10 acres from 1978 to 1987. In 1987 when cumulative production reached about 16.1 MMSTBO injection was reduced to almost half to cut operating expenses as a reaction to decreased oil prices. An aggressive fracture stimulation program began in 1993 (at 16.5 MMSTBO) which resulted in flattening decline rates within the unit. From 1998 forward, the low price of oil resulted in cost cutting measures that resulted in the decline seen at the end of the cumulative production curve.

MONTHLY PRODUCTION VERSUS CUMULATIVE PRODUCTION

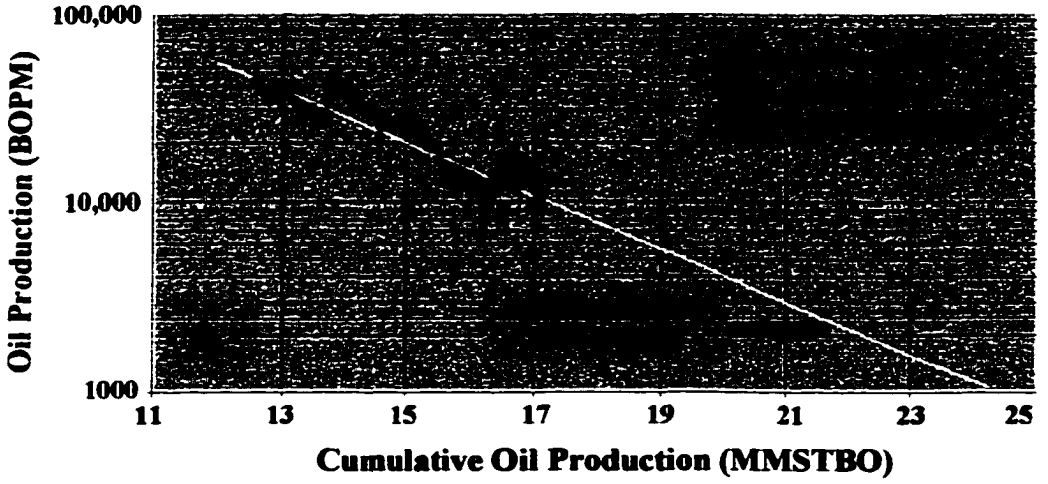

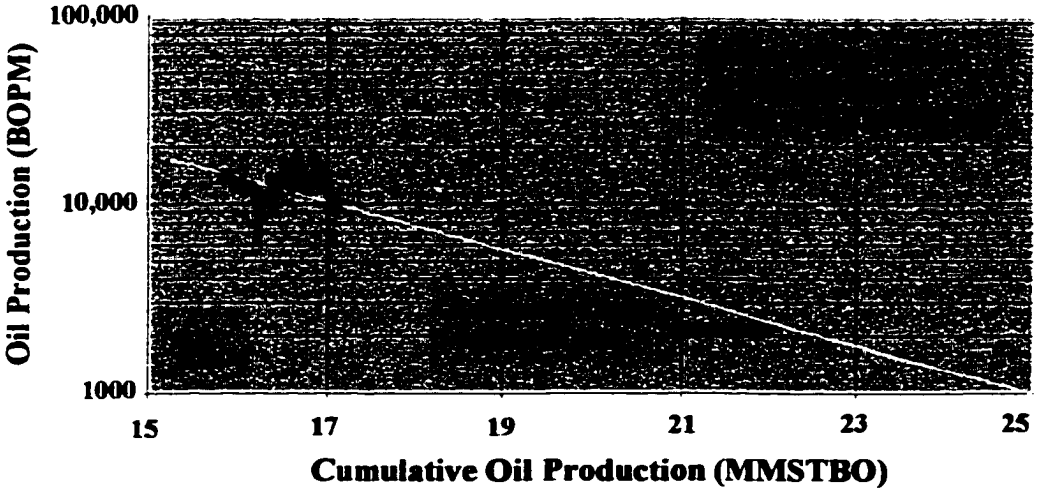

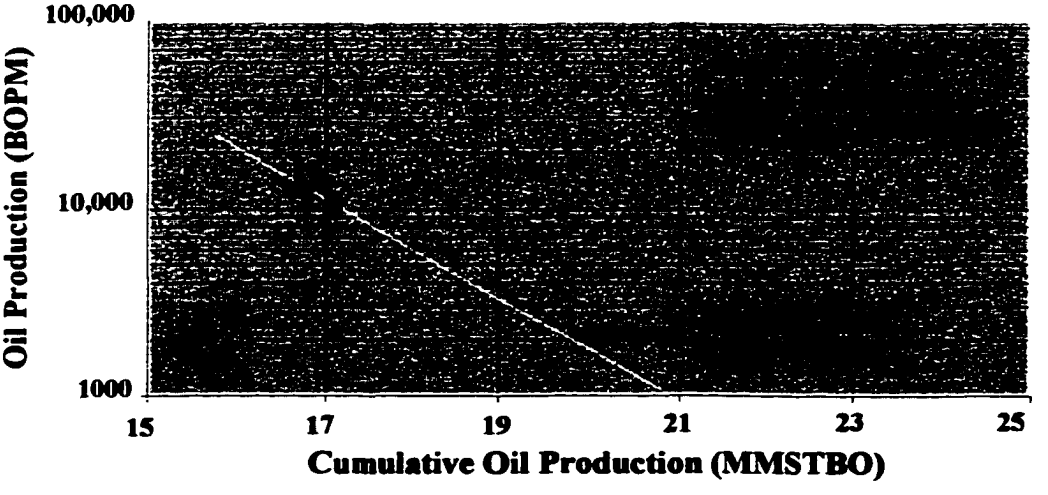

Figure 99. Decline curve analysis for the West Jordan unit. Semi-log plots of exponential curve fits through two models were constructed (A and D). Hyperbolic declines were calculated for exponents of 0.8 and 2.0 for each model to estimate gross ultimate recovery factors (GUR). Hyperbolic curves are believed to be more realistic due to the recognition that reservoirs tend to have a hyperbolic decline toward the end of secondary recovery versus an exponential decline during primary recovery. For this reason the decline curve analysis method using hyperbolic declines is considered more accurate than exponential curves for estimating GUR values in both methods 1 and 2. Decline analysis curves used for this method are considered conservative based on the overall flattening of the decline curve over the last six years of production within the unit. The drop in production at the end of the curve is reflective of cost cutting measures applied during low oil prices in 1998 and 1999.

MODEL 1

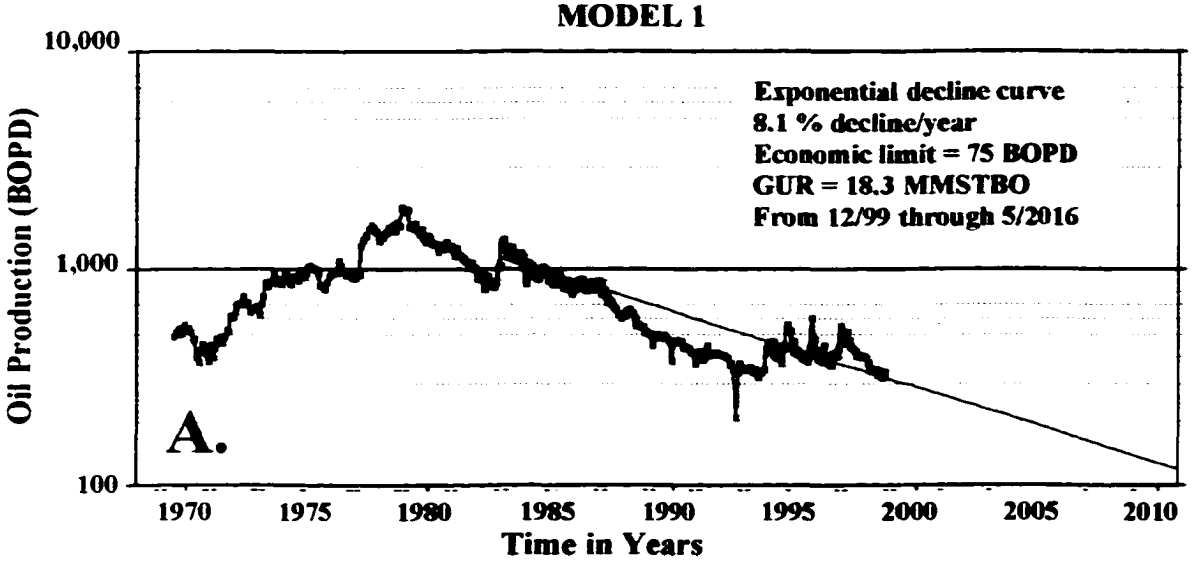
Exponential decline curve
8.1 % decline/year
Economic limit = 75 BOPD
GUR = 18.3 MMSTBO
From 12/99 through 5/2016
A.
Oil Production (BOPD)
10,000
1,000
100
1970
1975
1980
1985
1990
1995
2000
2005
2010
Time in Years

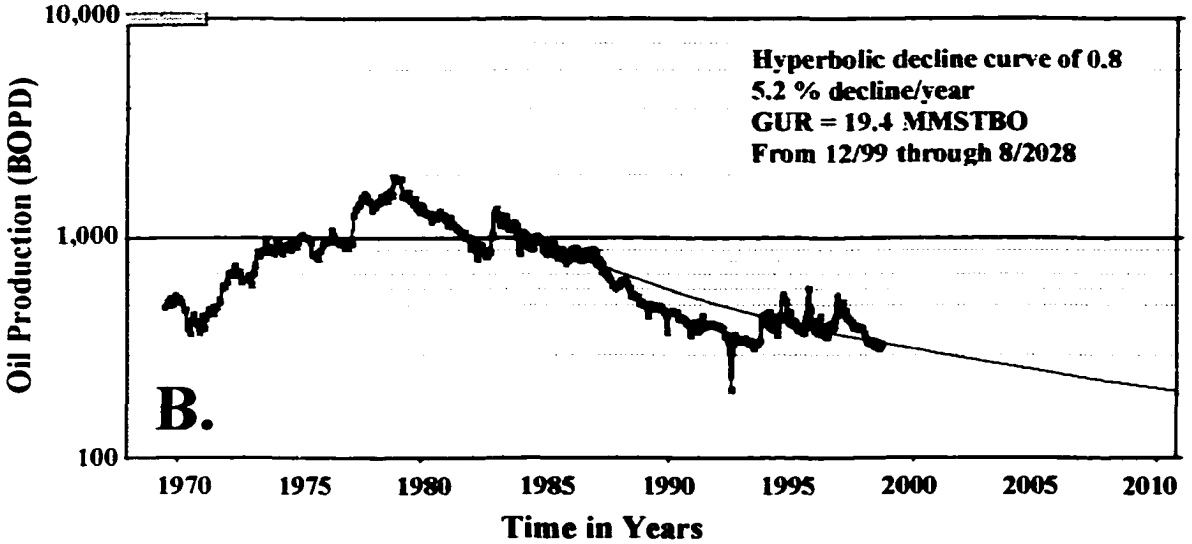
Hyperbolic decline curve of 0.8
5.2 % decline/year
GUR = 19.4 MMSTBO
From 12/99 through 8/2028
B.
Oil Production (BOPD)
10,000
1,000
100
1970
1975
1980
1985
1990
1995
2000
2005
2010
Time in Years

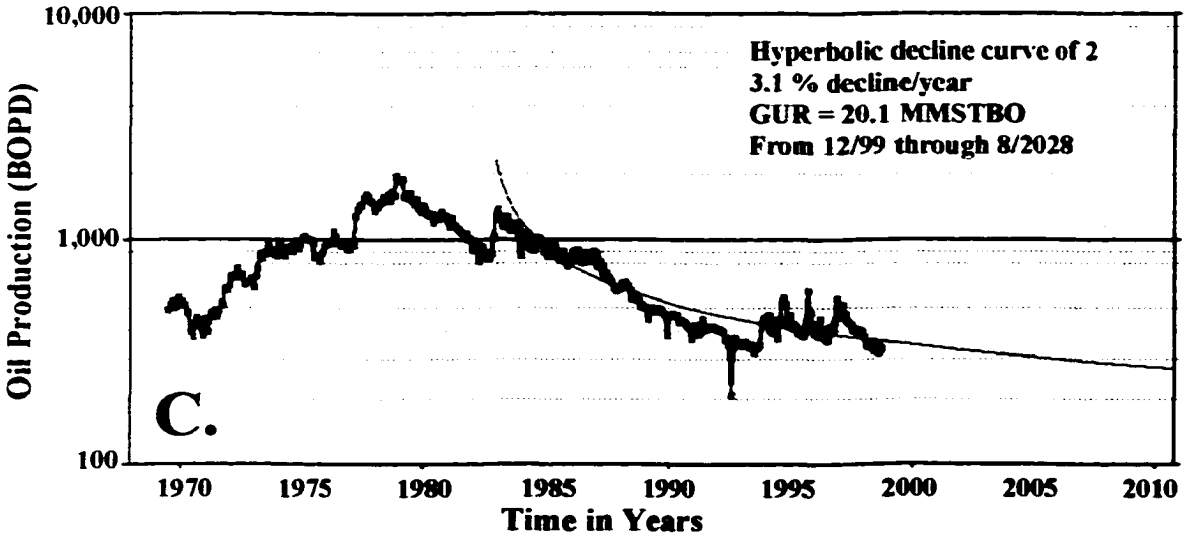
Hyperbolic decline curve of 2
3.1 % decline/year
GUR = 20.1 MMSTBO
From 12/99 through 8/2028
C.
Oil Production (BOPD)
10,000
1,000
100
1970
1975
1980
1985
1990
1995
2000
2005
2010
Time in Years

RVE ANALYSIS FOR THE WEST JORDAN UNIT

curve
BOPD
BO
5/2016

2005 2010

urve of 0.8
BO
8/2028

2005 2010

urve of 2
BO
8/2028

2005 2010

MODEL 2

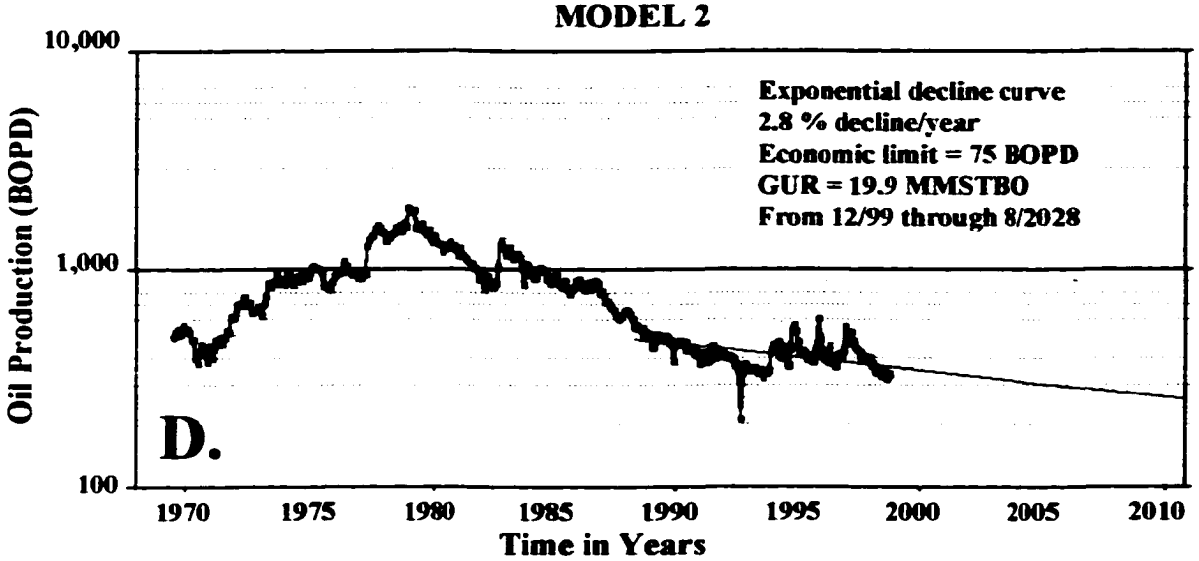

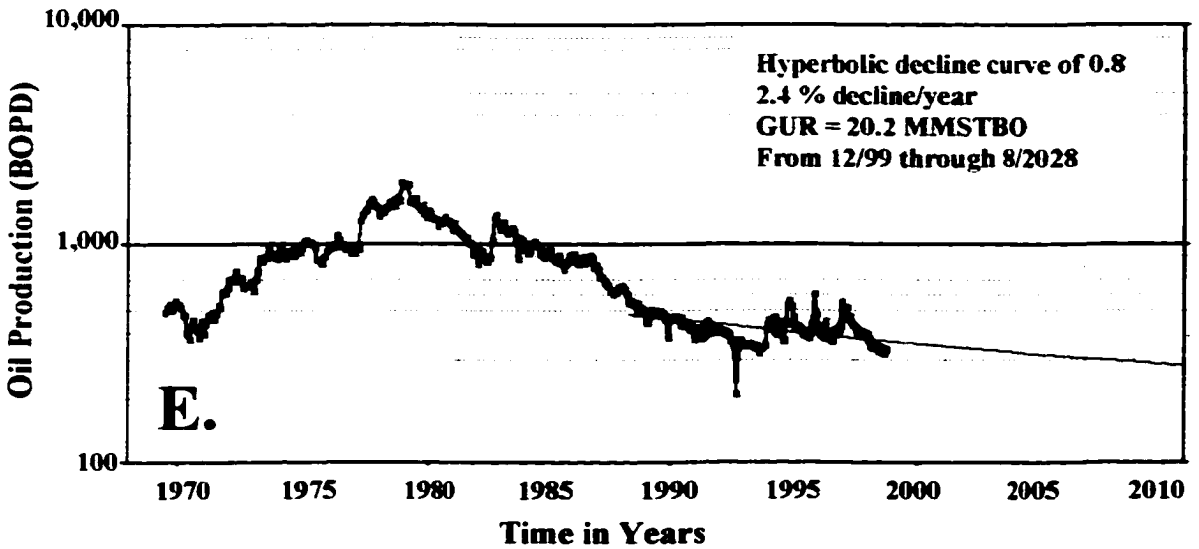

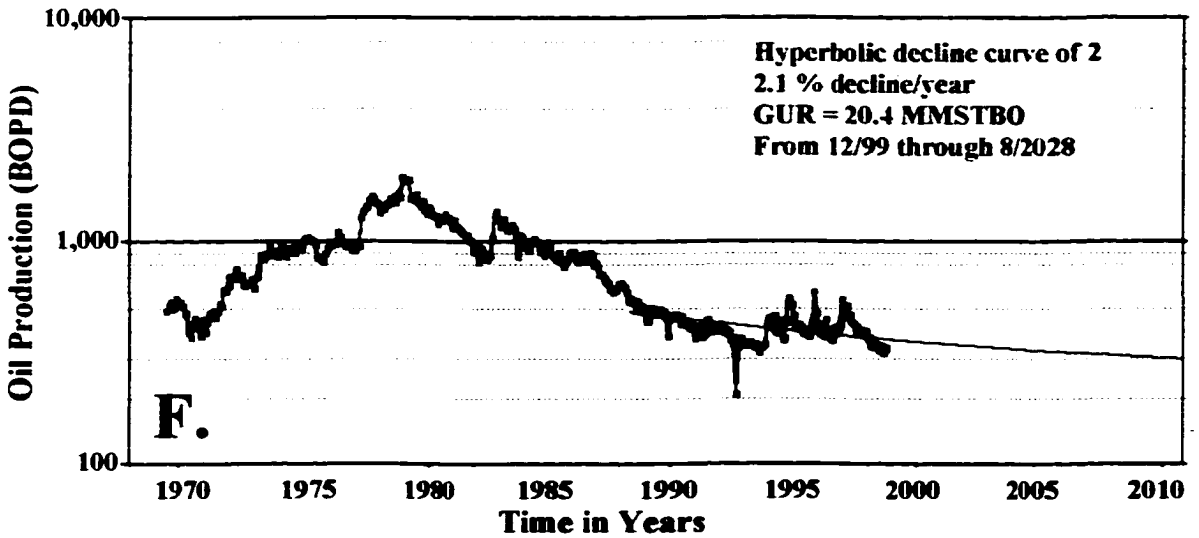

TABLE 3 - WEST JORDAN UNIT OIL RECOVERY SUMMARY

Primary Recover (to 6/1/69)	
Total production prior to unitization	**8,922,166 STOB**
Secondary Recover (6/1/69 to 12/1/99)	**8,297,958 STOB**
Gross Ultimate Recovery (as of 12/1/99)	**17,220,124 STOB**

CALCULATED RECOVERY FACTORS FROM THE GEOSTATISTICAL MODEL USING A 0.1 MILLIDARCY CUTOFF WHERE:

Original Oil in Place (OOIP)	**57,010,138 STOB**
Primary Recovery Efficiency (Rp)	**15.7%**
Secondary Recover Efficiency (Rs)	**14.6%**
Gross Ultimate Recovery (GUR)	**30.2%**

TOTAL OIL RECOVERY ESTIMATIONS FOR PRIMARY AND SECONDARY WATERFLOOD PROGRAM

METHODS	GUR (MMSTBO)	Recovery Factor (%)
I. Geostatistical 0.5 Millidarcy Flow Model	**21.9**	**38.45**
II. Oil Production versus Cumulative Production Curves	**GUR (MMSTBO)**	**Recovery Factor (%)**
A. From 1/1980 to 12/1999	**21.8**	**38.24**
B. From 1/1990 to 12/1999	**22.3**	**39.12**
C. From 1/1995 to 12/1999	**19.7**	**34.56**
III. Decline Curve Analysis	**GUR (MMSTBO)**	**Recovery Factor (%)**
A. Exponential decline 8.1 %/yr	**18.3**	**32.10**
B. Hyperbolic decline 5.2 %/yr	**19.4**	**34.03**
C. Hyperbolic decline 3.1 %/yr	**20.1**	**35.26**
D. Exponential decline 2.8 %/yr	**19.9**	**34.91**
E. Hyperbolic decline 2.4 %/yr	**20.2**	**35.43**
F. Hyperbolic decline 2.1 %/yr	**20.4**	**35.78**
Average of Recovery Estimates From Above	**20.4**	**35.79**

its GUR of 21.92 MMSTBO. As seen in table 4A the majority of the unrecovered oil, 32.69 percent, is present in zone IV-A. Other tertiary techniques will have to be utilized in order to recover oil within these tighter zones.

The second method used to predict oil recovery values was analysis of oil production versus cumulative production (fig. 98). Gross ultimate recovery estimations are determined by an exponential fit of monthly oil production versus cumulative production on a semi-log plot. Three different semi-log plots were constructed to measure total GUR values represented from different time periods of production in order to determine the precision of this method. This method resulted in a GUR values of 21.8, 22.3, and 19.7 MMSTBO for A, B, and C respectively (fig. 96). Decline rates ranged from 9 percent to 15.8 percent per year and recovery factors were between 34.56 and 38.24 percent. GUR values and recovery factors for all methods are provided in table 3.

The third method used to estimate GUR for the unit was decline curve analysis. Production data for the unit since the initiation of the waterflood in late 1969 was plotted versus time on a semi-log scale. Two exponential decline curves, models 1 and 2 were fit through data points to give reasonable representations of the data (fig. 99 A and D). Hyperbolic decline curves with exponents of 0.8 and 2.0 were then calculated for each of the two curve fits (models 1 and 2) to determine a realistic range of GUR values from the production data. Model 1, using data from 1983 forward, has higher decline rates per year than model 2 that incorporates data from 1987 forward. The hyperbolic decline curve with an exponent of 2 for both models results in higher GUR values than the exponent of 0.8.

Reservoirs tend to move from an exponential decline under primary production to hyperbolic decline during secondary production stages (Hinterlong, verbal communication, 2000). For this reason the decline curve analysis method using hyperbolic declines is considered more accurate than exponential curves for estimating GUR values in both methods 1 and 2. From 1993 to 1997 production within the unit had become relatively flat (fig. 99). Low oil prices during 1998 and 1999 resulted in decreased production within the unit due to cost cutting measures. Decline analysis curves used for method 3 are considered conservative based on the overall flattening of decline within the unit over the last six years of production.

The average GUR and recovery factor for all methods are 20.4 MMSTBO and 35.79 percent, respectively. This average recovery factor was multiplied by OOIP values from the 0.1 millidarcy geostatistical model to determine remaining OOIP for each zone based on the average of all methods (Table 4 B). These values were then compared to remaining oil in place determined from GUR values in the 0.5 millidarcy geostatistical model (table 4 A versus 4 B). Remaining oil in place calculated from the average recovery shows more oil remaining in zone IV-E1 and IV-E2 and less in zone IV-A than the 0.5 millidarcy cutoff model. The 0.5 millidarcy model is considered to be more accurate based on knowledge of the rock fabric, petrophysical characteristics of the cycle boundaries and results of the geostatistical models. Nevertheless, an average recovery factor based on methods II and III (table 3) can be applied as a fairly accurate method of calculating remaining oil in place in the absence of geostatistical analysis.

TABLE 4

A. REMAINING OIL IN PLACE BY ZONE CALCULATED FROM GEOSTATISTICAL MODELS

ZONE	MODEL 1 OOIP of the 0.1 md Model	MODEL 2 GUR of the 0.5 md Model	Remaining OOIP MODEL 1 - MODEL 2	Remaining OOIP (MMSTBO)	Remaining OOIP (Percent)
Zone I	298598.1469	297032.6067	1,565.54	0.00	0.00
Zone II	10834072.46	5074030.198	5,760,042.26	5.76	16.42
Zone III	562181.6517	86868.38672	475,313.27	0.48	1.35
Zone IV-A	12023081.11	552673.8591	11,470,407.25	11.47	32.69
Zone IV-B	3216306.791	111726.1097	3,104,580.68	3.10	8.85
Zone IV-C	7491606.038	1299436.514	6,192,169.52	6.19	17.65
Zone IV-E1	14897145.55	8473237.9	6,423,907.65	6.42	18.31
Zone IV-E2	7687145.822	6028360.567	1,658,785.26	1.66	4.73
TOTAL	57010137.57	21923366.14	35,086,771.43	35.09	100.00

B. REMAINING OIL IN PLACE BY ZONE CALCULATED FROM AVERAGE RECOVERY FACTOR OF ALL METHODS

ZONE	MODEL 1 OOIP 0.1 md Model	Average Recovery Factor (Ra) from Methods I-III (35.79%)	Remaining OOIP MODEL 1 - Ra	Remaining OOIP (MMSTBO)	Remaining OOIP (Percent)
Zone I	298598.1469	106868.2768	191,729.87	0.19	0.52
Zone II	10834072.46	3877514.532	6,956,557.92	6.96	19.00
Zone III	562181.6517	201204.8132	360,976.84	0.36	0.99
Zone IV-A	12023081.11	4303060.73	7,720,020.38	7.72	21.09
Zone IV-B	3216306.791	1151116.201	2,065,190.59	2.07	5.64
Zone IV-C	7491606.038	2681245.801	4,810,360.24	4.81	13.14
Zone IV-E1	14897145.55	5331688.393	9,565,457.16	9.57	26.13
Zone IV-E2	7687145.822	2751229.49	4,935,916.33	4.94	13.48
TOTAL	57010137.57	20403928.24	36,606,209.33	36.61	100.00

THREE DIMENTIONAL VISUALIZATION OF THE WEST JORDAN UNIT AND RECOMMENED ACTIONS FOR RESERVOIR RECOVERY IMPROVEMENT

Three-Dimensional Visualization Models

Three-dimensional models were built to better visualize reservoir compartmentalization within the West Jordan unit. Accurate determination of reservoir compartmentalization is fundamental to defining methods for improving waterflood performance within the reservoir. Three-dimensional models were created in Stratigraphic Geocellular Modeling (SGM) software a product of Stratamodel, Incorporated and EarthVision, a product of Dynamic Graphics Incorporated. EarthVision was found to be a more powerful tool for defining and viewing compartmentalization within the reservoir.

The comparison of porosity and permeability geobodies created in EarthVision provided an excellent method for visualizing compartmentalization within the reservoir. The creation of geobodies allowed for detailed analysis of porosity and permeability three-dimensional grids created in GriSTAT. The distribution of porosity using a 10 percent cutoff illustrates the pore space available within the reservoir for containment of oil (fig. 100). Even using a porosity cutoff of 12 percent illustrates the capacity of the San Andres to contain large volumes of oil (fig. 101). The problem lies in extracting that oil from tight dolomitized carbonates. As original oil in place calculations have shown, only slightly over 30 percent of the oil in place within the unit has been recovered under combined primary and secondary waterflood programs as of December 1999. Most of this oil has come from permeable zones defined by geobodies represented in the

Figure 100. Diagrams of porosity geobodies generated with a 10 percent porosity cutoff from the geostatistical model. Note that a large volume of pore space is available throughout the reservoir for the storage of oil. Although the reservoir shows lateral and vertical discontinuities within these geobodies a considerable amount of lateral continuity is present. This can be misleading when modeling a reservoir based on porosity attributes.

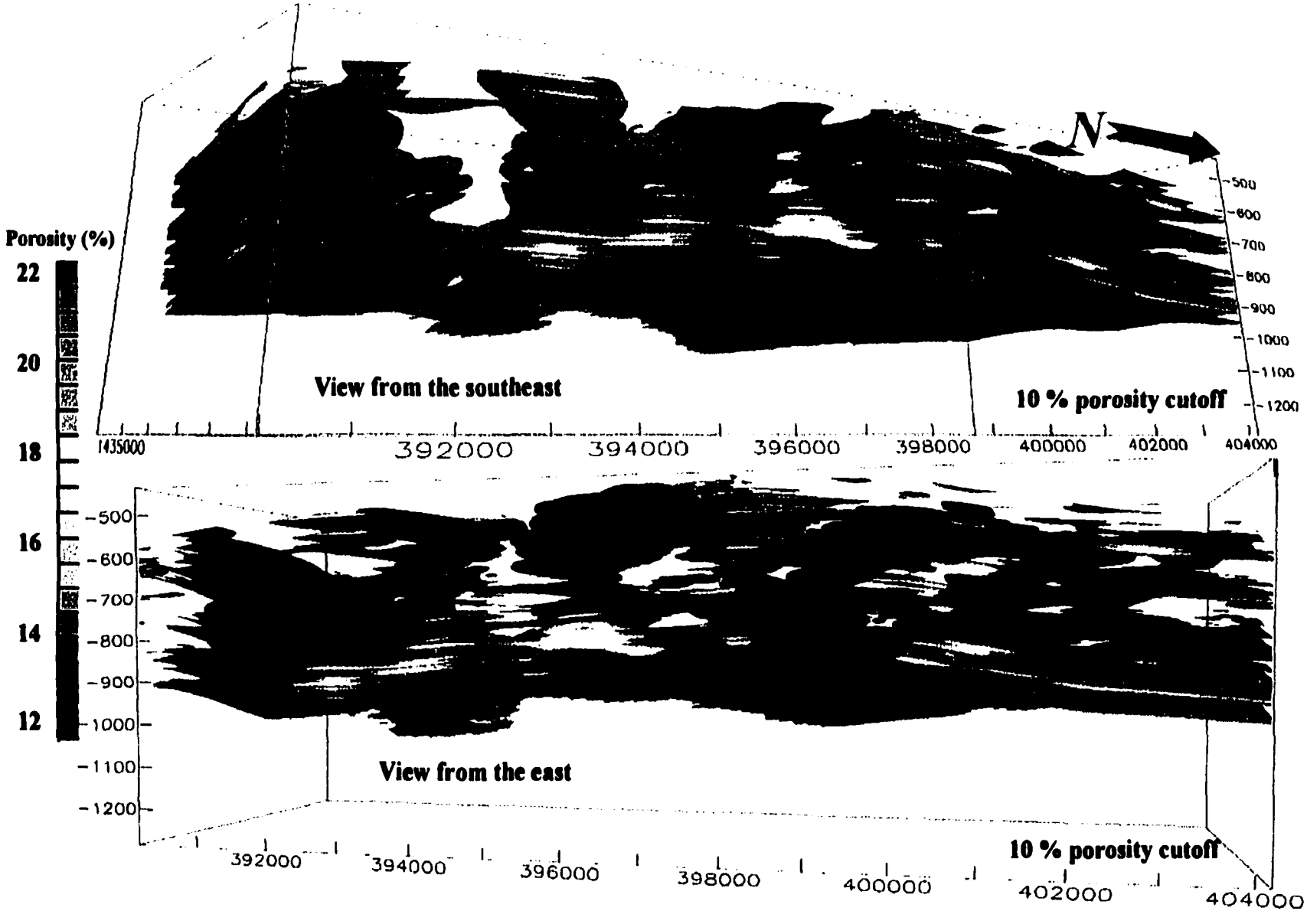
Porosity (%)
22
20
18
16
14
12
N
View from the southeast
10 % porosity cutoff
1435000
392000
394000
396000
398000
400000
402000
404000
500
600
700
800
900
1000
1100
1200
View from the east
10 % porosity cutoff
392000
394000
396000
398000
400000
402000
404000
-500
-600
-700
-800
-900
-1000
-1100
-1200

Figure 101. A diagram of porosity geobodies generated with a 12 percent porosity cutoff from the geostatistical model. Reservoir compartmentalization is more evident when using this higher porosity cutoff. This geobody model does not delineate accurately areas of the reservoir that are being effectively produced under waterflood, as does the permeability model.

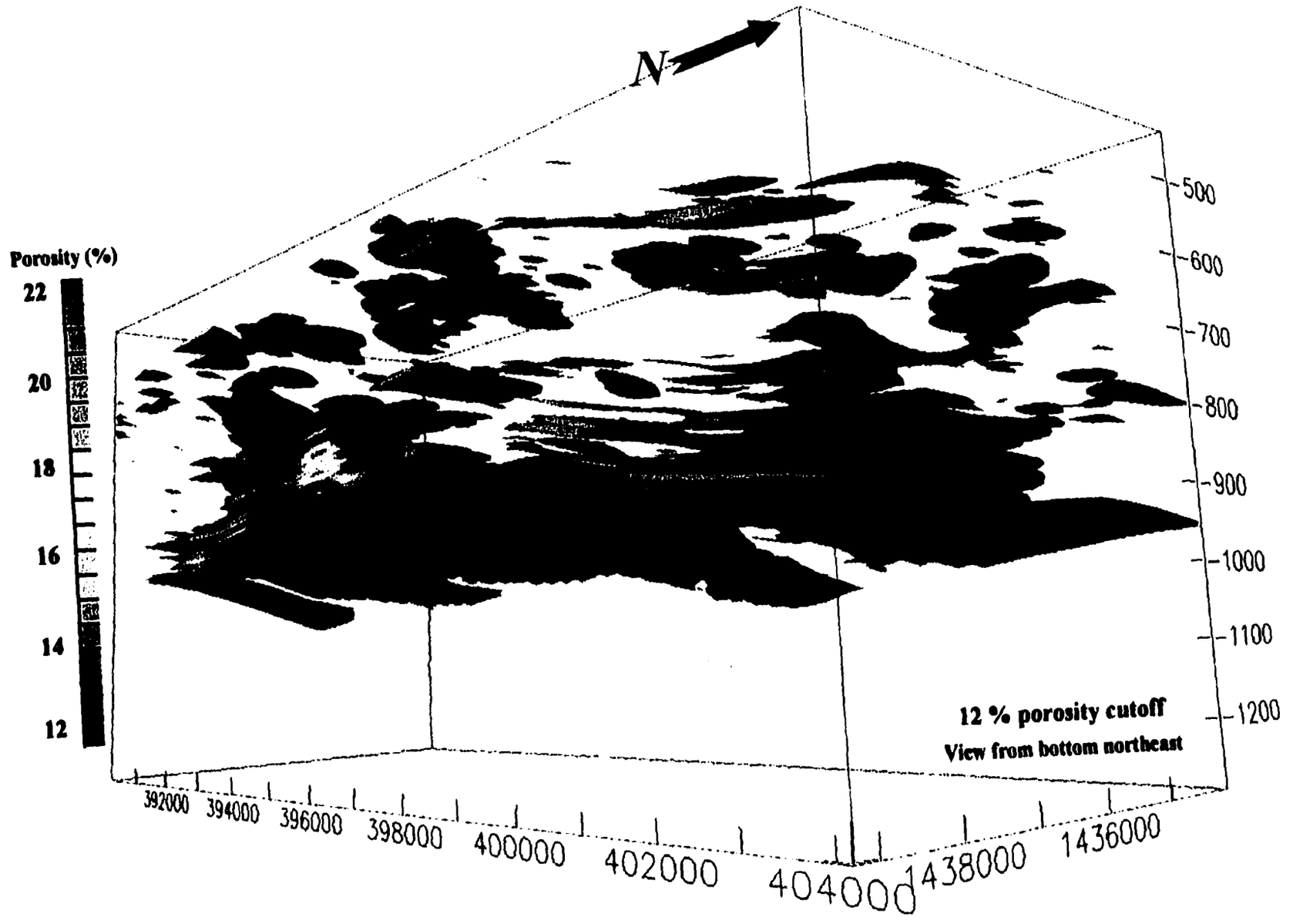
N
Porosity (%)
22
20
18
16
14
12
500
600
700
800
900
1000
1100
1200
12 % porosity cutoff
View from bottom northeast
392000
394000
396000
398000
400000
402000
404000
1438000
1436000

permeability model (figs. 102 and 103). These geobodies show areas within the reservoir that are being swept under secondary waterflood techniques. Geobody distribution illustrates the lack of vertical and horizontal continuity for both porosity and permeability attributes. The stacked nature of shoal bodies within the lower zones of the reservoir is evident from looking at geobodies of permeability (figs. 102 and 103).

By plotting well perforation data, continuity between injection and producing wells and the effectiveness of well drainage patterns can be easily visualized. A lack of continuity between injection and producing wells is common within the West Jordan unit. Injectors often are perforated at the base of one cycle boundary and nearby producers are perforated at the top of the underlying cycle boundary. Cycle boundaries act as permeability barriers to flow because changing water depths resulted in deposition of more mud-rich facies. The models of porosity and permeability geobodies show clearly a sufficient amount of vertical and lateral compartmentalization produced by cycle boundaries to cause waterflood performance problems. Perforations in one cycle are highly unlikely to result in waterflood sweep of another cycle.

Wells should also be examined to determine if they have been completed to the maximum depth of pay above the oil-water contact. The visualization was very useful in determining anomalous areas of low production. These areas were often identified as wells that had been shut in or plugged and abandoned because of completion problems or an excess of water production following large fracture treatments near the oil-water contact and may indicate potential infill drilling locations.

Figure 102. A diagram of permeability geobodies generated with a 0.5 millidarcy permeability cutoff from the geostatistical model. This model closely resembles the cumulative production patterns of the West Jordan unit since initiation of the waterflood. Note the considerable compartmentalization that occurs laterally and vertically within the reservoir and the stacked nature of the shoal bodies. Porosity seen within the upper part of the reservoir in the lower diagram is from fenestral pores within zone II. Little permeability is present in the rocks deposited in the middle ramp environments (zones IV-A and IV-B, and the upper part of zone IV-C).

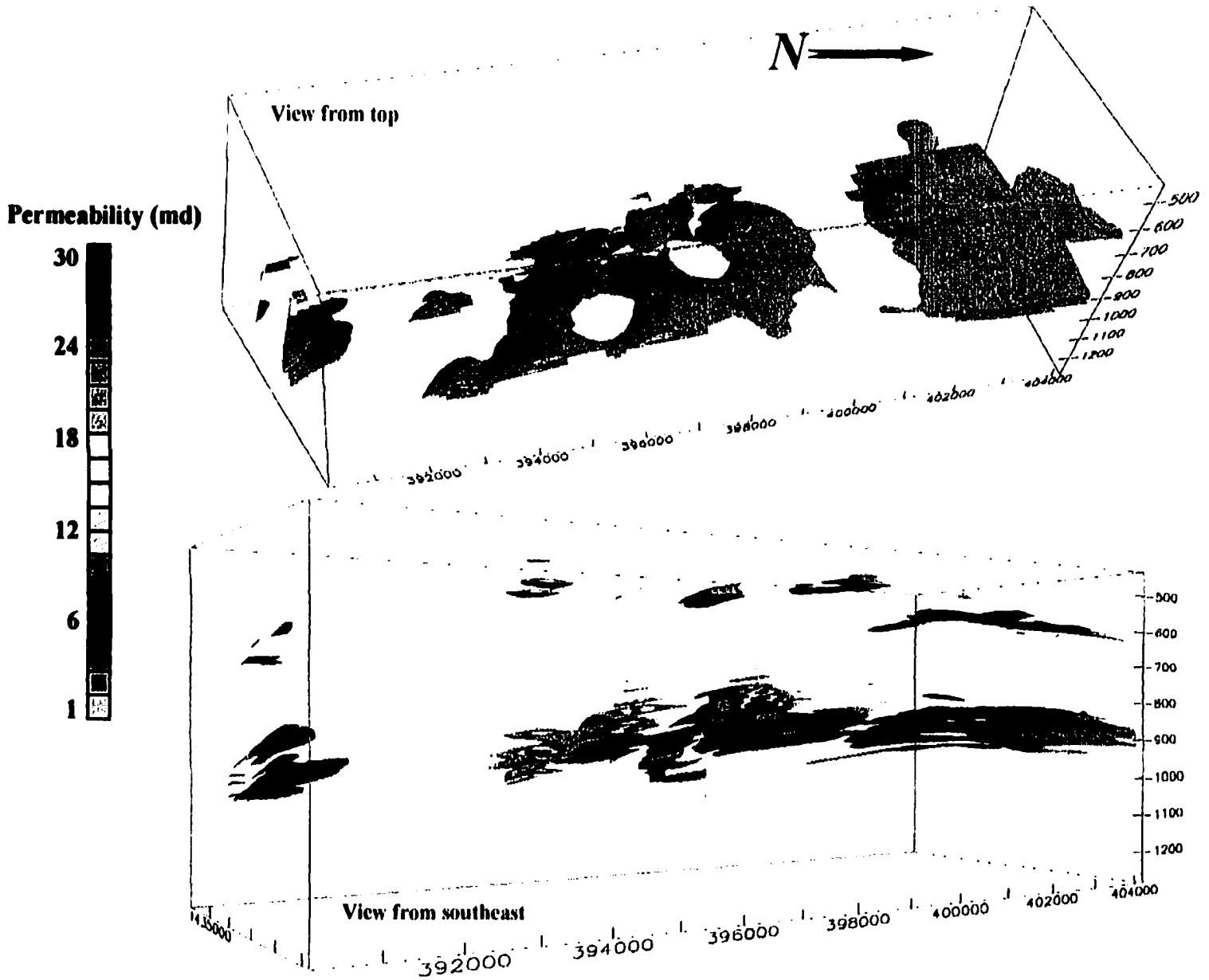
Permeability (md)
30
24
18
12
6
1
N
View from top
392000
394000
396000
398000
400000
402000
404000
500
600
700
800
900
1000
1100
1200
View from southeast
392000
394000
396000
398000
400000
402000
404000
500
600
700
800
900
1000
1100
1200

Figure 103. A diagram of permeability geobodies viewed from the bottom southeast and generated with a 0.5 millidarcy permeability cutoff from the geostatistical model. A lack of continuity was found between many injection and producing wells within individual shoal bodies. This is a main cause for inefficient waterflood sweep within the lower productive zones of the reservoir.

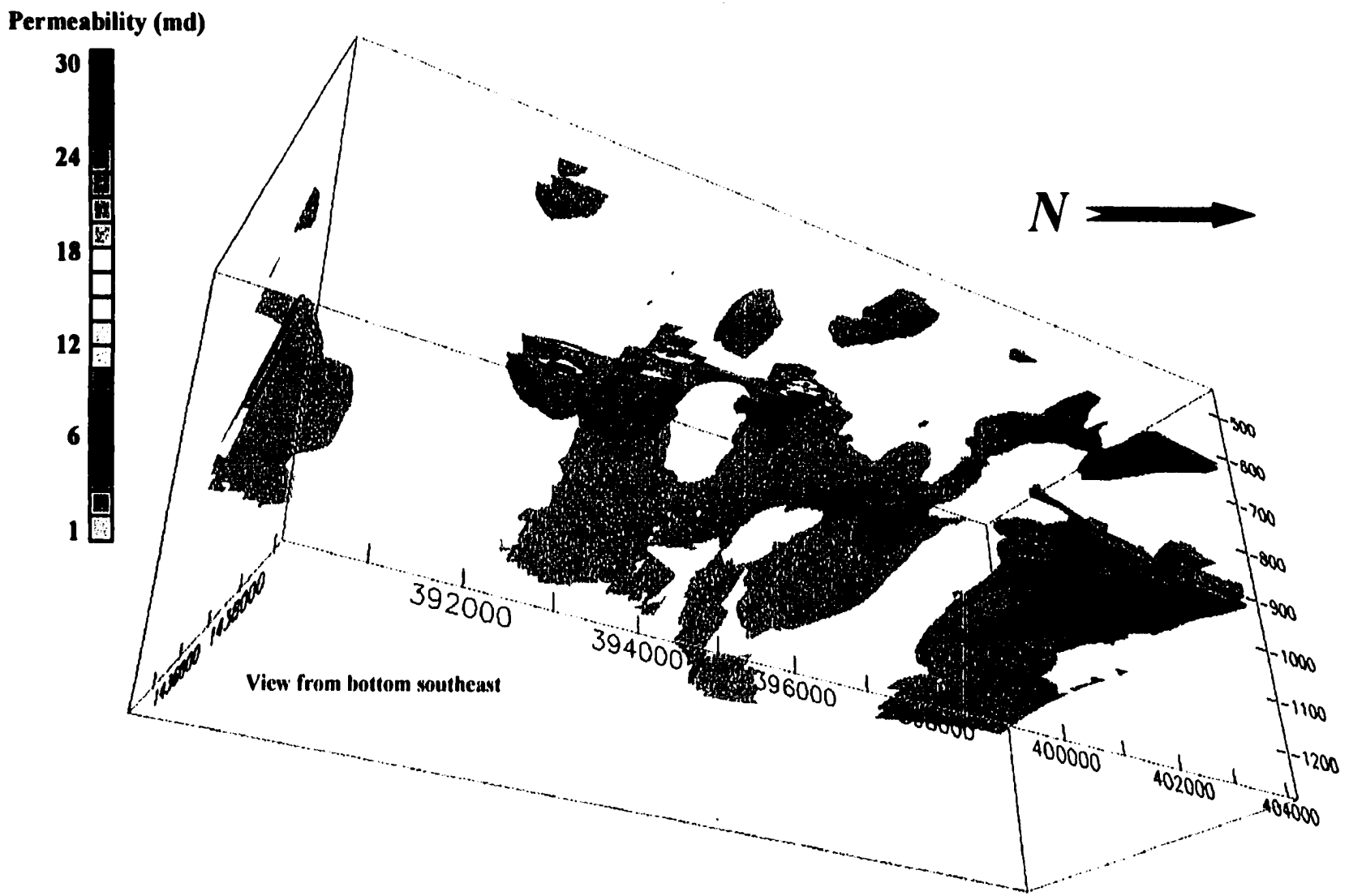
Permeability (md)
30
24
18
12
6
1
N
392000
394000
396000
400000
402000
404000
500
600
700
800
900
1000
1100
1200
View from bottom southeast

Recommendations for Waterflood Improvement

The first issue that should be addressed within the West Jordan unit is the lack of flow unit continuity between injection and producing wells. Injection patterns should be determined to connect injection wells to producing wells within permeable geobodies within the same cycle. An earlier inverted nine-spot waterflood pilot program was a failure because injection and producing wells were improperly placed relative to productive shoal bodies and non-productive intershoal areas.

Analysis of cumulative production patterns, geostatistical models, and detailed core examination has determined that fractures and stylolites within zone IV-A are channeling over 32 percent of the injection water through the reservoir without effectively sweeping matrix porosity. Channeling of water through this "thief zone" must be eliminated before an efficient waterflood can be achieved. This will be a daunting task because old casing and large fracture treatments may have propagated fractures out of zone.

A number of wells were found that could be deepened to contact shoal bodies or to contact more reservoir pay within an already penetrated shoal. This should be done with caution to remain above the –875 feet subsea elevation that represents the oil-water contact for the reservoir. Completion techniques should insure that fracture stimulation does not extend below this depth. Large fracture completion jobs have resulted in the plugging of several wells (WJU #.s 503, 506 and 602) that had potential pay (fig. 43). Nearby wells (WJU # 403, 501, 507, and 601) that are structurally lower have been

economic wells within the reservoir. Wells that have been identified for potential deepenings are listed in Table 5.

Infill drilling may be an option near wells that have been shut in due to completion problems such as the WJU # 1413 and 1406 wells. In addition, a large portion of the central shoal body area (fig. 43) does not appear to be adequately drained because the WJU #.s 1303, 1402 and 1412 wells are shut in. Although this may be advantageous to the neighboring Jordan University unit it appears to be an area of potential for the West Jordan unit. Geobody analysis shows that shoal bodies within the lower zones are vertically compartmentalized in a stacked nature as seen in outcrop photos and depositional environment models (figs. 42, 44, and 45). Directional laterals from existing wellbores have the potential to penetrate stacked, compartmentalized shoal bodies thus providing increased pay.

Because no resistivity data is available prior to waterflood and because production data for individual zones is not available, it is not possible to directly calculate remaining hydrocarbons in place for each zone within the reservoir. Nevertheless, reserve estimates based on methods described in the last section have identified zones that still contain large volumes of oil in place, particularly zone IV-A. Producing this oil will require favorable economics for alternative tertiary recovery techniques not yet being employed within the West Jordan unit. Possible tertiary recovery techniques include: horizontal laterals; carbon dioxide (CO_2) miscible floods; the combination of horizontal wells in conjunction with polymer floods; and microbial enhanced recovery which is being studied as a possible application in the adjoining Penwell unit. Tertiary recovery projects

on nearby units should be evaluated for their economic recovery of additional oil from the West Jordan unit.

TABLE 5

WEST JORDAN UNIT WELL CANDIDATES FOR DEEPENING

Priority deepening candidates: Central shoal area and structural high

#605	3680' to 3710'
#606	3670' to 3700'
#613	3670' to 3700'
#612	3664' to 3710'
#1301	3675' to 3705'
#1302	3565' to 3700'

Marginal candidates: Northern shoal area

#302	3650' to 3710'
#403	3662' to 3700'
#404	3660' to 3720'
#501	3630' to 3710'
#504	3657' to 3700'
#605	3680' to 3710'
#613	3670' to 3700'

Marginal candidates: Southern shoal area

#1411	3650' to 3710'
#1423	3682' to 3710'
#1502	3650' to 3685'
#1504	3623' to 3685'
#1507	3630' to 3690'
#1508	3620' to 3690'
#1602	3580' to 3685'
#1702	3545' to 3685'

CONCLUSIONS

1. The two most critical variables in defining reservoir flow properties are accurate chronostratigraphic correlations and a detailed knowledge of pore types and their distribution within the reservoir.
2. Pore types within the reservoir vary substantially from cycle to cycle, however, individual cycles were found to be dominated by one primary pore type. These pore types control flow within the unit, each exhibiting vastly different petrophysical behaviors that further compartmentalize the reservoir based on cycle boundaries.
3. Predictive tools related to chronostratigraphic relationships seen within the West Jordan unit can be applied to all San Andres reservoirs along the eastern margin of the Central Basin platform in order to better understand the nature of compartmentalization occurring within these fields.
4. Significant chronostratigraphic cycle boundaries have been defined within this study that will allow for the prediction of productive shoal facies within similar San Andres reservoirs along the eastern margin of the platform.
5. Productive shoal bodies are seen in outcrop and within this study to develop at the culmination of a high frequency sequence (HFS I within the West Jordan unit) marking a highstand systems tract (HST 1 for the unit) across the platform areas.
6. Depending on local paleotopography, position on the platform margin, and associated water depths, shoals may be found to develop in other fields at the top of highstand systems tract 2 as well as HST 1.

7. As evidenced from outcrop and within this study, development of shoals bodies during the culmination of the highstand systems tract produces vertically and laterally discontinuous geometries resulting in considerable compartmentalization of the reservoir within these ramp crest facies tracts. These geometries are the effect of available accommodation space associated with HST 1.
8. The level of compartmentalization seen within the West Jordan unit should be present within most if not all San Andres reservoirs along the platform. A thorough understanding of this reservoir compartmentalization is needed to adequately and economically develop these fields.
9. Stacked shoal body geometries are found to be between five and thirty feet thick in the vertical direction and to extend from one thousand to four thousand feet laterally. Non permeable intershoal mud-flat and tidal channel facies compartmentalized productive shoal facies in both the lateral and vertical direction.
10. Ramp crest facies tracts where productive shoal facies occur are seen in outcrop and within the West Jordan unit to develop behind middle ramp facies tracts, the product of a well-formed lagoonal environment. Cycles within middle ramp facies tracts contain a predominance of moldic pore types and were found to lack permeability.
11. Diagenetic features influencing porosity and permeability development are also believed to be related to the culmination of highstand systems tracts. Sulfate occlusion of pore throats and solution enhanced porosity both occur during periods of highstand within the reservoir and suggest that water depths during these periods had a significant control on diagenetic processes within associated cycle boundaries. This

lends another area of predictability to understanding diagenetic complexities of San Andres reservoirs along the eastern margin of the Central Basin platform.

12. The association of increased crystal size, porosity, and permeability within HFS I can be used as a predictive tool for other San Andres reservoirs along the Central Basin platform. Several workers within the area have now documented the relationship of increased crystal size with depth suggesting this is a common characteristic of the San Andres along platform margins of the Permian basin.
13. Geostatistical and cumulative production pattern analysis indicate that a minimum permeability value of 0.5 millidarcies is needed for flow within the reservoir under secondary waterflood conditions. The majority of strata within the reservoir containing consistent permeability values greater than 0.5 millidarcies are found in zones IV-E2, IV-E1 and II.
14. The primary flow units within the West Jordan unit are compartmentalized shoal bodies within zones IV-E2 and IV-E,1exhibiting well-developed intercrystalline porosity. Zone II is also considered a flow unit within the reservoir, although to a lesser extent.
15. Zone IV-A acts as a waterflood "thief zone" within the unit, channeling over 32 percent of injection water through fractures and large amplitude stylolite seams without contacting matrix porosity. Zones I and IV-C are considered flow barriers within the reservoir.
16. Core data is a necessity for understanding San Andres carbonates. Core data is essential to chronostratigraphic correlations defining cycle boundaries within these

reservoirs. Accurate characterization of these reservoirs cannot be completed without adequate core data distributed throughout the reservoir.

17. For these reservoirs to be produced in the most efficient and economic manner, reservoir characterization studies should be implemented early in the field discovery prior to secondary recovery programs.
18. A thorough understanding of the reservoir during early development can eliminate potential damage to the reservoir such as large fracture treatments that go out of zone resulting in uneconomic wells due to water production.

REFERENCES

Adams, D. C., and G. R. Keller, 1993, Possible extension of the Midcontinent Rift in West Texas and eastern New Mexico, Canadian Journal of Earth Science, v. 31, p. 709-720.

Adams, J. E., and nine others, 1939, Standard Permian section of North America: American Association of Petroleum Geologists Bulletin, v. 23, p. 1673-1681

Adams, J. E., and Rhodes, M. L., 1960, Dolomitization by seepage refluxion: American Association of Petroleum Geologists Bulletin, v. 44, no. 12, p. 912-920.

Arbenz, J. K., 1989, The Ouachita system, *in*, The Geology of North America, Vol. A, The Geology of North America – An overview, Geological Society of America, p. 371-396.

Asquith, G. B., 1986, Handbook of log evaluation techniques for carbonate reservoirs: AAPG Methods in Exploration, Series No. 5, 47 p.

Asquith, G. B., 1995, Determining carbonate pore types from petrophysical logs *in* Carbonate facies and sequence stratigraphy: Practical applications of carbonate models: PBS-SEPM Publication 95-36, p. 69-79.

Barnaby, R. J., and W. B. Ward, 1995, Sequence stratigraphic framework, high-frequency cyclicity, and three-dimensional heterogeneity: Grayburg Formation, Brokeoff Mountains, New Mexico, in P. H. Pause and M. P. Candelaria, eds., The San Andres in outcrop and subsurface: Permian basin Section, Society Economic Paleontologists and Mineralogists Publication 95-37, p. 37-49.

Bebout D. G., J. J. Lucia, C. R. Hocott, G. E. Fogg., and G. W. Vander Stoep, 1987, Characterization of the Grayburg Reservoir, University Lands Dune Field, Crane County, Texas: Bureau of Economic Geology, Report of Investigations 168, 98 p.

Bebout D. G., and P. M. Harris, eds.,1986, Hydrocarbon reservoir studies, San Andres/Grayburg Formations, Permian Basin: Permian Basin Section, Society of Economic Paleontologists and Mineralogists Publication No. 86-26, 143 p.

Bebout D. G., and P. M. Harris,1990, Preface, *in* D. G. Bebout and P. M. Harris, eds., Geological and engineering approaches in evaluation of San Andres/Grayburg hydrocarbon reservoirs-Permian basin: University of Texas at Austin, Bureau of Economic Geology, p. iii

Bebout D. G., and ten others, 1991, Integrated characterization of Permian Basin reservoirs, University Lands, West Texas: Targeting the remaining resource for

advanced oil recovery, Bureau of Economic Geology Report of Investigations No.203, 136 p.

Bebout, D. G., F. J., Lucia, C. R. Hocott, G. E. Fogg, and G. W. Vander Stoep, 1987, Characterization of the Grayburg reservoir, University Lands Dune field, Crane County, Texas: The Bureau of Economic Geology Report of Investigations No. 168, 98 p.

Bein, A., and L. S. Land, 1982, San Andres carbonates in the Texas Panhandle: sedimentation and diagenesis associated with magnesium-calcium-chloride brines: The University of Texas at Austin, Bureau of Economic Geology Report of Investigations No.121, 48 p.

Boyd, d. G., 1958, Permian sedimentary facies, central Guadalupe Mountains, New Mexico: New Mexico Bureau of Mines and Mineral Resources Bulletin 49, 100 p.

Caldwell, C. D., K. J. Harpole, and M. G. Gerard, 1998, Reservoir characterization of the Upper Permian Grayburg Formation in preparation for a horizontal-well CO2 flood, South Cowden Unit, west Texas *in* Stoudt, E. L., D. W. Dull and M. R. Raines eds., Permian basin core workshop – DOE funded reservoir characterization projects: Permian Section, SEPM Publication No. 98-40, pages not numbered.

Carozzi, A. V., and D. Von Bergen, 1987, Stylolitic porosity in carbonates: a critical facor4 for deep hydrocarbon production: Journal of Petroleum Geology, v. 10, p. 267-282.

Choquette, P. W., and Pray, L. C., 1970, Geologic nomenclature and classification of porosity in sedimentary carbonates: American Association of Petroleum Geologists Bulletin, v. 54, p. 207-250.

Cowan, P. E., and P. M. Harris, 1986, Porosity distribution in the San Andres Formation (Permain), Cochran and Hockley Counties, Texas: American Association of Petroleum Bulletin, v. 70, p. 888-897.

Davies, D. K., R. K. Vessell, L. E. Doublet, and T. A. Blasingame, 1997b, Improved characterization of reservoir behavior by integration of reservoir performance data and rock type distributions: Fourth International Reservoir Characterization Technical Conference Proceedings, p. 645-699.

Dawson, W. C., 1988, Stylolite porosity in carbonate reservoirs abst.: American Association of Petroleum Geologists Bulletin, v. 72, p. 176.

Dedman, R. G., and S. L. Dorobek, 1993, Sequence stratigraphic relationships of the Grayburg Formation, Foster, North Cowden, and Midland Farms fields, Central Basin

platform, west Texas, *in* J. Gibbs and D. Cromwell, eds., New dimensions in the Permian Basin: west Texas Geological Society, Publication 93-93, p. 19-27.

Dickinson, W. R., 1974, Plate tectonics and sedimentation: *in* W. R. Dickinson, ed., Tectonics and sedimentation: Special Publication of the Society of Economic Paleontologists and Mineralologtists, v. 22, p. 1-27.

Dulaney, J. P., and A. L. Hadik, 1990, Geologic description of Mobil-operated units in Slaughter (San Andres) Field, Cochran and Hockley Counties, Texas: *in* D. G. Bebout and P. M. Harris, eds., Geologic and engineering approaches in evaluation of San Andres and Grayburg hydrocarbon reservoirs-Permian Basin: Bureau of Economic Geology, p. 53-74.

Dull, D. W., E. A. Horvath, and K. D. Miller, 1994, Geologic reservoir description, San Andres CO_2 project, Mabee Field: Internal Texaco Report.

Dull, D. W., 1995, Reservoir characterization and application of geostatistics to three-dimensional modeling of a shallow ramp carbonate, Mabee San Andre3s Field, Andrews and Martin Counties, Texas: *in* Stoudt, E. L., and P. M. Harris, Hydrocarbon reservoir characterization – Geologic framework and flow unit modeling, SEPM Short Course No. 34 p. 155-197.

Dunham, R. J., 1962, Classification of carbonate rocks according to depositional texture, *in* Ham, W. E., ed., Classification of carbonate rocks : American Association of Petroleum Geologists Memoir 1, p. 108-121.

Dutton, S. P., 1980a, Depositional systems and hydrocarbon resource potential of the Pennsylvanian System, Palo Duro and Dalhart Basins, Texas Panhandle: The University of Texas at Austin, Bureau of Economic Geology Geological Circular 80-8, 49 p.

Dutton, S. P., 1980b, Petroleum source rock potential and thermal maturity, Palo Duro Basin, Texas: The University of Texas at Austin, Bureau of Economic Geology Geological Circular 80-10, 48 p.

Eacmen, Jim, D. Lorenz, and D. Pfeffer, 1998, Introduction to geostatistics manual to in-house Texaco school and GridSTAT users manual, 120 p.

Ebanks, W. J., 1990, Geology of the San Andres reservoir, Mallet Lease, Slaughter Field, Hockley County, Texas: implications for reservoir engineering projects, *in* D. G. Bebout and P. M. Harris, eds., Geologic and engineering approaches in evaluation of San Andres and Grayburg hydrocarbon reservoirs-Permian Basin: Bureau of Economic Geology, p. 75-86.

Eisenberg, R. A., P. M. Harris, C. W. Grant, D. J. Groggin, and F. J. Connor, 1994, Modeling reservoir heterogeneity within outer ramp carbonate facies using and outcrop analog, San Andres Formation of the Permian Basin: AAPG Bulletin, v. 78, No. 9, p. 1337-1359.

Elam, J. G., 1967, The tectonic style in the Permian basin and its relationship to cyclicity, *in* J. G. Elam and S. Chuber, eds., Cyclic sedimentation in the Permian Basin: west Texas Geological Society Publication 69-65, p. 55-80.

Elam, J. G., 1984, Structural systems in the Permian Basin: west Texas Geological Society Bulletin, v. 24, no. 1, p,.7-10.

Elliot, L. A., and J. K. Warren, 1989, Stratigraphy and depositional environment of lower San Andres Formation in subsurface and equivalent outcrops: Chaves, Lincoln, and Roosevelt Counties, New Mexico: American Association of Petroleum Geologists Bulletin, v. 73, p. 1307-1325.

Ewing, T. E., 1990, The tectonic framework of Texas; Text to accompany "The Tectonic Map of Texas": Bureau of Economic Geology, The University of Texas at Austin, 36 p.

Fields, M. E. and J. J. Nelson, 1996, West Jordan unit workover development study and competitor analysis; In house Report, Texaco Exploration and Production Inc., Midland, Texas

Fischer, A. G., and M. Sarntherin, 1988, Airborne silts and dune-derived sands in the Permian of the Delaware Basin: Journal of Sedimentary Petrology, v. 58, p. 637-643.

Fogg, G. E., and F. J. Lucia, 1990, Reservoir modeling of restricted platform carbonates: geologic/geostatistical characterization of interwell-scale reservoir heterogeneity, Dune field, Crane County, Texas: The University of Texas at Austin, Bureau of Economic Geology Report of Investigations No. 190, 66 p.

Frenzel, H. N., and 13 others, 1988, The Permian basin Region, *in* Sloss, L. L. ed., Sedimentary Cover-North American Craton; U. S., Boulder, Colorado, Geological Society of America, The Geology of North America, v. D-2, p. 261-289.

Friedman, G. M., S. K. Ghosh, and S. Urschel, 1990, Petrophysical characteristics related to depositional environments and diagenetic overprint: A case study of the San Andres Formation, Mabee field, West Texas *in* D. G. Bebout and P. M. Harris, eds., Geological and engineering approaches in evaluation of San Andres/Grayburg hydrocarbon reservoirs-Permian basin: University of Texas at Austin, Bureau of Economic Geology, p. 125-144.

Galley, J. E., 1958, Oil and geology in the Permian basin of Texas and New Mexico, *in*, Weeks, L. G., ed., Habitat of oil – A symposium: American Association of Petroleum Geologists, p. 395-446.

Garber, R. A., and P. M. Harris, 1986, Depositional facies of Grayburg/San Andres dolomite reservoirs – Central Basin platform, Permian Bsin: *in* Bebout D. G., and P. M. Harris, eds.,1986, Hydrocarbon reservoir studies, San Andres/Grayburg Formations, Permian Basin: Permian Basin Section, Society of Economic Paleontologists and Mineralogists Publication No. 86-26, p. 61-68.

Garber, R. A., and P. M. Harris, 1990, Depositional facies of Grayburg/San Andres dolostone reservoirs, Central Basin platform, Permian Basin, *in* D. G. Bebout and P. M. Harris, eds., Geological and engineering approaches in evaluation of San Andres/Grayburg hydrocarbon reservoirs-Permian basin: University of Texas at Austin, Bureau of Economic Geology, p. 1-20.

George, D. T., 1999, personal communication, Texaco Exploration and Production, Inc., Midland, Texas

Grammer, G. M., 2000, personal communication, Texaco Upstream Technology Department.

Grant, C. W., D. J. Goggin, and P. M. Harris, 1994, Outcrop analog for cyclic-shelf reservoirs, San Andres Formation of the Permian Basin: stratigraphic framework, permeability distribution, geostatistics, and fluid-0flow modeling: American Association of Petroleum Geologists Bulletin, v. 78, p. 23-54.

Guiseppe, A. C., and R. C. Trentham, 1999, Stratigraphic framework and reservoir delineation of the McCamey field (Grayburt-San Andres), Upton County, Texas: in D. T. Grace and G. D. Hinterlong, eds., The Permian Basin: providing energy for America, West Texas Geological Society Publication, #99-106, p. 43-53.

Handford, C. R., and R. G. Loucks, 1993, Carbonate depositional sequences and systems tracts – responses of carbonate platforms to relative sea-level changes: *in* R. G. Loucks and J. F. Sarg eds., Carbonate sequence stratigraphy, recent developments and applications, American Association of Petroleum Geologists, Memoir No. 57, p. 3-41.

Hanson, B. M., B. K. Powers, C. M. Garrett Jr., D. E. McGookey, E. H. McGlasson, R. L. Horak, S. J. Mazzullo, A. M. Reid, G. G. Calhoun, J. Clendening, and B. Clayton, 1991, The Permian Basin, in H. J., Gluskoter, D. D. Rice, and R. B. Taylor, eds., Economic geology, United States: Geological Society of America, The Geology of North America, v. P-2, p. 339-356.

Harris, P. M., C. A. Dodman, and D. M. Bliefnick, 1984, Permian (Guadalupian) reservoir facies, McElroy field, West Texas, *in* Harris, P. M., ed., Carbonate sands: Society of Economic Paleontologists and Mineralogists Core Workshop No. 5, p. 136-174.

Harris, P. M., and S. D. Walker, 1990, Development geology of a dolostone reservoir, Permian Basin, West Texas: *in* D. G. Bebout and P. M. Harris, eds., Geological and engineering approaches in evaluation of San Andres/Grayburg hydrocarbon reservoirs-Permian basin: University of Texas at Austin, Bureau of Economic Geology, p. 275-296.

Harris, P. M., C. Kerans, and D. G., Bebout, 1993, Ancient and modern examples of platform carbonate cycles-implications for subsurface correlation and understanding reservoir heterogeneity, in R. G., Loucks, and J. F. Sarg, eds., Carbonate sequence stratigraphy: recent development and applications: American Association of Petroleum Geologists Memoir 57, p. 476-492.

Harris, P. M., and W. S. Kowalik, 1994, Satellite images of carbonate depositional settings: : American Association of Petroleum Geologists Methods in Exploration Series, No. 11, 147 p.

Hayes, P. T., 1959, San Andres limestone and related Permian rocks in Last Chance Canyon and vicinity, southeastern New Mexico: American Association of Petroleum Geologists Bulletin, v. 43, no. 9, p. 2197-2213.

Hayes, P. T., 1964, Geology of the Guadalupe Mountains, New Mexico: United States Geological Survey Professional Paper 446, p. 1-69.

Hill, C. A., 1990, Sulfuric acid speleogenesis of Carlsbad cavern and its relationship to hydrocarbons, Delaware basin, New Mexico and Texas: American Association of Petroleum Geologists Bulletin, v. 74, p. 1685-1694.

Hills, J. M., 1970, Paleozoic structural directions in the southern Permian Basin, west Texas and southeastern new Mexico: American Association of Petroleum Geologists Bulletin, v. 54, p. 1809-1827.

Hills, J. M., 1972, Late Paleozoic sedimentation in west Texas, Permian Basin: American Association of Petroleum Geologists Bulletin, v. 56, p. 2303-2322.

Hills, J. M., 1985, Structural evolution of the Permian basin of west Texas and New Mexico, *in*, Dickerson, P. W., and Muehberger, W. R., eds., Structure and Tectonics of Trans-Pecos Texas: west Texas Geological Society Publication 85-81, p. 89-99.

Hinrichs, P. D., F. J. Lucia, and R. L. Mathis, 1986, Permeability distribution and reservoir continuity in Permian San Andres shelf carbonates, Guadalupe Mountains,

New Mexico, *in* Bebout, D. G., and P. M. Harris, eds., Hydrocarbon reservoir studies, San Andres/Grayburg formations, Permian Basin: Permian basin Section, Society of Economic Paleontologists and Mineralogists Publication 86-26, p. 31-36.

Holtz, M. H., S. C., Ruppel, and C. R. Hocott, 1992, Integrated geologic and engineering determination of oil-reserve-growth potential in carbonate reservoirs: Journal of Petroleum Technology, v. 44, p. 1250-1257.

Holtz, M. H., and R. P. Major, 1994, Geological and engineering assessment of remaining oil in a mature carbonate reservoir: An example from the Permian Basin, west Texas *in* SPE Permian basin oil and gas recovery conference, p. 5650576.

Horak, R.L., 1985, Trans-Pecos tectonism and its effect on the Permian Basin, *in* Dickerson, P. W., and Muehberger, W. R., eds., Structure and Tectonics of Trans-Pecos Texas: west Texas Geological Society Publication 85-81, p. 81-87.

Horvorka, S. D., H. S. Nance, and C. Kerans, 1993, Parasequence geometry as a control on porosity evolution: examples from the San Andres and Grayburg Formations in the Guadalupe Mountain, *in* Loucks, R. G., and J. F. Sarg, eds., Carbonate sequecne stratigraphy: recent development and applications: American Association of Petroleum Geologists Memoir 57, p. 493-514.

Houde, R. F., 1979, Sedimentology, diagenesis, and source bed geochemistry of the Spraberry sandstone, subsurface Midland Bsin, West Texas: The University of Texas, Dallas, Unpublished Masters Thesis, 168 p.

Inden, R. F., and C. H. Moore, 1983, Beach environment, *in* Scholle, P. A, D. G. Bebout, and C. H. Moore, eds., Carbonate depositional environments: American Association of Petroleum Geologists Memoir 33, p. 268-295.

Isaaks, E. H., and R. M. Srivastava, 1989, Applied Geostatistics: Oxford University Press, Inc., 561 p.

Jones, T. S., and H. M. Smith, 1965, Relationships of oil composition and stratigraphy in the Permian basin of west Texas and New Mexico: American Association of Petroleum Geologists Memoir 4, p. 101-224.

Keller, G. R., Hills, J. M., and Djeddi, R., 1980, A regional geological and geophysical study of the Delaware Basin, New Mexico and west Texas: New Mexico Geological Society Guidebook, 32st Field Conference, Trans-Pecos Region, p. 105-111.

Keller, G. R., Lidiak, E. G., Hinze, W. J., and Braile, L. W., 1983, The role of rifting in the tectonic development of the Midcontinent U.S.A. Tectonophysics, 94, p. 391-412.

Keller, G. R., Hills, J. M., Baker, M. R., and Wallin, E. T., 1989, Geophysical and geochronological constraints on the extent and age of mafic intrusions in the basement of west Texas and eastern New Mexico: Geology, v. 17, p. 1049-1052.

Keller, G. R., 1993, Evaporite geometries and diagenetic traps, Lower San andres, Northwest Shelf, New Mexico: American Associaton of Petroleum Geologists Bulletin Southwest Section Meeting, p. 183-193.

Kerans, C., H. S. Nance, 1991, High-frequency cyclicity and regional depositional patterns of the Grayburg Formation, Guadalupe Mountains, New Mexico, *in* Meader-Roberts, Sally, Candelaria, M. P., and Moore, G. E., eds., Sequence stratigraphy, facies and reservoir geometries of the San Andres, Grayburg, and Queen Formations, Guadalupe Mountains, New Mexico and Texas: Permian basin Section, Society of Economic Paleontologists and Mineralogists Publication 91-32, p. 53-96.

Kerans, C., W. M. Fitchen, M. H. Gardner, M. D. Sonnenfeld, S. W. Tinker, and B. R. Wardlaw, 1992, Styles of sequence development within uppermost Leonardian through Guadalupian strata of the Guadalupe Mountains, Texas and New Mexico, *in* strategies: applications of sequence stratigraphic and reservoir characterization concepts: west Texas Geological Society Symposium, 92-91, p. 1-7.

Kerans, C., and S. C. Ruppel, 1994, San Andres sequence framework, Guadalupe Mountains: Implications for San Andres type section and subsurface reservoirs, *in* R. A. Garber and D. R. Keller, eds., Field Guide to the Paleozoic Section of the San Andres Mountains: Permian basin Section, Society of Economic Paleontologists and Mineralogists Publication 94-35, p. 105-115.

Kerans, C., F. J. Lucia, and R. K. Senger, 1994, Integrated characterization of carbonate ramp reservoirs using Permian San Andres Formation Outcrop Analogs: American Association of Petroleum Geologists Bulletin, v. 78, p. 181-216.

Kerans, C., and W. M. Fitchen, 1995, Sequence hierarchy and facies architecture of a carbonate-ramp system: San Andres Formation of Algerita Escarpment and Western Guadalupe Mountains, west Texas and New Mexico: The University of Texas at Austin, Bureau of Economic Geology Report of Investigations No. 235, 86 p.

King, P. B., 1942, Permian of west Texas and southeastern New Mexico: American Association of Petroleum Geologists Bulletin, v. 25, p. 535-763.

King, P. B., 1948, Geology of the southern Guadalupe Mountains, Texas: United States Geological Survey Professional Paper 215, 138 p.

King, P. E., and five others, 1942, Resume of the geology of the southern Permian Basin, Texas and New Mexico: Geological Society of America Bulletin, v. 53, p. 539-560.

Kittridge, M. G., G. L. Lake, F. J. Lucia, and G. E. Fogg, 1990, Outcrop/subsurface comparisons of heterogeneity in the San Andres Formation: Society of Petroleum Engineers Formation Evaluation, p. 233-240.

Kluth, C. F., 1986, Plate tectonics of the Ancestral Rocky Mountains, in J. A. Peterson, ed., Paleotectonics and sedimentation: American Association of Petroleum Geologists Memoir 41, p. 353-370.

Kluth, C. F., and P. J. Coney, 1981, Plate tectonics of the Ancestral Rocky Mountains: Geology, v. 9, p. 10-15.

Leary, D. A., and J. N. Vogt, 1986, Diagenesis of the San Andres Formation (Guadalupian), Central Basin platform, Permian Basin, *in* D. G. Bebout and P. M. Harris, eds., Hydrocarbon reservoir studies San Andres/Grayburg Formations, Permian Basin: Permian Basin Section, Society of Economic Paleontologists and Mineralogists Publication No. 86-26, p. 67-68.

Leary, D. A., and J. N. Vogt, 1990, Diagenesis of the San Andres Formation (Guadalupian), Central Basin platform, Permian Basin, *in* D. G. Bebout and P. M. Harris, eds., Geological and engineering approaches in evaluation of San Andres/Grayburg hydrocarbon reservoirs-Permian basin: University of Texas at Austin, Bureau of Economic Geology, p. 21-48.

Lee, W. T. and G. H.Girty, 1909, The Manzano Group of the Rio Grande Valley, New Mexico: United States Geological Survey, Bulletin 389, p. 1-141.

Lewis, F. E., 1941, Position of San Andres group, west Texas and New Mexico, American Association of Petroleum Geologists Bulletin, v. 25, p. 73-103.

Lindsey, R. F., D. L. Hendrix, R. H. Jones, C. M. Keefer, D. I. Lindsey,m S. P. McDonald, and D. J. Rittersbacher, 1992, role of sequence stratigraphy in reservoir characterization: an example from the Grayburg Formation, Permian Basin, *in* D. H. Mruk, and B. C. Curren, (eds.), Permian basin production and exploration strategies: applications of sequence stratigraphic and reservoir characterization concepts: west Texas Geological Society Symposium, p. 19-26.

Longacre, S. A., 1980, Dolomite reservoirs from Permian biomicrites, *in* R. B. Halley and R. G. Loucks, eds., Carbonate reservoir rocks: Notes for Society of Economic Paleontologists and Mineralogists Core Workshop No. 1, Denver, Colorado, p. 105-117.

Longacre, S. A., 1983, A subsurface example of a dolomitized middle Guadalupian (Permian) reef from West Texas, *in* P. M. harris, ed., Carbonate buildups: Society of Economic Paleontologists and Mineralogists Core Workshop No. 4, 304-326.

Longacre, S. A., 1990, The Grayburg reservoir, North McElroy unit, Crane County, Texas, *in* D. G. Bebout and P. M. Harris, eds., Geological and engineering approaches in evaluation of San Andres/Grayburg hydrocarbon reservoirs-Permian basin: University of Texas at Austin, Bureau of Economic Geology, p. 239-273.

Lucia, F. J., 1962, Diagenesis of a crinoidal sediment: Journal of Sedimentary Petrology, v. 32, p. 848-865.

Lucia, F. J., 1983, Petrophysical parameters estimated from visual descriptions of carbonate rocks: A field classification of carbonate pore space: Journal of Petroleum Technology, March, v. 35, p. 626-637.

Lucia, F. J., D. G. Bebout, and C. R. Hocott, 1990, Reservoir characterization through integration of geological and engineering methods and techniques: Dune (Grayburg) Field, University Lands, Crane County, Texas, *in* D. G. Bebout and P. M. Harris, eds., Geologic and engineering approaches in evaluation of San Andres and Grayburg hydrocarbon reservoirs-Permian Basin: Bureau of Economic Geology, p. 197-238.

Lucia, F. J., C. Kerans, and R. K. Senger, 1992, Defining flow units in dolomitized carbonate-ramp reservoirs: Washington, D. C., Society of Petroleum Engineers Annual Meeting, publication SPE 24702, p. 399-406.

Lucia, F. J., and R. P. Major, 1994, Porosity evolution through hypersaline reflux dolomitization, *in* B. Purser, M. Tucker, and D. Zenger, eds., Dolomites: International Association of Sedimentologists Special Publication 21, p. 325-341.

Lucia, F. J., 1995, Rock-fabric/petrophysical classification of carbonate pore space for reservoir characterization: AAPG Bulletin, v. 79, p. 1265-1300.

Lucia, F. J., 1999, Carbonate reservoir characterization; Springer-Verlag, Berlin, Heidelberg, New York, 226 p.

Majewske, O. P., 1974, Recognition of Invertebrate fossil fragments in rocks and thin sections: E. J. Brill, Leiden, Holland, 101 p.

Major, R. P., D. G. Bebout, and F. J. Lucia, 1988, Depositional facies and porosity distribution, Permian (Gaudalupian) San Andres and Grayburg formations, P. J. W. D. M. field complex, Central Basin platform, west Texas, *in* A. J. Lomando and P. M. Harris, eds., Giant oil and gas fields: a core workshop: SEPM Core Workshop 12, p. 615-648.

Major, R. P., G. W., Vander Stoep, and M. H. Holtz, 1990, Delineation of unrecovered mobile oil in a mature dolomite reservoir: East Penwell San Andres Unit, University Lands, West Texas: The University of Texas at Austin, Bureau of Economic Geology report of Investigations No., 194, 52 p.

Major, R. P., G. W., Vander Stoep, and M. H. Holtz, 1990, Geological and engineering assessment of remaining mobile oil, East Penwell San Andres unit, Ector County, Texas, *in* D. G. Bebout and P. M. Harris, eds., Geological and engineering approaches in evaluation of San Andres/Grayburg hydrocarbon reservoirs-Permian basin: University of Texas at Austin, Bureau of Economic Geology, p. 175-196.

Major, R. P., and M. H. Holtz, 1990, Depositionally and diagenetically controlled reservoir heterogeneity at Jordan field: Journal of Petroleum Technology, v. 42, no. 10, p. 1304-1309.

Major, R. P., M. H. Holtz, and R. D. Dommisse, 1992, Calibration of porosity logs and delineation of flow units in a San Andres reservoir: Keystone Field, West Texas, *in* Mruk, D. H., and Curran, B. C., eds., Permian basin exploration and production strategies: applications of sequence stratigraphic and reservoir characterization concepts: west Texas Geological Society Publication 92-91, p. 100-105.

Major, R. P., and M. H. Holtz, 1997, Predicting reservoir quality at the development scale: methods for quantifying remaining hydrocarbon resource in diagenetically complex carbonate reservoirs, *in* J. A. Kupecz, S. Bloch, and J. Gluyas, eds., Reservoir quality prediction in sandstones and carbonates: AAPG Memoir 69, p. 231-248.

Major, R. P., and M. H. Holtz, 1997, Identifying fracture orientation in a mature carbonate platform reservoir: AAPG Bulletin, v. 81, No. 7, p. 1063-1069.

Mazzullo, S. J., and P. M. Harris, 1992, Mesogenetic dissolution: its role in porosity development in carbonate reservoirs: American Association of Petroleum Geologists Bulletin, v. 76, p. 607-620.

McGlasson, E. H., 1968, The Siluro-Devonian of west Texas and southeast New Mexico, *in*, west Texas geological guidebook – Ddelaware basin: west Texas Geological Society Publication 68-55, p. 35-44.

Meissner, F. F., 1972, Cyclic sedimentation in middle Permian strata of the Permian Basin, west Texas and New Mexico, in J. G. Elam and S. Chuber, eds., Cyclic Sedimentation in the Permian basin 1st edition: west Texas Geological Society Symposium, p. 203-232.

Murray, R. C., 1960, Origin of porosity in carbonate rocks: Journal of Sedimentary Petrology, v. 30, p. 59-84.

Needham, C. E., and R. L. Bates, 1943, Permian type sections in central New Mexico: Bulletin of the Geological Society of America, v. 54, p. 1653-1667.

Peterson, F., 1988, Pennsylvanian to Jurassic eolian transportation systems in the western Unite States, *in* G. Kocurek, ed., Late Paleozoic and Mesozoic eolian deposits of the Western Interior of the United States: Sedimentary Geology, v. 56,. P. 207-260.

Pinsonnault, S. M., 1996, Sequence stratigraphy of the Upper San Andres and Grayburg Formations, Waddell Field, Crane County, Texas: implications for hydrocarbon reservoir distribution: Unpublished Masters Thesis, Texas A and M University, 94 p.

Pray, L. C., 1985, The Capitan massive and its proximal reef, Walnut Canyon area, Carlsbad Caverns National Park, New Mexico, *in* Cunnigham, B. K., and Hedrick, C. L., eds., Permian carbonate/clastic sedimentology, Guadalupe Mountains: analogs for shelf and basin reservoirs: Permian basin Section, SEPM Publication 85-24, p. 25-41.

Purser, B. H., and G. Evans, 1973, regional sedimentation along the Trucial Coast, South East Persian Gulf, *in* Purser, B. H., ed., The Persian Gulf-Holocene carbonate sedimentation and diagenesis in a shallow epicontinental sea: Berlin, Springer-Verlag, p. 211-213.

Purves, W. J., 1990, Reservoir description of the Mobil Oil Bridges State Leases (upper San Andres) reservoir, Vaccum Field, Lea County, New Mexico, *in* D. G. Bebout and P. M. Harris, eds., Geologic and engineering approaches in evaluation of San Andres and Grayburg hydrocarbon reservoirs-Permian Basin: Bureau of Economic Geology, p. 87-112.

Ramondetta, P. J., 1982, Genesis and emplacement of oil in the San Andres Formation: The University of Texas at Austin, Bureau of Economic Geology Report of Investigations No. 116, 39 p.

Rhodes, E. G., 1992, Reservoir engineering methods, *in* D. Morton-Thompson and A. M. Woods, eds., Development geology reference manual, American Association of Petroleum Geologists Methods in exploration series, No. 10, p. 501-540.

Ross, C. A., 1986, Paleozoic evolution of the southern margin of Permian basin: Geological Society of America Bulletin, v. 97, p., 536-554.

Ruppel, S. C., and H. S. Cander, 1988a, Dolomitization of shallow-water platform carbonates by sea water and seawater-derived brines: San Andres Formation (Guadalupian), West Texas, *in* Sedimentology and geochemistry of dolostones: Society of Economic Paleontologists and Mineralogists, Special Publication No. 43, p. 245-262.

Ruppel, S. C., and H. S. Cander, 1988b, Effects of facies and diagenesis on reservoir heterogeneity: Emma San Andres Field, West Texas: Bureau of Economic Geology, Report of Investigations 178, 67 p.

Ruppel, S. C., 1990, Facies control of porosity and permeability: Emma San Andres reservoir, Andrews County, Texas, *in* D. G. Bebout and P. M. Harris, eds., Geological and engineering approaches in evaluation of San Andres/Grayburg hydrocarbon reservoirs-Permian basin: University of Texas at Austin, Bureau of Economic Geology, p. 145-173.

Ruppel, S. C., Charles Kerans, R. P. Major, and M. H. Holtz, 1995, Controls on reservoir heterogeneity in Permian shallow-water platform carbonate reservoirs, Permian Basin: implications for improved recovery: The University of Texas at Austin, Bureau of Economic Geology Geologic Circular 95-2, 30 p.

Ruppel, S. C., and F. J. Lucia, 1996, Diagenetic control of permeability development in a highly cyclic, shallow-water carbonate reservoir: South Cowden Grayburg filed, Ector County, Texas, *in* Martin, R. L., ed., Permian basin oil and gas fields: keys to success that unlock future reserves: west Texas Geological Society Publication p. 96-101.

Ruppel, S. C., ad D. G. Bebout, 1996, Effects of stratal architecture and diagenesis on reservoir development in the Grayburg Formation: South Cowden Field, Ector County, Texas: Fossil Energy, DOE, BC/14895010, Bartlesville Project Office, 80 p.

Ruppel, S. C., and F. J. Lucia, 1998, Cycle stratigraphy and diagenesis of the Grayburg Formation: South Cowden Field, Ector County, Texas *in* Stoudt, E. L., D. W. Dull and M. R. Raines eds., Permian basin core workshop – DOE funded reservoir characterization projects: Permian Section, SEPM Publication No. 98-40, pages not numbered.

Saller, A. H., and N. Henderson, 1998, Distribution of porosity and permeability in platform dolomites: Insight from the Permian of West Texas: AAPG Bulletin, v. 82, No. 8, p. 1528-1550

Sarg, J. F., and Lehmann, P. J., 1986, Lower-Middle Guadalupian facies and stratigraphy, San Andres-Grayburg Formations, Permian Basin, Guadalupe Mountains, New Mexico, *in* Moore, G. E., and Wilde, G. L., eds., Lower and Middle Guadalupian facies, stratigraphy and reservoir geometries, San Andres-Grayburg Formations, Guadalupe Mountains, New Mexico and Texas: Permian basin Section, Society of Economic Paleontologists and Mineralogists Special Publication No. 86-25, p. 1-36.

Schmoker, J. W., and R. B. Halley, 1982, Carbonate porosity versus depth: a predictable relation for south Florida: American Association of Petroleum Geologists Bulletin v. 66, p. 2561-2570.

Senger, R. K., F. J. Lucia, C. Kerans, G. E. Fogg, and M. A., Ferris, 1993, Dominant control on reservoir-flow behavior in carbonate reservoirs as determined from outcrop studies, in Linville, William, ed., Reservoir characterization III: Proceedings, Third

International Reservoir Characterization Technical Conference: Tulsa, Oklahoma, Penwell Books, p. 107-150.

Shumaker, R. C., 1992, Paleozoic structure of the Central Basin Uplift and adjacent Delaware Basin, West Texas, American Association of Petroleum Geologists Bulletin v. 75, No. 11, p. 1804-1824.

Silver, B. A., and R. G. Todd, 1969, Permian cyclic strata, northern Midland and Delaware Basins, west Texas and southeastern New Mexico: American Association of Petroleum Geologists Bulletin, v. 53, p. 2223-2251.

Sonnenfeld, M. D., 1991, High-frequency cyclicity within shelf-margin and slope strata of the upper San Andres sequence, Last Chance Canyon, *in* Meader-Roberts, Sally, Candelaria, M. P., and Moore, G. E., eds., Sequence stratigraphy, facies and reservoir geometries of the San Andres, Grayburg, and Queen Formations, Guadalupe Mountains, New Mexico and Texas: Permian basin Section, Society of Economic Paleontologists and Mineralogists Publication 91-32, p. 11-51.

Sonnenfeld, M. D., 1993, Anatomy of offlap: upper San Andres Formation (Permian Guadalupian), Last Chance Canyon Guadalupe Mountains, New Mexico, *in* Love, D. W., and others, eds., New Mexico Geological Society Guidebook, 44th Field Conference, Carlsbad Region, New Mexico and West Texas,, p. 195-204.

Sonnenfeld, M. D., and T. A. Cross, 1993, Volumetric partitioning and facies differentiation within the Permian Upper San Andres Formation of Last Chance Canyon, Guadalupe Mountains, New Mexico, *in* R. G. Loucks and J. F. Sarg, eds., Carbonate sequence stratigraphy: recent developments and applications: American Association of Petroleum Geologists, Memoir 57 p. 435-474.

Sun, S. Q., 1995, Dolomite reservoirs: porosity evolution and reservoir characteristics: American Association of Petroleum Geologists Bulletin, v. 79, p. 186-204.

Todd, R. G., 1976, Oolite-bar progradation, San Andres Formation, Midland Basin, Texas: American Association of Petroleum Geologists Bulletin, v. 60, p. 907-925.

Thomas, W. A., 1983, Continental margins, orogenic belts and intracratonic structures: Geology, v. 11, p. 270-272.

Trentham, R. C., W. C. Robinson, and R. E Weinbrandt, 1998, The use of core in an integrated 3D siesmic, Geological and engineering study of the Grayburg/San Andres of Foster and South Cowden Fields, Ector County, Texas *in* Stoudt, E. L., D. W. Dull and M. R. Raines eds., Permian basin core workshop – DOE funded reservoir characterization projects: Permian Section, SEPM Publication No. 98-40, pages not numbered.

Tyler, N., Bebout, D. G., Garrett, C. M. Jr., Guevara, E. H., Hocott, C. R., Holtz, M. H., Hovorka, S. D., Kerans, C., Lucia, F. J., Major, R. P., Ruppel, S. C., and Vander Stoep, G. W., 1991, Integrated characterization of Permian basin Reservoirs, University Lands, West Texas: Targeting the remaining resource for advanced oil recovery; Bureau of Economic Geology Report of Investigations, No. 203, p. 136.

Tyler, N., R. P. Major, D. G. Bebout, C. Kerans, F. J. Lucia, S. C. Ruppel, and M. H. Holtz, 1992, Styles of heterogeneity in dolomitized platform carbonate reservoirs: Examples from the Central Basin platform of the Permian Basin, southwestern USA: Journal of Petroleum Science and Engineering, v. 6, p. 301-339.

Tyler, R., H. S. Hamlin, S. J. Clift, M. H. Goltz, S. P. Dutton, and W. Yang, 1998, Reservoir characterization and the State of Texas advanced oil and gas resource recovery program, *in* W. D. DeMis and M. K. Nelis, eds., The search continues into the 21st Century, West Texas Geological Society Publication, No. 98-105, p 167-172.

Walker, D. A., J. Golonka, A. Reid, and S. Tomlinson, 1991, The effects of Late Paleozoic paleolatitude and paleogeography on carbonate sedimentation in the Midland Basin, Texas; *in* M. Candelaria, ed., Permian Basin plays – Tomorrow's technology today, West Texas Geological Society Symposium, Publication No. 91-89, p. 141-162.

Walper, J. L., 1977, Paleozoic tectonics of the southern margin of North America: Gulf Coast Association of Geological Societies Transactions, v. 27, p. 230-241.

Wang, F. P., and F. J. Lucia, 1993, Comparison of empirical models for calculating the vuggy porosity and cementation exponent of carbonates from log responses: University of Texas at Austin, Bureau of Economic Geology, Geological Circular 93-4, 27 p.

Wanless, H., 1979, abs. Pervasive pressure solution and association dolomitization, Paleozoic limestones: American Association of Petroleum Geologists Geological Conference on Deep Burial Diagenesis in Limestones, p. 23.

Ward, R. F., C. G. St. C. Kendal, and P. M. Harris, 1986, Upper Permian (Guadalupian) facies and their association with hydrocarbons-Permian, Basin, west Texas and New Mexico: American Association of Petroleum Geologists Bulletin, v. 70, p. 239-262.

White, T. C., 1984, Dolomitization, sulfate solution, and porosity development: the San Andres Formation, Howard-Glasscock field, Howard County, Texas, *in* G. E. Moore and G. Wilde, eds., West Texas Geological Society Publication SWS-84-78, p. 91-102.

Whitman, C. F., and R. E. Clemons, 1993, Lithofacies analysis of the Rio Bonito Member (Leonardian-Guadalupian) of the San Andres Formation in the Southern

Sacramento Mountains, Otero County, New Mexico: American Association of Petroleum Geologists Bulletin, Southwest Section Meeting, p. 195-200.

Wuellner, D. E., Lehtonen, L. R., and James, W. C., 1986 Sedimentary-tectonic development of the Marathon and Val Verde basins, West Texas, U.S.A.: A Permo-Carboniferous migrating foredeep, *in*, Allen, P., and Homewood, P., eds., Foreland Basins: International Association of Sedimentologists Special Publication 8, p. 15-39.

Yang, K. M. and S. L. Dorobek, 1993, Late Paleozoic synorogenic stratigraphy and tectonic evolution of the Permian Basin, west Texas and New Mexico, *in* J. Gibbs and D. Cromwell, eds., New Dimensions in the Permian Basin: west Texas Geological Society, Publication 93-93, p. 8-18.

Yang, K. M. and S. L. Dorobek, 1995, The Permian basin of west Texas and New Mexico: Tectonic history of a composite foreland basin and its effects on stratigraphic development, *in* S. L. Dorobek and G. M. ross, eds., Stratigraphic evolution of foreland basins, Society for Sedimentary Geology Special Publications 52, p. 149-174.

APPENDIX A - AVAILABLE WELL LOG DATA, WELL LOG NORMALIZATION, AND LOG SUMMATION MAPPING TECHNIQUES

Available Well Log Data

GR = Gamma Ray Log
SGR = Spectral Gamma Ray Log
GNT = Gamma Ray –Neutron Count Log
ACOUST = Acoustic/Sonic log
RES = Resistivity Log
LL = Laterolog
MLL = Micro Laterolog
DLL = Dual Laterolog
MSFL = Micro Spherically Focused Laterolog
CNLL/LDT = Compensated Neutron Litho Density Log
CNL = Compensated Neutron Log
ACE = Acoustic Cement Evaluation Log
CAL = Caliper
IPL = Injection Profile Log

Well Number	Available Logs
101	GR, ACOUST, LL, MLL, IPL
102	GR, ACOUST, LL, IPL
201	GNT, IPL
202	GNT
203	GR, ACOUST, LL
204	GR, ACOUST, IPL
301	GNT, IPL
305	GNT
306	GNT
307	GNT, IPL
308	GR, ACOUST,RES
309	GNT
311	GNT
312	GNT
313	GNT
314	GNT
315	GR, CNL
401A	GR, CNL, ACE

Well Number	Available Logs
402	GNT
405	GNT
406	GNT, IPL
406	GNT
503	GNT
504	GR, MLL
506	GNT
507	GNT
601	GR, CNL
603	GR, DLL, MSFL, CNLL/LDT, SPG, NPHI
604	GR, CNL
606	GR, CNL
607	GR, CNL, IPL
608	GNT, IPL
609	GNT
611	GNT
612	GNT
613	GNT
614	GNT
615	GNT, ACE
616	CDL/CNL, CAL, GR, DLL, MLL
701	GNT, IPL
704	GNT, IPL
705	GNT
706	GNT
707	GNT
708	GNT
801	GNT
802	GNT, IPL
803A	GNT
804	GNT, IPL
901	GR, LL, RES, IPL
902	GR, ACOUST, RES
1101	GNT, IPL
1102	GNT, IPL
1103	GNT
1201	GNT
1202	GNT
1203	GNT, IPL
1204	GR, CNL, DL, BHC
1205	GR, ACOUST
1206	GNT, IPL
1207	GNT

Well Number	Available Logs
1303	GR, DLL, MSFL, CNLL/LDT, NGT, SPG, NPHI
1304	GR, CDL/CNL, DLL, MLL, CAL, ACOUST
1305	GNT, IPL
1306	GNT, IPL
1308	GNT
1401	GNT, ACOUST
1402	GNT, IPL
1403	GNT, CAL, IPL
1404	GR, CNL/DL, DLL/RXO, NGT
1405	GR, CNL
1406	GNT
1407	GR, LDT/CNL, DLL, CAL, MSFL
1409	GR, CNL
1410	GNT, IPL
1411	GR, SP, RES, ACOUST.
1412	GNT, IPL
1413	GNT
1414	GNT
1415	GNT
1416	GNT, IPL
1417	GNT
1418	GNT, IPL
1420	GNT, IPL
1421	GNT
1422	GNT
1423	GNT
1424	GNT
1501A	GNT
1504	GR, LL RES, ACOUST, IPL
1505	GR, LL RES, ACOUST.
1506	GNT
1507	GR, LL RES, ACOUST.
1508	GR, LL RES, ACOUST.
1509	GR, LL RES, ACOUST.
1510	GNT
1512	GNT, IPL
1513	GNT, ACE
1514	GNT
1601	GNT
1602	GR, LL RES, ACOUST.
1603	GNT, IPL
1604	GNT
1605	GNT

Well Number	Available Logs
1701	GNT
1703	GNT
1704	GNT

Well Log Normalization

Log normalization was completed by Energy Data Services in June, 1996 prior to the initiation of this study. All porosity data available for the West Jordan unit was normalized prior to being used for porosity calculations. One hundred and fourteen wells contained porosity data, of these, only four modern log suites were available. Neutron logs were calibrated directly to core data to provide a reasonable estimate of dolomite and gypsum corrected porosity. Dolomite porosity was calibrated against core porosity that had been processed at high heat (vacuum retort) to drive off bound water as a result of gypsum. Gypsum porosity was calibrated against core porosity from samples processed at temperatures low enough to preserve the gypsum. Only two cores within the reservoir underwent low temperature core analysis.

Eighty percent of the gamma ray – neutron count logs (GNT) were corrected for casing and drift problems and then normalized prior to giving reasonable porosity values. There are eighteen sonic (acoustic) logs and four litho-density logs available for the unit. These logs were inspected to ensure dolomite and anhydrite beds had comparable values from well to well. None of these curves were found to require normalization.

Neutron Curve Normalization

Normalization of the neutron curve required the identification of a consistently low porosity rock type and a consistently high porosity rock type in each well. The low

porosity rock presented few problems, since there are an abundance of impure anhydrite or anhydrite dolomite lenses within the unitized interval. These lenses were set to zero porosity for the compensated neutron curves and a different value was used for the GNT neutron curves. The interbedded shales and carbonates within zone III (fig. 10) were selected as the high porosity rock.

The average neutron response from both shales and carbonates for the GNT curves was set at eight porosity units based on a comparison with core porosities in dolomites and twelve porosity units for the compensated neutron curve based on a comparison with the other normalized compensated neutron curves. An average maximum porosity for the San Andres was rejected because no consistently correlative high porosity rock type was found within the unit. Porosity development was found from density and sonic curves to vary greatly from well to well and shale intervals with similar gamma ray signatures were found to be much more dependable for porosity calibration than dolostones.

Casing Effects for GNT tools

Run changes, casing shoes, and water levels produced an abrupt change in neutron response in many logs. This change does not affect zero counts/second on gamma ray-neutron count logs, but it does affect the tool "sensitivity". When the counts/second are presented as the logarithm of the counts/second, these changes are seen as a shift in the curve. If the distance, in log of neutron units, between the shale line and the tight carbonate line is very different from the regional pattern it indicates the zero was improperly recorded for that well. If the same low porosity beds are present both above and below the change, the data can be corrected by simply shifting the lower portion of

the curve to fit the tight carbonate line seen in the upper part of the curve. The antilog of that curve can then be used as the corrected counts/second curve. There are three problems associated with the use of this method in the West Jordan unit: 1) the lower interval may not have any comparable low porosity development, therefore, shifting to the pattern of the overlying interval is problematic, 2) the casing shoe or other change may not be where it is supposed to be and their may be a real change that is not indicated on the log header or readily evident by inspection, 3) the logging engineer may have done something undetectable with the zero across the change. These corrections were applied as consistently as possible according to the rules above and arbitrary changes to the log curves were avoided when on of the three problems above were not clearly demonstrated.

Drift Problems within GNT Logs

Drift was found to occur up and down the wellbore within many of the GNT logs. In order to correct for problems of drift within the GNT logs a baseline was defined for each log and low porosity streaks (anhydrite) that appeared every thirty feet or so were set at the same counts/second value. After baselines were determined for core data, it was determined that a better fit with core porosities was achieved by setting the minimum rock porosities at three percent. After baseline corrections were made it was found that core to log porosity fit was as good or better for the GNT neutron curves as for the compensated neutron curves. The following observations were made while completing corrections for drift: 1) for most GNT curves, baselining the GNT curve on hard streaks with a baseline node about every thirty feet resulted in much better porosity interpretations than assuming no drift in the curve is present, and 2) some errors in porosity interpretation after baselining are inherent when there is no core porosity to use

as a guide. Most of these errors are caused by lower porosity streaks that have a real porosity somewhat greater than three percent. This results in a reduction of the apparent neutron porosities in some intervals. Errors resulting in porosity interpretations that are too high are much less frequent.

Measuring the Effect of Gypsum

Only two wells within the unit had both high temperature and low temperature core analysis to measure the effect of gypsum on porosity. Of these, the WJU #1511 well has 323 feet of core plug data compared to only 79 feet of core plug data for the WJU #1702 well. Regression analysis showed that in the WJU #1511 well, on the average the low temperature porosity could be obtained by multiplying the high temperature porosity by 0.82. It was determined that gypsum occludes 18 percent of the dolomite porosity. Errors with this method occur as a result of variations in the amount of pore space filled with gypsum as you move from zone to zone. Petrographic analysis completed for the present study found gypsum to be present in greater amounts in some zones versus others. Gypsum was seen to be more prevalent within the upper parts of the reservoir than in the lower zones (IV-C through IV-E2), although gypsum cement was seen within all zones at some concentration. Log analysis techniques applied to porosity data assumed that on average 20 percent of the dolomite porosity was filled with gypsum. This technique is believed to have potentially resulted in too low of porosity values in some zones where less gypsum may be present.

It was determined from log analysis that sonic porosity logs using a dolomite matrix tended to lump gypsum in with the dolomite and neutron porosity logs tended to lump gypsum in with porosity. Little difference was seen between Pe logs between

gypsum and dolomite providing little leverage for performing a gypsum correction. The use of the normal cross plot porosity (limestone, dolomite and quartz) was found to be more misleading than helpful in the four wells that contained both density and neutron curves.

Log Summation Mapping Techniques

The mapping software package used within this study is PETRA™ a product of geoPLUS Corporation. PETRA is multidisciplinary software program that integrates geological, geophysical, petrophysical and engineering data. The following is a brief description of log summation mapping techniques applied within PETRA which were used to calculate porosity maps within the study. Log footage summation functions within PETRA were used to extract reservoir parameters from digital log curve data based on applied cutoff criteria. The following porosity maps were made within the completion of this study: net and gross isopachs, porosity feet (PHIH), and average porosity (PHIA). The following calculations were completed for each of the maps listed above.

Gross Isopach Map - The isopach map thickness is based on the zone's upper and lower depth. No cutoffs are used in this calculation.

Net Isopach Map – The summation of the total number of feet where the porosity curve passes its cutoff criteria. All cutoffs are checked for passing cutoff criteria.

Porosity Feet (PHIH) – The summation of each sample interval multiplied by each porosity curve value passing all cutoff criteria. A porosity cutoff of seven percent was used for making PHIH maps of the reservoir prior to the geostatistical model.

Average Porosity Feet (PHIA) – The arithmetic mean value of all porosity curves values passing all cutoff criteria. A porosity cutoff of 13 percent was applied to PHIA maps constructed of zones IV-E1 and IV-E2.

APPENDIX B - CORE DESCRIPTIONS AND XRD DATA ANALYSIS

Core Descriptions and XRD Analysis

The foundation of this study is based on information gained through detailed core description from nine cores distributed throughout the West Jordan unit. Core analysis reports were available for each core, and additionally, three other cores that had not been located at the initiation of this study. Over three hundred thin sections were made from cores for petrophysical analysis. This data was combined to determine cycle boundaries of chronostratigraphic significance within the reservoir. Individual zone characteristics are presented in Appendix C.

Core Data

A total of over 2800 feet of core data was examined for the completion of this project. This core was provided by Texaco Exploration and Production, Inc., and the Bureau of Economic Geology in Austin, Texas. All cores required reconstruction prior to core description. This was done by comparison to original sample numbers from core analysis reports and through painstaking fitting of core pieces using log data as quality control. All cores were photographed after reconstruction had been completed. Cores diameters ranged from 2.5 inches to 4 inches with the majority of the cores examined being the standard 3.5 inch diameter. Two of the cores (WJU #.s 1511 and 1702) examined were analyzed under low temperature conditions to prevent the dehydration of gypsum. These cores were used in the log normalization process to determine the effect of gypsum on porosity logs within the reservoir. The remainder of the cores were all subject to high temperature analysis or the vacuum retort process.

Core Description Chart

All cores were described on a laptop computer using a core description form that was tailored for San Andres rocks seen within the Texaco operated West Jordan and Penwell units. This form was modified after a core description form used for a reservoir characterization study completed on the East Penwell unit by Applied Geoscience, Incorporated. The first column on the core chart provides the depth of the cored interval in half foot intervals and the location and depth of thin section samples (fig. 104). Oil staining is documented in the second column. Oil staining within cores that have undergone high temperature cleaning processes can be difficult to determine. The third column provides the textural classification used to describe all cores. This follows the depositional texture classification defined by Dunhan (1962). Columns within the textural classification are arranged with mud-dominated fabrics located to the right and grain-dominated fabrics located to the left. The columns represent an overall increase in grain-dominated, higher energy environments to the left and mud-dominated lower energy environments to the right and approximate the gamma ray log response expected on log curves. Rock type fabrics that lie on the border between two fabric types are transitional between the two.

The fourth column shows lithofacies described from each five-foot interval. The microfacies key is provided in Figure 105. The column may show up to three lithofacies that are predominant within the cored interval. The fifth column of the core chart is the rock lithology (figs. 104 and 106). Dolomite is the primary lithology seen within all cores although thin intermittent lenses of clay and anhydrite were also recorded for most cores. Sedimentary and diagenetic structures are described in the sixth column (fig. 104).

Figure 104. The core chart used to describe cores for the West Jordan unit. All cores within the unit were described using this detailed core analysis chart. Cores were described every half-foot using a binocular microscope. After the visual core inspection thin sections were analyzed to further define specific fields within the chart. This chart is from the WJU #1416 core and provides information on rock texture, fabric, grain components, sedimentary and diagenetic features, pore and cement types, vertical facies successions and other important features for each core.

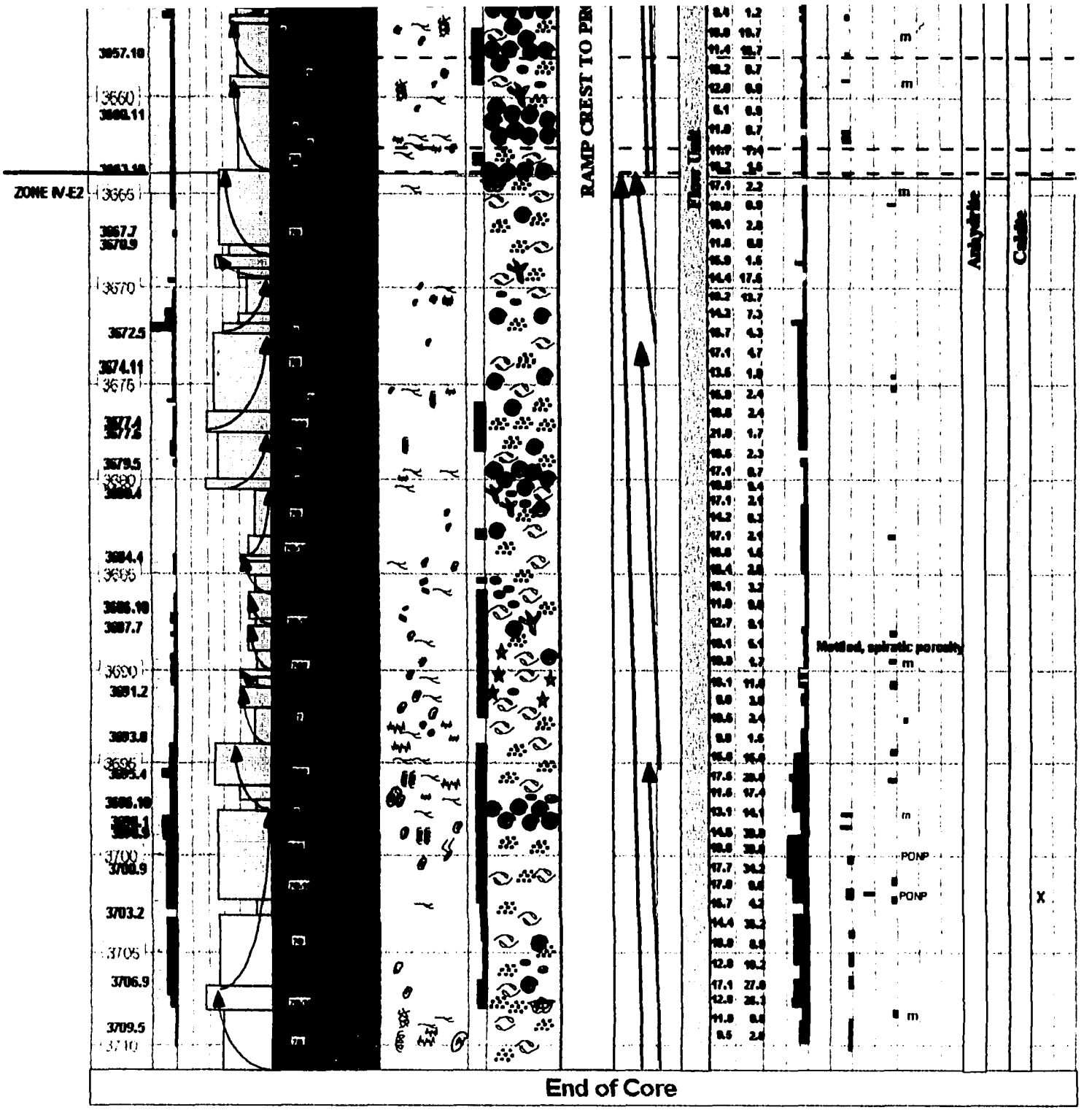
ZONE IV-E2
RAMP CREST TO PR
Flow Unit
Anhydritic
Calcite
Mottled, spiratic porosity
PONP
PONP
m
X
End of Core

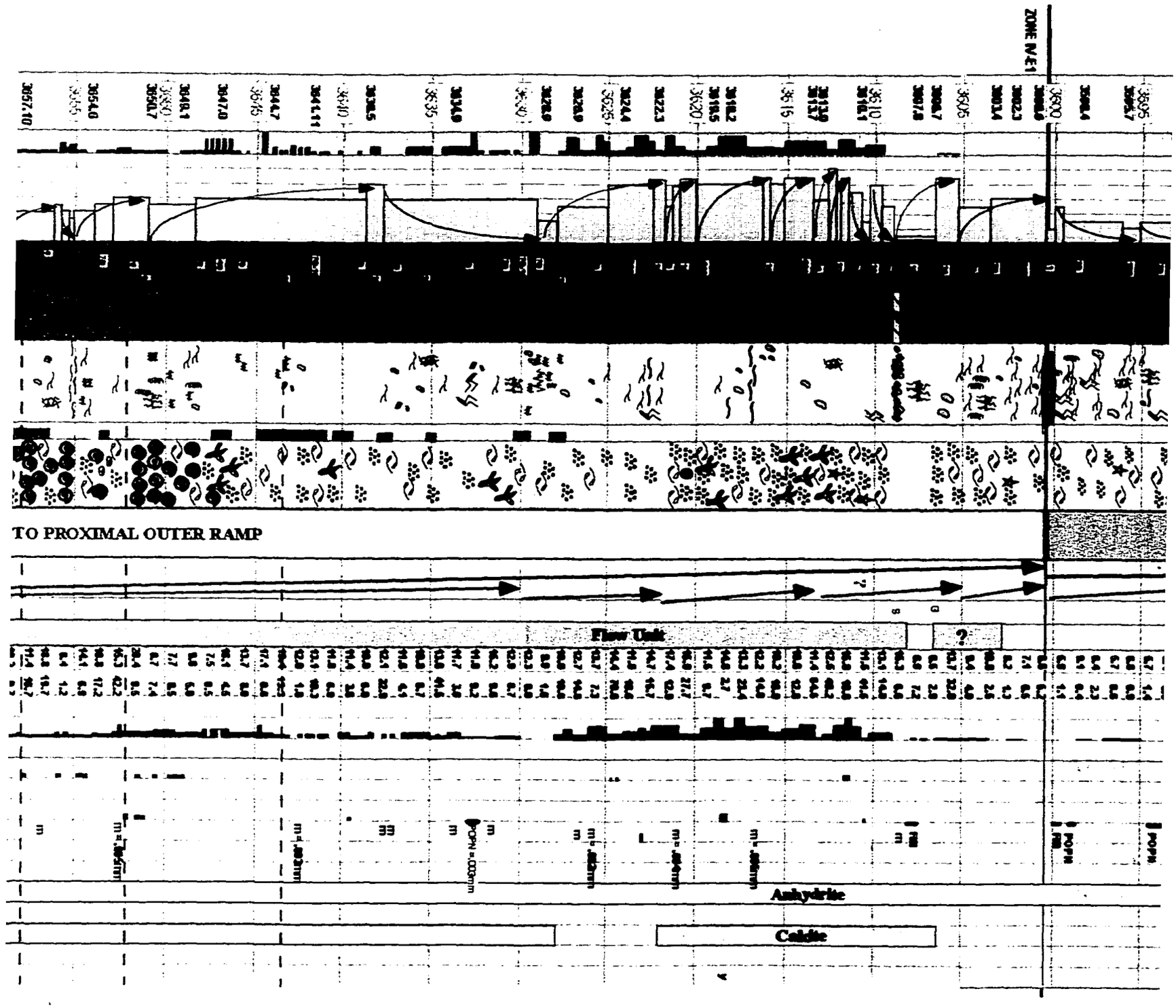
ZONE IV-E1
TO PROXIMAL OUTER RAMP
Flow Unit
?
Anhydrite
Calcite

Anhydrite
EMP CRISS FORMATION LAGOON
ZONE IV-C
PORN
MS
8
9
7.5
7.8

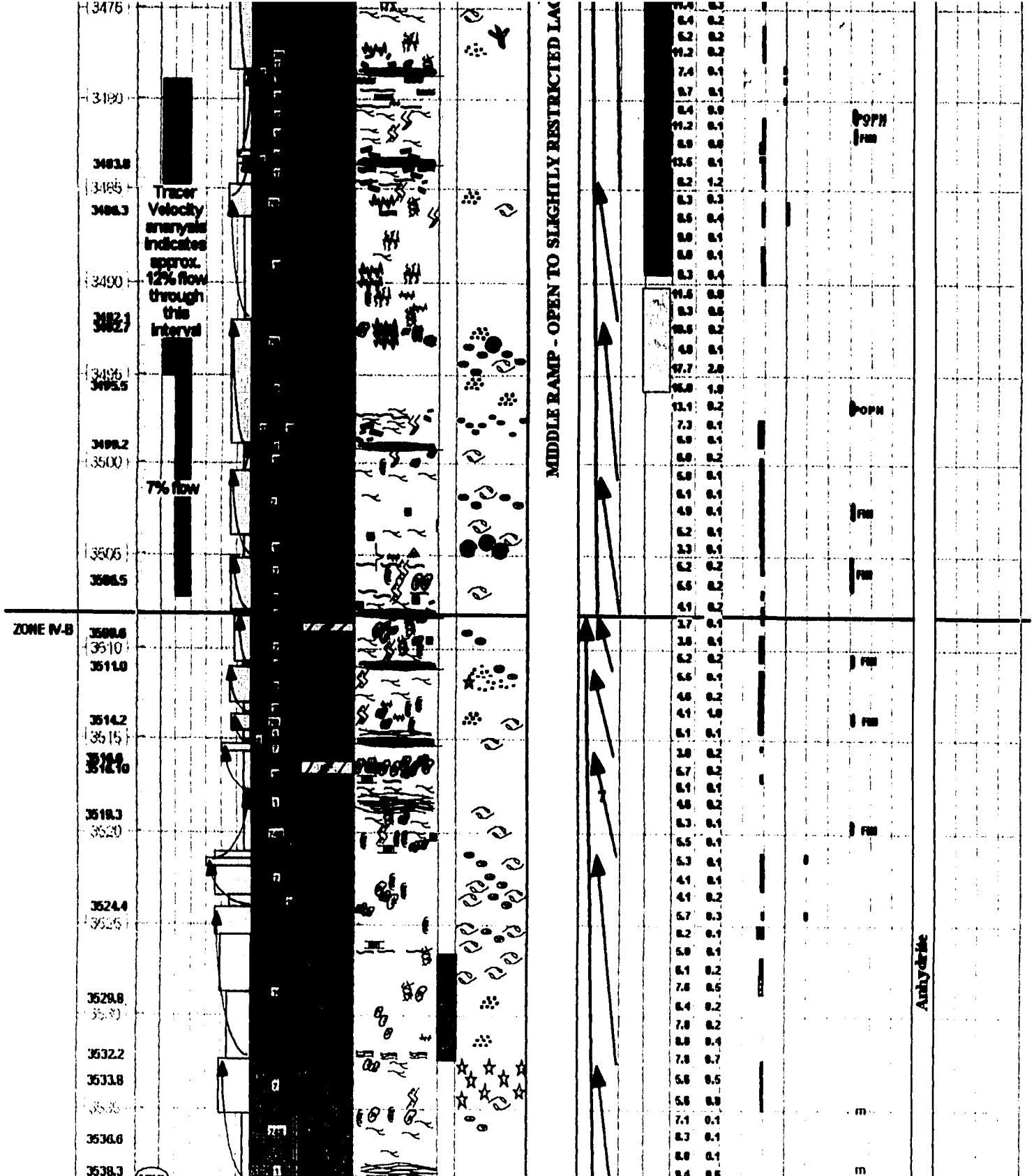
3475
3490
3483.8
3485
3488.3
3490
3492.1
3492.7
3495
3495.5
3498.2
3500
3505
3506.5
ZONE IV-B
3508.6
3510
3511.0
3514.2
3515
3518.3
3520
3524.4
3525
3529.8
3530
3532.2
3533.8
3535
3536.6
3538.3
Tracer Velocity analysis indicates approx. 12% flow through this interval
7% flow
MIDDLE RAMP - OPEN TO SLIGHTLY RESTRICTED LA
OPN
FRM
Anhydrite

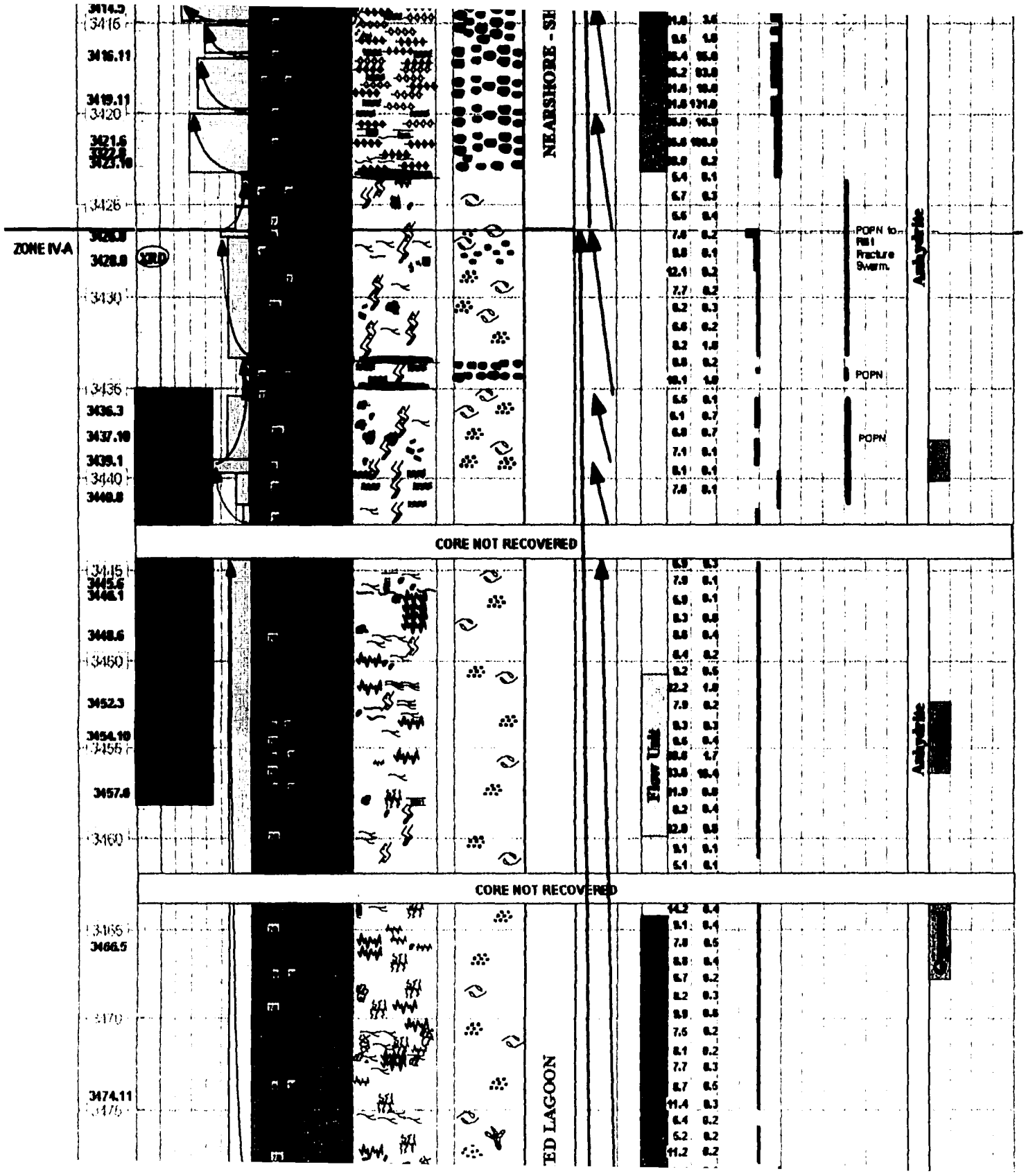
ZONE IV-A
3428.8
XRD
NEARSHORE - SH
POPN to Rill Fracture Swarm
POPN
POPN
Anhydrite
CORE NOT RECOVERED
Flow Unit
Anhydrite
CORE NOT RECOVERED
3466.5
3474.11
ED LAGOON

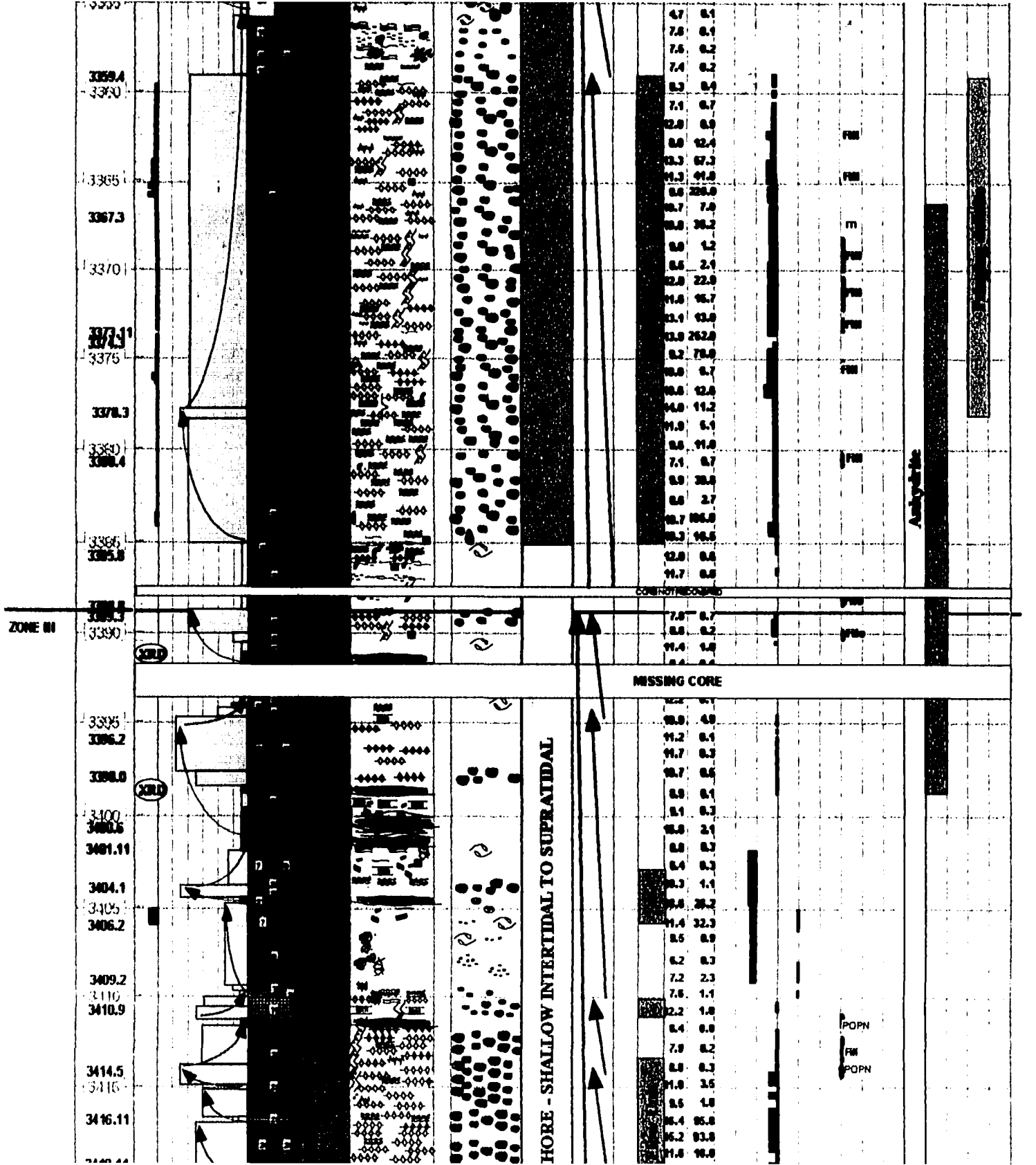
ZONE III
MISSING CORE
Anhydrite
SHORE - SHALLOW INTERTIDAL TO SUPRATIDAL
3359.4
3367.3
3378.3
3395
3396.2
3398.0
3401.11
3404.1
3406.2
3409.2
3410.9
3414.5
3416.11

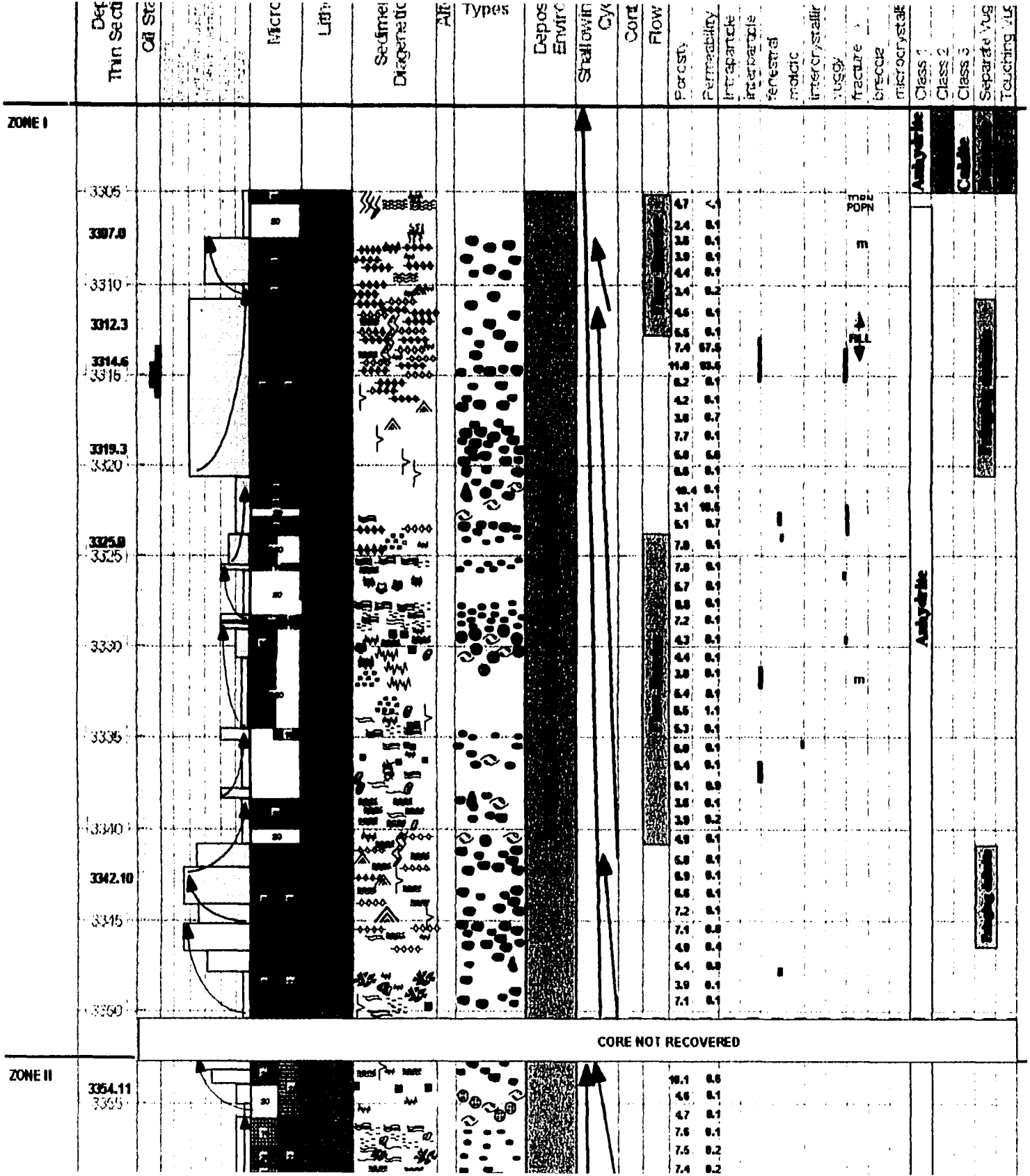
Depth
Thin Section
Oil Stain
Micro
Lith
Sedimentary
Diagenetic
Types
Depos Environ
Shallowing
Cycles
Flow
Porosity
Permeability
Intraparticle
Interparticle
Venular
moldic
intercrystalline
vuggy
fracture
breccia
microcrystalline
Class 1
Class 2
Class 3
Separate Vug
Touching Vug
ZONE I
3305
3307.0
3310
3312.3
3314.6
3316
3319.3
3320
3325.0
3325
3330
3335
3340
3342.10
3345
3350
Anhydrite
Anhydrite
Calcite
CORE NOT RECOVERED
ZONE II
3354.11
3355

West Jordan Unit
Core #1416
Ector County, TX

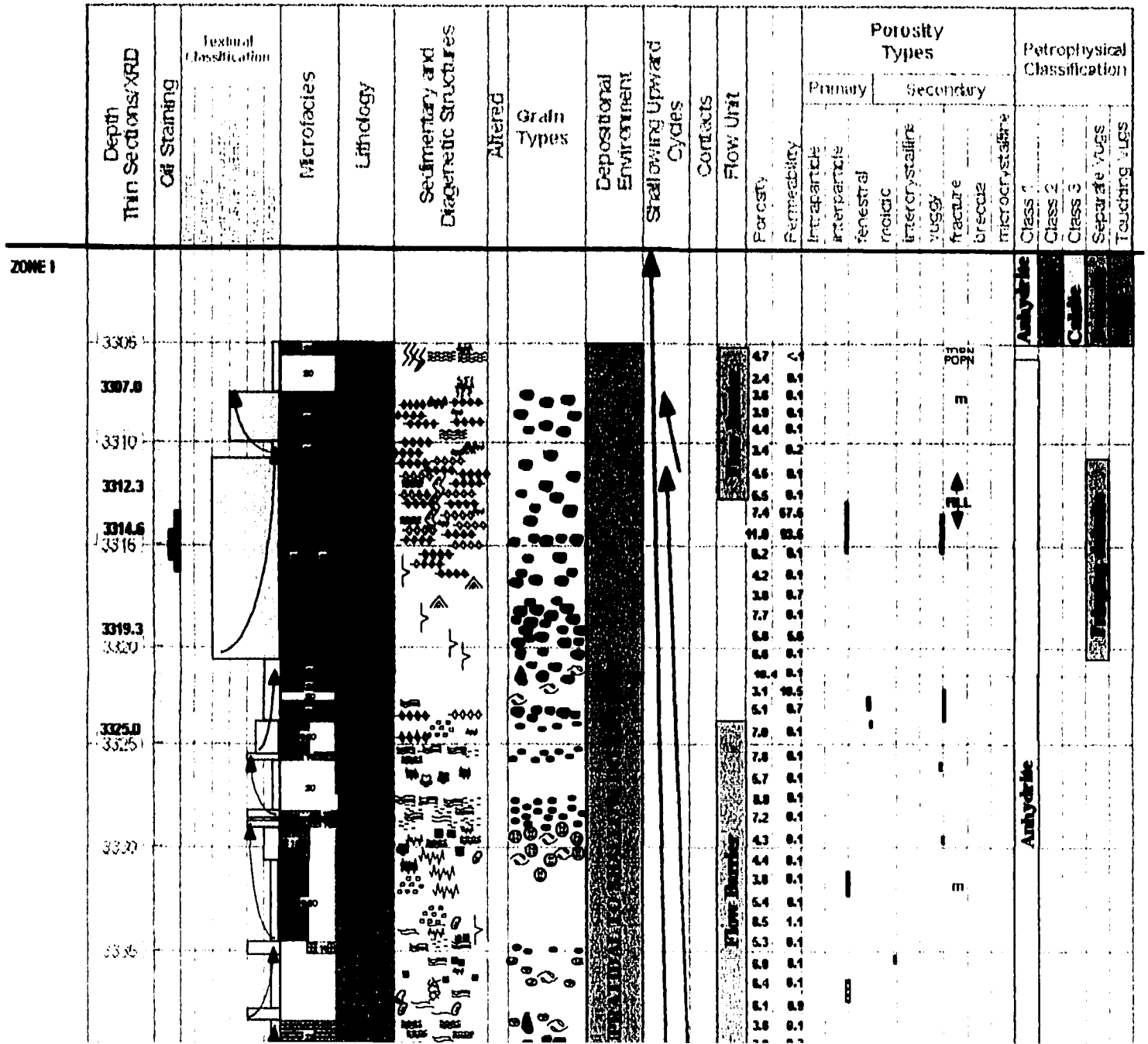
Depth
Thin Sections/XRD
Oil Staining
Textural Classification
Microfacies
Lithology
Sedimentary and Diagenetic Structures
Altered
Grain Types
Depositional Environment
Shallowing Upward Cycles
Contacts
Flow Unit
Porosity
Permeability
Porosity Types
Primary
Secondary
Intraparticle
interparticle
fenestral
moldic
intercrystalline
vuggy
fracture
breccia
microcrystalline
Petrophysical Classification
Class 1
Class 2
Class 3
Separate Vugs
Touching Vugs
ZONE I
3306
3307.0
3310
3312.3
3314.6
3316
3319.3
3320
3325.0
3325
3330
3335
Anhydrite
Anhydrite
Anhydrite

Figure 105. The key for microfacies observed within the West Jordan area. This lithofacies key was designed prior to examining the West Jordan cores in detail. Several cores were observed from the West Jordan, Penwell, East Penwell and Jordan University units to design a microfacies chart representative of the facies observed from cores within these units. After the completion of this chart and a basic familiarity with these facies was gained, the West Jordan unit cores were examined in detail.

LEGEND - MICROFACIES SYMBOLS

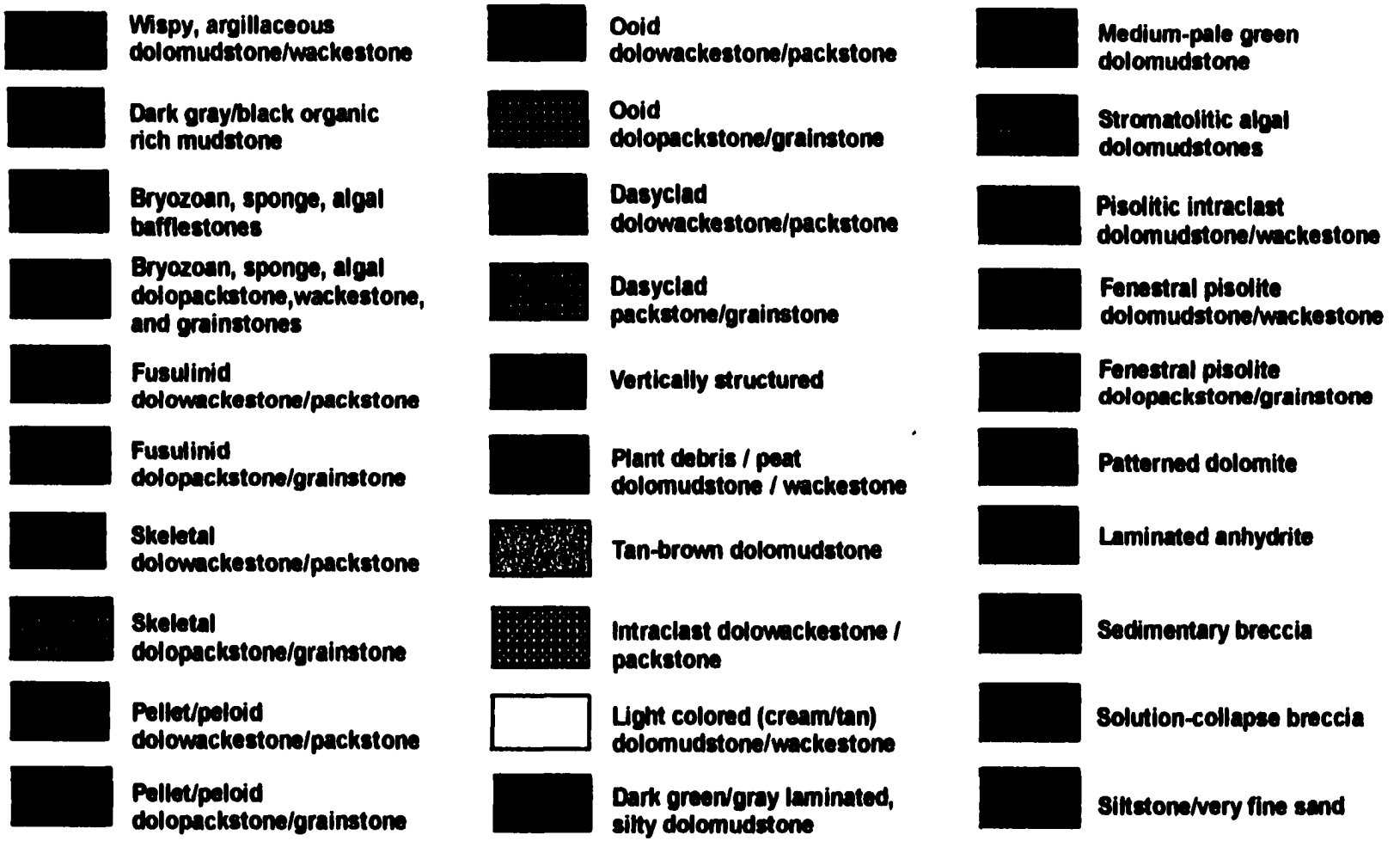

Figure 106. Legend of lithologic symbols used for core descriptions. The West Jordan cores were composed almost entirely of dolomite with intermittent clay and anhydrite intervals.

LEGEND - LITHOLOGIC SYMBOLS



This column documents the presence of anhydrite nodules, laminations, exposure surfaces, stylolites, fractures and so forth (fig. 107). These features provide information on environments of deposition and also influence flow within the reservoir. The development of clay laminations, anhydrite intervals, and stylolite swarms can act as flow barriers within the reservoir and fractures and large amplitude stylolites have been found to act as channels for injection fluids. In the sixth column, "altered" refers to the vertically structured fabric seen in many San Andres reservoirs. This fabric has been shown to be productive within several reservoirs along the eastern margin of the Central Basin Platform and therefore it was felt it should be specifically documented within cores.

Grain types are listed in the eighth column (figs. 104 and 107). Grain types are important indicators of depositional environments including water depth, salinity, and energy. Depositional environments for each core are presented on the core chart in column nine. These include supratidal, middle ramp (lagoon), ramp crest, and proximal outer ramp facies tracts. Each one of these broad depositional environments represents facies being deposited within a variety of microenvironments. Shallowing upward cycles are seen in the next column, as well as on the textural classification. Individual vertical facies successions (red arrows) occur next to textural fabrics in the textural classification. Grouped vertical facies successions (blue arrows) and cycle boundaries (red arrows) are seen in the column shallowing upward cycles. The next two columns indicate the nature of lithologic contacts being gradational, sharp, or moderate and probable flow units identified from visual core description.

Figure 107. Legend for grain types, sedimentary structures, and diagenetic features described within cores. Sedimentary and diagenetic structures are found in the sixth column of the core description chart and grain types are recorded in the eighth column.

LEGEND - GRAIN TYPES, SEDIMENTARY STRUCTURES, & DIAGENETIC FEATURES

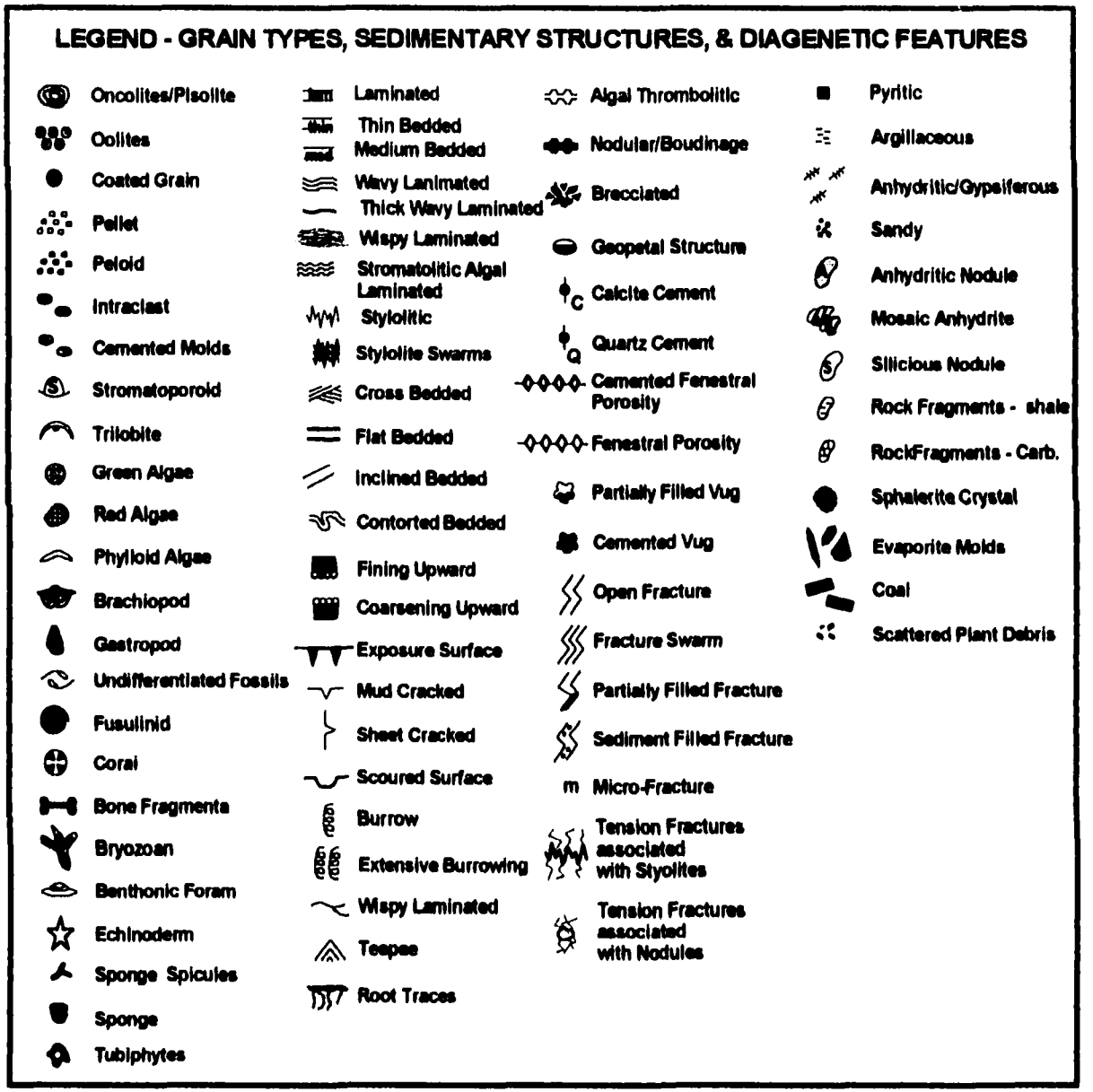

Core porosity and permeability data from core analysis sheets are provided in columns thirteen and fourteen and were used as a guide while visually describing core. Many porous intervals within the core are very difficult to recognize in hand samples and under a binocular microscope. This data was used to alert attention to zones where significant porosity and permeability had been measured from core analysis and was also very helpful in depth correcting core and log data. Porosity types are listed in the next column. Porosity types are divided into primary and secondary. Each porosity column shows porosity increasing to the left on a relative scale ranging from low (present on the right hand side of the column), medium (extending to the middle of the column), and high (extending to the left hand side of the column). Porosity types and the degree of porosity seen are based on hand samples described under a binocular microscope prior to examination of thin sections. The last column on the core description form is a recording of cement types seen within the reservoir. This column was completed after thin section analysis in order to identify cement types such as calcite and gypsum within the reservoir.

X-Ray Diffraction (XRD) Analysis

X-ray diffraction was applied to twelve samples from three cores (WJU #.s 1307, 1416, and 1419) within the unit to determine properties that would aid in the definition of cycle boundaries. Dolostones within the unit are interspersed with thin organic rich intervals that are abundant in siliciclastics. These siliciclastic rich clay intervals are found within the upper and lower parts of the reservoir. Originally it was believed that clays within the upper part of the reservoir might have had different origins than those from lower parts of the reservoir. The purpose of the XRD analysis was to potentially

define: 1) the origin of these intervals, primarily can they be identified as being similar in origin or from varying environments, 2) what water depths were they deposited in, 3) are they laterally extensive throughout the unit, and 4) what environmental significance do they represent. It was hoped that these intervals could be substantiated as marine flooding surfaces (MFS) representing correlative, well-defined chronostratigraphic markers across the unit. These intervals tend to have high gamma ray log readings that could be used to extrapolate from core to well logs.

Samples were analyzed from zone III within the inner ramp facies tract, from zone IV-B in middle ramp facies tract, and from zone IV-C within the ramp crest facies tract. Samples were collected in the upper and middle intervals of zone III from dark green-to-black colored clays. Core samples were taken from the middle of zone IV-B and from the upper and middle part of zone IV-C, both from dark gray to black colored clays. Results from XRD analysis are presented in Tables 5 and 6. Total clays for the samples ranged from 15 to 46 percent for inner ramp samples (blue), 9 to 39 percent for middle ramp (red) samples and 13 to 40 for ramp crest (green) samples (table 5). Clay percentages were almost entirely illite with minor amounts of Kaolinite (table 6). A high percentage of quartz was found in most samples. Inner ramp facies had the highest dolomite percentages in the WJU #1307 and #1419 cores. Pyrite within the samples ranged from 7 to 23 percent. The high percentage of illite in the clay fraction is likely responsible for high gamma ray log readings. No relationships were observed from the XRD analysis that would enable differentiation of depositional controls for samples from each zone.

TABLE 5 - Whole Rock Mineralogy (wt%)

Well Number	Depth (ft)	TCL (%)	QTZ (%)	KSP (%)	PLAG (%)	DOL (%)	PYR (%)	SID (%)	Anhy (%)	GYP (%)	FOM (%)
1307	3400	42	34	3	8	2	7	2	1	ND	1.17
1307	3437	15	10	1	ND	63	11	ND	ND	ND	1.29
1307	3570.5	30	9	2	2	40	14	2	1	1	1.44
1307	3590.6	20	13	2	1	50	11	1	1	1	1.46
1416	3391.1	37	35	3	8	2	11	2	1	ND	1.33
1416	3433.6	33	23	3	2	13	20	2	1	2	1.53
1416	3558.8	34	20	2	ND	18	7	3	15	2	1.09
1416	3578.4	40	21	2	2	11	18	2	2	2	1.45
1419	3422.6	ND	4	ND	ND	96	ND	ND	ND	ND	0.91
1419	3451	46	21	3	4	ND	23	2	1	1T	1.42
1419	3581.9	39	32	3	2	4	15	2	2	2	1.44
1419	3600.4	30	18	2	1	34	13	2	1	ND	1.33

TCL = Total Clay and Mica
QTZ = Quartz
KSP = Potasium Feldspar
PLAG = Plagioclase Feldspar
DOL = Dolomite
PYR = Pyrite
SID = Siderite
Anhy = Anhydrite
GYP = Gypsum
T = Trace
ND = Not Detected

Comment: FOM - Figure of Merit in XRD analysis. The FOM is based on a mass balance calculation. An FOM of 1.0 indicates a perfect mass balance. Values other than unity may indicate the presence of amorphous material or there is a preferred orientation

TABLE 6 - Clay Fraction (<2 um) Mineralogy (wt%)

Well Number	Depth (ft)	Illite (%)	Kaolinite (%)	Non-clays (%)
1307	3400	100	T	Q,D, F, Anhy
1307	3437	100	T	Q,D, F, Anhy
1307	3570.5	100	ND	Q,D, F, Anhy
1307	3590.6	96	4	Q,D, F, Anhy
1416	3391.1	100	ND	Q, F, Anhy
1416	3433.6	98	2	Q,D, F, Anhy
1416	3558.8	100	ND	Q,D, F, Anhy
1416	3578.4	100	T	Q,D, F, Anhy
1419	3422.6	100	T	Q,D, F, Anhy
1419	3451	100	T	Q, F, Anhy, Phil
1419	3581.9	97	3	Q, F, Anhy, Phil
1419	3600.4	94	6	Q,D, F, Anhy

Legend:

Q = Quartz
D = Dolomite
F = Feldspar
Anhy = Anhydrite
Phil = Phillipsite
T = Trace
ND = Not Detected

Comment: The quantity estimates and the associated error are not certain and could be as high as +/- 10%

**These estimates refer to the relative quantities of clay minerals only.

APPENDIX C - ZONE CHARACTERISTICS

Zone IV-E2 and IV-E1

Zones IV-E2 and IV-E1 are similar in character, both consisting of subtidal facies that are interpreted to have been deposited in open marine, shallow water environments. Predominant facies consist of peloidal and fusulinid dolowackestones to grain-dominated dolopackstones, skeletal dolowackestones to mud-rich packstones, and crinoidal dolowackestones. Less commonly occurring are thin, isolated bioherm facies with bryozoan, sponge, and algal grains. In addition, vertical structuring is seen in these zones. This texture has been described in detail throughout reservoirs (Clear Fork, San Andres and Grayburg) along the Central Basin platform and has been given several different names including "diagenetically altered", "altered", "mottled" and so forth. Vertically Structured facies exhibit a distinct vertically oriented mottling due to porosity variation believed to be the result of intense vertical burrowing within these facies. (Longacre, 1980, McElroy field; Bebout et al, 1987, Dune field; Ruppel and Cander, 1988a, Emma field; Major, et al, 1990, East Penwell Unit; Leary and Vogt, 1990, Seminole field; Ruppel and Lucia, 1998, South Cowden field; and Caldwell, et al, 1998, South Cowden field). Although this texture was not seen as a key productive facies at West Jordan unit, it has been related to significant production in nearby fields listed above.

Zone IV-E2 is approximately 76 meters (200 feet) thick and extends from the base of Zone IV-E1 to the correlative marker used to define the base of the West Jordan unit. The division between zones IV-E2 and IV-E1 is based on a minor marine flooding

surface indicating a small sea level rise that appears to be correlative throughout most of the unit. Structurally zone IV-E2 occurs from about –800 to –1,030 feet subsea within the unit boundaries (fig. 12). Although wells drilled into this zone can be very productive along structurally higher areas of the anticline, much of the zone encountered in wells along the western half of the unit is below the oil/water contact, which occurs at –875 feet subsea. Because only a few wells penetrate the entire thickness of this zone, no isopach map was constructed.

Structure contour maps show zone IV-E1 to extend from –740 to –970 feet subsea (fig. 12). Isopach maps show zone IV-E1 to range from 54 to 72 feet with a mean thickness of about 64 feet (fig. 13). The isopach map shows a general thinning along the western margin of the unit. This westward thinning reflects shallowing paleo water depths to the west, the landward position on the shelf platform during deposition of facies within this zone. Local paleotopography resulted in the deposition of laterally discontinuous shoal bodies as documented from core. Thick intervals seen within the isopach are areas where shoals are developed. The well-defined thin channel like area trending generally west-to-east across the unit is an intershoal area. Zone IV-E1 is capped by peloidal grain-dominated packestone to dolograinstone facies or its interpreted equivalent, marking the top of a shallowing upward cycle.

The primary porosity is intercrystalline with dolomite crystal size typically ranging from 70 to 200 microns (μm). Within these two zones, intercrystalline, interparticle and moldic porosity have been appreciably enlarged by dissolution of the dolomite crystals and removal of sulfate cement that may have been present within the

reservoir during earlier time periods. Porosity and permeability values measured from core data for these two zones range from less than 2 to 21 percent and from less than 0.1 to over 70 millidarcies, respectively. Average porosity and permeability values for these zones are 10.25 percent and approximately 4 millidarcies. Interpretation of core, PHIH (porosity feet) and PHIA (average porosity) maps of the lower zones suggest that a series of shoal and intershoal areas formed within the West Jordan unit during deposition of zones IV-E2 up through the middle of zone IV-C

Zone IV-C

Zone IV-C is composed of ramp crest, flanking ramp crest and middle ramp facies. Middle ramp facies consist of alternating clay lenses, light brown dolomudstones, and peloidal, fusulinid, crinoidal, and skeletal dolowackestones to mud-rich dolopackstones. Ramp crest facies include peloidal and skeletal grain-dominated dolopackstones and dolograinstones. Flanking facies are primarily mixed siliciclastics and peloidal and skeletal mud-rich dolopackstones. Where ramp crest and associated grain-dominated facies were observed from core, they were almost always occluded by sulfate cement (primarily anhydrite) within this zone. Clay lenses increase in number and thickness towards the top of zone IV-C. Peloidal dolograinstones from shoal facies are present within the central part of the interval, however they are not laterally correlative.

Zone IV-C ranges from a structural high of –700 to approximately –920 feet subsea at the western margins of the unit (fig. 12). The general overall geometry of the anticlinal structure is continues up section within the San Andres Formation. Zone IV-C is relatively thin compared to other zones within the unit having a mean thickness of 36

feet. An isopach map of zone IV-C indicates a general thinning to the west as seen in zone IV-E1 (fig. 13). Isopach maps from zones IV-E1 and IV-C show similar patterns of thick and thin areas. Core data from most wells identified a number of shoal facies within zone IV-C, however extreme dolomitization within the lower zones has obliterated original grain fabric. Within most thin sections only faint "ghosts" of original grains are visible.

The clays at the top of zone IV-C are extremely rich in organic matter including large particles of plant debris. Clay intervals within this zone are prevalent within the West Jordan unit but do not appear to extend far to the east or north. Because of their restricted occurrence within the unit and the large quantities of plant debris found within the upper parts of this interval, it is believed that these clay intervals were deposited in a restricted lagoon that formed during the latest deposition of zone IV-C. Therefore, the top of zone IV-C is placed at the top of the uppermost clay interval within the zone, it having been interpreted as the shallowest water deposit that can be correlated across the unit prior to sea level rise initiating deposition of zone IV-B. Because of the frequent occurrence of these clay intervals and the cemented nature of grain-dominated facies within this zone it is considered as a probable barrier to reservoir flow.

Crystal size within this zone was found to range from 20 μm to 70 μm for the dolowackestone to mud-rich packestone facies with clays and dolomudstones typically less than 20 μm. Porosity for this zone ranges from 0.5 to 14.5 percent and averages a little over 6 percent. Permeability ranges from less than .1 to 8 millidarcies with an average of 0.36 millidarcies.

Zone IV-B

Zone IV-B is composed of dolowackestones and mud-rich dolopackstone facies. Overall mud content is greater for zones IV-B and IV-A than in underlying zones IV-C through IV-E2. Common grains include peloids, skeletal material (primarily mollusk), and crinoidal fragments. Fusulinid dolowackestones occur rarely in zone IV-B and are believed to be the result of deposition during storm activity or strong tides. Clay intervals occur less often than in zone IV-C and are believed to have been deposited during minor periods of sea level rise based on vertical facies successions stacking patterns. This zone exhibits vertically structured facies similar to those seen in zones IV-E2 and IV-E1. Vertically structured fabric occurring within highstand systems tracts has been attributed to the reaction of burrowing organisms to changing water depths (Ruppel, 1998).

The top of zone IV-B ranges from approximately –630 to –880 feet subsea within the boundaries of the unit (fig. 12). The mean thickness of this zone is 47.5 feet. Isopach maps indicate a thickening of sediments over the structurally highest area of the unit (fig. 13) Zone IV-B is thicker toward the north and is thinner toward the southwest. A distinct change occurred from the deposition of zone IV-C to that of IV-B. Facies observed in cores suggest that zone IV-B was deposited within a quite, calm, fresh marine to slightly restricted lagoonal environment. The contact between zones IV-B and IV-A is placed at the base of a thin, laterally extensive, correlative clay which is believed to represent a minor marine flooding surface marking the beginning of the cycle boundary.

Porosity and permeability values for zone IV-B reach a maximum of 14 percent and 14 millidarcies respectively. Average values for the zone are 6 percent porosity and 0.20 millidarcies permeability. Cores taken throughout the reservoir show that moldic

porosity is the dominant pore type within zone IV-B. Associated with the increase in moldic porosity and decrease in dolomite crystal size is a decrease in overall porosity values. Isolated porosity and permeability streaks are seen within the cores, however, they are typically very thin and it is doubtful that they extend any great distance from the wellbore. Log data suggests that this zone may have limited potential in localized areas, nevertheless, low permeability values associated with moldic pore types limit the potential of this zone. Advanced recovery techniques such as horizontal drilling may offer improvement in producing mobile oil within these zones (IV-B and IV-A) but at this time it is not considered economically justifiable.

Zone IV-A

Zone IV-A consists of facies similar to those seen in zone IV-B, except for a greater occurrence of dolomudstones. Grains seen within this zone are peloids, skeletal (mollusk), sparse fusulinids, and crinoid material. Toward the top of zone IV-A thin algal dolowackestones and pisolite dolopackstones are present in some cores indicating a continuation of the prograding, shallowing upward cyclic nature of the San Andres reservoir within the unit. Dolomite crystal size for this zone is typically less than 20 μm. Although isolated streaks of porosity and permeably are present within this zone, overall it is very tight. The primary porosity types are moldic and fracture with fine intercrystalline porosity present within some of the dolowackestones and mud-rich dolopackstones.

Zone IV-A, ranging from about 65 feet to over 100 feet thick, is one of the thicker zones mapped within the unit. The mean thickness of this zone is 83.5 feet. The

structural elevation of zone IV-A ranges from –560 feet subsea at the crest of the structure to below –800 feet subsea along the deeper western limits of the unit (fig. 12). Similar to zone IV-B, an isopach map of zone IV-A shows the zone is thicker in the north and thinner in the southwestern part of the unit (fig. 13).

Sedimentary and diagenetic controls must have isolated this zone from those above and below it. Fracturing is very common in this zone as are large stylolite seams along which core separates when brought to the surface. Anhydrite nodules commonly exhibit radiating, irregular "diagenetic" fractures that are short in length. These diagenetic fractures suggest late stage formation of anhydrite nodules after solidification of the surrounding strata. Large stylolite seams up to 3 inches (7.5 cm) and stylolites with excessive tension fractures developing from stylolite teeth all indicate considerable pressure solution occurred within this zone. The intense diagenetic fracturing occurring around anhydrite nodules and tension gashes from stylolites may also indicate that this zone was at one time considerably overpressured or particularly sensitive to overburden stress. A high original concentration of clay and organic material may also be the cause of excessive stylolite formation in this zone. In addition to diagenetic fractures, late stage tectonic and/or regional fracture networks are indicated from core. These are most likely associated with the stress fields formed during the development of the anticlinal feature and possibly later Laramide and Basin and Range tectonism.

Zone IV-A is relatively tight throughout much of the reservoir although fracture porosity may have contributed considerable oil during primary production these fractures probably do not contribute to production after years of secondary waterflood recovery. It is felt that injection water is channeled through these fracture and stylolite networks

resulting in zone IV-A being a waterflood thief zone. The contact between zone IV-A and zone III occurs at the base of a clay zone which often overlies a thin pisolite-algal dolograinstone.

Zone III

Zone III is composed of mixed subtidal, intertidal and supratidal facies. Subtidal facies are typically dolomudstone to dolowackestones with sporadic moldic porosity. Primary grains are skeletal fragments (mollusk), peloids, intraclasts and algal grains. Algal laminated dolomudstones are common intertidal facies within this zone. Pisolite dolograinstones and grain-dominated dolopackstones are also common within zone III and some of these intervals were seen in cores are up to ten feet thick.

Zone III occurs at a structural elevation ranging from –520 to –750 feet subsea for the crest of the anticlinal structure and western margins of the unit, respectively (fig. 12). The isopach map of zone III shows a distinct change in deposition illustrated by a thickening of the supratidal facies in the landward direction of the unit, to the west and southwest (fig. 13). As the San Andres continued to prograde basinward, thicker sequences of supratidal pisolite and algal facies were deposited over shallow marine and restricted lagoon facies. In some cored wells the supratidal, pisolite facies has very well developed porosity and permeability reaching up to 16.5 percent and 131 millidarcies respectively. Light brown dolomudstones and clay rich intervals up to several feet thick are also common within this zone.

The top of zone III is usually correlated on the top of a thick (up to five feet) clay to clay-rich dolomudstone, which is correlative across the unit. Immediately underlying

this clay interval is a pisolite dolograinstone that varies in thickness from core to core. The majority of zone III is composed of non-permeable dolomudstones that act as a barrier to reservoir flow, particularly in the vertical direction. Although thin, isolated permeable intervals within pisolite dolograinstones are present they are not believed to be laterally extensive.

Zone II

Over much of the unit, zone II is comprised of a thick (20-25 feet) pisolite dolopackstone-grainstone bed that has excellent porosity and permeability that reach 23 percent and 250 millidarcies respectively, the highest values recorded within the San Andres reservoir at the West Jordan unit. Porosity within this pisolite facies is the result of the development of fenestral pores within a slightly submerged to exposed tidal flat environment. Other facies that occur to a significantly less degree within zone II are cream and green colored dolomudstones, algal laminated dolomudstones, intraclasts, and dark gray to green clay intervals.

Zone II occurs at a structural elevation ranging from –480 to –720 feet subsea within the unit boundaries (fig. 12). The zone ranges from 29 to 42 feet in thickness and as indicated from the isopach map is one of the more consistent zones correlated within the unit (fig. 13). The mean thickness for zone II is 36 feet. The unit thickens subtly to the southwest across the unit. As previously seen in zone III this is in response to thicker supratidal deposition in the landward direction.

Rocks with high values of fenestral porosity often are not considered good reservoir rock because they lack permeability. However, this does not appear to be the

case at West Jordan unit. This facies exhibits high permeability values observed in core descriptions and measured in core analysis across much of the unit. This suggests that good permeability should be present in the interwell areas where this facies is present. Zone II is therefore considered a flow unit within the West Jordan unit and a possible candidate for horizontal drilling. The top of zone II is placed at the top of a greenish-gray clay interval that occurs below the base of zone I.

Zone I

The highly porous and permeable pisolite facies that occurs in zone II is also present in zone I. However the pisolite facies present in zone I is almost without exception completely occluded by sulfate cement. Other facies seen within zone I include light cream colored dolomudstones, green, algal laminated to clay-rich dolomudstones and thin intervals of intraclasts. Rare peloidal and skeletal dolomudstone to dolowackestone facies are also found some of which exhibit moldic porosity. The most common grain constituents within this zone are pisolites. Gastropod, mollusk and mizzia grains are the most common skeletal grains found within this zone. The thin intraclast dolograinstone lenses observed in almost every core suggest periods of extremely shallow water or subaerial conditions during which these grains were eroded and redeposited nearby.

Although a few thin porous intervals occur in pisolite dolograinstones near the bottom of zone I, for the most part it is completely impermeable except for the development of fractures. Most fracture planes within the zone are also occluded by sulfate cement although some fractures remain partially open. The high degree of sulfate

cementation that has occurred within this zone and the predominance of nonporous dolomudstones make this zone a barrier to flow and the primary seal for the West Jordan unit reservoir.

The highest elevation of the San Andres reservoir within the West Jordan unit occurs at a subsea elevation of –432 feet (fig. 12). Localized exposure or non-deposition marks the end of the San Andres deposition. Thinning in zone I is indicated from cross section and isopach mapping within the north, central and southern parts of the unit (fig. 13). This upper zone within the unit ranges in thickness from 34 to 65 feet with a mean thickness of 47 feet. Core data contain exposure features such as mud cracks, soil zones, teepee structures and localized thin brecciated zones that indicate the possibility for exposure during late San Andres deposition.

The San Andres and Grayburg boundary is significant, marking a major drop in relative sea level. Where the lowermost Grayburg Formation is present in cored wells, its contact with the upper San Andres is sharp with siliciclastics of the Grayburg lying directly on top of supratidal pisolite and dolomudstone facies. These siliciclastics thin to the east into the basin and can be readily correlated across the area using gamma ray logs. Either localized paleotopographic highs existed over which there was non-deposition of upper San Andres sediments or localized exposure and truncation of exposed upper San Andres strata occurred during latest San Andres or earliest Grayburg time. In either case, paleo structure must have been present in some manner to influence depositional environments and their related facies.